Diffuse interstellar bands and the structure of the ISM

Martin Cordiner

Thesis submitted to the University of Nottingham
for the degree of Doctor of Philosophy

August 2005

"It's not about a salary, it's all about reality"

— Lawrence Parker aka KRS-One

Supervisor: Prof. Peter Sarre

Abstract

Results are presented of three different studies into the nature of the diffuse interstellar bands, their carriers and the environments in which they are located.

1. Optical observations of small-scale structure in the distribution of large molecules and/or dust grains in the ISM are examined in the first dedicated study of its type. Evidence is presented for variation in the strengths of fifteen out of sixteen measured narrow diffuse interstellar bands, over spatial scales from $\lesssim$ 370 AU to $\lesssim$ 20,000 AU, observed towards the component members of nearby (< 1.5 kpc distant) early-type binary and multiple star systems. Variations in diffuse interstellar band (DIB) equivalent widths of about five to ten percent are found between the sightlines towards ρ Oph A and B (separated by approximately 370 AU in the plane of the sky). The λ5780, λ5797, λ5850, λ6376, λ6379, λ6439, λ6614 and λ6660 DIBs are found to be significantly stronger towards ρ Oph B by an amount comparable to the differences in the column densities of interstellar K I and Ca II in these sightlines. The upper limit on the variability of the λ6284 DIB is approximately 1.5%. Different DIBs are subject to different degrees of variation, and in some cases different signs of variation, for example the λ5850 DIB is stronger towards ρ Oph C than ρ Oph A, whereas λ6614 is stronger towards A than C, proving the existence of chemical differences between the DIB carriers. The λ6614 DIB is found to show a variation in its pattern of sub-structure between ρ Oph A and C, which, interpreted within the 'Webster hypothesis' (Webster 1996), is consistent with a $\sim$ 4% enhancement in the interstellar $[^{12}C]/[^{13}C]$ ratio towards ρ Oph A relative to C. In other star systems observed: The λ5780, λ6196 and λ6614 diffuse interstellar bands are found to be stronger towards β^2 Sco than β^1 Sco (sightlines separated by $\sim$ 2200 AU). The λ6614 DIB is found to be stronger towards HD 150136 than HD 150135 ($\sim$ 12,500 AU separation) but no significant variation is found in the strengths of any other DIBs in the spectra of this binary system. The λ5780, λ6196 and λ6614 DIBs are detected in the lightly-reddened sightlines towards the two members of the μ Cru system, and are found to be approximately 50 to 200% stronger towards μ^2 Cru than μ^1 Cru. Weak interstellar K I absorption is detected and is found to be 122 ± 80% stronger (at 1σ confidence) towards μ^2 Cru than μ^1 Cru.

   The λ5780, λ6196, λ6203 and λ6614 diffuse interstellar bands are detected in the well-known 'time-variable' sightline towards κ Vel. Spectra are presented that

show the interstellar K I column density in this sightline to be N(K I) = 3.43 ± 0.13 × 10^{10} cm^{-2} in June 2004, corresponding to approximately a 35% increase in N(K I) since the time of the last measurement in March 2002 by Crawford (2002). During this period, the sightline moved $\lesssim$ 5 AU. DIB strengths towards κ Vel are compared between observations made in January 1995 and June 2004, during which time the sightline moved $\lesssim$ 25 AU across the interstellar medium (ISM) and the neutral potassium column density approximately doubled. No significant variation in the strength of λ5780 is found, with an upper limit on the change in equivalent width of ±41%.

The variation of diffuse interstellar band strengths over small spatial scales is interpreted as due to variations in the abundances of the carriers. Possible causes of small-scale DIB variability are discussed, including the degree of ionisation and excitation of the carriers.

2. The hypothesis that the cyanomethyl anion CH_2CN^- is responsible for the relatively narrow diffuse interstellar band at 8037.8 ± 0.15 Å is examined. The absorption spectrum arising from the $^1B_1 \longleftarrow {}^1A'$ origin band transition from the ground electronic state to the first dipole-bound state of the anion is calculated. Assuming that the distribution of ground state rotational level populations is in thermal equilibrium with the 2.74 K cosmic microwave background radiation, the transition results in a rotational contour with a peak wavelength of 8037.78 Å. CH_2CN^- is found to be a plausible candidate for the carrier of the λ8037 diffuse interstellar band provided a mechanism exists by which the rotational contour is broadened by an approximately Gaussian dispersion function with a width characterised by a Doppler b parameter between 16 and 33 km s^{-1} depending on the specific sightline in which the DIB is observed. Doppler broadening is found to be sufficient to cause such a dispersion in heavily-reddened sightlines, as demonstrated by the velocity structure of the interstellar gas in the sightline towards HD 183143, which is examined for K I, Na I, Ca I, Ca II, Ti II, CH, CH^+ and CN. Convolution of the calculated CH_2CN^- transitions with the optical depth profile of either Ca II or Ti II successfully reproduces the profile of the narrow λ8037 DIB observed towards HD 183143.

   The 2.74 K thermal distribution of ground-state rotational level populations may be modified by the nuclear spin statistics of the molecule. This situation is modelled and results in the appearance of additional strong spectral features at around 8024.8 Å and 8049.6 Å that are not seen in the observed interstellar spectra. If (a) no chemical mechanisms exist for the conversion of 'ortho' CH_2CN^- (hydrogen nuclear spins parallel) to 'para' CH_2CN^- (hydrogen nuclear spins antiparallel) or (b) the CH_2CN^- formation mechanisms do not result in a distribution of K_a'' levels approaching a 2.74 K Boltzmann distribution, then it is found that CH_2CN^- cannot be the carrier of the λ8037 diffuse interstellar band.

3. The strengths of diffuse interstellar bands and atomic lines in the ISM of the Large Magellanic Cloud (LMC) are analysed and compared with Galactic data.

Using optical spectra obtained along six reddened sightlines towards early-type stars in the LMC, at a resolution of ~ 3 km s^{-1} and a signal-to-noise of ~ 200, the velocity structure and column densities of interstellar K I, Na I, Ca II and Ti II are derived. Evidence is presented that the spectrum of diffuse interstellar bands in the LMC is similar (in strength and structure) to that found in the Galaxy, with the measurement of the equivalent widths of eleven DIBs at the Doppler-shifted wavelengths expected for the radial velocity of the LMC, including λ4430, λ5705, λ5780, λ5797, λ5850, λ6196 λ6203, λ6284, λ6376, λ6379 and λ6614. The observation of λ5705, λ5850, λ6196 and λ6203 constitutes the first reported detection of these DIBs in the LMC, and for λ5850, in any location outside of the Galaxy. All of the expected DIBs were observed towards the 30 Dor targets Sk −69°223 and Sk −69°243, and with strengths approximately equal to, or only slightly weaker than, those in Galactic 'σ-type' (strongly UV-irradiated) sightlines with similar reddenings and neutral potassium column densities. This result shows that there are interstellar clouds in the vicinity of 30 Dor that provide favourable environments for the existence of DIB carriers. The velocities of the carriers of the λ5780, λ5797, λ5850, λ6196 λ6379 and λ6614 diffuse interstellar bands in the LMC are found to be coincident with the velocities of the peaks of the atomic column density distributions at radial velocities of between 240 and 300 km s^{-1} relative to the local standard of rest. The least-squares fitted velocity of the λ6614 DIB is found to be shifted by ~ +5 km s^{-1} relative to the other DIBs in three out of four sightlines. This may be interpreted as evidence that the profile of sub-structure of the λ6614 DIB is skewed towards the red in these three sightlines (Sk −68°135, Sk −69°223 and Sk −69°243) to a greater degree than that found in the Galactic ISM.

Compared to Galactic trends, the LMC DIBs are found to be weak with respect to the reddening and neutral potassium column density towards Sk −67°2 and Sk −68°135. This may be attributable to a combination of the high UV flux and reduced shielding of interstellar clouds due to the low metallicity of the interstellar gas of the LMC, and results in the destruction of DIB carriers by photodissociation and/or photoionisation. Relative to N(H I) the λ6284 DIB observed in four LMC sightlines is shown to be approximately 1/5 to 1/2 of its average strength in the Milky Way. This supports the idea that the metallicity and/or dust-to-gas ratio of the ISM is closely linked with the chemistry that governs the abundance of DIB carriers relative to N(H I). Variations in the N(Ca II)/N(Ti II) ratio are found over at least an order of magnitude in the LMC ISM, and are taken as evidence for significant variation in the Ca II/Ca III ionisation balance. Derived logarithmic titanium depletions are found to be relatively low in the six LMC sightlines studied, with values between approximately −0.8 and −1.9, which are similar to the levels of depletion generally seen in the warm, shocked interstellar medium of the Galaxy.

Acknowledgements

Special thanks to Mum, Dad and Naomi for creating my universe. Thanks to Peter Sarre, captain of the interstellar cruiser, for being the brains behind this whole operation, for providing an endless source of positive energy, and for letting me participate in his exciting and unique scientific studies. Thanks to June McCombie for keeping me vigilant. Thanks to Phil Couch for letting me absorb some of his masterful data reduction abilities and skills with the Linux-box, and also for endowing me with the gift of 1-D radiative transfer. Extra-special thanks to 'the life and soul of East Midlands astrochemistry': Ross, Rad and Arfon whose wit, wisdom and friendship have been indispensable during my time in Nottingham. Whenever I look to the night sky in the direction of NGC 3372, I will be fondly reminded of them. Formal acknowledgement is required for Arfon Smith's assistance in reduction of the June 2004 AAT/UCLES dataset. Thanks and my eternal gratitude to Steve Fossey for teaching me to become wise in the ways of the spectra, for his knowledge, impeccable judgment and scientific precision that were instrumental in the outstanding success of the 'SSS DIB' project. Thanks to Nick Cox for company and assistance on my journey to the LMC (and beyond?). Special thanks to the mighty George Herbig for the excellent Keck HIRES spectra and raw data. Thanks of the highest order to Ian Howarth for the VAPID software, including speedy service, bug-fixing and fulfilment of my ridiculous requests. While my acknowledgement-sack still bulges with gratitude, I must also thank Moody for innumerable enlightening theoretical discussions and capricious conversations, Walkley for ridiculous comic capers and for company on the long nights writing this thesis, and Mr. Deathe for 3D dipole-bound state visualisation and a last-minute monitor in my hour of need. A generous thank you to In-Ok Song for a favourable Far-Eastern friendship, to Andy G for my introduction to computational chemistry and to Jules for accepting (and being worthy of) the honourable task of making sure the spirit of W1A lives on! Finally, I wish to acknowledge the EPSRC for funding the work involved in this thesis, and conclude with the motto of every shrewd observational astronomer: This research has made use of the simbad database, operated at CDS, Strasbourg, France.

Contents

Abstract 2

Acknowledgements 5

Thesis overview 10

1 Introduction 13

1.1 The interstellar medium 13

1.1.1 Interstellar Matter 16

1.1.2 Ionisation balance 23

1.1.3 The structure and distribution of interstellar matter 24

1.1.4 Diffuse interstellar cloud chemistry 25

1.2 Diffuse interstellar bands (DIBs) 28

1.2.1 DIB strengths and families 32

1.2.2 DIB profiles 32

1.2.3 DIB carriers 34

2 Optical echelle spectroscopy 38

2.1 The visible spectrum 38

2.2 The echelle spectrograph 41

2.2.1 Optics and detectors 41

2.2.2 Calibrations 44

2.3 Echelle data reduction in IRAF 47

2.4 Interstellar absorption line analysis 48

2.4.1 Optically thick absorption lines 48

2.4.2 VAPID interstellar absorption line analysis 52
2.4.3 Optically thin absorption lines and diffuse interstellar bands . 54

3 Diffuse interstellar bands and atomic lines in the LMC 56
3.1 Introduction to Chapter 3 56
3.2 The interstellar medium of the LMC 57
3.2.1 Comparison with the Galaxy 57
3.2.2 Diffuse interstellar bands 62
3.2.3 Atomic spectroscopy 64
3.3 Targets, instruments and observations 66
3.4 Spectra 70
3.4.1 Photometric uncertainties and reddening 71
3.4.2 Atomic and ionic spectra 73
3.4.3 Diffuse interstellar band spectra 78
3.5 Structure and composition of the ISM towards the LMC 87
3.5.1 $N_v(v)$ profiles and apparent optical depth (AOD) analysis . . . 87
3.5.2 Diffuse interstellar band carrier velocities 99
3.5.3 Integrated atomic gas properties 104
3.5.4 Galactic foreground gas and dust 108
3.5.5 LMC interstellar cloud component analysis 112
3.6 Discussion 114
3.6.1 LMC DIB strengths compared with E_{B-V}, N(K I) and Galactic data 114
3.6.2 Sk −67°2 122
3.6.3 Sk −67°5 124
3.6.4 Sk −68°135 125
3.6.5 Sk −69°223 128
3.6.6 Sk −69°243 129
3.6.7 Sk −70°120 132
3.7 Summary of factors affecting DIB strengths in the LMC 133
3.7.1 Gas and Dust 133
3.7.2 Metallicity 135

3.7.3 UV field strength 136
3.7.4 UV extinction 137
3.8 Key findings of Chapter 3 138

4 Diffuse interstellar bands and the small-scale structure of the ISM 142
4.1 Introduction to Chapter 4 142
4.2 Observations 150
4.3 Results: The discovery of small-scale spatial variation in DIB strengths towards multiple star systems 155
4.3.1 Standard stars 155
4.3.2 β Sco 155
4.3.3 ν Sco 170
4.3.4 ρ Oph 177
4.3.5 μ Cru 203
4.3.6 HD 150135/6 209
4.3.7 HD 164863/313693 217
4.3.8 Small-scale spatial variation in the velocity structure of the ISM towards HD 164863/313693 223
4.4 The time-variable sightline towards κ Vel 227
4.4.1 Interstellar K I column density variations 227
4.4.2 The search for time-variable DIBs 231
4.5 Discussion 235
4.5.1 Small-scale structure in the DIB-carrier distribution 235
4.5.2 DIBs as probes of SSS cloud conditions 241
4.5.3 Small-scale structure and λ6614 profile variability 242
4.6 Conclusion to Chapter 4 246

5 CH_2CN^-: Possible carrier of the λ8037 diffuse interstellar band 250
5.1 Introduction to Chapter 5 250
5.1.1 Organic interstellar anions 250
5.1.2 Dipole-bound anionic states 256
5.1.3 CH_2CN^- as possible carrier of the λ8037 DIB 259
5.2 Observations of the λ8037 DIB 260

5.3 The $^1B_1$ DBS ⟵ $^1A'$ GS transition of CH_2CN^- 262
5.3.1 Rotational spectroscopy of polyatomic molecules 262
5.3.2 Spectroscopy of CH_2CN^- 264
5.4 Modelling CH_2CN^- as the λ8037 DIB carrier 271
5.4.1 Rotational contour calculations 271
5.4.2 Comparison of model with observations 274
5.4.3 Velocity structure of the interstellar gas towards HD 183143 . 278
5.4.4 Interstellar CH_2CN^- velocity structure 286
5.4.5 'Ortho' CH_2CN^- transitions 291
5.5 Discussion 294
5.6 Conclusion to Chapter 5 300

Bibliography **302**

List of Figures **316**

List of Tables **322**

Thesis overview

Chapter 1

An introduction to the interstellar medium (ISM), a brief history of spectroscopic observations of interstellar atoms and molecules, dust and dust extinction properties, an outline of basic diffuse cloud chemistry, and an examination of the known properties of the diffuse interstellar band (DIB) spectrum.

Chapter 2

Details of the fundamental properties of optical echelle spectra and a summary of the basic data acquisition, reduction and analysis techniques employed for the spectra involved in this thesis.

Chapter 3

A study of the properties of the diffuse interstellar band spectrum in the Large Magellanic Cloud (LMC) and an analysis of the abundance, velocity structure and spatial distribution of Na I, Ca II, Ti II and H I in six sightlines towards reddened LMC OB supergiants (including the composite object Sk −69°243). The analysis is based primarily on spectra obtained using the UVES spectrograph on the VLT. DIB strengths, sightline reddenings and atomic abundances, depletions and abundance ratios are compared with Galactic data to examine the differences between the interstellar media of the LMC and the Milky Way.

Chapter 4

A study of the variability of diffuse interstellar band strengths over distance scales from approximately 370 to 43,000 AU in the local ISM (at radial distances up to approximately 1.5 kpc). Based on optical spectra of the members of six binary/multiple star systems using the UCLES instrument on the AAT, this work provides the first unequivocal evidence for 'small-scale structure' in the spatial distribution of DIB carriers in the ISM. Small-scale variation in DIB strengths is reported in sightlines towards four systems for which small-scale structure has previously been observed using interstellar Na I, and in a sightline-pair for which no small-scale structure has been previously observed. A search for variation in the strengths of the DIBs towards the high velocity star κ Vel between January 1995 and June 2004 is also reported.

Chapter 5

A critical examination of the hypothesis that a transition from the ground state to the first dipole-bound state of CH_2CN^- is responsible for the relatively narrow diffuse interstellar band located near 8037 Å. The transition is modelled using accurate molecular parameters and compared to Keck HIRES spectra of eight heavily-reddened Galactic sightlines. The velocity structure of the interstellar K I distribution in the sightlines is studied, and additionally of the species Na I, Ca I, Ca II, Ti II, CH^+ and CN in the sightline towards HD 183143. The plausibility of CH_2CN^- as the carrier of the λ8037 DIB is assessed based on its postulated velocity distributions, required interstellar abundances, and possible formation mechanisms, with the conclusion that CH_2CN^- cannot be ruled out as possible carrier of the λ8037 DIB.

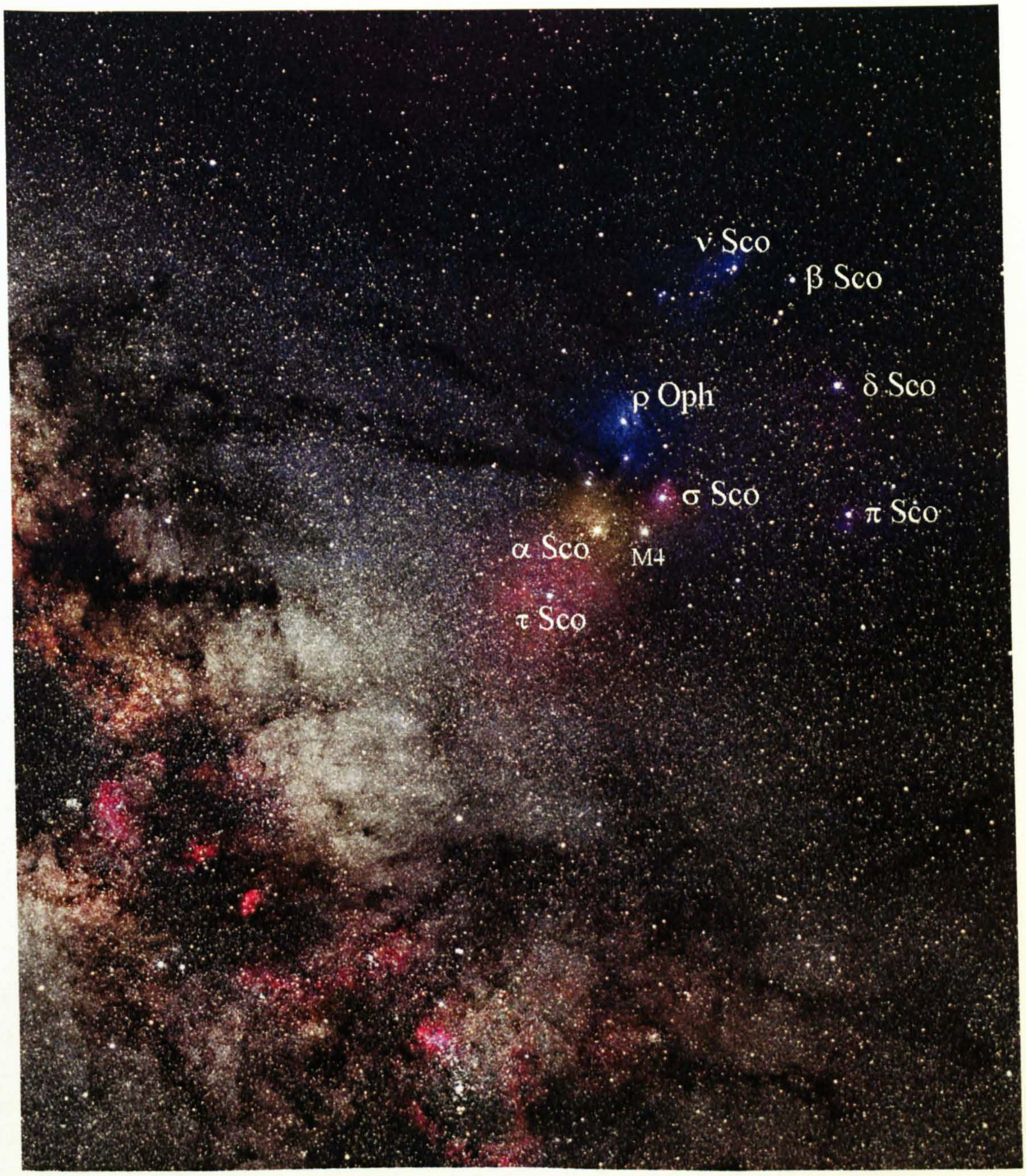

Figure 1: Annotated optical image of the night sky in the direction of the Scorpius-Ophiuchus constellations. The horizontal field of view spans ~ 20°. The labeled stars lie only ~ 150 pc away and are part of the Sco OB2 association, though M 4 is a globular cluster about 2 kpc distant. The bright blue nebulae surrounding α Sco, ρ Oph and ν Sco are caused by scattering of starlight by the dust in the ISM in the vicinity of these stars, but the red/pink glow surrounding σ and τ Sco is caused by emission from hot, hydrogen gas, excited by intense ultraviolet radiation. Dust particles obscure the light from background stars, and the Galactic centre is hidden behind a mass of thick dust clouds that obscure the bright region to the lower left of the image centre. Image courtesy of Tony and Daphne Hallas (www.astrophoto.com, used with permission), taken from S. E. Arizona, USA using a Pentax 6x7 camera with 45 mm lens at f/5.6 and an exposure time of approximately 90 minutes on Kodak PPF 400.

Chapter 1

Introduction

1.1 The interstellar medium

The interstellar medium (ISM) plays a fundamental role in the evolution of stars and galaxies. Comprising about a fifth of the baryonic mass of the Galactic disc (Whittet 2003), interstellar matter in galaxies throughout the cosmos represents a significant fraction of the mass of the Universe. The ISM is an integral part of the life cycle of the stars and planets, an active environment for the formation and destruction of complex molecules, and a laboratory for the study of extreme physical and chemical processes that are not easily reproduced on Earth.

The structure and composition of the ISM is determined by a complex combination of macroscopic and microscopic processes, with matter cycling between the stellar and interstellar phases over a time-scale of approximately 6×10^9 years (Tielens 1995). Gravitationally collapsing clouds of interstellar matter heat up to temperatures sufficient to initiate nucleosynthetic processing of atomic nuclei, resulting in the birth of a star. During a stars' lifetime, radiation pressure blows metal-enriched[1] matter back into the ISM as a stellar wind. High mass stars and Wolf-Rayets have particularly strong winds, sending enriched atomic and ionic matter far into the surrounding space. The cool, dense atmospheres of carbon and oxygen-rich stars provide sites for the efficient formation of complex molecules and granular material that is ejected into space as these stars end their lives. The deaths of massive stars as supernovae are responsible

[1] 'Metals' refers to elements heavier than hydrogen and helium.

for much of the mass returned to the interstellar medium. Their powerful explosions send metal-rich matter, cosmic rays and energetic shockwaves across the Galaxy.[2]

As a galaxy ages and the baryonic matter cycles between stars and interstellar space, the ISM becomes progressively richer in metals, resulting in an evolution of the abundances of the different reagents available to fuel astrochemical reactions. Energy is supplied to the ISM predominantly by stellar radiation and winds, cosmic rays, X-rays and supernova explosions, and these provide kinetic energy to support the gas against gravitational collapse. The heat balance is determined from the rate of energy input compared to the rate at which energy is lost to the intergalactic medium through radiative processes involving spectroscopic transitions of atoms, molecules and dust grains.

In the solar neighbourhood, the interstellar medium is tenuous, consisting of about one particle per cubic centimetre (Whittet 2003). However, there exist several phases of the ISM spanning a continuum of density and temperature regimes. The 'hot intercloud' medium has a low particle number density ($n \sim 0.003$ cm^{-3}) and a kinetic temperature T of $\sim 10^6$ K (Tielens 1995), filling much of the Galaxy and its halo, which is predominantly atomic and in a state of high ionisation. Distinguished by the fraction of hydrogen in neutral form, the 'warm ionised medium' ($n \sim 0.3$ cm^{-3}, $T \sim 8000$ K) and the 'warm neutral medium' ($n \sim 0.5$ cm^{-3}, $T \sim 8000$ K) also constitute a large fraction of the total ISM and cool *via* the high-energy Lyman alpha (Lα) transition and a transition of neutral atomic oxygen at ~ 6300 Å (Tielens 1995). A new stable phase of the ISM generally reflects the onset of a new cooling mechanism or the removal of a heating source (Tielens 1995): the diffuse ISM phase (also known as the 'Cold Neutral Medium'), with $n \sim 100$ cm^{-3} is believed to cool primarily *via* the $^2P_{3/2} \longrightarrow {}^2P_{1/2}$ transition of C II (Dyson & Williams 1997). The ionised carbon atoms extract kinetic energy from the gas predominantly by collisions with atomic and molecular hydrogen and free electrons, then radiate it away such that these clouds reach temperatures of ~ 100 K.

Heating of the diffuse ISM by cosmic rays and FUV photons (with 6 eV $\lesssim h\nu \lesssim$ 13.6 eV) prevents kinetic temperatures of the diffuse atomic gas from getting too low. However, where clouds are dense enough for molecular hydrogen to form without being rapidly photodissociated, H_2 provides an additional cooling mechanism *via* its

[2]Supernovae occur relatively rarely from a human's perspective; the last known in our Galaxy was Kepler's supernova, which exploded over 400 years ago (see Blair 2005 for details).

electric quadrupole transitions, allowing temperatures to drop to several tens of Kelvin. The cold and warm phases of the neutral interstellar medium are characterised by the presence of neutral atomic hydrogen (H I). The cold phase is generally in the form of relatively compact clouds, filaments and sheets embedded in the surrounding warm neutral or ionised phase (Lequeux 2005).

Dense molecular clouds contain the greatest fraction of the mass of the ISM, and have particle densities $n \gtrsim 300$ cm^{-3} though they are typically small in size (1 $\sim$ 50 pc; Lequeux (2005)). Opaque to dissociating and ionising radiation due to shielding, predominantly by dust grains, molecules form and persist in these environments and their rotational transitions permit the further cooling of the gas to $T \sim 10$ K.

The environments whose conditions span the intersection between the diffuse and the dense regimes provide an interesting opportunity for the study of interstellar molecules. In the so-called 'translucent' clouds (see for example Black & van Dishoeck 1991), particle densities are typically $\sim$ 300 to 1000 cm^{-3} and high abundances of complex molecules are found (Turner *et al.* 1999). Molecular formation mechanisms must proceed rapidly in order for significant abundances to be reached in the relatively unattenuated UV fields found in these environments. Localised variations in the concentrations of different species and the presence of density inhomogeneities in the gas may give rise to variations in the radiation field and in the molecular formation (and ion recombination) rates, due in part to the density-dependence of particle collision rates. As column densities (and number densities) increase, molecules may start to be shielded from dissociating UV photons by dust grains or by other members of the same species (self-shielding[3]). Molecular hydrogen self-shielding turns on at an H_2 column density of $N(H_2) \simeq 2 \times 10^{14}$ cm^{-2} (Black & van Dishoeck 1991), and at particle column densities of $\gtrsim 10^{20}$ cm^{-2}, the majority of hydrogen is predicted to be in molecular form. Shielding by dust is more important for the survival of less abundant molecules such as CO, and turns on at a much greater depth into a cloud (at $N(CO) \simeq 2 \times 10^{15}$ cm^{-2}). The abundance of CO is also sensitive to the gas density and the gas-phase carbon and oxygen abundances (Black & van Dishoeck 1991). Many polyatomic molecules begin to be seen in appreciable abundances with the appearance of CO in the translucent ISM as observed, for example by Lucas & Liszt (1996b), including HCN, HCO^+ and c-C_3H_2.

[3]The molecules at the edges of a cloud use up photons in dissociative transitions.

Where a sufficiently powerful source of UV photons is present, for example in the vicinity of an OB star (thousands of times more luminous than the Sun), hydrogen is ionised, and extremely destructive photons with $h\nu > 13.6$ eV travel through the gas. Electrons recombining with H II cascade down through the energy levels and give rise to the spectacular Hα λ6563 emission as part of the Balmer series of recombination lines. In H II regions, temperatures are $\sim 10,000$ K and proton densities can be up to $n_{\rm H} \sim 10^5$ cm^{-3} (Tielens 1995). Other atomic ions emit strongly in these regions, and heated dust may be present in the plasma (Whittet 2003), but such highly irradiated clouds contain no significant molecular abundances. Electron densities in H II regions may reach $n_e \sim 10^5$ cm^{-3}, compared to typical values of ~ 0.01 to 1 cm^{-3} in diffuse interstellar clouds.

Major advances in the investigation of the chemistry of the interstellar medium have occurred over the last thirty years, stimulated by the observation of an increasing number of molecules in various types of circumstellar and interstellar environment. Frequent new discoveries regarding molecules and their properties, such as internal excitation, macroscopic kinetic motions and spatial distribution, requires the continual updating of existing theories and the creation of new models to develop understanding of the ISM and its constituents. The full picture of the physics and chemistry that governs the formation and destruction of molecules in the ISM is far from complete.

1.1.1 Interstellar Matter

1.1.1.1 Gas

The study of the ISM began with the observation of narrow atomic absorption lines in the optical spectra of binary stars. Unlike the (usually) broader 'stellar' spectral lines originating in the stars themselves, narrow 'stationary' lines were found not to participate in the periodic Doppler shifts observed in spectroscopic binaries, indicating an origin in cool gas somewhere in the line of sight to the stars.

The first record of such observations was made by Hartmann (1904) for the 'K' line of ionised calcium (Ca II) towards δ Ori, who also speculated on the interstellar origin of the calcium H and K lines and the sodium D lines based on observations of their invariance during the 'flare up' of Nova Persei in 1901. Thus, for more than one

hundred years the gas between the stars has been the subject of intense scrutiny by astronomers. Each advance in instrumental capability and analysis technique yields more information about the nature of the ISM.

In 1919 Heger identified stationary lines in the spectra of β Sco and δ Ori and found a close correspondence between the radial velocities of the Ca II and the Na I lines. Subsequent surveys (see Heger 1922) lead to the discovery of additional unidentified absorption features at around 5780 and 5797 Å (constituting the first documented discovery of diffuse interstellar bands; see Section 1.2), that appeared to behave in the same way as the stationary sodium and calcium lines but were considerably broader in character.

Plaskett's work in 1923 on narrow Ca II lines was invaluable in confirming that stationary, or 'detached' lines were not phenomena observed only towards spectroscopic binaries, but towards early-type stars in general. Early speculations as to the origin of the interstellar matter consisted of theories of stellar mass loss due to high pressure metallic winds (see for example Evershed 1924).

The body of evidence to confirm the interstellar origin of the narrow metal lines expanded greatly during the 1920's (see the review by Thorndike 1930) and the 1930's, accompanied by the discovery of a plethora of new interstellar species. Neutral calcium and potassium were first observed by Dunham (1937). The assignment of several unidentified narrow spectral lines in the blue and NUV to absorption by interstellar CH, CH^+ and CN can be attributed predominantly to the work of Swings & Rosenfeld (1937), McKellar (1940), Douglas & Herzberg (1941), Swings (1942) and Adams (1943a).

Thus, the presence of a molecular component of the diffuse interstellar medium was confirmed, requiring a radical rethink of the processes occurring in the ISM that could give rise to such molecules. The advent of sensitive radio instruments permitted the discovery of 1.7 GHz interstellar OH emission by Weinreb *et al.* (1963), spawning a new branch of radio and millimetre 'molecular astrophysics'. The H_2O molecule was discovered in dense interstellar clouds by Cheung *et al.* (1969), followed by CO in 1970 by Wilson *et al.*. Rocket-borne astronomical instruments enabled the observation of many previously unobserved interstellar species through their UV absorption spectra, including, most notably, the discovery of H_2 towards ξ Per by Carruthers (1970).

Increases in instrumental precision facilitated the measurement of the detailed characteristics of interstellar atomic and molecular lines — including their strengths, relative intensities and profiles, which allowed the precise calculation of the properties of the ISM. Atomic and molecular abundances, free electron densities, dust extinction properties and gas kinetic, turbulent and radiation temperatures were derived (see for example Lequeux (2005) for details of some of the techniques), the explanation of which required the construction of detailed physical and chemical models.

Over one hundred interstellar molecules are now known (see for example Herbst 1995), including alcohols, sugars and amino-acids. A list of the (currently 129) known circumstellar and interstellar molecules is maintained on the National Radio Astronomy Observatory web-page located at http://www.cv.nrao.edu/ awootten/allmols.html. Dark molecular clouds are the most favourable environments for the production of organic molecules, where dust shields them from UV photons. Millimetre surveys by Turner (1989) and Nummelin *et al.* (2000) for example, show the richness of the chemical composition of these types of clouds. The possibility of the presence of complex molecules in the more diffuse phases of the ISM had been widely dismissed until relatively recently. Research has now shown that diffuse clouds provide favourable environments for polyatomic chemistry, exemplified by the work of Liszt and Lucas (2000; 2001) and Lucas and Liszt (1996a; 1996b; 1998; 2000) who used millimetre-wave absorption by gas in sightlines to distant quasars to observe molecules such as HCO^+, HCN, H_2CO, C_2H and *c*-C_2H_3 at fractional abundances (relative to H_2) that are comparable with those found in dark interstellar clouds.

1.1.1.2 Dust and depletion

Hints as to the presence of a particulate form of interstellar matter were provided by observations of apparently diminishing densities of stars with distance from the Sun (see for example Struve 1847), and in observations of dark patches of the sky where starlight was apparently obscured, as though blocked by solid matter. An early explanation of the diffuse radiation surrounding the Pleiades cluster was that it occurred as a result of starlight scattering by small particles adrift in space (Slipher 1912).

The apparent 'reddening' of stars in the Galactic plane presented another mystery, again explainable by the presence of an interstellar component that causes selective

'extinction' of the bluer wavelengths in a stellar spectrum. Trumpler (1930) showed that the amount of starlight extinction at a given wavelength, A_λ (measured in magnitudes), increased with the star's distance and varied as a function of $1/\lambda$ (λ being the radiation wavelength). The form of the wavelength-dependence law implies scattering by particles with a size comparable to the wavelength of visible light ($\sim$ 0.1 to 1 μm) that contain $\sim 10^9$ atoms (Whittet 2003). Formally, the visual extinction A_V is related to the apparent visual magnitude V, the absolute visual magnitude M_V and the distance d of the star by (see for example Whittet 2003)

$$V - M_V - A_V = 5 \log d - 5. \tag{1.1}$$

In the Johnson photometric system (Johnson & Morgan 1953) the V magnitude is measured from the integrated stellar flux observed through a yellow filter (centered on 5500 Å) and corrected for atmospheric attenuation. B is the corrected magnitude observed through a blue filter (centered on 4400 Å). The degree of reddening of a star (often referred to as 'colour excess', or simply the 'reddening' E_{B-V}) is calculated according to

$$E_{B-V} = (B - V) - (B - V)_0 \tag{1.2}$$

where $(B - V)_0$ represents the 'unreddened' colour index of the star, intrinsic to its particular spectral type (temperature) and luminosity class (mass). The E_{B-V} value measures how much 'slope' is introduced into the stellar spectrum as a result of the wavelength-dependent dust extinction law A_λ.

The shape of the 'extinction law' is measured by comparison of the spectrum of the star of interest with that of an unreddened 'standard' star with identical spectral type. Differences between the shapes of the spectral energy distributions are due to interstellar extinction. To facilitate comparison of the extinction between different sightlines, A_λ is usually normalised with respect to E_{B-V} or A_V and plotted against $1/\lambda$ in the form of an 'extinction curve' (see for example Cardelli *et al.* 1989; Fitzpatrick & Massa 1990). Variability of the extinction curve between sightlines is negligible for wavelengths $\lambda \approx 5000$ Å (Cardelli *et al.* 1989). It is in the UV that the extinction curve shows the most interesting variations, leading to in-depth discussion of the 'UV extinction curve' by many authors. The most notable feature is the 2175 Å 'bump', the

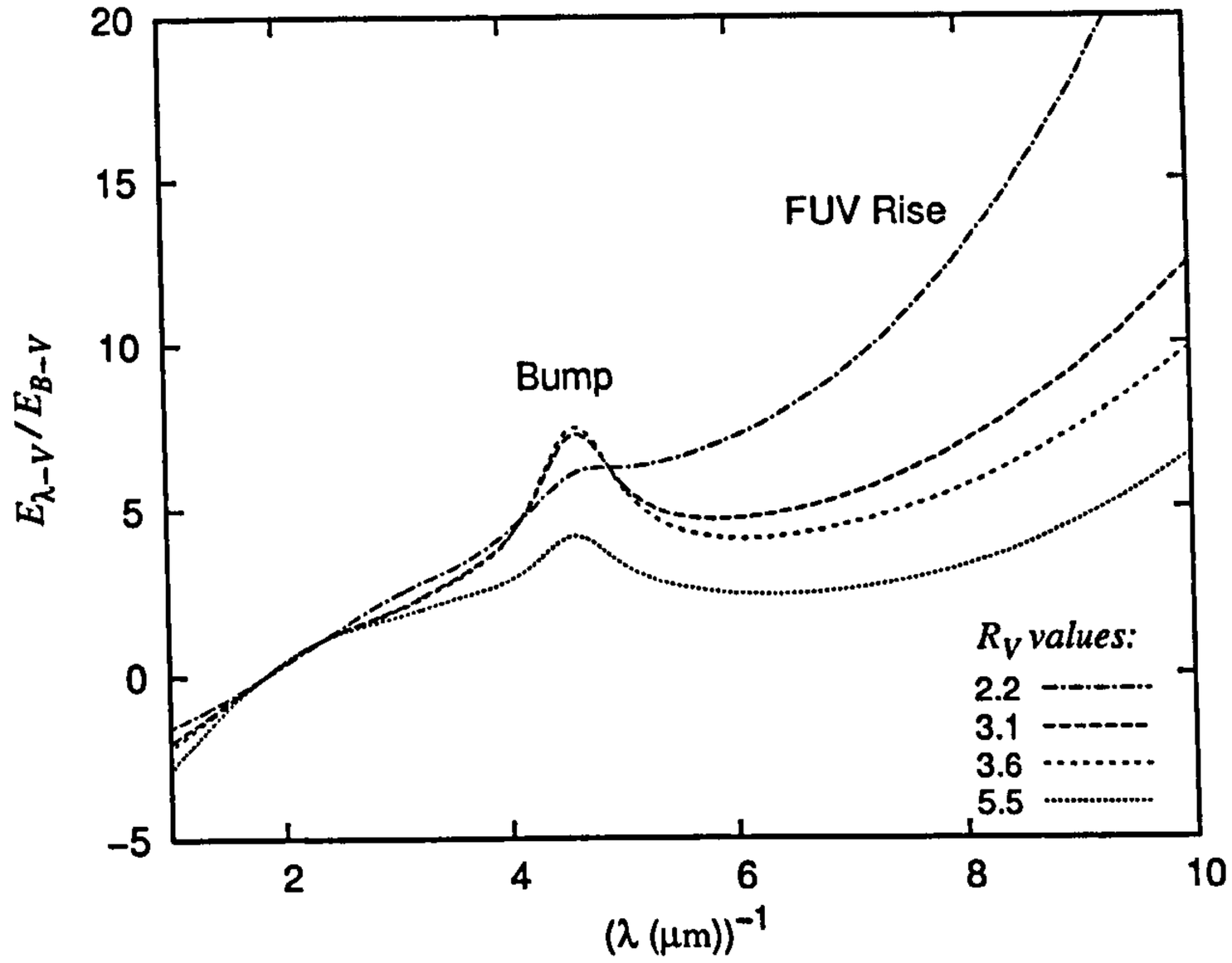

Figure 1.1: Examples of 'standard' interstellar UV extinction curves parameterised by R_V. Data provided by E. L. Fitzpatrick, based on work presented by Fitzpatrick (2004).

observational properties of which have been reviewed by Draine (1989), and is found to arise ubiquitously in the Galactic diffuse and dense ISM with a variable strength of up to a factor of two either side of the mean. The 'bump' width is also subject to a small degree of variability, with a broader bump generally associated with denser material. The other main feature is the 'far-UV (or FUV) rise' that describes the behaviour of the extinction curve at wavelengths $\lesssim$ 1650 Å and typically shows a smooth steepening of the extinction law towards shorter wavelengths. The rate of steepening can be highly variable between sightlines. Some examples of different-shaped extinction curves are shown in Figure 1.1.

Regardless of the variablility of the extinction law in the UV, the normalised extinction law between the B and V wavelengths remains relatively invariant (observe the region between 1.8 and 2.3 μm^{-1} in Figure 1.1). Thus, E_{B-V} remains a good measure of dust column density.

Cardelli *et al.* (1989) found that the observed range of different Galactic UV extinction curves could be parameterised by a single variable, chosen to be R_V, the ratio of visual to selective extinction:

$$R_V = \frac{A_V}{E_{B-V}}, \tag{1.3}$$

which led to the result that the factors affecting the extinction law in the Galaxy operate continuously and in a consistent way over the entire wavelength range. The strength of the bump and the steepness of the FUV rise were both found to correlate inversely with R_V.

In modelling the extinction properties of the interstellar dust, the variations in the UV extinction curve can be understood in terms of variations in the size distribution and composition of the dust grains. The most significant body of evidence points towards small graphitic particles as carriers of the 2175 Å bump (see Draine 1989), and it is generally agreed that very small dust grains (~ 100 Å in size, probably silicates — see, for example Draine & Lee (1984)) and/or PAHs (see Desért *et al.* 1990) are responsible for the FUV rise. A reduction in steepness of the FUV rise is therefore understood as being due to a reduction in the abundance of very small grains (or PAHs) resulting in an increase in R_V, and *vice versa*. Thus, R_V is often used as an indicator of the overall dust grain size distribution, or more specifically, the fraction of very small grains. In the local Galactic diffuse ISM, the average value for R_V is about 3.1 (Seaton 1979).

The quantities B, V, A_V and E_{B-V} are expressed in units of magnitude throughout this thesis, though the units are generally not explicitly stated.

Observational evidence points towards a population of interstellar dust grains between 0.001 and 1 μm in diameter, composed of primarily C, N, O, Mg, Si and Fe, and constituting at most 2% of the mass of the ISM (see Whittet 2003). The mass constraint arises from measurements of 'elemental depletion', a subject reviewed by Jenkins (1989). The cosmic abundance ratios of interstellar elements are well known from studies of meteorites that fall to earth (see Anders & Grevesse 1989, for example) or from measurements of the abundances of species in stellar atmospheres (including the Sun) or emission nebulae (see for example Sofia & Meyer 2001). UV and optical observations of the ISM show that interstellar gas-phase elemental abundances are extremely variable, and that many species vary in abundance with respect to their cosmic value by factors of up to ~ 1000. The implication is that atoms in the gas phase stick to the dust grains upon impact. The tendency for the atoms of different species to stick depends on

their condensation temperature[4]; those with high condensation temperatures coagulate efficiently into solid particles and tend to stick to dust grains as the temperature falls.

In the cool, quiescent diffuse ISM, 'refractory' elements with high condensation temperatures such as Ca, Ti, Fe and Ni are highly depleted from the gas phase and their depletions are strongly dependent on the density and temperature of the gas (Jenkins 1989). Elements with lower condensation temperatures such as Zn, K, Na and C do not readily deplete onto grains in the diffuse ISM and their depletions are broadly invariant to changes in interstellar conditions. The fraction of Ti and Ca in the gas phase is often less than 0.1% (*e.g.* Crinklaw *et al.* 1994), but in high temperature clouds or clouds previously exposed to intense shocks from supernovae, collisions between grains or thermal sputtering processes (Draine & Salpeter 1979) release the condensed species back into the gas phase. In shocked or hot interstellar clouds, such as those found in the Galactic halo, Ca and Ti depletions are of the order of −0.8 dex (Welty *et al.* 1999), though it is possible for *all* of the refractory species to be released back into the gas phase, with the implication of complete dust grain destruction (Lipman & Pettini 1995). The large variations in the sodium-to-calcium ratio of interstellar clouds observed by Routly & Spitzer (1952) provided the first evidence for the depletion of calcium; a trend was found whereby calcium abundances were relatively higher in clouds with higher mean radial velocities relative to the local standard of rest. The energetic processes responsible for accelerating these clouds to higher velocities were interpreted as responsible for shocking of the dust and the subsequent release of calcium atoms back into the gas phase (the 'Routly-Spitzer effect').

Formally, the depletion of an element X, denoted δ_X, is expressed as the logarithm (to base 10) of the observed fractional gas-phase abundance[5] relative to solar, though in environments where intrinsic elemental abundance ratios are non-solar due to a different 'metallicity' (such as in other galaxies where the metal-enrichment of the ISM has proceeded at a different rate), a more general expression is required:

$$\delta_X = \log\left(\frac{n_X}{n_H}\right) - \log\left(\frac{n_X}{n_H}\right)_\odot + \log Z_X. \qquad (1.4)$$

Z_X is the factor by which the intrinsic fractional abundance of element X in the envi-

[4]The condensation temperature of an element is defined as the gas kinetic temperature below which more than 50% of the atoms are condensed into the solid phase.

[5]Fractional abundances are conventionally expressed relative to the number of hydrogen nuclei, n_H.

ronment of interest differs, in the absence of any depletion, from the solar abundance. Typically $Z_X = Z$ is assumed, where Z is the average metallicity, *i.e.* the average of Z_X for all heavy elements for which data is available.

The fact that elements deplete out onto dust grains is of great significance for astrochemistry. It is now well known that the primary reaction involved in the production of H_2 requires the 'meeting' of two H atoms on a dust grain surface such that the energy of the exothermic association process is transferred to the grain. When species such as O and OH deplete onto grains, surface chemistry takes place to produce H_2O. Surface hydrogenation and oxidation reactions produce many other molecular species including CH_4, NH_3, CO_2 and CH_3OH (see Whittet 2003).

In dense interstellar environments rapid atom-grain collision rates result in the formation and build-up of icy molecular mantles that may later release their molecules into the gas phase upon heating of the dust. This can be due, for example, to shock-induced sputtering (Draine *et al.* 1983) or thermal desorption due to the release of gravitational potential energy as molecular clouds collapse under their own weight, or if a new star is born nearby, bathing the cloud in radiation.

1.1.2 Ionisation balance

Photoionisation of atomic gas by the interstellar radiation field results, for most atoms, in the population of a distribution of ionisation states, each with a very different (usually non-coincident) electronic spectrum. To calculate the total abundance of a given element requires the summation over all the ionisation states in which it resides. Generally, the principal mechanisms that control the distribution of ionisation states are believed to be photoionisation and electron recombination (Spitzer 1978). If other processes that might affect the level of ionisation are neglected, then at equilibrium the photoionisation rate Γ of an atomic species labelled X, in ionisation level i, balances the electron density-dependent recombination rate α of the atom in the next highest ionisation level $i + 1$ such that

$$n(\mathrm{X}^i)\Gamma = n(\mathrm{X}^{i+1})n_e\alpha \tag{1.5}$$

(see for example Lequeux 2005). The quantities $n(X^p)$ denote the abundance (number density) of X in ionisation level p, where p is an integer between 0 and z, and represents the number of electrons removed from the neutral atom up to a maximum of z, the proton-number of X. It is common to assume that the different ionisation states of an atom co-exist spatially such that the number densities $n(X^p)$ can be substituted for column densities $N(X^p)$, which are much easier to derive observationally.

Photoionisation rates (Γ) depend on the ionisation cross-section of the species and the incident radiation flux, the latter being affected by factors such as A_V and the proximity to OB stars. The recombination rate depends on how readily the species attaches electrons (determined by its electronic structure), and on the kinetic temperature and density n_e of the free electron gas.

In the diffuse interstellar medium it is common for an element to occur predominantly in a single ionisation state. The energy gaps between successive ionisation states are such that most atoms can only be singly ionised in the diffuse ISM due to the lack of photons with energies > 13.6 eV. Most neutral atoms have a first ionisation potential (the energy required to go from X^0 to X^1) of < 13.6 eV, and subsequent ionisation potentials > 13.6 eV. Calcium is an exception, with a first ionisation potential of 6.1 eV (Lequeux 2005) and a second ionisation potential of 11.9 eV (Welty *et al.* 2003) such that it commonly co-exists in three different ionisation states: Ca I, Ca II and Ca III (corresponding to X^0, X^1 and X^2 respectively). In very diffuse clouds, Ca III is expected to be the dominant form, whereas in denser clouds the relatively high Ca III recombination rate combined with the relatively low Ca II ionisation rate means that Ca II is expected to be dominant (Welty *et al.* 2003).

The main processes that are believed to disrupt the ionisation equilibrium of Equation (1.5) involve the transfer of electrons between dust grains/large molecules and atomic species (see Welty *et al.* 2003). The importance of such processes and the degree to which they affect the ionisation balance are presently not firmly established.

1.1.3 The structure and distribution of interstellar matter

Early evidence for non-uniformity in the distribution of interstellar matter was presented by Adams (1943b) in observations of the multiplicity of interstellar Ca II H and K lines which implied that the gas is not homogeneously spread between the stars in

the Galaxy. Instead, it is concentrated within discrete 'clouds' that may be separated in their mean line-of sight radial velocities, with narrow internal (kinetic and/or turbulent) velocity distributions. The dominant component of diffuse interstellar gas, H I, is contained in structures with sizes ranging from ~ 1 kpc (~ 10^8 AU) to ~ 10 AU, the lower limit imposed by the current maximum angular resolution of VLBI instruments of ~ 0.1″ (see Dickey & Lockman 1990).

In this thesis, the term 'cloud' is used to refer broadly to agglomorations of interstellar matter spanning the complete range of size and density. Where greater specificity is required, the term 'clump' refers to small ($\lesssim$ 1 pc diameter), typically denser ($\gtrsim$ 100 particles cm^{-3}) clouds. 'Core' refers to a compact region of well-shielded, predominantly molecular material that may be found at the heart of a diffuse or translucent cloud. The properties of diffuse clouds at the lower end of the size range are not yet well understood, but research continues apace (see 4.1).

1.1.4 Diffuse interstellar cloud chemistry

Stimulated by measurements of diatomic molecular abundances in sightlines through diffuse interstellar clouds, successful models of diffuse cloud gas-phase chemistry have been developed, most notably by van Dishoeck & Black (1986). Their models incorporate chemical reaction 'networks' that simulate the reaction rates for ~ 100 different molecules until equilibrium abundances are reached; the basic reaction mechanisms are described in Hartquist & Williams (1998) in their Chapter 4.

Densities in the diffuse ISM are too low for significant numbers of three-body collisions to occur, so the principal chemical reactions involve only two-body processes, with the exception of dust grain assisted reactions where the grain acts as a catalyst for the reaction of two (or possibly more) other species. Due to the lack of available free energy in the cold interstellar medium, the reactions that occur are predominantly exothermic, such that ion-neutral reactions provide a major contribution to the polyatomic chemistry of the ISM (Herbst & Klemperer 1973). In diffuse clouds, the main cause of ionisation is the UV field, so in denser clouds where the UV cannot penetrate the chemistry is driven by cosmic-ray (or sometimes X-ray) ionisation.

Helium is rather inert, so hydrogen, by its overwhelming over-abundance relative to other species, is the most important reagent in the initialisation of interstellar chem-

istry. Reactions of the type $X^+ + H_2 \longrightarrow XH^+ + H$ are instrumental in the formation of polyatomic ions (Herbst & Klemperer 1973), including the production of the 'universal protonator' molecule H_3^+:

$$H_2^+ + H_2 \longrightarrow H_3^+ + H. \tag{1.6}$$

As discussed by Herbst & Klemperer (1973), H_3^+ is of fundamental importance in astrochemistry, initiating many of the chemical reaction networks responsible for the wealth of molecules observed in dense molecular clouds, for example:

$$O + H_3^+ \longrightarrow OH^+ + H_2 \tag{1.7}$$

$$OH^+ + H_2 \longrightarrow H_2O^+ + H \tag{1.8}$$

$$H_2O^+ + H_2 \longrightarrow H_3O^+ + H \tag{1.9}$$

$$H_3O^+ + e \longrightarrow H_2O + H \text{ or } OH + H_2 \text{ or } O + H + H_2 \tag{1.10}$$

for the production of gas-phase water and the hydroxyl radical.

In the diffuse ISM, C^+ provides a reactive source of carbon, and initiates the 'carbon chemistry' (van Dishoeck & Black 1986) through the reactions

$$C^+ + H_2 \longrightarrow CH^+ + H - 0.4 \text{ eV} \tag{1.11}$$

(Hartquist & Williams 1998, Chapter 4), and

$$C^+ + H_2 \longrightarrow CH_2^+ + h\nu. \tag{1.12}$$

The latter takes place at a very slow rate (Black & Dalgarno 1973), but the former is endothermic and can only proceed rapidly where sufficient energy is available, for example at the shock front of a supernova explosion where the carbon ions are accelerated relative to neutral H_2 (see for example Draine & Katz 1986).

The reaction of CH^+ with H_2 then produces CH_2^+ that undergoes dissociative recombination to form CH.

The main route to the formation of CO in diffuse clouds (van Dishoeck & Black 1986) is

$$C^+ + OH \longrightarrow CO^+ + H \text{ or } CO + H^+ \tag{1.13}$$

that leads to the formation of HCO^+ *via* reaction with H_2:

$$CO^+ + H_2 \longrightarrow HCO^+ + H. \tag{1.14}$$

Reactions involving nitrogen are generally less well understood (Hartquist & Williams 1998, Chapter 4). Because of its high ionisation potential (14.5 eV), nitrogen is predominantly neutral in the diffuse ISM, and NH is believed to be formed (van Dishoeck & Black 1986) by the reaction

$$N + H_3^+ \longrightarrow NH_2^+ + H \tag{1.15}$$

followed by

$$NH_2^+ + e \longrightarrow NH + H \tag{1.16}$$

from which CN is produced *via*

$$C^+ + NH \longrightarrow CN + H^+. \tag{1.17}$$

In the absence of H_3^+, chemical models fail to reproduce the observed abundances of NH and CN in diffuse clouds by a considerable degree (Wagenblast *et al.* 1993), whereas the abundances of other species can still generally be accounted for. Thus Wagenblast *et al.* (1993) were led to the inclusion of grain surface reactions in their chemical model, whereby, for example, nitrogen atoms colliding with grains react with hydrogen to form NH that is subsequently returned to the gas phase. The efficiency of NH production in this manner was determined to be about 30% for each N atom-grain collision. Dust may be an important catalyst in many chemical reactions in the

diffuse ISM, with the potential for forming complex organic molecules that cannot be produced by conventional gas-phase chemistry.

Black & van Dishoeck (1991) addressed the issue of cloud structure as a potentially important factor in the modelling of diffuse and translucent interstellar clouds. Typically, models consider plane-parallel, homogeneous slabs of matter, but recent observations of small-scale structure in the diffuse ISM (see for example Heiles 1997; Crawford 2003) call the validity of such models into question. The nature of small-scale structure of the ISM is poorly understood, but more information regarding its properties is uncovered with each new study. Inevitably, marked fluctuations in the abundances of interstellar species over spatial scales of $\sim$ 10 AU must impact upon the chemistry associated with these clouds and their surroundings. The chemical modelling of small-scale density enhancements in the interstellar medium has begun (see Bell *et al.* 2005, for example), predicting observable abundances of molecules where, prior to the discovery of wide-spread small-scale structure, negligible amounts were expected.

1.2 Diffuse interstellar bands (DIBs)

The diffuse interstellar bands (DIBs) represent a set of broad absorption features in the spectra of stars observed through clouds of interstellar gas and dust. Heger (1922) observed 'stationary' absorption bands at 5780 Å and 5797 Å in the spectra of early-type spectroscopic binaries as part of a study on the possible interstellar nature of the sodium D and calcium H and K lines. Approaching 300 different DIBs have since been discovered in the spectra of reddened stars (Jenniskens & Desért 1994; Galazutdinov *et al.* 2000b), each characterised by a unique wavelength[6]. The interstellar origin of the λ5780, λ5797, λ6203, λ6270, λ6284 and λ6614 DIBs was confirmed by Merrill and co-workers (Merrill 1934; Merrill & Wilson 1938) in a systematic study that measured no shift in the wavelengths of the DIBs relative to the shifting stellar lines of binary stars. The DIBs were described as 'somewhat diffuse' with a similar breadth to stellar absorption lines, and a Doppler broadening mechanism arising from kinetic motion

[6]In this thesis, individual DIBs are identified by their (average) rest peak absorption wavelength rounded to the nearest angstrom, for example, the DIB with average peak-absorption at 6613.56 Å (Galazutdinov *et al.* 2000b) is labelled λ6614. However, for historical reasons the broad diffuse band that peaks at 4428.39 Å (Snow 2002) is referred to as λ4430.

of the interstellar gas was deemed very improbable. Merrill & Wilson (1938) noted that the strengths of λ5780 and λ6284 were correlated, and that their equivalent widths (see Section 2.4.3) scaled with the amount of dust (measured by E_{B-V}), indicating a possible origin in small solid particles that are known to exhibit relatively narrow absorption lines when their temperatures approach absolute zero.

From their good correlation with the amount of extinction and their location in the visible-NIR region, DIBs could be considered to represent structure in the optical extinction curve. Diffuse interstellar bands are apparently observed wherever dust is present, even in sightlines with exceptionally low E_{B-V} (Galazutdinov *et al.* 1998) and in sightlines showing a lack of any gas-phase molecular material (Krełowski *et al.* 1992). However, the correlation between DIB equivalent widths and reddening is imperfect, with an equivalent width scatter of about a factor of two about the mean for a given E_{B-V} for the well-studied λ5780 DIB (Herbig 1993). Dust grain properties are known to vary between different interstellar sightlines as implied by the variations in the UV extinction curve, however, correlations between DIB equivalent widths and the UV extinction curve parameters (bump height, bump width, FUV rise) are rather weak (Desért *et al.* 1995), indicating that the DIB carriers are not the same as the small dust grains responsible for the behaviour of the UV extinction curve. The strength of λ5780 was found to weakly anti-correlate with the steepness of the FUV rise, which itself correlates with the CH and H_2 abundances. Overall, DIB strengths were found to be much more variable than the observed variations in the UV extinction curve, suggesting that factors other than the properties of the dust have a significant effect on the abundance of the DIB carriers. The study by Desért *et al.* (1995) showed no link between R_V and the DIB strengths.

Although not as tight as the correlations with E_{B-V}, DIB strengths also correlate well with the column densities of H I and Na I as demonstrated by Herbig (1993). In addition, a lack of correlation was found between DIB strengths and the amount of H_2. It is apparent that factors other than the total column density of dust or the total amount of gas influence the DIB strengths, and that the abundances of their carriers are not strongly associated with the conventional diffuse-cloud chemistry that is generally believed to give rise to the small polyatomic molecular species that have a chemistry that is closely coupled to H_2. Indeed, the fact that DIBs are observed in the relatively un-

shielded[7] diffuse clouds with low extinction indicates that their carriers are relatively resistant to destruction by UV, such that they either cannot be small molecules, or they must be produced very rapidly, by chemical mechanisms that are poorly studied (or unknown).

The principal set of interstellar variables that seem likely to affect the strengths of the DIBs include (a) the rates of the chemical mechanisms that produce (and, perhaps, maintain the abundances of) the carriers; (b) the strength of the radiation field that has the potential to modify the carriers by photodissociation or photoionisation; (c) the kinetic temperature of the ISM and the shape and strength of the radiation field, that might modify the degree of excitation of the carriers, or alter the properties of mantles built up on solid interstellar particles; (d) the precise chemical composition of the individual carriers, alterations of which could lead to changes in the DIB spectrum; and (e) the electron density and electron temperature of the gas in which the carriers reside, factors that are capable of altering dissociative electron recombination rates and the ionisation balance and internal temperature of the carriers. Transient interstellar processes such as supernova shocks may result in significant processing of the interstellar dust and would cause alterations to the chemistry of the shocked region (Draine & Salpeter 1979), with the potential to affect DIB carrier abundances. Many physical and chemical factors are involved in modifying the variables mentioned above such that determining the factors important for the behaviour of the DIBs presents a formidable task. Understanding the processes that affect the DIB spectrum should assist in constraining the nature of the carriers.

The observation that different DIBs behave differently to each other in sightlines with distinct physical and chemical characteristics has lead to significant advances in the understanding of the properties of the carriers. Due to their proximity in wavelength and relatively large equivalent widths, the λ5780 and λ5797 DIBs have been studied intensively in this respect.

Krełowski & Walker (1987) and Krełowski & Westerlund (1988) showed that the strength ratio $\lambda5780/\lambda5797$ (expressed using either the central depths or equivalent widths of the features) is variable by a factor of up to three for a given E_{B-V}. The line of sight towards ζ Oph represents the archetypal case of λ5797 being relatively strong

[7] *i.e.* not shielded from the UV photons liable to cause photoionisation and photodissociation of small molecules.

	ζ-type	σ-type
W_{5780}/W_{5797}	$\lesssim 3$	$\gtrsim 4$
FUV rise	Steep	Flat
2175 Å bump	Broad	Narrow
Narrow (KW III) DIBs	Strong	Weak
'Weak DIBs'	Many	Few
Small molecules	Present	Absent

Table 1.1: Summary of some of the observed relative characteristics of ζ and σ-type diffuse interstellar clouds.

compared to λ5780, and σ Sco the opposite, with λ5780 relatively strong compared to λ5797. This was taken as evidence that the two bands are caused by different carriers that occur in variable relative abundances across a range of interstellar environments. The properties of 'σ-type' clouds (those with a λ5780/λ5797 strength ratio similar to that towards σ Sco) were deemed to be different in some way to the properties of 'ζ-type' clouds (those with a λ5780/λ5797 strength ratio similar to that towards ζ Oph).

Subsequent research has shown a plethora of differences between ζ-type and σ-type clouds (reviewed by Krełowski & Sneden 1995), including the steepness of the FUV rise in the extinction curve, the width of the 2175 Å bump and the presence or absence of of 'weak DIBs'. Particularly notable is the presence of large abundances of molecules (including H_2, CH and CN) in ζ-type clouds that are usually absent from σ-type clouds. A summary of some of the observational differences between ζ and σ-type clouds is shown in Table 1.1.

The relationship between the λ5780/λ5797 ratio and the molecular content of interstellar clouds has been studied by Krełowski *et al.* (1999) and Weselak *et al.* (2004), with the conclusion that λ5797, and other associated (usually relatively narrow) DIBs are stronger in denser clouds where the UV radiation is attenuated and diatomic molecules are abundant. The λ5780 DIB is relatively weak in such clouds, with the implication that its carrier apparently favours a less dense, more strongly UV-irradiated environment.

Apparently both λ5797 and λ5780 vary in different ways as a function of cloud density. It has been shown (Fossey & Somerville 1995) that the λ5780 DIB is weakened with respect to E_{B-V} (and also with respect to the strength of λ5797) when observed along relatively dense interstellar sightlines and in sightlines with high CH column densities relative to reddening. Similar effects have been observed for other DIBs, and

Ehrenfreund & Jenniskens (1995), among others, have shown that DIBs are generally weaker with respect to reddening along denser sightlines. Different diffuse bands were found to weaken with respect to E_{B-V} at different rates as the density of the matter in the sightline increased, interpreted as a consequence of differing ionisation potentials of the carriers that cause differential variations in their abundances following the attenuation of interstellar UV-field with increasing cloud density.

1.2.1 DIB strengths and families

The good correlation between the strengths of λ5780 and λ6284 observed by Merrill & Wilson (1938) has since been extended extended to include a close correlation with the DIBs λ6196 and λ6203 and λ6270 (Chlewicki *et al.* 1987). As discussed above, λ5780 and λ5797 are not correlated, but Chlewicki *et al.* found that λ5797 correlates well with λ6376 and λ6614.

Thus, diffuse interstellar bands may be classified into groups or 'families'. The members of a family exhibit similar patterns of strength variation between different sightlines, but poor correlations with the members of different families. From observations of correlated DIB behaviour in different sightlines, Krełowski & Walker (1987) and Westerlund & Krełowski (1989) classified some of the stronger DIBs into three families: KW I — including the very broad, relatively shallow λ6180 and λ4430 DIBs; KW II — including the relatively symmetric, generally moderately broad λ5780, λ6196, λ6203, λ6270 and λ6284 DIBs; and KW III — including the narrow, asymmetric λ5797, λ5850, λ6376 and λ6379 DIBs. It is interesting to note that the KW III DIBs are strong only in relatively dense interstellar environments (as inferred from the presence of molecules), and that this family consists only of narrow, asymmetric DIBs.

1.2.2 DIB profiles

DIBs generally have peak absorption strengths of up to $\sim$ 30%[8]. Each DIB has an apparently different absorption profile, with a full-width at half-maximum (FWHM) in the range 0.5 Å $\lesssim$ FWHM $\lesssim$ 30 Å (see Jenniskens & Desért 1994). It is generally the

[8]Strengths correlate with the amount of extinction, though most DIBs are weaker than 10% even in heavily-obscured sightlines. New weaker DIBs are found with each increase in survey sensitivity.

case however, that a particular DIB profile, aside from overall equivalent width, shows little or no apparent variation between sightlines characterised by markedly different physical and chemical conditions. Using the DIB profiles observed in the sightline towards HD 186745 (a sightline that shows little Doppler splitting in the gas traced by K I), Herbig & Soderblöm (1982) determined that the narrow λ6196 and λ6614 diffuse interstellar bands towards the heavily obscured star HD 183143 could be decomposed into separate contributions at Doppler velocities corresponding to the two separate interstellar K I Doppler components along this sightline. Thus, the concept of 'intrinsic' DIB profiles was born, advanced by Westerlund & Krełowski (1988) in studies of sightlines with clear Doppler splitting in interstellar Na I. It was shown that the profiles of the λ5780, λ5797, λ6196 and λ6203 DIBs could be reproduced using a sum of Doppler shifted intrinsic DIB profiles from sightlines with single, narrow (in velocity space) clouds of Na I. The DIB component velocities matched the Na I component velocities, but the DIB component strengths did not always match those of the Na I components in the same ratio. Apparently, the DIB profiles are very similar in different clouds; time and again, almost identical profiles are observed by different studies down lines of sight towards stars in different parts of the Galaxy as can be seen, for example by comparison of the DIB surveys of Jenniskens & Desért (1994); Galazutdinov *et al.* (2000b); Seab & Snow (1995); Krełowski & Schmidt (1997).

From further high resolution, high signal-to-noise studies of DIBs, a wealth of information has emerged regarding the presence of intrinsic structure located within their profiles. Performing such analyses requires the observation of DIBs in 'single-cloud' sightlines, *i.e.* those whose atoms and ions show a single, narrow (Gaussian) component in velocity space, free of Doppler splitting. It is difficult to satisfy this criterion exactly, but even the narrowest intrinsic DIB profiles have FWHM $\gtrsim$ 20 km s^{-1} when placed on a velocity scale, such that they are affected little by a small velocity dispersion (*e.g.* Gaussian with FWHM $\lesssim$ 5 km s^{-1}) in the gas in which they are produced.

The λ6614 and λ5797 DIBs were first observed at ultra-high resolution (capable of resolving features with FWHM $\sim$ 0.5 km s^{-1}) in single-cloud sightlines by Sarre *et al.* (1995) and Kerr *et al.* (1996), who discovered 'triplet' and 'doublet' structure respectively in these two DIBs. In λ6614, the structure was convincingly modelled as a rotational contour arising from the vibronic transitions of a large ($\sim$ 20 atom), symmetrical molecule. The narrowest structures inside the profile of the λ6614 absorption

band had a FWHM of ~ 7.5 km s^{-1}, significantly broader than the velocity distribution of the interstellar gases in the sightlines studied. The λ5797 profile was shown by Kerr *et al.* (1996) to exhibit weak 'ultra-fine structure' components in the base of its absorption profile, with Doppler FWHM ~ 1.7 km s^{-1}, comparable to the velocity spread of the neutral atomic gas in the three sightlines for which observations were made.

Sub-structures inside diffuse interstellar band absorption profiles were also found by Krełowski & Schmidt (1997) for λ5850, λ6234, λ6379 and λ6660. Fascinatingly, the relative intensities of the sub-structure peaks were found to be variable for the λ6614 and λ5797 bands between different sightlines. No sub-structure variability was observed for λ5780 (similar to the results of Seab & Snow 1995), or for λ6196. The variations of the intrinsic sub-structure of the λ6614 and λ5797 DIBs has been studied in detail by Walker *et al.* (2000) and Galazutdinov *et al.* (2002), confirming the result that there exist small but significant variations in the profiles of some of the diffuse interstellar bands. In a detailed study of the strong λ4430 DIB by Snow (2002), the band profile was not shown to exhibit any significant variations between sightlines, and showed no evidence for any sub-structure. The profile of λ4430 was found to be well described by a Lorentzian function with FWHM ~ 18 Å, implicating lifetime (natural) line-broadening as a possible cause of the diffuseness of this DIB.

One explanation for the structure of the profiles of the narrower DIBs is that they result from 'rotational contours' of molecules which are sufficiently massive that their rotational absorption lines are very closely spaced and therefore 'blend' together into a continuous profile. The observed variations in the sub-structure of the bands is then explained as arising from temperature-dependent variations in the rotational level populations (see for example Cami *et al.* 2004). Alternatively, Webster (1996) hypothesised that the structures arise from variations in the number of ^{13}C atoms in a large molecule (of 50 ~ 100 atoms) composed predominantly of ^{12}C.

1.2.3 DIB carriers

Attempts to assign diffuse interstellar bands to the spectroscopic transitions of solid-state or gas-phase species have been largely unsuccessful. The subject recently received a comprehensive review by Herbig (1995). The only DIB to have received a firm assignment is located at 1369.1 Å (its identity as a true DIB may have been ques-

tionable anyway due to its wavelength being well short of the main DIB spectrum), and was found by Watson (2001) to coincide with a vibronic transition of gas-phase CH, broadened by pre-dissociation.

The correlation of DIB strengths with E_{B-V} led many authors to suspect that they are caused by solid particles that make up (part of) the population of interstellar dust grains. Early theories were developed by, for example van de Hulst (1948), who proposed that the DIB carriers were 'impurities', perhaps rare-earth ions, embedded within spherical dust particles. Such impurities would give rise to resonances in the light scattering cross-section at the wavelengths of the impurity's electronic transitions, producing a broad, symmetric absorption profile. The theory predicted emission fringes on the blue side of the absorption feature, but such 'emission wings' have not been conclusively observed. This theory was advanced by Shapiro & Holcomb (1986), with the conclusion that the observed profiles of λ5780 and λ6614 could not be matched by impurities in graphite or magnetite, but impurities in grains of dirty silicates or ices with sizes up to $\sim 0.1\ \mu$m could be made to fit the observations. However, the required specific impurity distributions were deemed too contrived to occur consistently in the diffuse ISM to produce DIBs with invariant profiles and peak absorption wavelengths.

Asymmetric dust grains cause polarisation of starlight, observed ubiquitously throughout the ISM. If a component of the dust grain population was responsible for the DIBs, then unless they were highly symmetric (which again seems contrived), wavelength-dependent variations in the polarisation of the starlight should be observed across the DIB profiles (Greenberg & Stoeckly 1971). Searches for changes in polarisation have so far shown no evidence for DIB polarisation, for example in the dedicated studies made by Martin & Angel (1974) and Adamson & Whittet (1992), casting further doubt over the possibility that DIBs are caused by solid particles. However, in these studies, the possibility that the DIBs are caused by a *weakly* polarising population of dust grains could not be ruled out.

Atoms in the gas phase, due to their high abundances and strong resonant transitions provide an attractive potential set of DIB carriers. Possible line-broadening mechanisms include pre-ionisation (with autodetaching upper levels) or transitions to very short-lived upper states. Herzberg (1955a) proposed that electronic transitions of atomic anions such as O^- or C^- with upper states close to the electron detachment

threshold could provide transitions in the optical. Similarly, Rudkjøbing (1969) proposed that the λ4430, λ4760, λ4890 and λ6180 DIBs were caused by auto-ionising transitions of H^-. The wavelengths of these DIBs are close to the energies of resonances in the electron scattering cross-section of neutral hydrogen, indicating the possible presence of energy levels to which transitions from the ground electronic state could occur. Several difficulties with this theory were raised by Herbig & Leka (1991), including doubts as to the reality of the transitions, leading to its rejection.

The remarkable constancy of DIB peak absorption wavelengths, the occurrence of narrow DIBs, and the presence of fine structure within their profiles leads to the likely conclusion that at least some of the diffuse interstellar bands are caused by vibronic transitions in gas-phase molecules. The apparent observation of DIBs in emission in the 'Red Rectangle' nebula surrounding the star HD 44179 (Scarrott *et al.* 1992) also suggests a molecular carrier. The large abundance of interstellar carbon, and its tendency to form complex molecules through sp^2 and sp^3 bond hybridisation makes organic molecules attractive candidates for at least some of the DIBs. Ehrenfreund & Foing (1997) considered the possibility of C_{60}^+ as carrier of two DIBs in the NIR, and $HCOOH^+$ was proposed by Herzberg (1988), although no definitive assignments have yet been made.

A new branch of DIB carrier studies was spawned in the 1980's when it was realised that species containing large carbon chains and aromatic structures could survive in the strong UV fields of the diffuse ISM, by absorbing photons and redistributing the energy into vibrational modes *via* the process of internal conversion (see for example Omont 1986). Their extreme stability allows PAHs (planar aromatic sp^2-bonded carbon rings with hydrogen atoms located around their periphery) to absorb photons that would cause the dissociation of other molecules. PAHs may contain up to several hundred carbon atoms and can be modified to form a vast array of different species that are likely to be found in the ISM, for example with the addition of oxygen or nitrogen-containing side-groups, or the removal of peripheral hydrogen atoms. The 'PAH-DIB' hypothesis has been reviewed by Crawford *et al.* (1985), Leger & D'hendecourt (1985) and more recently by Salama *et al.* (1999) and these molecules continue to receive much attention as a viable explanation for at least some of the diffuse interstellar bands. Studies have shown that PAHs and their ions possess strong electronic transitions in the optical (see for example Salama & Allamandola 1994; Ruiterkamp *et al.* 2002) though

even after extensive laboratory and *ab initio* studies of the spectroscopy of a plenitude of PAHs and their related structures, no DIB has yet been assigned to any PAH-type molecule.

Chapter 2

Optical echelle spectroscopy

2.1 The visible spectrum

Even without modern detectors, the science of astronomy flourished for thousands of years using only the visible spectrum. A large proportion of the baryonic matter in the Galaxy is luminous in visible light, rendering much of the local Universe directly observable — at least, that which is not obscured by dust — which is why optical astronomy remains so important. In contemporary cosmological theories, baryonic matter accounts for only ~ 4% of the total energy budget of the universe, but the effects of non-baryonic dark matter on the physical and chemical processes with which this thesis is concerned are generally considered to be negligible.

Using an optical spectrograph of modest resolution and a suitable detector, it is possible to derive the abundances and temperatures of different atoms in the solar photosphere and chromosphere based on the profiles of their absorption spectra, superimposed on the solar continuum. Examination of a typical absorption line reveals a smooth, broad 'bowl-shaped' profile that arises predominantly as a result of the Sun's rotation. The Maxwellian velocity distribution of atoms in the hot atmospheric gas,'pressure-broadening' (caused by distortion of atomic energy level structures in atom-atom collisions), and turbulent motion of the gas also contribute towards the shape of the line-profile. From precise measurements of spectral line shapes, information about these processes can be obtained.

In contrast to stellar lines, interstellar atomic absorption lines are much narrower, rep-

resenting predominantly cool gas with relatively low kinetic temperatures and turbulent velocities. Temperatures and densities in the cool ISM are so low that pressure-broadening is insignificant, and the lengths of gas columns typically observed are sufficiently long that localised turbulence is averaged out into a Gaussian velocity distribution.

The information that can be derived from an astronomical spectrum depends on the properties of the object being observed, and on the characteristics of the spectrum obtained. Many parameters are important in defining the properties of a spectrum, but the main four of interest for this work are as follows:

1. The resolving power,

$$R = \frac{\lambda}{\Delta\lambda}. \tag{2.1}$$

$\Delta\lambda$ is the FWHM of the spectrograph's point spread function (PSF), and is essentially the smallest wavelength separation between two narrow, equally intense emission features that can still be distinguished by eye. For spectrographs that use a grating to disperse the light, R is approximately constant over the whole range of wavelength coverage, and depends on the density of grooves in the grating, and other characteristics of the spectrograph's optics. Spectral resolving power is often quoted as a velocity 'resolution' c/R to identify the smallest directly observable Doppler shift between two discrete, cold (*i.e.* narrow intrinsic line-width), gas clouds. R is also dependent on the width of the entrance aperture of the spectrograph, usually a slit, which if opened past its optimal width in order to accommodate a larger object image (caused, for example by poor seeing) degrades the resolution because the slit projects to a finite width on the detector.

2. The dispersion,

$$D = \frac{d\lambda}{dx}, \tag{2.2}$$

where x is distance along the dispersion direction of the spectrum at the detector. D measures how 'spread out' the spectrum will be, with implications for the smallest measurable wavelength step $d\lambda$, and the intensity, and therefore the S/N of the spectrum.

3. The signal-to-noise ratio (S/N),

$$(\mathrm{S/N}) = \frac{I(\lambda)}{\sigma(\lambda)}, \tag{2.3}$$

defined as the ratio of intensity $I(\lambda)$ at a given wavelength λ to the standard deviation per detector pixel $\sigma(\lambda)$, of the Gaussian distribution of the noise of the data (under the assumption of Poisson statistics). $I(\lambda)$ and $\sigma(\lambda)$ are usually measured in the spectral continuum and averaged over a discrete wavelength range. The S/N gives a measure of the size of the minimum discernible change in $I(\lambda)$ from one pixel to the next, and depends on the brightness of the object being observed, the length of exposure (integration time), the dispersion of the spectrum and the efficiency of the telescope, the spectrograph and the detector's optics. When 'Poisson statistics' are achieved, in the situation that the Poisson noise of the signal far exceeds noise in the spectrum introduced by other sources (detector noise, fringing etc.), σ scales as $\sqrt{N}$, where N is the number of photons collected per pixel.

4. The wavelength coverage, *i.e.* the range of wavelengths recorded in the final spectrum.

For observations of the diffuse ISM, a range of spectrograph parameters are applicable, depending on what is being studied. In most cases, there is a compromise between the above parameters that prevents the optimum of any one parameter from being achieved, although D is largely determined by the size of the pixels on the detector and the required resolution. Balancing the wavelength coverage with the required signal-to-noise and resolution creates the main difficulty, as interstellar atomic and diatomic molecular lines are very narrow due to the low kinetic temperature of the gas, but are located over a broad range of wavelengths spanning most of the optical region. It is desirable to achieve the highest S/N and resolution possible for detailed analysis of interstellar gas from optical lines.

For the study of the diffuse interstellar bands, the resolution constraint may be relaxed somewhat in favour of increased S/N for these weak absorption features. A S/N in the continuum of $\gtrsim 500$ is desirable to achieve a relative S/N of ~ 50 inside the stronger DIBs (with peak absorbtion strengths $\sim 10\%$). Although sub-structure is detected in some of the DIBs up to the resolving power limit of $R \sim 10^6$ provided by the best

presently available spectrographs[1], the majority of the known fine structure in DIB profiles is reproduced accurately at $R \gtrsim 5 \times 10^4$ (see Krełowski & Schmidt 1997). Reduced resolving power permits higher S/N per pixel as the dispersion can be reduced, focusing more light into each pixel.

The shortest wavelength a diffuse interstellar band has been observed at is 1369.13 Å (Tripp *et al.* 1994), and the longest at 13,175 Å (Joblin *et al.* 1990). DIBs are generally not found in the UV, and soon after its discovery, the λ1369.13 'DIB' was assigned to a pre-dissociating transition of CH by Watson (2001) (see Section 1.2.3). The vast majority (~ 95%) of the known DIBs lie between 4000 and 8000 Å (Herbig 1995), so that the DIB spectrum can be studied almost entirely using optical spectroscopy. The current instrument of choice for DIB observations is the echelle spectrograph due to its combination of high resolution and dispersion with broad wavelength coverage and efficient optics.

2.2 The echelle spectrograph

2.2.1 Optics and detectors

Employing a finely ruled echelle grating and a cross-dispersing prism, the echelle spectrograph takes starlight (passed through a slit and colimated) and produces an image of its spectrum as a series of near-parallel strips across the detector. Details of the design and function of a typical echelle spectrograph, HIRES (mounted on the Keck telescope on Mauna Kea, Hawaii), can be found in Vogt & Penrod (1988). A schematic diagram showing the principle of operation of the echelle spectrograph is shown in figure Figure 2.1 and a colour image of a typical echelle spectrum (referred to as an 'echellogram') as produced on the detector is shown in Figure 2.2. Each strip of spectrum spans a short wavelength range of typically $\lesssim$ 100 Å. Therefore, around 50 to 100 strips are required to cover the whole of the optical wavelength range from around 3000 to 10,000 Å. The wavelength coverage achieved for a given dispersion is generally limited by the size and wavelength response of the detector. It is therefore common to image a portion ($\lesssim$ 5000 Å) of the total optical spectrum at a time, using one CCD optimised to

[1]The Ultra High Resolution Facility (UHRF) of the Anglo Australian Telescope, Siding Spring Observatory, Australia achieves $R \sim 10^6$, at very high dispersion.

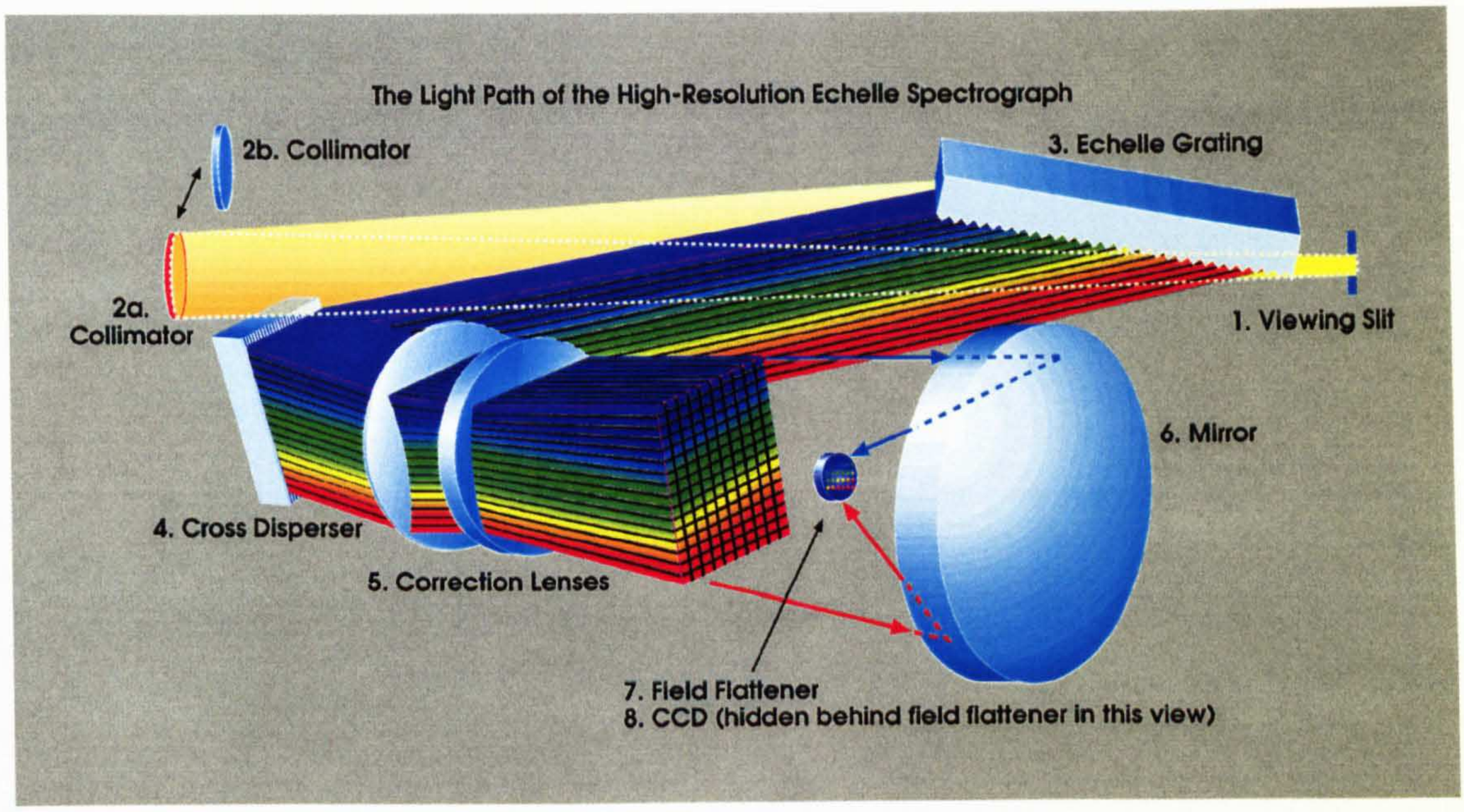

Figure 2.1: Schematic diagram showing the light path and the most important optical elements of the Keck HIRES, a typical echelle spectrograph (image used with the permission of S. S. Vogt). Starlight enters from the telescope through the viewing slit (1) on the right, is collimated (2), then split into a series of spectra by the echelle grating (3) which are then separated by the cross disperser (4). Optical elements (5, 6 and 7) focus the image of the spectrum onto the CCD detector (8).

record wavelengths in the UV, blue and yellow, and a different, red-sensitive detector for the orange, red and IR. The quantum efficiency of the detector is thus optimised for the particular wavelength of light received, also helping to reduce fringing of the spectrum in the red and IR (caused by internal reflections in modern, thin CCDs) that can cause severe degradation of S/N.

Practical considerations make it difficult to change detectors during the night, so that systems involving a separation of the starlight into two halves: 'red' and 'blue', divided near the yellow and sent through separate spectrometers to separate detectors, are now being used. Thus, near-complete coverage of the optical region in a single exposure can be achieved.[2]

Successive strips of spectrum correspond to successive orders of the diffraction fringes of the echelle grating. To achieve the high dispersion required by high resolution observations, order numbers of between ~50 and 150 are used, and hence the spectra

[2]The UVES spectrometer on the Very Large Telescope (VLT), European Southern Observatory, Chile, for example.

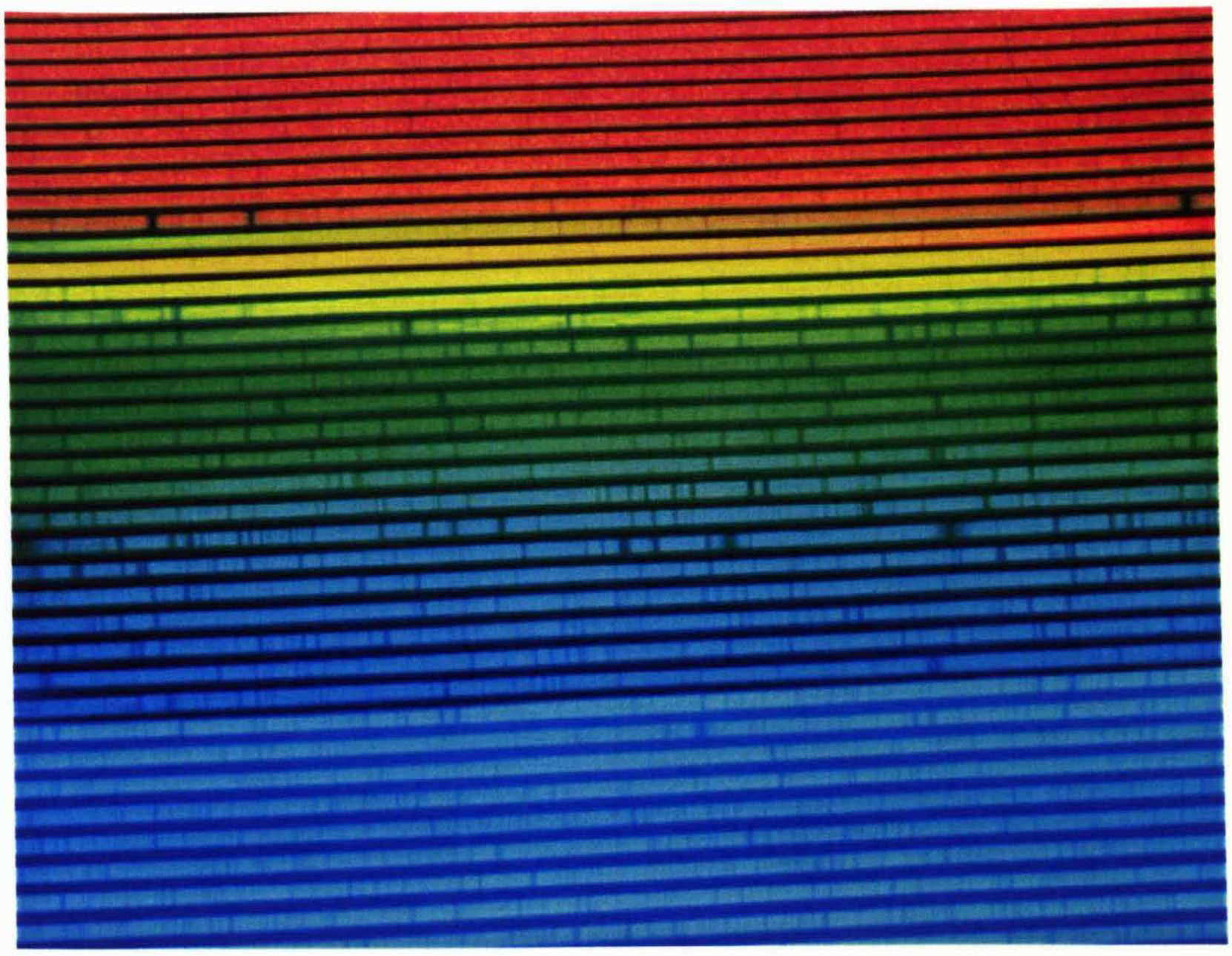

Figure 2.2: This image of an UCLES spectrum is an example of a typical echelle spectrum (or 'echellogram'), produced on the CCD detector at the Anglo-Australian Telescope, Siding Spring Observatory, Australia. The strips of spectrum are images of the different diffraction orders produced by the echelle grating, separated vertically by the cross-disperser. Numerous dark absorption lines are visible in the stellar continuum.

overlap. Adjacent superimposed orders are displaced in wavelength with respect to each other by an amount called the free spectral range (FSR). Blazing the echelle grating to direct light into only these orders means that each order is only illuminated over a small wavelength range, the centre of which differs between successive orders by the FSR. Each order drops rapidly in intensity away from the central wavelength, so it is usual to blaze adjacent orders such that their wavelength ranges overlap. This has the useful consequence of introducing redundancy into the spectrum to cross-check features, as any one wavelength may be reproduced in two or more different orders on different parts of the detector. A cross-dispersing prism splits the orders spatially (in the direction perpendicular to the dispersion), to ensure they do not overlap on the detector.

2.2.2 Calibrations

Modern CCD detectors suffer very little from dark current during observations, and for the high signal levels of the spectra concerned in this thesis, the dark current represents a negligible fraction of the total signal, and has been ignored.

Each pixel in the CCD detector responds at a different rate to received photons (*i.e.* with different quantum efficiency), and for each pixel, this rate also varies independently as a function of wavelength. In conjunction with the spectrum of interest, spectra of a uniform white light source (usually a quartz-lamp), are obtained to correct for this. Free of spectral features, exposing the CCD to such a spectrum will give an image of the response-rates of the pixels relative to each other. Based on the very closely linear response of the pixels, dividing the stellar spectrum through by the quartz 'flat field' spectrum cancels out the variations in pixel response rate, leaving a true representation of the stellar spectrum. 'Bad pixels' on the CCD (those that do not behave linearly), may also be identified this way and interpolated away using neighbouring pixels.

Troublesome fringing of spectra in the NIR-IR can be largely removed by flat-fielding; fringing is present in the quartz-lamp's spectrum, and is removed during flat-field division. Fringe cancellation is rarely complete however, and residuals are left in the object spectrum where fringing is severe. Increasing the frequency of flat-fields taken during the observing period can help if fringing is time-variable, for example if the spectrograph's optical configuration changes during the night.

Slight movements of the intricate optics of a spectrograph over time, due to vibrations or temperature fluctuations, mean that periodic wavelength calibration exposures are essential throughout the observing period. Subtle changes in the position of the spectrum relative to the detector pixels may thus be monitored. Typically, a Thorium-Argon (Th/Ar) lamp is used to give a wavelength scale because of the high density spectrum of well known emission lines. The Th/Ar emission line spectrum was assigned using wavelengths in air at 15 °C, pressure 760 mmHg (see de Cuyper & Hensberge 1998, and references therein).

On the detector, two principal axes of the spectrum are recorded, the wavelength axis (along the dispersion direction), and the spatial axis (parallel with the slit of the spectrograph, recording the portion of sky permitted by the slit's dimensions). Spectrograph optics may create a distorted image of the spectrum, manifested as curvature in

the principal axes relative to the CCD pixel rows. This results in a degradation in the resolution and a distortion of the shape of the point spread function and wavelength scale. In echelle spectra, the slit length is typically short (~ 5″), so that spatial distortion of the spectrum is small. In this case, the wavelength scale applicable to the spatial centre of the spectrum also applies with negligible error at the edges. However, if the curvature is very severe it is necessary to trace the position of the arc lamp emission lines along the spatial direction of the spectrum, measuring how the wavelength varies as a function of distance along the spatial axis. This creates a 2 dimensional 'distortion map' of $\lambda = \lambda(x, y)$ where (x, y) are rectangular spatial co-ordinates on the detector, and allows the distortion of the object spectrum to be removed through resampling and interpolation of the CCD image.

Another basic calibration for echelle spectra is to remove the artificial intensity distribution imposed on each order by the blaze of the grating. For a stellar spectrum $I(\lambda)$, the recorded spectrum of a given order n is $I(\lambda)B_n(\lambda)$, where $B_n(\lambda)$ is the 'blaze function' of order n. If the quartz-lamp spectrum has been subjected to the same optical processing as the starlight, and assuming the quartz-lamp spectrum does not vary as a function of λ, the flat-field spectrum for order n is $AB_n(\lambda)$, where A is a constant that may be removed by normalising the the flat-field. Thus the blaze function for each order is known, and may be divided out. One caveat of this method is that the quartz-lamp is often located in a convenient place near to the spectrograph, and so its light does not take an *identical* path to that of the starlight and the resulting quartz-lamp spectrum's blaze function ends up as $B'_n(\lambda) \neq B_n(\lambda)$, though generally $B'_n(\lambda) \simeq B_n(\lambda)$, which is sufficient for the 'blaze-correction' of most spectra. Differences between the quartz-lamp and stellar spectrum blaze functions are small, but may be significant, particularly at the edges of the orders.

An alternative way to determine $B_n(\lambda)$ is to take an exposure of a 'standard' star that has a relatively flat spectrum and then normalise the orders to peak intensities of 1. Because of the inherent shape of a star's black-body spectrum, and the stellar and telluric absorption and emission lines, stellar spectra are generally not very flat. However, a polynomial function can be fitted to the shape of the standard star spectrum in each order, and narrow atmospheric stellar and telluric absorption lines rejected from the fitting procedure. The black-body function is slow moving, so can be assumed to be flat across a single echelle order. Nevertheless, it may be desirable to include the black-

body shape in a calculation of a modified blaze function $B_n^m(\lambda) = I_{\text{black-body}}(\lambda)B_n(\lambda)$ to be divided out. If the temperature of the standard star is chosen to match that of the programme star of interest, then removal of the black-body shape from the programme star's spectrum may be achieved by dividing by $B_n^m(\lambda)$, such that a purely interstellar (and stellar photospheric) spectrum remains. The obvious problem with using a standard star instead of a quartz-lamp is that very broad features in the standard star's spectrum cannot be rejected in fits to the order profiles, so this must be considered when looking at the final, blaze-corrected interstellar spectra.

The presence of stellar atmospheric absorption or emission features poses a challenging problem for interstellar absorption studies. To examine a true interstellar spectrum towards an OB star, it would be necessary to remove the numerous atomic and ionic absorption lines that litter a star's spectrum, but the critical problem is that each star is different. The Harvard (MK) classification system attempts to put spectroscopically similar stars into categories. The correlation between the stellar features of stars within a given category is good, but not perfect. The detailed shapes and intensities of features are specific to the macroscopic temperature and density structure and precise composition of the stellar atmosphere, and generally cannot be modelled well enough to be predicted and removed with confidence. Each case of stellar line 'contamination' must be treated individually to assess the degree to which interstellar features are affected. In cases where stellar lines are broad compared to interstellar features, provided their profiles are smoothly varying, they can usually be fitted and divided out without significantly affecting the profiles of the interstellar features.

Stellar spectral lines are Doppler-broadened due to stellar rotation, with a corresponding reduction in core intensity. If the rotation speed is high enough, weak features are smeared so thin that they become almost invisible, and sufficiently broad that narrow interstellar features are easily distinguishable against them. O and B-type stars have relatively few metal lines in their optical spectra, providing the best targets for optical interstellar observations.

A final step is the removal of narrow telluric absorption features caused primarily by water and diatomic oxygen in the Earth's atmosphere. Particularly severe in the red and IR, the spectrum of telluric absorption spans a range of optical depths $\tau \sim 0 - 10$, though the majority of features have $\tau \lesssim 0.1$.

A spectrum of a 'telluric standard' (ideally a bright, unreddened, rapidly-rotating early-

type star) is observed, preferably at around the same time as the programme star and at a similar sky elevation so as to sample approximately the same air mass[3]. Dividing this into the programme star spectrum removes the telluric lines. High S/N of the telluric standard spectrum is imperative so as not to degrade the S/N of the programme star spectrum. Slight shifting and scaling may be required to match the telluric features exactly to account for any shifts in the spectrograph's optics and any differences in the optical depth of the atmosphere between observation of the star and standard. For selected telluric lines in flat regions of the spectrum, least-squares maximisation of the correlation function between the telluric standard and programme star gives the least biased values for the best shift and scale to apply. 'Telluric-correction' of the spectra used in this thesis was performed using the IRAF **noao.onedspec.telluric** procedure. The correlation maximisation function occasionally gave spurious results, in which case the shift and scale were manually adjusted 'by eye' to achieve the best possible cancellation (minimum residual RMS) of isolated telluric features. Thus, complete removal of telluric absorption was achieved for telluric line optical depths with $\tau \lesssim 0.5$. The main spectral regions of interest subject to telluric contamination with line-depths $\tau \gtrsim 0.5$ were around the diffuse interstellar bands at λ6284 Å, λ6993 Å and λ7224 Å. In these cases, incomplete telluric cancellation typically left residual 'spikes' in the spectra with an amplitude of between ~ 0.5 and 5% relative to the continuum.

2.3 Echelle data reduction in IRAF

For all of the datasets, preliminary CCD frame reductions and the calibration procedures outlined in Section 2.2.2 were performed using the standard packages available in NOAO IRAF version 2.11[4]. Scattered light surface fitting and subtraction, and the extraction and wavelength calibration of multiple echelle orders was facilitated by the tasks contained in **noao.imred.echelle.** Spatial/dispersion axial distortion correction, where necessary, was performed for single orders in **noao.twodspec.**

Following blaze and telluric-correction, further reduction steps included Doppler shift-

[3]Air mass is defined as the path-length through the Earth's atmosphere towards the target of observation.

[4]IRAF is distributed by the National Optical Astronomy Observatories, which are operated by the Association of Universities for Research in Astronomy, Inc., under cooperative agreement with the National Science Foundation.

ing the spectra into the LSR (local standard of rest) frame, correcting for the rotation and orbital motion of the Earth and the motion of the Sun through the LSR, using **astutil.rvcorrect**. Continuum flattening, including the removal of broad stellar features, unwanted interstellar features, and ripples caused by imperfect blaze-correction was performed using the **icfit** routines available in the **noao.onedspec.splot** task.

Continuum flattening, where necessary, was performed by dividing by the smoothest possible polynomial function[5] that gave a good fit to regions assumed to be continuum, or the local continuum defined by very broad DIBs or stellar lines. Effort was made to ensure a slow-moving fit ($d^2g(\lambda)/d\lambda^2 \simeq 0$ for the fitted polynomial $g(\lambda)$), across the interstellar features of interest. Narrow DIBs and atomic or diatomic absorption features were excluded from the fits by selecting 'sample regions', or more generally by using several ($\sim$ 10), rejection iterations — deleting those points that lay greater than $F\sigma_{\rm RMS}$ away from the fit in each iteration, then re-fitting the function. $\sigma_{\rm RMS}$ is the root-mean-square deviation of the fit from the spectrum at each iteration. F is a constant factor between between 1.5 and 2.5, set manually depending on the amplitude of the features to be excluded compared to other features in the continuum being fitted and on the order of the polynomial $g(\lambda)$.

2.4 Interstellar absorption line analysis

2.4.1 Optically thick absorption lines

The Beer-Lambert law dictates that the intensity of light travelling through a homogeneous opaque medium will be attenuated by the fraction

$$\frac{I(\lambda)}{I_0(\lambda)} = \mathrm{e}^{-\kappa(\lambda)\rho x}, \tag{2.4}$$

where $I_0(\lambda)$ is the initial spectral light intensity, x is the optical path-length of the light ray through the medium, $\kappa(\lambda)$ is the opacity and ρ is the number density (absorbers per unit volume). The optical depth of the light-path is $\tau(\lambda) = \kappa(\lambda)\rho x$. In the 'optically

[5]Chebyshev polynomials were used by default due to their inherent smoothness; cubic spline polynomials were used when necessary for a better fit to the continuum or for fitting peculiarly shaped stellar features.

thick' regime, $\tau \gtrsim 1$ and the fractional light intensity at the detector ($I(\lambda)/I_0(\lambda)$) is significantly less than 1.

In the absence of light scattering, the opacity of the medium as a function of frequency ν depends on the oscillator strength of the transition *via* the equation

$$\kappa(\nu) = \frac{\pi e^2 f}{m_e c}\phi_T(\nu), \tag{2.5}$$

(for the derivation of this equation, see for example Lequeux 2005), where m_e is the electronic mass, e the electronic charge, c the speed of light and $\phi_T(\lambda)$ the total area-normalised 'spectral-spread function' of the transition. The oscillator strength $f = f(\lambda_t)$ of a transition at a wavelength λ_t is equal to 1.4992×10^{-14} times the 'Einstein A' coefficient of the transition. $\phi_T(\nu)$ acts to broaden transition lines from delta functions with infinitesimal frequency width into spectral features with finite FWHM. When the absorption line is formed against a background light source with a flat continuum and observed using a spectrograph, the form of $\phi_T(\nu)$ is defined by a convolution of the natural (Lorentzian) line-broadening function $\phi_L(\nu)$, with the Gaussian Doppler velocity spread of the (assumed gaseous) medium $\phi_G(\nu)$, and the approximately Gaussian PSF[6] of the spectrograph, $\phi_S(\nu)$. Expressed in wavelength space,

$$\phi_T(\lambda) = \phi_L(\lambda) \otimes \phi_G(\lambda) \otimes \phi_S(\lambda). \tag{2.6}$$

The natural line-broadening function is given by

$$\phi_L(\lambda) = \frac{\Gamma_L}{\pi(\lambda - \lambda_t)^2 + \Gamma_L^2}, \tag{2.7}$$

where the Lorentzian FWHM is defined by

$$\Gamma_L = \frac{\lambda_t^2}{4\pi c\gamma}, \tag{2.8}$$

and γ is the radiation damping constant, or sum over Einstein A transition probabilities for allowed transitions to all energy levels below the upper and lower levels involved in

[6]The actual form of the spectrograph's PSF (point spread function) $\phi_S(\nu)$ depends on the optics of the spectrograph, but is usually well approximated by a Gaussian function.

the transition. The Gaussian shape introduced by random thermal and turbulent motion of the gas is characterised by

$$\phi_G(\lambda) = \frac{1}{\sqrt{2\pi\sigma_G^2}} e^{-\frac{(\lambda-\lambda_t)^2}{2\sigma_G^2}}, \tag{2.9}$$

where σ_G is related to the FWHM, Γ_G of the Gaussian by

$$\sigma_G = \frac{\Gamma_G}{\sqrt{8\ln 2}}. \tag{2.10}$$

The 'Doppler b' parameter is commonly used in interstellar line studies due to its convenience in parameterising the Gaussian velocity distribution and is related to σ_G by

$$b = \frac{\sqrt{2}\sigma_G c}{\lambda_t}, \tag{2.11}$$

such that in velocity space,

$$\phi_G(v) = \frac{1}{b\sqrt{\pi}} e^{-\frac{(v-v_c)^2}{b^2}}, \tag{2.12}$$

where v_c represents the central velocity of the Gaussian distribution of absorber velocities. The central wavelength of the distribution is at λ_c, displaced from the 'rest wavelength' of the transition λ_t due to bulk Doppler motion of the gas in the radial direction along the line of sight such that

$$v_c = \frac{c(\lambda_c - \lambda_t)}{\lambda_t} = \frac{\Delta\lambda}{\lambda_t}, \tag{2.13}$$

in the non-relativistic limit of $v_c \ll c$.

The echelle spectrographs used in this study have a PSF practically indistinguishable from a Gaussian, defined by

$$\phi_S(\lambda) = \frac{1}{\sqrt{2\pi\sigma_S(\lambda)^2}} e^{-\frac{(\lambda-\lambda_t)^2}{2\sigma_S(\lambda)^2}}, \tag{2.14}$$

where $\sigma_S(\lambda) = \lambda/(\sqrt{8\ln 2}R)$. At wavelengths close to the transition wavelengh such that $|\lambda - \lambda_t|/\lambda_t \ll 1$, variation of the PSF as a function of wavelength is negligible and $\sigma_S(\lambda) = \sigma_S \simeq \lambda_t/(\sqrt{8\ln 2}R)$.

By definition, $\tau(\lambda) = \kappa(\lambda)\rho x$, so introducing the 'total column density' of the absorbing species X as $N(\mathrm{X}) = N = \rho x$, from Equation (2.5),

$$\tau(\nu) = \frac{N\pi e^2 f}{m_e c}\phi_T(\nu). \tag{2.15}$$

Changing variable to wavelength space, the integrated optical depth of the line $\tau = \int_{-\infty}^{\infty}\tau(\lambda)d\lambda$ is related to N as follows:

$$\tau = \frac{N\pi e^2 f}{m_e c}\frac{\lambda_t^2}{c}\int_{-\infty}^{\infty}\phi_T(\nu)d\lambda. \tag{2.16}$$

Based on the fact that $\phi_T(\nu)$ is normalised and integrates to 1, rearranging this equation yields a formula for the total column density as a function of the integrated optical depth:

$$N = \frac{m_e c^2}{\pi e^2 f \lambda_t^2}\tau. \tag{2.17}$$

If the natural line-broadening component of $\phi_T(\nu)$ is narrow enough to be neglected (*i.e.* $\Gamma_L \ll \Gamma_G$) as is common in observations of the strong interstellar resonance transition lines (*e.g.* Na I, K I and Ca II), and if the resolving power of the spectrograph is sufficiently high that the contribution of $\phi_S(\lambda)$ to the line-shape is negligible, then the Gaussian Doppler motions of the gas dominate the observed spectral line profile. Under such circumstances the column density profile $N(\lambda)$ of the gas cloud can be derived from its optical depth profile $\tau(\lambda)$ using

$$N(\lambda) = \frac{m_e c^2}{\pi e^2 f \lambda_t^2}\tau(\lambda). \tag{2.18}$$

The situation of a negligible point spread function is rarely realised for real observations of narrow interstellar lines. Thus, the optical depth profile recorded with a spectrograph, or 'apparent optical depth' $\tau_a(\lambda) = \ln(I_0(\lambda)/I(\lambda))$, is a convolution of $\tau(\lambda)$ with $\phi_S(\lambda)$:

$$\tau_a(\lambda) = \tau(\lambda) \otimes \phi_S(\lambda), \tag{2.19}$$

making the precise determination of $N(\lambda)$ difficult without first deconvolving $\phi_S(\lambda)$ from the recorded spectrum. The technique of optical depth correction (see Section 3.5.1) is able to overcome this problem. The more conventional approach for moderate to high resolution data however, is to use absorption profile fitting and line modelling procedures.

2.4.2 VAPID interstellar absorption line analysis

In the general case of interstellar absorption spectroscopy, where the light from a distant source (with flat continuum) has passed through a set of i clouds at velocities v_i, with Gaussian internal velocity distributions defined by b_i and total column densities N_i, the resulting absorption spectrum will be complex and difficult to interpret. For a known transition, it is possible to construct a model for the optical depth profile of the spectrum in $\tau(\lambda)$ space by generating a set of i Gaussians parameterised by v_i, b_i and N_i that correspond to the i clouds in the line of sight. This 'cloud model' is then convolved with the natural line-shape of the transition, converted to fractional intensity ($I(\lambda)/I_0(\lambda)$) space[7], and then convolved with the PSF of the spectrograph to form the spectral line model. Comparison of the model with the recorded spectrum allows independent adjustment of the parameters ($[v,\ b,\ N]_i$) until a satisfactory match is achieved.

In velocity space, from Equations 2.15, 2.6 and 2.12, the optical depth profile $\tau_i(v)$ of each cloud is given by

$$\tau_i(v) = \frac{N_i \pi e^2 f \lambda_i^2}{m_e c^2} \frac{1}{b_i \sqrt{\pi}} \mathrm{e}^{-\frac{(v-v_i)^2}{b_i^2}} \otimes \phi_L(v) \otimes \phi_S(v). \tag{2.20}$$

The final model for the spectrum is formed by summation of the optical depth profiles ($\sum_i \tau_i(\lambda)$) of the i clouds in the model. The model parameters are optimised by non-linear least squares minimisation of the sum of the squared residuals χ^2 of the model

[7]From now on in this thesis, $I_0(\lambda)$ refers to the spectral continuum intensity (*i.e.* including stellar absorption, interstellar reddening and atmospheric attenuation, but excluding interstellar line/band absorption).

compared to the recorded spectrum. This is performed by the VAPID code developed by I. D. Howarth (see for example Howarth *et al.* 2002) that employs the Levenberg-Marquardt algorithm (Levenberg 1944; Marquardt 1963) to obtain a rapid and precise convergence of parameters to those that produce the χ^2 minimum.

The 'best fitting' final set of optimised parameters should closely represent the physical parameters of the absorbing clouds. However, the model may not represent a unique solution, particularly when there are many clouds (and therefore, many free parameters) in the model, or if the input set of initial $[v,\ b,\ N]_i$ are far from the true physical parameters of the clouds. Thus, the number of clouds in the model is kept to a minimum and clouds are added one by one until the desired quality of fit is achieved.

The initial set of $[v,\ b,\ N]_i$ is estimated based on the appearance of the spectrum, constrained by knowledge of interstellar cloud physics. For example, Doppler b parameters of cold interstellar gas clouds are around 1 km s^{-1}. Column densities are estimated using the equivalent widths of the lines and Equation (2.22).

The occurrence of local χ^2 minima in $[v,\ b,\ N]_i$ space cannot be precluded, but is unlikely provided that the number of clouds is kept to a minimum and that the clouds do not overlap each other too severely. In the regime of high enough S/N and resolution to resolve *all* of the individual clouds in a spectrum, optimised model parameters should be accurate. When these criteria are not met, each case must be carefully examined for possible problems in the optimisation procedure. In addition, the importance of accurate continuum rectification is stressed, in order that optical depth profiles are accurate.

When a species is observed in absorption through more than one transition involving the same lower state (the sodium D and UV lines or the calcium H and K doublet, for example), all of the transitions can be modelled simultaneously using VAPID and the model parameters are optimised by χ^2 minimisation of the residuals for every transition. Thus, more accurate determination of parameters is achieved. Narrow spectral lines originating in transitions with different strengths experience a different degree of optical depth degradation due to the spectrograph's point spread function, dependent on their b value, which provides an extra degree of information about the Doppler b values of the clouds. In addition, the detrimental effects of spurious artifacts in the data or incompletely cancelled telluric features are reduced by utilising multiple datasets that contain degenerate information.

To obtain accurate cloud model parameters, the transition wavelength λ_t and oscillator strength f must be accurately known. In this thesis, unless otherwise stated, the values used for the optical atomic resonance lines are from Morton (2003).

Once good convergence of model parameters is achieved, VAPID can compute error estimates for $[v,\ b,\ N]_i$ using a Monte Carlo algorithm. Based on the assumption of Poisson statistics of the spectral noise, the input spectra are replicated and random Gaussian noise (of RMS equal to the continuum RMS of the input spectrum) is added to each pixel. Up to 1000 'replicated datasets' are produced, and the model parameters are refit for each independently.

In parameter space, the distributions of the replicated model parameters are approximately Gaussian, and thus the mean of the distribution and the Gaussian σ can be found for each parameter. For a given parameter, 1σ from the mean covers 68.3% of the replicated models, 2σ covers 95.5% etc. The number of replications required to achieve complete coverage of all the possible noise scenarios is very large (approaching infinity), however, tests of real data observed at different S/N show that 50 replications provides a reasonable error analysis, and anything over 100 is good; 1000 replications should be rigorous provided the assumption of Poisson statistics holds.

2.4.3 Optically thin absorption lines and diffuse interstellar bands

For $\tau \lesssim 0.1$, saturation of line depths in intensity space is very low ($\lesssim 0.5\%$), such that $(I_0(\lambda) - I(\lambda))/I_0(\lambda) \simeq \ln(I_0(\lambda)/I(\lambda))$ and therefore $\tau(\lambda) \simeq (I_0(\lambda) - I(\lambda)/I_0(\lambda))$. In this 'optically thin' regime the area of an absorption line depends almost linearly on the number of absorbers. It is useful to define the equivalent width W_λ as the integrated area of an absorption feature at a wavelength λ:

$$W_\lambda = \int_{-\infty}^{\infty} \frac{I_0(\lambda) - I(\lambda)}{I_0(\lambda)} d\lambda \simeq \int_{-\infty}^{\infty} \tau(\lambda) d\lambda. \tag{2.21}$$

From Equation (2.17) and remembering that the spectral line-spread function $\phi_T(\lambda)$ is normalised, the column density of absorbers is found using

$$N \simeq \frac{m_e c^2}{\pi e^2 f \lambda_t^2} W_\lambda. \tag{2.22}$$

Most diffuse interstellar bands have a maximum absorptance of less than 10% and the condition $\tau \lesssim 0.1$ is fulfilled. Thus, W_λ is a useful measure of DIB strength, and scales almost linearly (negligible deviation for the purposes of this study) with the column density of the carrier species. Similarly, equivalent widths of weak atomic and molecular absorption lines can be used as a measure of the column density of the species that cause them, but must be done with caution because any features with peak absorptance greater than ~ 15% will be noticeably saturated.

Chapter 3

Diffuse interstellar bands and atomic lines in the Large Magellanic Cloud

3.1 Introduction to Chapter 3

It is expected that the study of the factors that influence the strengths of the diffuse interstellar bands will help to build understanding of the mechanisms involved in the formation and destruction of their carriers. The Milky Way provides a diverse range of interstellar environments characterised by various physical and chemical parameters, including particle number density, kinetic temperature, molecular content, gas-to-dust ratio, metallicity, dust grain composition and size distribution, free electron density, spectral energy distribution and intensity of pervading radiation field, turbulence, flows and shocking of the material, and the history of the ISM with respect to variations in these parameters. The ubiquitous presence of the DIBs where dust is found shows how resistant their carriers are to variations in cloud conditions. Across the spectrum of environments probed by diffuse band studies, the detailed balance of the factors critical to the maintenance of DIB carrier abundances is still to be determined.

To expand the range of conditions over which DIBs are observed, and to broaden the range of parameters with respect to which their carriers may be correlated and analysed, it is valuable to look outside of the Milky Way to different galaxies where differences in star formation rates, elemental abundance ratios, and galactic structure and kinematics offer markedly different interstellar conditions. Due to its proximity, size,

reduced metallicity and dust-to-gas ratio, and abundance of hot, bright stars suitable for optical absorption line studies, the Large Magellanic cloud presents an ideal target.

DIBs have been observed in other galaxies, including the SMC (Morgan 1987), dusty starburst galaxies (Heckman & Lehnert 2000) and the spiral galaxy NGC 1448 (Sollerman *et al.* 2005). Recent work on the dust and metal content of damped Lyman α systems (see for example Calura *et al.* 2003) has stimulated a search for DIBs in these strange, distant objects using absorption against background quasars (*e.g.* Lawton & Churchill 2004). Presently however, the LMC remains the first target of choice for extragalactic DIB work.

3.2 The interstellar medium of the LMC

3.2.1 Comparison with the Galaxy

The Large Magellanic Cloud is a dwarf irregular galaxy, gravitationally bound to the Milky Way and with about 1/10 of its mass, and presently at a heliocentric distance of 50.1 kpc (van der Marel *et al.* 2002). From H I mapping (Staveley-Smith *et al.* 2003), the LMC is seen to have a circular disc viewed as nearly face-on from our perspective, with concentrations of diffuse gas in several tidal arms. Staveley-Smith *et al.* (2003) derive a mean integrated heliocentric H I radial velocity of $v_{\rm HEL} = 273$ km s^{-1} and an H I diameter at 1 M$_\odot$ pc^{-2} of 9.3 kpc. The peak H I column density in their survey is located just to the south of the 30 Dor H II complex at 5.6×10^{21} cm^{-2}.

The relatively blue colour of the LMC and its under-abundance of heavy elements relative to the Milky Way is evidence of slow and/or sporadic star formation rates over the LMC's history (Westerlund 1997). Low metallicity has been measured in the chemical composition of its stars and H II regions. In H II regions, supernova remnants and Herbig-Haro objects, Dufour *et al.* (1982) and Russell & Dopita (1990) measured the C/H ratio to be about 25%, and the N/H ratio about 50%, of the respective ratios found in the Galaxy. Other species including O, Ne, S and Ar were measured to be about 50 – 80% less abundant than in Galactic H II regions relative to neutral hydrogen. In F-type supergiants (Hill *et al.* 1995), OB main-sequence stars (Rolleston *et al.* 2002) and red giants (Smith *et al.* 2002) the elements C to Fe are under-abundant by ~ 50%. There is considerable scatter between some of the values found in the

literature for various elements, but the overall consensus is that the LMC has about half the metallicity of the Milky Way. The situation has been reviewed by Rolleston *et al.* (2002), who conclude a general metal-deficiency of $\log Z = -0.3 \pm 0.04$ dex.

The gas-to-dust ratio measured by $G = N(\mathrm{H\,I})/E_{B-V}$ is known to be about a factor of four greater in LMC sightlines than in the Galaxy, as studied by Koornneef & Mathis (1981), Koornneef (1982) and Fitzpatrick (1985, 1986) using damped Lyman α absorption. Koornneef's value of 2.4×10^{22} cm^{-2} mag^{-1} is widely quoted, and, combined with the Galactic determination of 4.8×10^{21} cm^{-2} mag^{-1} by Bohlin *et al.* (1978), results in a value of G five times greater in the LMC than the Galaxy. If Fitzpatrick's value of 2×10^{22} cm^{-2} mag^{-1} is used for the LMC, a ratio of closer to four is found. In a sample of stars studied by Gordon *et al.* (2003), gas-to-dust ratios (measured by $N(\mathrm{H\,I})/A_V$), were found to be about twice the Galactic value, with a range between about 1 and $\gtrsim 5$ times Galactic and a trend for larger values to be found in sightlines inside the 30 Dor H II region.

The reasons for the greater gas-to-dust ratio in the LMC are not fully understood, but it is likely that diminished metallicity is at least partly responsible given that interstellar dust is composed mainly of carbonates and silicates. If one measures the amount of dust with respect to the abundance of gas-phase 'condensable species' that form the dust (Clayton & Martin 1985), one finds in the LMC $N(\mathrm{C,N,O})/E_{B-V} = 6.7 \times 10^{18}$ cm^{-2} mag^{-1}, whereas in the Galaxy $N(\mathrm{C,N,O})/E_{B-V} = 3.4 \times 10^{18}$ cm^{-2} mag^{-1}. A discrepancy of around a factor of two leads to the conclusion that a significantly different relationship exists between the gas and dust in the LMC compared to in the Galaxy. Koornneef (1982, 1984) considered the problem in terms of 'missing dust', and sought a solution that involved dust with a diminished reddening efficiency. However, it may be the case that the greater value of G in the LMC is due to the lower dust enrichment of the ISM, due to lower past rates of star formation and hence slower dust production compared to the Galaxy due to diminished numbers of mass-losing red giants, carbon rich AGB and post-AGB stars and supernovae.

The interstellar medium of the LMC has significantly different dust properties from those generally found in the Milky Way, evidence of which was provided by ultraviolet spectroscopy of the interstellar UV extinction curve (Koornneef & Mathis 1981; Clayton & Martin 1985; Fitzpatrick 1986). The average UV extinction curve in the LMC from Fitzpatrick (1986) is shown compared with the local average Milky Way data

from Seaton (1979) in Figure 3.1. The 2175 Å extinction bump strength is markedly smaller, and the FUV extinction is greater, coupled with a steeper FUV rise, as compared with the average Galactic curve. These differences are further accentuated in the sample of stars located in the 30 Dor H II region. A recent study by Gordon *et al.* (2003) shows differences between the average LMC and Milky Way extinction curves of a similar pattern, but with less discrepancy in the FUV rise (see Figure 3.2). The greatest deviation from Galactic extinction curves was seen towards the LMC2 supershell, just East of 30 Dor. Weakness of the 2175 Å bump is generally interpreted as a relative lack of graphitic particles in the dust grain distribution (see Section 1.1.1.2), assuming that graphitic grains cause the bump. The enhancement of the FUV extinction rise may be due to a greater abundance of small grains in the ISM of the LMC (see Clayton & Martin 1985, for example).

The ratio of total to selective extinction $R_V = A_V/E_{B-V}$ measures the slope of the extinction curve in the blue, and is closely related to the interstellar dust's UV extinction properties (see Section 1.1.1.2). In the Galaxy, lower values typically correspond to steeper extinction curves, though this is not the case when comparing R_V with the extinction curve shape for the LMC and Galactic averages (R_V = 3.4 and 3.1 respectively (Gordon *et al.* 2003)). The conclusion is that average UV extinction curves in the LMC are different to those measured locally in the Galaxy, and cannot be parameterised using R_V in precisely the same way. The properties of the dust grains and, by the relationship of DIB strengths with E_{B-V} (see Section 1.2), the properties of the DIBs in the LMC, may both be expected to be different as a result.

The 30 Dor (or Tarantula Nebula) region is remarkable in that it is the only extragalactic H II region visible to the naked eye. Around 1 kpc in diameter, it is an evolved, highly structured, brilliantly emitting mass of filamentary hydrogen, fueled by the excess of massive OB stars in the 30 Dor region. The majority of the illuminating flux is provided by the massive (~ 1000 $M_\odot$) star-forming region at its centre that produces a luminosity of about 10^8 $L_\odot$. One of the most active star forming regions known, it was proposed by Schmidt-Kaler & Feitzinger (1976) to be the 'active galactic nucleus' of the LMC. It is likely that the immense energy associated with this region in the form of radiation and mass-flows has modified the structure of the interstellar dust in such a way as to alter its properties, producing some of the differences in the average 30 Dor UV extinction observed in Figure 3.1. No differences in NIR extinction characteristics

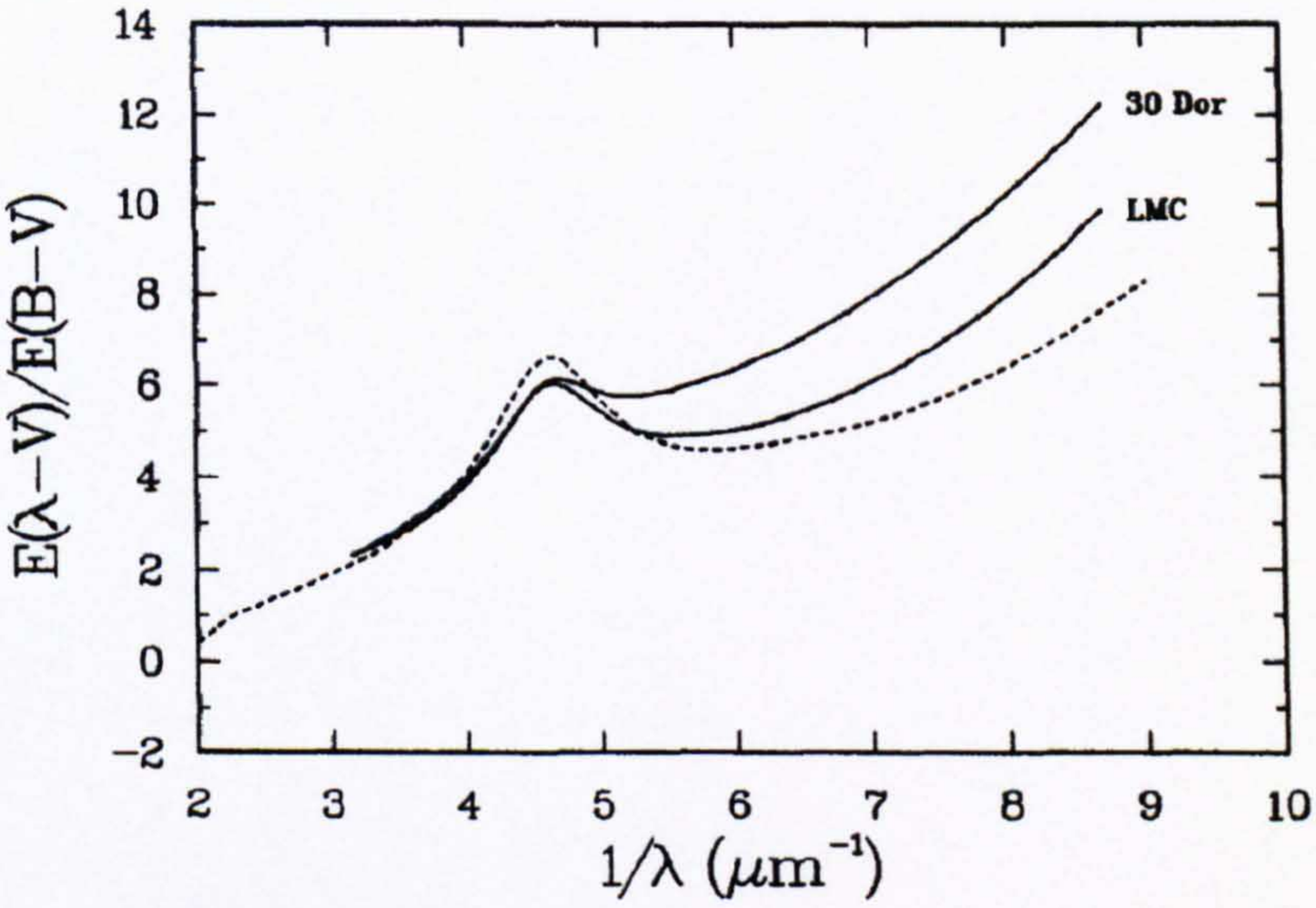

Figure 3.1: Figure taken from Fitzpatrick (1986) (with the permission of E. L. Fitzpatrick) showing the representative average UV extinction curves for samples of stars from the LMC and a subsample from the region around the 30 Doradus H II nebula, compared to the Galactic average curve (Seaton 1979) with $R_V \simeq 3.1$ (shown as a dotted line).

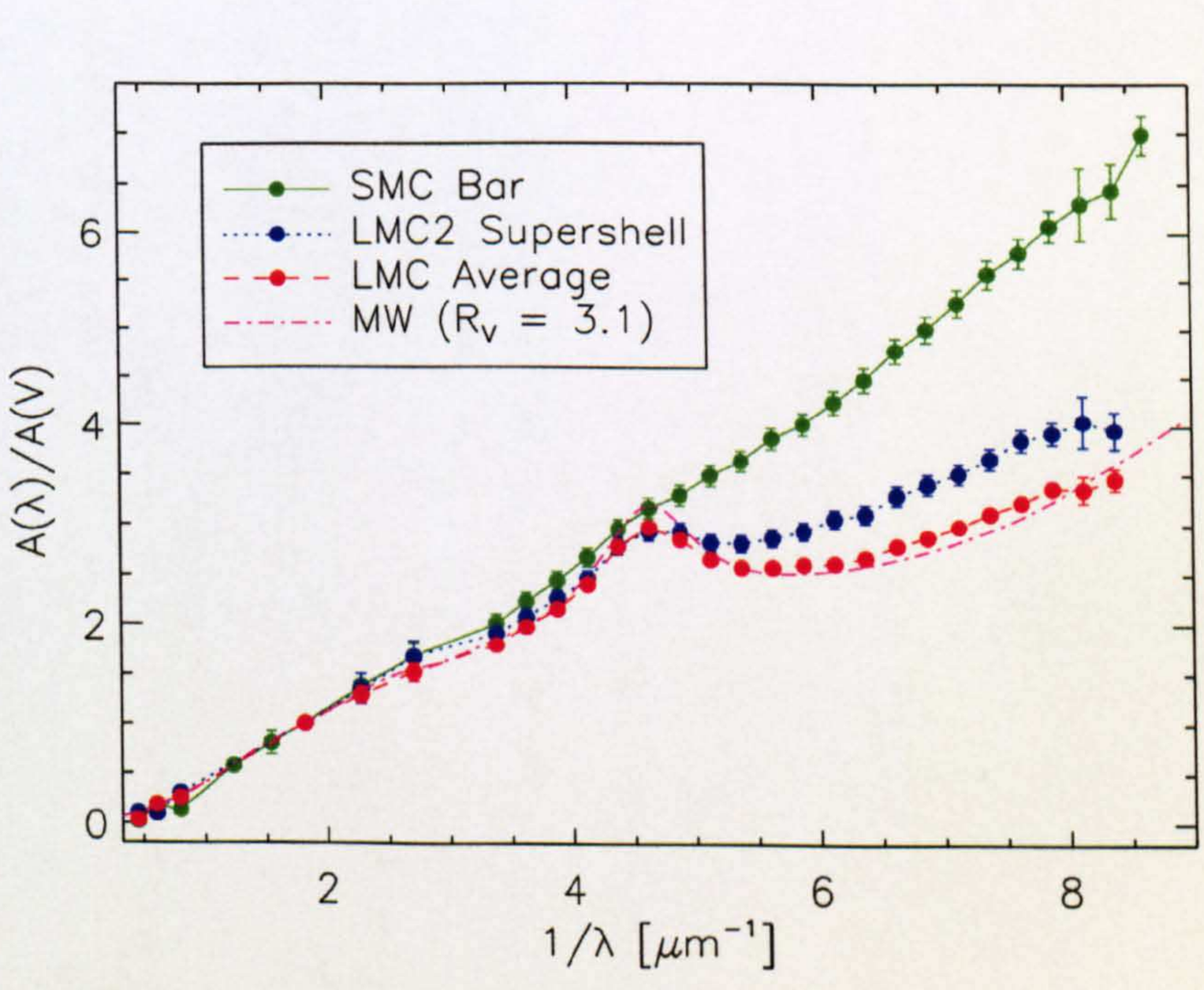

Figure 3.2: UV extinction curves for the LMC and SMC and Milky Way from the analysis of IUE data for a selection of stars by Gordon *et al.* (2003) (used with the permission of K. D. Gordon).

between the LMC and the Galaxy have been observed (Koornneef 1982).

It is worth noting that, in the study of the 30 Dor nebula by Feast (1961), the electron temperatures ($\sim 10^4$ K) and densities ($n_e \sim 100 - 2000$ cm^{-3}) were found to be in accord with typical values found in bright Galactic H II regions such as the Orion nebula.

The low mass of dust in the LMC, coupled with the high UV flux from H II regions such as 30 Dor leads to an above average strength of UV field in many parts of the LMC. Bolatto *et al.* (1999) found that the UV field in the vicinity of 30 Dor is ~ 3000 times stronger than the local Galactic average. The observation that neutral atomic species are particularly under-abundant (as compared to photoionised species) in the LMC (Welty *et al.* 1999; Vladilo *et al.* 1993) is probably due to the increased photoionisation rates caused by higher UV field strengths. A high UV field strength has been suggested by many studies. Martin *et al.* (1989) proposed that the average interstellar UV field strength in the LMC is at least 5 times that typically found in the Galaxy.

Other properties of the LMC ISM that are different to the Galaxy include the molecular content, which is found to be rather low by many studies, *e.g.* Tumlinson *et al.* (2002) who derived an average H_2 fraction of the LMC ISM about 1/8 of the Galactic value. This was interpreted as being due to a diminished H_2 production rate, caused by reduced dust grain abundances[1], coupled with an increased photodissociation rate due to the high UV field intensity. Their models require a mean LMC UV radiation field strength 10 – 100 times the galactic mean to reproduce the observed H_2 fractional abundances.

Israel (1997) measured the relative fraction of H_2 compared to CO throughout the LMC (the 'H_2 to CO conversion factor'), and found that it was between three and seven times greater than in the Galaxy. This result was attributed in part to the reduced CO abundances in the LMC caused by reduced metallicity, but predominantly to the higher interstellar radiation density, which is expected to result in increased photodissociation of CO relative to H_2. Column densities of CO are *much* lower than those of H_2 so that CO exhibits less self-shielding, and is therefore photodissociated more rapidly than H_2 when the radiation field is strong. The lack of dust in the LMC ISM (relative to H

[1]Dust grains are a catalyst for H_2 formation, providing a reaction site for two H atoms to combine and dissipate energy. The result of Tumlinson *et al.* (2002) implies that the dust grain abundance is a rate-limiting step in the reaction $H + H \longrightarrow H_2 + h\nu$.

atoms) further reduces CO shielding compared to the Galaxy.

The study of interstellar H_2 by André *et al.* (2004) identified the probable presence of small ($\sim 10^2 - 10^3$ AU diameter), dense ($n \sim 10^3 - 10^5$ cm^{-2}) clumps or filaments of gas and dust towards several LMC stars, as inferred by the large abundances of CO and H_2 along a few sightlines.

Marx-Zimmer *et al.* (2000) used H I absorption studies to probe the cool, dense gas of the LMC, and reached the conclusion that such gas is either at a lower temperature in the LMC than in the Galaxy — at an average temperature of ~ 30 K in the LMC *vs.* ~ 60 K in the Galaxy — or that the cool phase is more abundant, comprising 35% of the LMC's ISM compared to 24% of the Galaxy's. The presence of cool H I is particularly enhanced around 30 Dor, where it comprises about 50% of the neutral H I mass.

Condensation rates of refractory elements onto dust grains (depletion) have been found to show broadly similar characteristics in the LMC and the Galaxy (de Boer 1991; Welty *et al.* 1999), although this issue is clouded somewhat by the effects of reduced metallicity on the gas-phase elemental abundances. Clouds moving at high radial velocity relative to the centre of the LMC disc show relatively less depletion than the lower velocity gas clouds, in accordance with the Routly-Spitzer effect observed in the Milky Way (Routly & Spitzer 1952). A recent study of the sightline towards LMC star Sk–70°115 by Welty *et al.* (2004) has shown weak depletions of Si and Mg, but very severe depletions of Fe and Ni, unlike any situation observed in the Galaxy. Clearly, further studies of depletion in the LMC are warranted. No significant differences between the polarisation characteristics of the dust in the LMC and the Galaxy have been observed (Clayton & Martin 1985).

To summarise, the ISM of the LMC presents an environment substantially different from the Galaxy in which to study the unidentified diffuse interstellar absorption bands. The most prominent quantifiable differences are the gas-to-dust ratio, the metallicity, and the strength of the pervading radiation field.

3.2.2 Diffuse interstellar bands

The first reported detection of DIBs in the LMC was by Hutchings (1966) using plates from the survey of bright LMC stars by Feast *et al.* (1960). His measurements of the

λ4430 DIB indicated that the band was stronger per unit E_{B-V} in the LMC than in the Galaxy. However, in studies of this broad (FWHM ~ 18 Å) diffuse band, it is impossible to separate the LMC component from the component caused by Galactic foreground material, because the shift due to Doppler motion of the LMC amounts to only ~ 4 Å at 4430 Å. Consequently, it is likely that the strength of this DIB was overestimated; it is now known that the Galactic contribution can easily represent half of the total line of sight material for weakly reddened LMC stars. In addition, a follow-up study by Blades & Madore (1979) showed that many of Hutchings's band strength measurements were erroneously large, and that the data are consistent with an *upper limit* for the strength of the band equal to that observed in the Galaxy.

Houziaux *et al.* (1980) and Nandy *et al.* (1982) reached a similar conclusion, and determined that the λ4430 DIB does not appear to be strongly correlated with the strength of the 2175 Å UV extinction bump or the far-UV rise. It should be noted that, although the λ4430 DIB has a very large equivalent width and central depth compared to other DIBs, its accurate measurement is made difficult by stellar line blends, and its correlation with E_{B-V} is still rather poorly established.

With the advent of solid-state detectors and high resolution spectrographs, observations of the weaker, narrower DIBs towards the faint reddened stars of the LMC became possible. Pettini & Dodorico (1986) observed the λ6376 and λ6379 DIBs towards RMC 136a, the centre of the massive star-cluster that illuminates the Tarantula Nebula. Their conclusion was that the strengths of these DIBs were consistent with the absorption arising only in the 'LMC foreground' gas and dust identified by Fitzpatrick & Savage (1984), rather than the 'nebular dust' associated with the 30 Dor H II region, both components being present along this sightline. Another interpretation is simply that these DIB are weak with respect to E_{B-V} in this sightline.

The explosion of SN 1987A presented the opportunity to study DIBs near 30 Dor with unprecedented S/N, as shown by studies of Vladilo *et al.* (1987) where the λ5780, λ5797 and λ6284 DIBs were clearly observed, and by Vidal-Madjar *et al.* (1987), who observed λ6614. For relatively narrow DIBs, at the resolution of the observations, the radial velocity of the LMC results in complete Doppler-separation of the Galactic and LMC absorption components.

Vladilo *et al.* (1987) noted that the ratio of DIB equivalent widths to N(Na I) was smaller for the LMC gas than for the Galactic gas in the line of sight, and that this

could be caused by differing abundances and/or depletions of the ISM constituents. The band strengths relative to E_{B-V} were also analysed with respect to those measured in the heavily-reddened Galactic star HD 183143. It was determined that the DIBs were about a factor of two weaker per unit E_{B-V} as compared to this Galactic sightline. However, important caveats to this result include the fact that the reddening towards the supernova is uncertain, and that the Galactic component of dust was probably underestimated by Vladilo *et al.* at $E_{B-V}^{\rm MW} = 0.03$, when it is more likely in the region of 0.08 (Gochermann *et al.* 1989). HD 183143 is also known to have very strong DIBs (Herbig 1975), and the relationship between DIB strength and reddening is not necessarily linear (Herbig 1995).

There is increasing evidence that the diffuse interstellar bands may be ubiquitous in the ISM of the LMC, but the relationship between the DIB strengths and the gas and dust is still poorly defined. Apart from λ4430, which is not an easy DIB to measure accurately, observations of diffuse bands in the LMC are sparse, and have been restricted to the region in and around the 30 Dor nebula. Two of the aims of this study are to expand the observational dataset of DIBs in the LMC, and to observe the full spectrum of strong DIBs for a range of LMC sightlines inside and outside of the 30 Dor region.

3.2.3 Atomic spectroscopy

The first moderately-resolved ($R = 20,000$), atomic line measurements of diffuse, singly ionised calcium in the LMC were presented by Blades & Meaburn (1980). In-depth study of the distribution and velocity structure of Ca II towards 48 supergiants in the LMC was performed by Songaila *et al.* (1986), who identified that the diffuse ISM was 'fragmentary' (*i.e.* discontinuous), across the LMC disc.

Na I and Ca II were observed at high resolution ($R = 40,000 - 100,000$) with S/N $\sim$ 50 towards a sample of LMC stars by Vladilo *et al.* (1993) and Molaro *et al.* (1993). Profile fitting enabled the derivation of velocities, column densities and Doppler b values of interstellar clouds down to the confusion limit imposed by the resolution and S/N. Ti II and Ca II were analysed in a similar way by Caulet & Newell (1996). A high resolution interstellar K I survey by Welty & Hobbs (2001) included three LMC stars, and interestingly, the Na I/K I ratio was found to be 15.5 for their sample compared to the Galactic average of about 90, identifying peculiar ionisation fractions

or depletions (compared to the MW) for the LMC gas probed. Songaila (1981) used Ca II and Na I spectra to explore the possibility that 'intermediate velocity' LMC clouds are the cooling remnants of a hot, filamentary phase of the ISM ($T \sim 10^6$ K, $n \sim 10^{-4}$ cm^{-3}) ejected from the LMC's disc by energetic winds from the centre of 30 Dor.

The neutral atomic hydrogen gas of the LMC has been studied through 21 cm emission (Rohlfs *et al.* 1984; Staveley-Smith *et al.* 2003) and Lyman α (Lα) absorption (Fitzpatrick 1985). The LMC shows complex, ordered H I structure in clouds with sizes down to the $\sim$ 15 pc resolution limit of the survey by Staveley-Smith *et al.* (2003). Comparison of Ca II and H I velocity component structure, combined with data on stellar radial distances, allowed Songaila *et al.* (1986) and McGee *et al.* (1983) to determine the three dimensional spatial location of H I clouds. A detailed study of the relationships between H I and the multiple atoms and ions accessible in the optical (Ti II, Ca II, Na I and K I) has yet to be performed, which identifies another aim of this study.

The ISM in the line of sight towards the LMC, may be divided into components originating in the Galactic disc, the Galactic halo, the LMC disc, and the LMC halo, based on the radial velocity of the gas clouds. According to the H I survey by Kim *et al.* (2003) and Staveley-Smith *et al.* (2003), Galactic gas towards the LMC lies in the velocity range $-65 \lesssim v_{\rm LSR} \lesssim 75$ km s^{-1}, and is distinct from the LMC gas that lies in the range $85 \lesssim v_{\rm LSR} \lesssim 410$ km s^{-1}.

IVCs (intermediate velocity clouds) and HVCs (high velocity clouds) spoil the clean categorization of gas into the locales of the Galaxy and the LMC however. They are seen at velocities from approximately 30 km s^{-1} to at least 180 km s^{-1}, with diffuse H I column densities up to 2.4×10^{19} cm^{-2}. The exact origin, location and properties of these small isolated clouds remains uncertain, and it is difficult to definitively categorise them as being associated with the LMC or the Milky Way based only on their velocities. Molaro *et al.* (1993) observed IVCs and HVCs in Ca II, but noted that they are rarely observed in Na I, which, taken as evidence of the Routly-Spitzer effect, lead them to the conclusion that they are highly deficient — or even entirely lacking — in dust.

Given the proximity of the LMC ($\sim$ 50 kpc), and the extent of the Milky Way halo ($\sim$ 60 – 80 kpc), the HVCs must lie within the bounds of the Galaxy's spatial extent and therefore are likely to move predominantly under its gravitational influence. It then

seems reasonable to classify line-of-sight gas into (a) a Galactic component that resides in the disc of the Galaxy, (b) a Galactic halo component, and (c) an LMC component. Examination of the studies of the location of HVCs by McGee *et al.* (1983), Wayte (1990), Molaro *et al.* (1993) and Welty *et al.* (1999) leads to the classification scheme used in this chapter that gas with $v_{\rm LSR} \lesssim 40\,{\rm km\ s^{-1}}$ is Galactic, clouds with $40 \lesssim v_{\rm LSR} \lesssim 135\,{\rm km\ s^{-1}}$ are in the Galactic halo (albeit possibly ejected from the LMC at some time in the past (Songaila 1981; Olano 2004))[2], and gas at $v_{\rm LSR} \gtrsim 140\,{\rm km\ s^{-1}}$ is in the LMC.

The ionised hydrogen of the LMC has been mapped by Davies *et al.* (1976) in Hα emission. Spectroscopic studies of H II regions and their physical and chemical properties have been carried out using metallic UV emission lines by Dufour *et al.* (1982). Optical emission lines have been analysed in detail by Russell & Dopita (1990), and an early study by Feast (1961) examined ionised oxygen emission lines in the 30 Dor nebula.

The principal aim of this chapter is to expand the present body of knowledge surrounding the diffuse interstellar band carriers and atomic species in the LMC and, for multiple lines of sight, to study the properties of the DIBs with respect to the LMC's unusual interstellar conditions, including metallicity, gas-to-dust ratio, interstellar radiation field, UV extinction law, and atomic gas properties.

3.3 Targets, instruments and observations

At a distance of 50 kpc, the brightest stars of the LMC have apparent visual magnitudes of around 10 to 12. To perform observations of adequate S/N (~ 200), at high resolving power ($R \sim 50,000 - 100,000$), requires lengthy exposures upwards of half an hour on a 10 metre class telescope. A very good instrument for these observations is the Ultraviolet and Visual Echelle Spectrograph (UVES), on the ESO VLT at the Cerro Paranal Observatory, Chile. This high altitude site provides exceptional atmospheric conditions, with minimal telluric absorption and a median seeing of $\sim 0.7''$.

Located at Naysmith B on the 8.2 m Unit Telescope 2 (KUEYEN), the UVES provides

[2]The study of Olano (2004) concluded that the HVCs were 'launched' into the Galactic halo around 570 Myrs ago following a collision of the LMC and SMC; $\sim 3 \times 10^9$ M$\odot$ of matter was liberated from the Magellanic Clouds into the surrounding space (Galactic halo) during the violent event hypothesised.

a resolving power of $R \approx 80,000$ with a slit width of 0.5″, which is ample for observing diffuse bands and low to moderate optical depth interstellar atomic absorption lines. Dividing the beam of starlight into blue and red 'arms' observed simultaneously on different detectors allows efficient observation of the wavelength range from 3000 Å to 10,000 Å with only a few small gaps in spectral coverage.

Targets were selected based on their early spectral type, brightness, reddening and location: three reddened targets were located in and around the 30 Dor nebula, two less reddened targets in the 'W' H I arm (see Staveley-Smith *et al.* 2003, Figure 1), to the North-West of the bar, and a very low reddening standard just East of the 'E' arm, South-East of the bar[3]. Figure 3.3 shows the location of the target stars. Their co-ordinates, spectral types and reddenings are given in Table 3.1. On the lower optical plate in Figure 3.3 (the magnified region surrounding the 30 Dor nebula), some of the Hα emission shells of the Tarantula Nebula can be seen. Much of the H II region is not bright enough to be seen in this image, but extends over a kiloparsec from 30 Dor's centre to well beyond Sk −68°135 and Sk −69°223.

Data were recorded on the nights of the 25^{th} to 27^{th} of September 2001 with excellent atmospheric conditions. Of the programme stars in Table 3.1, all but Sk −69°223 were recorded at the default UVES settings of '346 + 590' and '437 + 860', where the numbers either side of the '+' refer to the central wavelength of the spectrum in nm for the blue and red arms respectively. The 346 + 590 spectra cover the region containing the Na I UV doublet lines at 3302.4 and 3303.0 Å, Ti II lines at 3242.0 and 3383.8 Å (the latter being the stronger), and the DIBs λ5705, λ5850, λ6196, λ6203, λ6284, λ6376, λ6379 and λ6614. The 437 + 860 spectra contain the Ca II H and K lines at 3968.5 and 3933.7 Å, the K I doublet lines at 7664.9 Å and 7699.0 Å, and the λ4430, λ6993 and λ7224 DIBs.

A problem was identified during observations that the echelle order containing the λ5780 and λ5797 DIBs was missing from the 346 + 590 setting, lying across the join between the two mosaicked red CCDs such that the entire order was lost. Correction of this problem lead to the use of setting 390+564 for Sk −69°223, in which the λ5780 and λ5797 DIBs and all the above mentioned features except for the K I doublet and DIBs λ6993 and λ7224 were observed in a single exposure.

[3]The 'bar', owing to its shape is the name of the optically bright, ~ 4 kpc long, concentration of stars near the kinematic centre of the LMC.

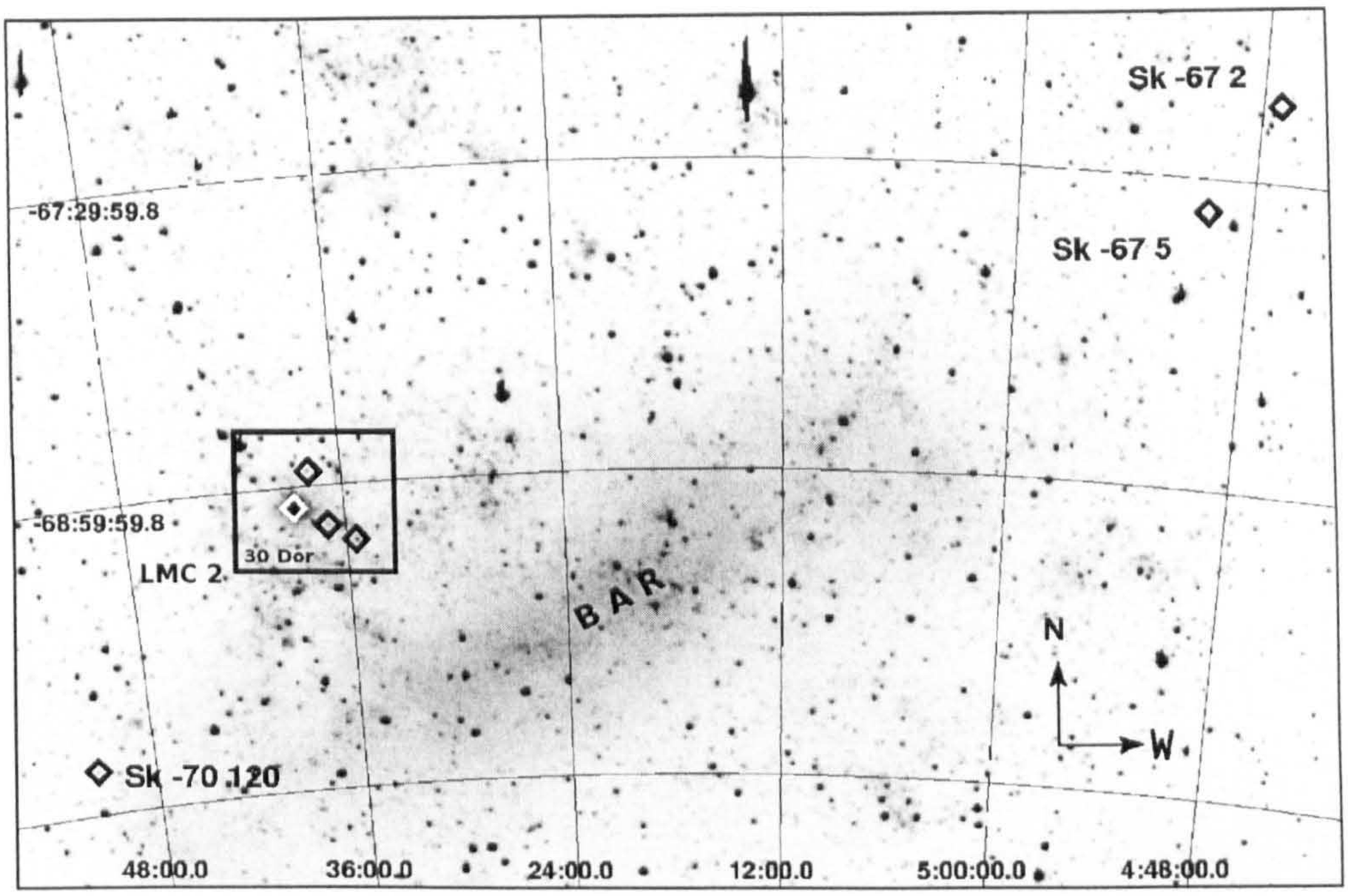

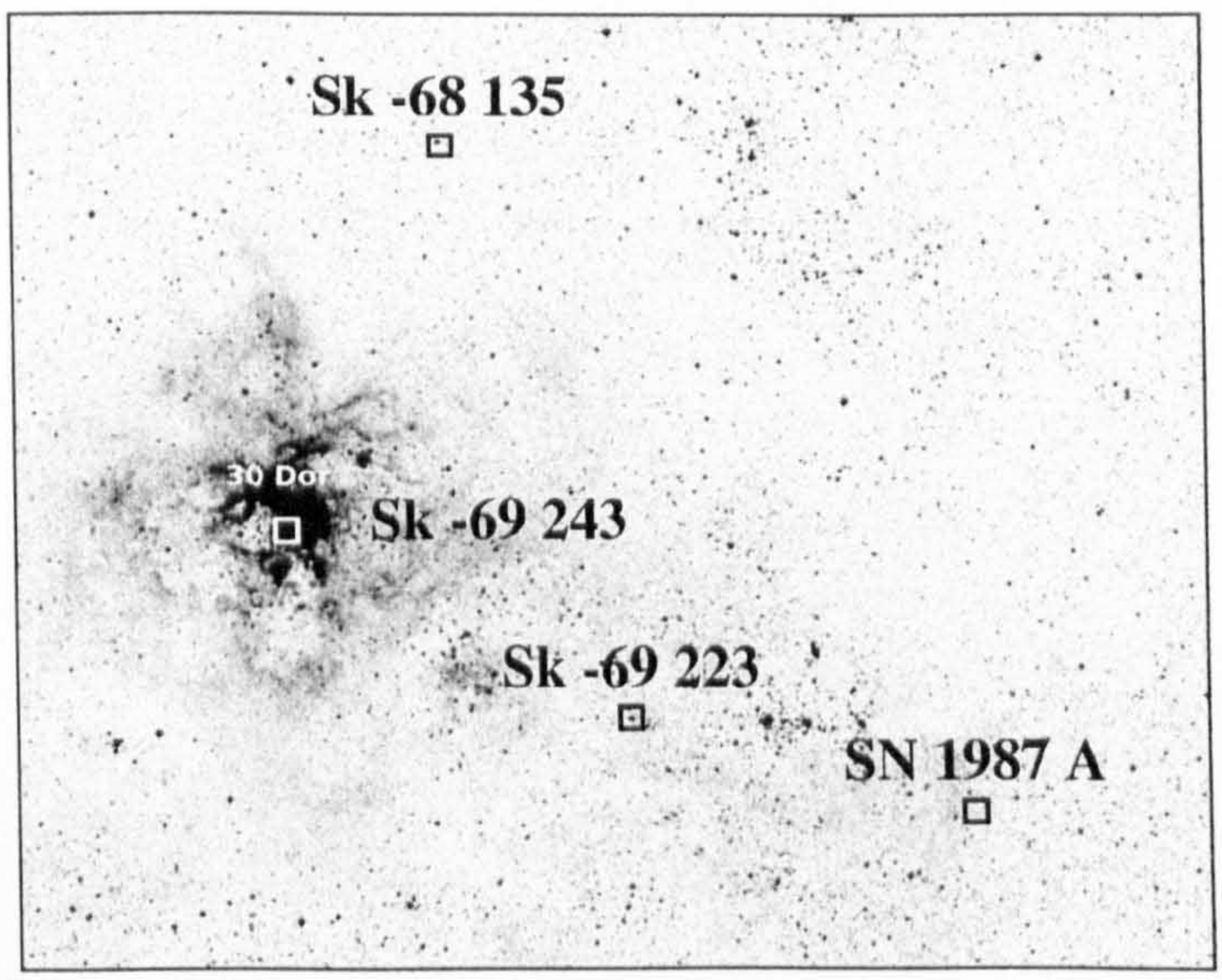

Figure 3.3: Optical images of the Large Magellanic Cloud and magnified 30 Dor region, showing the positions of the observed targets. SN 1987A, the LMC bar, and the LMC2 H II supershell are also marked. Images courtesy of K. D. Gordon (private communication), with additional annotations.

Target	HD number	RA (J2000)	DEC (J2000)	MK type	V	$B-V$	E_{B-V}
Sk −67°2	270754	04 47 04	-67 06 53.1	B1.5 Ia[a]	11.27[a]	0.10[a]	0.26
Sk −67°5	268605	04 50 19	-67 39 37.9	O9.7 Ib[b]	11.34[f]	-0.12[f,h]	0.11
Sk −68°135	269896	05 37 49	-68 55 08.0	B0 Ia[c]	11.35[f]	0.00[f]	0.22
Sk −69°223	38029	05 36 55	-69 11 37.3	WC4+OB (B1.5 Ia)[d]	11.59[g]	0.11[g]	0.38[i]
Sk −69°243	38268	05 38 43	-69 06 03.9	Composite (O3)[e]	9.50[g]	0.13[g]	0.40
Sk −70°120	270196	05 51 21	-70 17 08.7	B1.5 Ia[a]	11.61[a]	0.05[a,h]	0.10

Table 3.1: Characteristics of the observed LMC targets. Photometric and spectral-type data are from references as labelled: '[a]' — Hipparcos catalogue (Perryman & ESA 1997); [b] — Walborn & Blades (1997); [c] — Feast *et al.* (1960); [d] — Breysacher *et al.* (1999), bracketed type derived from this study; [f] — Ardeberg *et al.* (1972); [g] — Feitzinger & Isserstedt (1983); [h] Fitzpatrick (1988). [e] denotes that Sk −69°243 is the composite object R136, studied by Massey & Hunter (1998), composed mainly of O3 supergiants. E_{B-V} values were calculated from the literature photometry and spectral type, using intrinsic colours for LMC supergiants from Fitzpatrick (1988). [i] denotes that the E_{B-V} of Sk −69°223 may be uncertain due to confusion in the literature over the nature of this apparently composite object, classified by most authors as a Wolf-Rayet but the primary object is found by this study to be a B1.5 Ia supergiant; the reddening cited in this table was derived using Wolf-Rayet narrow-band colours (Smith 1968; Smith *et al.* 1990; Breysacher *et al.* 1999) — see discussion in text (Section 3.4.1).

A continuum S/N of between 100 and 200 was achieved for all spectral regions of interest in all targets, except for the regions containing the Na I UV doublet and the stronger of the Ti II lines for Sk −69°223, where vignetting at the compromised echelle setting reduced the continuum S/N to ~ 30 and ~ 60 respectively.

The resolution of the final spectra was $R \simeq 86,000$ ($\simeq 3.5$ km s^{-1}) for all wavelengths shorter than 6800 Å recorded on the 346 + 590 and 390 + 564 settings, as measured from unblended Th/Ar arc lamp lines. For the far-red-NIR data (recorded on setting 437 + 860), a resolving power of $R \simeq 100,000$ ($\simeq 3.0$ km s^{-1}) was measured in the vicinity of the K I doublet.

3.4 Spectra

The initial part of the reduction of the raw CCD images was undertaken as part of a collaboration with N. L. J. Cox (see Cox *et al.* 2005) using the MIDAS echelle reduction procedures, including routines tailored specifically to UVES data reduction.

Reductions were carried out by the author as described in Chapter 2 to shift the spectra to LSR (local standard of rest) wavelength, normalise the continua and divide out telluric features. The lightly-reddened standard star Sk −70°120 was used for telluric division except for the spectral region containing the Na D lines, due to Galactic Na I absorption in the Sk −70°120 spectrum. The unreddened star α Eri (Achernar) was used instead, which shows no evidence of interstellar Na I. Raw data and calibration frames for Achernar (recorded using UVES), were obtained from the ESO data archive[4], and reduced using IRAF according to the procedures outlined in Chapter 2 of this thesis.

The K I λ7665 line is overlapped by a telluric O_2 band of substantial optical depth, and cannot be used reliably for column-density measurement, whereas the K I λ7699 line lies *between* telluric absorption lines of the same O_2 band. Removal of these telluric features was performed by fitting and subtracting Gaussians; $\sigma_f \approx \sigma_c$ was checked in each case, where σ_f is the residual RMS of the fitted Gaussian compared to the spectrum, and σ_c is the RMS of the noise in the continuum. Small telluric features are

[4]Observations made with ESO Telescopes at the Paranal Observatory under programme ID (60.A-9022(A)).

known to exist between the major absorptions in the O_2 band, but the dryness of the atmosphere at the Cerro Paranal Observatory site renders them insignificantly small and their effects negligible at this S/N.

For the Ca II H lines, removal of several broad stellar hydrogen and helium absorption features was necessary. This was accomplished by fitting and subtracting Gaussians (under the assumption of a Gaussian stellar absorption line-shape). Again, $\sigma_f \approx \sigma_c$ was checked in each case. Excellent agreement between the profiles of the Ca II H and K lines was obtained after this process.

3.4.1 Photometric uncertainties and reddening

Uncertainties in the Johnson UBV photometry for the stars in Table 3.1 are typically $\sim 0.01-0.02$ magnitudes. Spectral types are well determined for Sk −67°2, Sk −67°5, Sk −68°135 and Sk −70°120. Sk −69°223 (HD 39029) is listed in the literature as a WC4+OB Wolf-Rayet (Feitzinger & Isserstedt 1983; Torres *et al.* 1986; Smith *et al.* 1990; Breysacher *et al.* 1999) named Brey 67 in LMC Wolf-Rayet survey of Breysacher (1981). Examination of the spectrum we obtained reveals no evidence for WC4 features, or indeed any of the He II, C III C IV, O IV or O V emission features associated with the WC class of objects. Smith *et al.* (1990) and Torres *et al.* (1986) both measure a logarithmic equivalent width of 1.89 log(Å) for the C IV 5801 Å emission feature but our spectra show no emission at this wavelength. From the ratio of the He I absorption line equivalent widths at 4009 Å and 4026 Å, the spectrum of Sk −69°223 can be classified in the Harvard system as B1.5 Ia, with a P-Cygni He II 6560 Å profile indicative of mass outflow. The spectrum of Sk −69°223 is almost identical to that of Sk −70°120, cited as a B1.5 Ia supergiant by Fitzpatrick (1988).

The acquisition image from the exposure of Sk −69°223 (Figure 3.4) suggests that the confusion over the spectral type of this object may be due to a case of mistaken identity. Past studies (Breysacher 1981; Feitzinger & Isserstedt 1983; Torres *et al.* 1986; Smith *et al.* 1990; Breysacher *et al.* 1999) make no mention of multiplicity in the visual constituents of this object, though the presence of OB stellar features has been noted (hence the WC4+OB classification), which in a WR spectrum is generally taken as evidence of an OB-type companion. From Figure 3.4 it is clear that the brightest star in Sk −69°223 (the star over which the spectrograph slit was placed), is separated

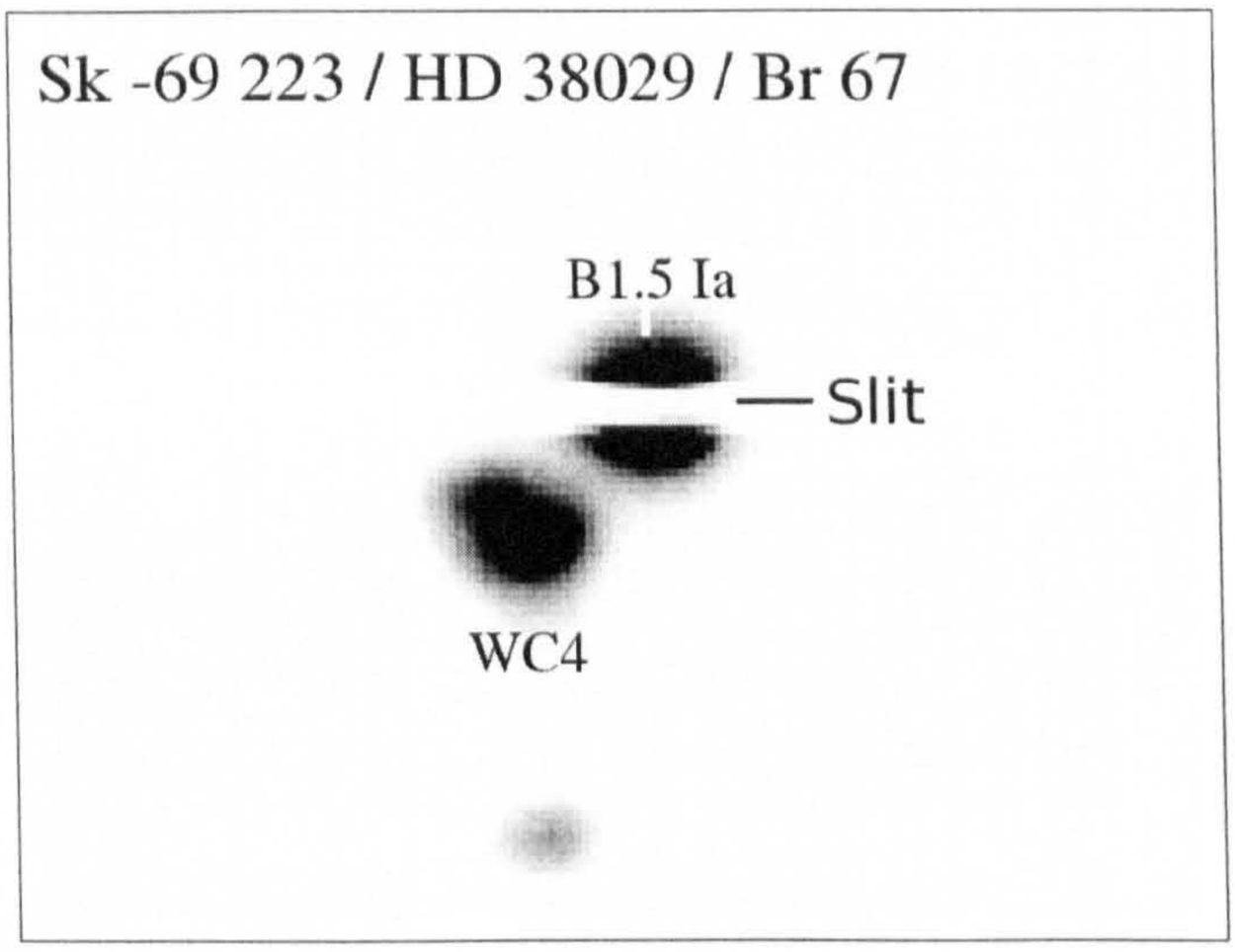

Figure 3.4: The acquisition image for one of the exposures of Sk −69°223. Slit width is 0.5″, seeing was ~ 0.6″. Sk −69°223 is a composite object consisting of a B1.5 Ia supergiant and a dimmer WC4 companion.

from the dimmer counterpart by between 1.5 and 2 arcseconds. Conceivably, past observations may have been made in conditions of poorer seeing such that the multiple components were not resolved. The primary component is of type B1.5 Ia, so by inference, the dimmer companion is the WC4 Wolf-Rayet, which itself appears to be a binary object.

Given the relative weakness of the continuum emission in Wolf-Rayet stars, the narrow-band colours of the 'composite object' Sk −69°223 will be dominated by the B1.5 Ia primary. Johnsson broad-band photometry is likely to be highly polluted by the WC4 He II, C III and C IV lines of the Wolf-Rayet. From the narrow-band photometry ($b-v = 0.02$) of Breysacher *et al.* (1999) and the relationship between $B-V$ and $b-v$ of Turner (1982), using B1.5 Ia intrinsic colours ($(B-V)_0 = 0.16$) from Fitzpatrick (1988)), a reddening of $E_{B-V} = 0.34$ is found for Sk −69°223. This is discrepant from the value of 0.38 derived in Table 3.1 using the WC4 intrinsic narrow-band colours of Smith *et al.* (1990), probably due to the contribution of the B1.5 Ia's flux to the overall observed continuum.

Sk −69°243 (or R136) is a composite object composed of around 65 massive (~ 100 $M_\odot$), hot stars (~ 50,000 K), and studied in detail by Massey & Hunter (1998) using the HST, who refer to it as a 'super star cluster'. This unusual object contains more O3 and O3 If* stars than have been observed anywhere else in the Universe, and is the source of much of the ionising radiation that fuels the huge 30 Dor H II emission neb-

ula. Also contained within the core are several unusually hot WN-type Wolf-Rayets. Examination of the observed spectrum of Sk −69°243 (contrasting the situation of Sk −69°223), reveals broad He II, N IV and N V emission features characteristic of the highly excited, nitrogen rich winds of WN stars. The stellar continuum is dominated by the O3 stars.

The reddening of Sk −69°243 was derived from Johnson photometry with the assumed intrinsic colours of an LMC O3 star (Fitzpatrick 1988). The E_{B-V} value of 0.40 so obtained agrees with the average value of 0.40 ± 0.06 derived by Massey & Hunter who fitted Kurucz model-atmospheres to 54 of the stars in R136 that have well defined spectral types.

3.4.2 Atomic and ionic spectra

Examples of the spectra observed towards the programme targets are shown for Ca II K in Figure 3.5, for the Na D lines in Figure 3.6 and for the Na I UV doublet in Figure 3.7. VAPID (see Chapter 2, Section 2.4.1) was used to construct cloud models for these spectra, utilising the air wavelengths and oscillator strengths from Morton (2003), except for the Na D lines, for which the hyperfine-splitting was modelled using the transition data from Welty *et al.* (1994). For Ca II, the H and K lines were fitted simultaneously, and for Na I, the Na D_1, D_2, Na I UV λ3302.4 and λ3303.0 lines were fitted simultaneously. The K I λ7699 line was fitted as a single transition. Reasonable convergence of models was achieved, with the residual RMS approaching the continuum RMS to within a factor of two in every fit. The S/N and resolution of the data allowed detection of clouds to a column density limit of $\gtrsim 2 \times 10^{10}$ cm^{-2} in Na I and K I, and $\gtrsim 3 \times 10^{10}$ cm^{-2} in Ca II.

A clear division in velocity space is evident between Galactic interstellar clouds (around $v_{\rm LSR} \simeq 0$ km s^{-1}) and LMC clouds (around $v_{\rm LSR} \simeq 275$ km s^{-1}), with small contributions to the overall column densities by IVCs and HVCs in the lines of sight. The overlap between LMC and Galactic components in the two lines of the Na D doublet is negligible for all stars except Sk −70°120, for which the D_2 line absorption at $v_{\rm LSR} \simeq 300$ km s^{-1} is severely blended with the Galactic D_1 absorption around $v_{\rm LSR} \simeq 0$ km s^{-1} (the LMC Na D_2 line begins to overlap the MW Na D_1 line at around 5895.5 Å). This problem is not apparent for other atomic doublet transitions.

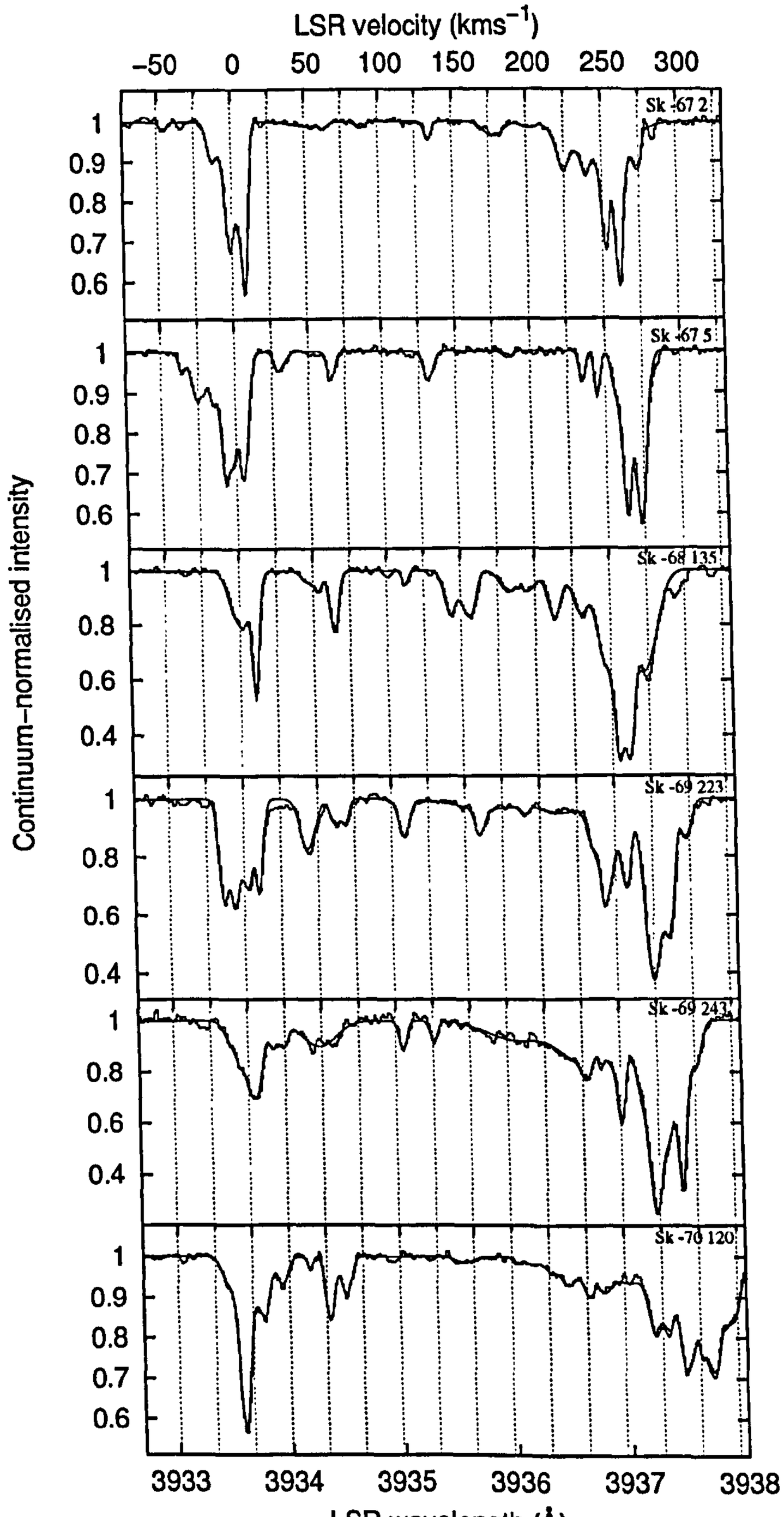

Figure 3.5: The histograms show the Ca II K spectra observed towards the six LMC targets, shifted to LSR frame and continuum-normalised. VAPID model fits are overlaid as smooth curves.

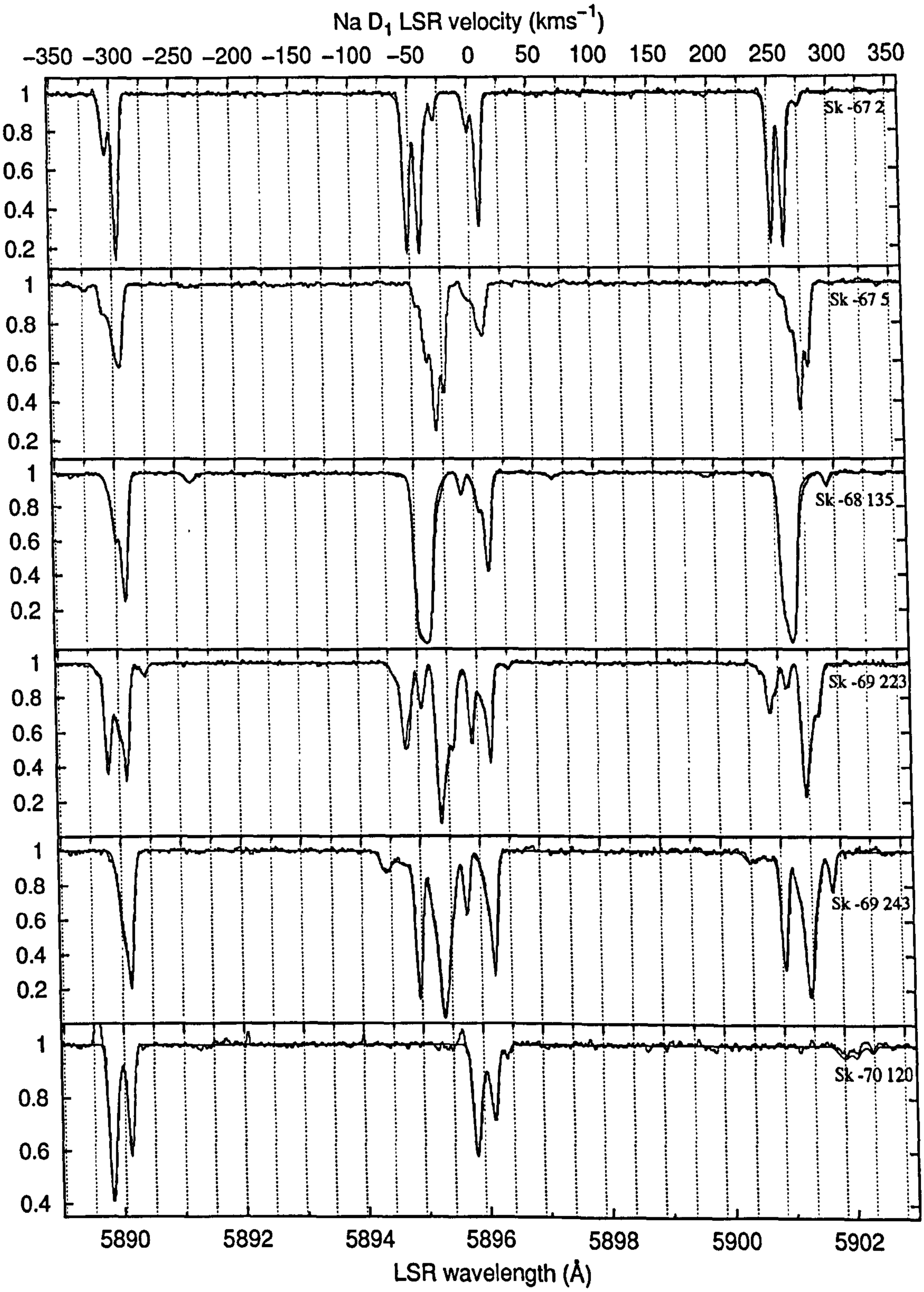

Figure 3.6: The histograms show the Na I D doublet spectra observed towards the six LMC targets, shifted to LSR frame, telluric-corrected and continuum-normalised. VAPID model fits are overlaid as smooth curves.

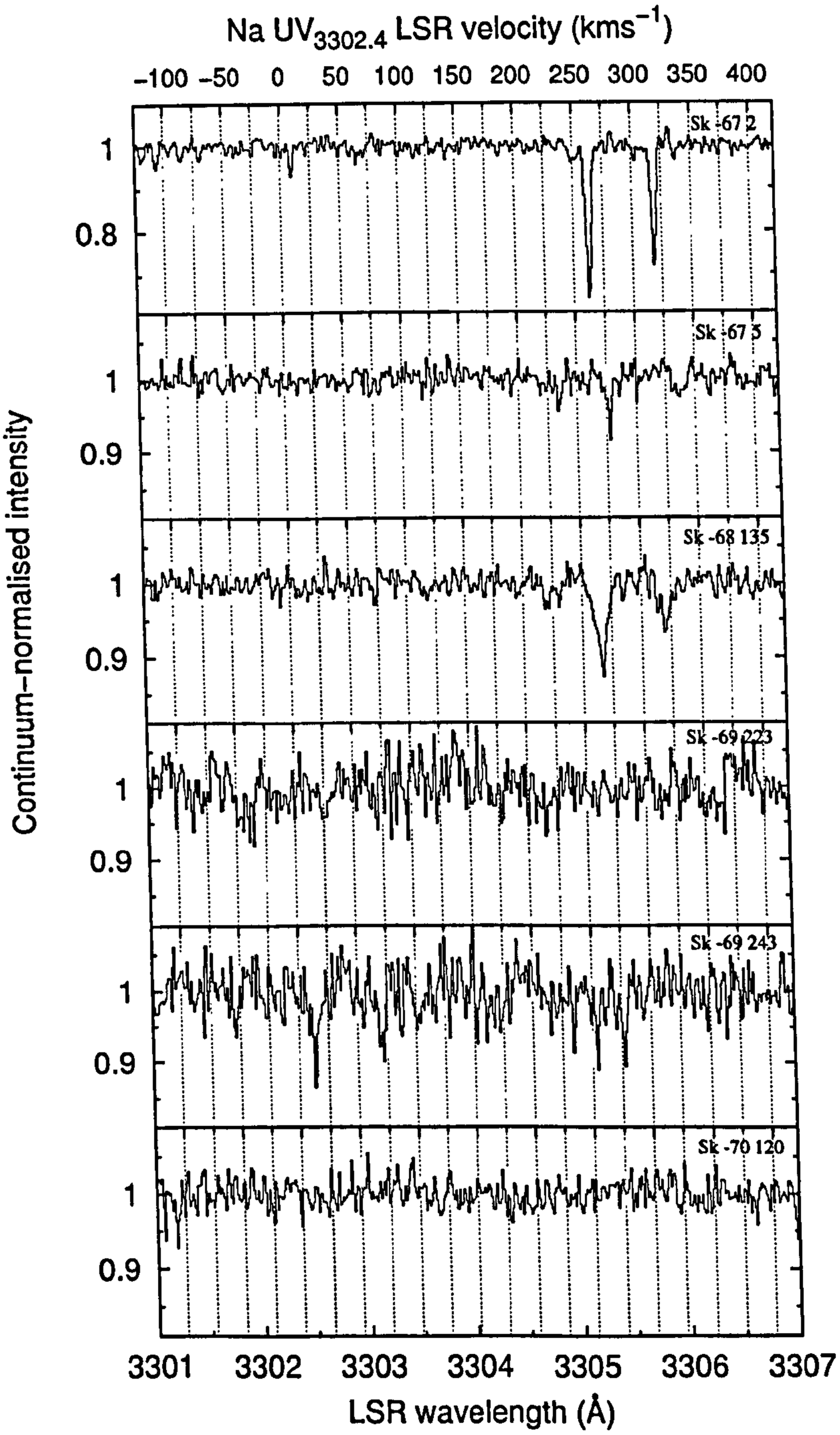

Figure 3.7: The Na UV doublet spectra observed towards the six LMC stars, shifted to LSR frame and continuum-normalised.

Comparison of the Sk −69°243 Ca II and Na I spectra with those obtained by Blades & Meaburn (1980), Molaro *et al.* (1993) and Vladilo *et al.* (1993) shows excellent correspondence between our data and those previously recorded for this sightline. Our spectra, however, are of higher resolution and S/N.

From Figures 3.5 and 3.6, the complexity of cloud component structure along the lines of sight is clear. A spatial scale-dependent variation of cloud parameters is evident: The most closely spaced sightlines are Sk −68°135, Sk −69°223 and Sk −69°243, approximately 20′ apart from each other. Given that most of the Galactic gas along these sightlines should be located $\lesssim$ 1 kpc away (Sembach & Danks 1994), the dramatic differences between the Na I and Ca II profiles in the vicinity of $v_{\rm LSR} = 0$ show that the Galactic gas probed must be highly fragmented over a scale of $\lesssim$ 6 pc. There is a relatively narrow cloud component seen in Ca II and Na I gas with $v_{\rm LSR} = 8-12$ km s^{-1} that remains of roughly similar strength and Doppler width across all sightlines. Although perhaps not a single, contiguous cloud, this component is suggestive of a sheet of interstellar matter spanning over 1 hour in RA in the direction of the LMC, with a spatial extent of $\gtrsim$ 250 pc. These results are in accord with those of Molaro *et al.* (1993), who, however, assume the gas to be located at a radial distance of less than 100 pc. Using this value leads to a cloud size of $\lesssim$ 0.6 pc for the variable Na I and Ca II components near $v_{\rm LSR} \simeq 0$ km s^{-1}.

The importance of the Na UV doublet (data shown in Figure 3.7) for deriving accurate column densities in profile fits must be noted; even at this high resolution (~ 3.5 km s^{-1}), it is not sufficient to use the Na D lines alone, even when they *appear* to be relatively unsaturated. The highly saturated Na D lines of Sk −68°135 clearly require the use of Na UV data because their core optical depths approach infinity. For the $v_{\rm LSR} \simeq 0$ km s^{-1} clouds towards Sk −69°243, VAPID least-squares column densities were about an order of magnitude less without the use of Na UV (Figure 3.7) data, even though the apparent optical depth of the Na D_2 line reaches only $\tau_a(\lambda) \simeq 1.6$. This reveals an unexpected result that the Galactic contribution to the Na I column density is greater than the LMC's contribution for this sightline.

Further discrepancies between Na D-derived column densities and physical reality are seen for the *second* of the pair of the LMC Na I clouds towards Sk −67°2 (at $v_{\rm LSR} \simeq 262$ km s^{-1}): from examination of the Na D spectra (Figure 3.6), this cloud and its partner at $v_{\rm LSR} \simeq 251$ km s^{-1} appear to have very similar column densities. However, the less

saturated Na UV data (Figure 3.7) show that the $v_{\rm LSR} \simeq 262$ km s^{-1} component actually has over ten times the column density of the component at $v_{\rm LSR} \simeq 251$ km s^{-1} that is hardly visible above the noise. Such discrepancies are caused by degradation of the apparent optical depth of narrow cloud components by the finite instrumental resolution. The narrower an absorption line is (*i.e.* low Doppler b), the greater the degradation in the apparent optical depth in its core due to the instrumental point spread function, resulting in a reduction in the measured column density (using Equation (2.18)) when the b value is unknown. Thus, a problem with using least-squares fits is identified: that when b cannot be reliably determined (for example, for very narrow, unresolved or heavily blended lines), the effects of optical depth degradation by the instrumental point spread function cannot be quantified. Such optical depth degradation, however, only affects integrated component column densities severely for high optical depths.

For Ca II K[5], $\tau_a(\lambda) < 1$ for all the recorded spectra, so unresolved saturated structure is less significant than for the Na D lines. The apparent optical depth $\tau_a(\lambda)$ remains below 0.55 for the observed Ti II spectra, and below 0.25 for K I, such that degradation of the true optical depth profile due to the spectral resolution is quite small for these data.

3.4.3 Diffuse interstellar band spectra

Diffuse interstellar bands were identified in the LMC spectra by reference to the surveys of Jenniskens & Desért (1994), Tuairisg *et al.* (2000) and Galazutdinov *et al.* (2000b) for wavelengths, profiles and expected strength ratios. Doppler shifted DIBs with components attributable to absorption in the LMC gas at $v_{\rm LSR} \simeq 270$ km s^{-1} were found in the spectra of Sk −67°2, Sk −67°5, Sk −68°135, Sk −69°223 and Sk −69°243. Table 3.2 lists the equivalent widths and approximate wavelengths of the DIBs observed in the LMC. Errors on the equivalent widths, σ_{W_λ}, are given in parentheses after each entry, estimated using $\sigma_{W_\lambda} = \sigma_c \Delta_\lambda$ where σ_c is the normalised continuum RMS of the spectrum and Δ_λ is the wavelength interval over which $(I_0(\lambda) - I(\lambda))/I_0(\lambda)$ was integrated to find W_λ. Upper limits on W_λ are given where no DIB was measured, calculated using $W_\lambda < 3\sigma_c\Gamma_\lambda$, assuming a triangular DIB shape and a $3\sigma_c$ detection limit on the peak absorption strength. DIB full width half maxima, Γ_λ, were taken from

[5]The stronger of the H and K lines.

Sightline	W_{4430} 4431.95	W_{5705} 5710.23	W_{5780} 5785.57	W_{5797} 5802.21	W_{5850} 5855.08	W_{6196} 6201.57	W_{6203} 6208.67	W_{6284} 6289.51	W_{6376} 6381.71	W_{6379} 6384.96	W_{6614} 6619.51
Sk –67°2	<250	9 (23)	–	–	10 (5)	5 (3)	17 (17)	150 (29)	<23	<10	13 (8)
Sk –67°5	<200	<28	–	–	<15	<7	2.5 (14)	<69	<17	<7	<13
Sk –68°135	<200	<23	–	–	5 (5)	<7	19 (14)	30 (30)	<20	<10	5 (3)
Sk –69°223	20 (160)	20 (9)	145 (21)	28 (6)	2 (6)	12 (3)	50 (20)	240 (21)	5 (6)	12 (4)	20 (8)
Sk –69°243	150 (180)	25 (21)	–	–	11 (6)	7 (3)	25 (14)	335 (47)	<28	15 (4)	50 (14)

Table 3.2: Equivalent widths W_λ (in mÅ) of the DIBs in the reddened LMC sightlines. Error estimates given in parentheses. DIBs are named according to peak wavelength, and the LMC wavelengths are given (in Å) based on $V_{\rm LSR} = 270\,{\rm kms}^{-1}$ for the LMC absorbing gas. Where no DIB detection was made, equivalent width upper limits are given. Dashes denote spectral regions missing from the data.

Tuairisg *et al.* (2000), with the assumption that the LMC and Galactic DIB profiles are approxiamately the same.

The targets with the strongest DIBs were Sk −69°223 and Sk −69°243, followed by Sk −67°2, then Sk −68°135 and Sk −67°5, in accordance with the total reddening along the lines of sight. Most of the targets show evidence for DIBs at the wavelengths expected for absorption arising in 'foreground' Galactic material (see *e.g.* Figure 3.10). Indeed, for Sk −70°120 (with low reddening, $E_{B-V} = 0.1$), the only observed DIBs are those at Galactic rest wavelengths, seen clearly in Figure 3.9.

In the spectra observed towards Sk −69°223, the λ4430, λ5705, λ5780, λ5797, λ5850, λ6196, λ6203, λ6284, λ6376, λ6379 and λ6614 DIBs were all detected. Marginal detections of the DIBs λ6993 and λ7224 were also made (not shown). The observed spectral regions containing the detected DIBs towards all the programme targets are shown in Figures 3.8 to 3.13.

A well-exposed reddened Galactic spectrum is shown (towards either HD 183143, β^1 Sco, or ρ Oph A), to provide a reference for expected DIB strength and profile. The vertical dotted lines represent the expected approximate wavelengths of the DIBs in the rest frame of the LMC (radial velocity ~ 280 km s^{-1} with respect to the local standard of rest). Spectra are continuum-normalised with low-order polynomials and shifted to the LSR reference frame, with vertical additive offsets for display in the figures.

The DIBs detected are those expected given the S/N levels achieved and the approximate reddenings of the targets. It is clear that there are substantial variations in the relative strengths of some of the DIBs between targets (see, for example Figure 3.12), sometimes precluding measurement of the weaker bands as they move below the detection threshold imposed by the S/N.

The λ4430 DIB was only detected reliably towards Sk −69°223 and Sk −69°243. This is a difficult DIB to observe in echelle spectra because it spans almost an entire echelle order (with a Lorentzian profile, FWHM ~ 20 Å), so small errors in blaze correction over the length of the order can change its strength and profile significantly, particularly when it is weak. The difficulty in achieving complete blaze correction is highlighted by the tail-off in the continuum at the blue end of the LMC spectra in Figure 3.8. However, all the spectra were blaze-corrected identically (using flat field spectra to determine the blaze function), so that *differences* between the spectra should be real.

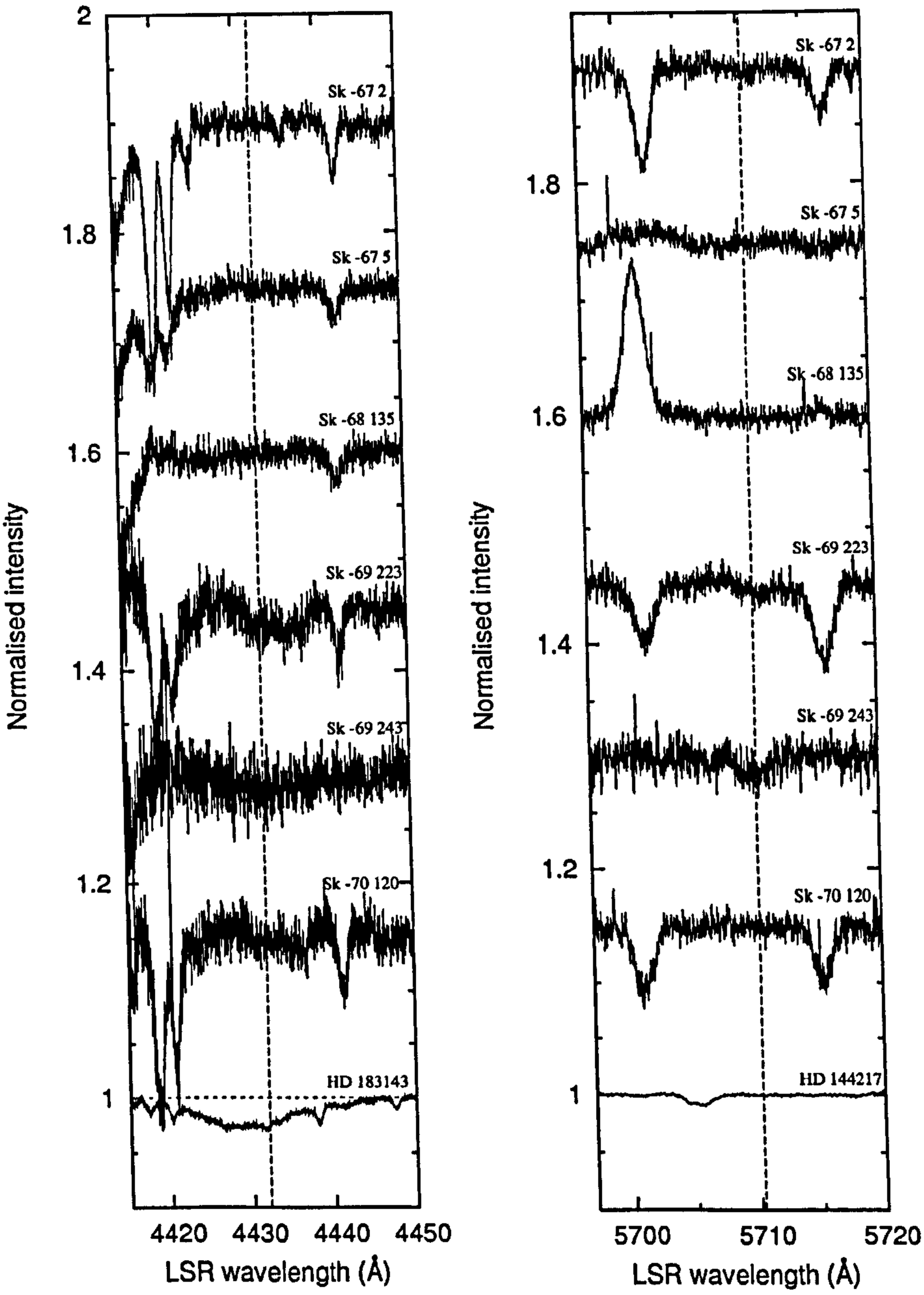

Figure 3.8: The spectral regions covering the λ4430 and λ5705 diffuse interstellar bands towards the six LMC sightlines. The vertical dashed lines represent the expected positions of the LMC DIBs based on the mean radial velocity of the LMC. HD 183143, shown as a Galactic comparison for λ4430, is scaled by a factor of 0.25 to give an approximate strength comparison between this heavily-reddened Galactic target (E_{B-V} = 1.27) and the moderately reddened LMC targets (E_{B-V} 0.2 ~ 0.3). HD 144217 (β^1 Sco, E_{B-V} = 0.22), is shown as a Galactic comparison for λ5705.

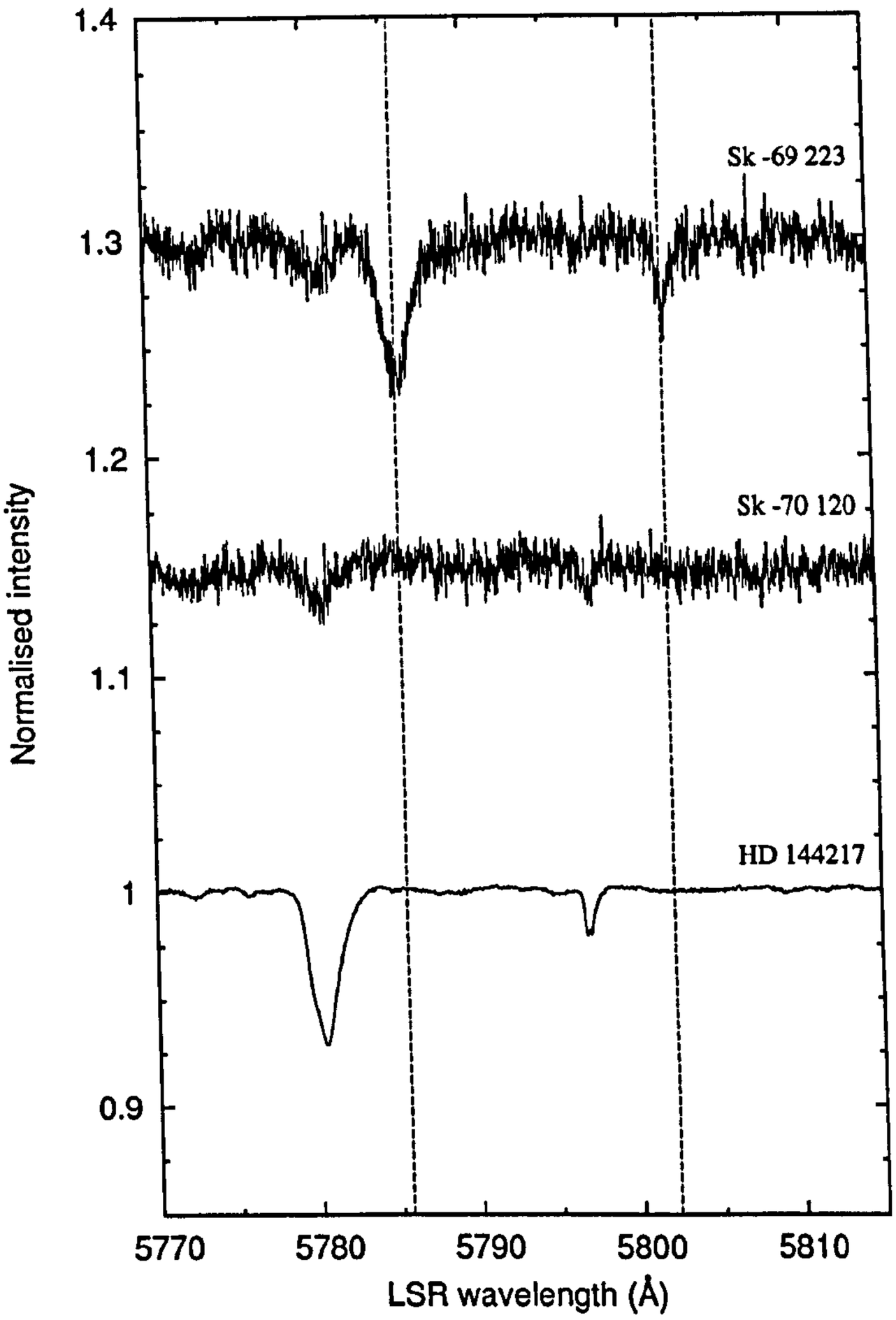

Figure 3.9: The spectral region covering the λ5780 and λ5797 diffuse interstellar bands towards Sk −69°223 and Sk −70°120. The vertical dashed lines represent the expected positions of the LMC DIBs based on the mean radial velocity of the LMC. HD 144217 (β^1 Sco, $E_{B-V} = 0.22$, σ-type sightline), is shown as a Galactic comparison.

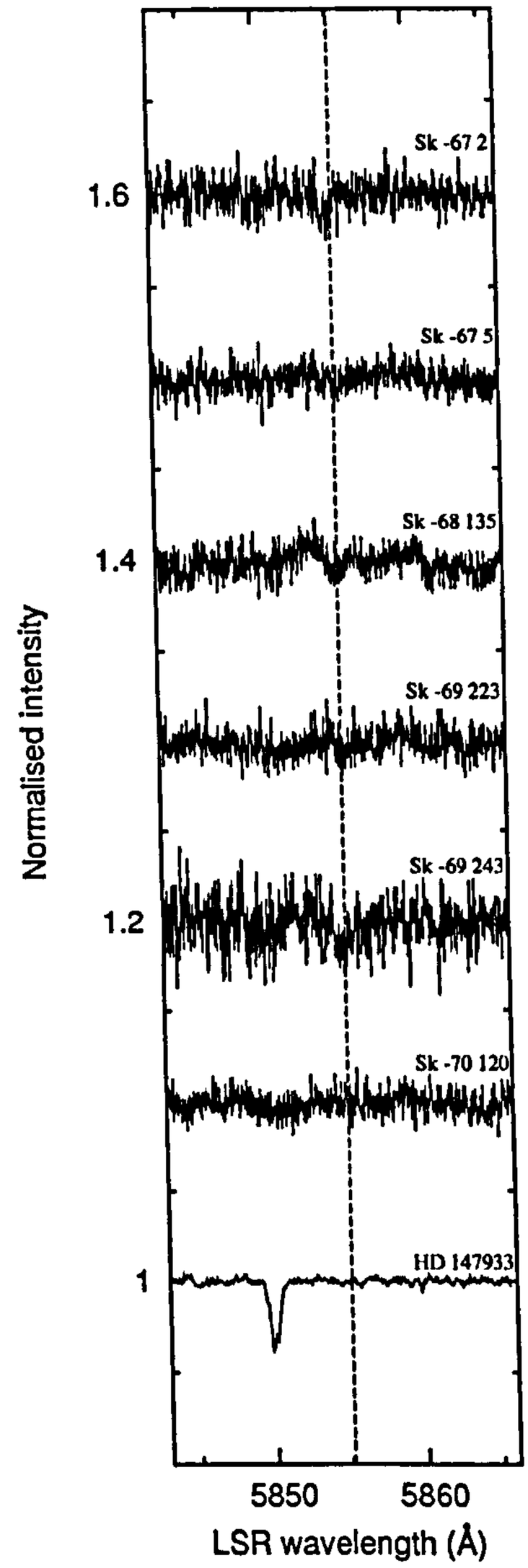

Figure 3.10: The spectral region covering the λ5850 diffuse interstellar band towards the six LMC sightlines. The vertical dashed line represents the expected positions of the LMC DIBs based on the mean radial velocity of the LMC. HD 147933 (ρ Oph A, $E_{B-V} = 0.48$), is shown as a Galactic comparison.

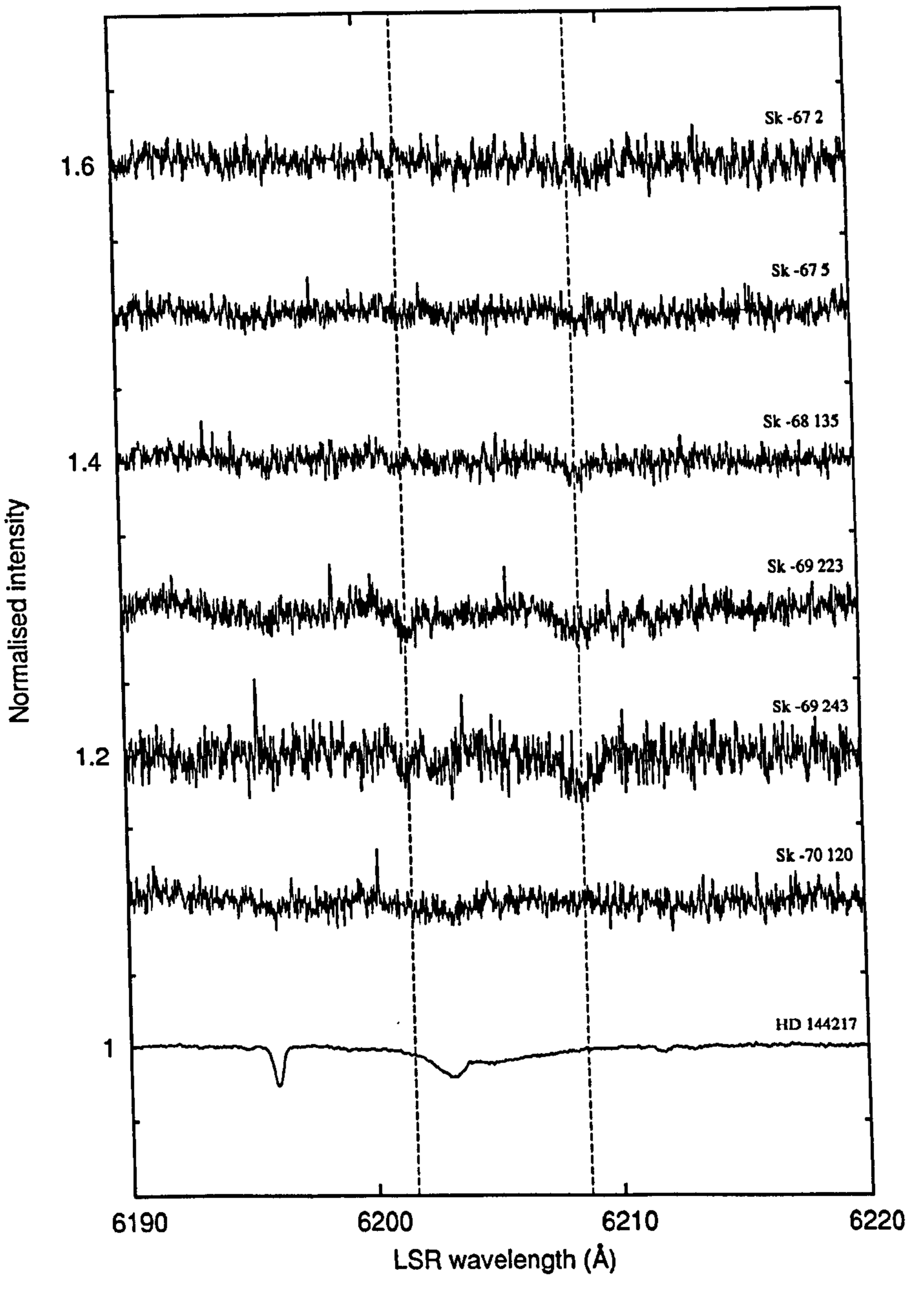

Figure 3.11: The spectral region covering the λ6196 and λ6203 diffuse interstellar bands towards the six LMC sightlines. The vertical dashed lines represent the expected positions of the LMC DIBs based on the mean radial velocity of the LMC. HD 144217 (β^1 Sco, $E_{B-V} = 0.22$, σ-type sightline), is shown as a Galactic comparison.

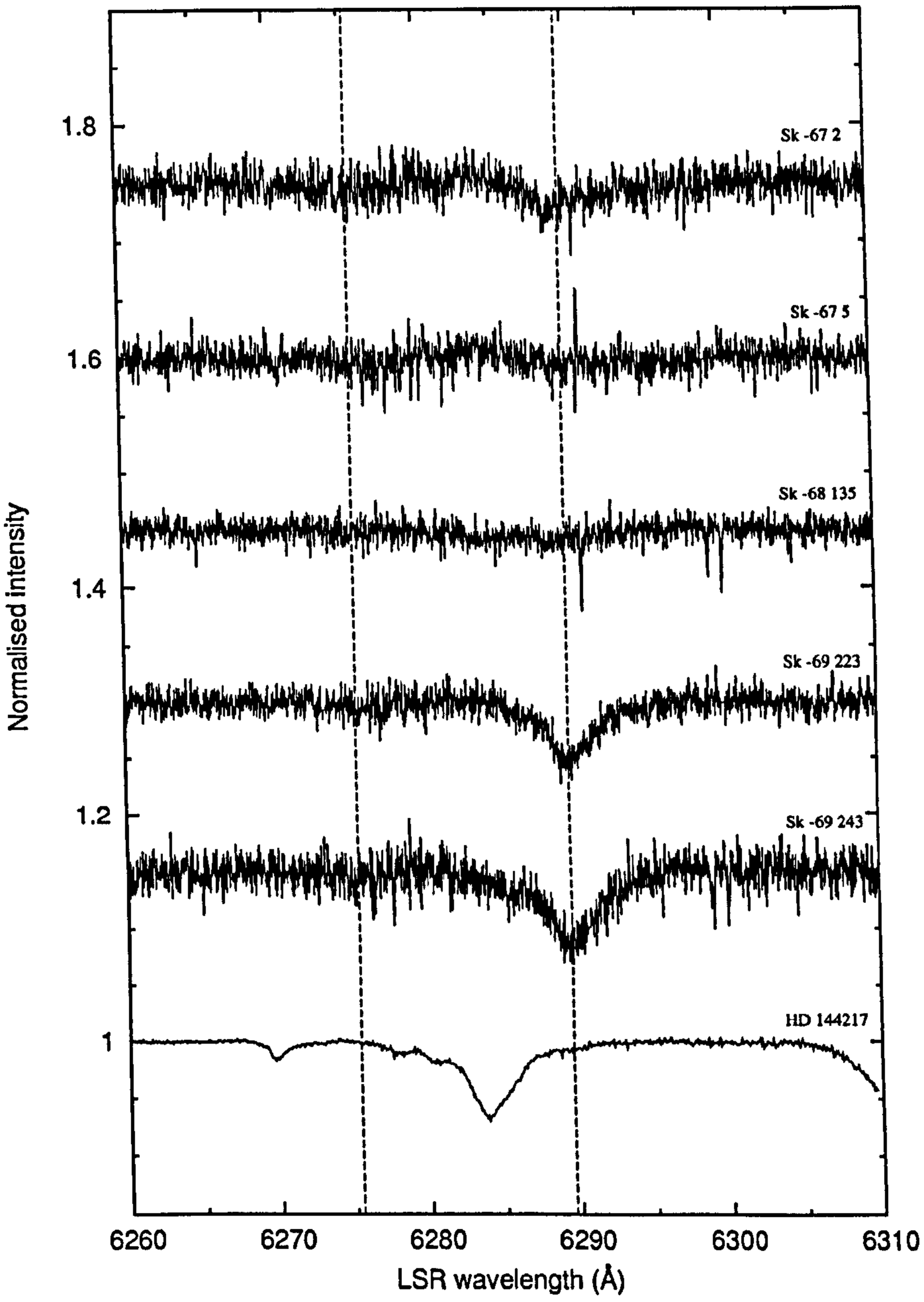

Figure 3.12: The spectral region covering the λ6270 and λ6284 diffuse interstellar bands towards the five sightlines reddened by LMC dust, telluric-corrected using the Sk –70°120 spectrum. The vertical dashed lines represent the expected positions of the LMC DIBs based on the mean radial velocity of the LMC. HD 144217 (β^1 Sco, $E_{B-V} = 0.22$, σ-type sightline), is shown as a Galactic comparison.

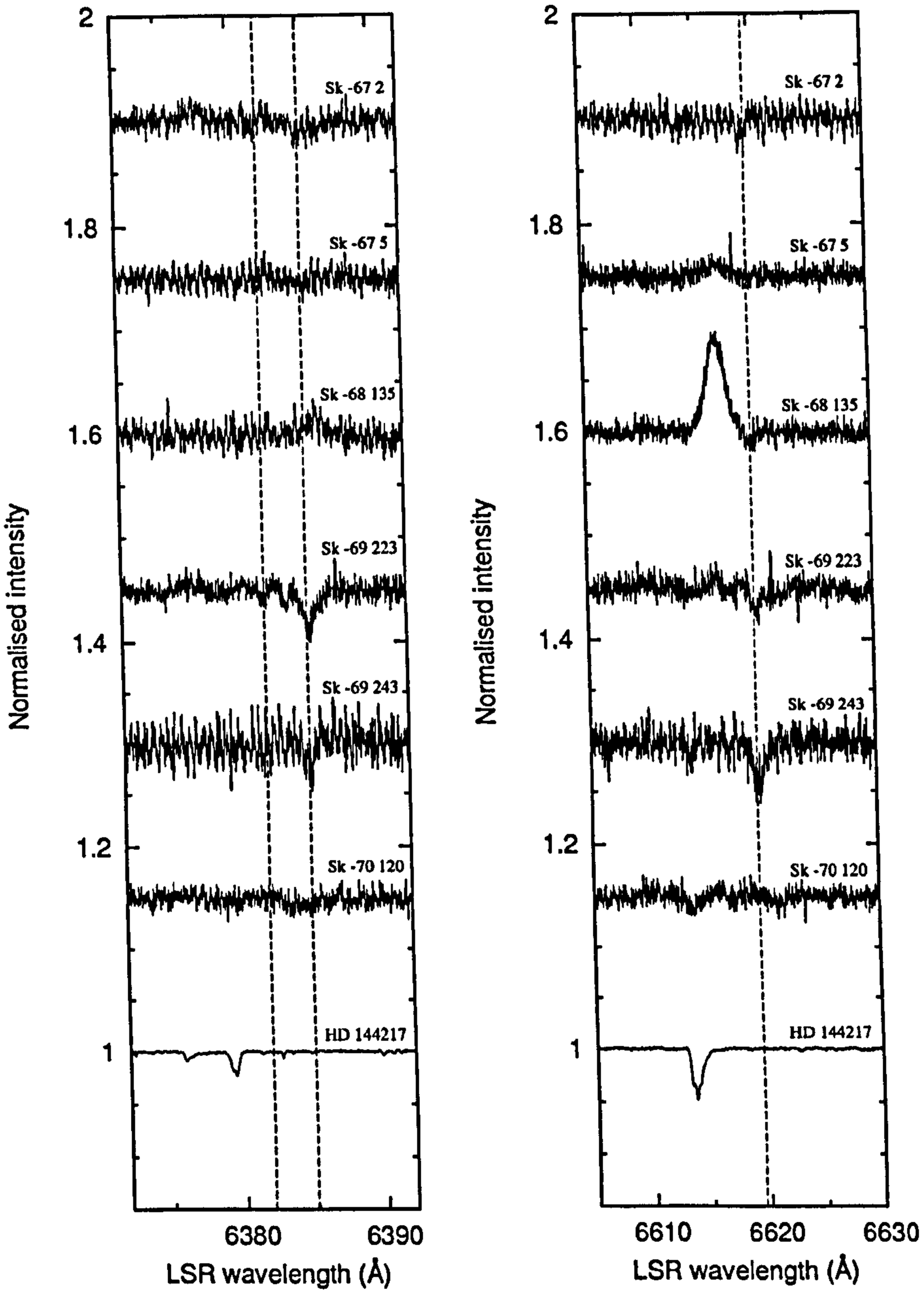

Figure 3.13: The spectral regions covering the λ6379 and λ6614 diffuse interstellar bands towards the six LMC sightlines. The vertical dashed lines represent the expected position of the LMC DIBs based on the mean radial velocity of the LMC. HD 144217 (β^1 Sco, E_{B-V} = 0.22, σ-type sightline), is shown as a Galactic comparison.

Their shared continuum shapes may be uncertain however. The rest of the detected diffuse interstellar bands are narrow enough to have reliable continua.

The spectra of the region around 5850 Å (Figure 3.10) constitute the first reported detection of the λ5850 DIB in an external galaxy. An apparent small emission feature to the blue of the LMC λ5850 feature towards Sk −68°135 is of unknown origin.

The only DIB detected towards Sk −67°5 is λ6203, seen in Figure 3.11. This is a marginal detection, but the profile of the DIB appears to be correct with respect to the Galactic reference spectrum of HD 144217.

Figure 3.12 shows the region containing λ6270 and λ6284 which are the only DIB spectra presented that required telluric correction. Near-perfect removal of the telluric oxygen absorption features was achieved by division by the Sk −70°120 spectrum. It was assumed that the Galactic foreground λ6284 component was of similar magnitude for all stars. In any case, the overlap between the Galactic and LMC λ6284 profiles is small enough for possible blending to have only a marginal effect on measured column densities. The λ6270 DIB's relative weakness puts it below the detection threshold of the spectra.

Further analysis of the DIB strengths requires knowledge of the Milky Way foreground reddening towards the targets in order to separate the Galactic and LMC contributions to the dust columns along the lines of sight. This information can be obtained with the aid of atomic species known to correlate with E_{B-V}.

3.5 Structure and composition of the ISM towards the LMC

3.5.1 $N_v(v)$ profiles and apparent optical depth (AOD) analysis

To facilitate analysis and inter-comparison of the velocity distributions of the observed atomic species, the spectra have been converted to '$N_v(v)$ profiles'. Each atomic spectrum was transformed into $\tau(v)$ space using $\tau(\lambda) = \ln(I_0(\lambda)/I(\lambda))$ and the air rest wavelengths from Morton (2003). The column densities $N(v)$ of the atomic species were then calculated per unit velocity for each data point in the spectra, based on the rela-

tionship between $\tau(v)$ and $N(v)$ derived (see Savage & Sembach 1991) from Equation 2.18:

$$N_v(v) = \frac{3.767 \times 10^{14}}{f\lambda_t}\tau(v). \tag{3.1}$$

$N_v(v)$ is the column-density per unit velocity (in units of cm^{-2} $(\mathrm{km\ s}^{-1})^{-1}$), and λ_t is in Ångstroms. The $N_v(v)$ profile may be integrated numerically to obtain the column density over a specified velocity range.

The limited resolution of the spectrograph smears the $\tau(v)$ distribution by convolution with the instrumental (Gaussian) PSF (see Section 2.4.1), degrading the strength of sharp peaks, increasing the strength of the line-wings, resulting in a modified (degraded) optical depth distribution $\tau_a(v)$ recorded in the image of the spectrum[6]. τ_a is known as the 'apparent optical depth' or AOD. When $\tau_a(v)$ is substituted for $\tau(v)$ in Equation (3.1), peak column densities are underestimated. The smearing occurs in intensity space, where the relationship between $I_0(v)/I(v)$ and $\tau(v)$ is exponential so that a change in $I_0(v)/I(v)$ at large $\tau(v)$ is much more significant than an equivalent change at small $\tau(v)$. Thus, where τ is low, integrated column densities are not severely reduced by instrumental degradation, but for high τ, the measured column density degradation is exponentially greater.

At the high resolution ($3 - 3.5$ km s^{-1}) of the LMC atomic spectra, the degradation of $\tau(v)$ into $\tau_a(v)$ represents only a small change in optical depth profile for all the atomic lines except for the Na D lines and some of the stronger, sharper Ca II H and K absorption components. Although the exact form of $\tau(v)$ is not known, and cannot be known without a spectrograph of infinite resolution, the quantity $\tau(v)/\tau_a(v)$ can be calculated using the ingenious technique developed by Jenkins (1996). Known as 'optical depth profile reconstruction', the method utilises the apparent optical depth profiles observed for two different transitions from the same atom (or molecule). Requirements for the technique are that the transitions must be of significantly different strength (*i.e.*, different $f\lambda_t^2$), and originate in the same lower energy level. Examples of such transitions are the spin-orbit doublets of the sodium D lines and the ionised calcium H and K lines where the $^2P_{3/2}$ spin-orbit energy levels are doubly degenerate (and the $^2P_{1/2}$ lev-

[6]The spectrum is recorded in intenity space ($I(\lambda)$), related to optical depth space by $\tau(\lambda) = \ln(I_0(\lambda)/I(\lambda))$ where $I_0(\lambda)$ is the continuum spectral intensity.

els singly degenerate), resulting in a pair of transitions where the shorter wavelength transition is approximately twice the strength of the longer.

The difference in intrinsic transition strength is utilised in standard curve of growth methods (see for example Jenkins 1986), where the degree of saturation in, for example, the Na D_1 line is deduced from the amount by which the ratio of the D_2 to D_1 line equivalent widths differs from the *unsaturated* ratio of 2. Curves of growth for the two lines can be constructed, with functional forms parameterised by a single Doppler b value (or an assumed ensemble of clouds with multiple b values), which when fitted to the equivalent widths of the two observed transitions, yields the column density. Clearly, this method will be inaccurate when knowledge of the velocity distribution (and Doppler b values) of the clouds is incomplete, as is commonly the case.

Jenkins (1996) developed this method for application to $\tau_a(v)$ profiles. Comparison of the Ca II H and K $\tau_a(v)$ profiles shows that the apparent optical depth of the K lines is generally twice that of the H lines except in the strongest, narrowest absorption components where instrumental resolution degrades the stronger profile (K) more than the weaker one (H). The velocities for which $\tau_a(v)_{\mathrm{Ca\ II\ K}} \lesssim 2\tau_a(v)_{\mathrm{Ca\ II\ H}}$ define the locations (in velocity space) of 'unresolved saturated structure'. Provided the ratio of $[f\lambda^2]^s/[f\lambda^2]^w$ is known for the strong (superscript s) and weak (superscript w) transition lines of the doublet, the characteristic ratio $\tau_a(v)^s/\tau_a(v)^w$ describes the amount of unresolved saturated structure for each point in v-space. No information about the functional form of the $\tau_a(v)$ profiles is required, and accordingly no arbitrary (and error prone) assumptions are made about the distribution of absorbing clouds and their Doppler b values.

By modelling interstellar absorption lines, Jenkins (1996) calculated an empirical relationship between $\frac{([f\lambda^2]^s/[f\lambda^2]^w)}{(\tau_a(v)^s/\tau_a(v)^w)}$ and $\tau(v)^w/\tau_a(v)^w$ and derived the relevant correction factor $C(v)$ by which $\tau_a(v)^w$ should be multiplied in order to restore the 'lost' optical depth. The reconstructed optical depth profile may be used with Equation 3.1 to generate column densities as a function of velocity, *i.e.* the $N_v(v)$ profiles.

Jenkins' simulations and comparisons with real data showed his method to be reliable and accurate for measuring column densities over a very wide range of cloud component distributions (parameterised by number of clouds and Doppler b distributions, with varying degrees of cloud overlap and superposition). The method was only seen to break down significantly when analysing lines with a few strongly saturated, narrow

components with a disproportionate amount of absorption caused by weak, unsaturated components. Another caveat is that the method of optical depth profile reconstruction is unable to retrieve the lost *velocity structure* information due to smearing caused by the spectrograph's resolution.

The optical depth profiles of the Na I D_1 and Ca II H lines were reconstructed and converted to $N_v(v)$ for each LMC sightline. Care was taken to ensure the matching of velocity scales to compare the lines of the doublets on an equal point-for-point basis in velocity space which necessitated interpolation of spectra to the same velocity binning using IRAF **sinterp**. Careful continuum placement was required for accurate extraction of $\tau_a(v)$, and this was straightforward in all cases except for the Ca II H line towards Sk −70°120, where a large stellar absorption line was present, fitted and removed under the assumption of a Gaussian profile[7].

A **C** algorithm was written to perform the conversion of normalised spectra $I(\lambda)/I_0(\lambda)$ into $N_v(v)$ profiles. Transition oscillator strengths f were taken from Morton (2003).

The results for Ca II were highly satisfactory, showing smooth variation in $C(v)$ across the strongest peaks of the spectra, as expected, with little or no optical depth correction required for weak and/or broad features. The strong saturation in some of the Na D lines (particularly towards Sk −67°2, Sk −68°135 and Sk −69°223, as noted in Section 3.4.2) resulted in failure of the algorithm where S/N and perhaps scattered light subtraction and continuum rectification errors caused incorrect derivation of $\tau_a(v)$; where lines are saturated to around the zero intensity level, these errors and other noise sources dominate the calculation of τ_a. Algorithm failure was manifested by discontinuities in the $C(v)$ profiles, and sometimes associated with unphysically large corrected column densities.

For the strongly saturated LMC gas components towards Sk −67°2 and Sk −68°135, the Na UV data were utilised, providing a much more accurate $N_v(v)_{\mathrm{Na\ I}}$, whereby composite $N_v(v)_{\mathrm{Na\ I}}$ profiles were formed using the high S/N, moderately saturated Na D data for the Galactic, IVC and HVC regions, and the Na UV data were used for the LMC region of velocity space.

A Galactic Na I component ($v_{\mathrm{LSR}} \simeq 10$ km s^{-1}), toward Sk −69°243 is very strong,

[7]The majority of stellar features in Sk −70°120 have profiles that may be modelled by Gaussians to within the S/N of the spectra.

as evidenced by the Na UV spectrum (Figure 3.7), and very narrow (low Doppler b), evidenced by the comparatively low (degraded) Na D line strength in Figure 3.6. This is suggestive of the dangerous situation mentioned by Jenkins (1996) and noted above, and probably explains why the algorithm broke down for this component, calculating an unphysically large column density at a few points in velocity space. A very similar situation occurred for the $v_{\rm LSR} \simeq 10$ km s^{-1} component towards Sk −69°223, which has a similar profile to that towards Sk −69°243 (see Figure 3.6). Unfortunately, the Na UV spectrum is poor for this sightline, so a high column density and small b value could not be confirmed. Fortunately, the region of unphysically large column density was narrow compared to the line width, so was interpolated across. The Na UV data was too poor to be of assistance in providing $N_v(v)_{\rm Na\ I}$ in these two cases.

S/N constraints prohibited the use of optical depth reconstruction for the Na UV doublet and the Ti II UV lines. However, due to the low optical depth of these lines, unresolved saturated structure has only a small effect on their measured column densities. Within the S/N, the 'optically thin' relation $W_\lambda \propto f\lambda_t^2$ was upheld in the ratio of equivalent widths of the Ti II λ3242 and λ3384 lines, and the Na UV doublet lines. Additionally, Ti II has a relatively smooth, unpeaked (relative to Ca II, Na I and K I), interstellar absorption spectrum (see Welty 1998) and is expected to be quite well resolved at $R \approx 3.5$ km s^{-1}. No doublet information was available for K I. Thus, Equation (3.1) was used directly for these spectra, using $\tau(v) = \tau_a(v)$ to create $N_v(v)$. The $N_v(v)$ profiles are plotted in Figures 3.14 to 3.19.

Neutral hydrogen 21 cm data was obtained for each sightline from the ATCA + Parkes survey conducted by Staveley-Smith *et al.* (2003) and Kim *et al.* (2003) using the online retrieval system[8] kindly provided by L. Staveley-Smith (private communication). With ~ 1′ angular resolution, the spatial resolution of the maps is ~ 15 pc at the distance of the LMC. Clearly, the ISM is variable on scales smaller than this, but probably at a low level such that the salient features of the spectra are expected to be correct. The H I data were made available in mosaic format and the pieces containing the RA and DEC of the required programme stars were retrieved. Sk −69°243 has a 21 cm continuum emission source associated with it, rendering the spectrum unsuitable for obtaining column densities, so the surrounding four mosaic pieces were used and averaged together. $N_v(v)_{\rm H\ I}$ profiles were calculated from the H I temperatures $T_b(v)$ using

[8]URL: http://www.atnf.csiro.au/research/smc_h1/get_spectrum.html

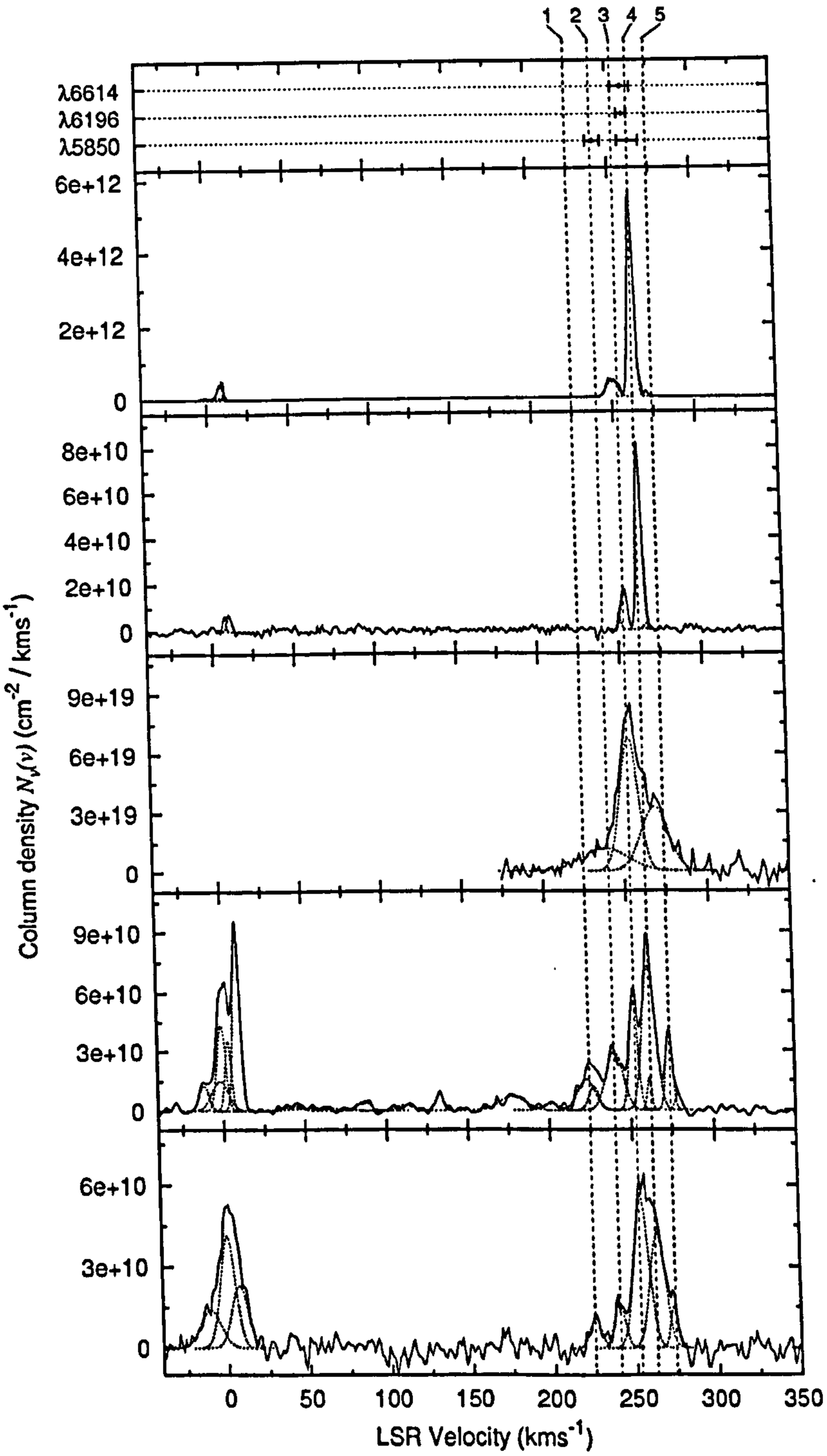

Figure 3.14: Sk −67°2 atomic interstellar column densities plotted as a function of LSR velocity. Principal clouds of the LMC and least-squares fitted velocities of the DIB carriers (with 1σ error bars) are labelled.

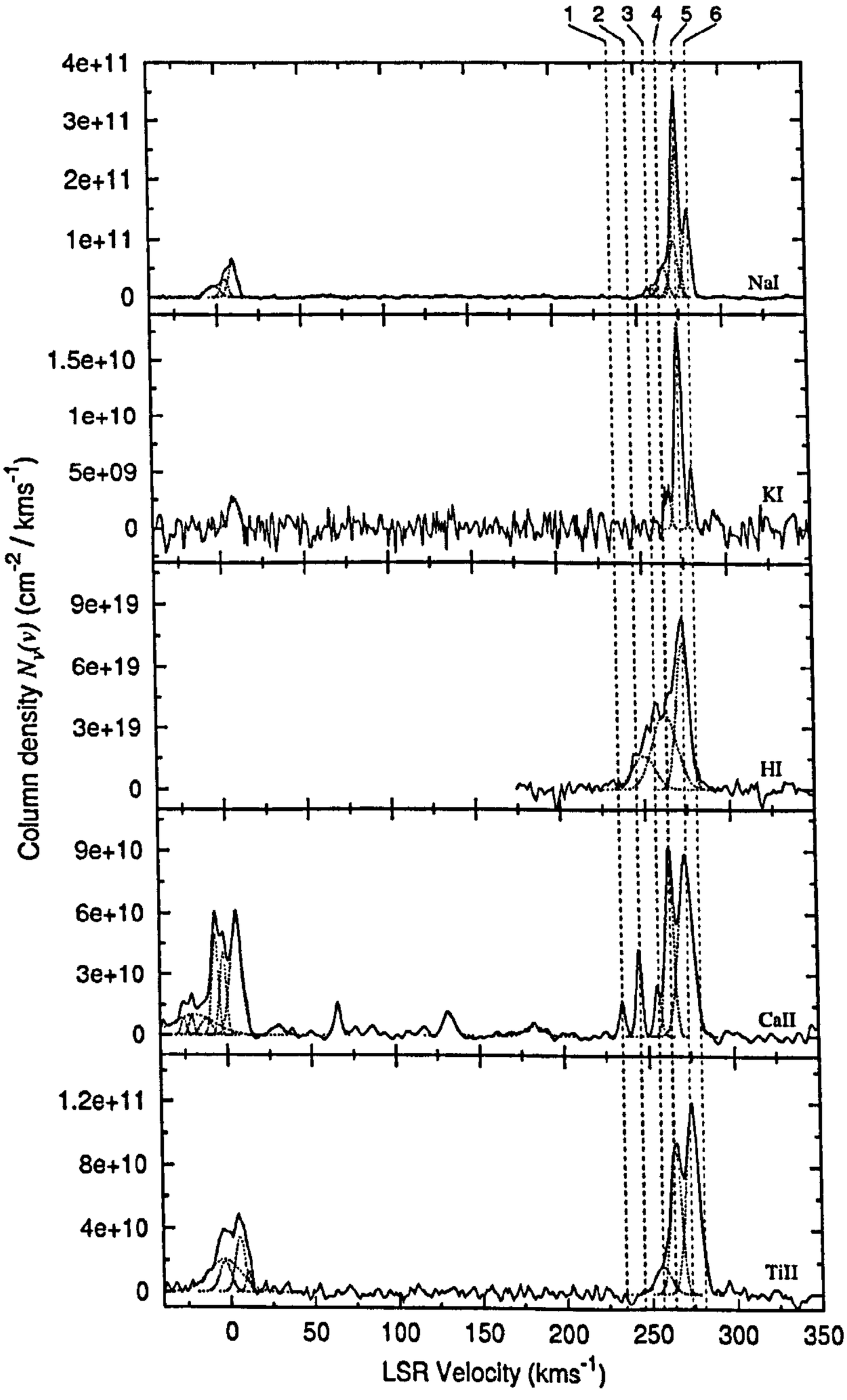

Figure 3.15: Sk −67°5 atomic interstellar column densities plotted as a function of LSR velocity. Principal clouds of the LMC are labelled.

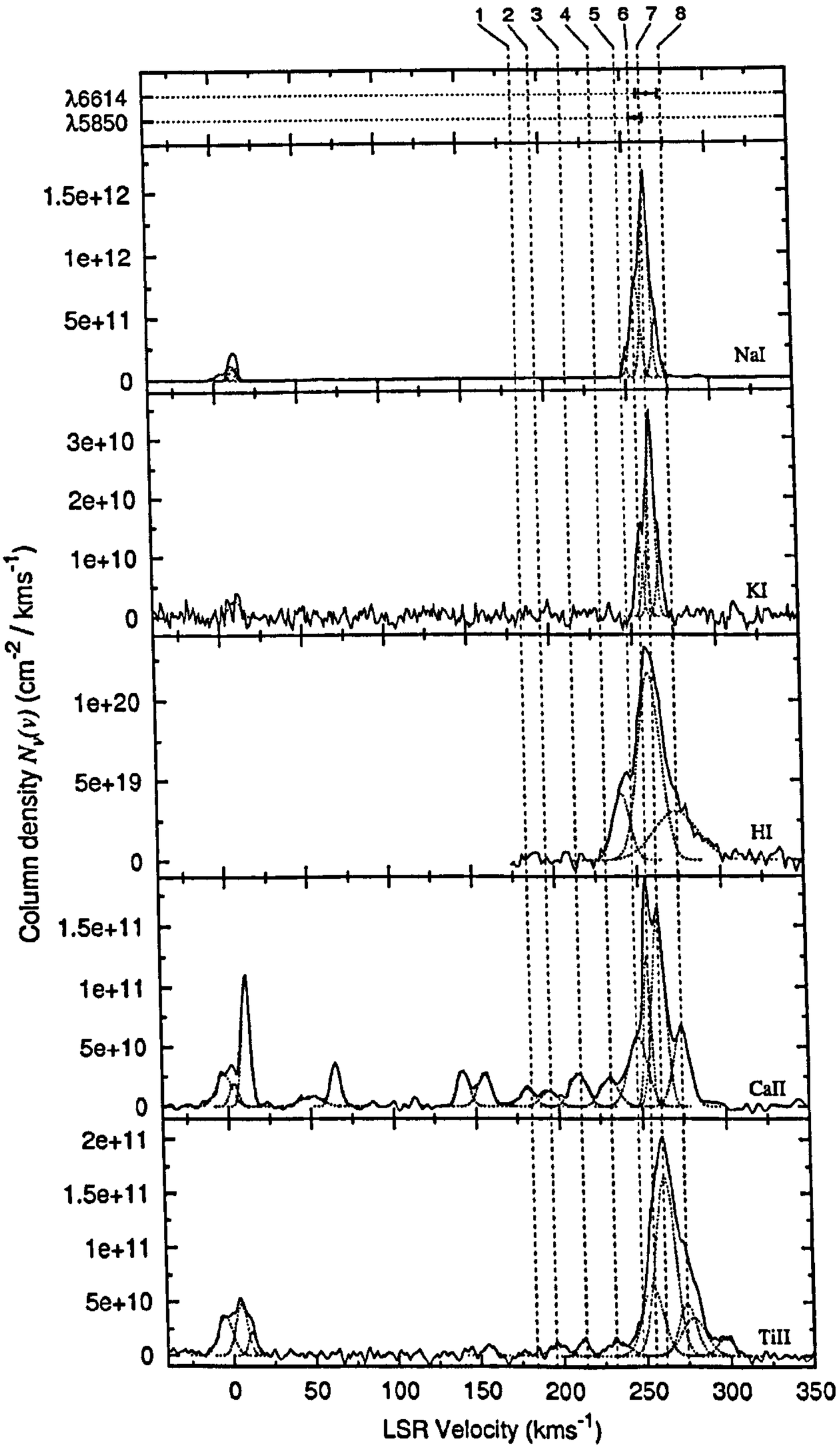

Figure 3.16: Sk −68°135 atomic interstellar column densities plotted as a function of LSR velocity. Principal clouds of the LMC and least-squares fitted velocities of the DIB carriers (with 1σ error bars) are labelled.

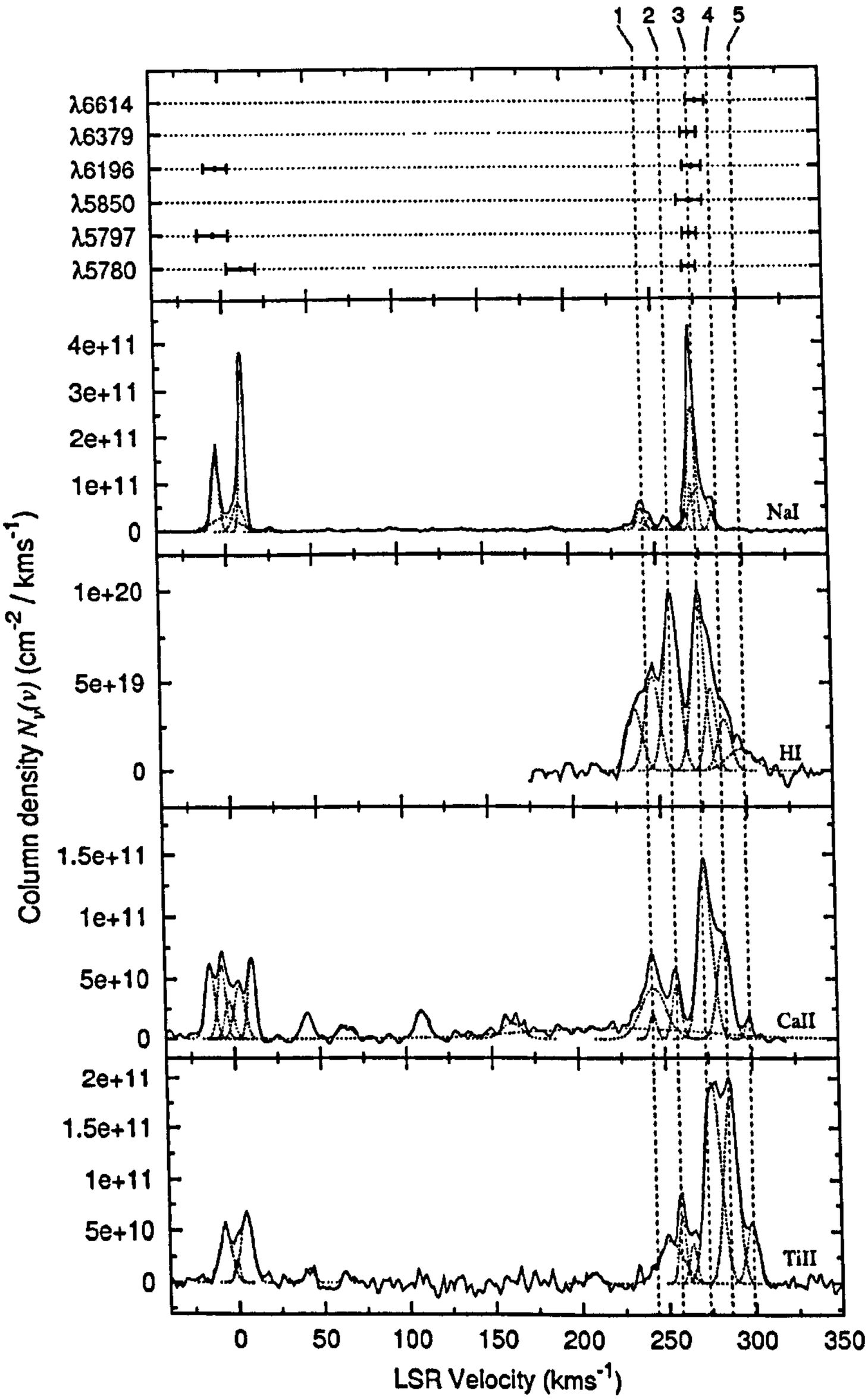

Figure 3.17: Sk −69°223 and atomic interstellar column densities plotted as a function of LSR velocity. Principal clouds of the LMC and least-squares fitted velocities of the DIB carriers (with 1σ error bars) are labelled.

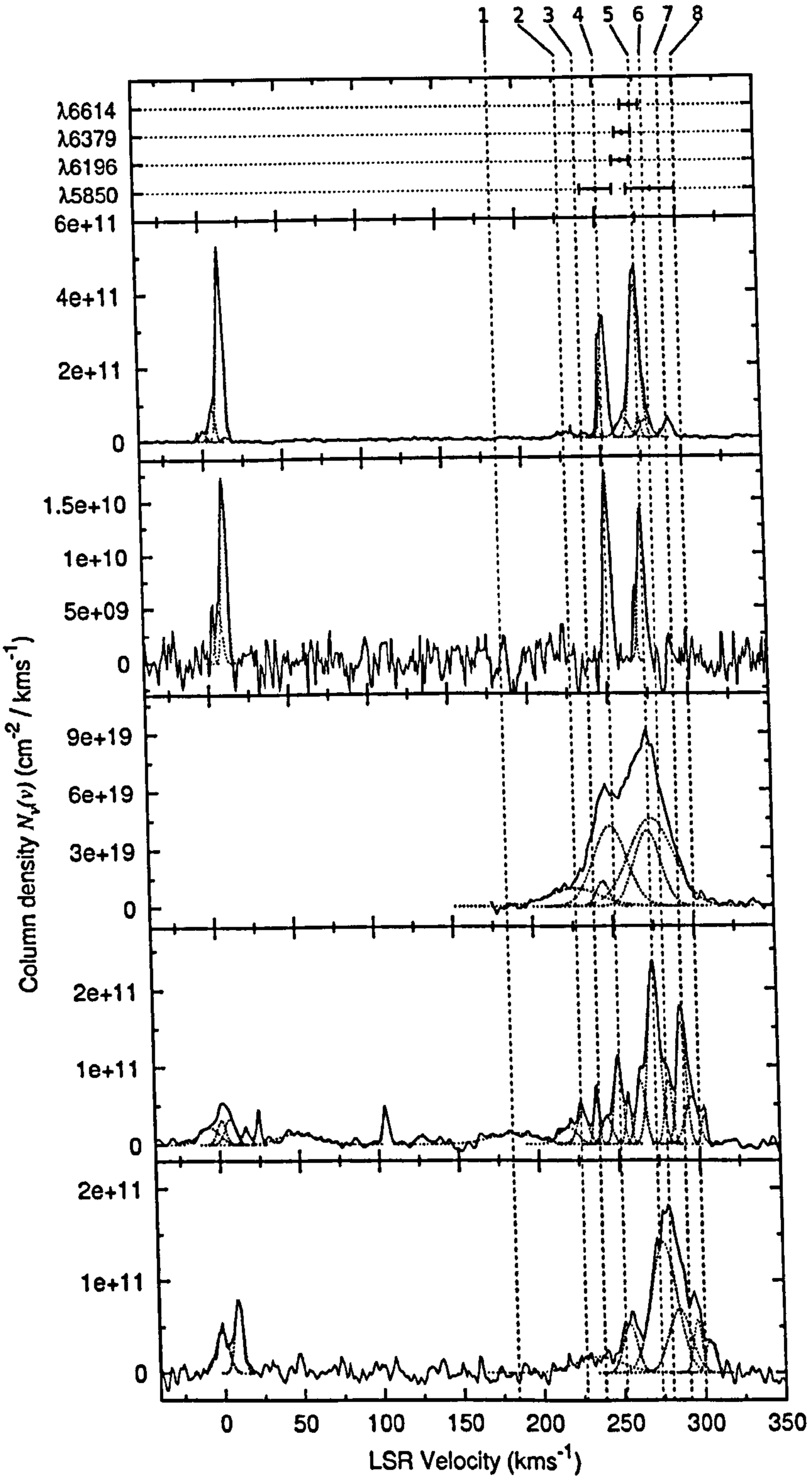

Figure 3.18: Sk −69°243 atomic interstellar column densities plotted as a function of LSR velocity. Principal clouds of the LMC and least-squares fitted velocities of the DIB carriers (with 1σ error bars) are labelled. H I data are the average of four mosaic pieces surrounding Sk −69°243 such as to exclude the 21 cm emission source.

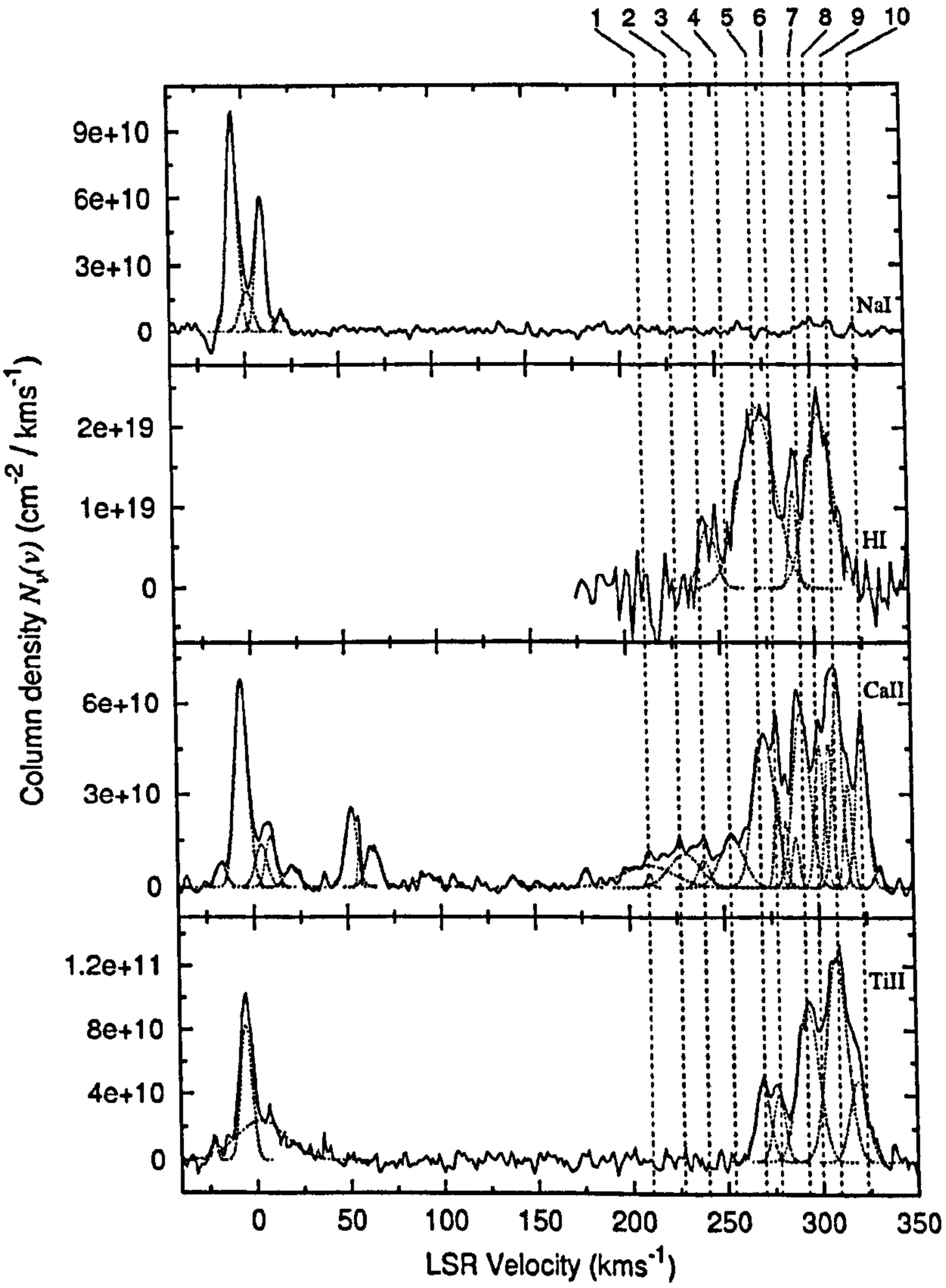

Figure 3.19: Sk −70°120 atomic interstellar column densities plotted as a function of LSR velocity. principal clouds of the LMC are labelled.

the optically thin approximation $N_v(v)_{\rm H\,I} = 1.823 \times 10^{18} T_b(v)$ (see Dickey & Lockman 1990). The spectra span the velocity range of the LMC gas only ($175 \lesssim v_{\rm LSR} \lesssim 350$ km s^{-1}) and have a velocity resolution of 1.6 km s^{-1}.

Line of sight H I 21 cm emission profiles suffer from the drawback that cloud components originating between us and the star are likely to be contaminated by emission originating *behind* the star. The degree of contamination is dependent on the location of the star within the disc of the LMC and on the LMC's H I distribution. Correspondence between $N_v(v)_{\rm Ti\,II}$ and $N_v(v)_{\rm H\,I}$ is reasonably good in all cases (see Figures 3.14 to 3.19), leading one to believe that the programme stars are behind at least 50% of the total line of sight H I, as would be expected for the programme targets, which were selected for their above-average reddening. Inevitable variations in the depletions and ionisation equilibria of the optical species preclude unambiguous identification of background H I components. In fact, examination of the $N_v(v)$ profiles (grouped by sightline) shows negligible evidence for H I components at velocities not represented in at least one of the optical species. N(Na I) and N(H I) are known to be well correlated (*e.g.* Hobbs 1974), so it is possible that the mismatch between peak Na I and H I column densities for Sk −67°2 is due to the presence of a background H I component, even though Ti II is strong at the peak H I velocity. The double-peaked H I profile is not well matched in any species towards Sk −69°223, indicating that the lower velocity peak may originate in the background. Instrumental calibration errors may have introduced offsets in the velocity scales of up to ~ 2 km s^{-1} in each species.

Neglecting the contribution to the $N_v(v)$ profiles by natural line-broadening, Gaussian components were fitted independently for each species using IRAF **splot** with central velocity, FWHM and column density as free parameters. A minimum-component rationale was employed, adding components to the fits until the overall residual RMS of the fits matched the continuum RMS of the $N_v(v)$ profiles. As such, each Gaussian component must represent at least one cloud in the line of sight. Signal-to-noise and resolution limitations prevent the discrete identification of all of the clouds. Clearly, very broad components must represent many clouds spanning a range in velocity, based on the median separation of K I clouds of 1.2 km s^{-1}, observed in the Galaxy by Welty & Hobbs (2001), and an expected Doppler b of about 1 km s^{-1} for individual clouds. It must be noted however, that the fitted component full-width half-maxima in this study *include* the UVES instrumental resolution of ~ 3.5 km s^{-1}. The results of the fitting

are shown as dotted Gaussians in Figures 3.14 to 3.19

3.5.2 Diffuse interstellar band carrier velocities

LSR velocities of the gas containing the diffuse interstellar band carriers in each sightline were derived by comparing the observed DIB spectra with a corresponding spectrum of a 'single-cloud' Galactic sightline.[9] As explained in Section 1.2.2, although the different DIBs can have very different profiles, examining a particular DIB shows the profile to be almost identical between different sightlines, Doppler-shifted to match the radial velocities of the interstellar gases. Subtle variations in the sub-structure of DIB profiles have only been observed at very high signal to noise for λ5797 and λ6614 (see for example Galazutdinov *et al.* 2002; Walker *et al.* 2000). Seab & Snow (1995) found no evidence for differences in the profile of λ5780 between different Galactic sightlines, and Galazutdinov *et al.* (2003) published 'intrinsic' DIB profiles of λ5850, λ6196 and λ6379 towards the single-cloud sightline HD 24398.

The single-cloud comparison sightline used here is β^1 Sco for intrinsic DIB profiles λ5797, λ5780, λ6196, λ6379 and λ6614, and ρ Oph for λ5850, due to the relative weakness of this DIB towards β^1 Sco. Spectra were of very high S/N ($\gtrsim$ 1000) and high enough resolving power ($\sim 50,000$) to reveal most of the known structure in the DIB profiles. Spectra were recorded on UCLES at the AAT in June 2004 by M. A. Cordiner, S. J. Fossey and P. J. Sarre and presented in this thesis in Chapter 4. β^1 Sco was chosen as the main Galactic DIB comparison because the sub-structure pattern observed in λ6614 lies halfway between the two extremes of variation observed for this DIB in the Galaxy by (Walker *et al.* 2000), Galazutdinov *et al.* (2002) and Cami *et al.* (2004). Intrinsic profiles were Doppler-shifted to the air rest frame using the single K I cloud peak velocities recorded in the same spectra and $\lambda_{\mathrm{K\ I\ rest}} = 7698.9645$ Å (Morton 2003).

The effect of variations in the λ6614 sub-structure on derived λ6614 DIB carrier velocities was assessed by applying the fitting procedure to three different Galactic λ6614 profiles that cover the observed extremes in this DIB's sub-structure variation (see the profiles published by Galazutdinov *et al.* 2002; Walker *et al.* 2000; Cami *et al.* 2004).

[9] 'Single-cloud' refers to the fact that in all species for which high resolution spectra are available, the absorption down the sightline is dominated by one narrow (FWHM $\lesssim$ 5 km s^{-1}), component.

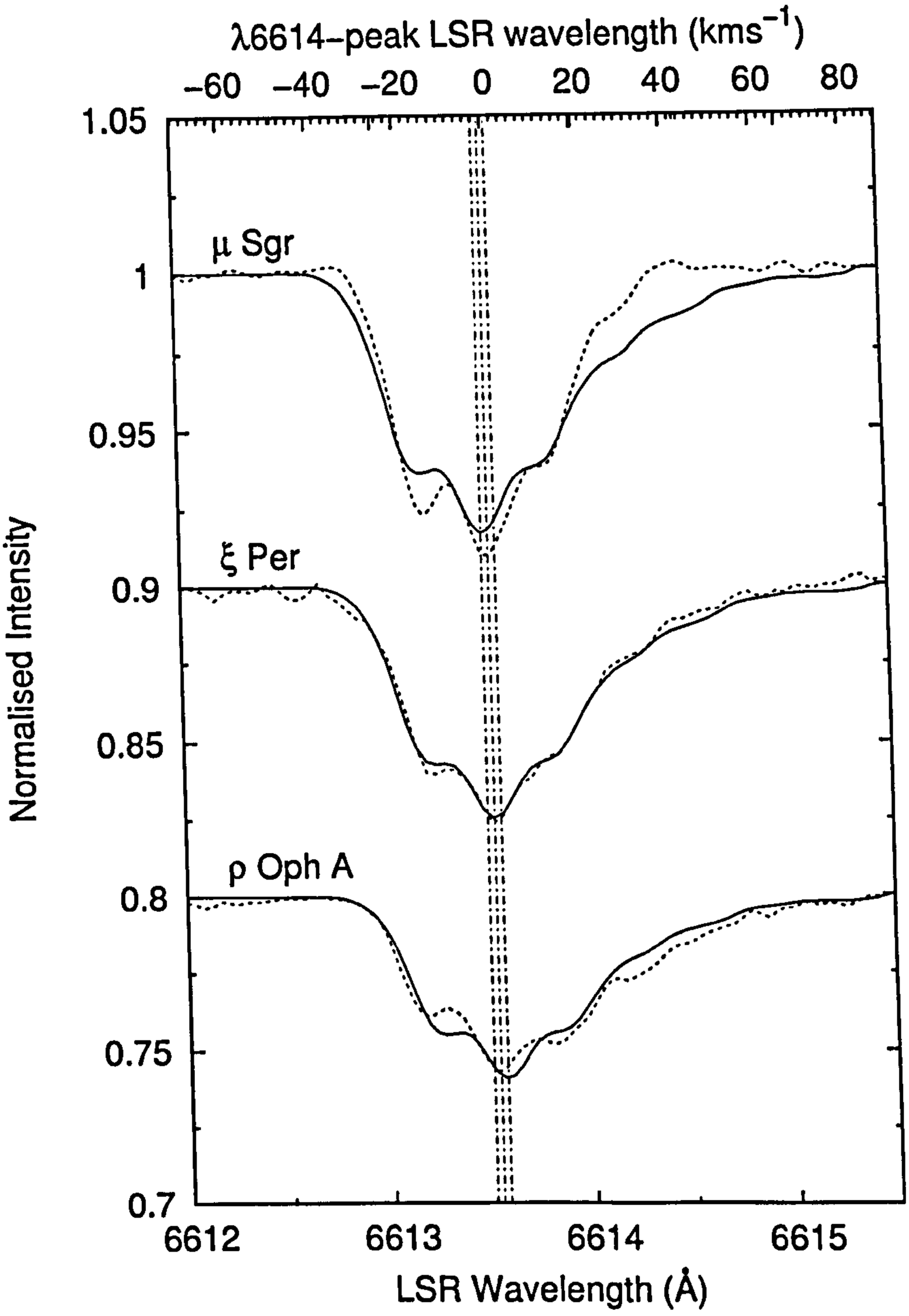

Figure 3.20: The three dotted traces show the telluric-corrected, continuum-normalised λ6614 spectra observed along three different single-cloud Galactic sightlines, exhibiting different patterns of sub-structure in each case. The spectra have been shifted to set the interstellar K I peak velocity at rest (using $\lambda_{\mathrm{K\,I\,rest}} = 7698.9645$ Å (Morton 2003), such that the carriers of this DIB are also at rest. The solid lines show the VAPID least-squares fits to the data, and the vertical dot-dashed lines show the least-squares velocities of the fits ($v_{6614}(\mu$ Sgr) = −2.3 km s^{-1}, $v_{6614}(\xi$ Per) = −0.8 km s^{-1} and $v_{6614}(\rho$ OphA) = 0.7 km s^{-1}). The zero of the velocity scale is set at 6613.55 Å, the peak absorption wavelength of the 'intrinsic' β^1 Sco λ6614 profile.

The DIB profiles and results of the fits are shown in Figure 3.20. For the 'bluest' type of profile, represented by the μ Sgr spectrum, the least-squares velocity was –2.3 km s^{-1}. For the 'reddest' type of profile, represented by the ρ Oph A spectrum, the least-squares velocity was 0.7 km s^{-1}; and the 'intermediate' λ6614 profile, observed towards ξ Per had a least-squares velocity of –0.8 km s^{-1}. Thus, variations in the λ6614 profile in the LMC sightlines should lead to relatively small errors in the least-squares λ6614 fitted velocities of no more than ±2.5 km s^{-1}, and likely less than 1 km s^{-1} in the 'red direction'. The μ Sgr λ6614 spectrum was published by Sarre *et al.* (1995), data provided courtesy of R. E. Hibbins (private communication). The ρ Oph A λ6614 spectrum is presented in this thesis, Chapter 4, Figure 4.38 and the ξ Per spectrum was part of the dataset provided by G. H. Herbig (private communication; see Section 5.2).

In extended trials of this fitting technique, DIB least-squares velocities were found to correspond with the principal K I cloud velocities along different sightlines to within ±1 km s^{-1} for all of the different DIBs tested (λ5797, λ5780, λ5850, λ6196 and λ6379). Fitting of double components also proved to be successful — the well known 'double-cloud' sightline HD 183143 has two narrow clouds of interstellar K I (and of many other species; see Figure 5.9 in Section 5.4.3) separated by about 15 km s^{-1}. As explained in Section 1.2.2 the λ6614 DIB was successfully 'decomposed' into two components by Herbig & Soderblöm (1982) with DIB component velocities and strengths matching the two K I clouds identically within the S/N. Their result was accurately reproduced using the fitting procedure described here. S/N level and differences in instrumental resolution were not found to significantly affect the precision with which the velocities of *single* component fits could be determined.

Using VAPID to perform least-squares fitting, it was necessary to down-sample the intrinsic DIB profiles to the number of data points (60), permitted by the software, input as a set of transitions. The integrity of the sub-structures in the DIB profiles was maintained at this sampling level.

In the fits, the strength, velocity and Doppler b were allowed to vary. Due to the limited S/N and the weakness of the LMC DIBs, the number of DIB-carrying clouds used in the fits was restricted to one unless the Doppler b became unphysically large, indicating the presence of DIB-carriers in multiple clouds well-separated in velocity space. This only occurred for the case of λ5850 towards Sk –67°2 and Sk –69°243, where a single component fit required b > 30 km s^{-1}. For all the other fits, least-squares optimised

b values were less than 15 km s^{-1}. Velocity error estimates were generated by VAPID using at least 200 Monte Carlo noise replications, with b fixed arbitrarily at 10 km s^{-1}.

Least-squares fitted DIB velocities are shown in Figures 3.14 to 3.18 with error bars (plotted at the tops of the Figures) that include a possible error of ±2.5 km s^{-1} due to sub-structure variability of λ6614, and ±1 km s^{-1} for the other DIBs. It must be noted that this analysis assumes 'intrinsic' DIB profiles to be the same in the LMC as they are the Galaxy, which may not be true. Such differences could introduce unquantifiable, potentially systematic, errors into the fit results. However, no evidence has thus far shown any of them to be any different, and the single-component fits herein obtained are statistically flawless within the S/N of the observations ($\sigma_{\rm fit} = \sigma_{\rm continuum}$ for each fit). The quality of fit to the strong λ5780 DIB towards Sk −69°223 is good evidence that at least this DIB has the same profile in the Galaxy and the LMC. Figure 3.21 shows the results of the fitting procedure for λ5780 towards Sk −69°223 with the intrinsic β^1 Sco λ5780 profile used in the fitting. There is little ambiguity in the Doppler velocity of the gas in which the LMC λ5780 absorption occurs, even for this relatively broad DIB. The rest of the DIBs fitted are significantly narrower.

As shown by the least-squares velocities of the DIBs in Figures 3.14 to 3.18, the DIB carriers are located at line-of-sight velocities coincident with the primary peaks of the atomic column density distributions.

With the exclusion of λ5850 towards Sk −69°243, the DIB-carrier velocities shown in Figures 3.16, 3.17 and 3.18 all show least-squares velocities of λ6614 shifted to the red slightly, by on average ~ 5 km s^{-1}, compared to the other DIBs. The shift is also apparent for Sk −67°2 and Sk −68°135 with respect to the peak Na I velocity. It is possible that this reflects a tendency for the λ6614 DIB to arise not in the denser clouds characterised by high neutral sodium abundances, but in those warmer regions characterised by the presence of Ca II and Ti II. The λ6614 velocity matches the peaks of the Ca II and Ti II velocity distributions towards Sk −67°2 and Sk −69°243, and a correlation between the velocity of Ca II absorption and the velocity of the λ6614 carrier was identified in the Perseus OB2 association by Sonnentrucker *et al.* (1999a). This suggests that the λ6614 carrier is more abundant in the warmer, more shocked clouds characterised by high calcium and titanium gas-phase abundances. Another plausible interpretation of the data however, is that the velocity shift represents a change in the intrinsic profile of the λ6614 DIB. As explained earlier, variations have been observed

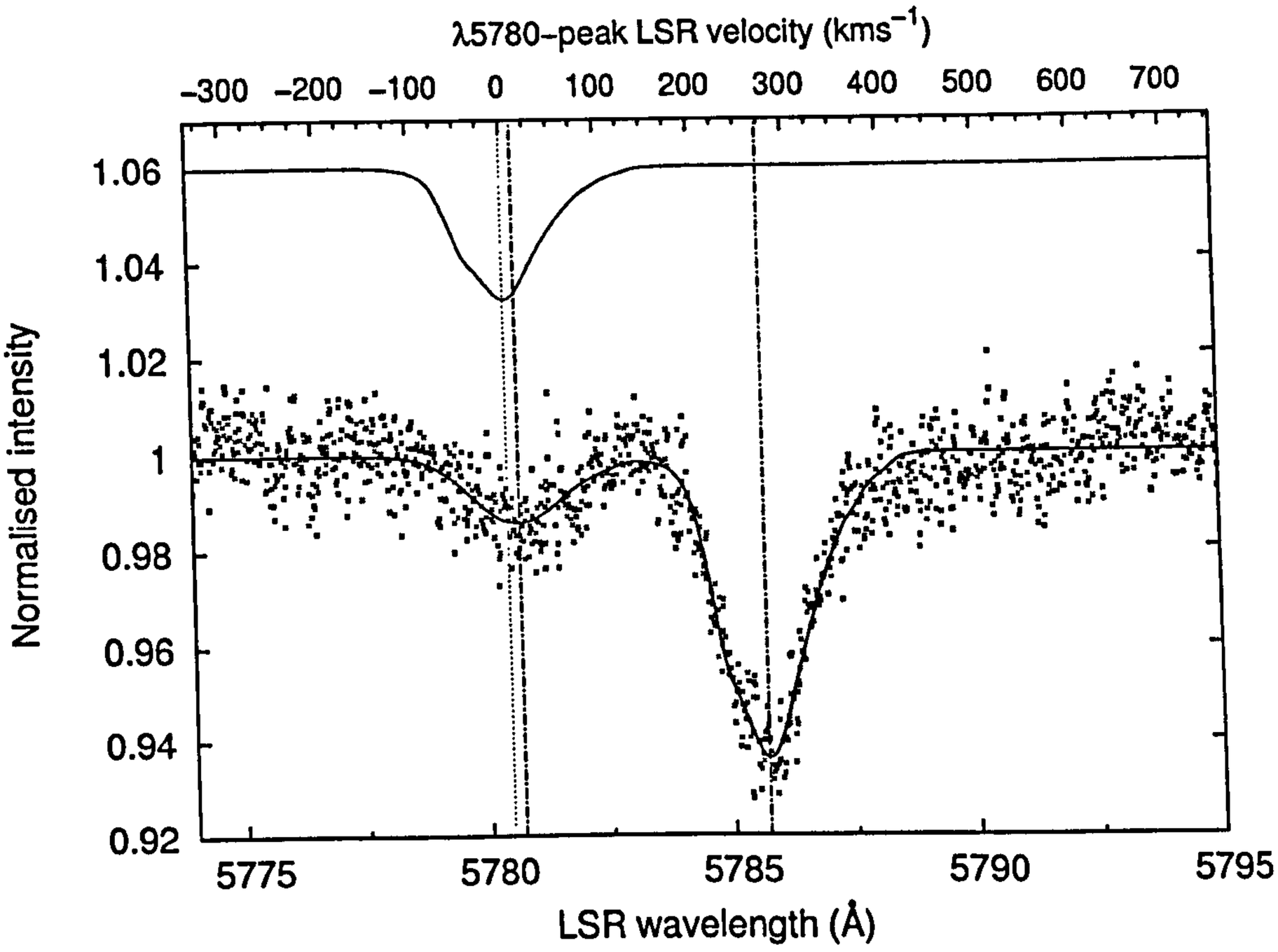

Figure 3.21: Results of intrinsic profile fitting the β^1 Sco rest λ5780 profile to the Sk −69°223 λ5780 spectrum. The intrinsic profile is shown in the upper part of the figure. The Sk −69°223 spectrum and VAPID least squares fit shows two Doppler separated components corresponding to diffuse interstellar absorption in the Galaxy (at v_{LSR} = 12.5 km s^{-1}), and the LMC (at v_{LSR} = 273.1 km s^{-1}), whose velocities are shown with dot-dashed lines. The Doppler b parameter of the LMC component is 0.6 km s^{-1}— negligible compared to the width of the DIB. The velocity scale in the plot (for display only) is defined with respect to the peak optical depth of the λ5780 intrinsic DIB profile (v_{LSR} = 0 km s^{-1} at 5780.457 Å).

in the pattern of substructure inside the λ6614 DIB in Galactic sightlines. The reasons for these changes have not yet been proven, but a theory has been proposed by Webster (1996) whereby the changes in sub-structure are understood as resulting from differences in the [^{12}C] to [^{13}C] ratio in the composition of large spheroidal carbon-based carrier molecules. It is possible that the magnitude of the observed shift in the λ6614 velocity is caused by a high ^{13}C content in the carrier. The shift of ~ 5 km s^{-1} is larger than the 0.7 km s^{-1} least-squares velocity in the fit to the λ6614 ρ Oph A profile (see Figure 3.20) that apparently lies at the extreme red end of the sub-structure variation spectrum seen in this DIB in the Galaxy. Thus, the λ6614 DIB in three of the four LMC targets would possess a pattern of sub-structure different from any yet measured in the Galaxy, provided its carriers are spatially coincident with the other DIB carriers

and the main Na I clouds.

In terms of the Webster hypothesis, a lower [^{12}C] to [^{13}C] ratio in the carrier molecule is required to shift the DIB profile peak to the red, which could result from a lower [^{12}C] to [^{13}C] ratio in the material that formed it. Another possible explanation for profile variability is that it results from changes in the level of internal excitation of the (molecular) carrier. Red-shifting of the λ6614 profile could perhaps result from an increase in the internal temperature of the carrier.

3.5.3 Integrated atomic gas properties

Dividing the gas into Galactic and LMC components based on the velocity criterion explained in Section 3.4.2, the integration of the $N_v(v)$ profiles yields atomic column densities shown in Table 3.3. The origin of each number is explained in the caption, with Na I column densities coming from a combination of the Na D_1 optical depth correction method, Na UV λ3303 apparent optical depth profiles, and VAPID modelling (see Section 3.5.1 for details). K I column densities are presented for all targets; where the K I spectral region was not recorded (as for Sk −69°223 and Sk −70°120), the column densities were calculated based on the known Galactic linear correlation between N(Na I) and N(K I) (Welty & Hobbs 2001).

Measured values of the Galactic ratio N(Na I)/N(K I) in this study are in line with the value of around 90 measured by Welty & Hobbs, but the average ratio for the LMC gas of 48 from this study is substantially greater than the value of 15 published for the three LMC sightlines observed by Welty & Hobbs. They noted that their value was unusually small, and somewhat difficult to explain. It is therefore postulated that their very low value is perhaps caused by underestimation of N(Na I) using only the Na D_1 line; the two highest values of N(Na I)/N(K I) in this study are seen towards Sk −67°2 (N(Na I)/N(K I) = 71), and Sk −67°5 (N(Na I)/N(K I) = 55), where the Na I column densities are reliable, measured from the (relatively unsaturated) Na UV λ3302.4 line. There is no reason to presume that the K I column densities are erroneous as these lines are also relatively unsaturated. Nevertheless, the average of the measured N(Na I)/N(K I) is taken with the three sightlines of Welty & Hobbs's study to form an average LMC N(Na I)/N(K I) ratio of 37, with an estimated error of ±20, which is used with N(Na I) to calculate an estimate for N(K I) towards Sk −69°223 and Sk −70°120.

		Integrated column densities					Ratios			
Sightline	Locale	Na I (10^{11} cm^{-2})	K I (10^{11} cm^{-2})	H I (10^{21} cm^{-2})	Ca II (10^{11} cm^{-2})	Ti II (10^{11} cm^{-2})	$\frac{\text{Ca II}}{\text{Na I}}$	$\frac{\text{Na I}}{\text{K I}}$	$\frac{\text{Ca II}}{\text{Ti II}}$	$\log \frac{\text{Na I}}{\text{H I}^2}$
Sk −67°2	MW	27.4[a]	0.39	–	12.3[a]	10.3	0.45	70	1.2	–
	LMC	312[b]	4.42	1.52 (0.51)	20.8[a]	14.3	0.07	71	1.5	-28.9
Sk −67°5	MW	7.18[a]	0.19	–	14.2[a]	9.46	1.97	37	1.5	–
	LMC	31.0[a]	1.22	1.21 (0.40)	18.5[a]	20.0	0.60	25	0.9	-29.7
Sk −68°135	MW	17.7[a]	0.24	–	11.2[a]	9.58	0.63	74	1.2	–
	LMC	176[b]	3.21	2.64 (0.88)	47.5[a]	53.8	0.27	55	0.9	-29.6
Sk −69°223	MW	59.1[c]	0.70[d]	–	16.8[a]	11.3	0.28	85	1.5	–
	LMC	38.9[a]	1.07[d]	2.85 (0.95)	47.5[a]	58.4	1.22	37	0.8	-30.3
Sk −69°243	MW	97.7[c]	1.10	0.7 (0.2)[e]	11.3[a]	9.27	0.82	89	1.2	-28.7
	LMC	69.9[a]	1.74	6.3 (2.0)[e]	76.15[a]	57.63	1.09	40	1.3	-30.8
Sk −70°120	MW	10.3[c]	0.12[d]	–	9.14[a]	14.0	0.89	85	0.7	–
	LMC	1.98[c]	0.05[d]	0.78 (0.26)	39.20[a]	42.85	19.8	37	0.9	-30.5

Table 3.3: Galactic and LMC atomic and ionic column densities and ratios, derived predominantly from AOD analysis. Ratios represent averages over multiple clouds in the velocity range of the given locale (MW or LMC). H I column densities were calculated from 21 cm emission data with 15 pc spatial resolution (Staveley-Smith *et al.* 2003), with error estimates calculated assuming $N(\text{H I}) = 0.75 \pm 0.25 \times N(\text{HI}_{21\text{cm}})$. [a] — calculated from doublet ratio optical depth correction; [b] — from Na UV 3302.4 Å line; [c] — from VAPID analysis; [d] — no K I data were available: column densities derived from $N(\text{Na I})^{\text{LMC}}$ and the linear relation between N(Na I) and N(K I) published by Welty & Hobbs (2001), supplemented by data from this table. [e] — from de Boer *et al.* (1980)'s Lα measurement. Errors on column densities for 'optical species' are $\lesssim 10\%$ as calculated using the continuum RMS or VAPID replicated fits where applicable.

H I sightline column densities for the LMC are calculated as 0.75 ± 0.25 of the integrated value from the 21 cm profiles (after Tumlinson *et al.* 2002), to account for the fact that the stars may be 'in front' of some of the emitting H I gas. The H I column density for Sk −69°243 is taken from the Lα absorption measurement of Koornneef & Mathis (1981) and is more accurate than the 21 cm data, also avoiding the problem of the 21 cm emission source in the vicinity the massive star cluster R136. Errors on other atomic column densities are ~ 10%, primarily resulting from Poisson noise in the spectra.

From the ratios of atomic and ionic column densities in Table 3.3, it is evident that the interstellar gas in the LMC sightlines is different from average Galactic interstellar gas in several respects. The difference in N(Na I)/N(K I) has already been mentioned; the average value of approximately 48 for the LMC is about the same as towards the Sco-Oph region of the Galaxy, where the ratio is quite discrepant (Welty & Hobbs 2001), about half the Galactic average. This may be due to an unusual combination of preferential ionisation of Na I, enhanced recombination of K II, or perhaps an unusual depletion pattern for Na and K which, in the Galaxy are usually very similarly behaved in these respects (Welty & Hobbs 2001).

The ratio of N(Na I)/N(H I)^2 is markedly lower towards the sample of LMC targets than is typically seen in the Galaxy (Welty & Hobbs 2001), where a logarithmic ratio of around −28.5 predominates.[10] The average of the six targets in the sample is −29.8. As for K I (not shown in the table), the Galactic ratio N(K I)/N(H I)^2 is about −30.2, and the average of the four LMC targets for which K I was observed is −31.2. These results are in accord with the measurements for LMC stars made by Welty & Hobbs (2001), and also show the slight trend towards a relatively lower abundance of Na I compared to K I in the LMC seen in their data. This might go some way to explaining the discrepant N(Na I)/N(K I) ratio. The reasons for N(Na I) and N(K I) being underabundant in the LMC compared to the Galaxy by about an order of magnitude probably reflect a combination of increased ionisation rate due to the enhanced UV field strength of the LMC, and the diminished metallicity of the gas.

Towards Sk −67°2, both the N(Na I)/N(H I)^2 ratio and the N(Na I)/N(K I) ratio are much more similar to the typical Galactic value than the other sightlines. The most dis-

[10] N(H I) is squared to reflect the approximately quadratic dependence of N(Na I) (and N(K I)) on N(H I) observed by Hobbs (1974).

crepant sightline in N(Na I)/N(H I)^2 is Sk −69°243, with a logarithmic ratio of −30.8, also with a discrepant N(Na I)/N(K I) ratio of 40. There are not enough sightlines to confirm a significant correlation between N(Na I)/N(K I) and N(Na I)/N(H I)^2.

The ratio N(Ca II)/N(Na I) is highly variable, spanning a range between 0.07 and 19.8 for the six observed sightlines, similar to the range seen in the Galaxy for a much larger sample of stars (Hobbs 1978; Crawford 1992; Bertin *et al.* 1993; Sembach & Danks 1994). As discussed by these authors, the Ca II/Na I ratio gives a diagnostic of the amount of Ca depleted onto grains and of the ionisation equilibrium between Ca III and Ca II within the gas, and highlights the presence of variable grain properties and cloud densities and thicknesses in interstellar gas. Sk −68°135, Sk −69°223 and Sk −69°243 show an enhanced Ca II/Na I ratio compared to the average Galactic diffuse ISM value of ~ 0.5, indicative of raised Ca II abundances due (at least in part), to shocking of the dust grains and hence liberation of calcium into the gas phase.

The Ca II/Ti II ratio is rather uniform (~ 1) for both the foreground Galactic (MW) gas and the LMC gas, shown in Table 3.3. This trend agrees with past studies of these two cations (*e.g.* Caulet & Newell 1996), where constancy of the ratio was taken as evidence for uniformity of the Ca III/Ca II ionisation balance, and a similar depletion rate for Ca and Ti. However, examination of the data from the Ti II and Ca II studies by Stokes (1978), Albert *et al.* (1993), Welsh *et al.* (1997) and Welty *et al.* (1996) shows that the average Galactic-disc diffuse ISM Ca II/Ti II ratio is ~ 3. Thus, the sightlines probed must have either an unusually low titanium depletion relative to calcium, due perhaps to modified dust grain properties, or an unusually small amount of calcium in the form of Ca II due to enhanced photoionisation of this species (or reduced recombination of Ca III), in clouds with low optical thickness. The discrepancy in the Ca II/Ti II ratio is further enhanced in the LMC clouds of the observed sightlines compared to the Galactic clouds.

The average MW and LMC Ca II/Ti II ratios of, respectively, 1.2 and 1.1 lie within the range found in Welsh *et al.*'s study, so the discrepancy could be caused by statistical bias due to the small number of sightlines observed here. However, this seems unlikely when examining the column densities for 15 sightlines towards the LMC and SMC published by Caulet & Newell (1996) and Welty *et al.* (2001), where ratios $\lesssim 2$ were seen in each case. The high UV field strength of the Magellanic Clouds (Tumlinson *et al.* 2002) — enhanced by the diminished metallicity that gives rise to a deficit of

shielding dust grains — is a likely cause of increased Ca II to Ca III photoionisation. If this is the case, then the high Ca II/Na I ratios observed are indeed representative of highly undepleted gas where large amounts of calcium are in the gas phase.

3.5.4 Galactic foreground gas and dust

The problem of measuring the amount of interstellar material in the 'Galactic foreground', between our telescopes and the boundary representing the outer edge of the LMC, has been addressed by many authors. Reliable determination of the properties of the Galactic foreground dust is fundamental to studies of intrinsic star colours (*e.g.* Fitzpatrick 1988), gas-to-dust ratios (*e.g.* Koornneef 1982), extinction curves (*e.g.* Gordon *et al.* 2003), interstellar lines (*e.g.* Savage & de Boer 1981) and diffuse interstellar bands (*e.g.* Vladilo *et al.* 1987). Dedicated research carried out by Gochermann *et al.* (1989) and Oestreicher *et al.* (1995) using stellar photometry and by Schwering & Israel (1991) using 21 cm, 60 μm and 100 μm emission, allowed the construction of foreground dust maps (E_{B-V} *vs.* RA and DEC). The resolution of these maps was limited, but gave valuable insight into the foreground dust distribution. The average foreground E_{B-V} is about 0.08, but varies between about 0.03 and 0.15 across the LMC, showing small scale fluctuations down to the resolution limit, and large scale trends over the whole LMC disc.

Presently, the best estimate of foreground reddening is from the map published by Staveley-Smith *et al.* (2003). With complete coverage of the whole of the LMC at an angular resolution of $\sim 1'$, their deep H I survey combined aperture synthesis and single dish data to provide accurate foreground H I column densities. Using the H I/E_{B-V} relation of Burstein & Heiles (1978) that was derived using the reddening of halo stars and extinction data from faint galaxy number counts, the intrinsic error in the estimation of the foreground reddening $E_{B-V}{}^{\rm MW}$ from N(H I) is about 0.02 mag.

It is also possible to derive an estimate of $E_{B-V}{}^{\rm MW}$ using the fact that N(Na I) is linearly correlated with E_{B-V} in the Milky Way (Hobbs 1974). The relationship is very similar along low density lines of sight through the Galactic halo (Sembach *et al.* 1993), probing interstellar material close to the galactic latitude of the LMC, and by proximity is expected to be similar to the foreground material towards the LMC itself. Least-squares fitting the N(Na I) *vs.* E_{B-V} data published by Sembach *et al.* (1993) with a

linear function, the relationship

$$E_{B-V}{}^{\mathrm{MW}} = (N(\mathrm{Na\ I})^{\mathrm{MW}} + 1.41 \times 10^{11})/3.79 \times 10^{13}$$

is found, with an RMS scatter of 0.053 in $E_{B-V}{}^{\mathrm{MW}}$. Using $N(\mathrm{Na\ I})^{\mathrm{MW}}$ from Table 3.3, reasonable agreement was found between $E_{B-V}{}^{\mathrm{MW}}$ calculated this way and that measured from the foreground reddening map of Staveley-Smith *et al.* (2003), except for the targets Sk −69°223 and Sk −69°243 for which the high Galactic Na I columns gave $E_{B-V}{}^{\mathrm{MW}} = 0.16$ and 0.26 respectively. Such high foreground reddening significantly exceeds any previous estimates for nearby sightlines (in the region of 0.08 ± 0.02), so are likely to be miscalculations, biased by a higher than average $N(\mathrm{Na\ I})/E_{B-V}$ ratio for the gas in these sightlines. Indeed, Sembach *et al.*'s dataset includes sightlines with high $N(\mathrm{Na\ I})$ but very low E_{B-V} compared to the average $N(\mathrm{Na\ I})/E_{B-V}$ ratio. However, small-scale ($\lesssim$ 100 AU) fluctuations in atomic, molecular and DIB-carrying gas column-density (see for example Heiles 1997; Crawford 2002; Meyer & Lauroesch 1999, and Chapter 4 of this thesis) appear to be ubiquitous in the diffuse medium, attributable at least in part to small-scale matter density variations, indicating the existence of small-scale structure in dust column densities on spatial scales smaller than the resolution of the Staveley-Smith *et al.* reddening map.

Where $E_{B-V}{}^{\mathrm{MW}}$ calculated using $N(\mathrm{Na\ I})$ was different to that measured from Staveley-Smith *et al.*'s reddening map, the latter was additively adjusted by up to 0.02 mag (the map's RMS scatter) towards the former value to go some way toward accounting for the discrepancy. The resulting values of $E_{B-V}{}^{\mathrm{MW}}$ are shown in Table 3.4, along with the resulting contribution to the dust column in the LMC, $E_{B-V}{}^{\mathrm{LMC}}$ obtained by subtraction (the dust contribution by IVCs and HVCs was assumed to be negligible, due to their low column densities and generally low dust content). For comparison with previous measurements, $E_{B-V}{}^{\mathrm{LMC}}$ for Sk −69°243 is in exact agreement with the value of 0.32 derived by Koornneef & Mathis (1981), and for Sk −67°5, with the value of 0.09 published by Tumlinson *et al.* (2002). $E_{B-V}{}^{\mathrm{LMC}} = 0.17$ for Sk −68°135 is different from Tumlinson *et al.*'s value of 0.20, presumably due to the use of different photometric data. This discrepancy is covered by our E_{B-V} error estimate of 0.06 that includes photometric uncertainties and the intrinsic uncertainty on the Staveley-Smith *et al.* data.

Sightline	$E_{B-V}{}^{\mathrm{LMC}}$	$E_{B-V}{}^{\mathrm{MW}}$	R_V	δ_{Ti}	$\frac{N(\mathrm{H\ I})}{E_{B-V}}$ (10^{21} cm^{-2} mag^{-1})
Sk −67°2	0.22 (0.06)	0.04	3.62 (0.35)[a]	-1.8 – -1.5	3.6 – 12.7
Sk −67°5	0.09 (0.07)	0.02	–	-1.6 – -1.3	5.0 – 80.6
Sk −68°135	0.17 (0.06)	0.06	4.35 (0.35)[b]	-1.5 – -1.2	7.8 – 33.6
Sk −69°223	0.26 (0.08)	0.08	3.8 (0.4)[b]	-1.5 – -1.2	5.6 – 21.1
Sk −69°243	0.32 (0.08)	0.08	3.2[c]	-1.9 – -1.6	10.8 – 34.6
Sk −70°120	0.05 (0.05)	0.05	–	-1.1 – -0.8	>5.2

Table 3.4: Contributions to the reddening of the LMC stars for the observed sightlines due to Galactic (MW), and LMC interstellar components. Errors on final $E_{B-V}{}^{\mathrm{LMC}}$ values (shown in parentheses) are the combined errors of the object's photometry, its intrinsic colour, and scatter in the relationship between N(H I) and E_{B-V} for the Galactic ISM (Burstein & Heiles 1978). Literature R_V values: [a] — from Gordon *et al.* (2003), [b] — from Cox *et al.* (2005) and [c] — from Fitzpatrick & Savage (1984). The range of possible integrated logarithmic Ti depletions δ_{Ti}, and gas-to-dust ratios $N(\mathrm{H\ I})/E_{B-V}$ for the LMC component are given, but are uncertain due to the uncertainty in the amount of H I in the background from the 21 cm data. The Lα H I column density (de Boer *et al.* 1980) was used for Sk −69°243 due to its greater precision.

The slope of the UV extinction law, R_V, taken from the literature, is given for the reddened sightlines in Table 3.4, along with other parameters of the LMC component of the ISM, calculated from the data in Table 3.3. The R_V values are high compared to the Galactic average of 3.1 and the LMC average of 3.4 (Gordon *et al.* 2003), which is perhaps indicative of larger-than-average dust grains.

The logarithmic Ti depletions $\delta_{\rm Ti}$ were calculated using Equation (1.4) and assuming a Ti under-abundance of $\log Z_{\rm Ti} = -0.3$ dex in the LMC (see Section 3.2.1) relative to the Galactic abundance of $n_{\rm Ti}/n_{\rm H} = 9.77 \times 10^{-8}$ given by Anders & Grevesse (1989). The values in Table 3.4 are consistent with titanium depletions found in the warmer phases of the Galactic ISM ($\delta_{\rm Ti} \sim -1.3$, see Welty *et al.* (1999), in contrast with $\delta_{\rm Ti} \sim -3$ for the cold neutral medium). With these integrated quantities, the depletion variations between individual clouds are lost, and given the complexity of the cloud structure along the LMC sightlines, there is bound to be substantial variation in the depletion levels between clouds where differing conditions of density, UV flux and shock history prevail. It is clear, however, that the warm phase must dominate the Ti II spectra, or this usually severely-depleted element would be present in far lower abundance. It is possible that these high gas-phase titanium abundances, coupled with the low Ca II/Ti II ratio are evidence for different depletion characteristics and hence different dust chemistry in the LMC compared to the Milky Way; in general Ca II and Ti II are depleted at the same rate (Crinklaw *et al.* 1994).

The depletion of Ti towards Sk −70°120 is especially low, reminiscent of depletion levels only seen far out into the Galactic halo (at distances of ~ 1 kpc; Lipman & Pettini (1995)) where, it is presumed, shocks and possibly total destruction of the dust grains has liberated the titanium into the gas phase. The uncertainties in the measured Ti depletions are due to the errors in the line-of-sight H I column densities. Background H I contaminating the sightline 21 cm profiles can only serve to artificially increase the depletions, such that the result that there is more Ti in the gas-phase in the LMC ISM than in the Galaxy is firm.

The gas-to-dust ratios N(H I)/E_{B-V} incorporate the range of possible errors in E_{B-V} and N(H I), rendering these values rather uncertain. N(H I)/E_{B-V} is likely to lie near the middle of the ranges given, and for Sk −70°120, the value of 5.2×10^{21}cm^{-2} mag^{-1} is a strict lower limit — this sightline shows such a small amount of Na I in the LMC velocity range, and such a low Ti depletion and high Ca II/Na I ratio that there must be

very little dust in this sightline relative to N(H I). The gas-to-dust ratio is not as high towards Sk −67°2 and Sk −69°223 as the LMC average of $\sim 20 \times 10^{21}$ cm^{-2} mag^{-1}. It is thus inferred that the relationship between gas and dust along these sightlines must be more similar to that typically found in the Galaxy.

3.5.5 LMC interstellar cloud component analysis

The $N_v(v)$ profiles (Figures 3.14 to 3.19) permit point for point inter-comparison of column densities for different species as a function of velocity. 'Principal clouds' in the LMC were identified from the Ca II profile for each sightline because this species shows the interstellar cloud component structure in more detail than Na I, Ti II or H I. The great complexity of the cloud velocity structure in the LMC is immediately apparent and is much more complex than the structures observed in the Galactic gas along the six sightlines studied. This may be a manifestation of the low depletion of much of the LMC ISM — perhaps reflecting a turbulent history — leading to more calcium in the gas phase.

The location of the DIB carriers within the principal (*i.e.* strongest), Na I cloud is clear for most of the sightlines in which DIBs were reliably measured. Towards Sk −69°243, the Na I and K I show two principal components, interestingly with differing Na I/K I ratios and markedly different Ca II/Na I ratios. Due to S/N limitations, it was not statistically favourable to fit two components to the DIB profiles, except for λ5850, so the DIB velocities for Sk −69°243 probably reflect a weighted mean from contributions in the two dominant Na I clouds shown in Figure 3.18.

As noted in Section 3.5.1, fits to $N_v(v)$ using Gaussian profiles are likely to represent the combined column density contributions from several different interstellar clouds. For the purposes of taking abundance ratios between different species, in order to make the best cloud-for-cloud comparison, it was decided that the peaks of the Gaussian fits should be used as the measure of the abundance of a particular species in each of the discrete 'clouds'. This eliminates the problem of different species having different thermal/turbulent Doppler b parameters (identified by Welty & Hobbs 2001) by taking the abundance at the mean cloud velocity, where all species are expected to co-exist. The Gaussian fits are helpful in minimising any errors between the velocity scales, and have the benefit of excluding contamination from adjacent 'clouds'. Where no

Sightline	Cloud #	Velocity (kms^{-1})	δ_{Ti}	log $\frac{Ca\ II}{Na\ I}$	$\frac{Ca\ II}{Ti\ II}$	$\frac{Na\ I}{K\ I}$
Sk −67°2	1	224.8	-1.3	>1.0	2.1	–
	2	240.0	-1.5	>1.1	1.9	–
	3	253.0	-1.8	-0.9	1	28
	4	261.4	-1.7	-1.8	2	68
	5	274.3	-2.0	>0.8	2.6	–
Sk −67°5	1	234.7	–	>0.7	>2.2	–
	2	245.3	-2.5	>1.1	>6.1	–
	3	257.5	-2.0	0.2	1.5	>7
	4	263.6	-1.4	0.2	0.9	17
	5	273.6	-1.5	-0.6	0.7	19
	6	280.4	-1.2	-1.0	0.5	27
Sk −68°135	1	183.6	–	>0.7	>1.6	–
	2	195.0	–	>0.7	1.2	–
	3	213.3	–	>1.0	1.7	–
	4	231.6	-1.2	>0.9	1.8	–
	5	246.9	-1.7	>1.3	0.9	–
	6	255.3	-1.6	-0.8	0.8	61
	7	261.4	-1.5	-1.0	0.9	49
	8	275.1	-1.3	>1.4	1.3	–
Sk −69°223	1	243.1	-2.0[a]	0.1	1.5	–
	2	257.5	-1.7[a]	0.2	0.7	–
	3	275.1	-1.3[a]	-0.4	0.7	–
	4	285.8	-1.0[a]	0.3	0.4	–
	5	298.7	-1.0[a]	>0.6	0.3	–
Sk −69°243	1	184.3	–	>0.5	>0.8	–
	2	227.0	-1.6	0.4	2.5	>4
	3	238.5	-2.0	0.7	3.5	>3
	4	251.4	-1.7	-0.5	2.1	19
	5	273.6	-1.5	-0.3	1.6	30
	6	280.4	-1.2	0.2	1.2	>14
	7	291.1	-1.2	0.5	2.2	>14
	8	300.3	-0.7	>0.9	1.1	–
Sk −70°120	1	214.8	–	>0.3	>0.7	–
	2	227.0	–	>0.4	>1	–
	3	237.7	–	>0.3	>0.8	–
	4	253.7	–	>0.6	>1.5	–
	5	270.5	-1.3	>1.1	1.1	–
	6	278.9	-1.4	>0.9	0.8	–
	7	291.1	-0.7	>1.2	0.6	–
	8	301.8	-1.1	1.0	0.4	–
	9	309.4	-0.6	1.1	0.5	–
	10	322.4	-0.1	1.1	1.1	–

Table 3.5: Properties and species abundance ratios of the LMC interstellar 'clouds' identified in Figures 3.14 to 3.19. Ti depletions were derived using H I 21 cm profiles; the values represent lower limits for a cloud where a H I 21 cm component lies *behind* the target; [a] denotes an uncertain depletion derived from the average of H I profiles adjacent to Sk −69°243 such as to exclude the 30 Dor continuum emission source. Dashes indicate a lack of column density data for one or both species due to S/N constraints.

Gaussian component was present for a 'cloud' of a given species, the $N_v(v)$ profile was used directly to obtain the species abundance at the required velocity.

Clouds are marked and numbered for each sightline in Figures 3.14 to 3.19, and Table 3.5 shows the calculated Ti depletions and species ratios for each cloud. Due to the possible contamination of the H I profiles by background components, the Ti II depletion values are lower limits; in the nomenclature of depletions, a larger number means less depletion.

The association of DIB carriers with particular 'clouds' can be made from examination of the DIB least-squares velocities plotted in Figures 3.14 to 3.18. There are clear variations across the different sightlines in the parameters of the clouds in which the DIB carriers reside. The least variable parameter is the titanium depletion, with lower limits ranging between −1.8 and −1.3, reflecting depletions of about an order of magnitude less than the value of −3 typical of the cold Galactic ISM (Welty *et al.* 1999) traced by Na I, where DIB carriers are usually observed to be strongest. The range of logarithmic Ca II/Na I ratios of between −1.8 and −0.3, and the Ca II/Ti II ratios of between 0.7 and 2 indicate high (compared to Galactic), variable UV field strengths. Compared to typical Galactic Ca II/Na I values, Sembach & Danks (1994) measured log Ca II/Na I to be about −0.3 on average for high Galactic latitude sightlines, and Crawford (1992) measured a value of −2 for typical cool, diffuse molecular clouds. The LMC Na I/K I ratio ranges between 30 and 70.

3.6 Discussion

3.6.1 LMC DIB strengths compared with E_{B-V}, N(K I) and Galactic data

The correlation between DIB equivalent widths and E_{B-V} has been studied in detail for a selection of diffuse interstellar bands (Herbig 1993). Although real deviations from linearity exist, the relationship between the amount of dust and the amount of DIB carriers is very close to linear. DIB strengths also correlate well with the column densities of the trace neutrals Na I and K I. Power law regressions with exponents of ~ 0.7 were found by Herbig (1993) in fits to extensive data on DIB equivalent widths

vs. Na I and K I column densities. Convincing *linear* fits between DIB equivalent widths and N(K I) were recently published by Galazutdinov *et al.* (2004).

The DIB strengths do not correlate well with the abundant H_2 molecule, nor with CO, CN or CH as expected from the close chemical relationships between these diatomics (Herbig 1993). The only diatomic molecule claimed to correlate directly with DIB strengths is C_2 (Thorburn *et al.* 2003), but only for a small selection of the weaker DIBs not concerned with this study.

A useful method for analysis of the LMC DIB strengths is to compare their equivalent widths with the Galactic correlations between DIB strengths, E_{B-V} and the column densities of trace neutrals. Any deviations from the Galactic correlations will aid the identification of the parameters that affect the DIB strengths. Thus, a compilation of Galactic data was assembled, primarily from the high S/N ($\sim$ 1000) DIB measurements made by Thorburn *et al.* (2003) and from the high resolution (0.5 $\sim$ 1.8 km s^{-1}) Na I and K I surveys by Welty *et al.* (1994) and Welty & Hobbs (2001). Supplementary DIB equivalent widths were taken from Herbig (1975), Herbig (1993), Tuairisg *et al.* (2000), Guarinos (1988) and from this thesis (Section 4.3). DIB equivalent widths for the sightline σ Sco were measured from spectra obtained from ancillary sources (N. L. J. Cox, private communication; S. J. Fossey, private communication). Supplementary atomic column densities were obtained from Herbig (1993) and Pan *et al.* (2004). The sightlines contained in the compiled dataset pass through a range of Galactic environments from molecular clouds to star forming regions and H II regions. The spectrum of cloud types characterised by the λ5780/λ5797 ratio is covered, and the range of line-of-sight E_{B-V} values lies between $\simeq$ 0 and $\sim$ 2. Sightlines probe gas at radial distances of up to 2 kpc which, although localised compared to the size of the Milky Way, should represent a diverse, though not necessarily complete sample of the Galactic ISM.

Data are plotted with point styles according to the key in Figure 3.22. Sightlines in the Galaxy known to exhibit peculiar properties are identified with unique point styles. Sightlines of extreme ζ type (with $W_{5780}/W_{5797} < 2$, high molecular content, standard UV extinction curve) are plotted with right filled triangles, and extreme σ-type sightlines ($W_{5780}/W_{5797} > 5$, low molecular content, low FUV extinction rise and low 2175 Å bump strength), are plotted with inverted filled triangles. The stars of the ρ Oph system lie behind a cloud with relatively high gas-to-dust ratio ($G = 1.5 \times 10^{22}$

Galactic (MW) sightlines –
ζ–type sightlines –
σ–type sightlines –
ρ Oph sightlines –
Orion sightlines –
Weak DIB sightlines –
Sk –67°2 –
Sk –67°5 –
Sk –68°135 –
Sk –69°223 –
Sk –69°243 –
Sk –70°120 –

Figure 3.22: Key for point styles used in LMC *vs.* Galactic DIB strength, E_{B-V} and atomic column density plots.

cm^{-2} mag^{-1}; Bohlin *et al.* (1978)) and high R_V value (~ 4.4; Cardelli *et al.* (1989)), and are labelled with crossed diamonds. The 'Orion' sightlines probe the ISM in the vicinity of the Orion Nebula H II region (plotted with crossed circles) and typically show exceedingly weak DIBs for the reddening, no evidence for diatomic molecules, and anomalously flat UV extinction curves (Cami *et al.* 1997). Sightlines known to exhibit anomalously weak DIBs for the reddening are shown with crossed pentagons. The $\zeta \longrightarrow \sigma \longrightarrow$ Orion progression of cloud properties is believed to reflect a trend for increasing interstellar UV field strength (Cami *et al.* 1997).

Figure 3.23 shows a comparison of the atomic correlations with E_{B-V} between the Galactic and LMC data. The lower depletion of titanium and greater gas-to-dust ratio the LMC sightlines is shown in the N(Ti II) *vs.* E_{B-V} plot (the lower panel), where the LMC sightlines have N(Ti II) about an order of magnitude greater than most of the Galactic data; N(Ti II) is apparently not correlated with E_{B-V} and the lack of distinction between the ζ and σ sightlines in the plot indicates that Ti depletion is probably not correlated with the W_{5780}/W_{5797} ratio.

The high gas-to-dust ratio in the LMC sightlines as expressed by $G = N(\mathrm{H\ I})/E_{B-V}$ is evident in the position of the data points in the N(H I) vs E_{B-V} plot (Figure 3.23, middle panel). The sightlines towards Sk –67°2 and Sk –69°223 lie short of the LMC average shown by the dashed line, with gas-to-dust ratios similar to those found in many Galactic sightlines (including ρ Oph). Within the large errors on G, it is possible

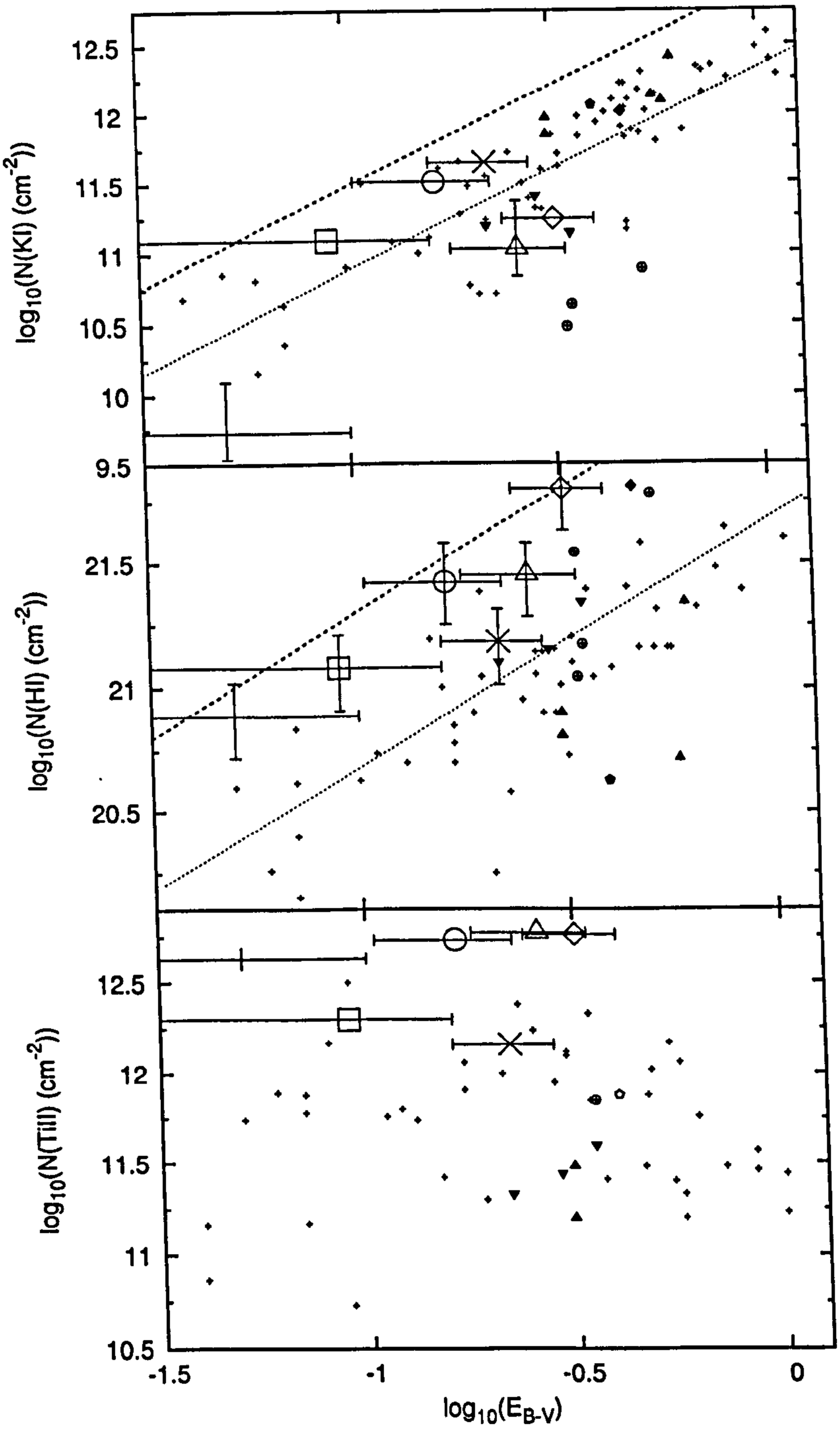

Figure 3.23: Logarithmic plots of LMC K I (top), H I (middle), and Ti II (bottom) column densities against E_{B-V}, compared with Galactic data. The weaker dotted line in the K I plot is the least-squares linear fit through the Galactic K I *vs* E_{B-V} data; the stronger dashed line shows this trend-line after a multiplication of N(K I) by a factor of 4 to simulate the LMC gas-to-dust ratio (see below). In the middle plot, the fainter dotted line represents the Galactic gas-to-dust ratio $G = \frac{N(\mathrm{H\ I})}{E_{B-V}}$ found by Bohlin *et al.* (1978); the stronger dashed line represents $4G$ and estimates the gas-to-dust ratio in the LMC where it is on average four times greater than in the Galaxy (Fitzpatrick 1986). H I data are from Savage & Jenkins (1972) and the Ti II data are from Stokes (1978). See key (Figure 3.22) for explanation of point styles.

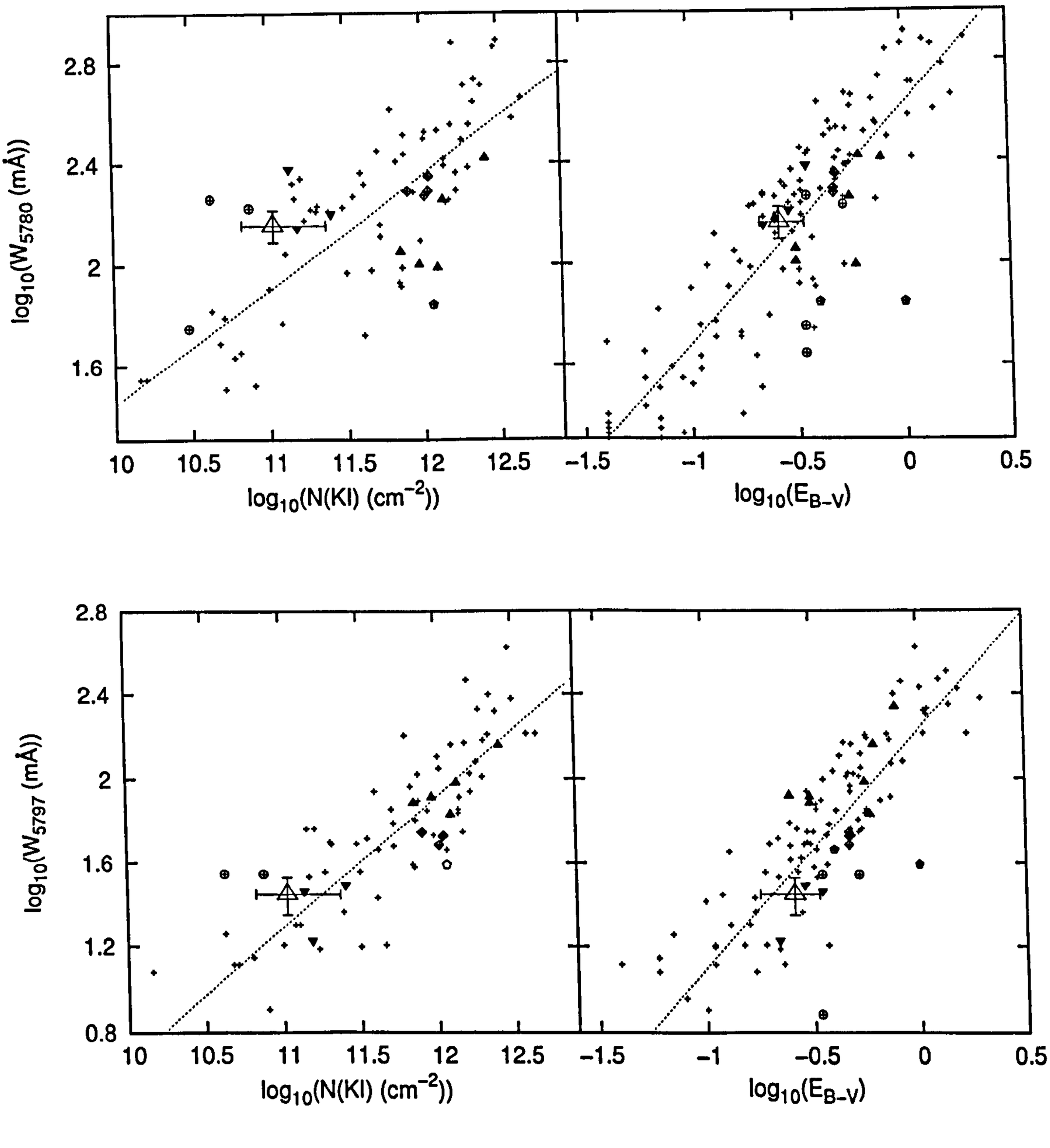

Figure 3.24: Logarithmic plots of the equivalent width of the λ5780 (top), and λ5797 (bottom) diffuse interstellar bands measured towards Sk −69°223, plotted with respect to K I column density (left) and E_{B-V} (right). Galactic data are plotted, with power law fits to the K I data and linear fits to the E_{B-V} data shown with dotted lines. See key in figure 3.22 for explanation of point styles.

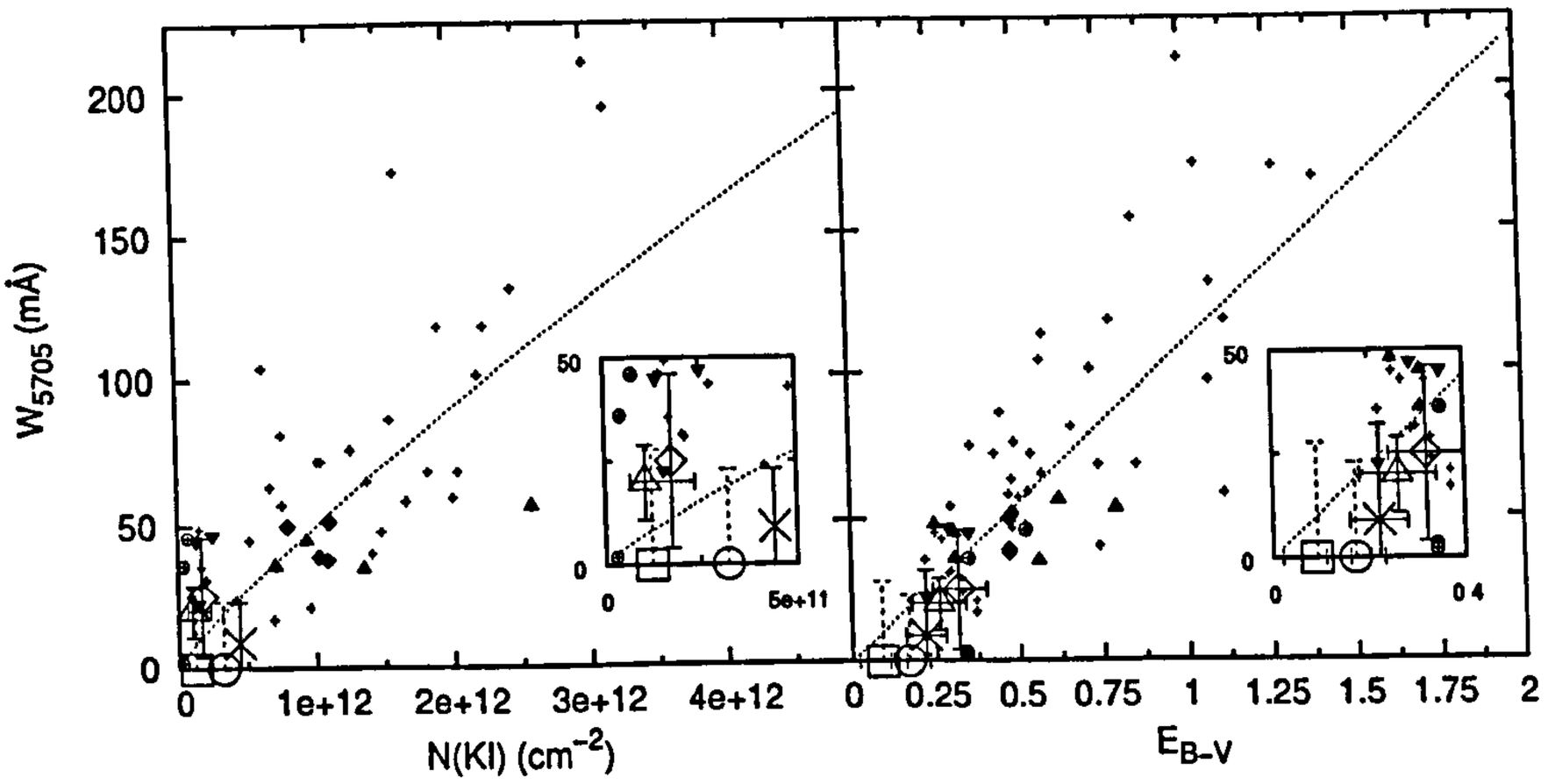

Figure 3.25: Equivalent widths of the λ5705 diffuse interstellar band measured towards the five reddened LMC targets, plotted with respect to K I column density (left) and E_{B-V} (right). Galactic data are plotted, with a power law fit to the K I data and a linear fit to the E_{B-V} data shown with dotted lines. See key 3.22 for explanation of point styles. Dashed error bars represent upper limits on DIB strengths (*i.e.* no DIB detected). Inserts show magnified regions around the LMC sightline data.

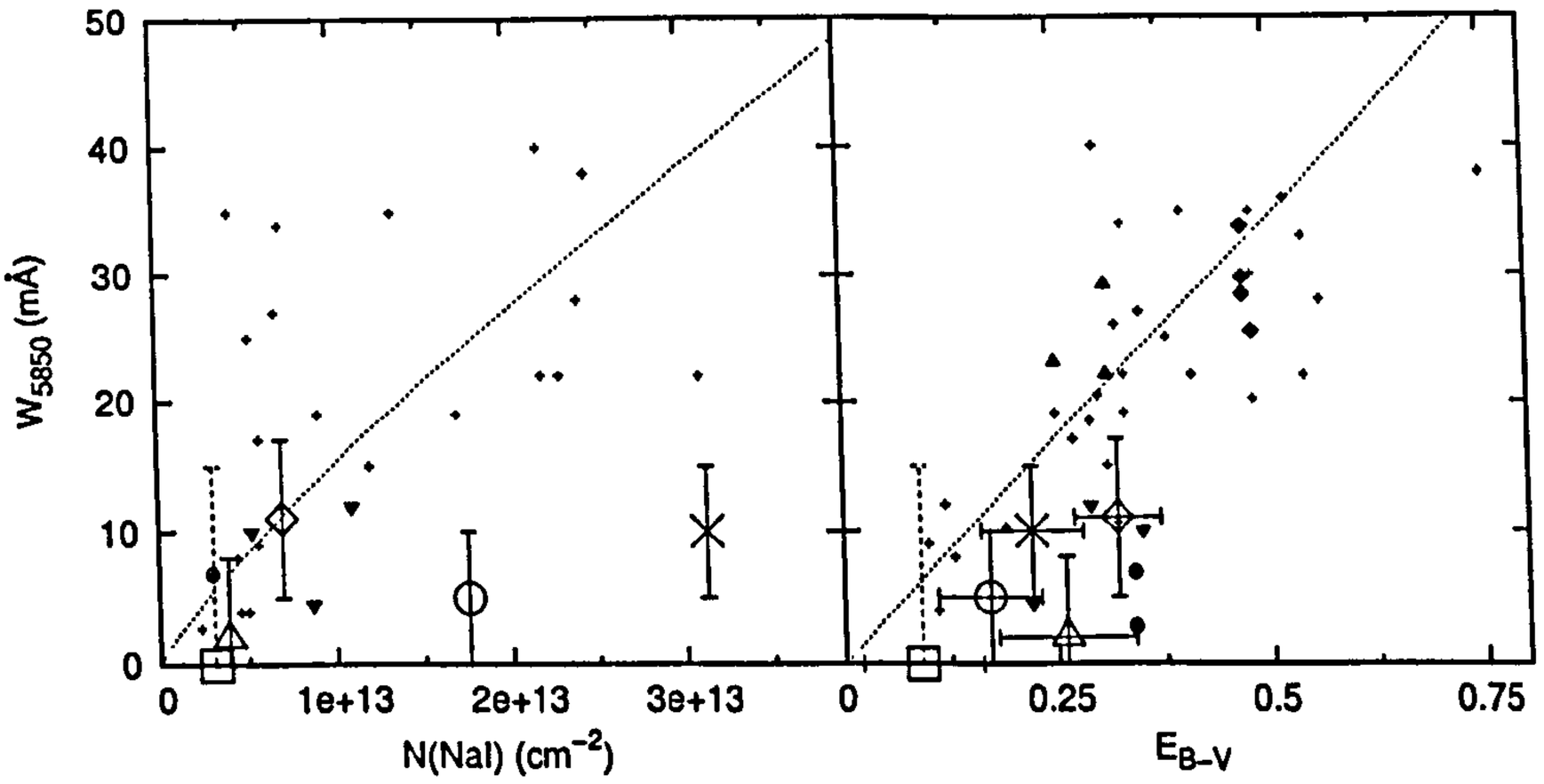

Figure 3.26: Equivalent widths of the λ5850 diffuse interstellar band measured towards the five reddened LMC targets, plotted with respect to Na I column density (left) and E_{B-V} (right). Galactic data are plotted, with a power law fit to the Na I data and a linear fit to the E_{B-V} data shown with dotted lines. ζ clouds are out of the plot range for N(Na I) due to exceptionally high column densities. See key in figure 3.22 for explanation of point styles. Dashed error bars represent upper limits on DIB strengths (*i.e.* no DIB detected).

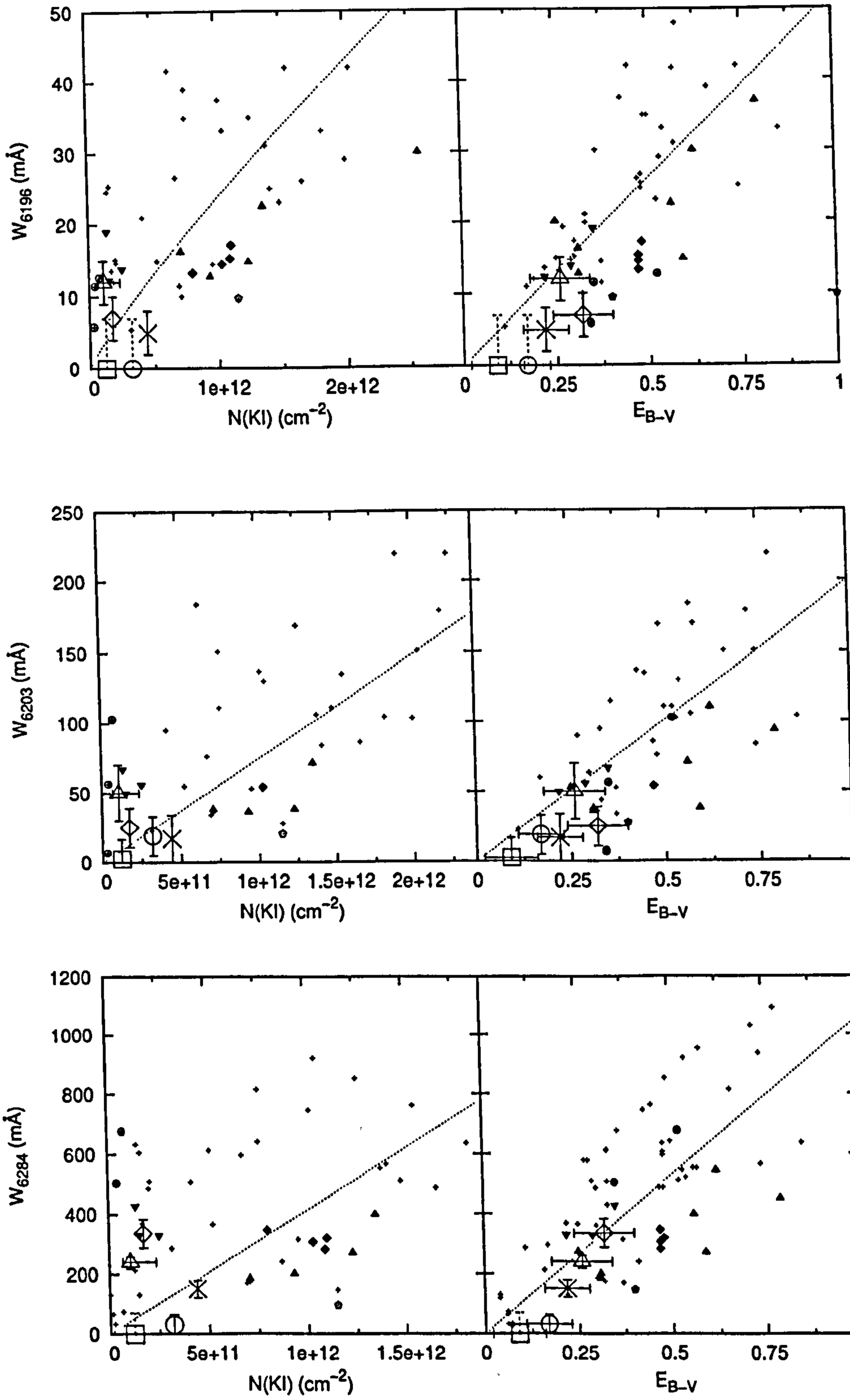

Figure 3.27: Equivalent widths of the λ6196 (top), λ6203 (middle), and λ6284 (bottom) diffuse interstellar bands measured towards the five reddened LMC targets, plotted with respect to K I column density (left) and E_{B-V} (right). Galactic data are plotted, with linear fits to the data shown with dotted lines. See key in figure 3.22 for explanation of point styles. Dashed error bars represent upper limits on DIB strengths (*i.e.* no DIB detected).

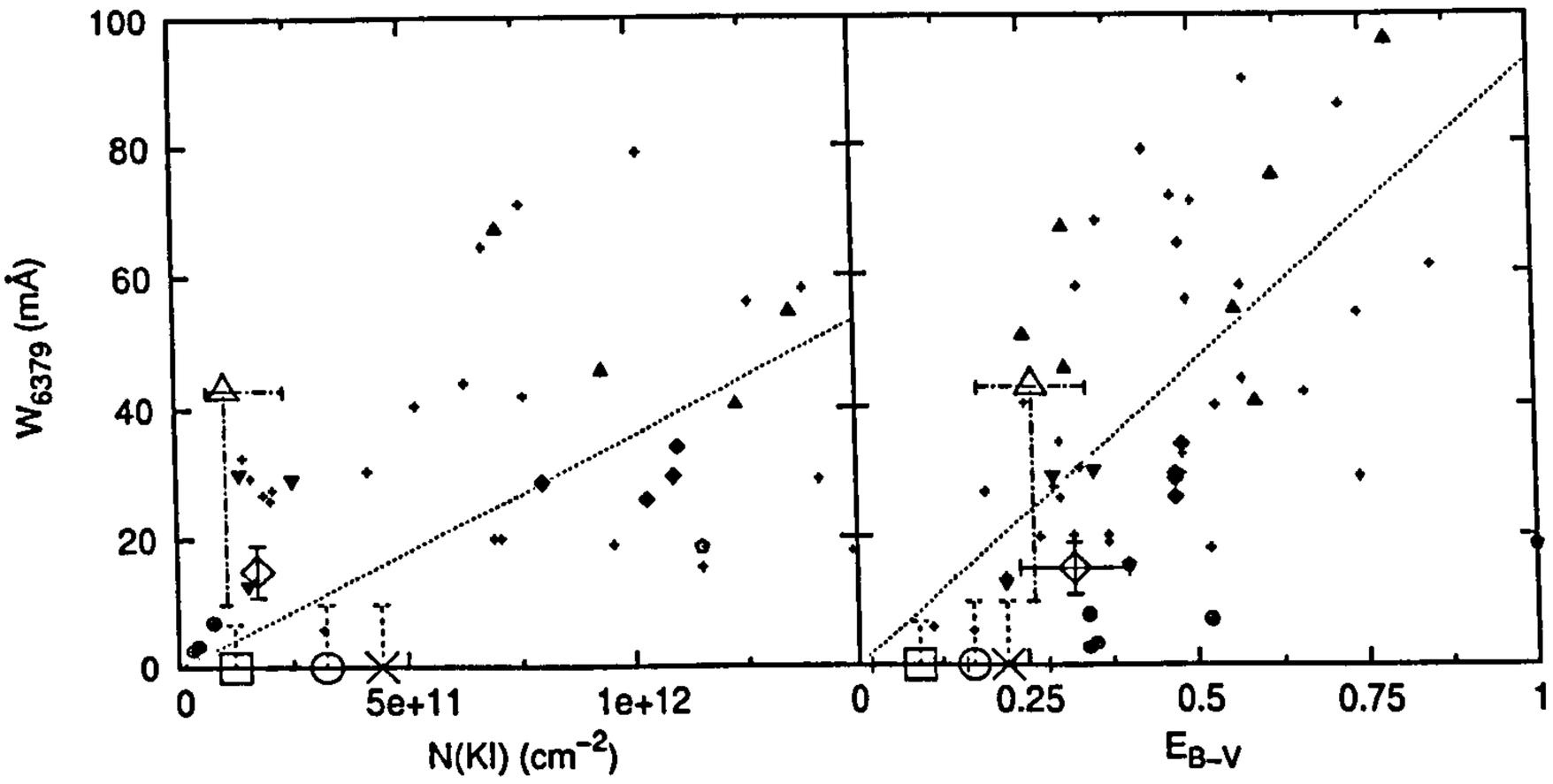

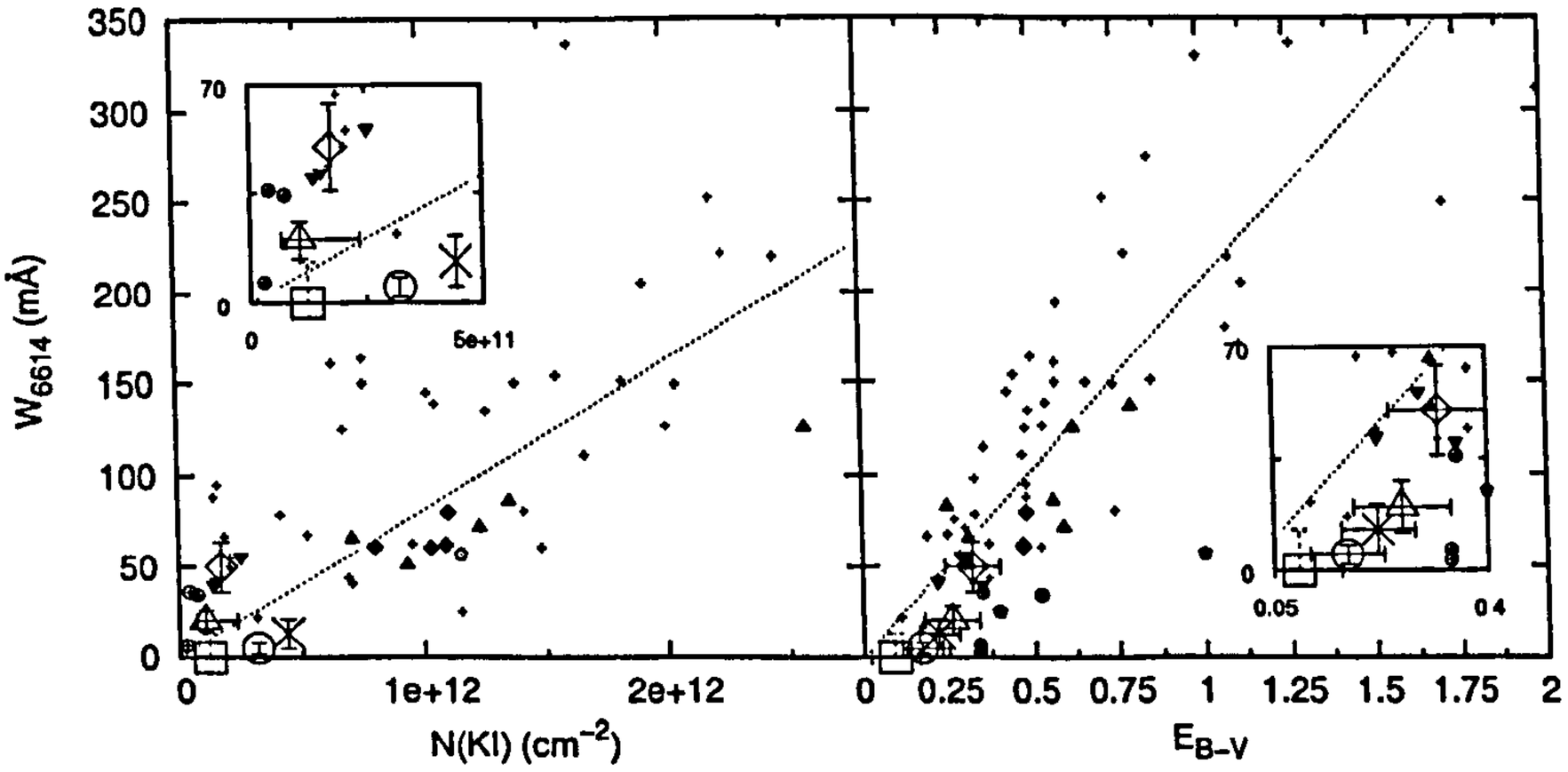

Figure 3.28: Equivalent widths of the λ6379 (top), and λ6614 (bottom) diffuse interstellar bands measured towards the five reddened LMC targets plotted with respect to K I column density (left) and E_{B-V} (right). Galactic data are plotted, with linear fits to the data shown with dotted lines. See key in figure 3.22 for explanation of point styles. Dashed error bars represent upper limits on DIB strengths (*i.e.* no DIB detected), dot-dashed error bar for Sk −69°223's λ6379 identifies that this data point may be uncertain due to a stellar line blend – the lower error limit was obtained by least-squares deblending a Gaussian stellar component and a single intrinsic λ6379 profile taken from β^1 Sco. Inserts show zoomed area surrounding LMC data points.

that the gas-to-dust ratio in the ISM towards Sk −67°2 could be equal to the Galactic average. The ζ and σ-type Galactic sightlines are separated, at least in part due to the significant fraction of hydrogen in molecular form in ζ clouds that is unaccounted for in this plot.

The progression $\zeta \longrightarrow \sigma \longrightarrow$ Orion is highlighted by their vertical displacement on the N(K I) *vs.* E_{B-V} plot (Figure 3.23, top panel), where a progression in UV field strengths is presumably responsible for ionising progressively more K I: N(K I) is exceptionally low for the amount of reddening in the Orion sightlines, probably due to the strong UV radiation field pervading this region. Although the error bars cloud the issue somewhat, broadly speaking the LMC sightlines all appear to have N(K I)/E_{B-V} ratios consistent with the ratios found along Galactic sightlines. Towards Sk −67°2, Sk −69°223 and Sk −69°243 the N(K I)/E_{B-V} ratios are well short of the ratio (naïvely) expected for the greater gas-to-dust ratio of the LMC — the strong dashed line in the plot represents the multiplication of the mean Galactic N(K I)/E_{B-V} ratio (weaker dotted line) by a factor of 4 to give the ratio that might be expected in the LMC ISM where the gas-to-dust ratio is ~ 4 times Galactic. The fact that the LMC sightlines lie short of this line shows that G is not the main factor governing N(K I)/E_{B-V}, and therefore the ionised potassium fraction and/or the level of depletion of K I in the LMC are greater than in the Galaxy. Given that K I depletion is relatively constant in the Galaxy (Welty & Hobbs 2001), it is likely that the relative reduction in N(K I) in the LMC sightlines is due to enhanced K I photoionisation, consistent with the occurrence of strong, relatively unattenuated UV fields pervading the LMC ISM (see Section 3.2.1). The reddening of Sk −70°120 is very uncertain, probably moving it off the left edge of the plot. Sk −69°223 and Sk −69°243 fall in the region of the σ-type sightlines, suggesting stronger pervading UV fields in the ISM towards these two targets than towards the others.

3.6.2 Sk −67°2

Of all the programme targets, Sk −67°2 has the greatest LMC Na I and K I column densities, and might therefore be expected to show the strongest DIBs. From the data in Figure 3.14 and Table 3.5, the principal Na I component with which the DIB carriers are associated has a 'normal' (with respect to the Galaxy) Na I/K I ratio and a logarithmic Ca II/Na I ratio of −1.8, characteristic of typical Galactic diffuse molecular

clouds (Crawford 1992). The Ca II/Ti II ratio of 2 is also within the normal range of values found in the Galaxy (Stokes 1978; Albert *et al.* 1993). Supported by the relatively high N(K I)/E_{B-V} and relatively low N(H I)/E_{B-V} compared to the other LMC sightlines (see Figure 3.23), the evidence suggests that this sightline bears the closest similarity to the Galactic diffuse ISM. However, examination of the correlation plots (Figures 3.26 to 3.28) shows that the DIB carriers observed in this sightline are underabundant by about a factor of two with respect to the trace neutral species, as compared with the Galactic averages shown by the trendlines. A possible exception to this result is λ6284, though this DIB is still weaker than typically observed in the Galaxy for similar values of N(K I).

The distribution of Galactic data points in the plots of DIB strength *vs.* E_{B-V} is different to those in the N(K I) plots, but all the Sk −67°2 DIB equivalent widths are still below the Galactic average. The weakness of the DIBs is particularly apparent for λ5850, λ6379 and λ6614 (members of the KW III family), and the ratio of λ6284 to λ6614 equivalent widths (about 11.5), is indicative of a σ-type sightline which typically shows a weakness of KW III DIBs and a strengthening of KW II DIBs (including λ6284) compared to E_{B-V}. The W_{6284}/W_{6614} ratio is greater than typical for σ clouds, almost reaching the high values observed towards Orion. In Galactic σ and Orion sightlines, the strength of λ6284 is generally enhanced compared to the mean, but the relative weakness of λ6284 towards Sk −67°2 compared with Galactic σ and Orion clouds — shown in Figure 3.6.1 — suggests that there is another factor at work that acts to weaken the DIB, other than those factors that distinguish ζ, σ and Orion sightlines in our own Galaxy.

As shown in Table 3.4 the R_V value of approximately 3.6 towards Sk −67°2 is in line with typical Galactic σ cloud values, indicating that the UV extinction curve and hence the dust grain composition and size distribution is similar to that found in the Galaxy. Residing to the West of the LMC bar, far from the intense star formation and ionising UV flux of 30 Dor, and indeed, at least 7 pc away from the nearest H II nebula N4 (Davies *et al.* 1976), the ISM towards Sk −67°2 appears to have no exceptional properties and represents a typical diffuse interstellar sightline apart from reduced DIB strengths and the reduced metallicity common to all the LMC sightlines. Metal abundances are $\lesssim$ 50% of those in the Galactic ISM, which could account for a reduction in DIB strengths relative to E_{B-V} *via* modifications to the physics and chemistry that

maintain the abundances of DIB carriers, suggesting that metals may play a crucial role in the processes responsible for DIB carrier formation and/or persistence in the ISM.

3.6.3 Sk −67°5

Noteworthy features of this sightline (also far West of the centre of the LMC but close to several bright H II regions) are the very low Na I/K I ratios within its principal clouds. Clouds 4, 5 and 6 (see Figure 3.15 and Table 3.5) have N(Na I)/N(K I) < 30, which is significantly lower than any values observed in the Galaxy by Welty & Hobbs (2001). Logarithmic Ca II/Na I ratios are fairly low (between −1 and 0.7), yet generally still greater than for most Galactic molecular clouds. $\log N$(Ca II)/N(Na I) = −1.0 is typical of diffuse, non-molecular clouds (Hobbs 1978). The Ca II/Ti II ratio is very low in this cloud (~ 0.5), probably due to increased photoionisation of Ca II by a high UV flux. Conversely, two high velocity clouds (1 and 2) moving at speeds of ~ 20 km s^{-1} and ~ 30 km s^{-1} towards us with respect to the local rest frame of the LMC ($v_{\rm LSR} \simeq 262$ km s^{-1}, measured from the HI velocity slices in Kim *et al.* (2003)), have high logarithmic Ca II/Na I ratios (greater than 0.7), and cloud 2 has a very high Ca II/Ti II ratio (greater than 6). The logarithmic Ti depletion measured in cloud 2 is −2.5, which is the greatest depletion of any cloud measured in this study. The only way this high depletion can be reconciled with the high Ca II/Na I ratio (usually taken as an indicator of *low* depletion) and high Ca II/Ti II ratio is if the Ca II abundance is being affected significantly by the ionisation equilibrium. This cloud must contain either an above average electron density, an above average abundance of negatively charged large molecules (which convert Ca III into Ca II by electron transfer), or a lower than average ionising UV field strength in order to increase the relative Ca II fraction. To decide which of these factors is responsible is beyond the scope of this study, but this result shows that it is incorrect to assume that the interstellar calcium ionisation equilibrium is constant (see for example Caulet & Newell 1996) for the purpose of deriving calcium depletions from Ca II/Na I ratios. There are many examples of a varying Ca II ionisation balance, evidenced by the greatly varying Ca II/Ti II ratios in the sightlines studied here. The varying Ca II/Ti II ratio can be seen from examination of the relative variations in the $N_v(v)$ profiles of these two species shown in Figures 3.14 to 3.19, for example, the IVCs around $v_{\rm LSR} \simeq 60$ km s^{-1} towards Sk −67°5 and

Sk −70°120, HVCs around $v_{\rm LSR} \simeq 130$ km s^{-1} towards Sk −67°5 and Sk −68°135, and the prominent Galactic disc component at $v_{\rm LSR} \simeq 10$ km s^{-1} towards Sk −68°135.

The DIBs towards this sightline are weak, as evidenced by the non-detection of all DIBs apart from λ6203. However, the limited S/N does not permit the assignment of equivalent width upper-limits small enough to confirm or deny a general weakness with respect to reddening or the trace neutrals. This sightline is indicated on most of the correlation plots with a dashed error bar to indicate the upper limits on dib equivalent widths. Certainly of interest, and perhaps of great importance, is the detection of λ6203 without any detection of λ6284. The strengths of these DIBs are correlated almost exactly in the Galaxy (correlation coefficient = 0.97, with a ratio $W_{6284}/W_{6203} = 5.7$ for the 54 sightlines in the Galactic dataset detailed in Section 3.6.1), showing that their carriers must have an intimately linked chemistry. This link appears to be broken in the LMC due possibly to the under-abundance of metals or high gas-to-dust ratio. The former is more likely as sightlines in the Galaxy with differing gas-to-dust ratios uphold the correlation between W_{6284} and W_{6203}. Other conditions along this sightline are not particularly unusual; the UV field is not exceptionally strong, calculated as ~ 3 times the local Galactic average by André *et al.* (2004). From examination of Figure 3.11 the quality of the detection of λ6203 for this sightline is not great, though it *is* statistically significant, with 6 pixels within the peak of the assumed DIB profile at least 2σ below the continuum, constituting at least a 4.9σ detection. The shape of the feature is as expected for this DIB, and no known spectral features of an O-type supergiant that could be responsible for such an absorption line are known to lie in this wavelength range.

3.6.4 Sk −68°135

Sk −68°135 lies ~ 300 pc to the north of the centre of 30 Dor, well within the extent of the ionised gas of the nebula. Figure 3.16 shows that the gas in the sightline towards Sk −68°135 is dominated by a single strong component in Na I that is shown in Ca II to be composed of several closely spaced clouds with differing Ca II/Na I ratios covering a range of conditions from the quiescent, dense, low velocity[11] regime (see Hobbs 1978,

[11]The local LMC H I rest frame is at $v_{\rm LSR} \simeq 265$ km s^{-1}, measured from the maps of Kim *et al.* (2003).

for example) of cloud 7 (with log N(Ca II)/N(Na I) = −1.0 at $v_{LSR} \simeq 261$ km s^{-1}), to the shocked, higher velocity gas of cloud 8 (with log N(Ca II)/N(Na I) = 1.4 at $v_{LSR} \simeq 275$ km s^{-1}). A system of clouds with log N(Ca II)/N(Na I) $\gtrsim$ 1 are shown by Ca II in the velocity range $v_{LSR} \simeq 184 - 232$ km s^{-1} (clouds 1 – 4), whose high velocities relative to the local rest frame of the LMC (with a radial velocity vector up to ~ 100 km s^{-1} towards us) suggests that they may have been pushed away from the main disc of the LMC by a strong force (see for example de Boer *et al.* 1980). Powerful winds from O-type stars and Wolf-Rayets around 30 Dor could perhaps supply the required energy, but supernova explosions are another possible explanation. Alternatively, similar to the HVCs, these clouds could be expanding remnants of gas and dust left over from a past collision between the LMC and SMC. From examination of Figure 3.16, the neutral hydrogen column densities in these clouds are low, such that the large gas-phase Ca II column densities — taken as evidence for low calcium depletions — give further evidence for a shocked history for these clouds. Ti was not detected in these clouds.

The carriers of the diffuse interstellar bands that were strong enough to permit a velocity measurement lie within clouds 6 and/or 7 (the clouds that show the strongest Ca II and Na I peaks respectively). Due to the error on the velocity measurement, it is not possible to constrain the existence of the DIB carriers to within one cloud or the other, but indicative of the environment most favourable for molecule formation is the fact that André *et al.* (2004) measured high H_2 column densities (log $N(H_2)$=19.87) in cloud 7 and negligible amounts in the surrounding clouds. Cloud 7 (see Table 3.5) has a low logarithmic Ca II/Na I ratio of −1.0, typical of cool diffuse clouds (Hobbs 1978; Sembach & Danks 1994). The substantial H_2 column, along with detections of HD and CO is surprising given the strength of the dissociating UV radiation permeating the cloud that was calculated by André *et al.* (2004) to be over 1000 times the average Milky Way interstellar radiation field. They hypothesised that this extremely high level of radiation must arise due to the close proximity of the cloud to the background star. On this basis, the molecular cloud is therefore the remnant of a dense cloud, presumably from which the star Sk −68°135 was born, and is in the process of being eroded away by the strong stellar radiation. The impact of such an interesting environment on DIB carrier abundances can be analysed.

The DIBs detected with certainty towards Sk −68°135 are λ5850, λ6203 and λ6284

and λ6614. It is unsurprising, given the observed weakness of these DIBs, that others were not detected. The gas-to-dust ratio and R_V are high and are similar to values observed for the molecular cloud in front of ρ Oph, a recent star-formation site. Ti depletions in the DIB-carrying gas ($\delta_{\rm Ti} \sim -1.5$ in clouds 6 and 7) are relatively low compared to the typical depletions $\delta_{\rm Ti} \sim -2.9$ in the cold neutral medium of the Galaxy (Welty *et al.* 1999). From examination of Figures 3.26 to 3.28, λ5850 and λ6614 are clearly weak compared to the Galactic average by at least a factor of two, though are not too dissimilar in relative strength to the σ and Orion sightlines. λ6284 is exceptionally weak for the amount of K I and E_{B-V}. λ6196 is also weak, though λ6203 appears to have a strength more in line with some of the weaker Galactic targets, especially when plotted with respect to E_{B-V}. From the presence of λ6614 and λ5850, and the ratio of $W_{6284}/W_{6614} \sim 6$ (showing that λ6284 is weak), the DIB-containing cloud is similar to a ζ-type, though there is no evidence for diatomic molecules (CH, CH^+ or CN) in the UVES spectrum.

Possible explanations for the extreme weakness of λ6284 and λ6196 include either (a) that the main cloud (number 7's) recent history as a cold, dense, quiescent molecular core caused the precipitation of the carriers of these DIBs into mantles on the dust grain surfaces, removing them from the gas phase, or (b) that the extreme UV field that now penetrates this cloud has largely destroyed these DIB carriers. The high R_V value and low Ti depletion in the cloud is evidence for the former, indicative of an overall distribution of dust grain sizes favouring larger grains with reduced FUV extinction efficiency, and less surface area available for depletion. This does not preclude the possibility that UV radiation has destroyed many of the DIB carriers, but the high H_2 abundance and the fact that λ5850 and λ6614 are present are evidence that some well-shielded parts of the cloud remain that the UV photons cannot penetrate.

Due to uncertainties in the reddening and the weakness of the DIBs (causing large relative errors in their equivalent widths), it is difficult to be certain about just how weak the DIBs are, but the results are consistent with them being less than half as strong in this sightline than the Galactic average. If λ6284 were a factor of two stronger, it would have a ratio W_{6284}/N(K I) similar to the ζ type sightlines shown in Figure 3.6.1.

3.6.5 Sk −69°223

The moderately reddened target Sk −69°223 displays some of the strongest DIBs observed in this study. Located among the ionised gas shells and filaments of the DEM 232, DEM 261 and DEM 263 H II nebulae (Davies *et al.* 1976), this hot, massive star lies towards the edge of 30 Dor in the direction of SN 1987A, about 200 pc from the central ionising O-star cluster R136 (Sk −69°243).

As shown by Figure 3.23, the amount of K I in the sightline (as inferred from the low N(Na I)) is very low for the reddening, and is similar to the amounts seen towards σ and Orion sightlines where, it is suggested, the strong UV fields photoionise K I. The N(Na I)/N(H I)^2 ratio is almost two orders of magnitude lower than the Galactic average, and distinguishes this sightline from Sk −67°2 which has a N(Na I)/N(H I)^2 ratio about 1.5 dex greater. This is suggestive of increased K I photoionisation in the gas towards Sk −69°223, which is supported by the low Ca II/Ti II ratio that probably results from increased Ca II photoionisation.

The gas-to-dust ratio is high at around twice the Galactic mean, but within the error estimate, is not significantly greater than many of the Galactic sightlines plotted. Ti depletion is very low ($\delta_{\rm Ti} \sim -1.3$), particularly in the principal cloud containing the DIBs and most of the Na I (cloud 3 — see Figure 3.17 and Table 3.5), providing evidence for the shocked history expected from the location in 30 Dor. Accordingly, Ca II/Na I ratios are rather high. These conditions are perhaps indicative of a combination of small, high density, clumps of gas and dust embedded within a more widely dispersed, warmer, less depleted medium with a much larger volume filling factor that dominates the overall depletion measures. To create such low Ti depletion and integrated sightline N(Na I)/N(H I)^2 ratio, it is likely that the ratio of warm to cold ISM is greater than in typical Galactic sightlines. The high R_V value is suggestive of a grain population biased towards larger grains.

With similar velocity ($v_{\rm LSR} \simeq 275$ km s^{-1}) and column densities of Na I and Ca II, it is plausible that the principal DIB-containing cloud (cloud 3) towards Sk −69°223 is part of the same sheet of material that causes cloud 5 towards Sk −69°243, as proposed by Vladilo *et al.* (1993). According to the H I velocity slices in Kim *et al.* (2003), the local H I rest frame is around $v_{\rm LSR} \simeq 265$ km s^{-1}, such that this cloud seems to be 'falling back' into the disc of the LMC. It is possibly a leftover remnant of the collapsing

molecular cloud that formed the young stars in and around 30 Dor $\lesssim 5 \times 10^6$ years ago (de Boer *et al.* 1980).

Clearly, the UV flux impinging on this cloud is high, resulting in a ratio $W_{5780}/W_{5797} \approx 5$, which is typical of σ-type sightlines. From Figure 3.24 it is clear that the strengths of these bands are exactly as one would expect for the amount of K I and E_{B-V}, and λ5780 is located among the σ-type sightlines on the correlation plots. With respect to K I, the λ5705, λ5780, λ6196, λ6203, λ6284, λ6379 and λ6614 DIBs are all on a gradient similar to the σ sightlines, showing a σ-type DIB strength pattern. The DIBs observed in this sightline are generally not weak with respect to E_{B-V}. A notable exception to this rule is λ5850 which is weak by at least a factor of 2 compared to the Galactic average for similar values of N(K I) *and* E_{B-V}.

Conditions of low depletion, high R_V and high UV flux in the ISM probed by this sightline appear not to have diminished the DIB strengths below those seen for high UV Galactic environments. Thus there is a component of the ISM in this sightline, lacking in Sk −67°2 and Sk −68°135, in which conditions are favourable for DIB carrier production to the degree found typically in the local Galactic ISM.

3.6.6 Sk −69°243

A site of active star formation, the > 50 massive, hot O-type stars and Wolf-Rayets in this composite object provide most of the ionising radiation that lights up the Tarantula Nebula. The radiation density in the nebula creates a FUV field ~ 4600 times the local Galactic interstellar value (Poglitsch *et al.* 1995). Feast (1961) calculated the temperature of the nebula as $\approx 10^6$ K, with $n_e = 100$ to 2000 cm^{-3}. According to de Boer *et al.* (1980) the sightline to Sk −69°243 probes clouds over a velocity range of ~ 100 km s^{-1} from dense, neutral gas around $v_{\rm LSR} \simeq 274$ km s^{-1} to highly exited O III-emitting gas at $v_{\rm LSR} \simeq 230$ km s^{-1}, with extremely excited coronal-type gas emitting in C IV at $v_{\rm LSR} \simeq 205$ km s^{-1}. C II and CO emission were found by Poglitsch *et al.* (1995) to co-exist in velocity space along this sightline, indicating the presence of an ionisation-bounded PDR containing dense ($n \sim 6800$ cm^{-3}), compact (~ 1 pc diameter) clumps of molecular gas, though the primary CO peaks that they recorded at $v_{\rm LSR} \simeq 260$ km s^{-1} and $v_{\rm LSR} \simeq 240$ km s^{-1} are apparently not coincident with the velocities of the principal Na I clouds with which the DIB carriers are associated.

From the relative position of the DIB least-squares velocities at $v_{LSR} \simeq 274$ km s^{-1} (see Figure 3.18), principal cloud number 5 contains the highest proportion of DIB carriers in this sightline, coincident with the primary H I peak. This cloud was calculated to have a number density of ~ 300 cm^{-3} and a temperature of ~ 100 K by de Boer *et al.* (1980), which is typical of cold Galactic diffuse clouds such as the one towards ζ Oph where DIBs are strong (van Dishoeck & Black 1986; Herbig 1993). This cloud has a much greater Na I/K I ratio (albeit still much smaller than in the Galaxy), and lower Ca II/Na I ratio than the other principal Na I cloud (number 4 at $v_{LSR} \simeq 251$ km s^{-1}). There appears to be a greater concentration of DIB carriers in cloud 5 than cloud 4 as inferred from the fact that the single-component fitted DIB peak-velocities are closer to cloud 5 than cloud 4 with a ratio of about 1 : 3 (see DIB velocities at the top of Figure 3.18). The reason for a greater relative Ca II abundance in the cloud containing the majority of the DIBs may be related to depletion, electron density (or density of electron-donating species), ionising radiation field strength, or some combination of these factors. Given that Ti depletion is known not to correlate with DIB strengths (Herbig 1993), and that UV field strength appears to have a differential effect on the strengths of λ6196 and λ6379[12], but noting that their location on the velocity diagram is the same (top of Figure 3.18), it appears that electron density or the concentration of large negatively charged molecules could be responsible for the observed differences in Ca II and DIB carrier concentration between clouds 4 and 5. Large negatively charged molecules can act as electron donors for atoms or molecules (Welty & Hobbs 2001), so the increased Ca II/Na I ratio in cloud 5 where the DIBs are more strongly concentrated is evidence in support of the hypothesis that the carriers of λ6196, λ6379 and λ6614 are neutral or anionic species.

Cloud 5 (at $v_{LSR} \simeq 274$ km s^{-1}), similar to cloud 3 described for Sk −69°223, is 'falling in' towards the LMC relative to the H I rest frame in the locality of Sk −69°243 (around $v_{LSR} \simeq 260$ km s^{-1}). Cloud 4 is moving towards us, away from the LMC at about 10 km s^{-1} with respect to the local LMC HI rest frame, and is probably located closer to the star, subject to a greater radiation field than the more quiescent cloud 5. It is possibly a 'wind blown' bubble created by the massive cluster R136 (Feitzinger *et al.* 1984).

[12]This statement is based on the relationship between W_{5780}, W_{6379} and E_{B-V} analysed by Sonnentrucker *et al.* (1999b), and the excellent correlation (coefficient = 0.98) between W_{5780} and W_{6196} in the data published by Thorburn *et al.* (2003).

From Figures 3.25 to 3.28, the location of the DIB strengths on the correlation plots is consistent with this sightline being similar to Galactic σ-type sightlines. According to Fitzpatrick & Savage (1984) the extinction curve towards Sk −69°243 has $R_V = 3.7$ (like σ Sco, with $R_V = 3.8$ (Snow & Krełowski 1994)). The dust in this sightline is believed to be composed of a contribution from an 'LMC foreground' component with steep FUV rise (and $E_{B-V} \simeq 0.14$) and a contribution from 'nebular' dust with a much flatter, Orion-type FUV rise (and $E_{B-V} \simeq 0.18$). The measured DIB strengths are generally lower than the Galactic average, but not significantly lower than the σ and Orion type targets where UV flux is high. W_{6284} is consistent with the strengths of this DIB in Galactic σ-type sightlines (see Figure 3.6.1). Notwithstanding the fact that the DIBs could be *stronger* than in the MW in one dust component than the other, it thus seems as though both types of material are highly effective in producing the DIB carriers, contrary to the theory of Pettini & Dodorico (1986) who postulated that the weakness of the KW III DIBs they observed towards R136a[13] was due to the inefficiency of the nebular dust at producing DIB carriers. Based on the fact that the 'nebular' dust is similar to that seen in Orion where KW III DIBs are weak (probably due to the high UV field), and that cloud 4 is believed to be closer to the ionising cluster Sk −69°243 where UV radiation is high, one can associate the nebular dust with cloud 4, so it is not surprising that the KW III DIBs observed by Pettini & Dodorico (1986) were rather weak. The DIB production efficiency may however be *marginally* less in this material, accounting for an overall reduction in DIB strengths compared to Sk −69°223 where the out-flowing, excited, strongly UV-pervaded nebular component is absent (or weak) in the atomic spectra. Thus, using the results of de Boer *et al.* (1980) and Fitzpatrick & Savage (1984), the DIB carriers in the ISM towards Sk −69°223 are apparently associated only with the denser, more quiescent, in-falling gas cloud left over from the massive cloud of gas and dust that formed 30 Dor. Towards Sk −69°243, the DIB carriers are also located within the 'nebular' dust component, in which they appear to be present in marginally reduced abundances relative to E_{B-V}, but in similar abundances as in Galactic σ and Orion-type sightlines.

[13]Spectra were obtained by Pettini & Dodorico (1986) using the Hubble Space Telescope to resolve a single component R136a of the composite object R136 (Sk −69°243).

3.6.7 Sk −70°120

The dust content of the ISM in the direction of Sk −70°120 is very low. From the Ti II and H I data it is clear that the fraction of titanium in the gas phase is around 10% of the total interstellar abundance. Gas-phase fractions this large are usually seen only in the high velocity clouds in the Galactic halo, whose grain populations have been largely destroyed through the rapid acceleration processes that drove the clouds to such high velocities. This is corroborated by the very high Ca II/Na I ratio, whose value is boosted by the low Na I column density.

Sk −70°120 is located off the Eastern edge of the main disc of the LMC in a line of sight with relatively low H I column density. The peak H I velocity is at $v_{\rm LSR} \simeq 310$ km s^{-1}, moving away from us about 40 km s^{-1} faster than the main disc of the LMC to which it lies adjacent. This steep velocity 'shelf' is evident in the H I velocity slices of Kim *et al.* (2003). The exceptionally low depletion and high velocity of this mass of gas suggests that it may have sheared away from the main disc of the LMC in a gravitational encounter with the SMC. Alternatively, if the metallicity of this gas is much lower than the assumed −0.3 dex relative to the Milky Way, then it could possess no dust content at all, with the conclusion that the gas is left over from the collapse and formation of the LMC from its primordial cloud, and now lies in orbit, disconnected from the main LMC disc.

The 'stream' of Ca II clouds moving towards us relative to the LMC at high velocities (around $v_{\rm LSR} \simeq 235$ km s^{-1}, see Figure 3.19), is notable. The presence of these high velocity clouds in spectra around 30 Dor has been taken by several authors (de Boer *et al.* (1980), Songaila (1981), Feitzinger *et al.* (1984), Vladilo *et al.* (1993) for example) as evidence of wind-blown gas, propelled away from the LMC by the extreme energetics of the environment. This is clearly not the case for these clouds, located in an isolated environment far (~ 1 kpc) from the edge of 30 Dor.

3.7 Summary of factors affecting DIB strengths in the LMC

The interstellar conditions in the sightlines probed by this study represent a set of environments distinct from any previously observed in the Galaxy. The implications for the diffuse interstellar bands of a combination of increased gas-to-dust ratio, very low Na I/K I ratios and reduced metallicity, combined with variations between sightlines in UV field strength, dust extinction properties, elemental depletions and ionisation equilibria have been studied. An important conclusion is that, despite markedly different environmental conditions, particularly the high pervading UV field-strength and low metallicity of the LMC's ISM, DIB carriers are still present in the interstellar gas in high abundance.

3.7.1 Gas and Dust

From the plots in Figures 3.24 to 3.28, a correlation between LMC DIB equivalent width and E_{B-V} was observed that is broadly consistent with that observed in Galactic σ and Orion-type sightlines (that probe diffuse clouds subject to high UV fields). If a gas-phase chemistry alone were responsible for the production and maintenance of DIB carriers, then a fourfold increase in gas-to-dust ratio might have been expected to also increased the DIB strengths relative to E_{B-V}. The reduced metallicity of the LMC would oppose this expectation to some degree, unless the DIB carriers are composed of similar materials to the dust grains. Given the large number of different DIBs and the complexity of their collective spectrum (Herbig 1995), it is likely that the DIB carriers are composed largely of carbon-based material, such that the chemical effects of a reduction in metallicity should affect the abundances of DIB carriers *and* the dust grains to a similar degree. Therefore, normalisation of DIB equivalent widths by E_{B-V} should divide out the metallicity's effects.

A range of gas-to-dust ratios were probed in this study, from approximately Galactic towards Sk −67°2 to four times Galactic towards Sk −69°243. No significant correlation between gas-to-dust ratio and DIB strengths was observed, thus strengthening the link between DIB carriers and their origins in a dust-dependent chemistry.

For the λ6284 DIB which has the most accurate equivalent width data in this study,

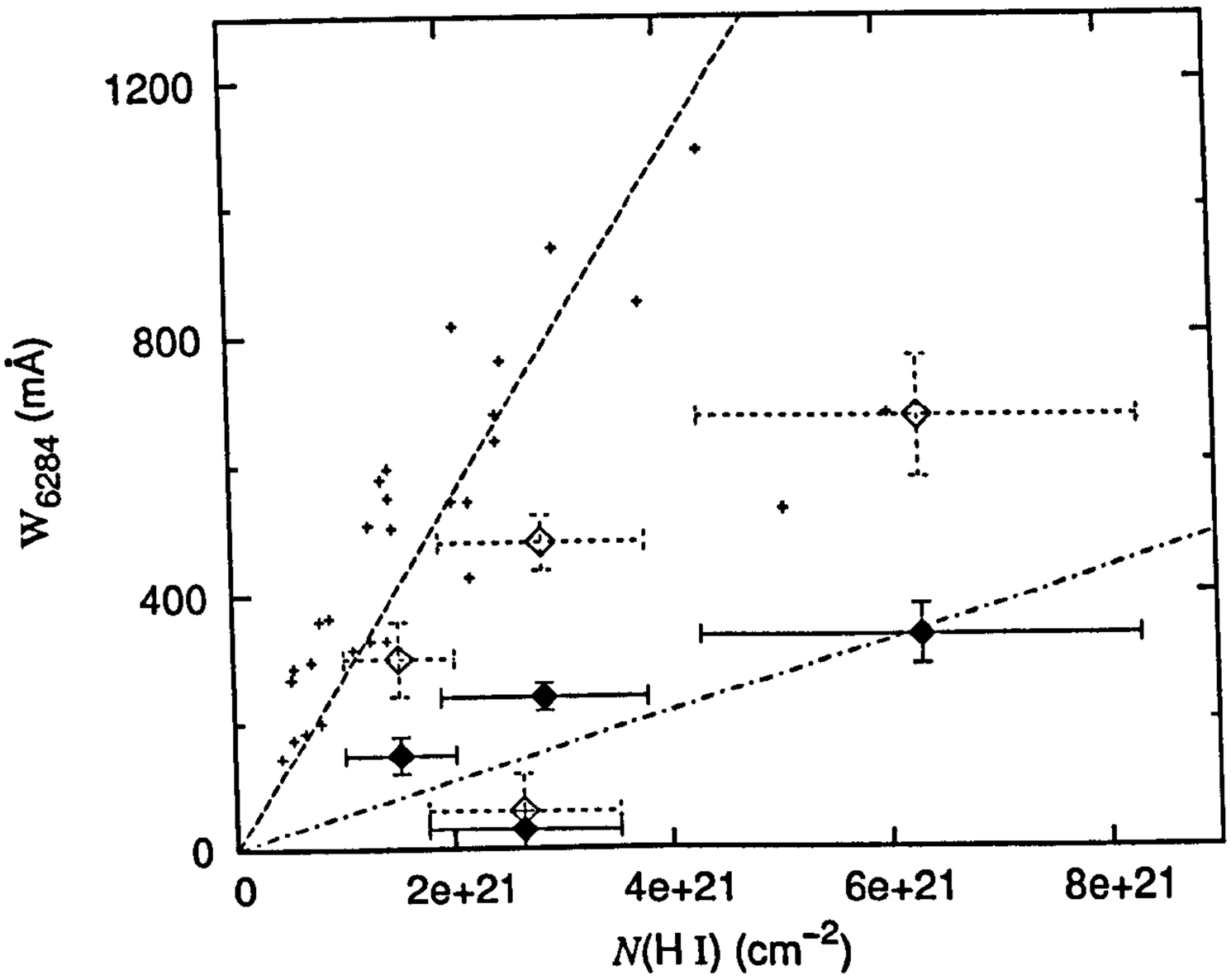

Figure 3.29: This graph shows λ6284 equivalent widths plotted against N(H I) for the LMC (filled diamonds) and the Galaxy (small crosses). The Galactic trend-line (dashed line) has a gradient 5 times that of the LMC (dot-dashed line). The open diamonds represent the LMC data points scaled by a factor of two to provide an approximate metallicity correction; error bars are scaled accordingly.

the relationship of the carriers of this DIB to the neutral hydrogen gas of the LMC is shown together with Galactic data in Figure 3.29. From the lines of best fit this DIB is weaker with respect to N(H I) by on average a factor of five compared to the Galactic sightlines in the plot. Thus it is evident that the carriers of this DIB are not directly related to H I. From the location of the open diamonds in the figure, the scaling of the DIB strengths by the ratio of Galactic to LMC metallicities (~ 2) is insufficient to account for the observed discrepancy in the relationships. Scaling by the *gas-to-dust ratio* (a factor of 4 to 5) would be a more effective method of reconciling the difference between Galactic and LMC trendlines. Unfortunately, large uncertainties in N(H I) and in the metallicities of the ISM towards the LMC targets preclude a definitive analysis.

Within the observational errors, the relationship between DIB strengths and the abundances of the trace neutrals Na I and K I was not distinguishably different from the Galactic relationship. The fact that N(K I) does not show any significant enhancement relative to E_{B-V} for sightlines with high gas-to-dust ratios (shown by Figure 3.23, and by the very low Na I/H I^2 ratios in Table 3.3) is evidence that the number densities of

the trace neutrals in denser, cooler diffuse clouds are governed not by the metallicity of the gas, but predominantly by the ionisation equilibrium. It is therefore a reasonable hypothesis that the DIB-carrier abundances are most strongly influenced by similar processes to those that determine the abundances of trace neutrals, *i.e.* ionisation and recombination.

The reasons for the high gas-to-dust ratio observed in the LMC are not clear (Koornneef 1984). The obvious suggestion is that the LMC has experienced a less active star formation history than the Milky Way, such that metal enrichment of the LMC's ISM has proceeded more slowly. Gas-to-dust ratios of galaxies are known to correlate approximately linearly with metallicity (Issa *et al.* 1990), and low metallicity stars are known to produce less dust, in proportion to their metal content (van Loon 2000). Therefore, taking an average LMC metallicity of –0.3 dex (corresponding to ~ 50% less metals in the LMC than the Galaxy), a twofold increase in gas-to-dust ratio relative to the Galaxy would be expected. The remaining factor of two required to obtain the fourfold (Fitzpatrick 1985) gas-to-dust enhancement of the LMC over the Galaxy is likely to arise from preferential sampling of low-dust content sightlines in past studies (Koornneef 1982; Fitzpatrick 1985). A turbulent history of the LMC's ISM, as indicated by the past interactions of the LMC, SMC and Galactic halo, would have caused shocking and destruction of dust grains. The strong UV field throughout much of the LMC would also be expected to erode the dust grains at a faster rate than in the local Galactic ISM, further reducing dust grain abundances and increasing the gas-to-dust ratio. In addition 'high latitude' sightlines are probed in any Earth-based observations of the LMC because its disc is viewed virtually face-on. These sightlines would be expected to exhibit greater gas-to-dust ratios than 'in plane' sightlines to correspond with the Galactic trend (Burstein & Heiles 1978). The magnitude of these effects is uncertain, but to explain qualitatively the 4 : 1 difference in the LMC : Galaxy gas-to-dust ratio, there appears to be no need to invoke a reduced reddening efficiency of the LMC dust relative to the Galaxy as suggested by Koornneef (1984).

3.7.2 Metallicity

Even with a lower abundance of metals available for producing DIB carriers and dust grains, assuming all other effects to be equal, the relationship between DIB strengths

and E_{B-V} should remain the same as in the Galaxy (see above discussion about gas-to-dust). However, the metallicity of the ISM has broader consequences than simply altering the abundances of the atomic constituents available for dust and molecule formation. Reduced molecular and dust fractions reduce the ability of the ISM to shield itself from impinging UV radiation (see for example Israel 1997), such that only the denser clumps of gas and dust are shielded to the extent common in the Galaxy. Although the majority of DIB strengths are not significantly weakened with respect to E_{B-V} towards Sk −69°223 and Sk −69°243, this cannot be said of Sk −67°2 and Sk −68°135. Thus, although the sample of sightlines in this study is small, it seems that the effects of metallicity are manifested for half of the sightlines observed. The inference is that the reduced ability of clumps in the LMC to self-shield, and the increased dissipation/destruction rate of molecular gas clouds by UV photodissociation and heating, have a detrimental effect on DIB carrier abundances in certain sightlines. Towards Sk −69°223 and Sk −69°243 it is likely that the combination of high UV from 30 Dor and a high abundance of gas and dust left over from the huge molecular cloud from which the many massive stars around 30 Dor formed provides a site conducive to the formation and maintenance of high DIB carrier abundances. The destruction of environments favourable for DIB-carriers through erosion of clouds by UV radiation is a plausible hypothesis to explain the weakness of the DIBs towards Sk −67°2 and Sk −68°135.

3.7.3 UV field strength

Classification of LMC sightlines into ζ, σ and Orion families seems to apply to the LMC as well as the Galaxy, and the fact that three of the four main DIB-containing sightlines seem to be of σ type supports the idea that UV field strength is critical in the division of clouds between these two types, given the high UV radiation strengths in the LMC. The notable exception, Sk −68°135 is believed to be a sightline containing very dense material left over from star formation and hence contains clouds of the better shielded, ζ type where high abundances of molecules are found and the abundances of DIB carriers from the KW II family, such as λ6284, are low.

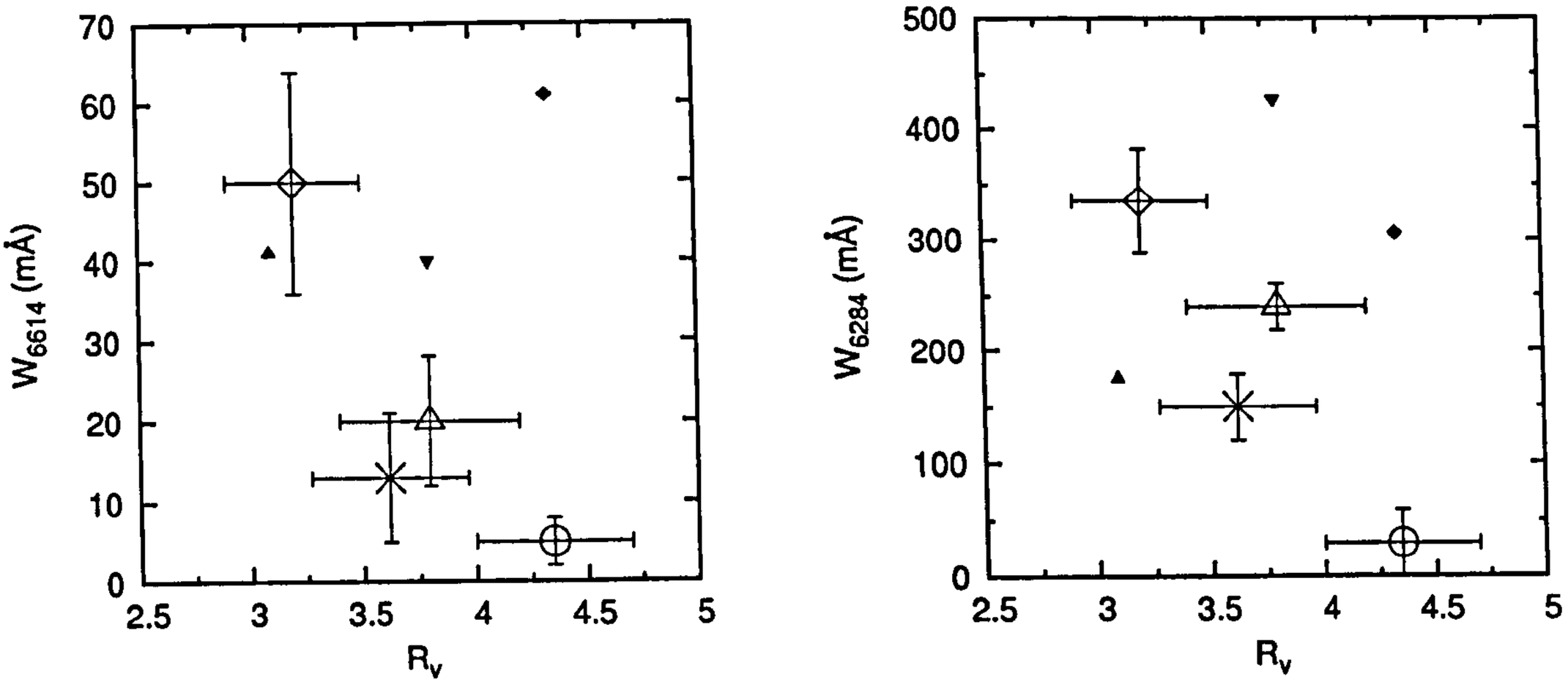

Figure 3.30: The equivalent widths of the λ6284 and λ6614 DIBs plotted against R_V for the four most heavily-reddened LMC sightlines. ζ Oph, σ Sco and ρ Oph A are shown for reference to Galactic observations with R_V values from Cardelli *et al.* (1989) and Snow & Krełowski (1994). Data point styles are as in Figures 3.22 to 3.28.

3.7.4 UV extinction

Past Galactic studies have failed to find significant, convincing links between the parameters of the extinction curve and the strengths of the diffuse interstellar bands (Desért *et al.* 1995). The difference in R_V between σ Sco and ζ Oph (Snow & Krełowski 1994) may be circumstantial, and have little bearing on the factors involved in DIB chemistry. Strengths of the λ6284 and λ6614 DIBs are plotted against R_V in Figure 3.30 with data points from selected Galactic sightlines for reference. The LMC, with its anomalous extinction curves and, for the sightlines probed in this study, higher than Galactic-average R_V values, has presented an environment ideal for probing this relationship, but no significant correlations have been found, in part due to the limited number of sightlines probed.

One plausible idea is that the general weakness of the DIBs can be linked with reduced 2175 Å bump strength of the LMC sightlines. Difficulties in accurately determining R_V, and the lack of reliable published extinction curves for the studied sightlines makes this an important area for further study.

3.8 Key findings of Chapter 3

- Evidence that the same diffuse interstellar band spectrum is present in the ISM of the Large Magellanic Cloud as in the Milky Way has been presented, as evidenced by the positive identification of 11 DIBs: λ4430, λ5705, λ5780, λ5797, λ5850, λ6196 λ6203, λ6284, λ6376, λ6379 and λ6614. The observation of λ5705, λ5850, λ6196 and λ6203 constitute the first reported detections of these DIBs in the LMC, and for λ5850, in any location outside of the Galaxy. Given the signal-to-noise of the spectra, and based on the known relationship between DIB strength and E_{B-V} in the Galaxy, all of the expected DIBs were observed towards the 30 Dor targets Sk −69°223 and Sk −69°243, showing that the ISM of the LMC is favourable as a site for DIB carrier formation. This suggests that the chemistry from which the carriers arise is likely to operate in other regions of the cosmos. As such, it is likely that DIBs can be expected as a general feature of the ISM in other Galaxies.

- Evidence for a redshift in the velocity of λ6614 relative to the other DIBs towards Sk −68°135, Sk −69°223 and Sk −69°243 is suggestive that either (a) the λ6614 carriers are preferentially located in different clouds to the λ5780, λ5797, λ5850, λ6196 and λ6379 DIBs, that happen to be at a systematically red-shifted velocity in the sightlines studied; or (b) the pattern of sub-structure exhibited by this DIB is systematically shifted towards the red in the sightlines studied. If a change in sub-structure is the cause of the redshift, then the typical LMC λ6614 profile must be unusual compared to the typical Galactic profile, perhaps as a result of the low dust-to-gas ratio and metallicity of the ISM of the LMC. The 'redshifting' of the λ6614 profile could also result from a change in the level internal excitation of the carrier in the LMC. The mechanisms that cause the λ6614 sub-structure variations are not understood, but present an interesting area for further research.

- Of the DIBs measured, most of the carriers are associated in velocity-space with the location of the peak Na I (and K I) column densities. The derived DIB carrier least-squares velocities match the velocity of the dominant Na I peak in each sightline to within the error bars, indicating a close association of the DIB carriers with high column density, cool clouds of predominantly neutral atomic (and

molecular) hydrogen. Due to the correlation between the $N_v(v)$ profiles of the different atomic species, the DIB velocities are also closely associated with the Ca II, Ti II and H I peaks (particularly λ6614). Towards Sk −69°243 the derived DIB velocities are not coincident with the velocities of the primary CO peaks observed by Poglitsch *et al.* (1995).

- The LMC DIBs are weak with respect to reddening and neutral potassium column density towards Sk −67°2 and Sk −68°135 compared to the Galaxy. This is attributable to reduced shielding of interstellar clouds due to the lower metallicity of the ISM, combined with the very high UV fields of the LMC, resulting in the destruction of DIB carriers and the environments favourable for their existence. DIBs observed towards Sk −69°223 and Sk −69°243 have strengths approximately equal to, or very slightly weaker than, those in extreme Galactic σ-type sightlines with similar reddening and neutral potassium column densities. The sightline towards Sk −67°2 also appears to represent σ-type conditions. The high UV flux in these LMC environments adds to the body of evidence that the ISM in σ-type sightlines is subject to a high UV field strength that modifies the diffuse band strengths in a predictable way. The strength of λ6614 is about a factor of two lower than the Galactic average in most of the LMC targets, and is similar to the strength of this DIB observed in the Orion Nebula where UV flux is high. Except for the anomalous (probably strongly irradiated, post-star-formation) cloud towards Sk −68°135, the strength of λ6284 is similar, if slightly weaker, towards the LMC targets as compared with the Galaxy, strengthening the hypothesis that this DIB carrier is more abundant where UV irradiation is strong. This suggests a cationic λ6284 carrier, or a carrier formed by UV-stimulated chemistry.

- The pattern of variation of DIB equivalent widths fits with classification schemes previously identified for the Galaxy (see Chapter 1, Section 1.2.1); the λ5780, λ6196 and λ6284 DIB strengths are correlated, as are λ5797, λ6379 and λ6614, but there is only a relatively weak correlation between the two sets. Thus the ζ/σ cloud classification is upheld in the LMC. The anomalous detection of λ6203 without detection of λ6284 towards Sk −67°5 is the only exception, providing evidence that the pattern of DIB strength ratios in the LMC may not always be identical to those observed in the Galaxy.

- Relative to N(H I) the DIBs observed in the LMC (represented in this case by λ6284) are approximately a factor of two to five weaker than in the Galaxy, reflecting the lower metallicities (~ 50% Galactic) and dust-to-gas ratios (~ 20 – 25% Galactic) of the LMC sightlines, showing a likely link between these factors and the rate of DIB carrier production relative to N(H I). The DIB carrier abundances are more closely linked with E_{B-V}, and hence dust chemistry.

- Variation of the Ca II/Ti II ratio over at least an order of magnitude in the LMC ISM is taken as evidence for significant variations in the Ca II/Ca III ionisation balance.

- Depletion of titanium from the gas-phase is relatively low in the LMC sightlines studied: approximately the level generally seen in the warm, shocked interstellar medium in the Galaxy. This indicates that the DIBs either form in a relatively smaller population of cooler, denser clouds in the LMC, or that DIB carriers reside in the warmer, less depleted medium in high abundances.

- Towards the 30 Dor targets Sk −69°223 and Sk −69°243, integrated Ca II/Na I ratios are larger than average for high-latitude Galactic diffuse sightlines by a factor of 2 to 3. Given the reduced Ca II/Ti II and Na I/H I ratios in these sightlines, the pervading UV radiation field appears to be very strong, causing rapid ionisation of Na I. Coupled with the low depletion of the gas that indicates shocked material in these sightlines, and the fact that the DIBs are about as strong with respect to E_{B-V} as in the Galaxy, DIB carrier formation must be rapid in regions located within the highly energetic, strongly irradiated conditions of the ISM in the 30 Dor Nebula.

- The low column density clouds identified in Ca II absorption around 30 Dor by many authors and confirmed by this study, moving towards us relative to the rest frame of the LMC by ~ 50 km s^{-1}, are often explained as resulting from expanding shells of gas and dust blown away from 30 Dor by the intense radiation fields and stellar winds emanating from the high density of massive stars located in the nebula. The abundant presence of these Ca II components towards the field star Sk −70°120 off the Eastern edge of the LMC far (~ 1 kpc) from 30 Dor, suggests an origin for these clouds either in the primordial gas that formed the LMC, or as gas ejected from the LMC in a past close-encounter with

the SMC. The low Ti depletion and high Ca II/Na I ratio of this gas indicates a very low dust content.

Chapter 4

Diffuse interstellar bands and the small-scale structure of the ISM

4.1 Introduction to Chapter 4

The distribution of interstellar gas and dust in the Milky Way is far from uniform. Early evidence for this was presented by Adams (1943b) in observations of the multiplicity of Ca II H and K lines towards 40 out of 50 stars observed. Interstellar gas was found to be concentrated in discrete clouds separated in their mean velocities, with narrow internal velocity distributions. A Gaussian distribution of atomic velocities within such clouds has been identified by countless studies since, using spectra recorded at resolutions $\lesssim 1$ km s^{-1}, which is sufficient to resolve the intrinsic absorption line profiles (*e.g.* Sembach *et al.* 1993; Welty *et al.* 1994; Welty & Hobbs 2001; Price *et al.* 2001). The discontinuous, clumpy structure of the ISM was hinted at by observations of ubiquitous spatial variation in the extinction towards stars and nebulae (see for example Kaplan & Pikelner 1970). Interstellar extinction was found to vary significantly over spatial scales of less than 10,000 AU by Lodén (1973), with the implication that the clouds responsible must contain structure approximately this size or smaller.

According to the review by Dickey & Lockman (1990), H I gas is contained in structures with sizes ranging from ~ 1 kpc (~ 10^8 AU) to ~ 10 AU, the lower limit imposed by the current maximum angular resolution of VLBI instruments (~ 0.1″). Supershells constitute the largest Galactic H I structures, created by the sweeping up of gas in su-

pernova shockwaves. About three quarters of the total interstellar H I is contained in large structures of various forms. These include shells, sheets and filaments as observed by Heiles (1967), who also identified a profusion of approximately solar mass 'cloudlets' with diameters of a few parsecs, embedded within the large structures.

Unequivocal evidence for small-scale structure (SSS) of the ISM has been collected over the last 30 years, beginning with the VLBI study of H I absorption towards the spatially extended extragalactic continuum source 3C 147[1] by Dieter *et al.* (1976). H I optical depth variations were observed to the 0.1″ limit of angular resolution, implying a spatial variation in H I column density over less than 70 AU perpendicular to the sightline. This result was confirmed by Diamond *et al.* (1989) who observed 3C 147 and two additional sources 3C 138 and 3C 380. Small-scale structure was observed towards each, and the H I opacity variations were explained by the presence of clouds around 25 AU in diameter and with densities $n_{\rm H} \sim 10^4 - 10^5$ cm^{-3}. Further quasar observations have since been carried out by Greisen & Liszt (1986), Davis *et al.* (1996) and Faison *et al.* (1998) who all identified variations in H I column density over spatial scales of about 10 AU, with the conclusion that small-scale structure is a widespread feature of the cold neutral medium of the Galaxy.

Towards pulsars with high proper motion, temporal variability in H I opacities has been observed by Frail *et al.* (1994). H I optical depths were between 0.1 and 2.5, and significant variations in optical depth were measured for all seven of the pulsars observed, indicating SSS on scales of 5 to 100 AU. These results have been questioned by Johnston *et al.* (2003) and Stanimirović *et al.* (2003) however, who failed to find such convincing opacity variations in most of the pulsars they observed.

'Extreme radio scattering events' observed by Fiedler *et al.* (1987) and Romani *et al.* (1987) have led to the interesting suggestion by Pfenniger *et al.* (1994) and by Pfenniger & Combes (1994) that cold ($T \sim 3$ K), dense ($n \sim 10^9$ cm^{-3}) molecular 'clumpuscules' about 30 AU across may constitute a mass of previously undetected material in spiral galaxies. They hypothesise that enough clumpuscules could exist to explain the missing mass required by flat galactic rotation curves, which are generally believed to be caused by some form of dark matter. Extreme scattering events manifest themselves as dramatic changes in radio flux of distant quasars over periods of weeks to months, and are interpreted as being due to the refraction of radiation in its passage

[1] A quasar with redshift $\Delta\lambda/\lambda \approx 0.5$.

through dense clouds of free electrons in the Galactic ISM. In the model by Walker & Wardle (1998), the electrons reside in an 'ionised skin' at the periphery of the dense, self-gravitating molecular clumps.

Direct observations of small-scale structure in molecular interstellar gas have been made in radio absorption studies of H_2CO (Marscher *et al.* 1993) and HCO^+ (Lucas & Liszt 2000) towards compact background sources moving transverse to the line of sight. Lucas & Liszt argue that from molecular emission constraints it is not possible for the observed structures to be caused by very small, high n_H inclusions in the gas, and that small-scale variations in the chemistry are instead responsible for raising the HCO^+ abundance in localised areas of the ISM.

Dense molecular condensations 27 – 230 AU across have been observed in 2 cm emission by Churchwell *et al.* (1987) using the VLA, embedded in ionised envelopes in the Trapezium and Orion KL regions. Number densities were estimated to be $\sim 10^6$ cm^{-3}. These molecular condensations may represent the contracting phase of pre-stellar objects.

In further studies, compact ($\sim$ 40 AU), dense ($n \sim 10^3$ cm^{-3}) molecular gas filaments have been invoked to explain the abundances of H_2 observed using FUSE along relatively diffuse sightlines in the Galaxy (Richter *et al.* 2003) and the LMC (André *et al.* 2004). Also, models of the molecular chemistry including H_3^+ and HCO^+ towards the Cygnus OB2 association (Scappini *et al.* 2002; McCall *et al.* 2002b) require the presence of compact clumps of gas with $n \sim 10^4$ cm^{-3} embedded in the surrounding diffuse medium (where $n \sim 10$ cm^{-3}), highlighting the likely importance of small-scale structure in successfully modelling gas-phase molecular chemistry in the diffuse ISM.

Recently, an explosion of studies focusing on the variability of optical and UV absorption lines towards binary/multiple star systems, globular clusters and 'runaway' stars (with high proper motion) has occurred. The first study of this type (by Münch & Unsöld 1962) identified a cloud of Ca II with an upper size limit of about 1 pc ($\sim$ 200,000 AU) diameter in the direction of α Oph, the size of which was constrained by the cloud's absence from the spectra of the nearby stars in the surrounding field. The spatial extent of small interstellar structures may be constrained by probing the clouds on smaller spatial scales. Meyer (1990) studied the Mg II and Mn II UV lines towards several binary systems and found $\approx$ 50% difference in the line strengths between the two components of κ CrA. At a distance of 120 pc, the 23″ separation of this binary

proved the existence of SSS over a scale of $\lesssim$ 2800 AU. The ubiquitous presence of SSS was confirmed by Watson & Meyer (1996), when all of the 17 binary/multiple star systems they observed showed variations in the interstellar Na D_1 absorption line profiles between the closely separated component stars. The inferred SSS size ranged from $\lesssim$ 480 AU for the pair ρ Oph AB to $\lesssim$ 29,000 AU for two components of the triple system HD 206267. Followed up by K I λ7699 observations for five of the systems, significant SSS was found in three cases (not in the other two, probably due to insufficient S/N and the relative weakness of K I lines), with an additional result that SSS was found to occur in clouds spanning a very wide range of column densities.

Another spectacular example of SSS can be seen towards the two stars of the binary system μ Cru, separated by about 6600 AU and observed in Na I D_1 and Ca II K at ultra-high resolution by Meyer & Blades (1996). Two distinct interstellar Na I components show strong variation between the two sightlines: a component at a heliocentric radial velocity $v_{\rm HEL} = -8.6$ km s^{-1} with N(Na I) = 7.0×10^{10} cm^{-2} towards μ^1 Cru is not present towards μ^2 Cru, and a component at $v_{\rm HEL} = 5$ km s^{-1} with N(Na I) = 6.8×10^{10} cm^{-2} towards μ^1 Cru is approximately four times as strong towards μ^2 Cru. Overall, there is about 50% more Na I towards μ^2 Cru than μ^1 Cru. The difference is less pronounced in Ca II, with only $\simeq$ 10% difference in the total column density. In a further study by Lauroesch *et al.* (1998), the interstellar Zn II profiles were found to be indistinguishable between the two μ Cru sightlines. Given that Zn II correlates well with H I it was therefore deduced that the H I column density is equal between the two sightlines and that the observed Na I differences were probably due to variations in the sodium ionisation balance rather than a density effect of the type observed in H I VLBI absorption studies. Based on the proper motion of the binary, a lower limit to the SSS scale-size of $\sim$ 10 AU was inferred from the invariance of the Na I profile over 21 months between subsequent observations of μ Cru.

If the velocity of interstellar matter perpendicular to our sightline is negligible compared to the proper motion p of the background star, then in a time t, the sightline moves across the cloud by an angle pt radians. The physical length of interstellar cloud covered by the sightline in this time must be less than dpt, where d is the distance to the star, because the cloud lies at an (often unknown) distance between zero and d. The effects of tangential motion of the gas are only significant for very nearby clouds (closer than about 100 pc), with tangential velocities greater than 50 km s^{-1}, such that

in most cases of SSS probed by runaway stars the stellar proper motion dominates the relative movement of the sightline across the cloud.

During the period from June 1994 to March 2002 the line of sight towards the bright nearby B2 IV star κ Velorum was monitored by Crawford *et al.* (2000) (see also Crawford 2002). At a distance of 165 pc, the proper motion of 15.5 mas yr^{-1} produced a movement of the sightline across the cloud of $\lesssim$ 20 AU over the eight-year observation period. During the first 69 months, the K I column density increased by $\simeq$ 40% from 1.62×10^{10} cm^{-2} to 2.29×10^{10} cm^{-2}, accompanied by $\simeq$ 15% increase in the Na I column density. The reduction in the Na I/K I ratio was taken as evidence that the structure passing through the sightline is cold and dense compared to the surrounding medium, belonging to the class of elongated, dense filaments ($\sim$ 30 AU diameter, $n \sim 10^4$ cm^{-3} with a temperature of $\sim$ 15 K) discussed by Heiles (1997). Over the following 24 months, the K I column density increased by a further 10%, consistent with a uniform rate of increase of 1.2×10^9 cm^{-2} yr^{-1} over the entire observation period; no significant variations in Ca II abundance were recorded. Simple chemical modelling of the Ca I/Ca II ratio and the observed CH^+ abundance in the time-variable cloud allowed calculation of the approximate depth (100 $\sim$ 1000 AU), and H I number density ($\gtrsim 10^3$ cm^{-3}) of the cloud along the line of sight. The inferred geometry matches that of Heiles' (1997) dense, elongated H I filaments.

Although significant quantities of molecular material such as CO are not typically associated with H I small-scale structures (Heiles 1997), recent detailed studies by Pan *et al.* (2004) (single epoch, towards members of multiple stellar systems in star-forming regions) and Rollinde *et al.* (2003) (multiple epoch, towards the runaway star HD 34078) have proved the existence of SSS in CN, CH and CH^+ gas distributions. Rollinde *et al.* found substantial structure in CH on a scale of $\sim$ 100 AU. Interpreted as due to a $\sim$ 100 AU diameter cloud, the inferred cloud density is $\sim 1.5 \times 10^5$ cm^{-3}, which could explain the relatively small amount of CH^+ variation because CH^+ reacts quickly with H_2 at this density, removing it from the cloud.

Using runaway stars allows the probing of SSS on the shortest distance scales; Lauroesch *et al.* (2000) observed the stars HD 32039/40 over 4.25 years and measured variations in N(Na I) with a size of approximately 15 to 21 AU. C I fine structure excitation analysis suggested a total number density of the order of 20 to 200 cm^{-3} for the variable cloud, which is significantly lower than that usually inferred for SSS in H I.

The Na I and Ca II column densities in a component of the gas towards HD 219188 were seen to increase by a factor of 2 to 3 by Welty & Fitzpatrick (2001) over 3 years, indicating structure on a scale of ~ 50 AU. The density of the cloud was deduced as $n_H \sim 25$ cm^{-3}, which is, again not dissimilar to the typical diffuse ISM and far less than the $n_H \sim 10^5$ cm^{-3} densities typically found in H I SSS. A ~ 12 AU structure was observed in Na I over 8 years by Lauroesch & Meyer (2003) towards ρ Leo. Again, C I excitation analysis suggested that the variable component had a remarkably low density of $\lesssim 20$ cm^{-3}; significant changes in the interstellar Ca II absorption profile were not observed. Lauroesch & Meyer (2003) suggested that the the density-dependence of the Na I ionisation equilibrium was responsible for the observed Na I spatial variability. Atomic recombination rates are dependent on electron density (see Equation (1.5), Section 1.1.2) such that small variations in number density may significantly alter the sodium ionisation balance. Following the reasoning of Lauroesch & Meyer (1999), for a neutral ideal gas in pressure equilibrium, with a constant electron abundance relative to n_H, the Na I (and K I) electron recombination rate is proportional to $n_H^{1.7}$. An associated implication is that species with lower ionisation rates such as Ca II should be able to travel further from denser regions before being ionised, resulting in an ionisation-rate dependent scale-size for SSS of a given species that is sufficient to explain the lack of observed Ca II variability (Lauroesch & Meyer 2003).

C I excitation analysis (Lauroesch *et al.* 2000; Lauroesch & Meyer 2003) has provided evidence that the total particle number density in the clouds responsible for small-scale structure observed by Na I absorption in the diffuse ISM, can be several orders of magnitude less than the number densities derived in H I absorption studies (reviewed by Heiles 1997). A possible interpretation is that the small-scale spatial variation observed in Na I (and in other species with ionisation potentials below 13.6 eV) occurs in the outer edges of denser, higher pressure clumps of interstellar matter, or perhaps in the dissipating remnants of expanding transient molecular clumps (Bell *et al.* 2005). A spatial gradient in the photoionisation rate would be expected across such regions, providing a mechanism capable of producing small-scale variations in ionisation equilibrium. With reference to the 'skin effect' (see below), DIB carriers are hypothesised to exist in greatest abundances in the outer layers of denser clouds. With proposed ionisation potentials < 13.6 eV (see for example Sonnentrucker *et al.* 1999b), the carriers might be expected to be subject to similar small-scale, ionisation-dependent variations as those observed in Na I and Ca II.

With regard to studies of the diffuse interstellar bands, it is a plausible hypothesis that the presence of SSS may be fundamental to the processes that maintain the DIB carrier abundances. The 'skin effect' (documented by Herbig (1995), Cami *et al.* (1997) and Snow (2002) for example) apparently causes variations in DIB strengths due to variations in the ambient UV field with distance into a cloud, and supposes that the DIB carriers are most abundant in a skin around the periphery of the cloud where UV photons aid their formation and/or excitation[2]. At the cloud edge, the DIB carriers are exposed to the full interstellar UV flux, but become increasingly well shielded towards the cloud centre where they may recombine or react to form different species. Clearly, the amount of cloud 'skin' in a given sightline is determined by the geometry and number of intervening interstellar clouds. If the skin effect is real then ubiquitous SSS should affect DIB strengths by providing regions in which the gas density gradient passes from the dense to the diffuse regime over a short distance. If the DIB carriers reside preferentially at a specific cloud density (at a certain distance from a SSS cloud 'core'), then the number of SSS clumps in a given sightline should be correlated with the strength of the DIBs. The thickness of the skin and the size of the SSS core would also be important in determining the size of the environment most favourable for the DIB carriers, and hence in determining DIB strengths. Identification of the nature of the relationship between DIB-carrier abundance and the radial distance of a sightline from the centre of a SSS clump will provide a useful probe of the nature of the poorly understood skin effect.

Little is known about the precise relationship between DIB carrier abundances and the gas density or pervading UV field strength. The studies by Krełowski & Walker (1987), Cami *et al.* (1997), Krełowski *et al.* (1998), Sonnentrucker *et al.* (1997) and Weselak *et al.* (2004) provide interesting evidence that the carriers of the narrow DIBs including λ5797 and λ6379 (of the family KW III) favour environments where UV fields are low, recombination rates are high, and diatomic molecules exist in abundance whereas the broader DIBs λ6284 and λ5780 (of the family KW II) are preferentially located in a medium exposed to stronger UV flux, where the ratio of ionisation to recombination rates is greater and fewer diatomic molecules exist. One of the aims of this study is to determine whether such effects are observable over very small spatial scales.

Reports of attempts to observe SSS in the DIB-carrier distribution are scarce or undoc-

[2]DIB carriers may be cations or electronically excited large molecules.

umented, but DIB carriers, with a preference to reside in diffuse, UV-irradiated clouds may provide a valuable probe of the nature of SSS. For example, Rollinde *et al.* (2003) observed a lack of variation in the λ5780 and λ5797 DIBs that was attributed to the density in the 'SSS cloud' being too high to allow the existence of significant numbers of DIB carriers. However, no definitive data on the density of the SSS cloud was available to test this hypothesis.

The single example of SSS in DIBs recorded in the literature is in the survey by Herbig (1975). Towards the binary ρ Oph AB (separation $\approx$ 375 AU), the equivalent widths of the λ5780 and λ5797 bands were measured and both were apparently stronger towards ρ Oph B by around 30%. However, the accuracy of these equivalent width measurements (obtained from photographic spectra) may be insufficient to permit these results as a reliable detection of SSS (Herbig, private communication). Other DIBs recorded towards ρ Oph AB did not display such variation. In the studies reported in this chapter, using modern solid-state detectors, the differences found are much smaller, of the order of 5%.

The exact nature of the gas responsible for small-scale structure in the ISM is still poorly understood. Although successful models have been constructed, important parameters such as density and temperature are poorly constrained by present observations. The naïve interpretation of SSS in Na I and K I as being due to small, high density, approximately spherical clouds does not fit with all of the observational evidence (Heiles 1997). Small-scale H I structures appear to be ubiquitous, and may be explained by a filamentary geometry, elongated in one direction (Heiles 1997). It is apparent that these high-density structures are not required to explain much of the SSS observed in optical absorption line studies, and indeed, cannot explain the HCO^+ SSS observed by Lucas & Liszt (2000). Small-scale variations in chemical equilibrium, with the possible addition of transient microstructures and a fractal geometry of gas cloud structures seem to be a necessary component of the ISM.

This study aims to search for the first definitive evidence of small-scale structure in the distribution of diffuse interstellar band carriers. Given that the DIBs represent one or more distinct classes of large molecules or small dust grains, an important question to answer is whether the DIB carrier distribution contains small-scale structure, and if so, what are its characteristics? It will be fascinating to examine the relationship of DIB strengths with the properties of SSS already observed, and to determine whether the

known correlations between the different DIBs and the trace neutral species (Na I, K I) are upheld over the very small spatial scales probed by SSS studies.

A problem that hinders DIB correlation studies and prevents the accurate analysis of DIB strengths with respect to particular interstellar variables is that between different Galactic sightlines (widely distributed throughout the local ISM), the interstellar conditions probed are liable to have differences in many different physical and chemical parameters. Over the very short spatial scales of SSS, turbulent and kinetic mixing of the interstellar gas should be thorough such that chemical abundances and elemental depletions are almost identical. If the specific properties of the SSS for a given sightline could be established, then their effects on the DIB spectrum could be directly assessed. The main aim of this programme was to study the strengths of DIBs towards a selection of sightlines that contain SSS that has already been studied. For less well characterised sightlines, the DIBs may provide a useful probe of the nature of the gas in small structures, based on knowledge of the environments in which DIBs arise. A search for 'new' SSS sightlines was also carried out, using the interstellar Na D lines, K I λ7699 line and a selection of the stronger diffuse interstellar bands.

4.2 Observations

To search for SSS in DIBs requires sightlines towards bright, early-type stars. Magnitudes of $\lesssim 6$ are desirable to achieve very high S/N ($\gtrsim 1000$) at high dispersion in feasible exposure times. For SSS observations of DIBs towards binary systems (to a lesser extent for narrow atomic lines), it is desirable that the spectral types of the stars should be closely matched so that their intrinsic spectra are as similar as possible, facilitating the identification of differences in interstellar features.

The amount of material in the sightline must be sufficient to produce DIBs that are strong enough that small variations in equivalent width can be readily observed. Targets were selected to achieve a balance between DIB strength, S/N, and amount of atomic column density variation observed in previous studies. The Sco OB2 association, due to its proximity (~ 170 pc), the substantial amount of intervening gas and dust, the plethora of past reports of DIBs, the abundance of bright young stars, and evidence for SSS already observed in atomic and molecular lines (Watson & Meyer 1996; Lauroesch & Meyer 1999; Pan *et al.* 2004), provided several suitable binary/multiple

targets: β Sco, ν Sco and ρ Oph (shown in Figure 1 on page 12) that formed the core of the observing programme.

The binary system μ Cru was chosen due to the brightness of its members and the very large ($\approx$ 50%) difference in Na I column density between the two stars. To probe shorter spatial scales, the time-variable sightline towards κ Vel was also selected. This star was observed at high dispersion to a S/N of $\sim$ 500 by S. J. Fossey in January 1995 (private communication), so that nearly 10 years had elapsed since the earlier observation of DIBs in this sightline, which provides a $\sim$ 25 AU SSS probe length due to the star's proper motion.

Two further binary systems were selected for which no past reports of SSS existed, taken from the Catalogue of the Components of Double and Multiple stars (Dommanget & Nys 1994): HD 150135/6, an O-type binary in the Ara OB1 association, and HD 164863/HD 313693, early B-type stars in the cluster NGC 6531. Details of the observed programme targets are shown in Table 4.1.

For the accurate determination of DIB equivalent widths, accurate continuum definition is vital. The best method of determining the shape of the stellar continuum is to compare with unreddened stars of the same spectral type such that any differences should be due to interstellar features. Stellar features can be easily identified in slowly rotating stars, which is important for assessing possible stellar contamination of DIB profiles. Spectra of bright, unreddened, rapidly rotating standard stars are also required for the removal of telluric features (see Section 2.2.2). Thus a range of standard stars covering the range of spectral types of the programme targets were observed (shown in Table 4.2) with a range of rotational velocities $v \sin i$, and to a S/N comparable with the main programme stars.

The observation programme placed exceptionally high constraints on the quality of the spectra in order to achieve very high S/N, requiring a highly stable spectrograph with efficient CCD response. Observations were carried out from June 5–7 2004 using the University College London Echelle Spectrograph (UCLES) on the 3.9 m Anglo-Australian Telescope, Siding Spring Observatory, Australia. The 31 lines/mm grating was used in conjunction with a 1″ slit width to achieve a resolving power of $\simeq 58,000$[3] on the MITLL3 CCD . Seeing varied from $\simeq$ 0.9″ to 2.2″. The entire wavelength range

[3]Resolution measured from the average FWHM of over 100 emission lines in the Th/Ar wavelength calibration spectra.

Name	HD	RA(2000)	DEC(2000)	Sp. Type	V	E_{B-V}	S/N
β^1 Sco	144217	16 05 26.2	-19 48 19.6	B0.5 V	2.6	0.22	2300
β^2 Sco	144218	16 05 26.6	-19 48 06.7	B2 V	4.9	0.22	2000
ν^1 Sco	145502	16 11 59.7	-19 27 38.5	B2 IV	4.4	0.29	1300
ν^3 Sco	145501	16 11 58.6	-19 27 00.2	B8/B9 V	6.5	0.19	1000
ρ Oph A	147933	16 25 35.1	-23 26 48.7	B2/B3 V	5.0	0.47[f]	1200
ρ Oph B	147934	16 25 35.1	-23 26 46.0	B2 V	5.9	0.47[f]	1000
ρ Oph C	147932	16 25 35.1	-23 24 18.8	B5 V[a]	7.3	0.47[f]	720
ρ Oph D	147888	16 25 24.3	-23 27 36.8	B3/B4 V	6.8	0.48[f]	850
μ^1 Cru	112092	12 54 35.7	-57 10 39.8	B3 IV[b]	4.0	0.02[g]	2500
μ^2 Cru	112091	12 54 36.9	-57 10 06.6	B5 Ve[b]	5.3	0.06[g]	2300
HD 150135	150135	16 41 20.4	-48 45 46.6	O6.5 IV[c]	5.7	0.47[h]	500
HD 150136	150136	16 41 19.5	-48 45 47.6	O3 + O5[d]	6.9	0.47[h]	700
HD 164863	164863	18 04 12.6	-22 30 03.4	B0[e]	7.3	0.28[i]	300
HD 313693	313693	18 04 11.2	-22 29 42.3	B1[e]	8.8	0.28[i]	220
κ Vel	81188	09 22 06.8	-55 00 38.4	B2 IV[b]	2.5	0.06[g]	2300

Table 4.1: Programme star characteristics grouped by system. RA and DEC and V magnitudes are from Hipparcos data (Perryman & ESA 1997) and spectral types from the Michigan Catalogue of Spectral Types (Houk & Smith-Moore 1988) except those labelled with superscripts: [a] — from Garrison (1967), [b] — from the modal average of the spectral types listed in the SIMBAD database (URL: http://simbad.u-strasbg.fr/), [c] — from Walborn (1972), [d] — from Niemela & Gamen (2005) who determined the spectral types of two binary components of HD 150136, the O3 component being the brighter, [e] — from Forbes (1996); E_{B-V} values were calculated using mean of the values in the SIMBAD database and $B-V$ photometry and the intrinsic colours of Wegner (1994) except those labelled: [f] — from Pan *et al.* (2004), [g] — where $B-V$ is from Hipparcos photometry (Perryman & ESA 1997), [h] — where $B-V$ is from photometry by Maíz-Apellániz *et al.* (2004), [i] — from Forbes (1996). The last column shows the measured S/N per pixel of the reduced spectra at approximately 6000 Å.

Name	HD	RA(2000)	DEC(2000)	Sp. Type	V	$v \sin i$ (km s^{-1})	S/N
α Eri	10144	01 37 42.8	-57 14 12	B5 IV	0.5	–	1100
θ^1 Eri	18622	02 58 15.7	-40 18 17	A3 V	3.2	70[a]	750
α^1 Cru	108248	12 26 35.9	-63 05 56	B0.5 IV	0.8	124[b]	1600
γ Mus	109026	12 32 28.0	-72 07 59	B5 V	3.8	–	2000
α Vir	116658	13 25 11.5	-11 09 41	B1 V	1.0	130[c]	1500
β Lib	135742	15 17 00.4	-09 22 59	B8 V	2.6	250[c]	1200
γ Lup	138690	15 35 08.4	-41 10 00	B3 V	2.7	283[b]	700
υ Sco	158408	17 30 45.8	-37 17 45	B2 IV	2.7	30[d]	1200
λ Sco	158926	17 33 36.4	-37 06 14	B2 IV	1.6	237[b]	1600
α Pav	193924	20 25 38.9	-56 44 06	B3 IV	1.9	24[b]	1300
α Gru	209952	22 08 14.0	-46 57 40	B5 V	1.7	–	1800

Table 4.2: Observed telluric and spectral type standards. RA and DEC and V magnitudes from Hipparcos data (Perryman & ESA 1997), spectral types from modal average of SIMBAD data. Stellar rotational velocities $v \sin i$ (accessed *via* SIMBAD) taken from [a] — Royer *et al.* (2002), [b] — Uesugi & Fukuda (1970), [c] — Abt *et al.* (2002), [d] — Bernacca & Perinotto (1970). The last column shows the measured S/N per pixel of the reduced spectra at around 6000 Å.

from 5000 to 10,000 Å was recorded for all targets over 58 echelle orders. Multiple exposures (15 for the case of β^1 Sco) were required to reach the desired S/N ($\gtrsim$ 1000) and prevent saturation of the CCD which occurs at about 100,000 electrons per pixel. Observations were made with the CCD in 'fast' readout mode (readout noise of 2.9 e/pixel) with a gain of 2.2 e/ADU.

Long flat-field exposures were required (several hours per night), with additional flat-fields taken through a blue filter to offset the enhanced red-sensitivity of the chip. Flat-fields were taken using a quartz lamp at the beginning, middle and end of the night. The flat-fielding accuracy of the CCD (*i.e.* the accuracy with which the varying pixel response rates could be corrected) was not guaranteed for S/N over 1000 with the MITLL3 CCD, so to achieve a S/N of $\gtrsim$ 2000 for κ Vel and μ Cru, two 'dithering' techniques were employed. When the seeing was good enough ($\lesssim$ 1.5″), it was possible to perform subsequent exposures of the same star at two different positions along the ~ 5″ long slit. Thus, the starlight was made to fall on different CCD pixels in the two positions, with the effect of reducing the total electron load experienced by each pixel for a given total exposure length. As seeing degraded past approximately 1.2″, the wings of the seeing function progressed outside of the aperture provided by the slit, resulting in loss of light such that the use of this method was then deemed inefficient. To pro-

vide dithering for stars observed in poor seeing, three different UCLES cross-disperser angles were used, changed between nights with the effect of moving the image of the spectrum on to a different set of CCD pixels. Dithering also ensured that any 'bad' or anomalously behaving pixels could be identified by comparing 'dithered' spectra, providing an internal consistency check of the data. Attempts were made during observations to ensure the same exposure level and dithering characteristics for stars that would later be compared for the presence of DIB strength variability, thus reducing the effects of potential differences in the scattered light produced by the spectrograph optics or any other time-variable optical anomalies. Star systems were observed in 'exposure sets', alternating between members in successive exposures such that any changes in seeing or drifts in the spectrograph optics would affect the spectra of all stars in a set as near to equally as possible, further enhancing the rigour of this study.

Spectra were reduced as described in Chapter 2, with an additional step to correct the MITLL3 CCD counts for a small non-linearity in its quantum efficiency. The non-linearity of a given pixel is well defined and behaves according to $N_m = N_t(1 + \alpha N_t)$, where N_m is the recorded counts, N_t is the 'true' number of counts (that would have been recorded for a truly linear CCD), and α is the non-linearity constant, equal to -0.15×10^{-6} for the MITLL3, obtained from the website of the Anglo-Australian Observatory[4]. The discrepancy between N_m and N_t was at most 1% for a single exposure.

Final reduced, co-added spectra all exhibited Poisson statistics in flat regions of stellar continuum, with S/N $\simeq \sqrt{N_e}$, even for the peak $N_e = 11$ million electrons per pixel obtained toward μ^1 Cru. Typical exposures were ~ 6.5 million electrons per pixel at 6000 Å for μ^1 Cru, but the duplication of several restricted spectral regions (around 5705 Å, 5780 Å, 5890 Å and 6200 Å for example), caused by overlaps in the wavelength coverage of adjacent echelle orders, effectively doubled the counts in these regions. Towards the very edges of the orders, low frequency ripples with amplitudes of up to ~ 10% of the continuum signal were present in the spectra due to blaze-correction artifacts. Such regions were *not* utilised when co-adding the spectra important to the main science goals of this chapter.

[4]URL: http://www.ast.cam.ac.uk/AAO/local/www/cgt/ccdimguide/mitll3.html

4.3 Results: The discovery of small-scale spatial variation in DIB strengths towards multiple star systems

4.3.1 Standard stars

The programme stars range in spectral type from O3 to B9, with the majority being of early B type. The contribution of stellar features to the spectra should therefore be small, although for these spectral types some stellar features are known to exist in the wavelength ranges spanned by some of the DIBs. The presence of strength variation in the relatively broad DIBs can only be determined definitively if there are no stellar features present over its wavelength range, or if stellar lines within a DIB profile are invariant between compared sightlines. For the purposes of stellar feature identification, the spectra of the standard stars are presented in Figures 4.1 to 4.3 for the wavelength ranges of the DIBs concerned by this study. The accompanying ρ Oph A spectra (top traces) indicate the spectral positions of the DIBs.

γ Mus, recorded as a standard for stars with spectral type around B5 shows a plethora of relatively narrow stellar absorption lines across the optical, which is unusual considering its early spectral type. The α Pav spectrum is more typical of a mid-B type, with absorption concentrated in fewer stronger stellar features. Although many of the lines in the γ Mus spectrum are not present in the programme stars of similar spectral type, it is useful as a comparison to indicate the *possible* locations of stellar lines.

4.3.2 β Sco

Residing in the nearby Sco OB2 association, the β Sco binary system exhibits a reddening of $E_{B-V} = 0.22$ for both stars. According to the Hipparcos parallax (Perryman & ESA 1997), the distance to β^1 Sco is 163 ± 3 pc, which combined with the separation between β^1 and β^2 Sco of 13.6″ yields a sky-projected distance between the binary pair of $\approx$ 2200 AU. It is reasonable to assume that the SSS cloud in this sightline (observed by Watson & Meyer 1996; Lauroesch & Meyer 1999) is part of the the dominant concentration of interstellar gas observed towards Sco OB2 that is located at a distance of $\approx$ 145 pc according to Cappa de Nicolau & Poeppel (1986). Using this distance, the length-scale probed by observation of $\beta^{1,2}$ Sco spans a sky-projected distance of

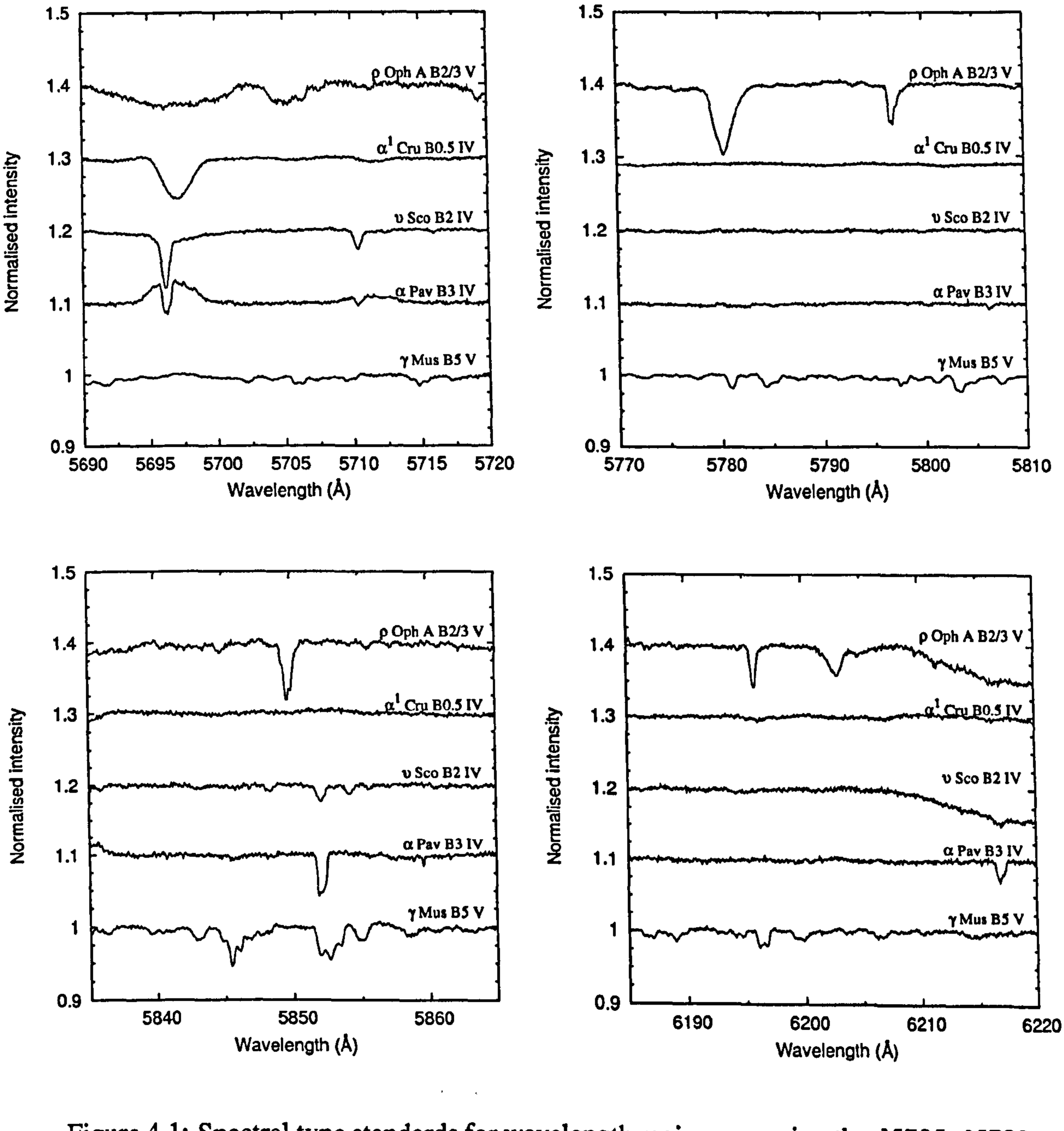

Figure 4.1: Spectral type standards for wavelength regions covering the λ5705, λ5780, λ5797, λ5850, λ6196 and λ6203 DIBs, telluric-corrected, normalised by low-order polynomials and shifted vertically for display. All spectra have been 'scaled up' by a multiplicative factor of two except for those covering λ5780 and λ5797. ρ Oph A spectra (top traces) shown to identify the spectral location of the DIBs.

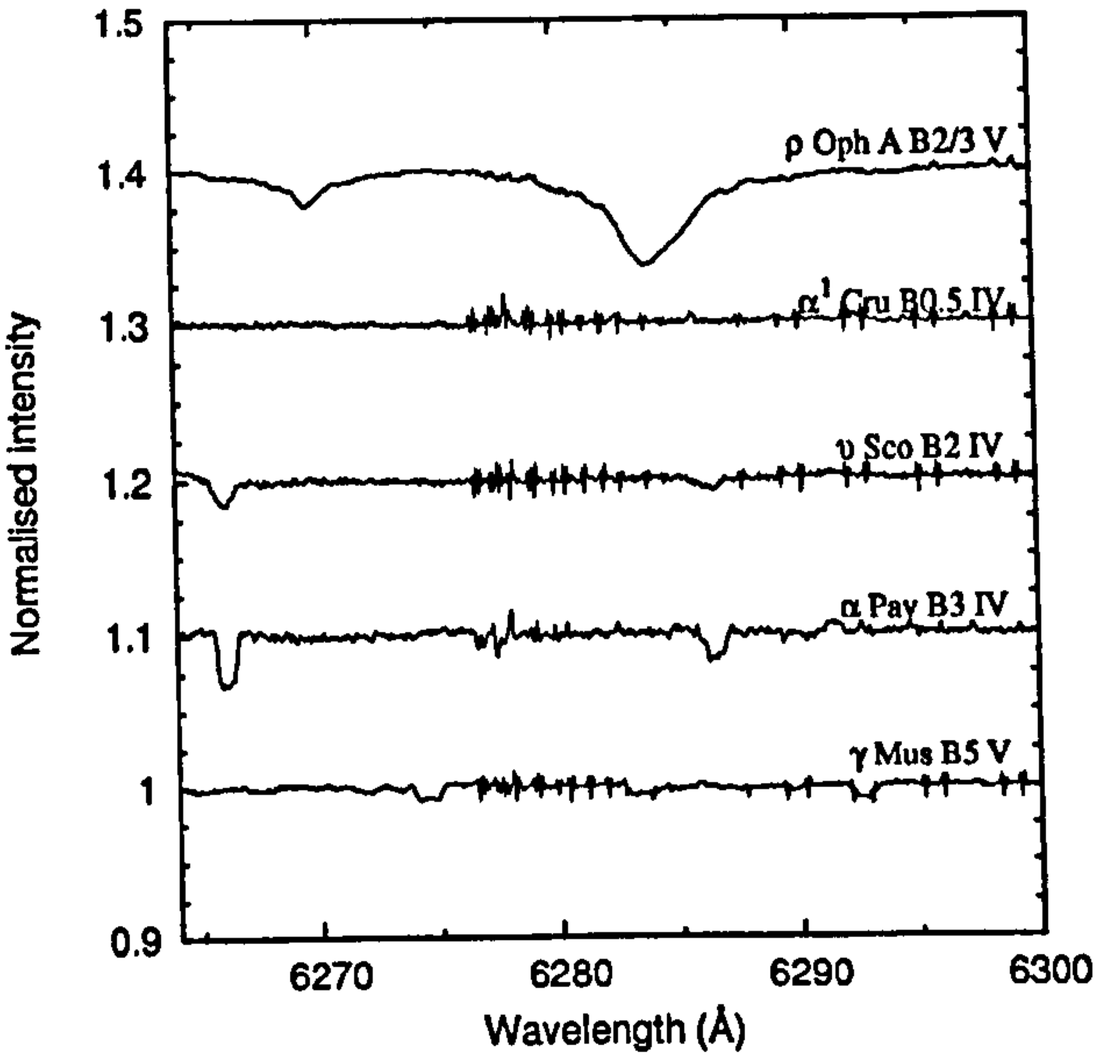

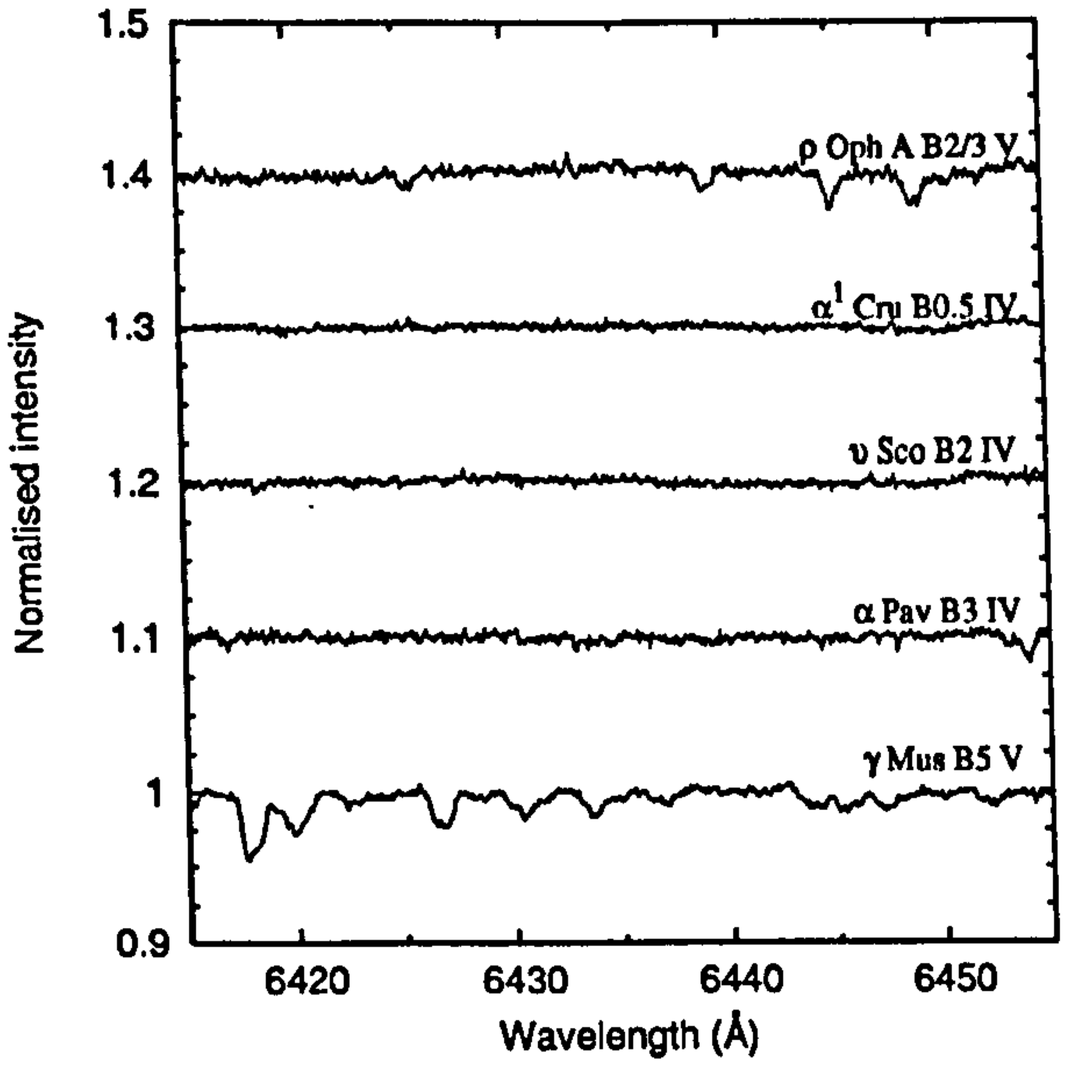

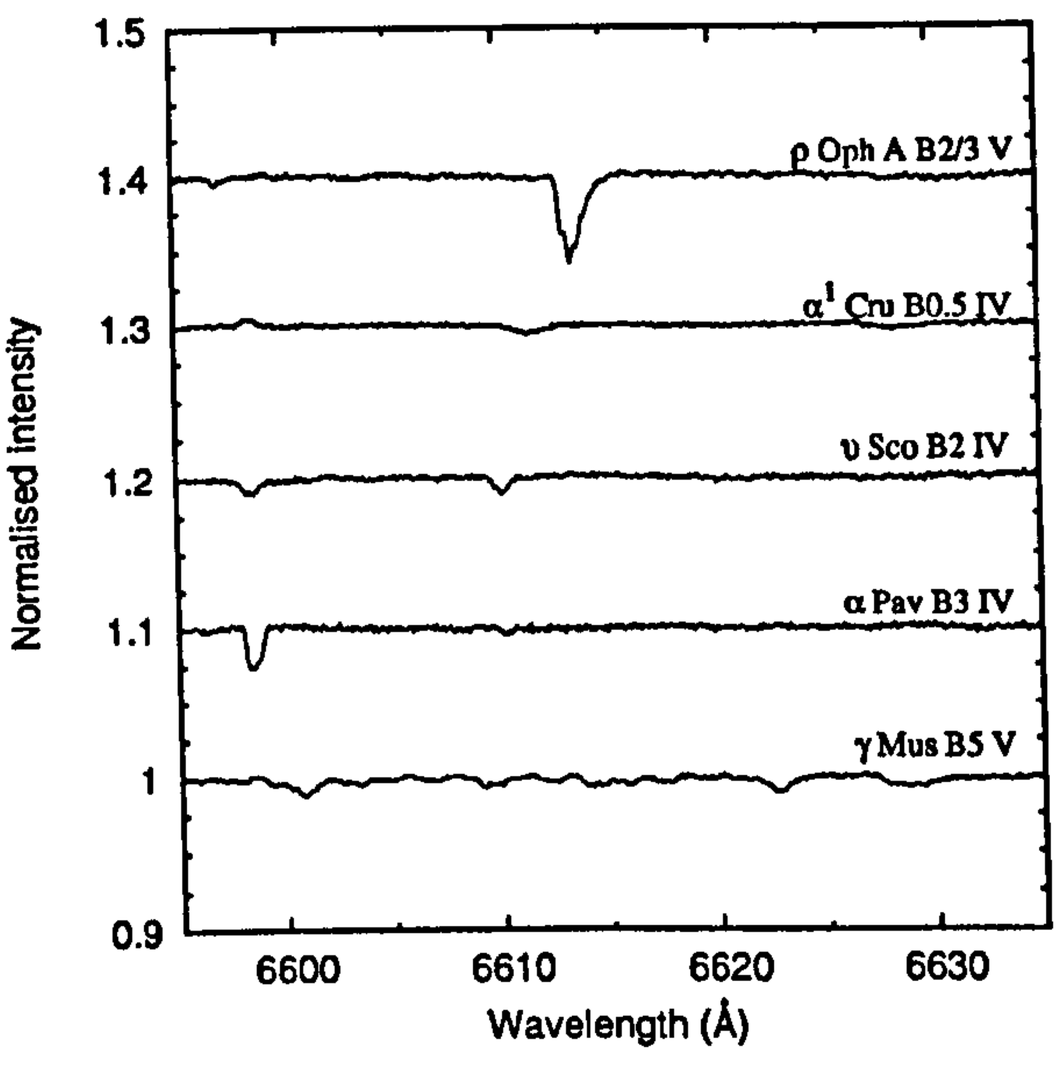

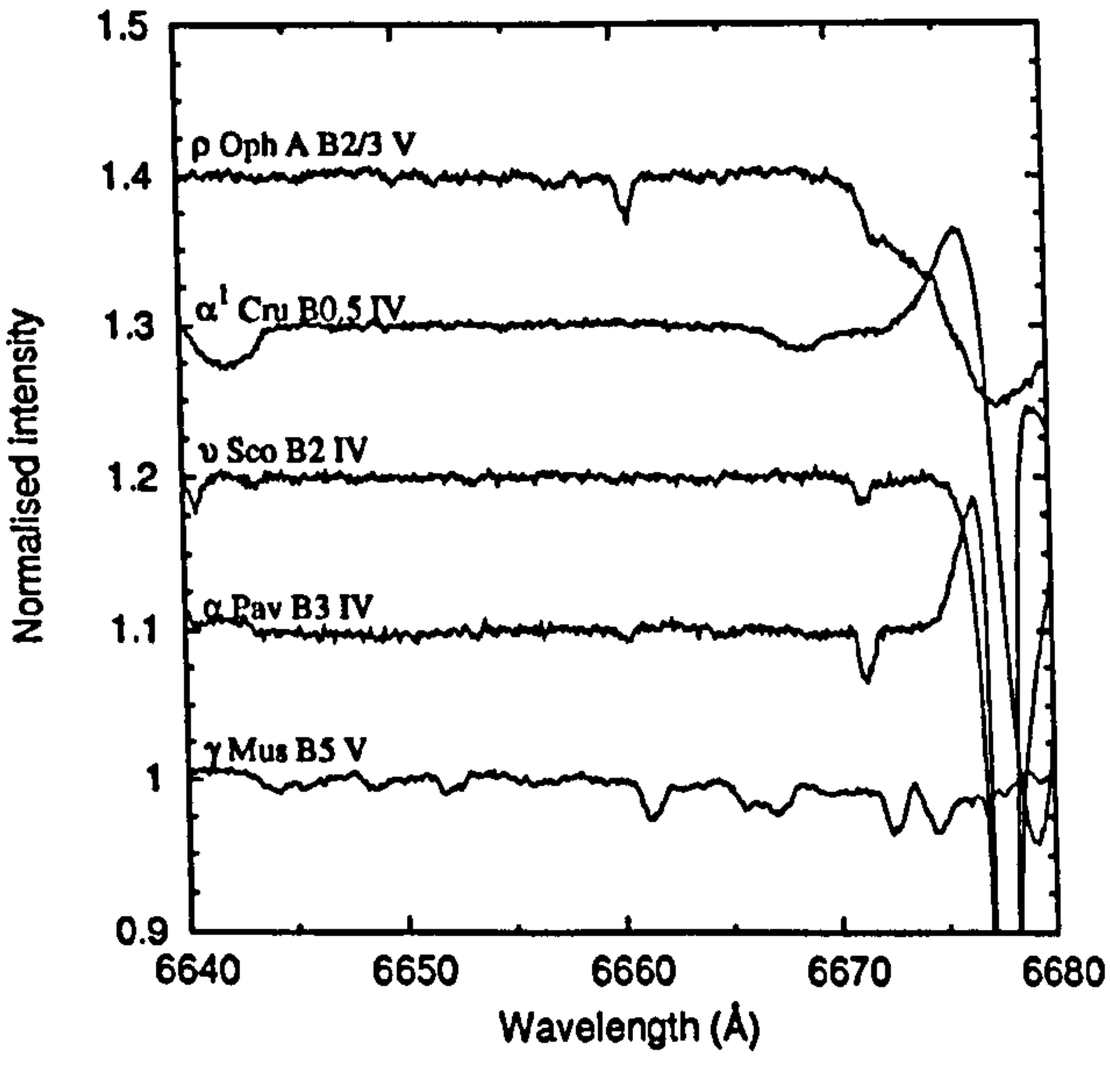

Figure 4.2: Spectral type standards for wavelength regions covering the λ6270, λ6284, λ6426, λ6439, λ6445, λ6614 and λ6660 DIBs, telluric-corrected, normalised by low-order polynomials and shifted vertically for display. All Spectra have been 'scaled up' by a multiplicative factor of two except for those covering the λ6284 and λ6614 regions. ρ Oph A spectra (top traces) shown to identify the spectral location of the DIBs. 'Noise' in the region of λ6284 is due to the incomplete cancellation of strong telluric O_2 absorption lines.

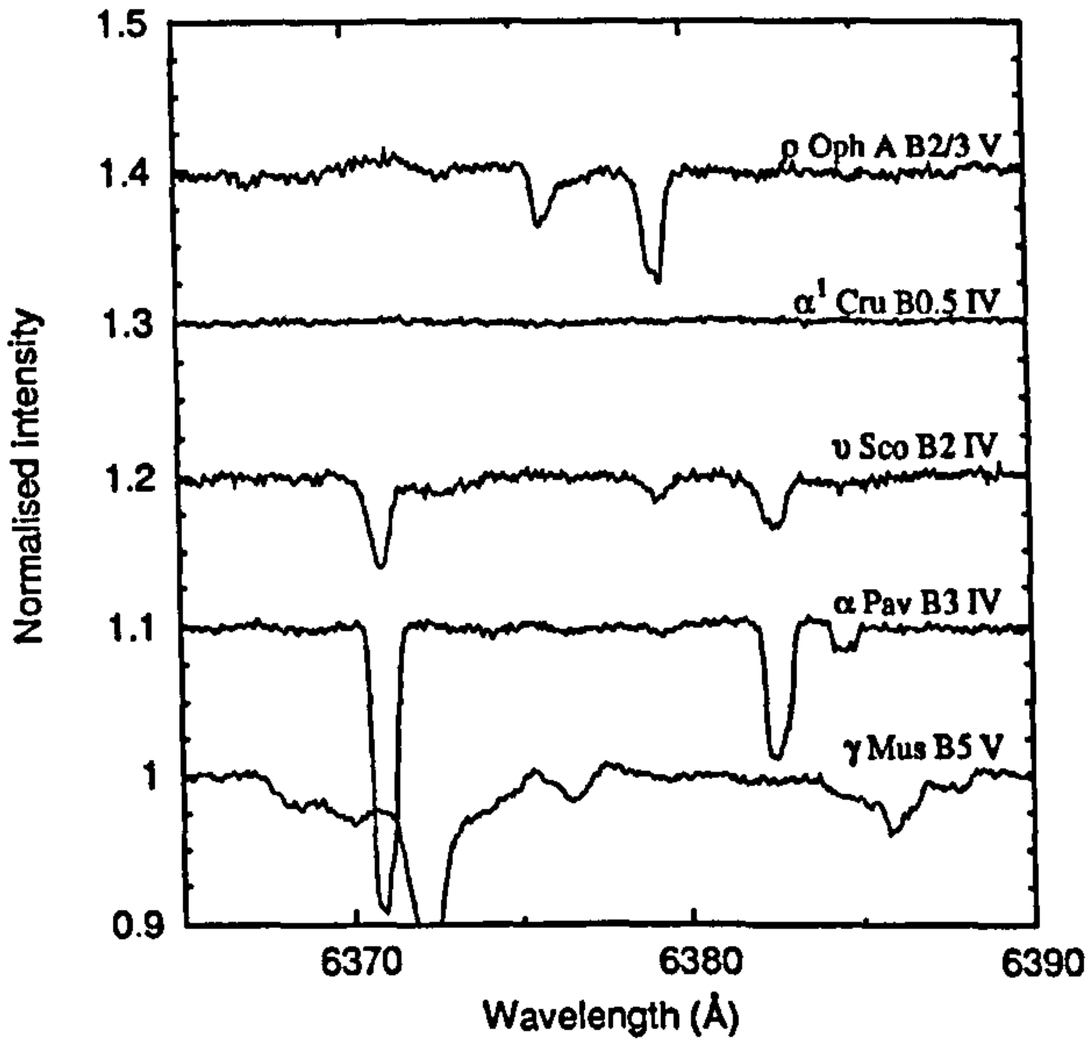

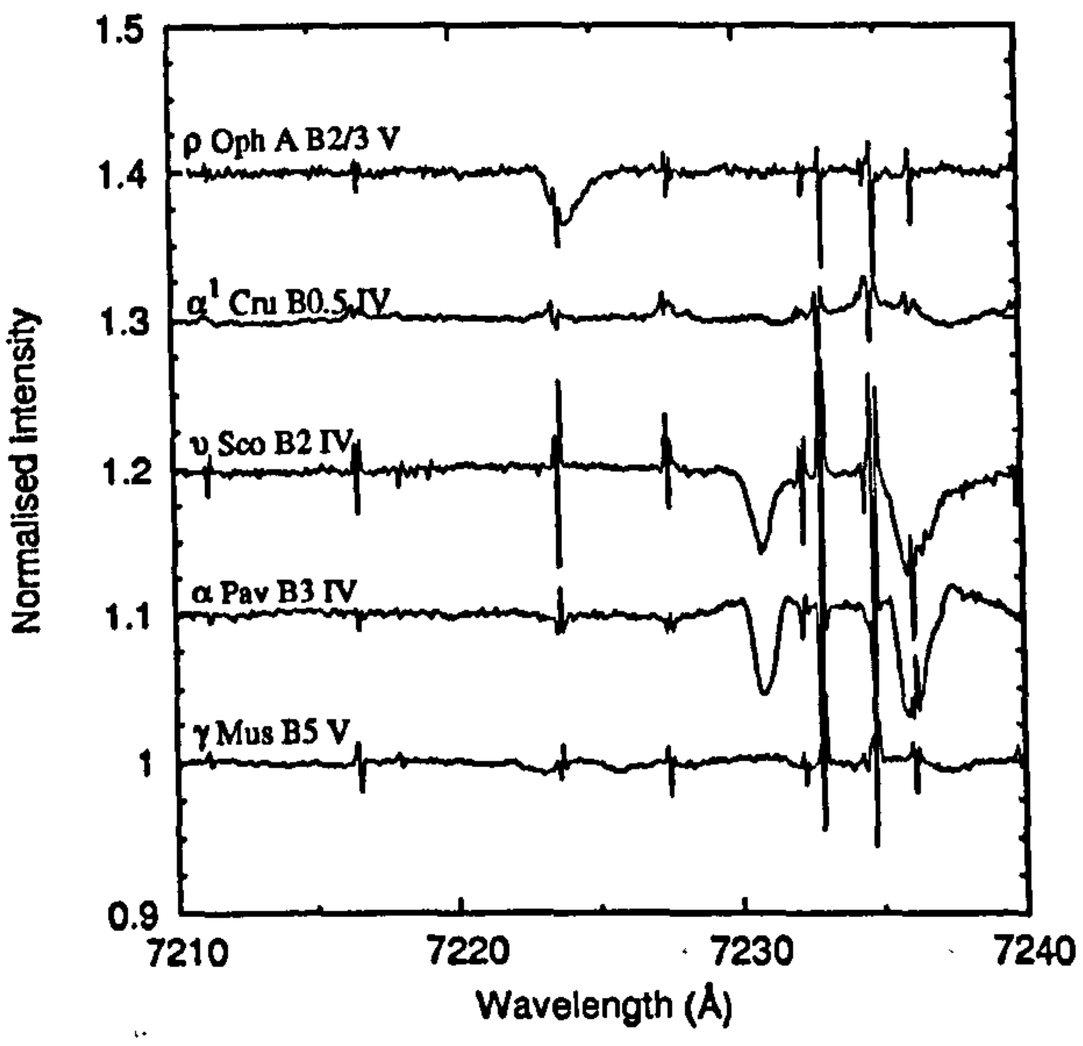

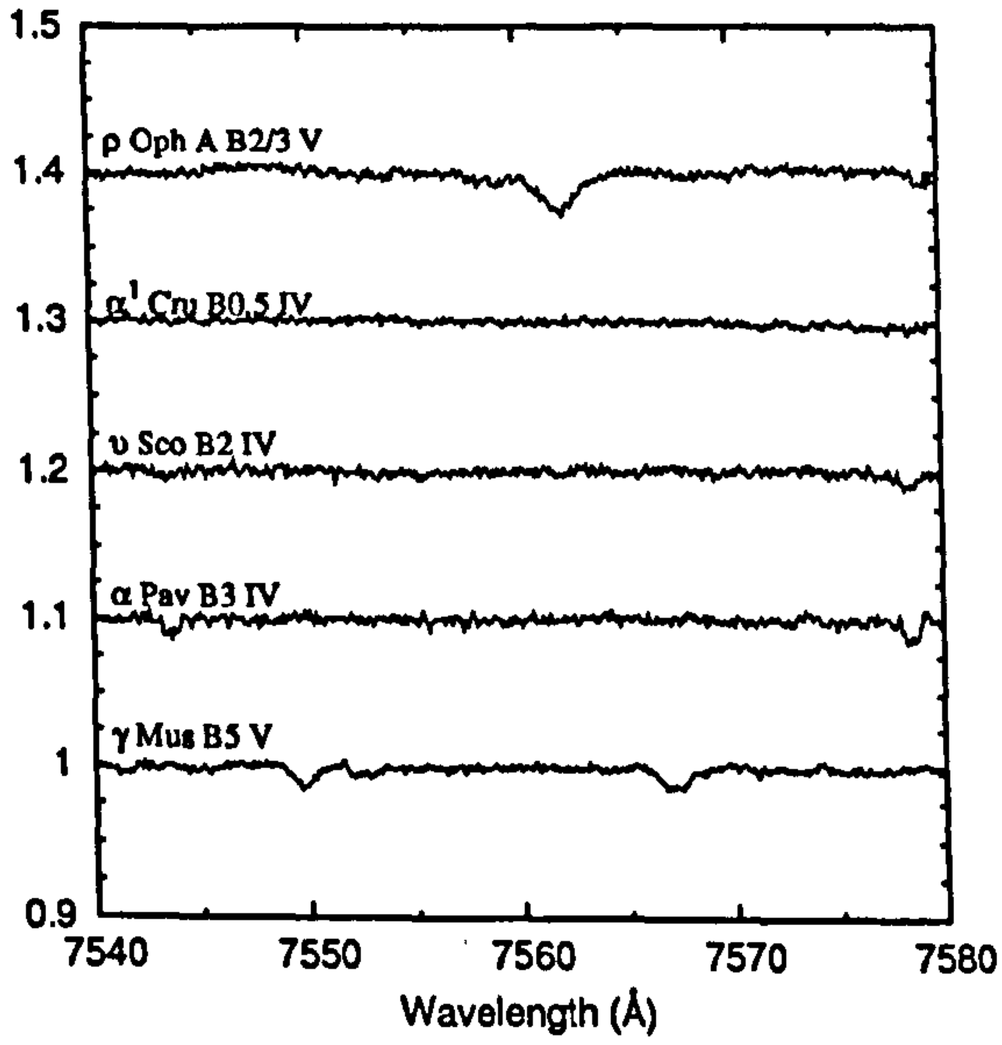

Figure 4.3: Spectral type standards for wavelength regions covering the λ6376, λ6379, λ7224 and λ7562 DIBs, telluric-corrected, normalised with low-order polynomials and shifted vertically for display. λ7562 spectral regions have been 'scaled up' by a multiplicative factor of two. ρ Oph A spectra (top traces) shown to identify the spectral location of the DIBs. 'Noise' in the region of λ7224 is due to the incomplete cancellation of several strong telluric absorption lines.

~ 2000 AU.

The Na I and K I column densities (Watson & Meyer 1996; Lauroesch & Meyer 1999) are greater towards β^2 Sco (see Table 4.3), so residual spectra were formed by subtracting normalised DIB spectra of β^1 Sco from those of β^2 Sco. Examination of the residuals facilitates the identification of differences between the spectra. Given the general invariance of diffuse interstellar band profiles, the residual spectrum over the wavelength range of a given DIB should match the shape of that DIB if it is stronger towards β^2 than β^1. The DIB profile should appear upside down in the residual plot if it is stronger towards β^1 than β^2. The presence of contaminating stellar features should be identifiable as distortions in the residual spectra.

Immediately striking from examination of Figures 4.4 to 4.14 is the very close similarity between the $\beta^{1,2}$ Sco spectra in the case of every DIB. This is not true of the stellar absorption lines; β^2 Sco is of later spectral type and contains several stellar lines absent from the β^1 Sco spectra. The stellar lines of β^2 Sco have an unusual shape (see, for example the lines at 6268 Å in Figure 4.8, or at 6372 Å in Figure 4.9) that suggest this star may be a composite object. It is relatively easy to identify these distinctive, narrow, multi-peaked stellar lines in cases where they may be blended with DIBs.

The equivalent widths of 16 of the strongest (narrow) DIBs observed are shown in Table 4.3. The statistical precision of the measurements is high Approximate equivalent width errors calculated using the formula $\sigma_{\rm RMS}\Delta_\lambda$ amount to $\lesssim$ 1.5 mÅ for all DIBs, where $\sigma_{\rm RMS}$ is the RMS noise in the (normalised) continuum and Δ_λ is the FWHM of the DIB in question. To calculate the DIB equivalent widths W_λ, the mean of the measurements for a given DIB towards both stars was taken (*i.e.* $W_\lambda(mean) = (W'_\lambda(\beta^1) + W'_\lambda(\beta^2))/2$). The difference between the two was then measured by integrating over the the residual DIB spectrum (with the constant 1 added to each data point), using the observed DIB profile from β^1 Sco to determine the limits of integration. This 'residual equivalent width' $[W_\lambda]_R$ was divided by two and applied as a relative difference to $W_\lambda(mean)$ for each star (*i.e.* $W_\lambda(\beta^2) = W_\lambda(mean) + [W_\lambda]_R/2$ and $W_\lambda(\beta^1) = W_\lambda(mean) - [W_\lambda]_R/2$). Averaging of the W_λ measurements in this manner reduced the errors in the final equivalent widths due to continuum placement and stellar contamination. Applying half the 'residual equivalent width' as a difference to both sightlines ensures greatest accuracy in the 'equivalent width difference' values $\delta(\beta^2/\beta^1)$.

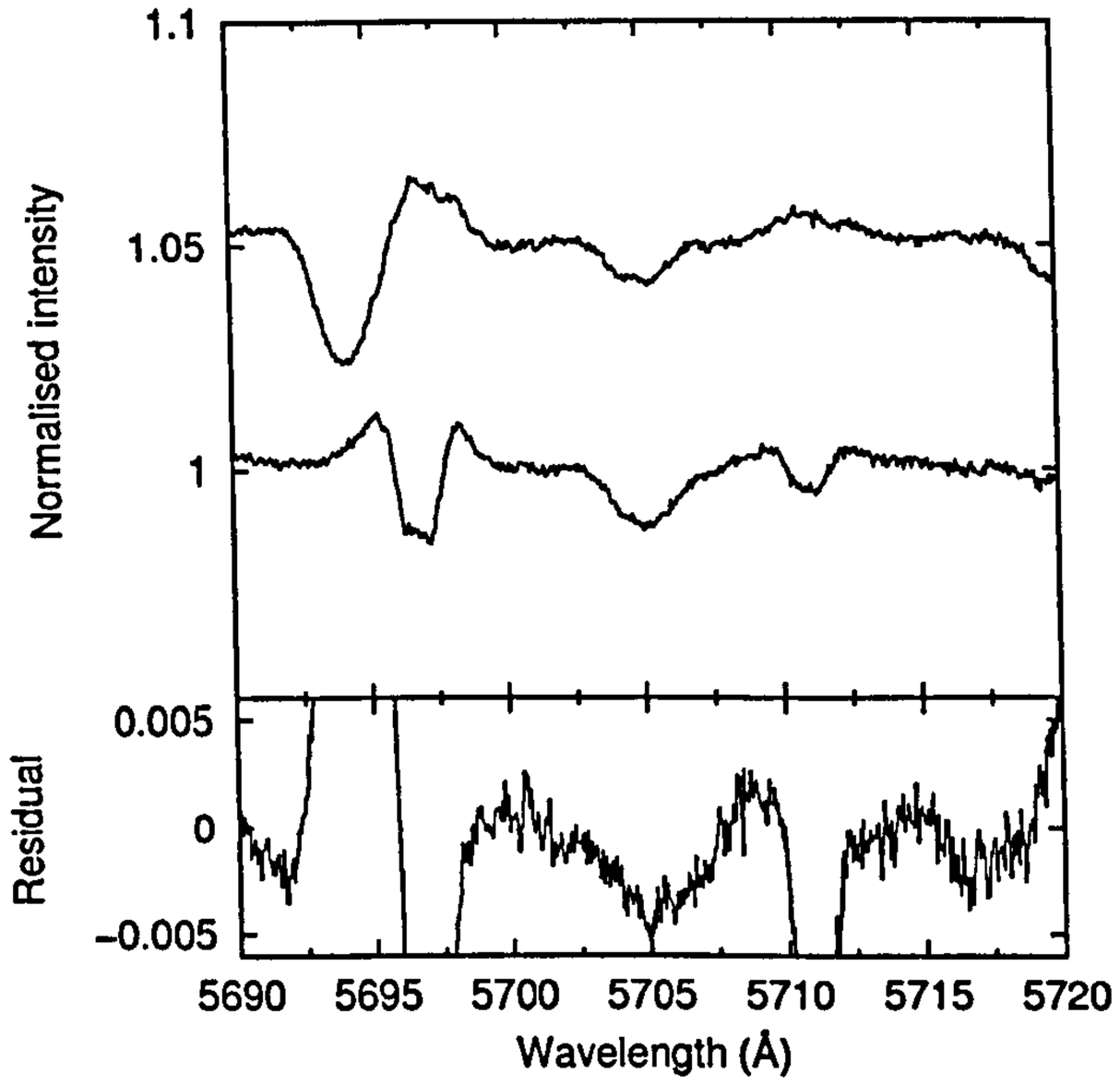

Figure 4.4: Spectra of $\lambda 5705$ recorded towards β^1 Sco (top) and β^2 Sco (middle), telluric-corrected and normalised with straight line continua. Lower trace shows the residual intensities of β^2 Sco $-$ β^1 Sco.

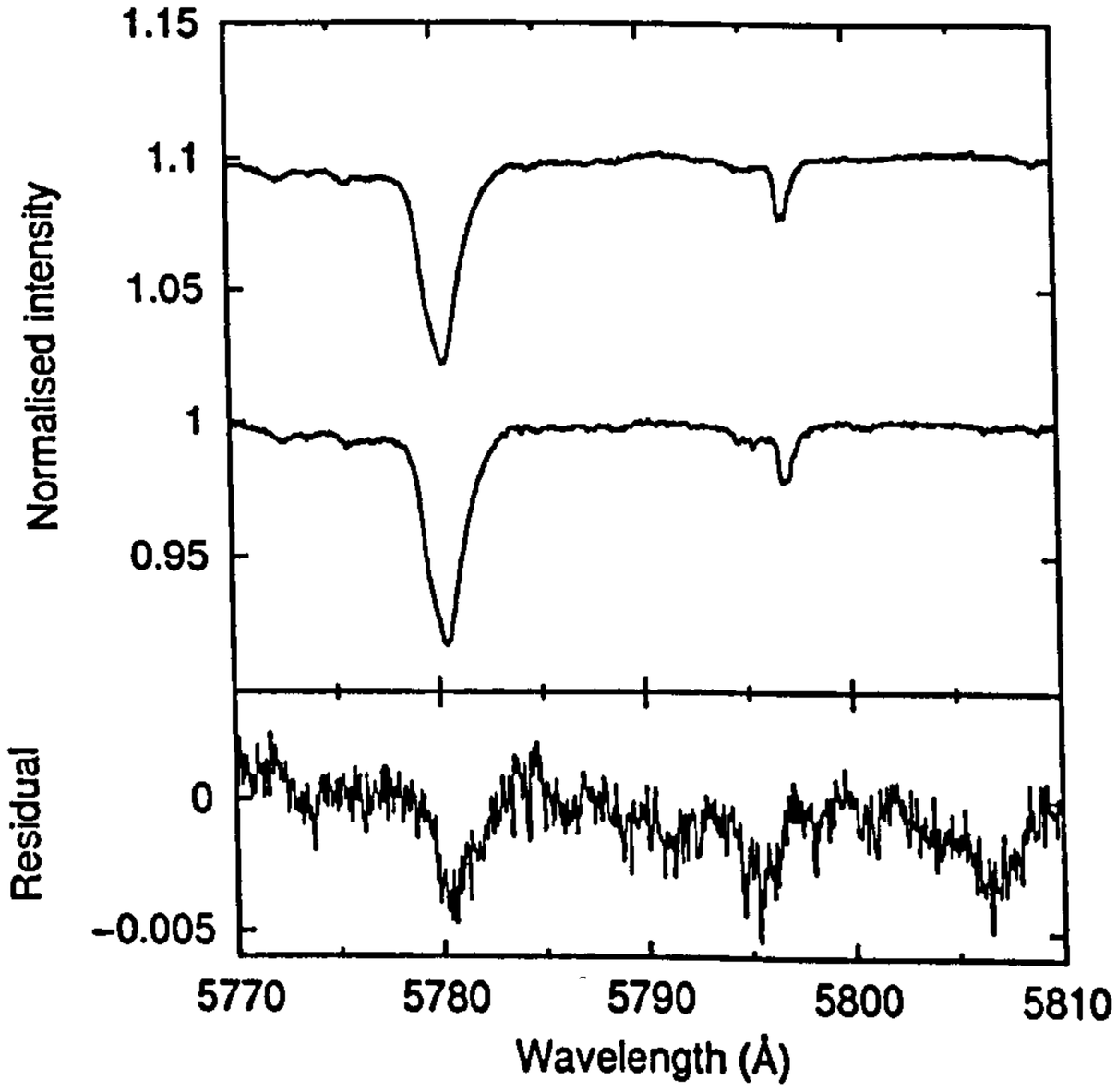

Figure 4.5: Spectra of $\lambda 5780$ and $\lambda 5797$ recorded towards β^1 Sco (top) and β^2 Sco (middle), telluric-corrected and normalised with straight line continua. Lower trace shows the residual intensities of β^2 Sco $-$ β^1 Sco.

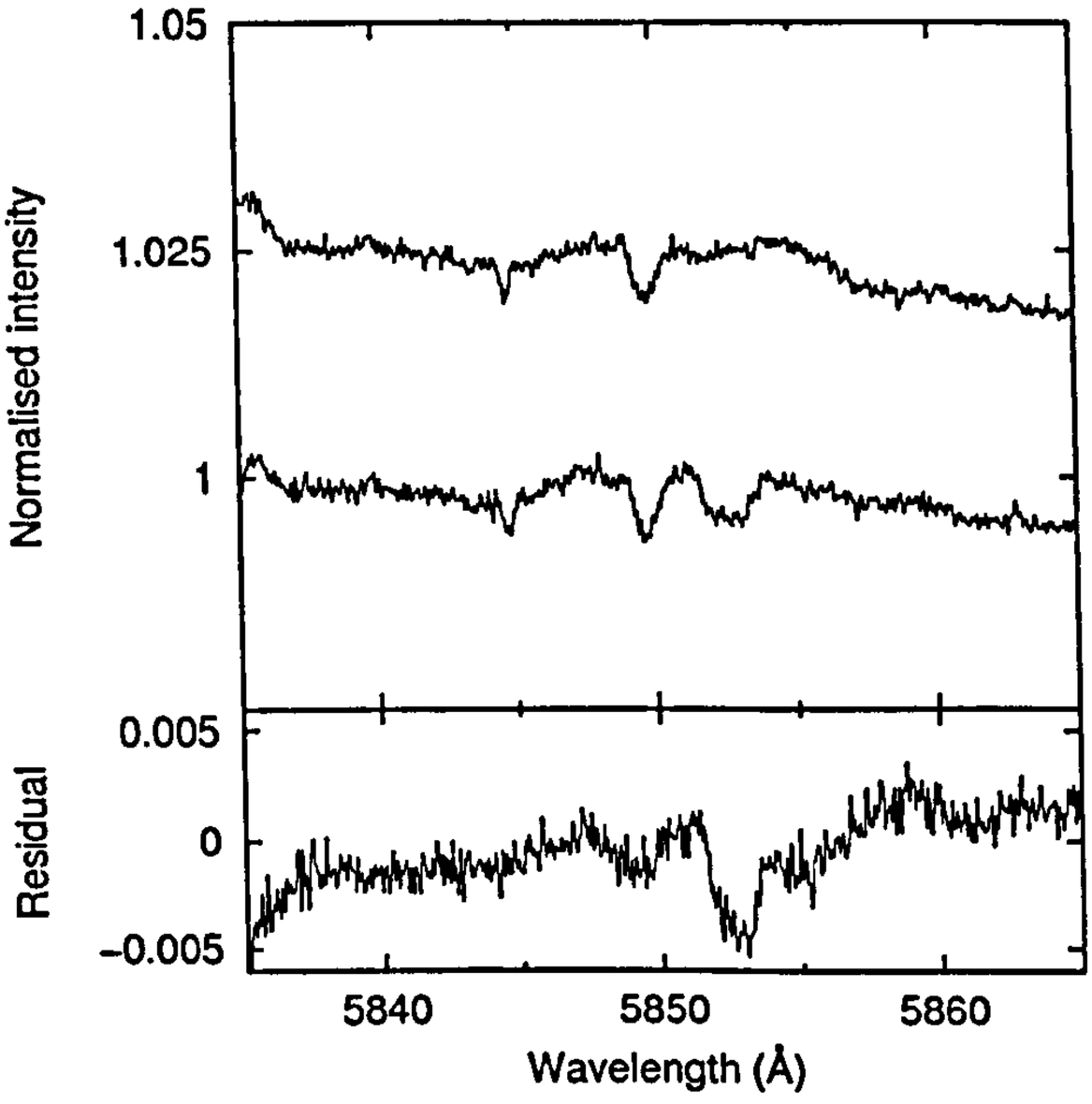

Figure 4.6: Spectra of λ5850 recorded towards β^1 Sco (top) and β^2 Sco (middle), telluric-corrected and normalised with straight line continua. Lower trace shows the residual intensities of β^2 Sco – β^1 Sco.

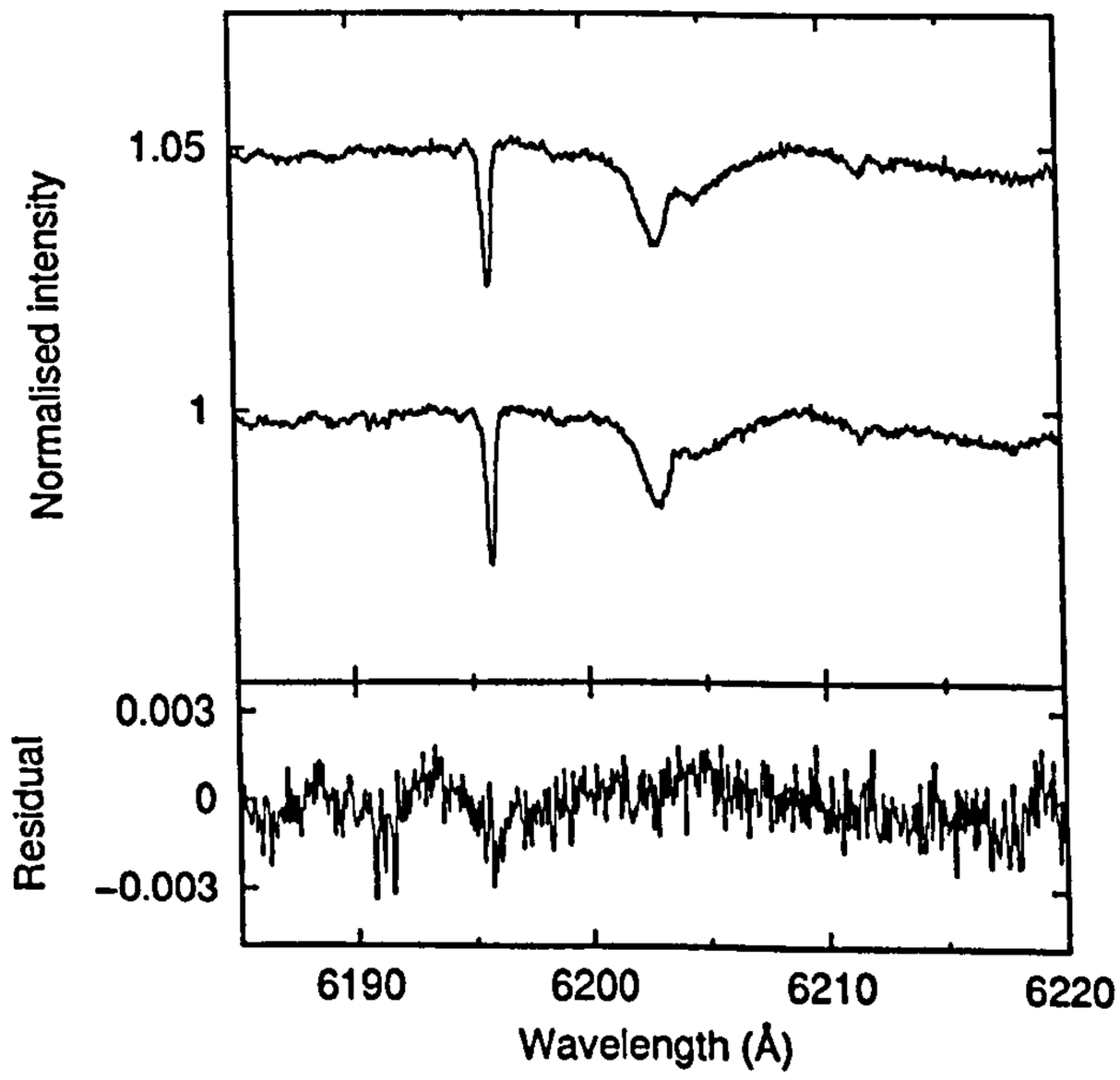

Figure 4.7: Spectra of λ6196 and λ6203 recorded towards β^1 Sco (top) and β^2 Sco (middle), telluric-corrected and normalised with low-order polynomial continua. Lower trace shows the residual intensities of β^2 Sco – β^1 Sco.

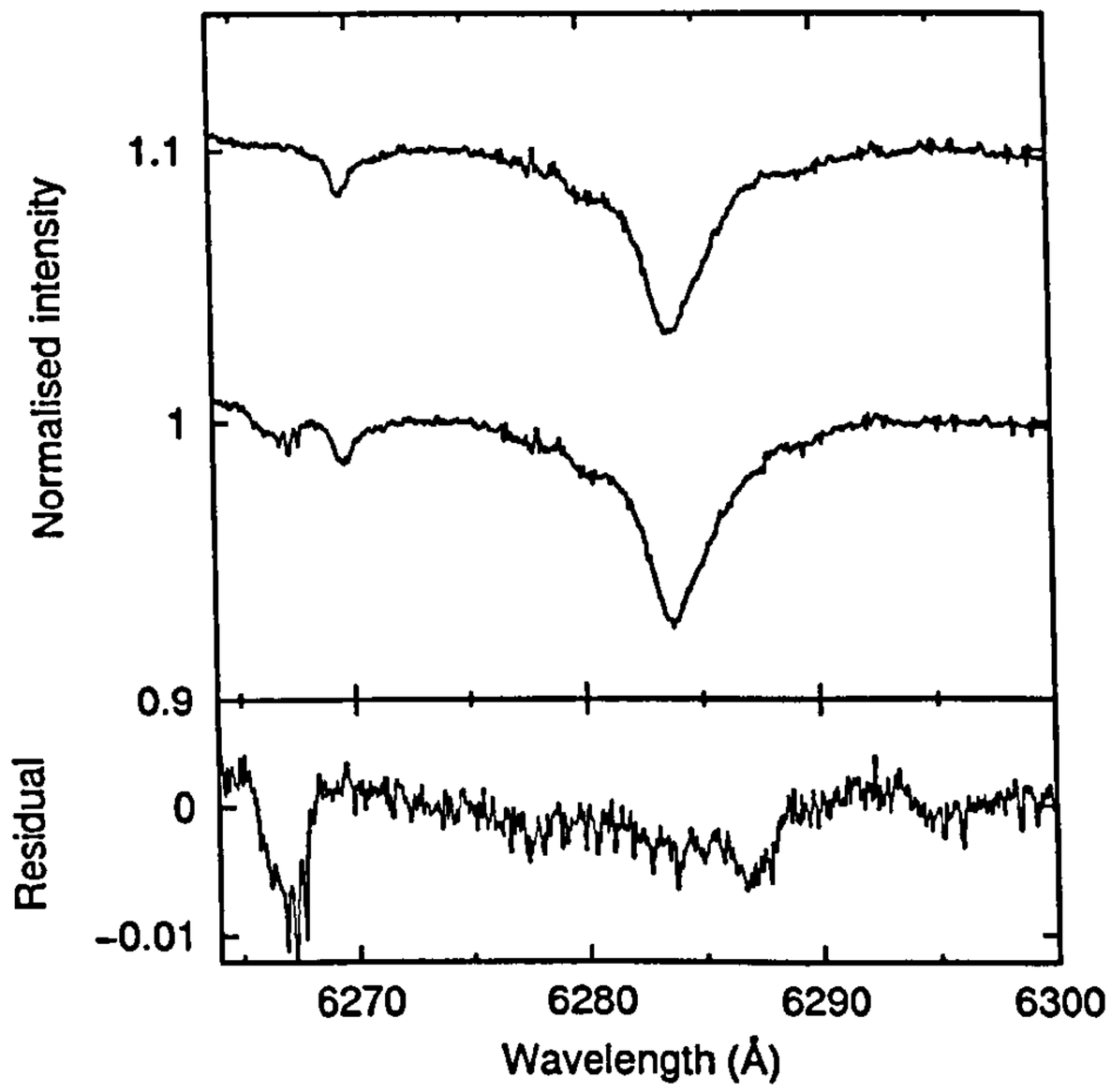

Figure 4.8: Spectra of λ6284 recorded towards β^1 Sco (top) and β^2 Sco (middle), telluric-corrected and normalised with straight line continua. Lower trace shows the residual intensities of β^2 Sco $-$ β^1 Sco.

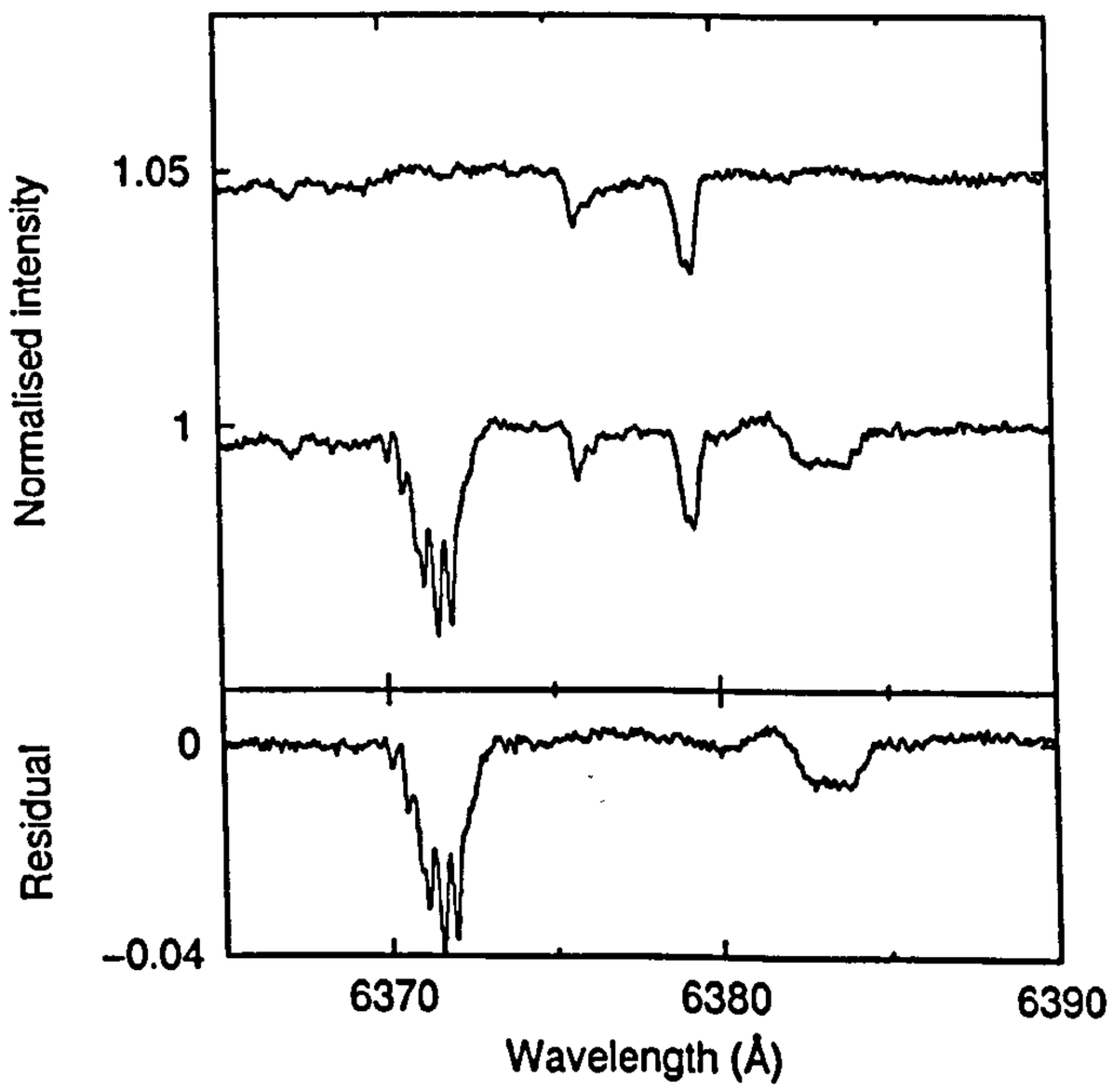

Figure 4.9: Spectra of λ6376 and λ6379 recorded towards β^1 Sco (top) and β^2 Sco (middle), telluric-corrected and normalised with straight line continua. Lower trace shows the residual intensities of β^2 Sco $-$ β^1 Sco.

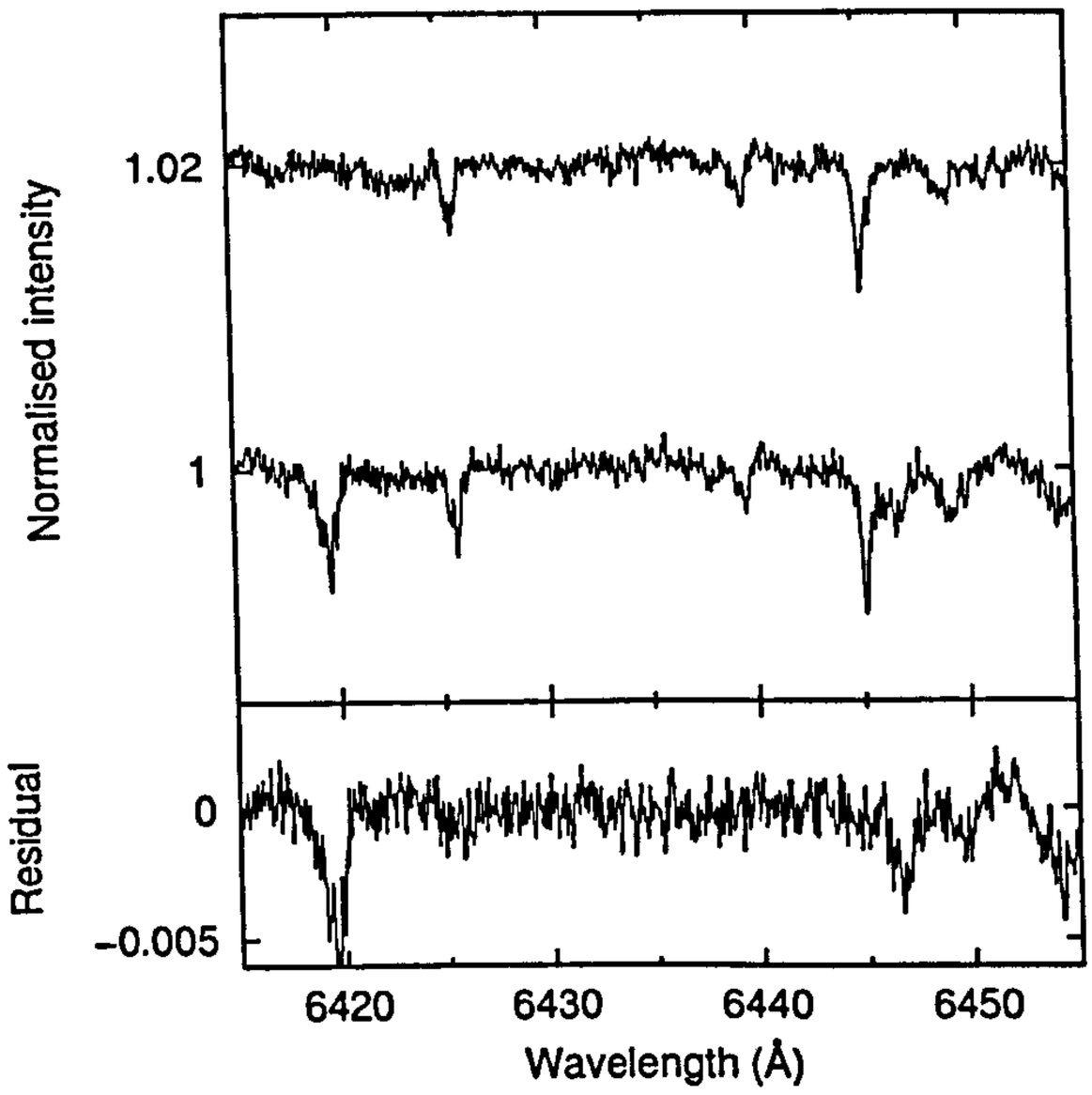

Figure 4.10: Spectra of λ6426 , λ6439 and λ6445 recorded towards β^1 Sco (top) and β^2 Sco (middle), telluric-corrected and normalised with low-order polynomial continua. Lower trace shows the residual intensities of β^2 Sco – β^1 Sco.

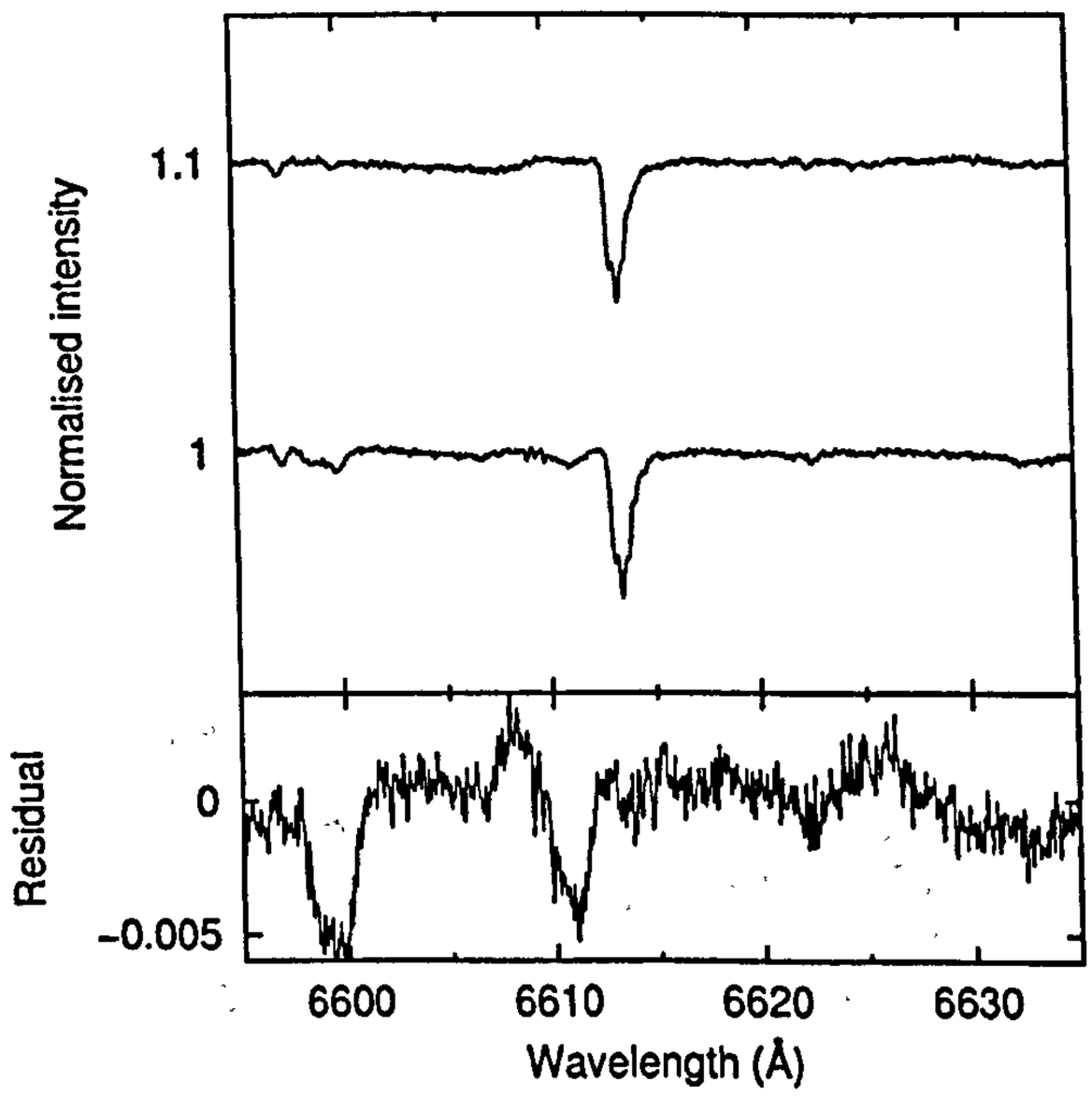

Figure 4.11: Spectra of λ6614 recorded towards β^1 Sco (top) and β^2 Sco (middle), telluric-corrected and normalised with straight line continua. Lower trace shows the residual intensities of β^2 Sco – β^1 Sco.

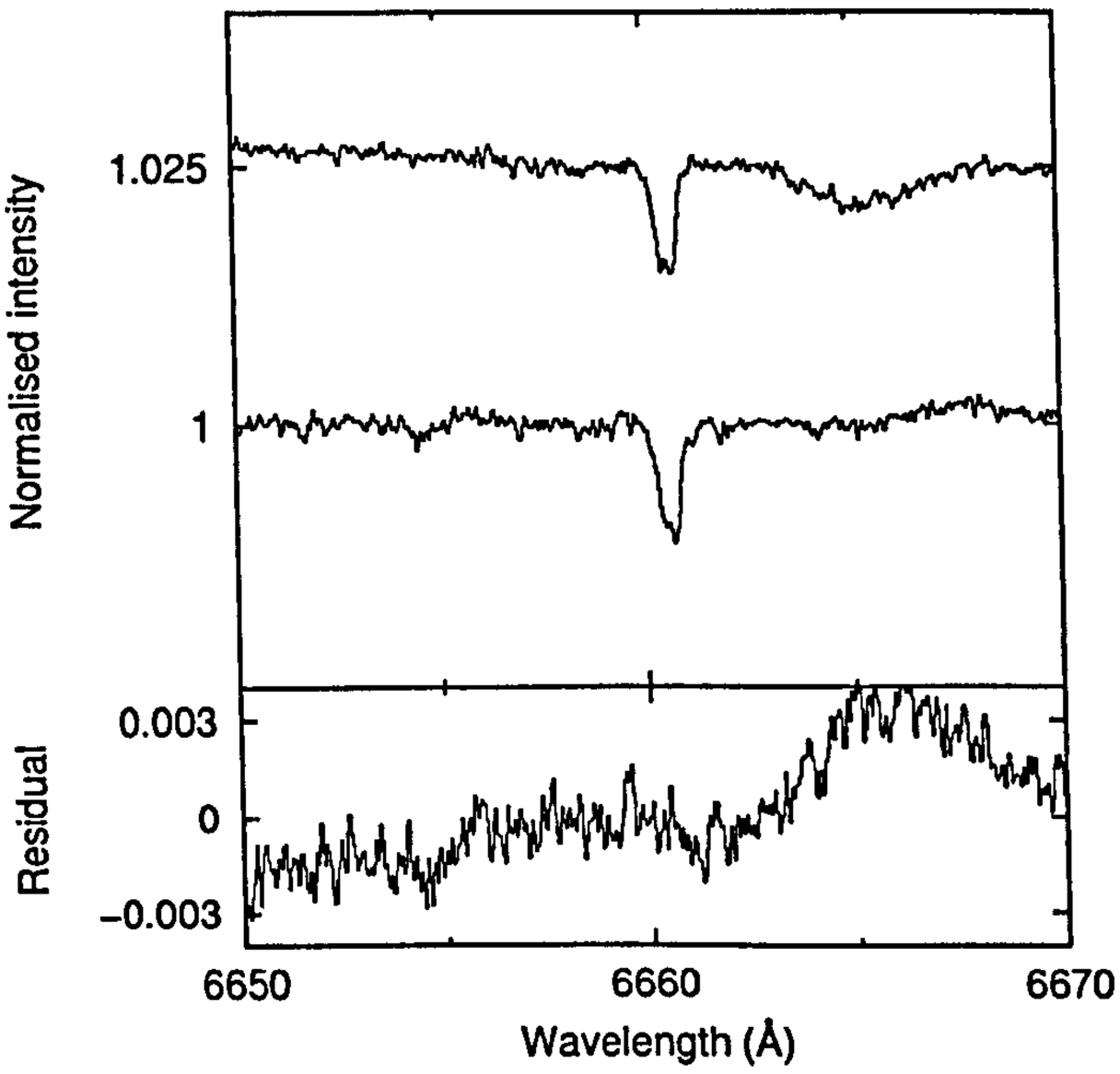

Figure 4.12: Spectra of λ6660 recorded towards β^1 Sco (top) and β^2 Sco (middle), telluric-corrected and normalised with straight line continua. Lower trace shows the residual intensities of β^2 Sco $-$ β^1 Sco.

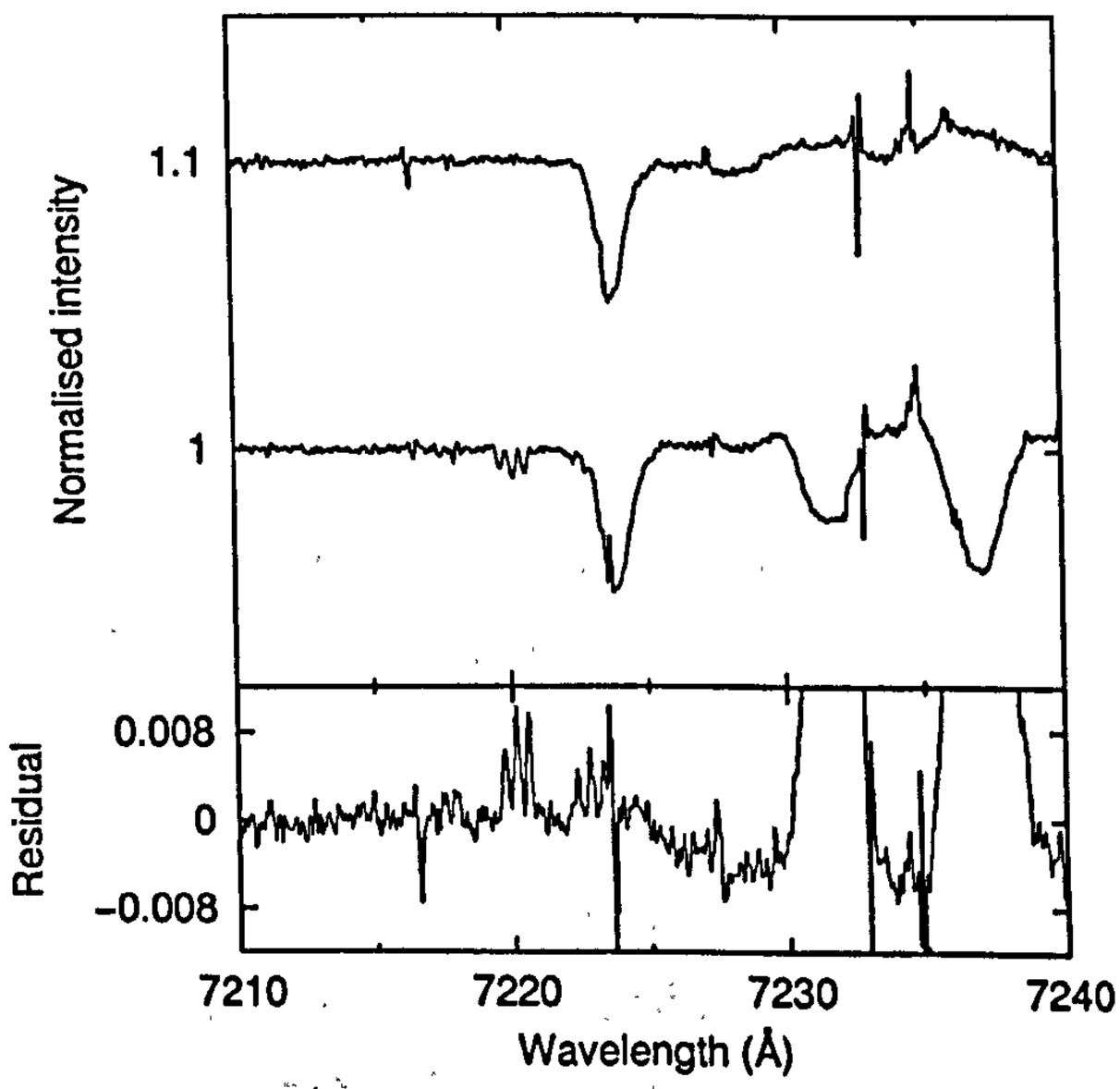

Figure 4.13: Spectra of λ7224 recorded towards β^1 Sco (top) and β^2 Sco (middle), telluric-corrected and normalised with straight line continua. Lower trace shows the residual intensities of β^2 Sco $-$ β^1 Sco.

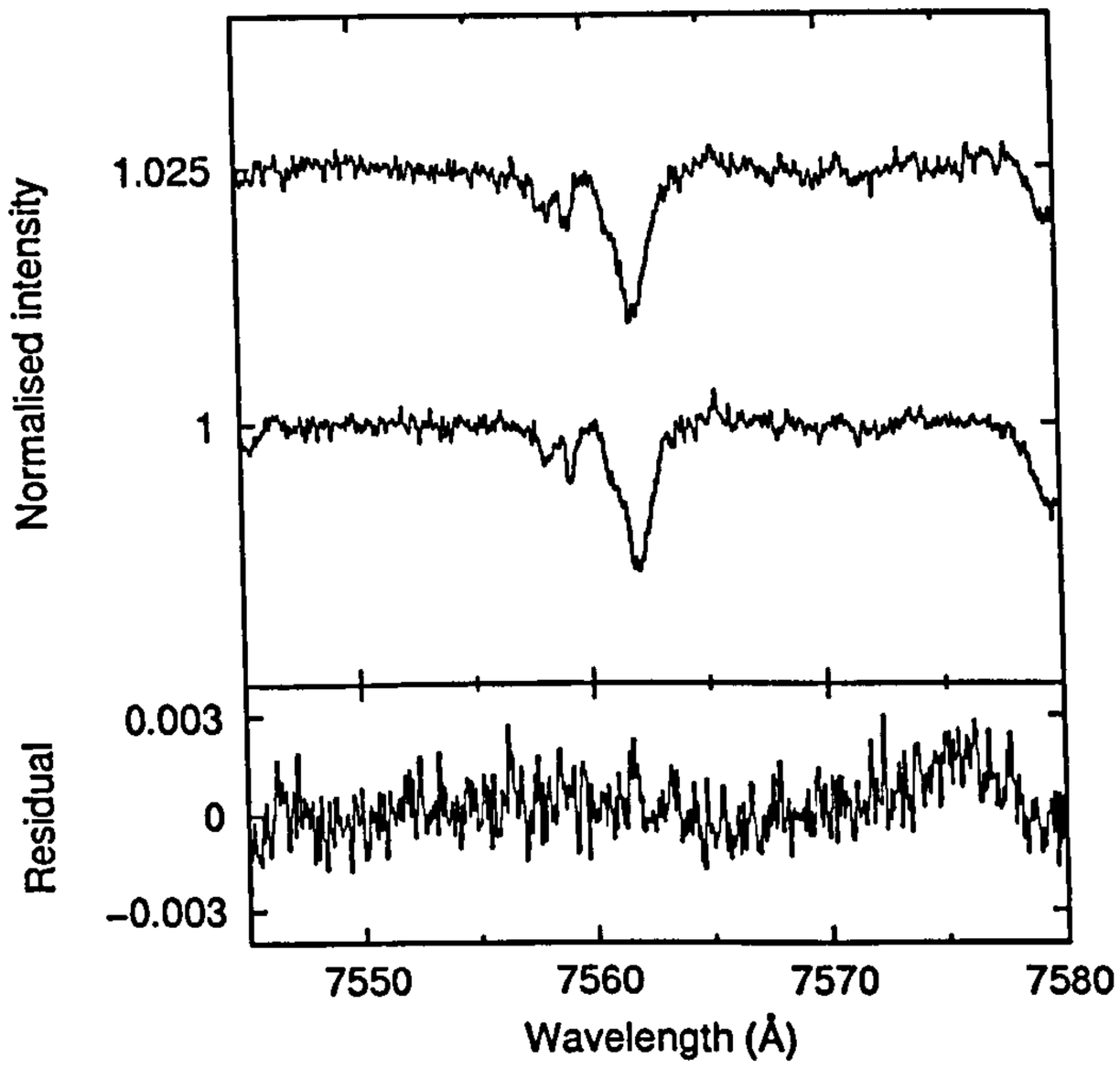

Figure 4.14: Spectra of $\lambda 7562$ recorded towards β^1 Sco (top) and β^2 Sco (middle), telluric-corrected and normalised with low-order polynomial continua. Lower trace shows the residual intensities of β^2 Sco $-$ β^1 Sco.

Equivalent width *differences* are denoted in this thesis by $\delta(X/Y)$, which gives the 'percentage excess' of $W_\lambda(X)$ (the equivalent width of a DIB in sightline X) compared to $W_\lambda(Y)$ (its equivalent width in sightline Y), calculated using

$$\delta(X/Y) = 100\left(\frac{W_\lambda(X)}{W_\lambda(Y)} - 1\right). \tag{4.1}$$

For the β Sco system, interstellar features are typically stronger towards β^2 than β^1, so percentage excesses were formed as $\delta(\beta^2/\beta^1)$ so as to give positive values for the typical case of $W_\lambda(\beta^2) > W_\lambda(\beta^1)$ and negative values for $W_\lambda(\beta^1) > W_\lambda(\beta^2)$. Combining the statistical errors from the individual spectra to calculate the RMS noise $\sigma_R(\beta^{1,2})$ of the residual plot using $\sigma_R(\beta^{1,2}) = \sqrt{\sigma(\beta^1)^2 + \sigma(\beta^2)^2}$, the error on $\delta(\beta^2/\beta^1)$ was then determined using $\sigma_R(\beta^{1,2})\Delta_\lambda$. Where no feature corresponding to a difference between the DIB spectra could be identified in the residual spectra, an upper limit on $\delta(\beta^2/\beta^1)$ was calculated using $\sigma_R(\beta^{1,2})\Delta_\lambda$. This is a reasonable two to three sigma upper limit because the peaks of the DIB absorption profiles span at least four to nine pixels in all cases and the statistical error scales inversely as the square root of the number of binned pixels for Poisson noise. Stellar line blends contaminate many of the DIBs,

Feature	W_λ (mÅ) β^1 Sco	W_λ (mÅ) β^2 Sco	$\delta(\beta^2/\beta^1)$ (%)	Blend?
λ5705	22.6	27.9	23 (8.3)	?
λ5780	142.3	151.5	6.5 (1.0)	N
λ5797	16.7	15.3	-8.4 (2.9)	Y
λ5850	5.4	5.5	1.9 (10)	Y
λ6196	12.3	13.5	9.8 (2.3)	N
λ6203	57	57	<4.7	N
λ6284	330	330	<0.8	Y
λ6376	5.5	5.5	<8.2	N
λ6379	13.3	13.3	<3.0	?
λ6426	2.1	2.6	24 (31)	N
λ6439	1.4	1.7	21 (37)	Y
λ6445	5	5	<9.0	N
λ6614	42.5	43.5	2.4 (1.4)	N
λ6660	7.3	7.3	<5.0	N
λ7224	62	62	<1.2	T
λ7562	32	32	<4.3	N
K I λ7699	22.9	25.6	11 (0.9)	
Na I D_1	147.4	154.7	5.0 (0.1)	
log N(K I)	11.193	11.276	21 (30)	

Table 4.3: Equivalent widths of interstellar features measured towards $\beta^{1,2}$ Sco. $\delta(\beta^2/\beta^1)$ is the percentage *excess* of β^2 Sco measurements compared to β^1 Sco, with error estimates given in parentheses. N(K I) data are from Lauroesch & Meyer (1999). In the last column, 'Y' indicates a definite or probable stellar blend contaminating the DIB spectra, 'N' indicates improbable or absent stellar blend and '?' is for indeterminate cases, 'T' indicates severe telluric contamination of results.

introducing unquantifiable errors into the equivalent width measurements. It is difficult to be certain about the presence or lack of such blends, but the effects of their presence can only be ruled out with confidence when the residual plots are flat in the region surrounding a DIB *and* the DIB profile is shown cleanly in the residual spectrum. Small-scale variations in DIB strengths are deemed to be present when the DIB profile is clearly present in the residual spectrum, and with a shape reasonably matching that observed directly towards either star.

Figure 4.4 shows the λ5705 DIB, and several distortions in the surrounding spectrum due to stellar lines, including broad inverted lines introduced by division by the telluric standard spectrum. The γ Mus spectrum in Figure 4.1 shows the possibility of stellar lines within the DIB profile, but the shape of the residual spectrum is roughly consistent with the profile of the DIB. Thus, there appears to be an enhancement in the strength

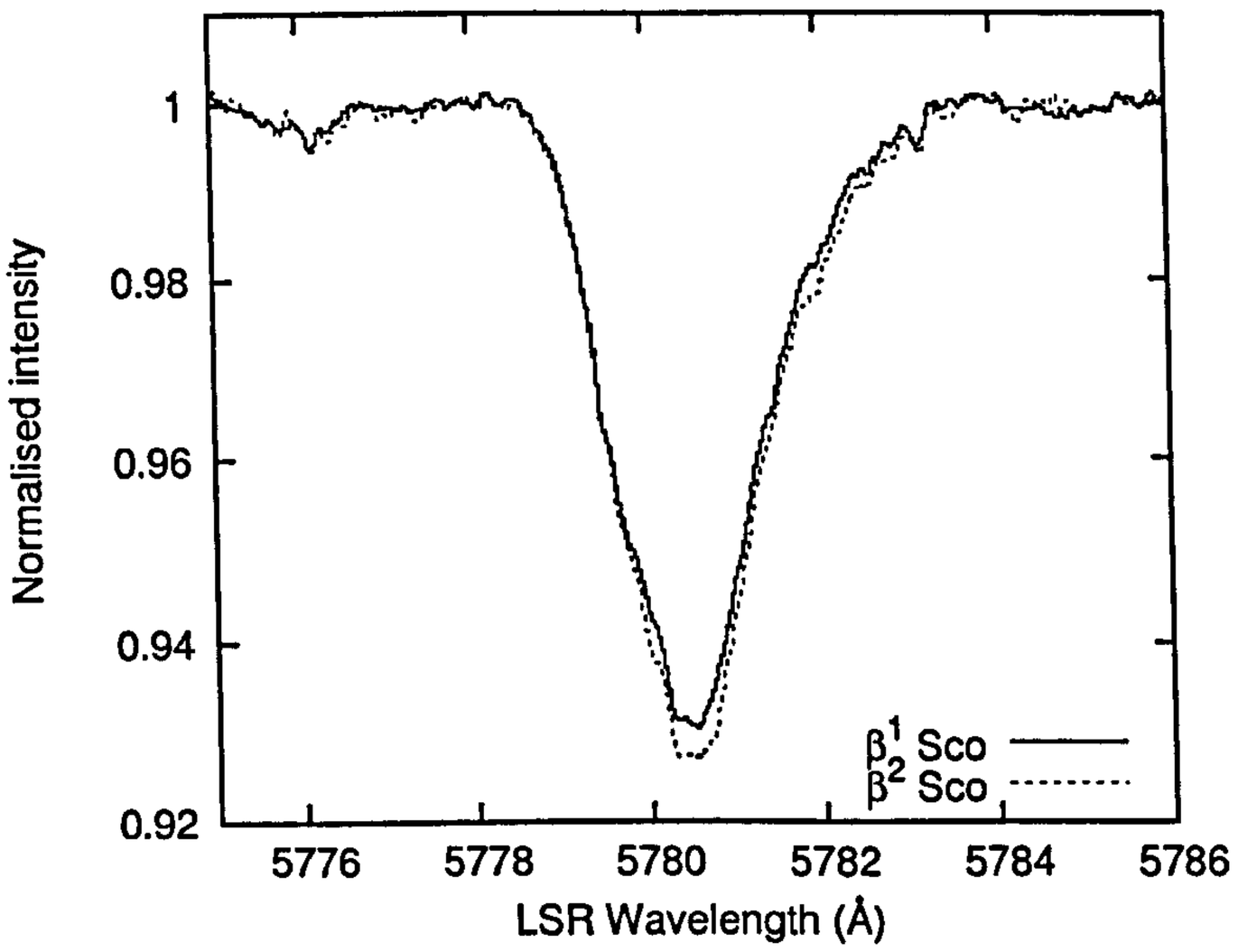

Figure 4.15: Overlaid $\beta^{1,2}$ Sco λ5780 spectra, telluric-corrected and normalised with low-order polynomial continua.

of λ5705 towards β^2 Sco by about 23% compared to β^1 Sco (see Table 4.3). Due to the strong stellar features adjacent to the diffuse band, a flat residual continuum cannot be defined however, so this cannot be considered a definite detection of small-scale structure in the λ5705-carrier distribution.

Towards $\beta^{1,2}$ Sco, differences in the strengths of the DIBs are observed with a high degree of confidence for λ5780 (see Figures 4.5 and 4.15) and λ6196 (Figures 4.7 and 4.16). As shown in Table 4.3, λ5780 is about 6.5 ± 1% stronger, and λ6196 is about 9.8 ± 2.3% stronger, towards β^2 Sco. These are two of the DIBs with the greatest central depths for this pair of sightlines. No significant stellar features appear to be contaminating the DIB profiles, and for both DIBs the residual spectra show an excess for β^2 Sco with a shape consistent with an overall increase in the strength of the whole DIB. The very strong λ6284 DIB (see Figure 4.8) does not show convincing evidence for variation consistent with a change in strength of the DIB between the two sightlines, and though a stellar feature is present on the red side of the profile towards β^2 Sco, the residual spectrum is flat (albeit sloping) around the DIB peak. Considering the statistical errors, this DIB apparently has the same equivalent width towards both stars to within 0.8%. It is plausible however, that the slope in the residual continuum could arise from a difference in the intrinsic profile of λ6284 between the sightlines.

Of other DIBs unlikely to have significant stellar line contamination, λ6426 and λ6614

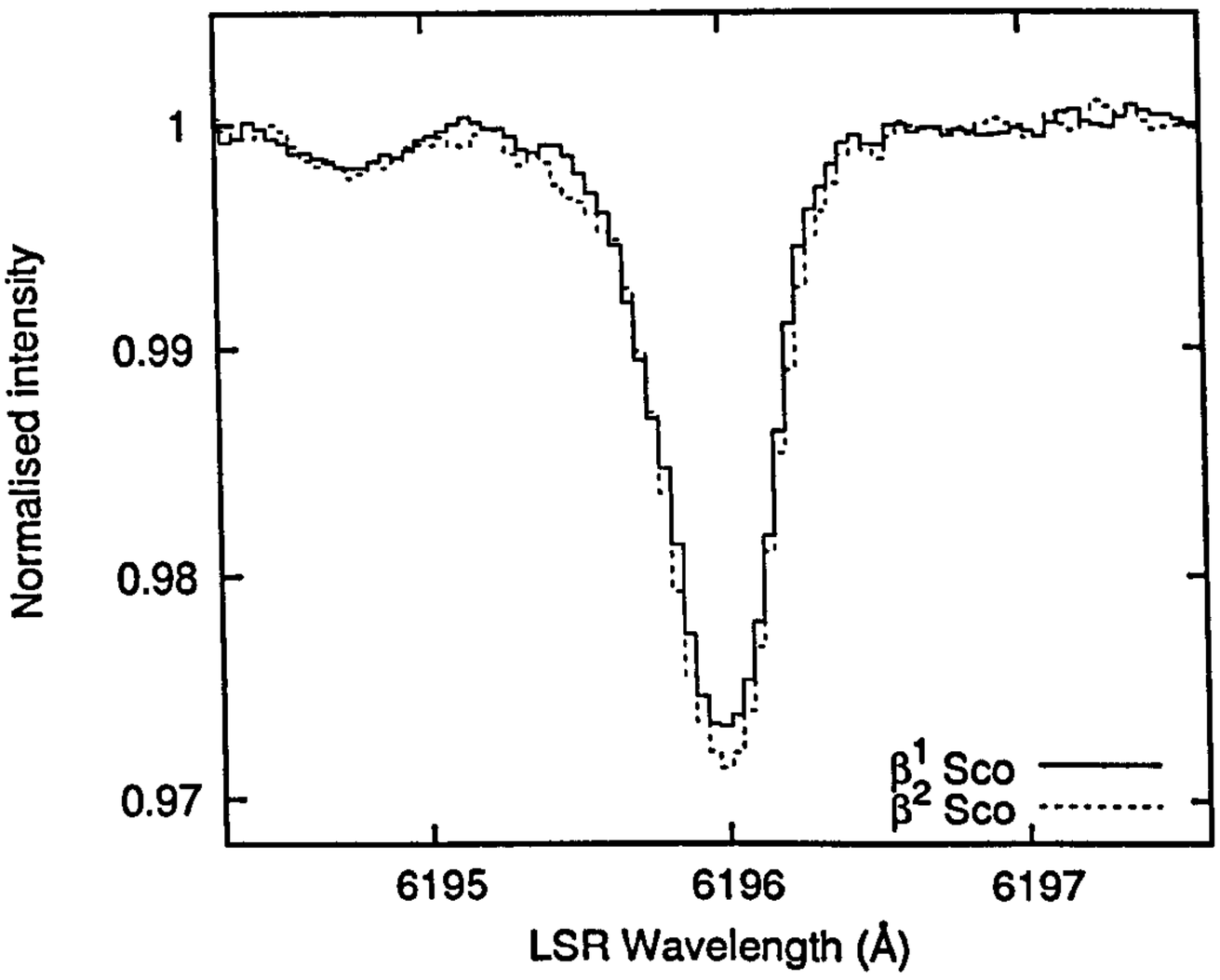

Figure 4.16: Overlaid $\beta^{1,2}$ Sco λ6196 spectra, telluric-corrected and normalised with low-order polynomial continua.

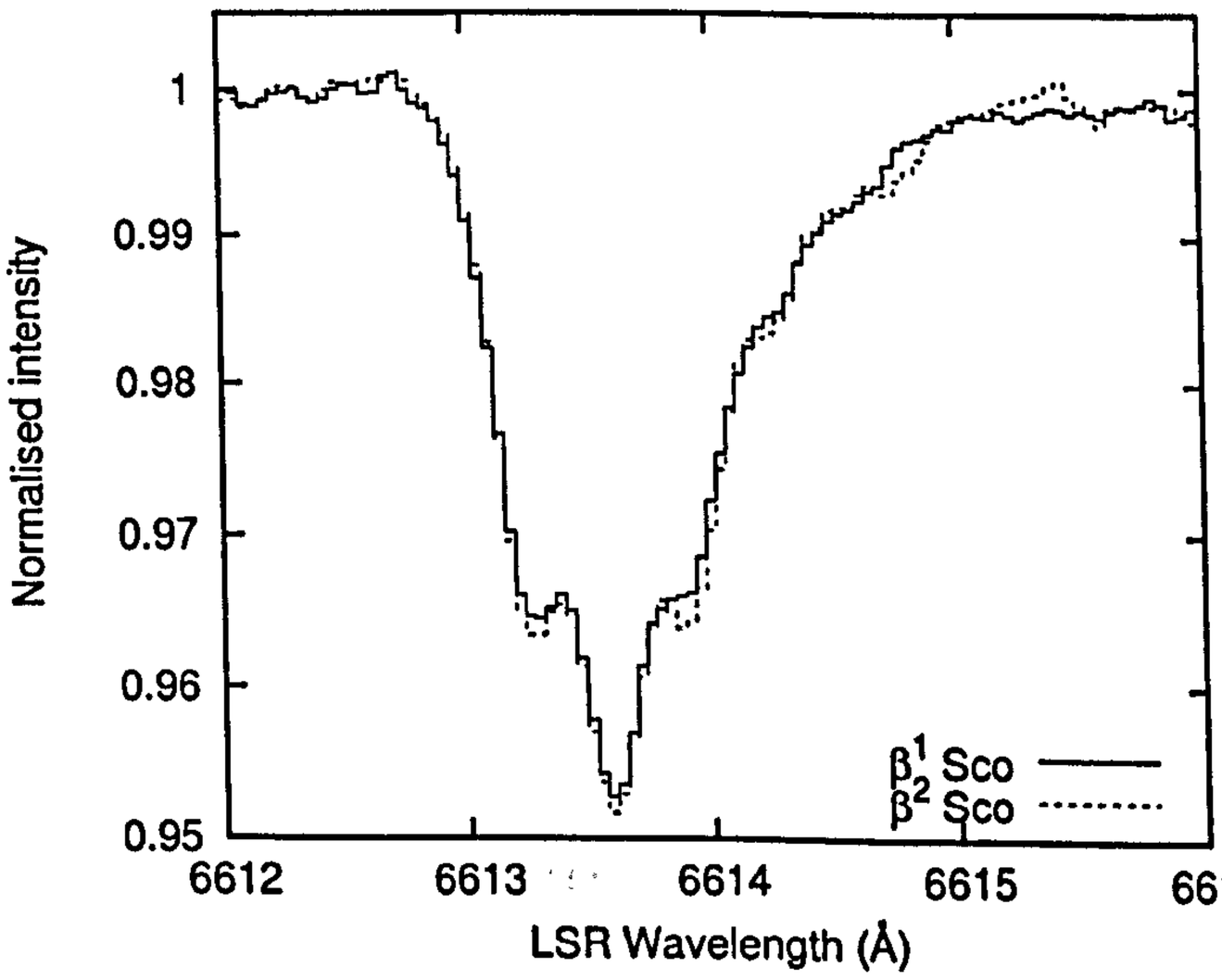

Figure 4.17: Overlaid $\beta^{1,2}$ Sco λ6614 spectra, telluric-corrected and normalised with low-order polynomial continua.

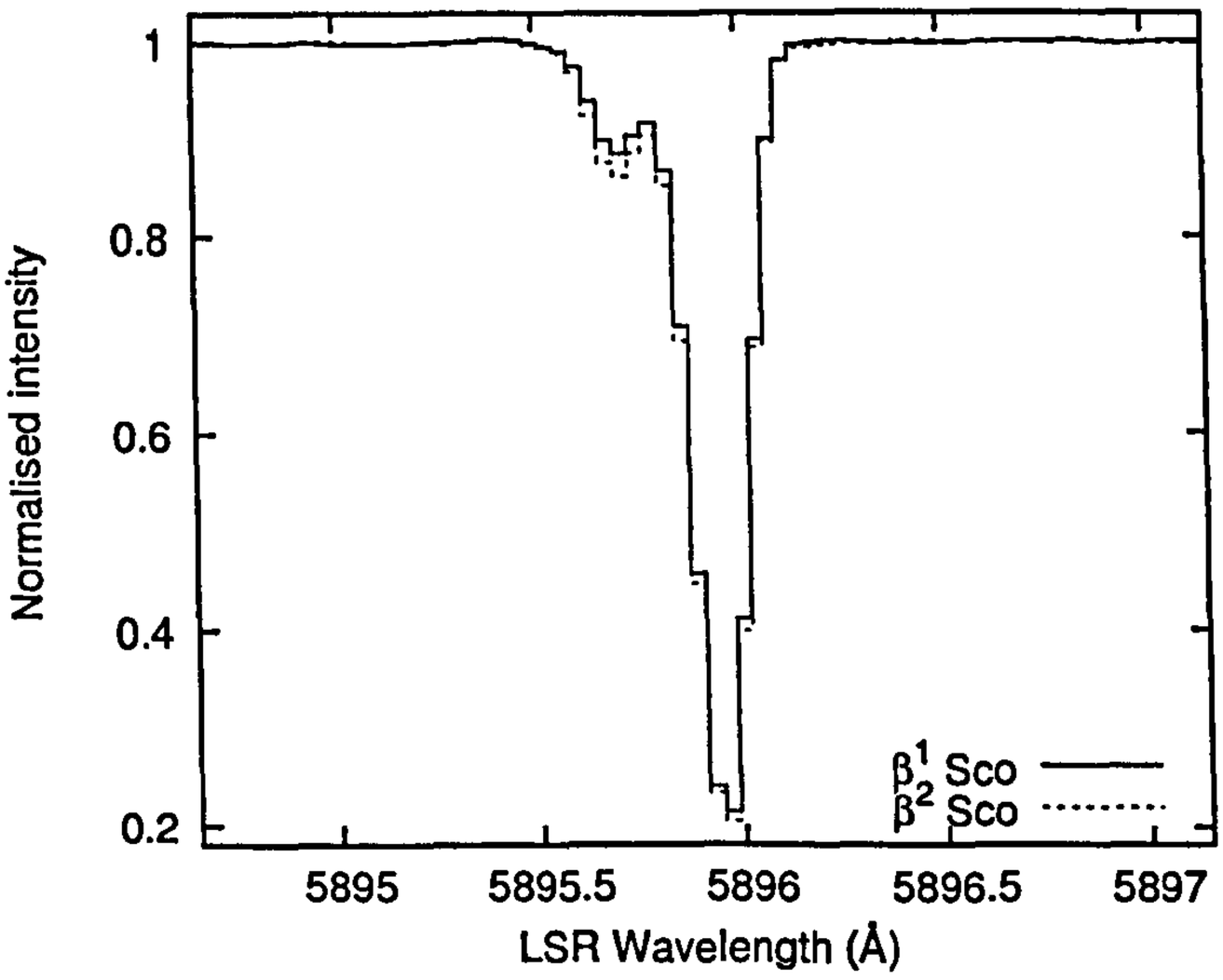

Figure 4.18: Overlaid $\beta^{1,2}$ Sco Na I D_1 spectra, telluric-corrected and normalised with low-order polynomial continua.

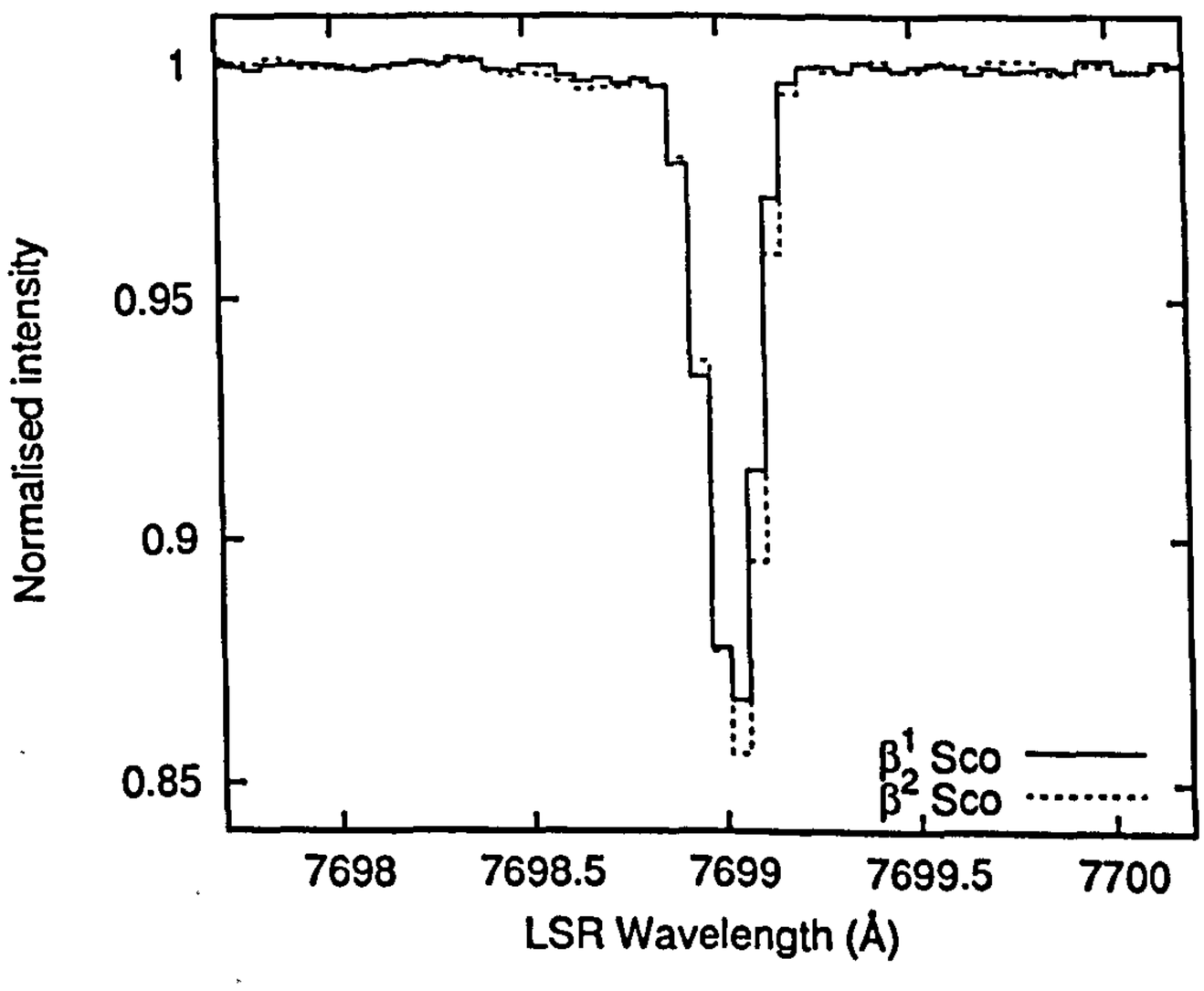

Figure 4.19: Overlaid $\beta^{1,2}$ Sco K I λ7699 spectra, telluric-corrected and normalised with low-order polynomial continua.

show strength enhancements towards β^2 Sco, though λ6426 is too weak for the difference to be significant within the estimated errors. From examination of the standard star spectra for those of similar type to $\beta^{1,2}$ Sco (see Figure 4.2), there is little possibility that the difference in the λ6614 absorption shown by Figures 4.11 and 4.17 is caused by stellar line-blends, so λ6614 is deemed to show band strength variation at a level of about 2.4%. Stellar blends due predominantly to lines in the β^2 Sco spectrum preclude a definitive analysis for λ5797, λ5850 and λ6439 (shown in Figures 4.5, 4.6 and 4.10 respectively), and though no severe stellar lines appear to contaminate λ7224 (Figure 4.13), incomplete cancellation of the strong telluric absorptions that overlap this DIB prevent accurate determination of its profile and any small-scale variation that it may exhibit.

λ6203, λ6660 and λ7562 (shown in Figures 4.7, 4.12 and 4.14 respectively) show no variation at the signal-to-noise of the observations, with upper limits on the variability of about 5%. Due to their relative weakness, upper limits on the variability of λ6376 and λ6445 (see Figures 4.9 and 4.10 respectively) are around 9%.

Although the spectrum of the spectral-type standard star υ Sco shows a significant stellar feature at 6379 Å, examination of Figure 4.9 shows a fairly flat residual spectrum and the absence of any 'DIB-shaped' difference between β^1 and β^2 Sco over the width of the DIB absorption. Precluding an accidental cancellation of any variation in this DIB by a stellar feature, it appears to be different by no more than 3% between β^1 and β^2 Sco.

The equivalent widths of Na D_1 and K I λ7699, whose profiles are shown in Figures 4.18 and 4.19 highlight the excess of these trace neutrals in β^2 over β^1 at the level expected for the variations in K I column density (21 ± 30%) published by Lauroesch & Meyer (1999) and given in Table 4.3.

4.3.3 ν Sco

The ν Sco system lies 134 ± 20 pc away as determined from the Hipparcos parallax (Perryman & ESA 1997) and is part of the Sco OB2 association. Separated by 41.1″, the sky-projected distance between ν^1 and ν^3 Sco is approximately 5500 AU. The fact that the ν Sco system illuminates a blue reflection nebula (see Figure 1 on page 12) indicates that it is probably associated with the 145 pc distant H I gas component

identified in Sco OB2 by Cappa de Nicolau & Poeppel (1986).

Of spectral type B2 IV, ν^1 Sco shows very similar spectral features to the standard star υ Sco (seen in Figures 4.1 to 4.3). Unfortunately, the later-type B8/9 V star ν^3 Sco exhibits a plethora of stellar absorption lines, similar to γ Mus (see Figures 4.1 to 4.3) throughout most of the wavelength ranges of interest. The only strong DIBs not severely contaminated by stellar lines in the ν^3 Sco spectrum are λ6203 and possibly λ6379 and λ6614 (see Figures 4.23, 4.25 and 4.26). Examples of the recorded spectra and residuals are shown for the stronger DIBs in Figures 4.20 to 4.26. The large difference in the λ5780 profile between ν^1 and ν^3 Sco shown in Figure 4.27 is almost certainly a result of the stellar features in the ν^3 Sco spectrum, combined with the continuum normalisation. However, the shape of the residual spectrum across the wavelength range of λ5780 (Figure 4.21) shows a close enough resemblance to the normal λ5780 profile that it is possible that stellar contamination is not severe. This is mere speculation given the similarity of the residual feature to other residual features of stellar origin, for example at 5784 Å.

The residual plot in Figure 4.23 indicates that the ν^1 Sco λ6203 DIB is slightly stronger than towards ν^3 Sco, but this difference lies within the error estimate. The residual plot for λ6379 (Figure 4.25) shows a feature of the correct width (*i.e.* the width of λ6379, $\sim$ 0.5 Å) at 6379 Å, consistent with this DIB being $7.2 \pm 2.3\%$ stronger towards ν^1 than ν^3 Sco (Table 4.4). However, from the υ Sco and α Pav spectra (of similar spectral type to ν^1 Sco) in Figure 4.3, it is seen that a contaminating stellar feature is likely at the wavelength of λ6379.

The most convincing case for small-scale structure variation in the ν Sco DIBs is for λ6614 (shown in Figure 4.26). Notwithstanding a difference in the intrinsic DIB profile between the two sightlines, there appears to be a stellar blend on the red side of the DIB that must at least partially overlap the ν^3 Sco λ6614 profile. The residual λ6614 spectrum has a steep blue side however, of the shape expected for an enhancement of the overall λ6614 strength in ν^3 Sco and is unlikely to be caused by stellar features. Measuring the equivalent width of the residual spectrum over the wavelength range of the ν^1 Sco λ6614 DIB gives a 14.1 mÅ difference, which amounts to a $26 \pm 2.4\%$ enhancement in DIB strength towards ν^3 Sco as shown in Table 4.4.

The K I λ7699 and Na I D_1 lines are both significantly stronger towards ν^1 Sco than ν^3 Sco (see Figures 4.28 & 4.29 and Table 4.4) and are largely unaffected by stellar

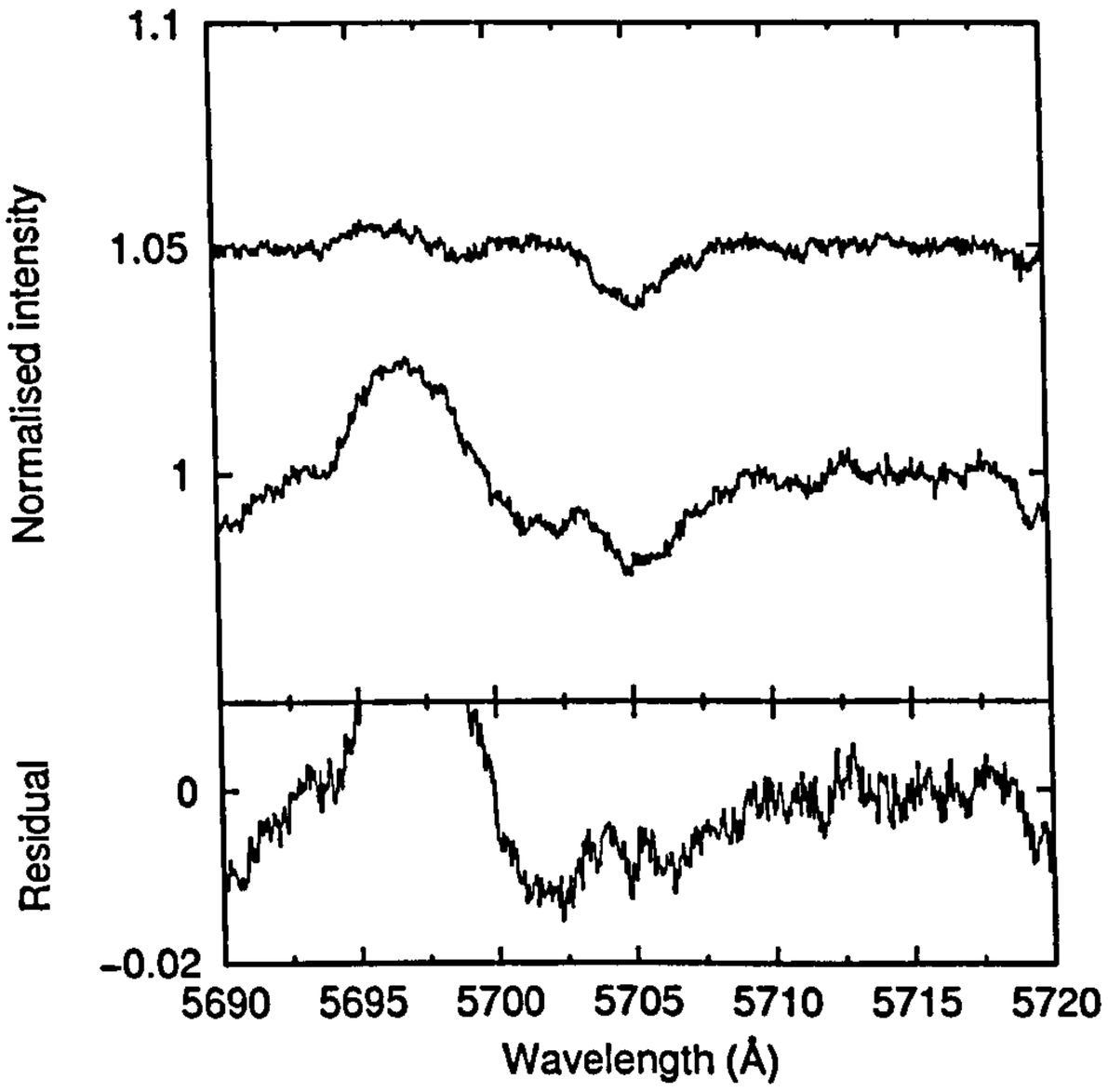

Figure 4.20: Spectra of $\lambda 5705$ recorded towards ν^1 Sco (top) and ν^3 Sco (middle), telluric-corrected and normalised with straight line continua. Lower trace shows the residual intensities of ν^3 Sco – ν^1 Sco.

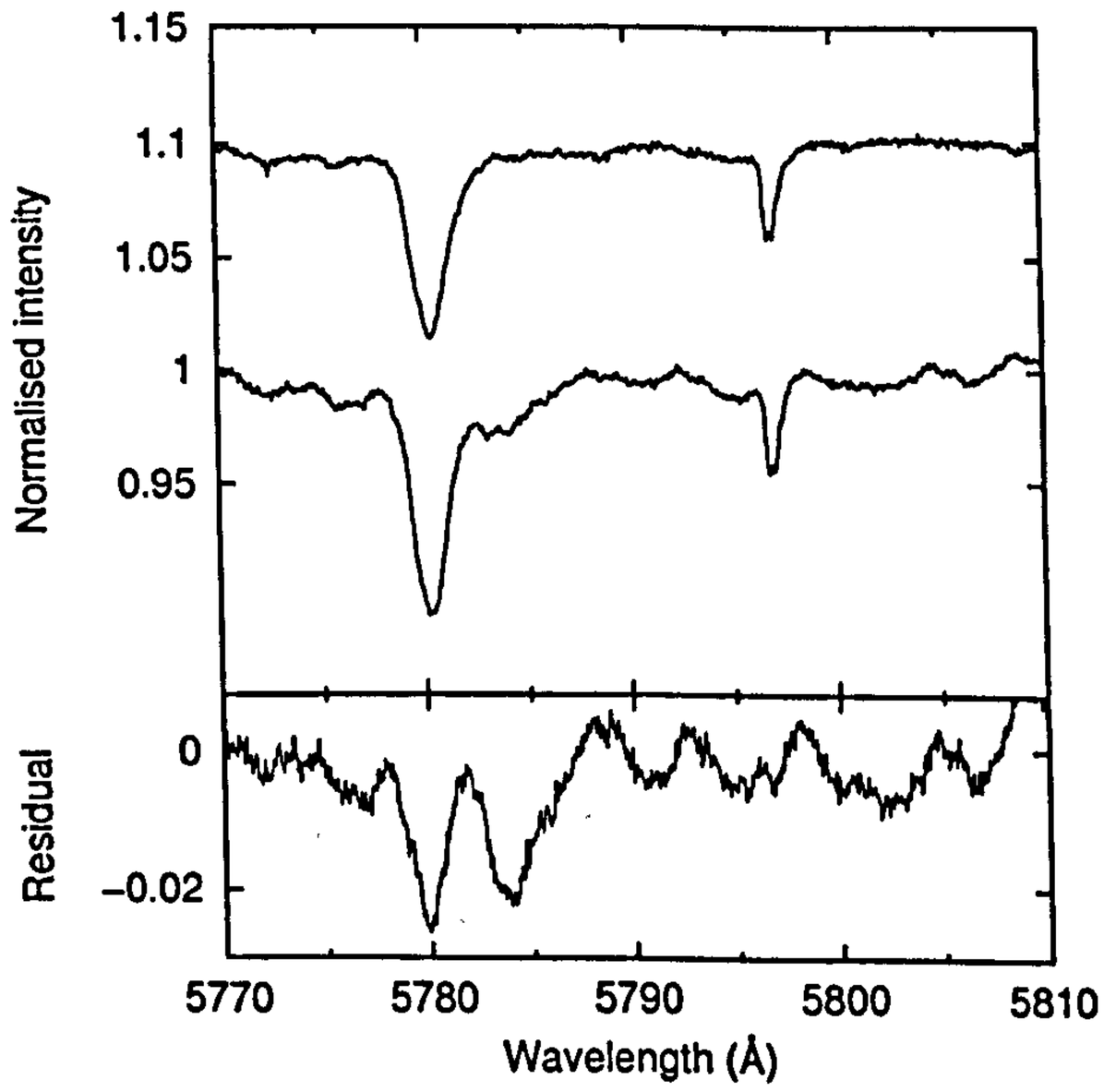

Figure 4.21: Spectra of $\lambda 5780$ and $\lambda 5797$ recorded towards ν^1 Sco (top) and ν^3 Sco (middle), telluric-corrected and normalised with straight line continua. Lower trace shows the residual intensities of ν^3 Sco – ν^1 Sco.

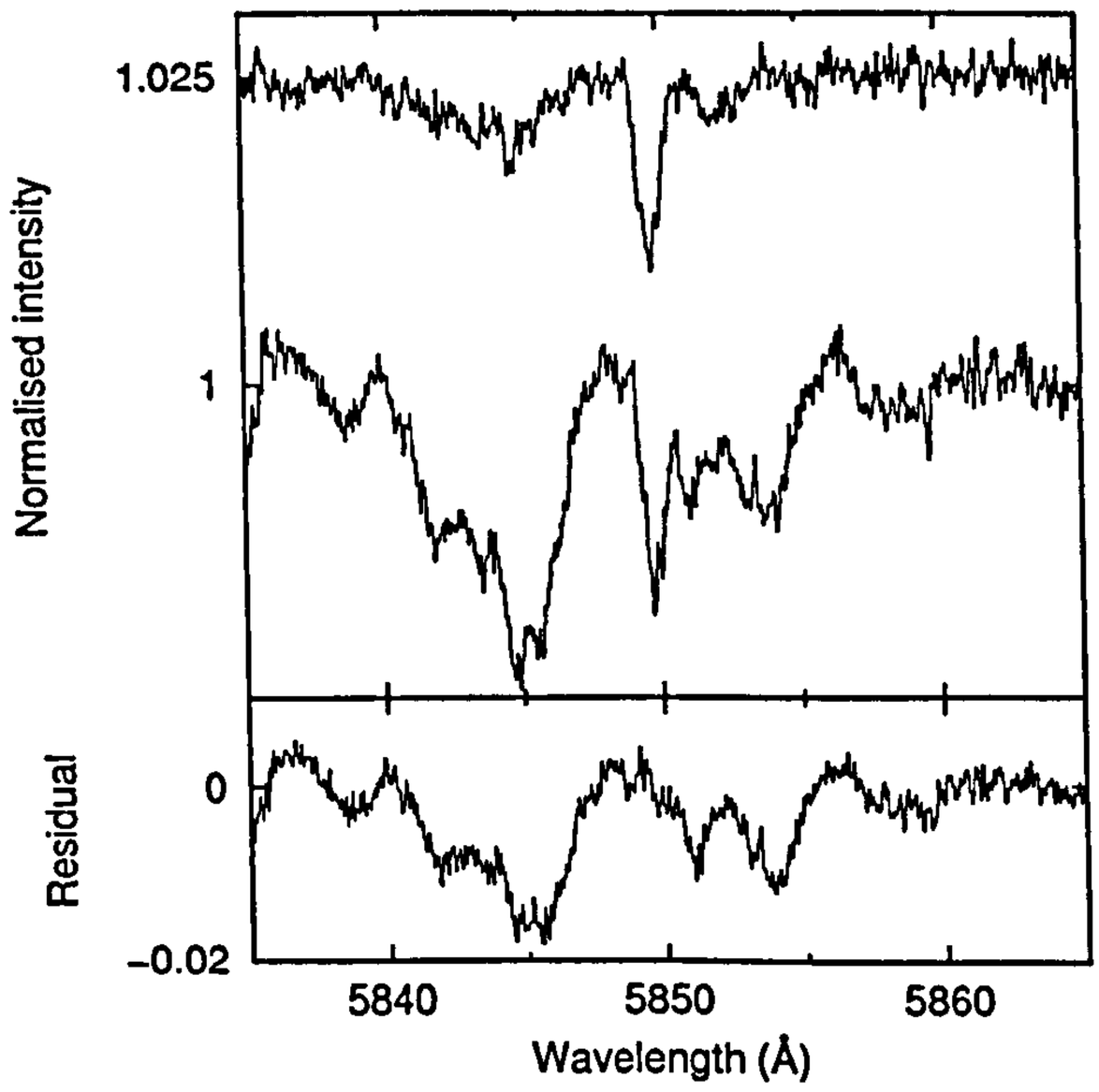

Figure 4.22: Spectra of λ5850 recorded towards ν^1 Sco (top) and ν^3 Sco (middle), telluric-corrected and normalised with straight line continua. Lower trace shows the residual intensities of ν^3 Sco – ν^1 Sco.

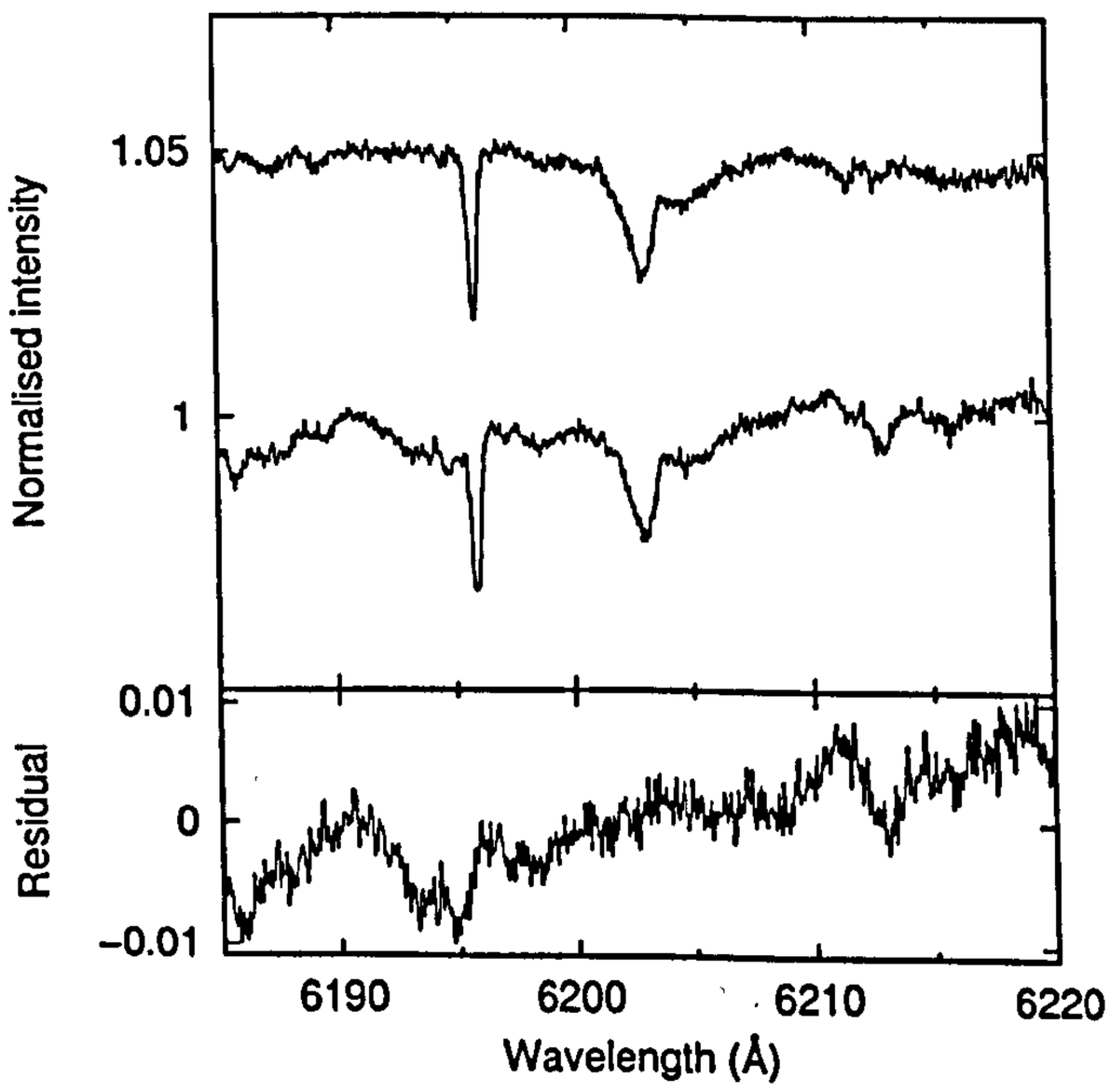

Figure 4.23: Spectra of λ6196 and λ6203 recorded towards ν^1 Sco (top) and ν^3 Sco (middle), telluric-corrected and normalised with low-order polynomial continua. Lower trace shows the residual intensities of ν^3 Sco – ν^1 Sco.

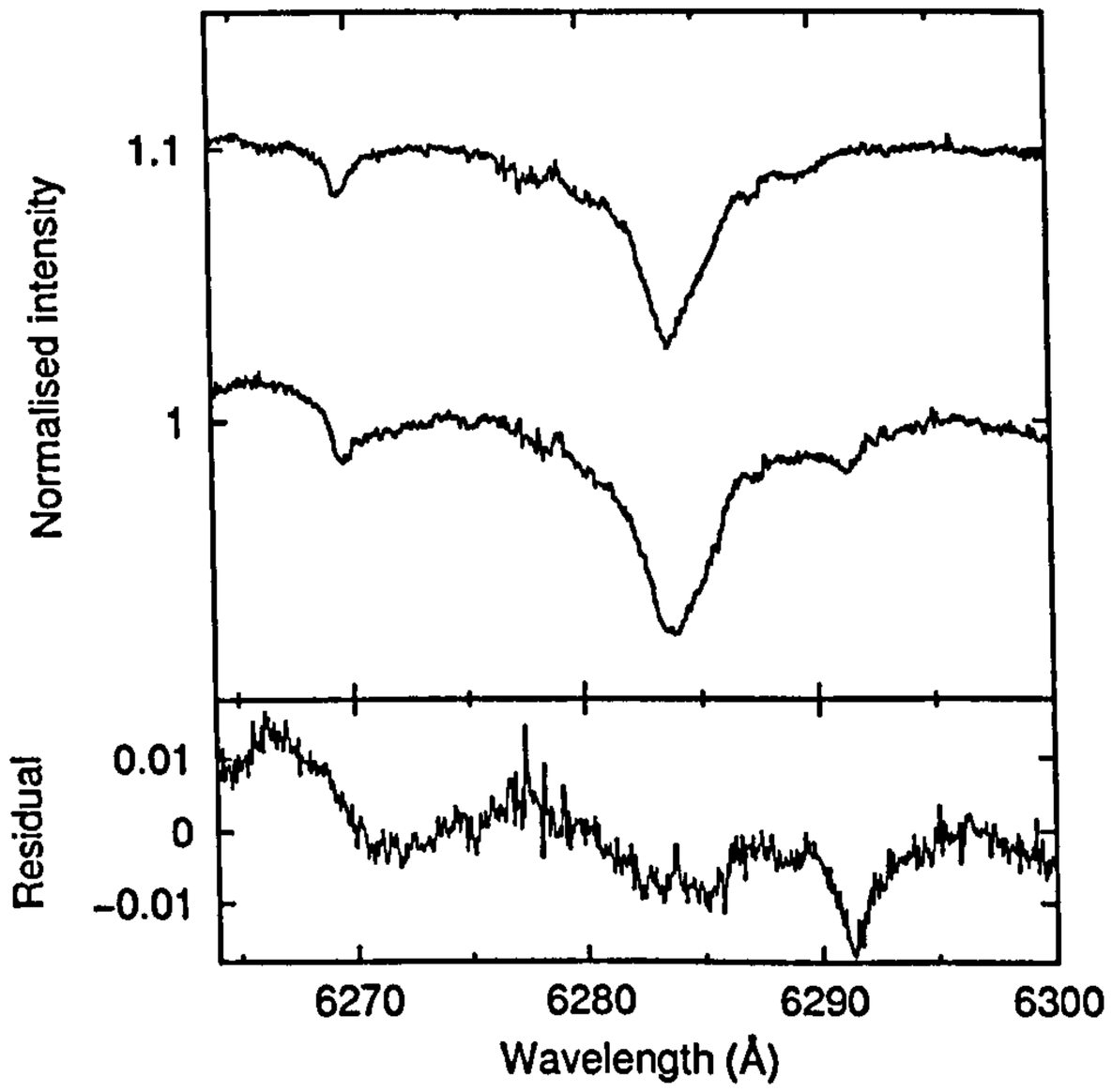

Figure 4.24: Spectra of λ6284 recorded towards ν^1 Sco (top) and ν^3 Sco (middle), telluric-corrected and normalised with straight line continua. Lower trace shows the residual intensities of ν^3 Sco – ν^1 Sco.

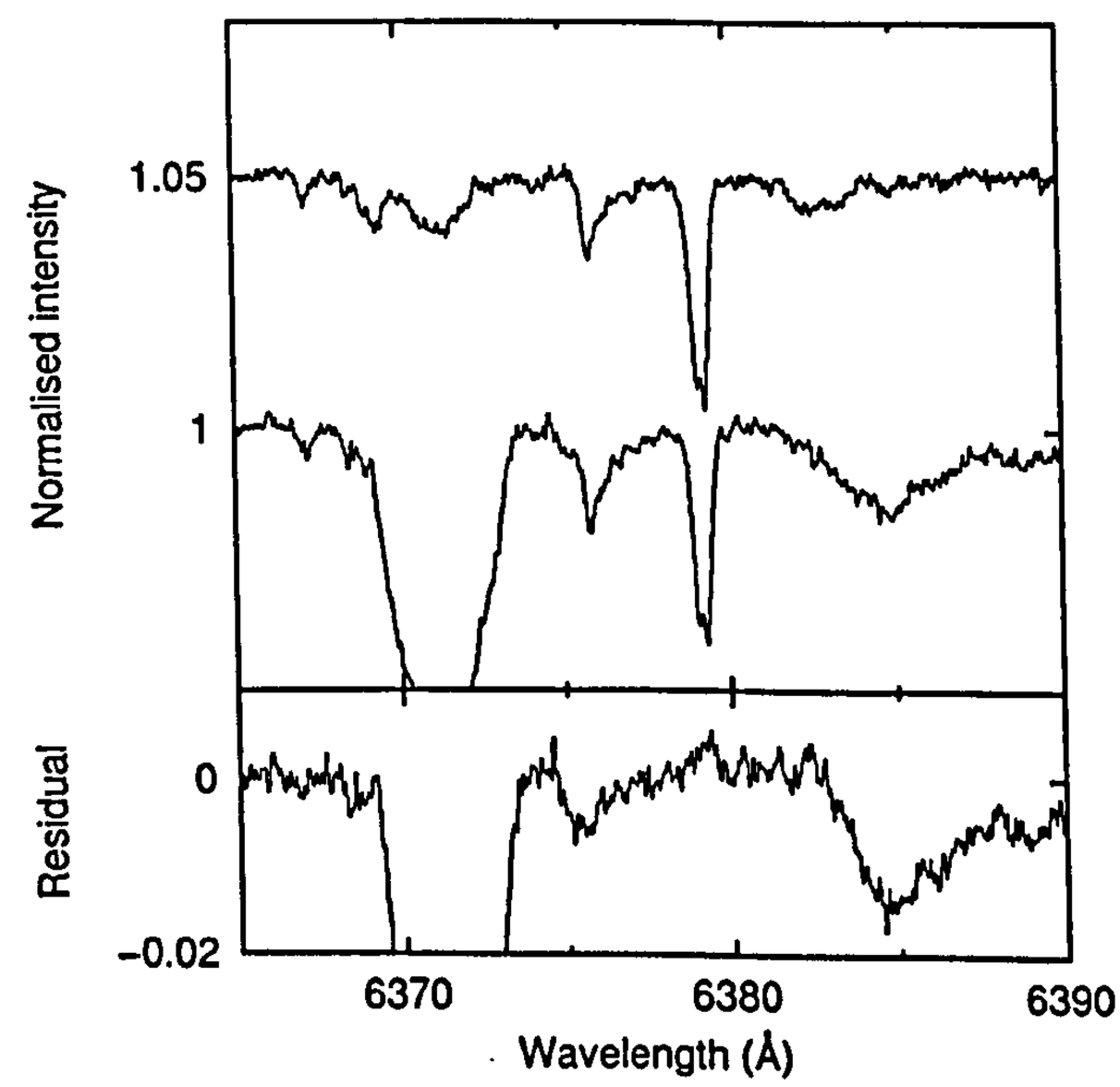

Figure 4.25: Spectra of λ6376 and λ6379 recorded towards ν^1 Sco (top) and ν^3 Sco (middle), telluric-corrected and normalised with straight line continua. Lower trace shows the residual intensities of ν^3 Sco – ν^1 Sco.

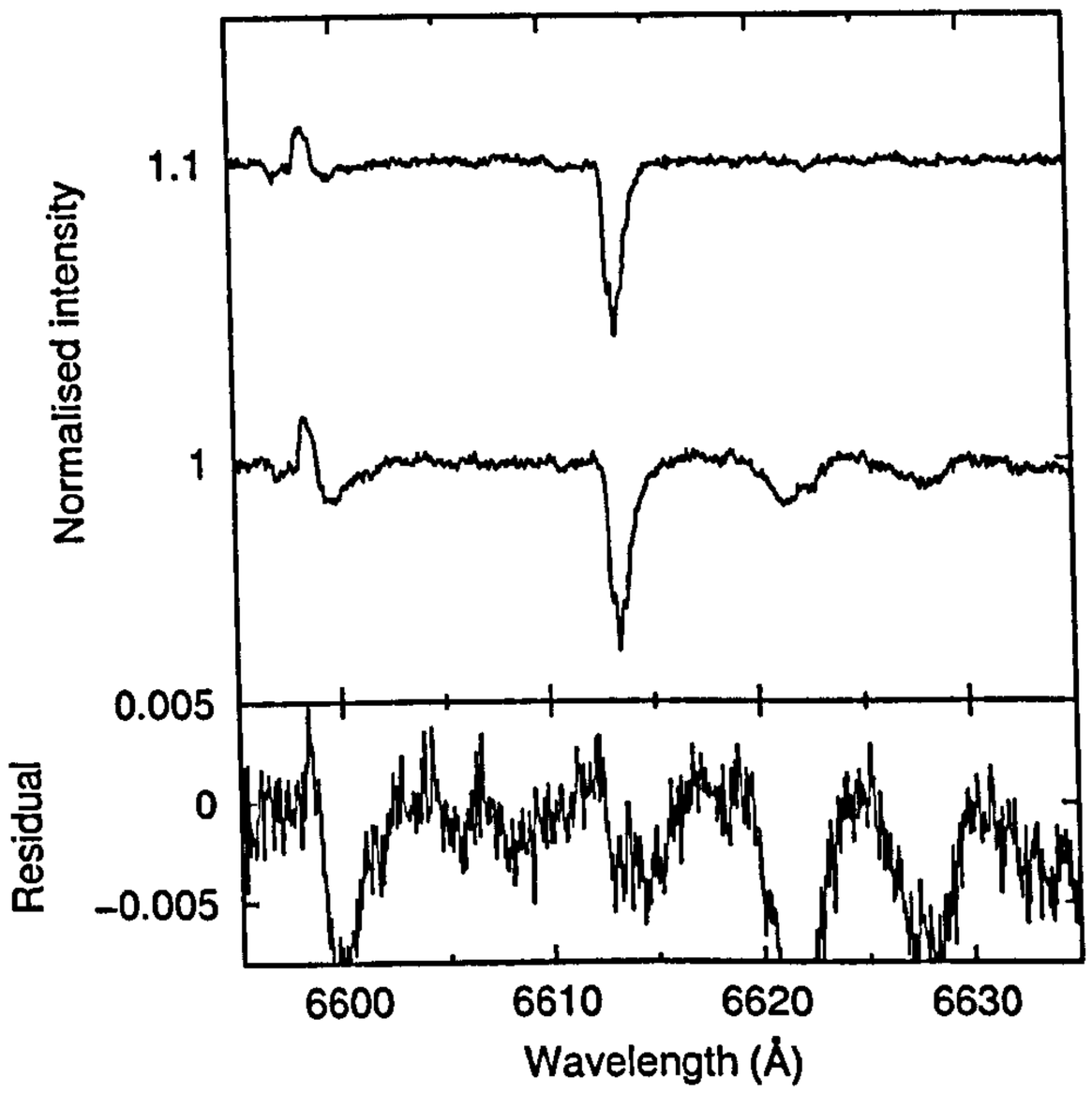

Figure 4.26: Spectra of λ6614 recorded towards ν^1 Sco (top) and ν^3 Sco (middle), telluric-corrected and normalised with straight line continua. Lower trace shows the residual intensities of ν^3 Sco – ν^1 Sco.

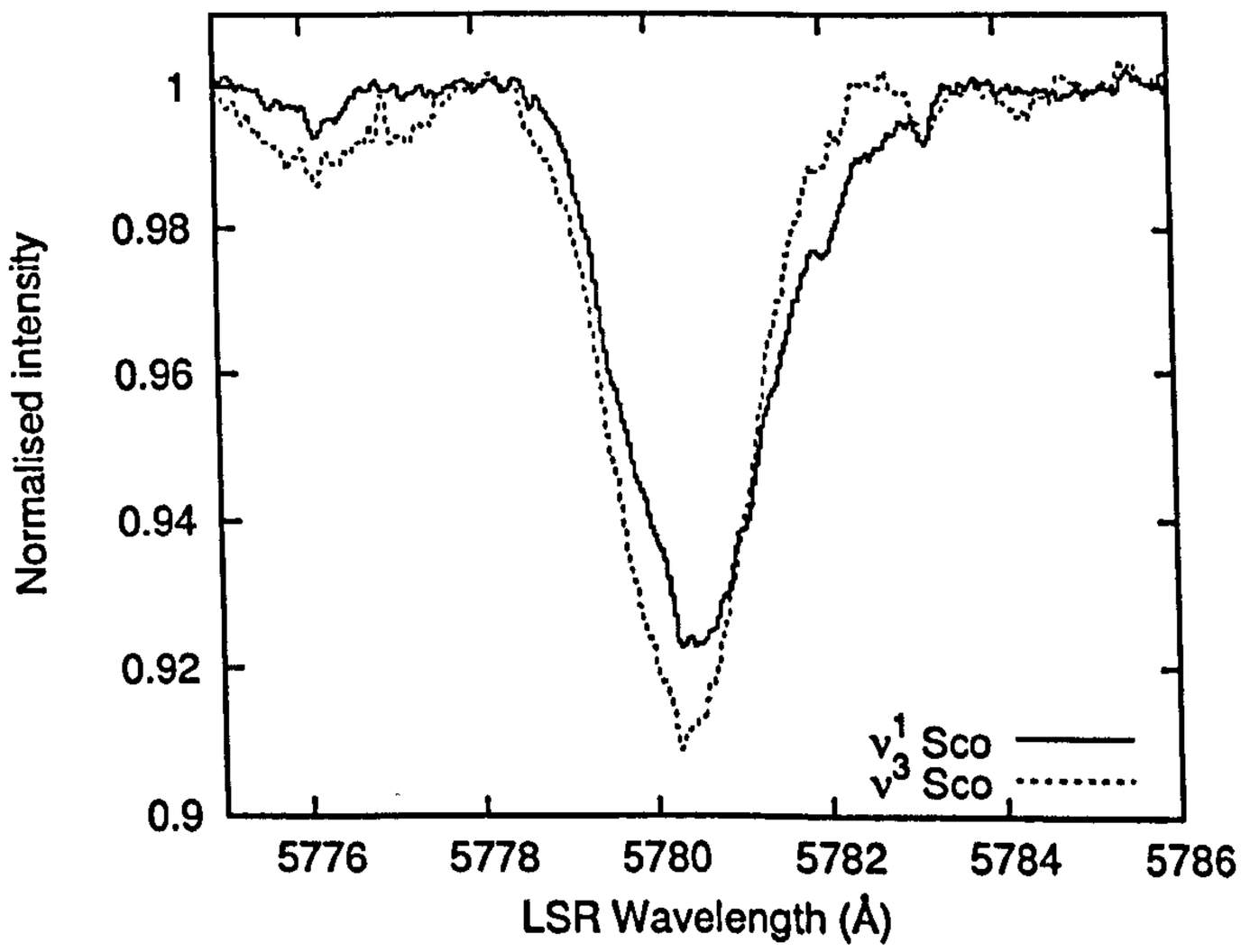

Figure 4.27: Overlaid $\nu^{1,3}$ Sco λ5780 spectra, telluric-corrected and normalised with low-order polynomial continua.

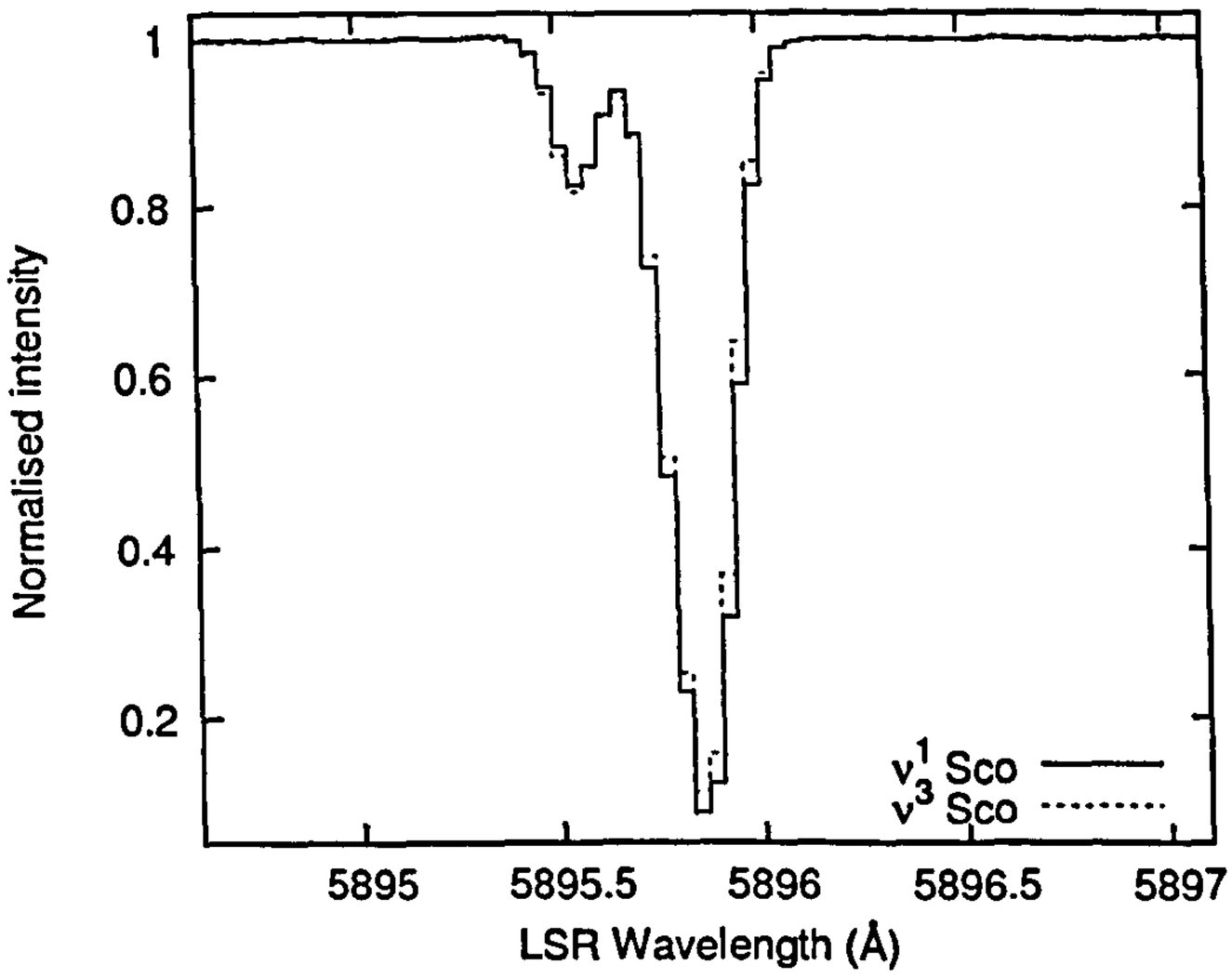

Figure 4.28: Overlaid $\nu^{1,3}$ Sco Na I D_1 spectra, telluric-corrected and normalised with low-order polynomial continua.

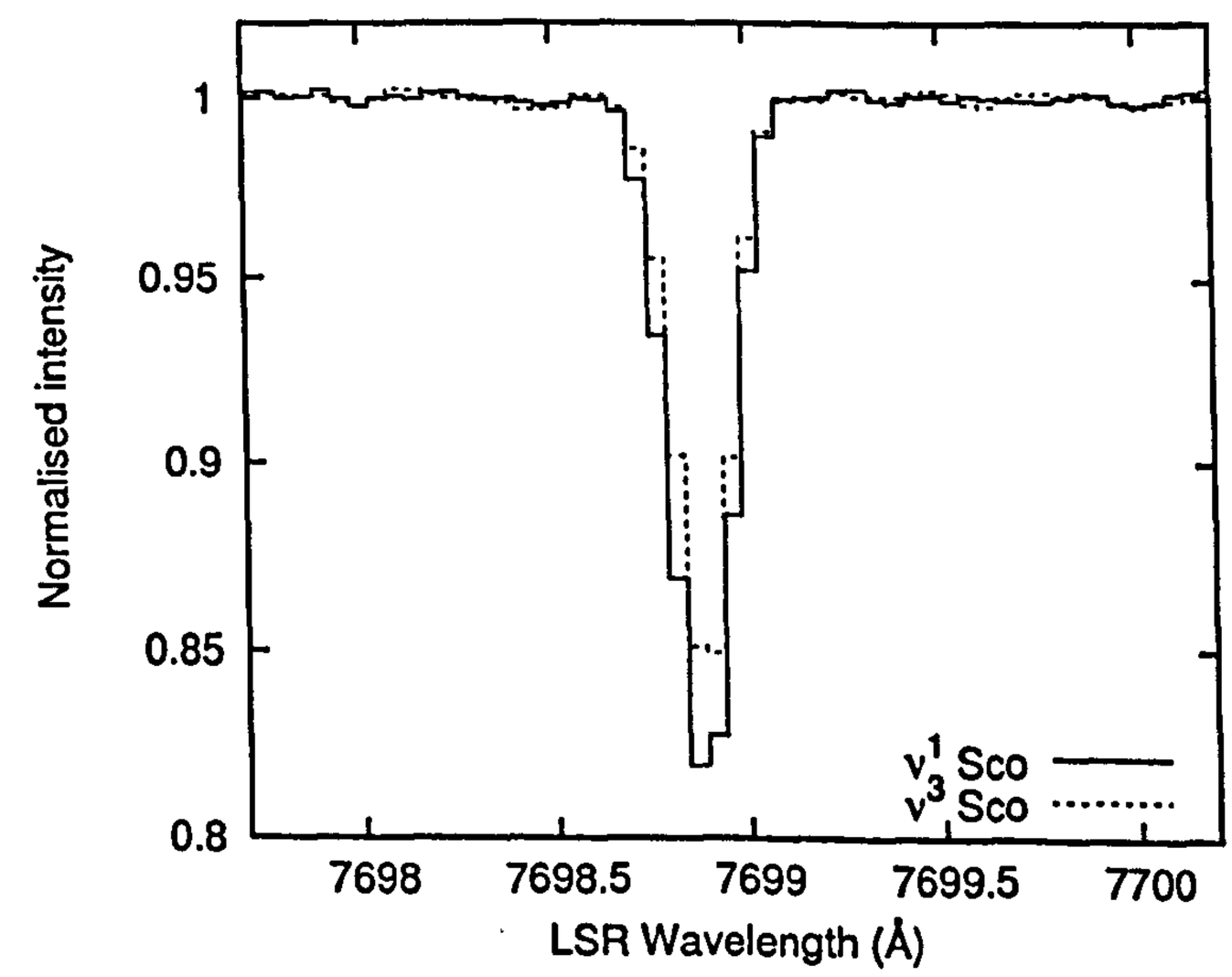

Figure 4.29: Overlaid $\nu^{1,3}$ Sco K I λ7699 spectra, telluric-corrected and normalised with low-order polynomial continua.

Feature	W_λ (mÅ) ν^1 Sco	W_λ (mÅ) ν^3 Sco	$\delta(\nu^3/\nu^1)$ (%)	Blend?
λ5705	39.7	43.6	9.8 (7.5)	Y
λ5780	161	176	9.3 (1.7)	Y
λ5797	31	35.8	15 (3.4)	Y
λ5850	11.9	10.3	-13 (8.4)	Y
λ6196	13.8	12	-13 (3.5)	Y
λ6203	65	67.2	3.4 (7.8)	N
λ6284	361	390.4	8.1 (1.4)	Y
λ6376	11	7.8	-29 (6.6)	Y
λ6379	29.2	27.1	-7.2 (2.3)	?
λ6426	2.6	9.1	250 (82)	Y
λ6439	2.7	2.7	<39	Y
λ6445	6.9	6.9	<13	Y
λ6614	54.7	68.8	26 (2.4)	Y
λ6660	9.2	13.8	50 (9.1)	Y
λ7224	65	65	<2.2	T
λ7562	30.5	32.9	7.7 (8.3)	Y
K I λ7699	36.1	29	-20 (1.0)	
Na I D_1	200.6	193.2	-3.7 (0.1)	
log N(K I)	11.39	11.30	23 (46)	

Table 4.4: Equivalent widths of interstellar features measured towards $\nu^{1,3}$ Sco. $\delta(\nu^3/\nu^1)$ is the percentage *excess* of ν^3 Sco measurements compared to ν^1 Sco, with error estimates given in parentheses. N(K I) data are from Lauroesch & Meyer (1999). In the last column, 'Y' indicates a definite or probable stellar blend contaminating the DIB spectra, 'N' indicates improbable or absent stellar blend and '?' is for indeterminate cases, 'T' indicates severe telluric contamination of results.

blends due to their combination of depth and narrowness.

4.3.4 ρ Oph

The ρ Oph system consists of five young, early-to-mid B-type dwarf stars (Dommanget & Nys 1994). Components A and B are separated by 3.1″ which is sufficient for the stars to be resolved in ground-based observations. During observations of the ρ Oph system, the seeing FWHM was $\simeq$ 0.95″, which converts to a separation between ρ Oph A and B of $\approx 8\sigma_{\rm seeing}$ and ensured negligible overlap in their light distributions. The separation between A and C is 150″, between A and D 169″ and between C and D 207″. An annotated image of the ρ Oph system is shown in Figure 4.30

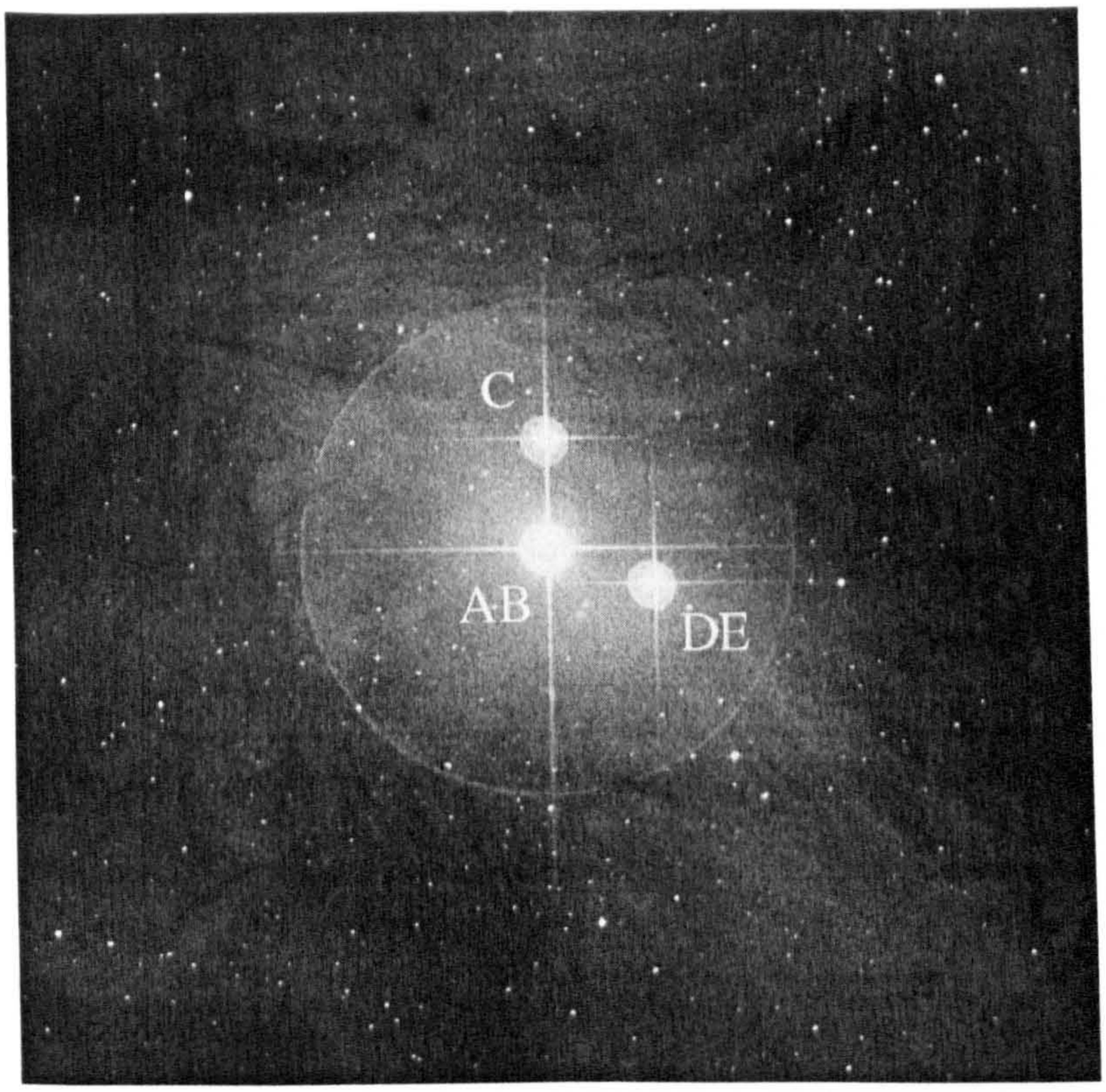

Figure 4.30: Annotated image of the early B-type multiple star system ρ Oph obtained from the Digitized Sky Survey. The image resolution is insufficient to resolve components A and B or components D and E. Reflection nebulosity is due to interstellar matter associated with the system. The Digitized Sky Surveys were produced at the Space Telescope Science Institute under U.S. Government grant NAG W-2166. The images of these surveys are based on photographic data obtained using the Oschin Schmidt Telescope on Palomar Mountain and the UK Schmidt Telescope. The plates were processed into the present compressed digital form with the permission of these institutions.

Component E is separated from D by only 0.6″, so these two stars cannot be observed independently using Earth-based telescopes without adaptive optics. During observation, the slit was positioned over the peak of the ρ Oph D + E light distribution. The visual magnitudes of D and E are 6.9 and 8.1 mag respectively (Dommanget & Nys 1994) so that D dominates the recorded spectrum.

Hipparcos parallax data (Perryman & ESA 1997) provide a distance to ρ Oph of between 115 and 170 pc for the components A + B (denoted AB hereafter), C and D + E (denoted DE hereafter). Using a distance to AB of 120 pc results in a sky-projected separation of approximately 370 AU between A and B; $\sim 18,000$ AU between AB and C; $\sim 20,000$ AU between AB and DE; and $\sim 25,000$ AU between C and DE.

In ρ Oph, the search for evidence of SSS in diffuse interstellar band spectra is greatly

facilitated by the similarities between the stellar spectra and a general lack of significant contaminating stellar photospheric features, epecially for ρ Oph A and B. Table 4.5 shows measurements of the equivalent widths of the 16 strongest narrow DIBs.

In the following discussion, DIB equivalent widths labelled $W'_\lambda(\Omega)$, where $\Omega = w$, x, y or z, were measured directly from the spectra. The indices w, x, y and z represent different arbitrary members of the ρ Oph system. Similar to the method employed for β Sco and the other *binary* systems, when DIB equivalent widths were found to differ between two component sightlines by $\lesssim$ 10%, the average was taken of the equivalent widths measured for each component (*i.e.* $W'_\lambda(w) + W'_\lambda(x)$). Differences between the $W'_\lambda(\Omega)$ were measured from the residual plots (Figures 4.31 to 4.41) then divided by two and applied to the relevant sightlines as an equivalent width correction. Where three components had mutually very similar $W'_\lambda(\Omega)$ ($\lesssim$ 10% different), the three equivalent widths $W_\lambda(\Omega)$ for $\Omega = x$, y, or z were calculated according to

$$W_\lambda(z) = \frac{W'_\lambda(x) + W'_\lambda(y)}{2} + \frac{[W_\lambda(z) - W_\lambda(x)]_R}{2} + \frac{[W_\lambda(z) - W_\lambda(y)]_R}{2}. \qquad (4.2)$$

The subscript R denotes that the quantities in square parentheses were measured from the residual spectra. Mutually consistent, averaged equivalent widths that preserve the SSS *equivalent width differences* were thus obtained, requiring the substitution of different ρ Oph component members as x, y and z to form three different permutations of the above equation. For the fourth component sightline, and for other cases where differences in two $W'_\lambda(\Omega)$ were $\gtrsim$ 10%, permutations of the following equation were used:

$$W_\lambda(z) = \frac{W'_\lambda(w) + W'_\lambda(x) + W'_\lambda(y)}{3} + \frac{[W_\lambda(z) - W_\lambda(w)]_R}{3} + \frac{[W_\lambda(z) - W_\lambda(x)]_R}{3} + \frac{[W_\lambda(z) - W_\lambda(y)]_R}{3}. \qquad (4.3)$$

Thus, equivalent width *differences* between the component sightlines should be accurate, though absolute equivalent widths may be in error by $\lesssim$ 5%. It is the equivalent width differences that are of primary importance for this study. The errors in the residual measurements were calculated as described for β Sco (Section 4.3.2). Due to the similar S/N of the four ρ Oph spectra, the errors on the equivalent widths are almost the same for each sightline, so the error column σ_{W_λ} in Table 4.5 was taken as the average of the individual sightline equivalent width errors.

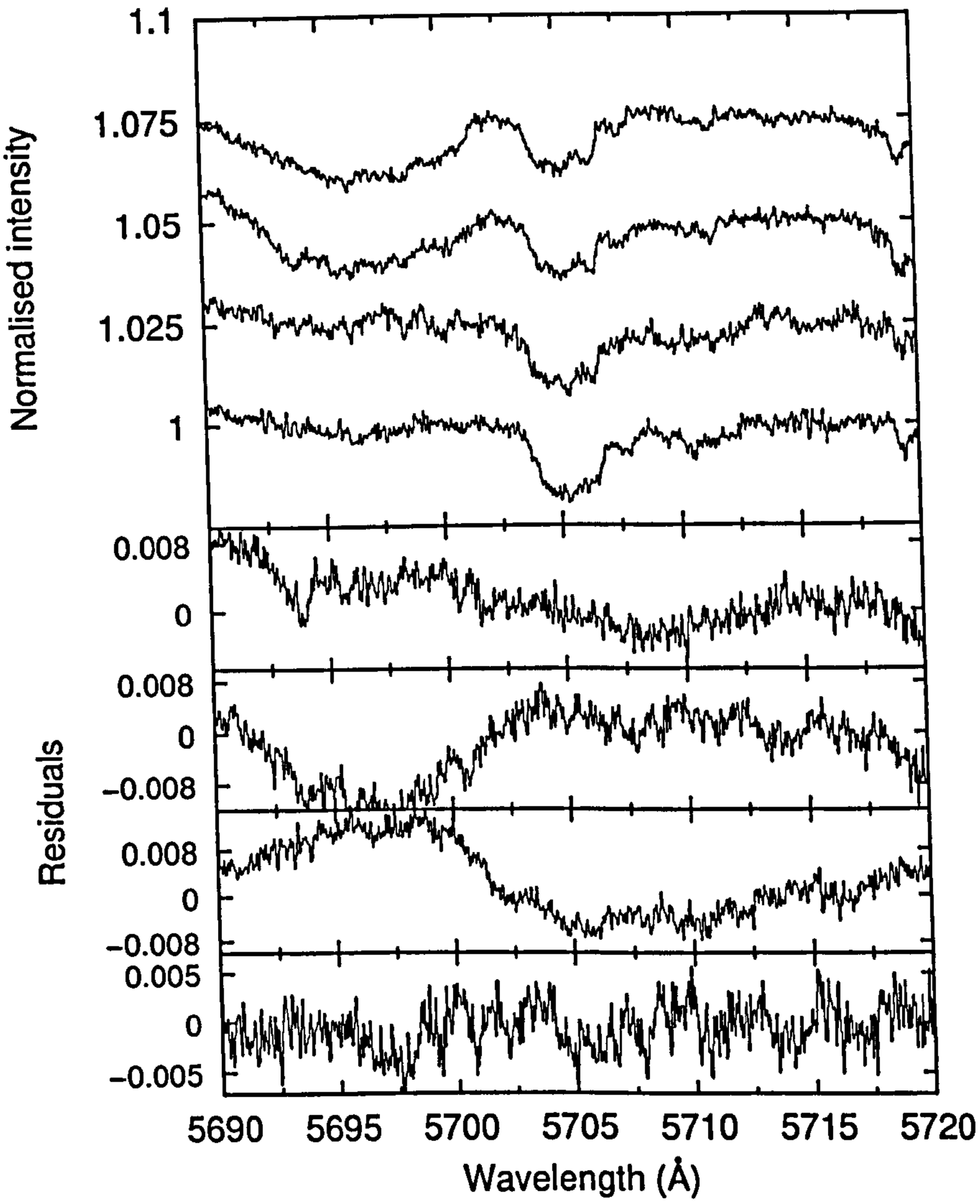

Figure 4.31: Spectra of λ5705 recorded towards (from top to bottom) ρ Oph A, ρ Oph B, ρ Oph C and ρ Oph DE, telluric-corrected and normalised with straight line continua. Lower section of the figure shows the residual intensities (from top to bottom) of (1) ρ Oph B − ρ Oph A, (2) ρ Oph B − ρ Oph C, (3) ρ Oph DE − ρ Oph A and (4) ρ Oph DE − ρ Oph C.

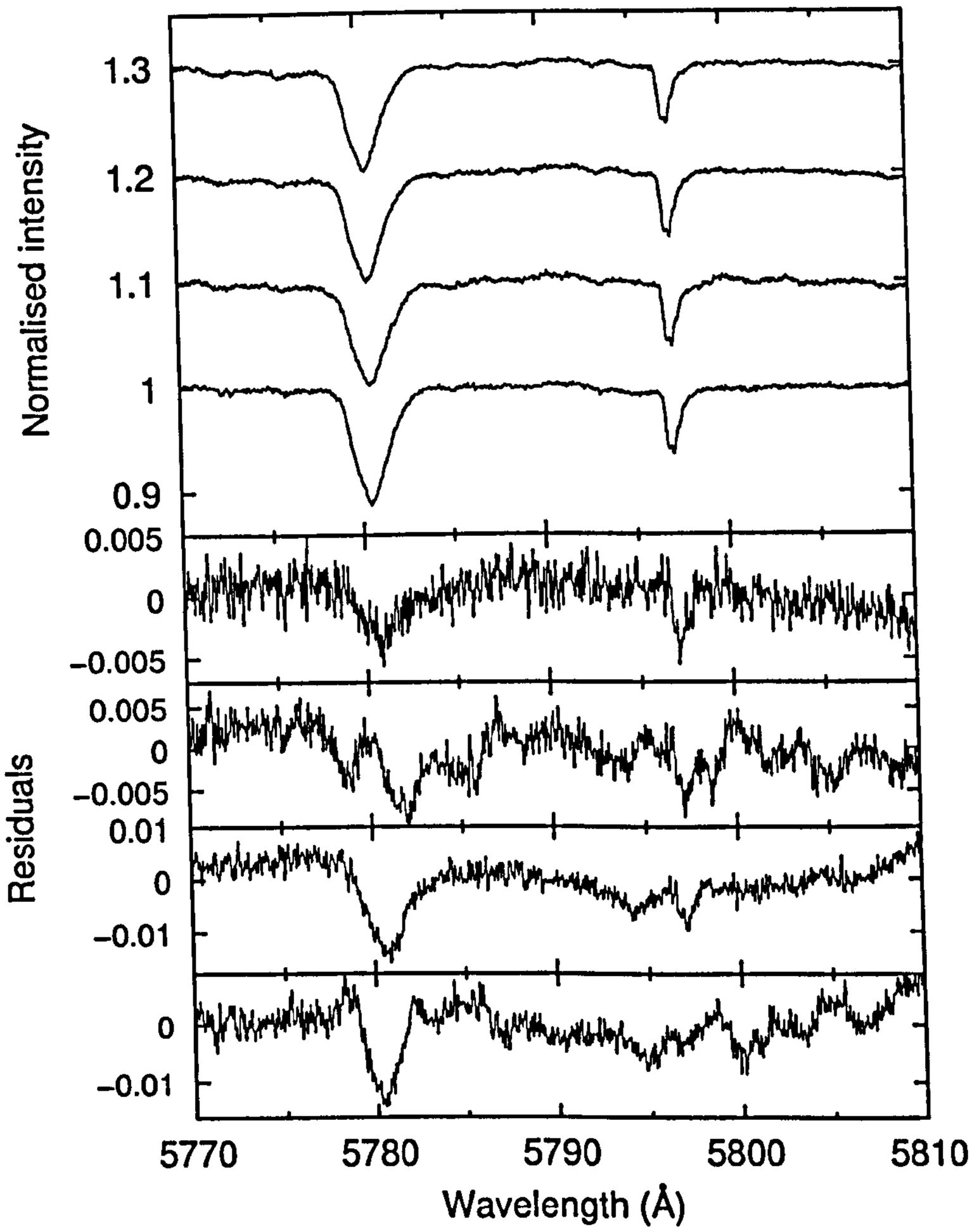

Figure 4.32: Spectra of λ5780 and λ5797 recorded towards (from top to bottom) ρ Oph A, ρ Oph B, ρ Oph C and ρ Oph DE, telluric-corrected and normalised with straight line continua. Lower section of the figure shows the residual intensities (from top to bottom) of (1) ρ Oph B – ρ Oph A, (2) ρ Oph C – ρ Oph A, (3) ρ Oph DE – ρ Oph A and (4) ρ Oph DE – ρ Oph C.

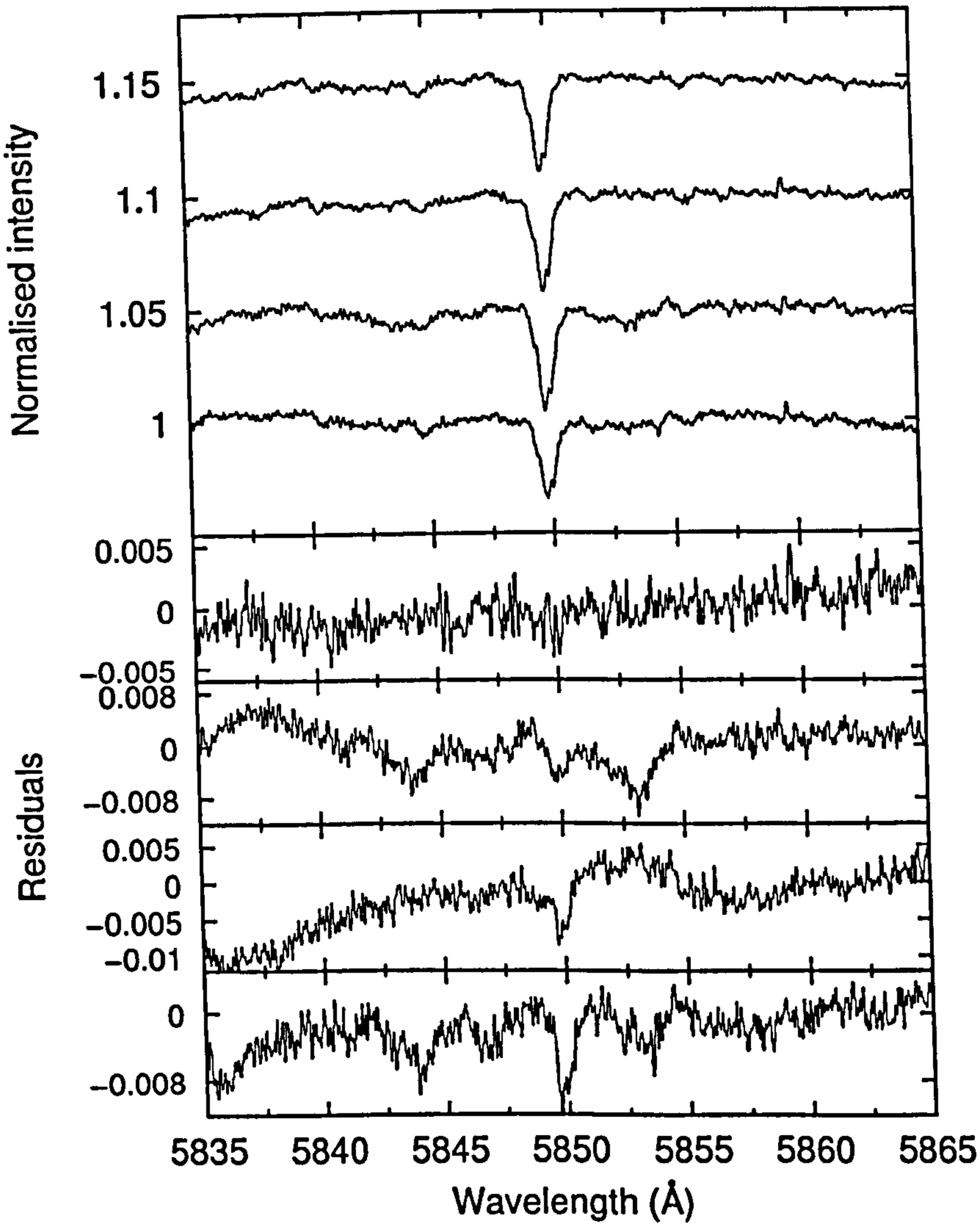

Figure 4.33: Spectra of λ5850 recorded towards (from top to bottom) ρ Oph A, ρ Oph B, ρ Oph C and ρ Oph DE, telluric-corrected and normalised with straight line continua. Lower section of the figure shows the residual intensities (from top to bottom) of (1) ρ Oph B – ρ Oph A, (2) ρ Oph C – ρ Oph A, (3) ρ Oph B – ρ Oph DE and (4) ρ Oph C – ρ Oph DE.

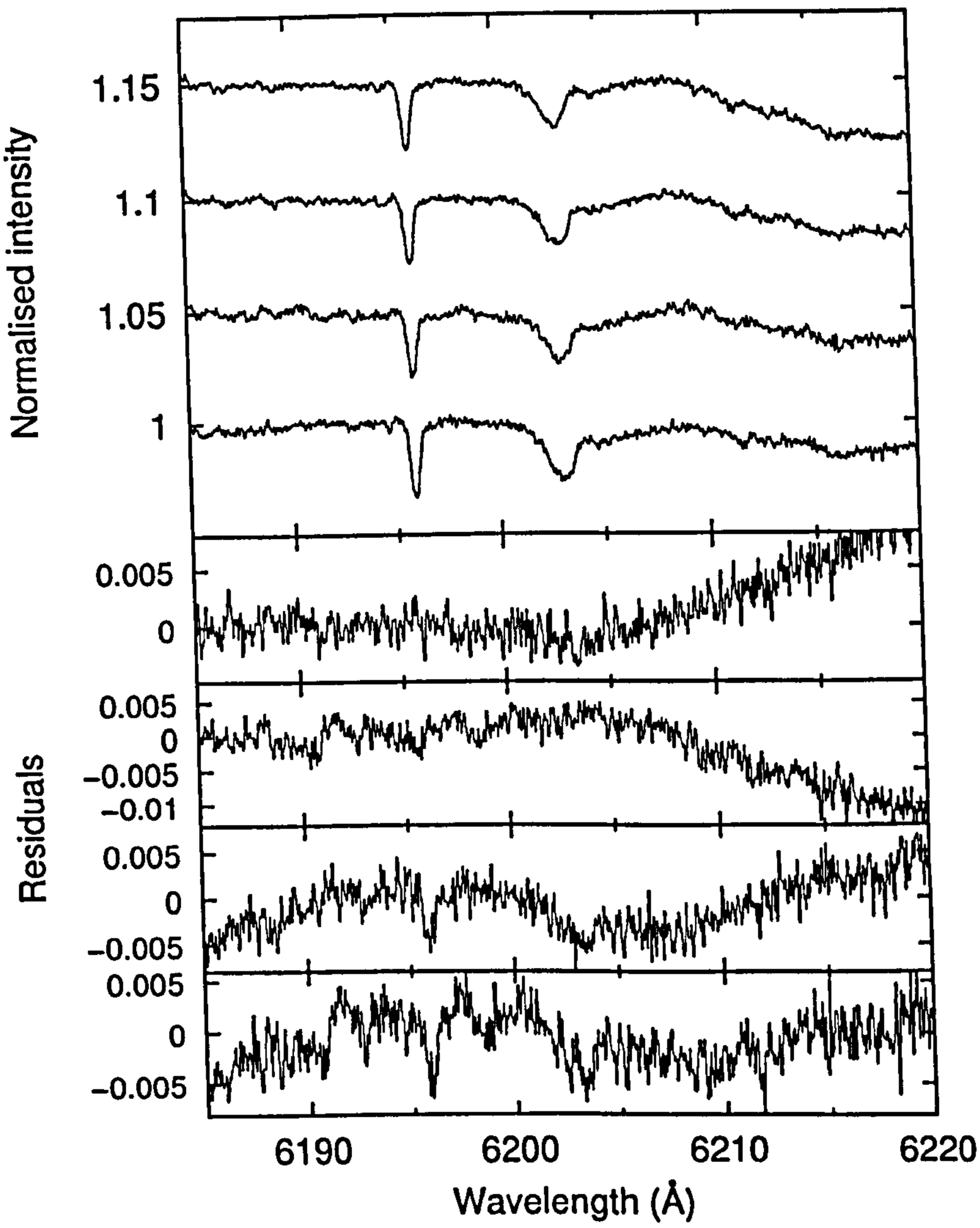

Figure 4.34: Spectra of λ6196 and λ6203 recorded towards (from top to bottom) ρ Oph A, ρ Oph B, ρ Oph C and ρ Oph DE, telluric-corrected and normalised with low-order polynomial continua. Lower section of the figure shows the residual intensities (from top to bottom) of (1) ρ Oph B − ρ Oph A, (2) ρ Oph A − ρ Oph C, (3) ρ Oph DE − ρ Oph B and (4) ρ Oph DE − ρ Oph C.

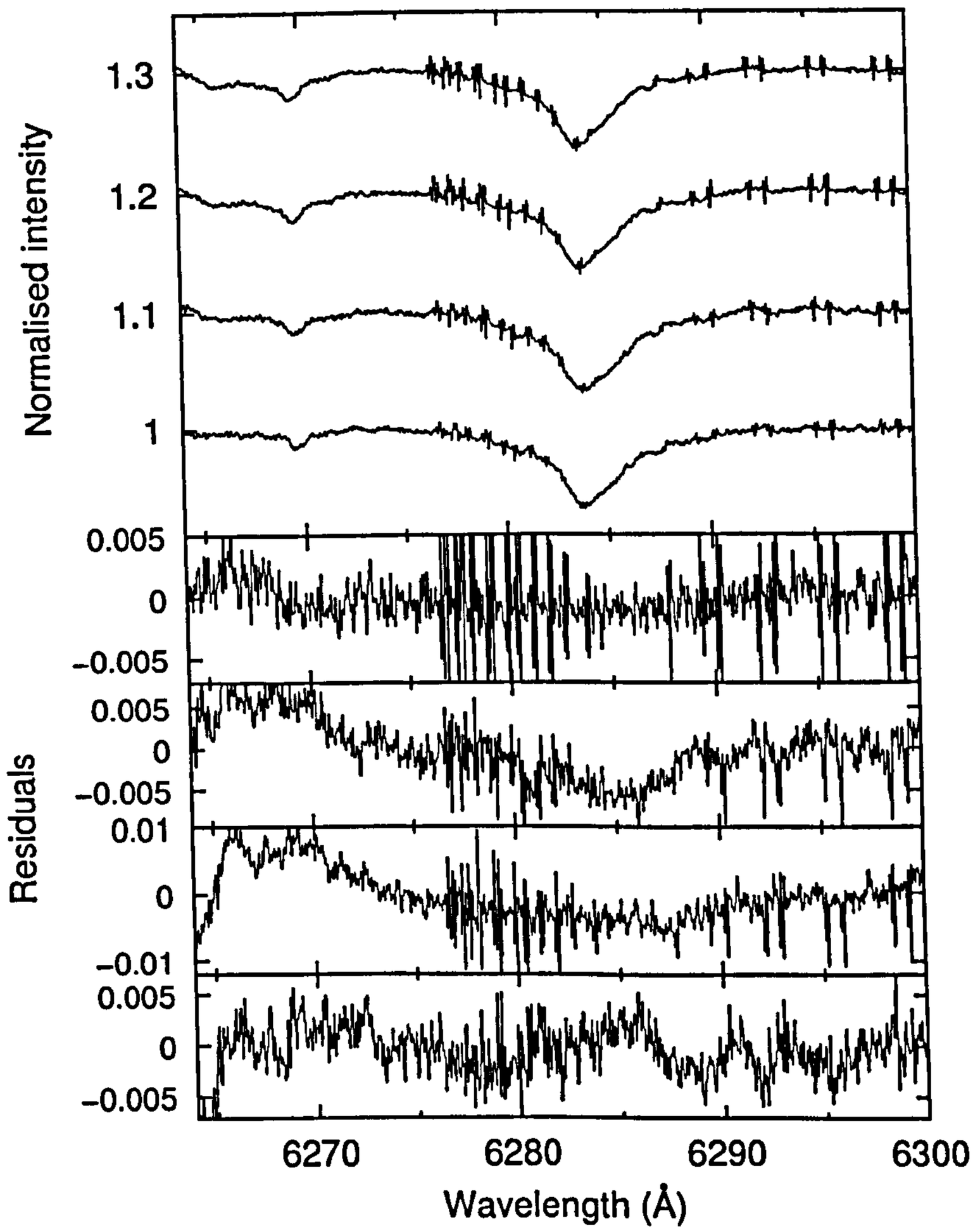

Figure 4.35: Spectra of λ6284 recorded towards (from top to bottom) ρ Oph A, ρ Oph B, ρ Oph C and ρ Oph DE, telluric-corrected and normalised with straight line continua. Lower section of the figure shows the residual intensities (from top to bottom) of (1) ρ Oph B – ρ Oph A, (2) ρ Oph C – ρ Oph A, (3) ρ Oph DE – ρ Oph A and (4) ρ Oph DE – ρ Oph C.

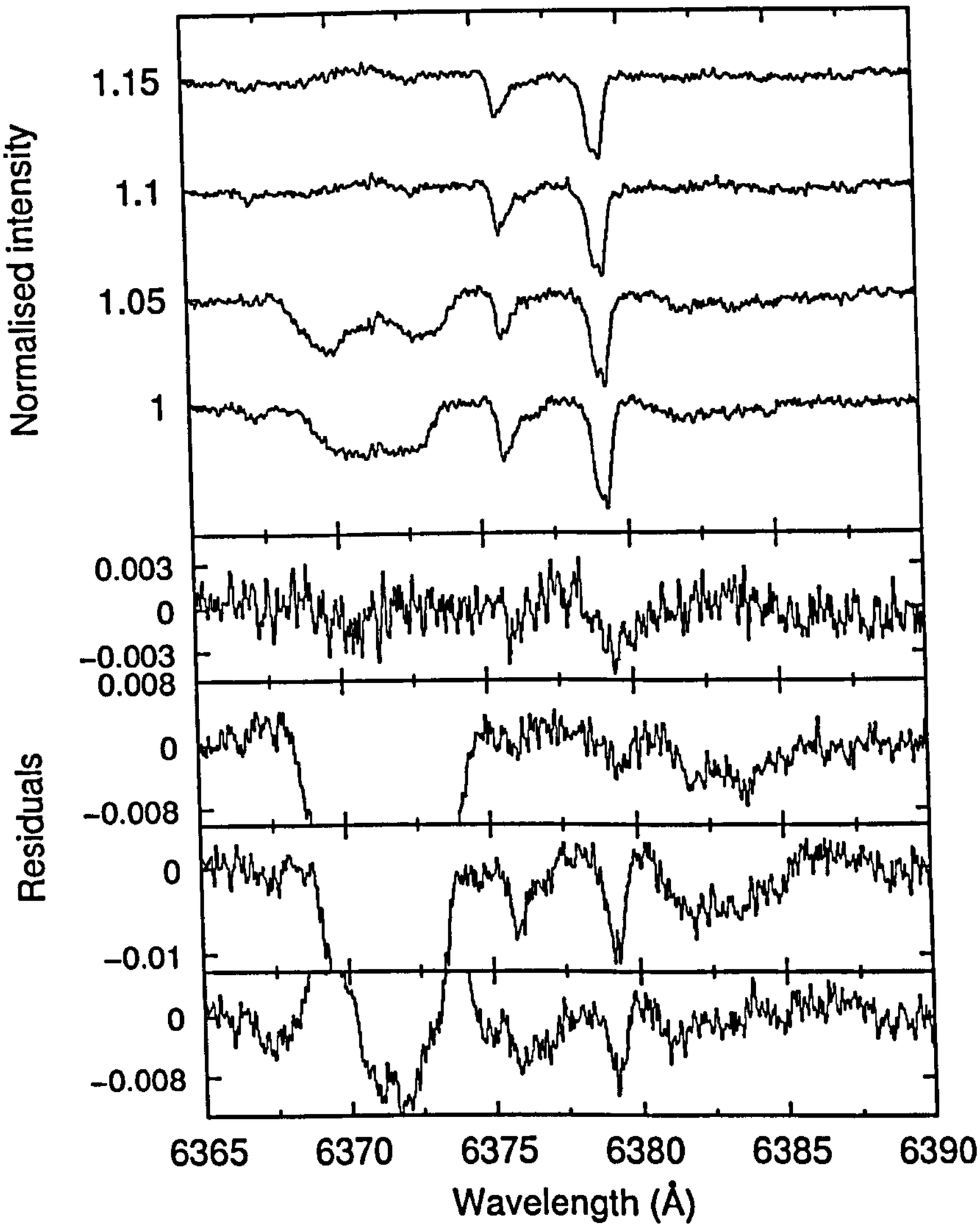

Figure 4.36: Spectra of λ6376 and λ6379 recorded towards (from top to bottom) ρ Oph A, ρ Oph B, ρ Oph C and ρ Oph DE, telluric-corrected and normalised with straight line continua. Lower section of the figure shows the residual intensities (from top to bottom) of (1) ρ Oph B – ρ Oph A, (2) ρ Oph C – ρ Oph A, (3) ρ Oph DE – ρ Oph A and (4) ρ Oph DE – ρ Oph C.

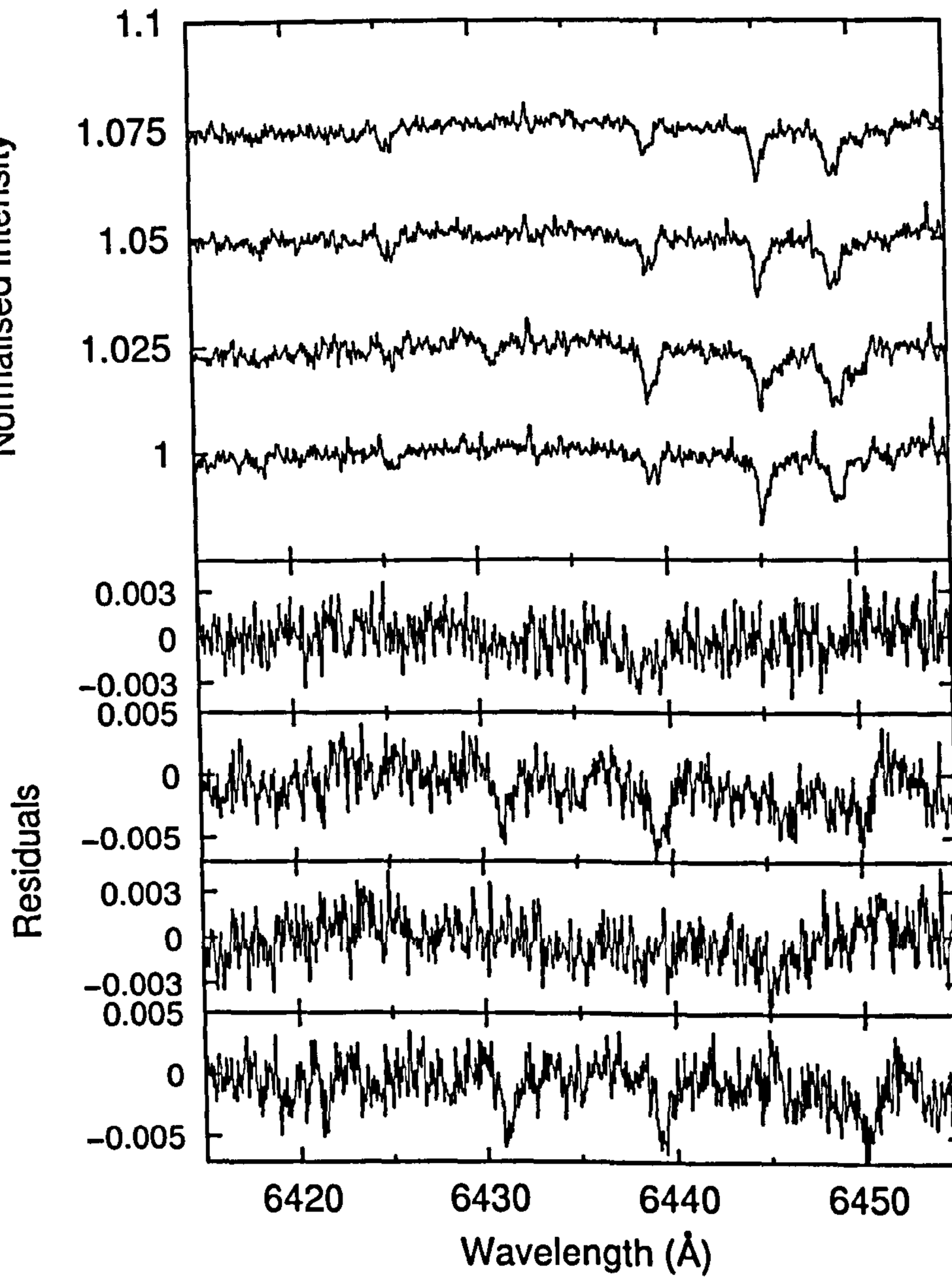

Figure 4.37: Spectra of λ6426, λ6439 and λ6445 recorded towards (from top to bottom) ρ Oph A, ρ Oph B, ρ Oph C and ρ Oph DE, telluric-corrected and normalised with low-order polynomial continua. Lower section of the figure shows the residual intensities (from top to bottom) of (1) ρ Oph B – ρ Oph A, (2) ρ Oph C – ρ Oph A, (3) ρ Oph DE – ρ Oph A and (4) ρ Oph C – ρ Oph DE.

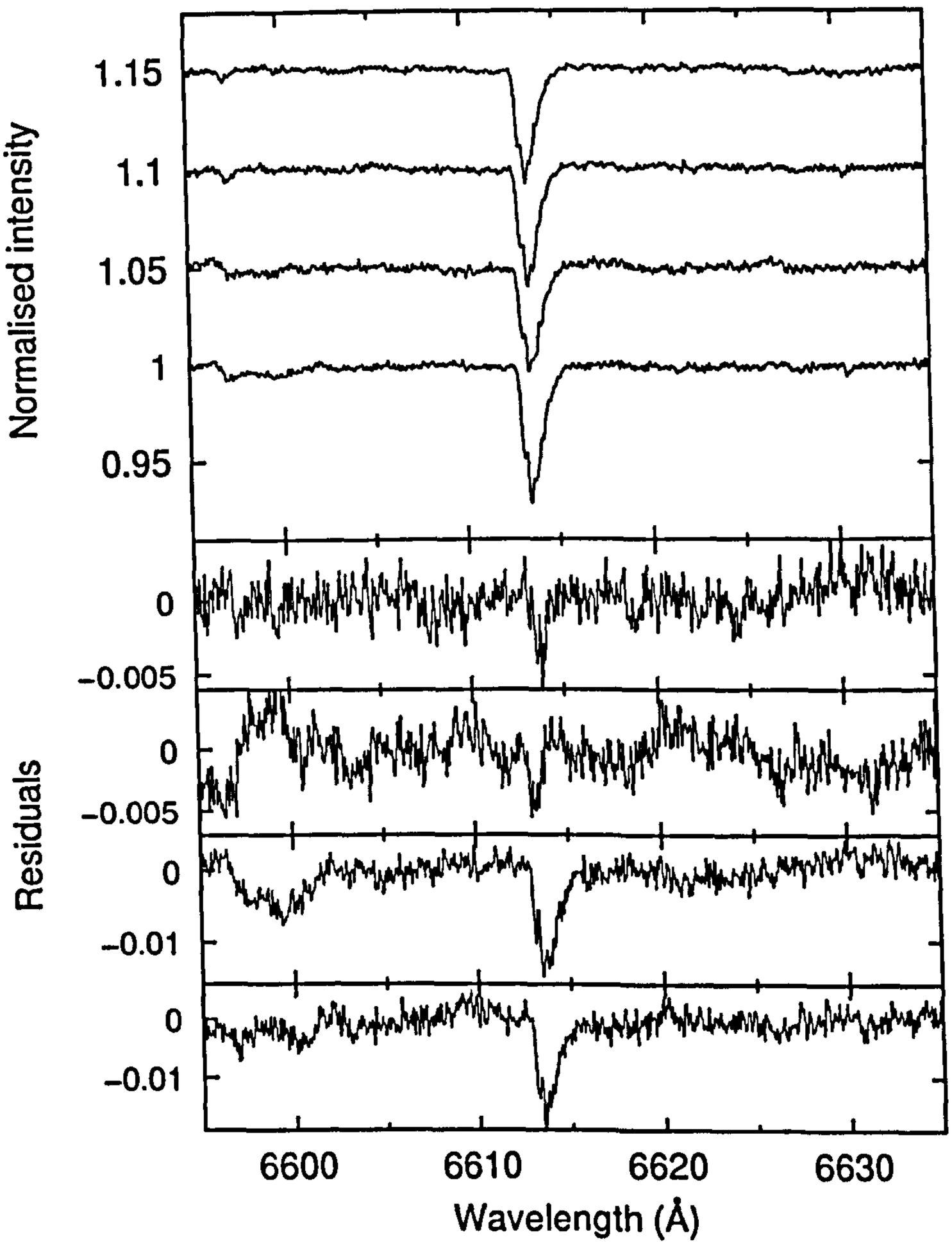

Figure 4.38: Spectra of λ6614 recorded towards (from top to bottom) ρ Oph A, ρ Oph B, ρ Oph C and ρ Oph DE, telluric-corrected and normalised with straight line continua. Lower section of the figure shows the residual intensities (from top to bottom) of (1) ρ Oph B – ρ Oph A, (2) ρ Oph A – ρ Oph C, (3) ρ Oph DE – ρ Oph A and (4) ρ Oph DE – ρ Oph C.

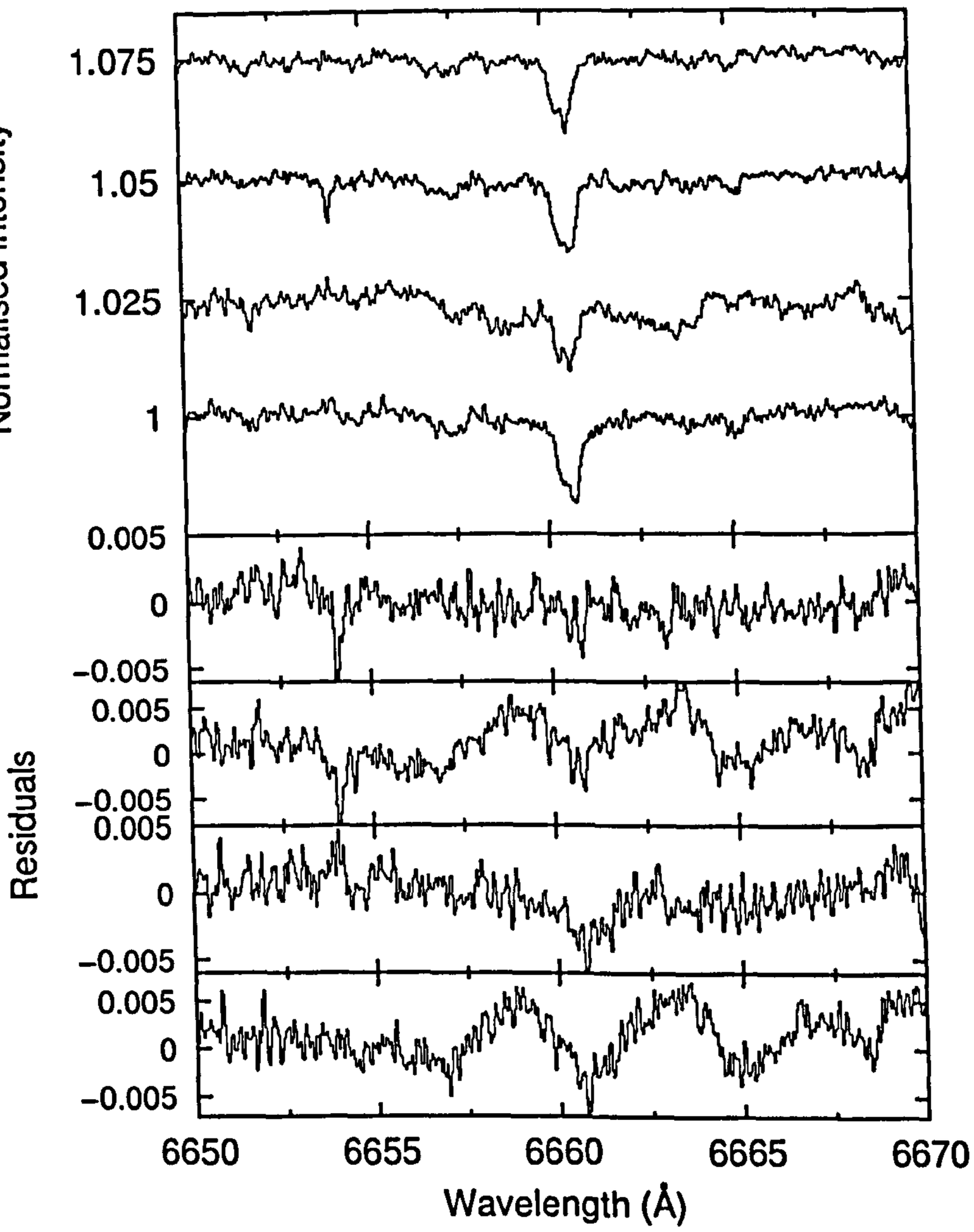

Figure 4.39: Spectra of λ6660 recorded towards (from top to bottom) ρ Oph A, ρ Oph B, ρ Oph C and ρ Oph DE, telluric-corrected and normalised with straight line continua. Lower section of the figure shows the residual intensities (from top to bottom) of (1) ρ Oph B – ρ Oph A, (2) ρ Oph C – ρ Oph C, (3) ρ Oph DE – ρ Oph A and (4) ρ Oph DE – ρ Oph C.

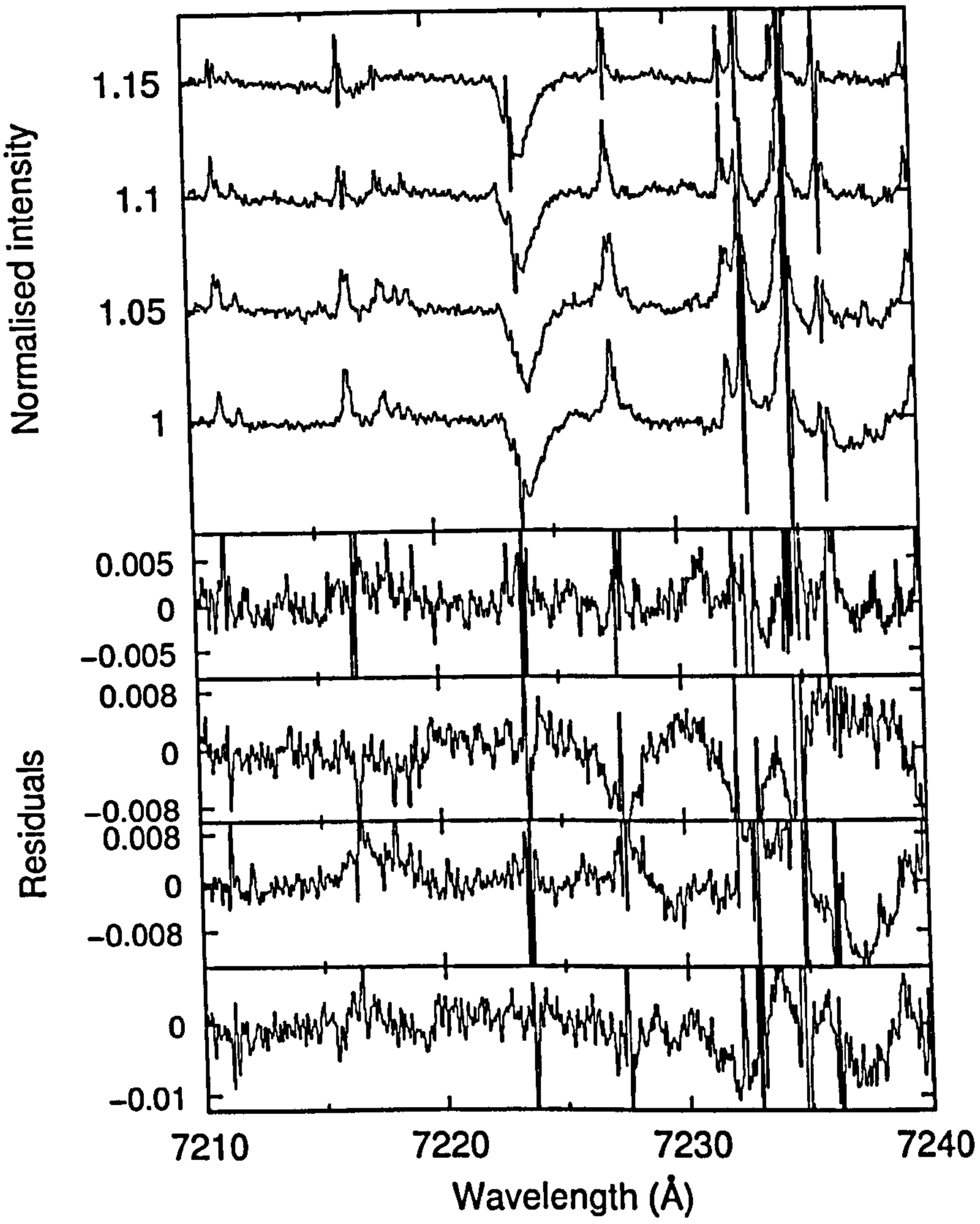

Figure 4.40: Spectra of λ7224 recorded towards (from top to bottom) ρ Oph A, ρ Oph B, ρ Oph C and ρ Oph DE, telluric-corrected and normalised with straight line continua. Lower section of the figure shows the residual intensities (from top to bottom) of (1) ρ Oph B – ρ Oph A, (2) ρ Oph B – ρ Oph C, (3) ρ Oph DE – ρ Oph A and (4) ρ Oph DE – ρ Oph C.

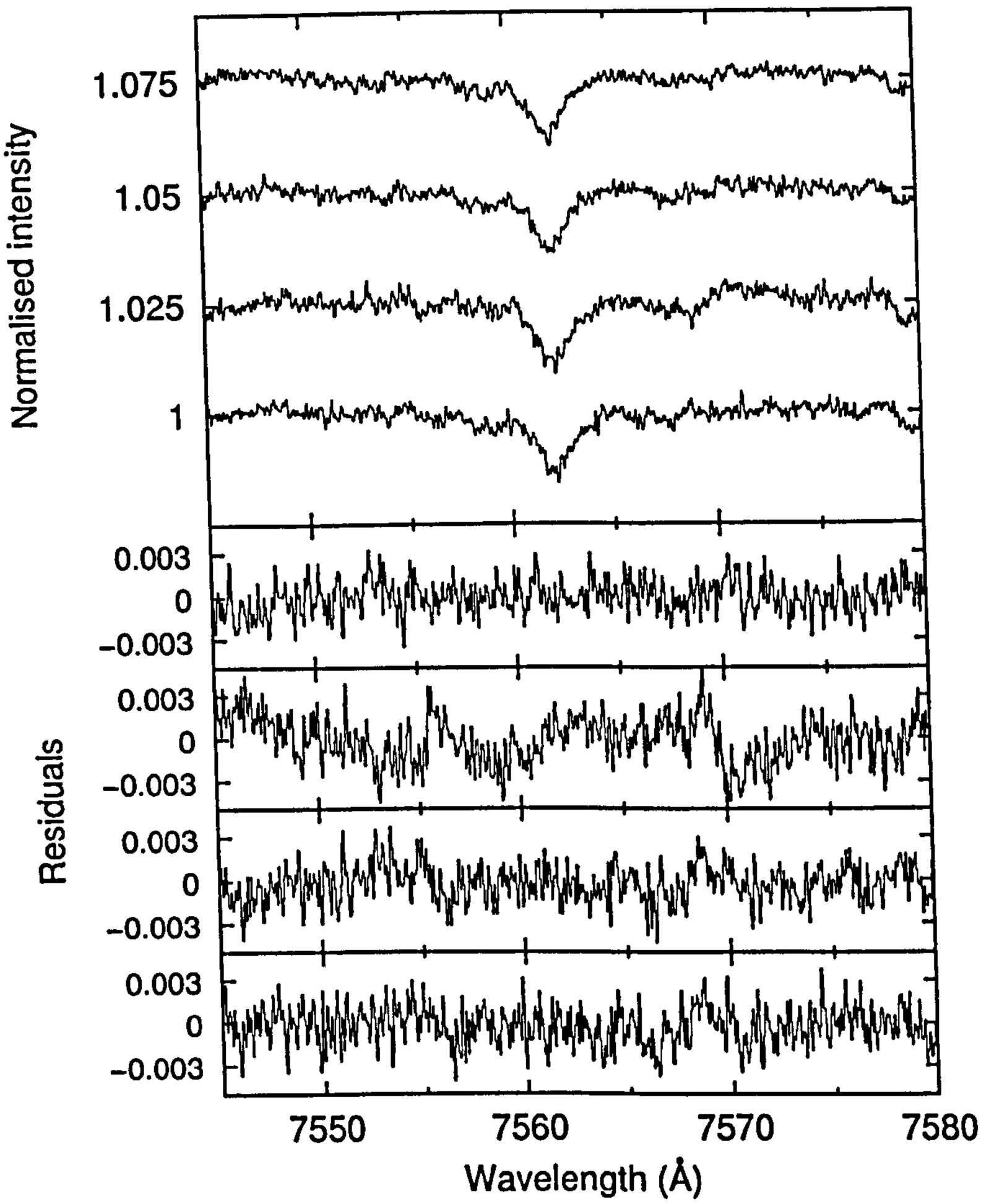

Figure 4.41: Spectra of λ7562 recorded towards (from top to bottom) ρ Oph A, ρ Oph B, ρ Oph C and ρ Oph DE, telluric-corrected and normalised with low-order polynomial continua. Lower section of the figure shows the residual intensities (from top to bottom) of (1) ρ Oph B − ρ Oph A, (2) ρ Oph A − ρ Oph C, (3) ρ Oph DE − ρ Oph A and (4) ρ Oph DE − ρ Oph B.

	W_λ (mÅ)					
Feature	ρ Oph A	ρ Oph B	ρ Oph C	ρ Oph DE	σ_{W_λ}	Blend?
λ5705	38.5	38.5	32.5	45	2.8	N
λ5780	188.3	202.4	207.2	240.1	2.6	C
λ5797	49.3	53.2	53.7	55.5	1.0	C
λ5850	28.4	30.2	33.8	24.3	1.1	N
λ6196	14.8	14.8	14.8	19	0.5	N
λ6203	40.4	41	41	45.3	4.9	N
λ6284	295	295	330.1	295	4.5	C
λ6376	13.5	14.7	14.7	20.2	0.8	N
λ6379	26	27.8	28.2	33.8	0.7	?
λ6426	2.9	2.9	2.9	2.9	1.2	N
λ6439	4.3	5.3	9.4	2.6	1.0	N
λ6445	6.8	6.8	8.6	9.2	0.8	Y
λ6614	63.5	66.5	59.9	84.7	1.1	N
λ6660	8.9	10	11.2	12.9	0.7	Y
λ7224	42.6	43.5	45.3	53.9	1.3	T
λ7562	36	36	36	36	2.2	N
K I λ7699	88.1	89.5	77.7	90.5	0.3	
Na I D_1	188.9	191.5	174.2	187	0.2	
$\log N$(K I)	12.01	12.04	11.90	12.04		
$\log N$(Ca I)	10.24	10.23	10.21	10.31		
$\log N$(Ca II)	12.25	12.29	12.28	12.29		
$\log N$(CH)	13.37	13.37	13.28	13.34		
$\log N(CH^+)$	13.20	13.16	12.85	12.88		
$\log N$(CN)	12.32	12.30	12.78	12.32		
$\log N(C_2)$	13.69			13.59		

Table 4.5: Equivalent widths of interstellar features measured towards the stars of the ρ Oph system. σ_{W_λ} gives an error estimate for the DIB equivalent widths in mÅ. Atomic and diatomic column densities are from Pan *et al.* (2004) except for the C_2 data, which are from Thorburn *et al.* (2003). In the last column, 'Y' indicates a definite or probable stellar blend contaminating the DIB spectra, 'N' indicates improbable or absent stellar blend and '?' is for indeterminate cases, 'T' indicates severe telluric contamination of results, 'C' indicates that a contaminating stellar feature is probably present for the ρ Oph C measurement.

Feature	δ(B/A)	δ(C/A)	δ(DE/A)	δ(C/B)	δ(DE/B)	δ(DE/C)	σ_δ
λ5705	<7.6	-16	17	-16	17	38	7.6
λ5780	7.5	10	28	2.4	19	16	1.3
λ5797	7.9	8.9	13	0.9	4.3	3.4	1.9
λ5850	6.3	19	-14	12	-20	-28	3.6
λ6196	<3.4	<3.4	28	<3.4	28	28	3.4
λ6203	1.5	1.5	12	<12	10	10	12
λ6284	<1.5	12	<1.5	12	<1.5	-10.6	1.5
λ6376	8.9	8.9	50	<5.8	37	37	5.8
λ6379	6.9	8.5	30	1.4	22	20	2.5
λ6426	<41	<41	<41	<41	<41	<41	
λ6439	23	119	-40	77	-51	-72	20
λ6445	<12	26	35	26	35	7.0	12
λ6614	4.7	-5.7	33	-9.9	27	41	1.7
λ6660	12	26	45	12	29	15	6.8
λ7224	2.1	6.3	27	4.1	24	19	2.9
λ7562	<6.2	<6.2	<6.2	<6.2	<6.2	<6.2	
K I λ7699	1.6	-13.4	2.7	-15.2	1.1	16.5	0.3
Na I D[1]	1.4	-7.8	-1.0	-9.0	-2.3	7.3	0.1
N(K I)	5.7	-22	6.7	-27	0.9	37	10
N(Ca I)	-2.9	-6.9	16	-4.1	20	25	10
N(Ca II)	11	9.1	10	-2.0	-1.0	1.0	10
N(CH)	-1.7	-19	-8.0	-18	-6.4	14	9
N(CH^+)	-10	-56	-53	-51	-48	7.1	6
N(CN)	-4.8	186	0.0	200	5.0	-65	13
N(C_2)			-20				38

Table 4.6: Tabulated here are the DIB and atom equivalent width *percentage* excesses of comparisons between interstellar absorption features towards pairs of stars in the ρ Oph system. For atomic and diatomic species, *column density* percentage excesses are given. The column $\delta(X/Y)$ is the percentage by which the equivalent width of the star designated by sightline 'X' is in excess of that designated by sightline 'Y', where X and Y are substituted for the names of the component stars in the ρ Oph system: A, B, C and DE. Error estimates on the percentages are given by the column σ_δ.

Table 4.6 shows the relative percentage differences between the DIB equivalent widths measured for the various components of the ρ Oph system. These are quoted as a percentage excess $\delta(X/Y)$ as described by Equation (4.1), page 165. As an example, from the first row of the table, the value of δ(DE/A) = 17 means that the DIB λ5705 is 17% stronger towards ρ Oph DE than towards ρ Oph A, but δ(B/A) < 7.6 means that this DIB shows a variation of varies less than 7.6% between ρ Oph A and B. Towards ρ Oph C, λ5705 is 16% *weaker* than towards ρ Oph A as denoted by δ(C/A) = −16. The error column σ_δ gives the error on $\delta(X/Y)$ averaged across all permutations of sightline pairs. These values, again, were similar enough to allow the average error to be used as representative of the individual errors in $\delta(X/Y)$ for the different combinations of sightline pairs.

The residual plots in Figures 4.31 to 4.41 show clear variations between the stars of the ρ Oph system in the equivalent widths of most of the diffuse interstellar bands measured. The DIBs λ5780, λ5797, λ5850, λ6376, λ6379, λ6614 and λ6660 all show a significant enhancement in equivalent width towards ρ Oph B compared with ρ Oph A. The strength enhancement is typically around 5%, and can be attributed to an increase in the strengths of the DIBs because the DIB profiles are present in the residual spectra for each case. Thus, any variations in the DIB profiles between sightlines must be small relative to the gross features of the profiles. The equivalent widths of the Na I D_1 and K I λ7699 lines measured here are about 1% greater towards ρ Oph B than A, but these lines are both rather saturated.

The DIBs for which no discernible differences could be detected between ρ Oph A and B are λ5705, λ6196, λ6284, λ6426, λ6445 and λ7562. No evidence for contamination of these results by stellar blends can be seen in the residual spectra for any DIBs apart from λ6379 and λ6439 where absorption features about 3 times as broad as the DIBs are present that cover the DIB profiles and are stronger in ρ Oph B than A. The telluric lines do not prohibit the accurate analysis of the residual spectrum of λ6284, where a flat residual continuum is clearly seen beneath the telluric-correction artifacts in Figure 4.35. The telluric artifacts are too severe to permit a proper analysis of the variability of λ7224, though it appears that this DIB does not exhibit any large variations between the sightlines.

Between the other ρ Oph sightlines, variations in DIB strengths are observed with broadly similar magnitudes as found for the case of A and B. Of slightly later spectral

type, the ρ Oph C spectrum contains more contaminating stellar lines, preventing an accurate analysis of the λ5780, λ5797 and λ6284 DIBs. Stellar features also contaminate the λ6660 region for ρ Oph C and DE. Towards DE, the DIBs are typically the strongest in the ρ Oph system, between 10 and 50% stronger than towards ρ Oph A. An exception is λ6284 which appears to be strongest towards ρ Oph C, but this may be due to stellar contamination, and if so, suggests that λ6284 may have the same equivalent width as towards the other sightlines of this system which appear to be identical to within $\approx$ 1.5%

The λ6196 diffuse band has the same equivalent width between A, B and C to within about 3.4%, but is stronger towards DE by about 28% (as shown by Figures 4.45 and 4.34). The only DIBs for which no differences in strength were observed between all four ρ Oph sightlines are λ6426 (Figure 4.37) and λ7562 (Figure 4.41). This is not surprising for the case of λ6426 which is very weak (W_{6426} = 2.9 mÅ), allowing only a 41% upper limit on its variability. λ7562 appears to vary by $\lesssim$ 6.2% between the four sightlines however.

The Na I D_1 and K I λ7699 equivalent widths follow the pattern of strengths W_λ(DE) > W_λ(B) > W_λ(A) > W_λ(C) except for $W_{\mathrm{Na\ I\ D_1}}$(DE) which lies in between that of A and C. The ρ Oph A and B Na I D_1 and K I λ7699 equivalent widths are only slightly stronger towards B; which is nevertheless a significant difference in these very high S/N spectra. From Figures 4.49 and 4.50 it is interesting to note the relative lack of K I towards ρ Oph C compared to the other three sightlines. This is not observed in the Na I spectrum, probably due to the saturation of the Na I D_1 line which approaches zero intensity in the line core; indeed the ρ Oph C line profile is noticeably narrower than the others in the Na I D_1 comparison plot.

A further result for the ρ Oph system is that the pattern of DIB equivalent width variations does not always follow that exhibited by the K I and Na I lines. The different DIBs show different patterns of strength variations between the four sightlines. The data for λ5705, λ6196 and λ6614 are consistent with the K I strength pattern of W_λ(DE) > W_λ(B) > W_λ(A) > W_λ(C). λ5850 expresses almost the opposite pattern however, with W_λ(C) > W_λ(B) > W_λ(A) > W_λ(DE). These results are displayed in the overlaid spectra of Figures 4.47 and 4.44. The close similarities between the spectra of A and B are clear, but W_λ(B) is significantly greater than W_λ(A) in both cases. The majority of DIBs for which significant variations in strength have been measured (includ-

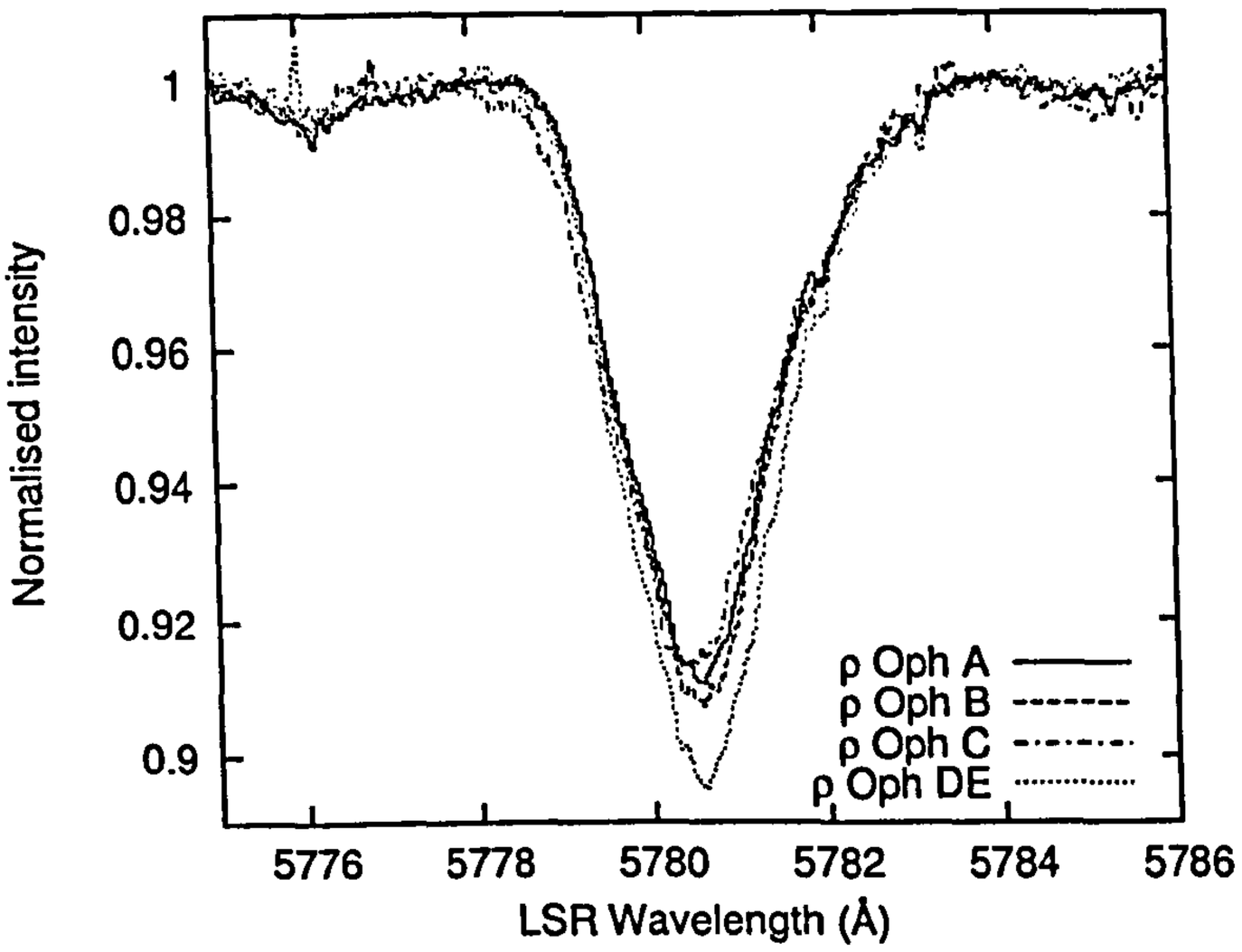

Figure 4.42: Overlaid ρ Oph A, B, C, DE λ5780 spectra, telluric-corrected and normalised with low-order polynomial continua.

ing λ5780, λ5797, λ6376, λ6379 and λ6446) show a strength pattern consistent with either W_λ(DE) > W_λ(C) > W_λ(B) > W_λ(A) or W_λ(DE) > W_λ(B) > W_λ(C) > W_λ(A). The equivalent widths towards sightlines B and C are very similar for these DIBs. For examples of this strength pattern, see Figures 4.42, 4.43 and 4.46.

The recent DIB study conducted by Thorburn *et al.* (2003) at similar resolution and high S/N provides an opportunity to compare our DIB equivalent width results for ρ Oph A and DE with past measurements. In their paper, equivalent widths with error estimates are given for ρ Oph A and D for many of the DIBs studied here. The equivalent width measurements all match to within 20%, except for λ6284 which is measured as about 30 to 40% greater by Thorburn *et al.* (2003). There is an apparent trend for the Thorburn *et al.* (2003) measurements to be in excess of those presented here, outside of the combined error estimates in many cases. As already explained, the absolute DIB equivalent widths presented here for ρ Oph may be in error by up to about 5%.

The largest source of error in high S/N DIB equivalent width measurements is the continuum definition, which can be different for different authors, making inter-comparison of results difficult. For any given author, the continuum definition should be consistent between different sightlines though. This was carefully controlled in this study to ensure the *differences* between DIB equivalent widths were measured accurately for the purpose of SSS detection. Thus, comparison between the *differences* in the ρ Oph

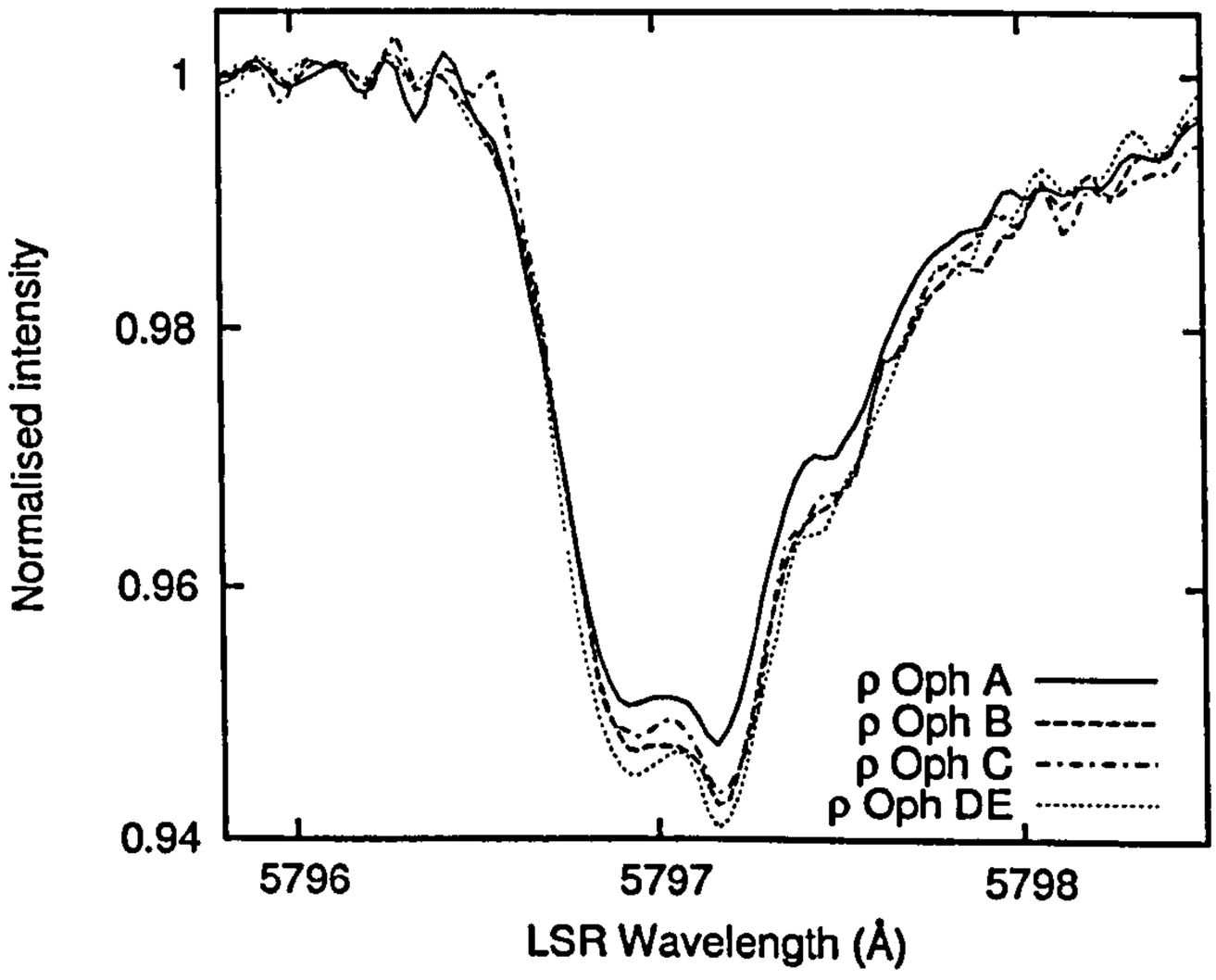

Figure 4.43: Overlaid ρ Oph A, B, C and DE λ5797 spectra, telluric-corrected and normalised with low-order polynomial continua.

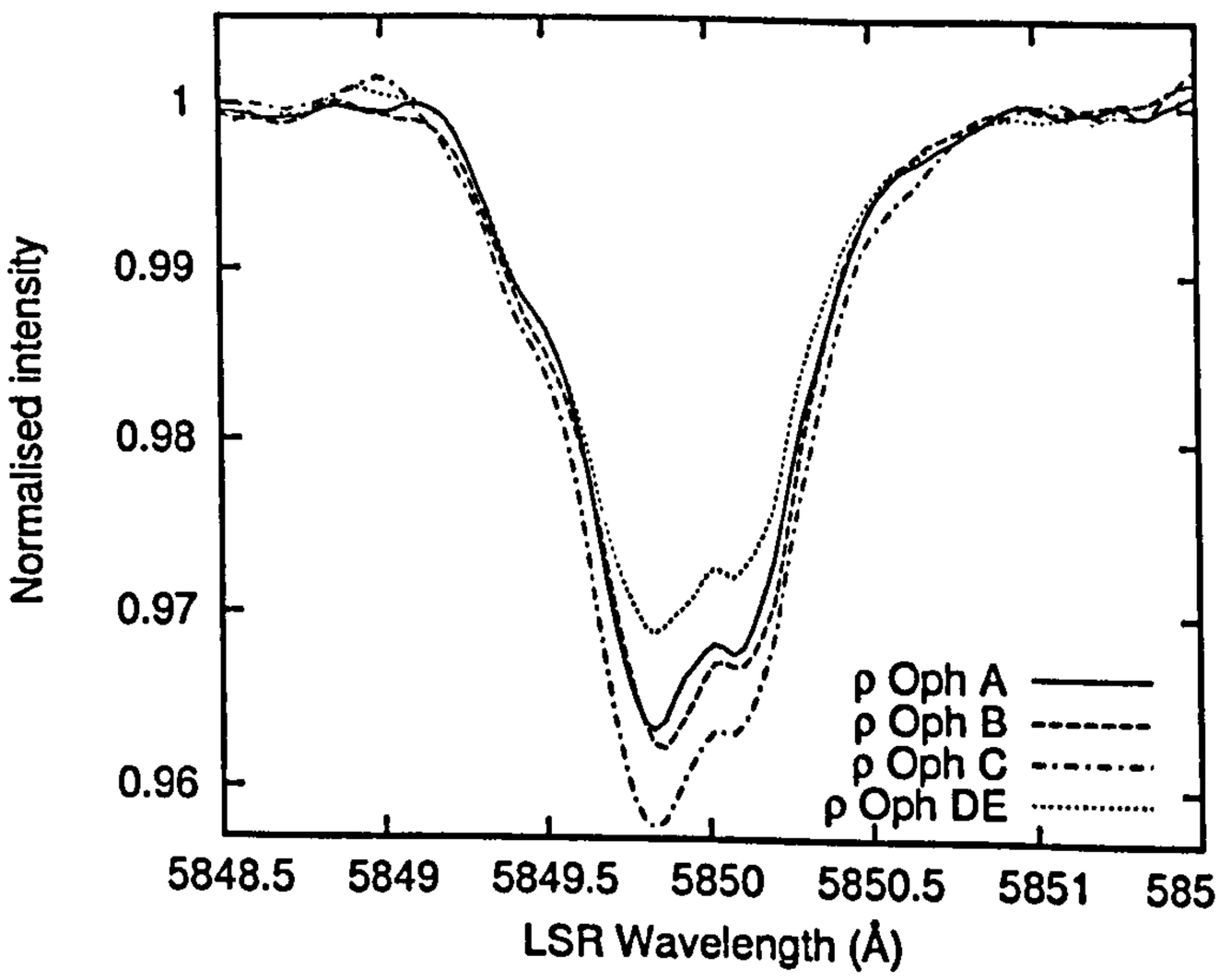

Figure 4.44: Overlaid ρ Oph A, B, C and DE λ5850 spectra, telluric-corrected, normalised with low-order polynomial continua and smoothed with a 5-pixel boxcar.

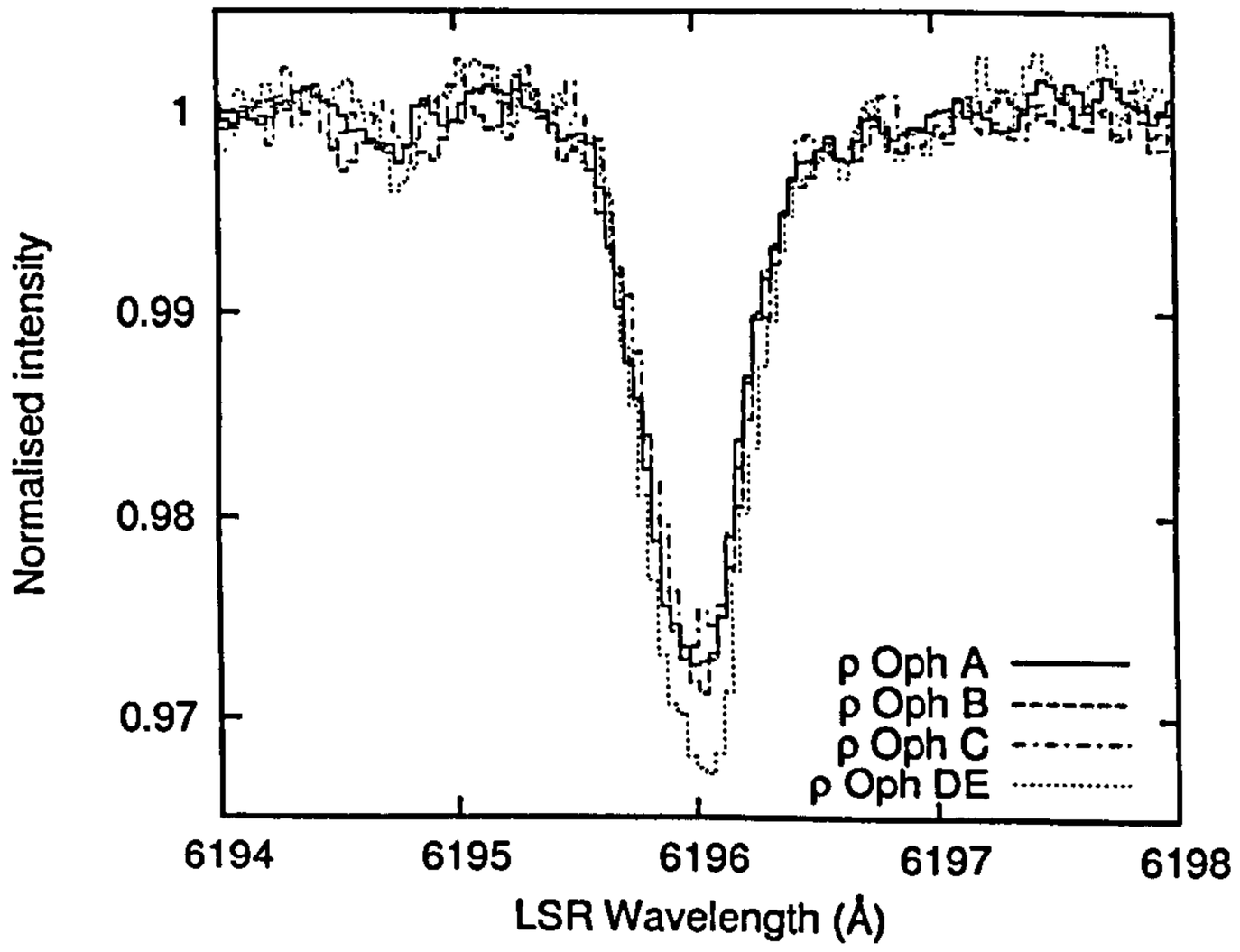

Figure 4.45: Overlaid ρ Oph A, B, C and DE λ6196 spectra, normalised with low-order polynomial continua.

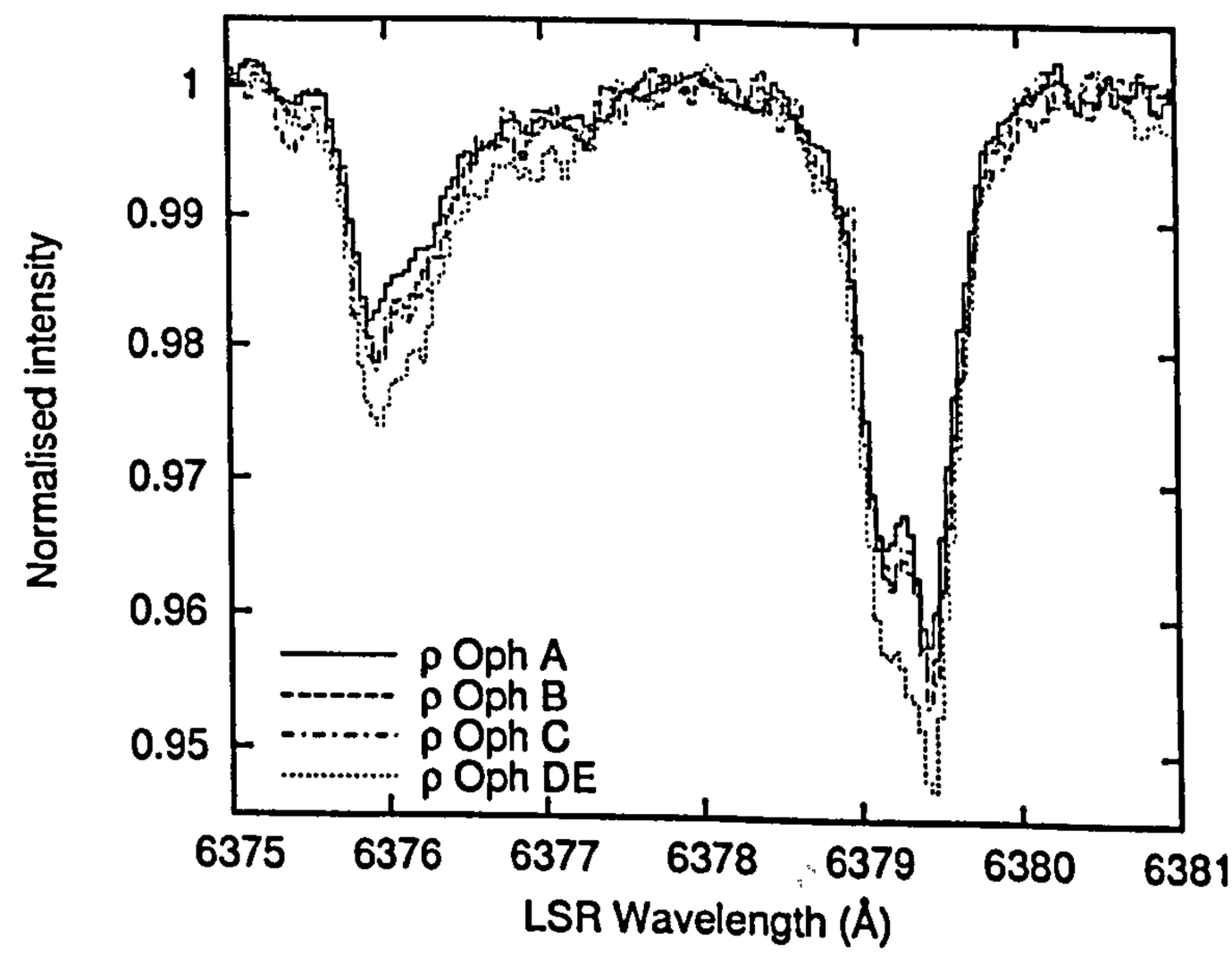

Figure 4.46: Overlaid ρ Oph A, B, C and DE λ6376 and λ6379 spectra, telluric-corrected and normalised with low-order polynomial continua.

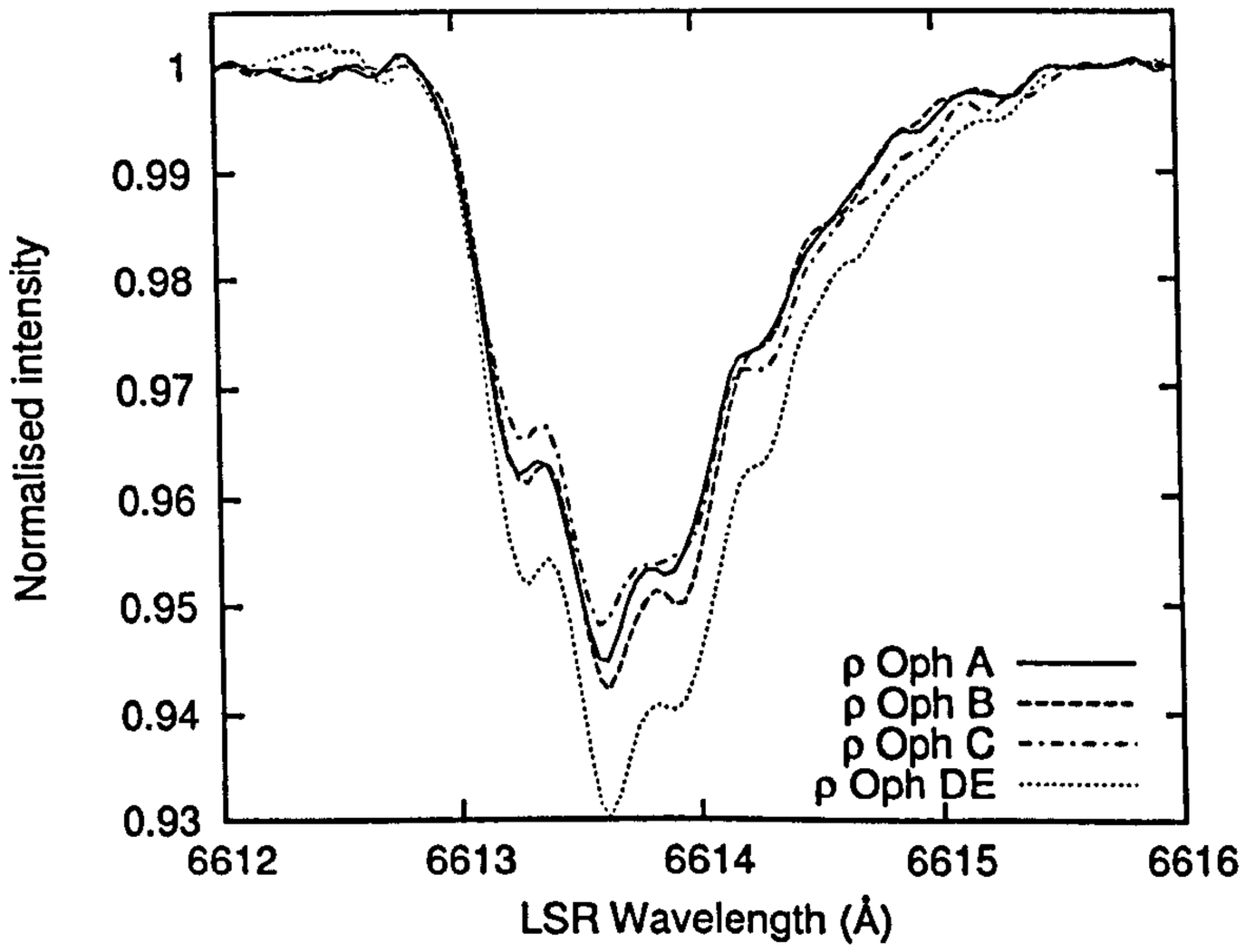

Figure 4.47: Overlaid ρ Oph A, B, C and DE λ6614 spectra, telluric-corrected, normalised with low-order polynomial continua, and smoothed with a 3-pixel boxcar.

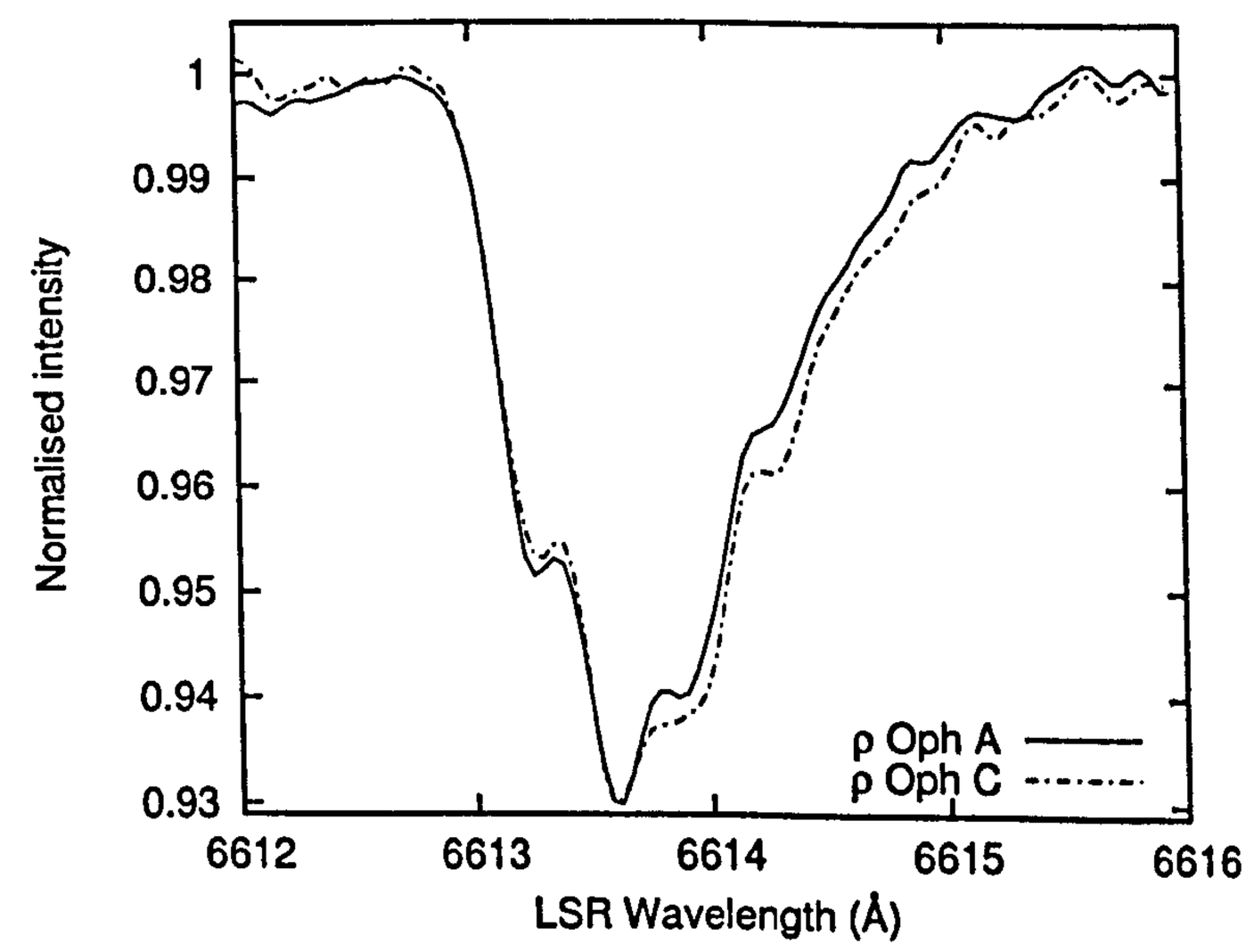

Figure 4.48: ρ Oph A and C λ6614 spectra, telluric-corrected, normalised with low-order polynomial continua, smoothed with a 3-pixel boxcar, scaled and shifted to a common peak-absorption intensity for display.

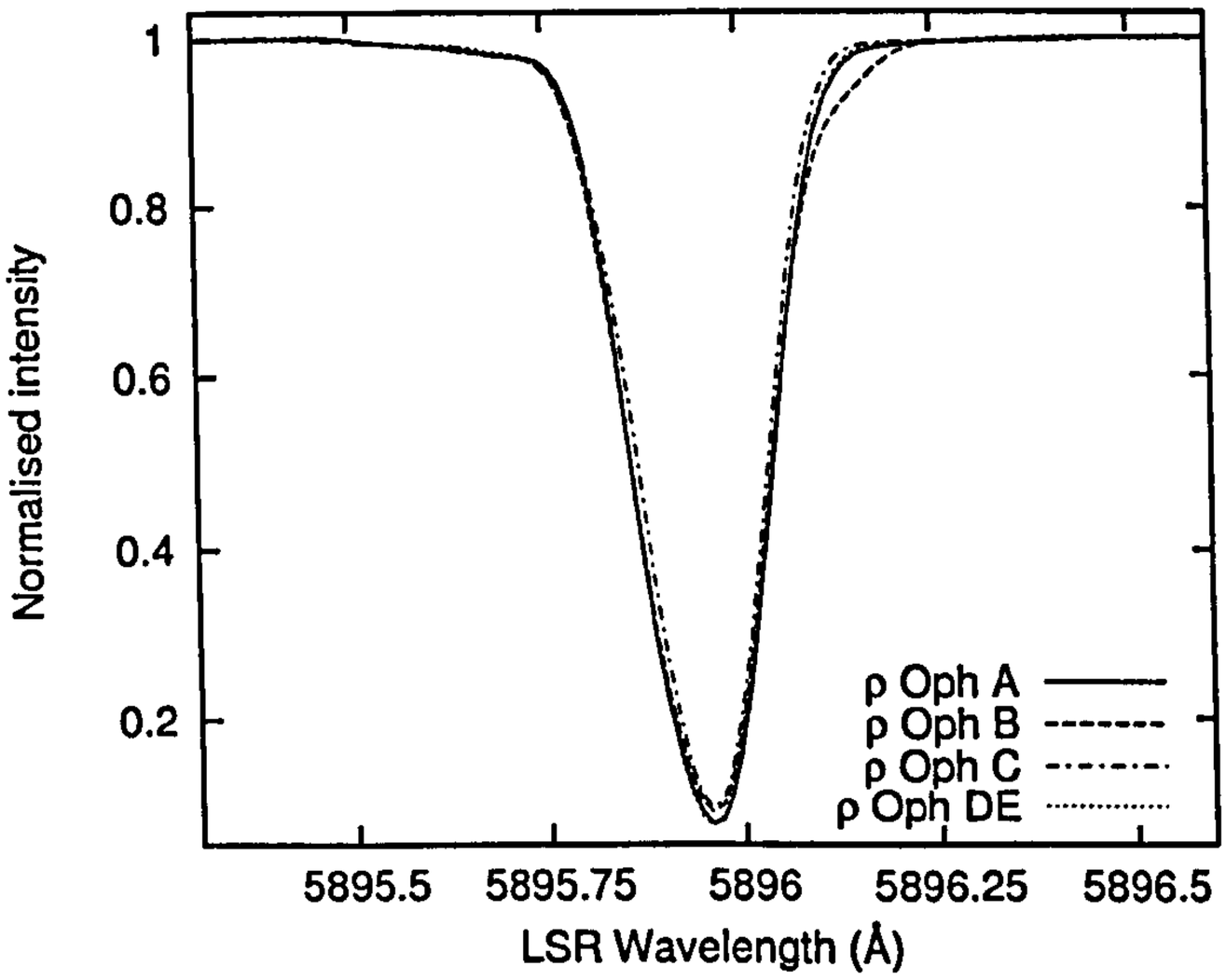

Figure 4.49: Overlaid ρ Oph A, B, C and DE Na D_1 spectra, telluric-corrected, normalised with low-order polynomial continua and plotted using cubic splines.

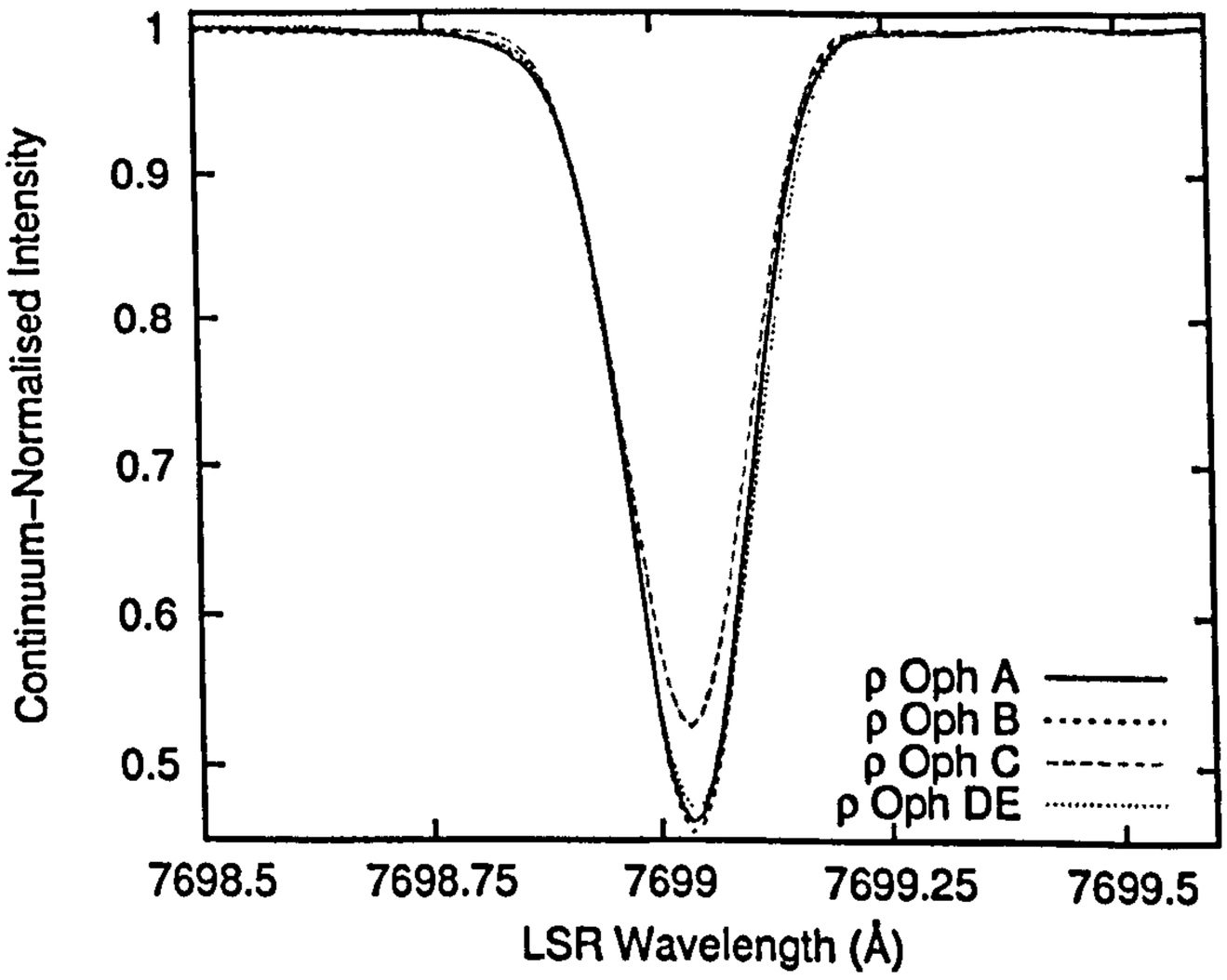

Figure 4.50: Overlaid ρ Oph A, B, C and DE K I λ7699 spectra, telluric-corrected, normalised with low-order polynomial continua and plotted using cubic splines.

A and DE equivalent widths reported by Thorburn *et al.* (2003) with the differences reported here may be more meaningful. Indeed, comparison of the ρ Oph A to DE equivalent width ratios shows good correspondence between our data and Thorburn *et al.*'s in all cases except for λ5797, where Thorburn *et al.* measure a significantly *reduced* λ5797 equivalent width in ρ Oph D compared to A, whereas our study finds the opposite. This is somewhat troubling given the reported accuracy of the Thorburn *et al.* spectra, though again, may be related to differences in continuum definition between our respective studies and is possibly a consequence of the blending of the λ5797 profile with the nearby, relatively broad λ5795 DIB. The broad λ5795 DIB is very weak in the ρ Oph spectra and was excluded from our equivalent width measurements. From the evidence presented in Figure 4.32 and Figure 4.43 it is difficult to refute that the narrow λ5797 DIB is stronger towards ρ Oph DE.

With regard to the previous results for ρ Oph A and B from photographic spectra reported by Herbig (1975), the overall result of that work was that both λ5780 and λ5797 are stronger towards ρ Oph B than ρ Oph A. Although these results are subject to large error bars (Herbig, private communication), Herbig's measurements support the results obtained herein. From Herbig (1975), W_{5780}(A) = 258, W_{5780}(B) = 326, W_{5797}(A) = 92 and W_{5797}(B) = 123.[5] A later, high resolution solid-state detector study by Herbig (1993) gave W_{5780}(A) = 219, W_{5797}(A) = 54. These values are compared with the results of our study: W_{5780}(A) = 188, W_{5780}(B) = 202, W_{5797}(A) = 49 and W_{5797}(B) = 53. The correspondence between the later measurements for ρ Oph A by Herbig (1993) and our results is reasonable considering potential differences in continuum definition: within about 10% for W_{5797} and about 16% for W_{5780}.

Utilising data from the recent high-resolution blue-NUV study of atomic and diatomic species towards the stars of the ρ Oph system by Pan *et al.* (2004), comparison between the abundances of the DIB carriers and the abundances of K I, Ca I, Ca II, CH, CH^+ and CN can be made. The data are shown in Table 4.5, and plotted in Figure 4.51 for a selection of the stronger DIBs apparently unaffected by stellar line blends. It is apparent that, in the ρ Oph system, the DIB strengths correlate better with N(K I) and N(Ca I) than with the diatomic molecules. The Ca II column density is relatively invariant between the ρ Oph sightlines. The substantial enhancement in CN towards ρ Oph C appears to have no effect on the strengths of different DIBs. The enhanced

[5] 'A' and 'B' in parentheses denote measurements of ρ Oph A and B respectively.

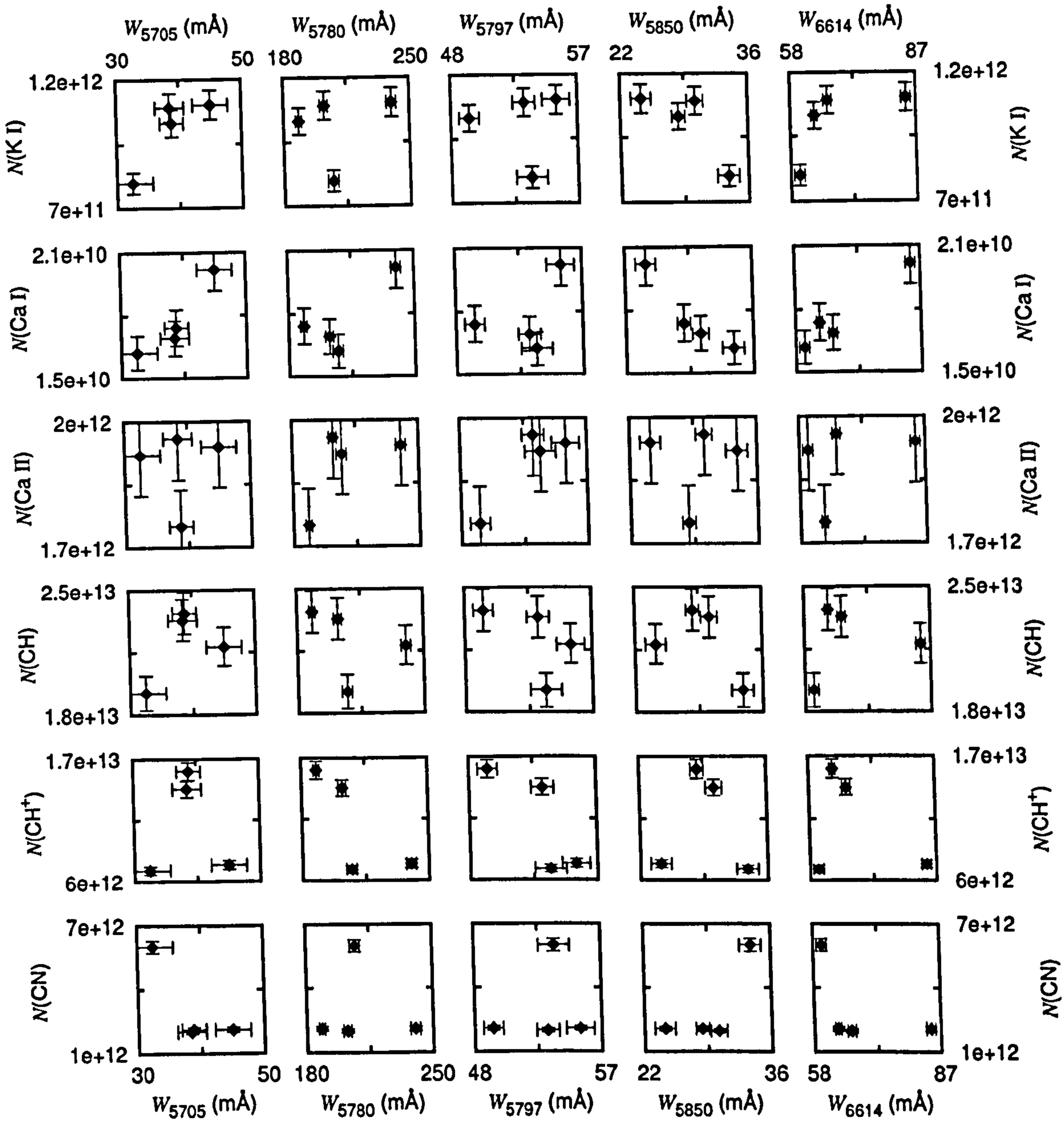

Figure 4.51: Atomic and diatomic column densities from Pan *et al.* (2004) plotted in units of cm^{-2} against DIB equivalent width measurements for ρ Oph A, B, C and DE.

CH^+ abundance towards A and B does not seem to have any direct effect on the DIBs plotted. Whereas most of the DIBs show a positive correlation with N(K I) and N(Ca I) as is typically observed in the wider Galactic ISM, the plots in Figure 4.51 show that λ5850 is anticorrelated with these quantities in the ρ Oph system.

As noted already, the profiles of all of the DIBs studied remain remarkably constant over the four ρ Oph sightlines, notwithstanding cases where stellar features contaminate the profiles. There is evidence, however that the profile of λ6614 exhibits a subtle difference towards ρ Oph C compared to the other sightlines. Careful examination of the pattern of residuals formed by subtraction of the ρ Oph C spectrum from that of ρ Oph A, shown in the second trace of the lower panel in Figure 4.38, reveals a displacement of the peak of the λ6614 residual feature by about 0.5 Å towards the blue with respect to the peak of the DIB profile. The peak absorption wavelength of the λ6614 DIB is identical between all four sightlines to within ~ 0.01 Å (the approximate wavelength calibration accuracy of UCLES during the period of observation), as shown by Figure 4.47. Given that this DIB is stronger towards ρ Oph A than towards C, the residual offset towards the blue suggests that the red side of the DIB should be more similar between A and C than the blue side where the residual intensity is greater. This would require an enhancement in the strength of C on the red side and/or a reduction in strength on the blue side relative to the profile for sightline A, resulting in a skewed λ6614 profile. This is exactly what is observed in Figure 4.47, where, relative to the profile of A, the ρ Oph C profile shows stronger absorption to the red of the central peak, and weaker absorption to the blue. For clarity, the profiles of λ6614 towards A and C have been scaled and additively shifted such that their peak absorption intensities are matched, shown plotted in Figure 4.48. Counting from the steep blue edge of the DIB profile, four absorption peaks are clearly seen in both profiles. Relative to the second peak (fixed for display by scaling and additive shifting), the first peak is stronger in the ρ Oph A profile, whereas the third and fourth peaks and the rest of the red side of the DIB are stronger in the ρ Oph C profile. Although subtle differences of this kind may also be discernible between the other ρ Oph sightlines, the profiles of A, B and DE are much more similar to each other within the S/N, C being the most distinctly different in the ρ Oph system. This profile difference is discussed in further detail in Section 4.5.3.

4.3.5 μ Cru

An early B dwarf binary system with very low reddening ($E_{B-V} \sim 0.05$), the μ Cru system lies 116 ± 8 pc away as derived from the Hipparcos parallax data (Perryman & ESA 1997). Due to its separation of 38.8″, the sky-projected distance between the binary pair is ~ 4500 AU. The detection of DIBs in this system was non-trivial and necessitated many hours of integration before DIBs could be identified reliably, particularly for the dimmer μ^2 Cru. Four DIBs have been detected with confidence; λ5780 (Figure 4.52), λ6196 and λ6203 (Figure 4.54), and λ6614 (Figure 4.56), displayed with residual spectra of μ^2 Cru – μ^1 Cru.

The DIBs detected towards μ^1 Cru are significantly weaker than those detected towards μ^2 and the results of the equivalent width measurements are given in Table 4.7. The recorded Na I spectra are shown in Figure 4.57, and appear as expected based on the previous measurements of these lines (Meyer & Blades 1996) and the lower resolution of our UCLES spectra. Interstellar K I has been detected in μ^1 and μ^2 Cru for the first time (see Figure 4.58). The lines are exceptionally weak, but the principal K I cloud is at $v_{\rm LSR} \simeq -1.3$ km s^{-1} ($v_{\rm HEL} \simeq 5$ km s^{-1}), matching the velocity of the strongest Na I cloud towards μ^2 Cru. The $v_{\rm LSR} \simeq -13$ km s^{-1} ($v_{\rm HEL} \simeq -8.6$ km s^{-1}) cloud (Meyer & Blades 1996; Lauroesch *et al.* 1998) was not reliably detected in K I towards either star. The K I spectra were modelled in VAPID to calculate column densities with 1σ error estimates. Logarithmic column densities of 9.74 ± 0.07 and 10.07 ± 0.09 were derived for μ^1 and μ^2 Cru respectively, so the K I column density towards μ^2 Cru is about twice that towards μ^1 Cru. However, within the error, the variation in N(K I) may not be different to the 53% variation in N(Na I) derived by Lauroesch *et al.* (1998) (no error estimate given).

The DIBs in μ^2 Cru are relatively weak compared to other Galactic sightlines as highlighted by the plots of DIB strengths versus N(K I) and E_{B-V} in Figure 4.59 and Figure 4.60.

For λ5780, the difference between the μ^1 and μ^2 profiles is striking, producing a residual λ5780 spectrum with a profile consistent with a pure increase in the strength of this DIB by about 85 ± 28% towards μ^2 compared to μ^1 Cru. Weak stellar features exist in this region (see Figure 4.1) for stars with early B spectral types, and an apparent emission feature is present on the red side of λ5780 towards μ^1 Cru, so it is probable

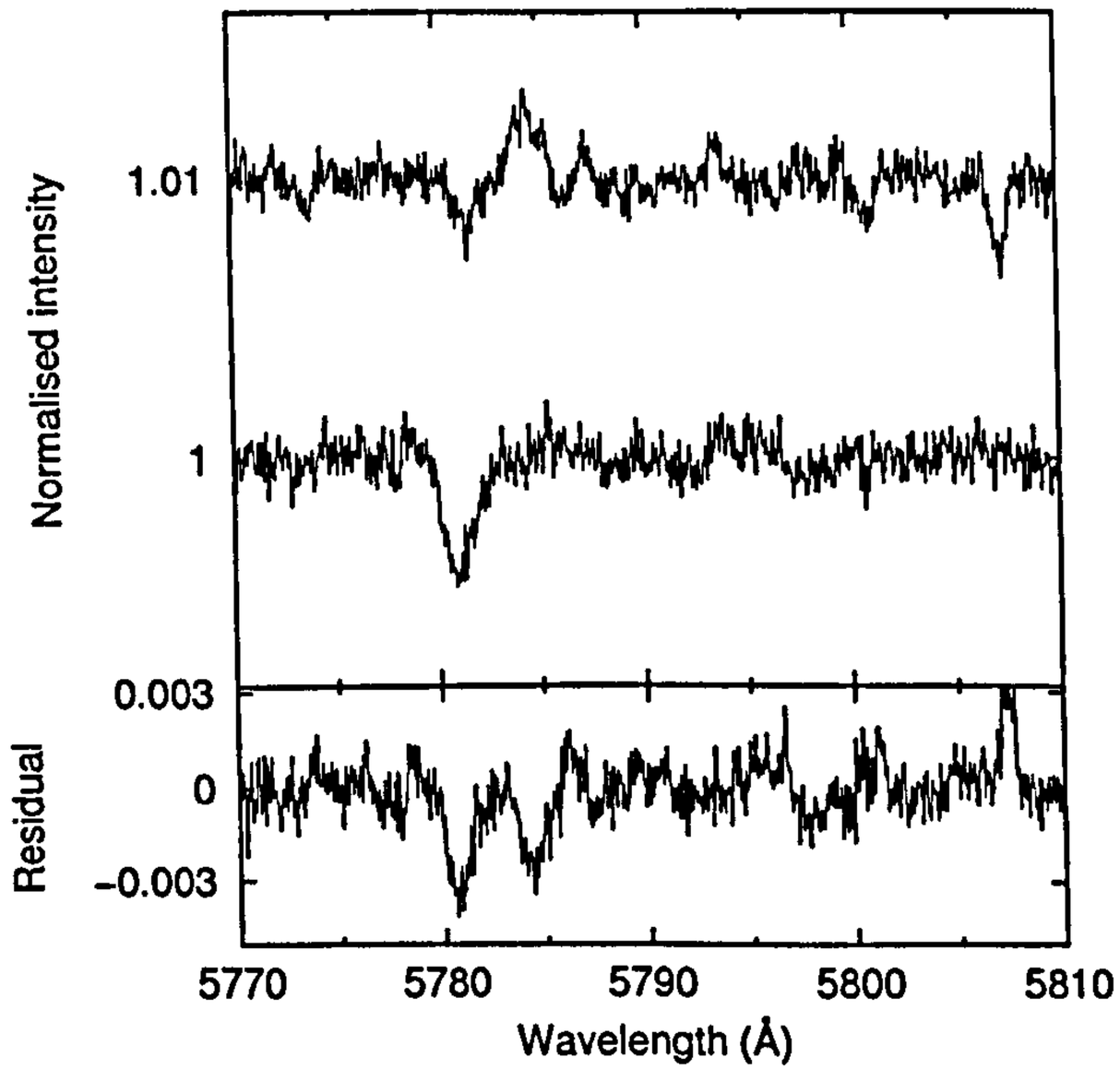

Figure 4.52: Spectra of λ5780 and λ5797 recorded towards μ^1 Cru (top) and μ^2 Cru (middle), telluric-corrected and normalised with straight line continua. Lower trace shows the residual intensities of μ^2 Cru $-$ μ^1 Cru.

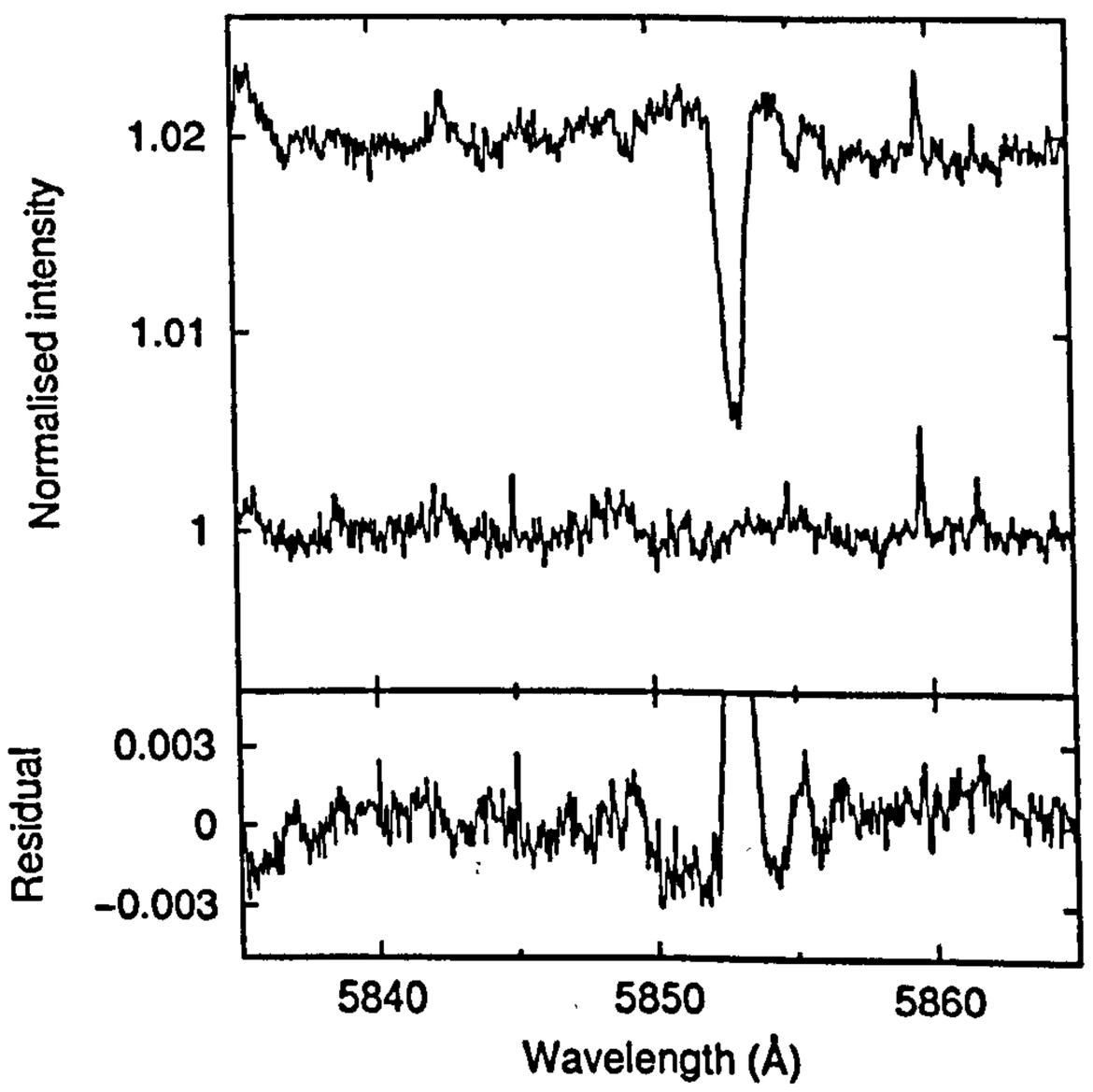

Figure 4.53: Spectra of λ5850 recorded towards μ^1 Cru (top) and μ^2 Cru (middle), telluric-corrected and normalised with straight line continua. Lower trace shows the residual intensities of μ^2 Cru $-$ μ^1 Cru.

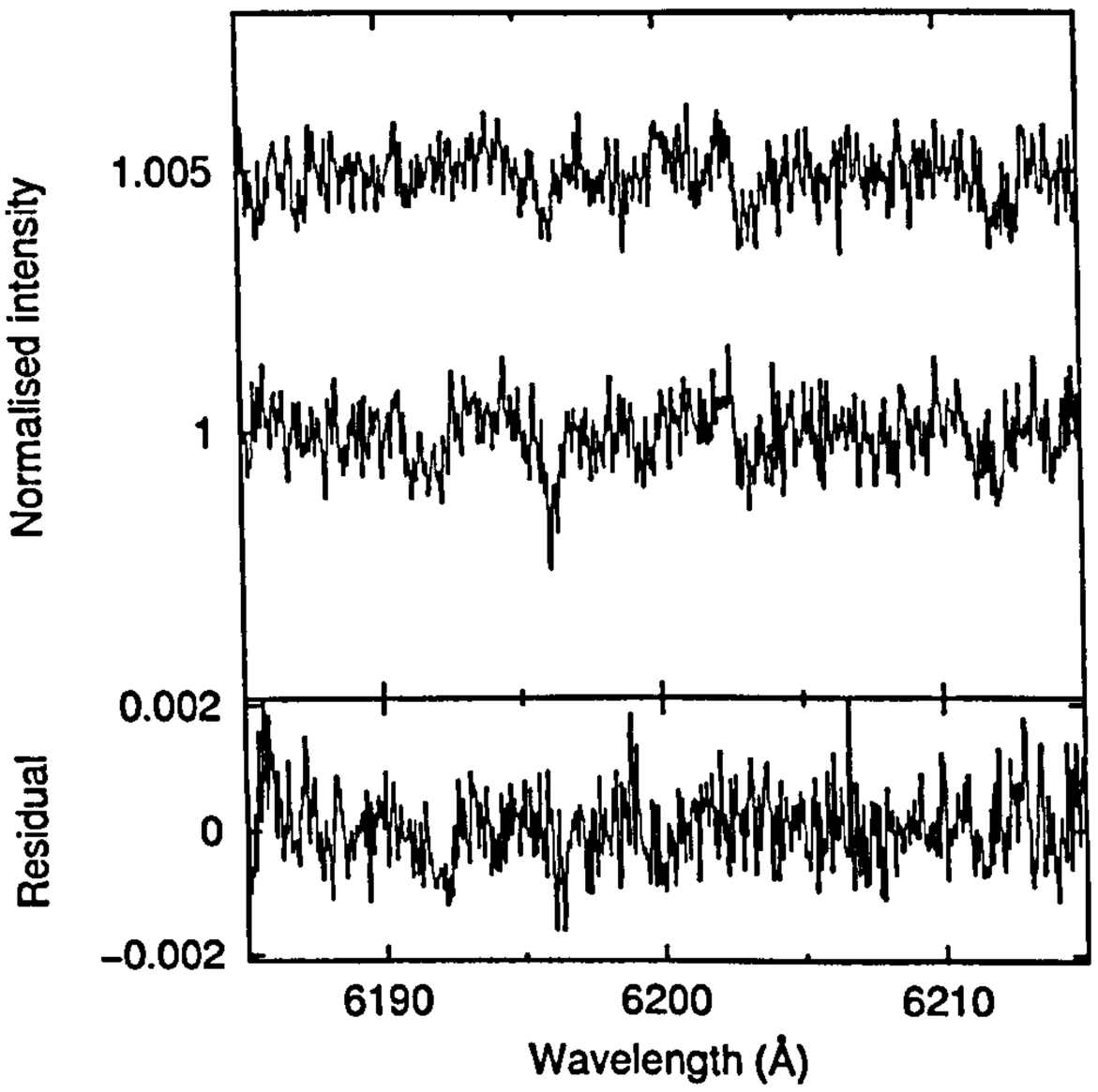

Figure 4.54: Spectra of λ6196 and λ6203 recorded towards μ^1 Cru (top) and μ^2 Cru (middle), telluric-corrected and normalised with low-order polynomial continua. Lower trace shows the residual intensities of μ^2 Cru – μ^1 Cru.

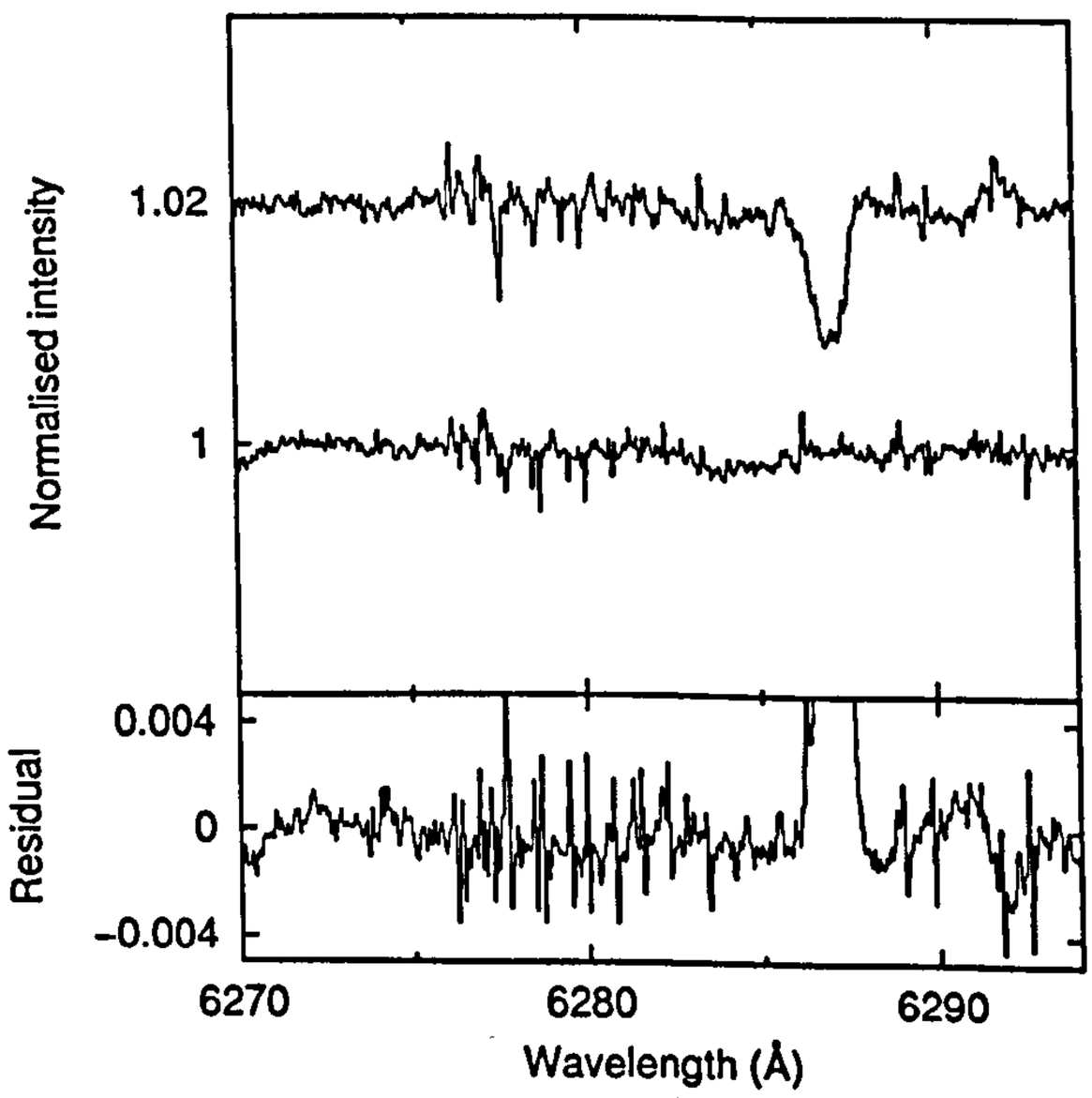

Figure 4.55: Spectra of λ6284 recorded towards μ^1 Cru (top) and μ^2 Cru (middle), telluric-corrected and normalised with straight line continua. Lower trace shows the residual intensities of μ^2 Cru – μ^1 Cru.

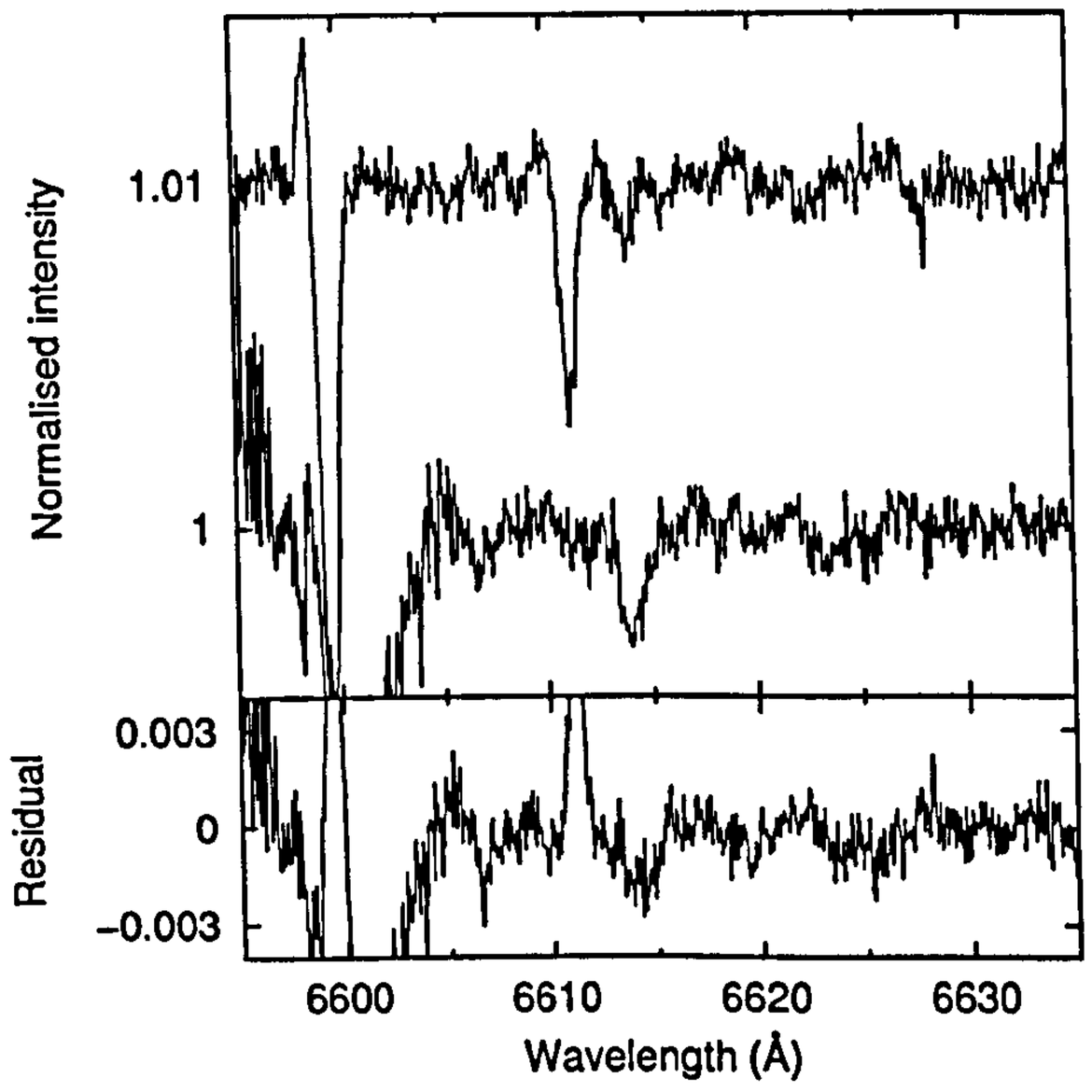

Figure 4.56: Spectra of λ6614 recorded towards μ^1 Cru (top) and μ^2 Cru (middle), telluric-corrected and normalised with straight line continua. Lower trace shows the residual intensities of μ^2 Cru – μ^1 Cru.

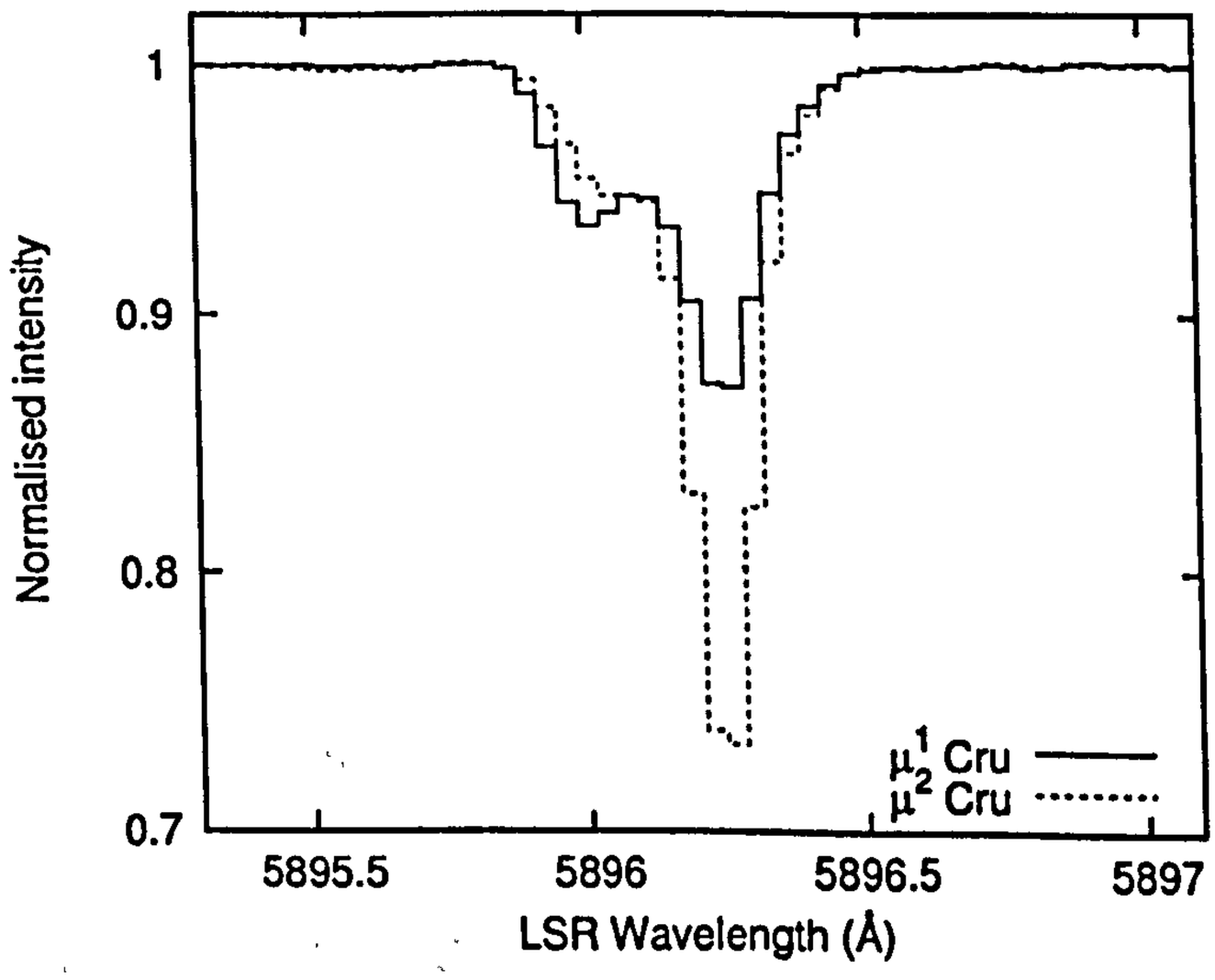

Figure 4.57: Overlaid $\mu^{1,2}$ Cru Na I D_1 spectra, telluric-corrected and normalised with low-order polynomial continua.

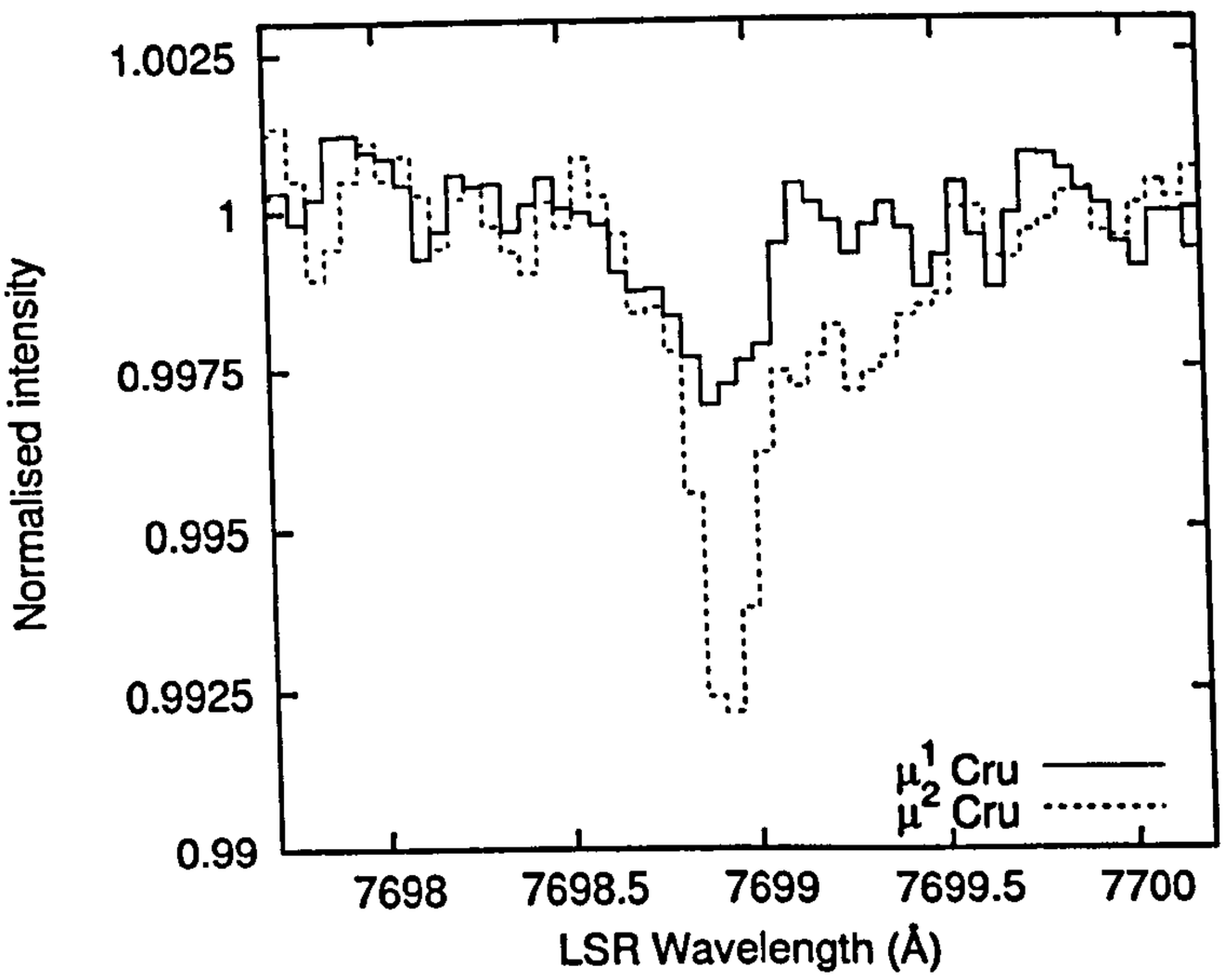

Figure 4.58: Overlaid $\mu^{1,2}$ Cru K I λ7699 spectra, telluric-corrected and normalised with low-order polynomial continua.

	W_λ (mÅ)		$\delta(\mu^2/\mu^1)$	
Feature	μ^1 Cru	μ^2 Cru	(%)	Blend?
λ5780	4	7.4	85 (28)	Y
λ5797	0	0	–	Y
λ5850	0	0	–	Y
λ6196	0.6	1.1	83 (40)	N
λ6203	1.1	1	-9.0 (104)	N
λ6284	3.7	5.5	49 (44)	?
λ6614	1.5	4.2	180 (33)	N
K I λ7699	0.9	2.3	155 (34)	
Na I D_1	34.3	49.8	45 (0.7)	
log N(K I)	9.736	10.072	122 (80)	
log N(Na I)	11.585	11.77	53	
log N(Ca II)	11.17	11.214	11	

Table 4.7: Equivalent widths of interstellar features measured towards $\mu^{1,2}$ Cru. $\delta(\mu^2/\mu^1)$ is the percentage *excess* of μ^2 Cru measurements compared to μ^1 Cru, with error estimates given in parentheses. N(K I) were calculated using VAPID, N(Na I) and N(Ca II) are from Meyer & Blades (1996). In the last column, 'Y' indicates a definite or probable stellar blend contaminating the DIB spectra, 'N' indicates improbable or absent stellar blend and '?' is for indeterminate cases, 'T' indicates severe telluric contamination of results.

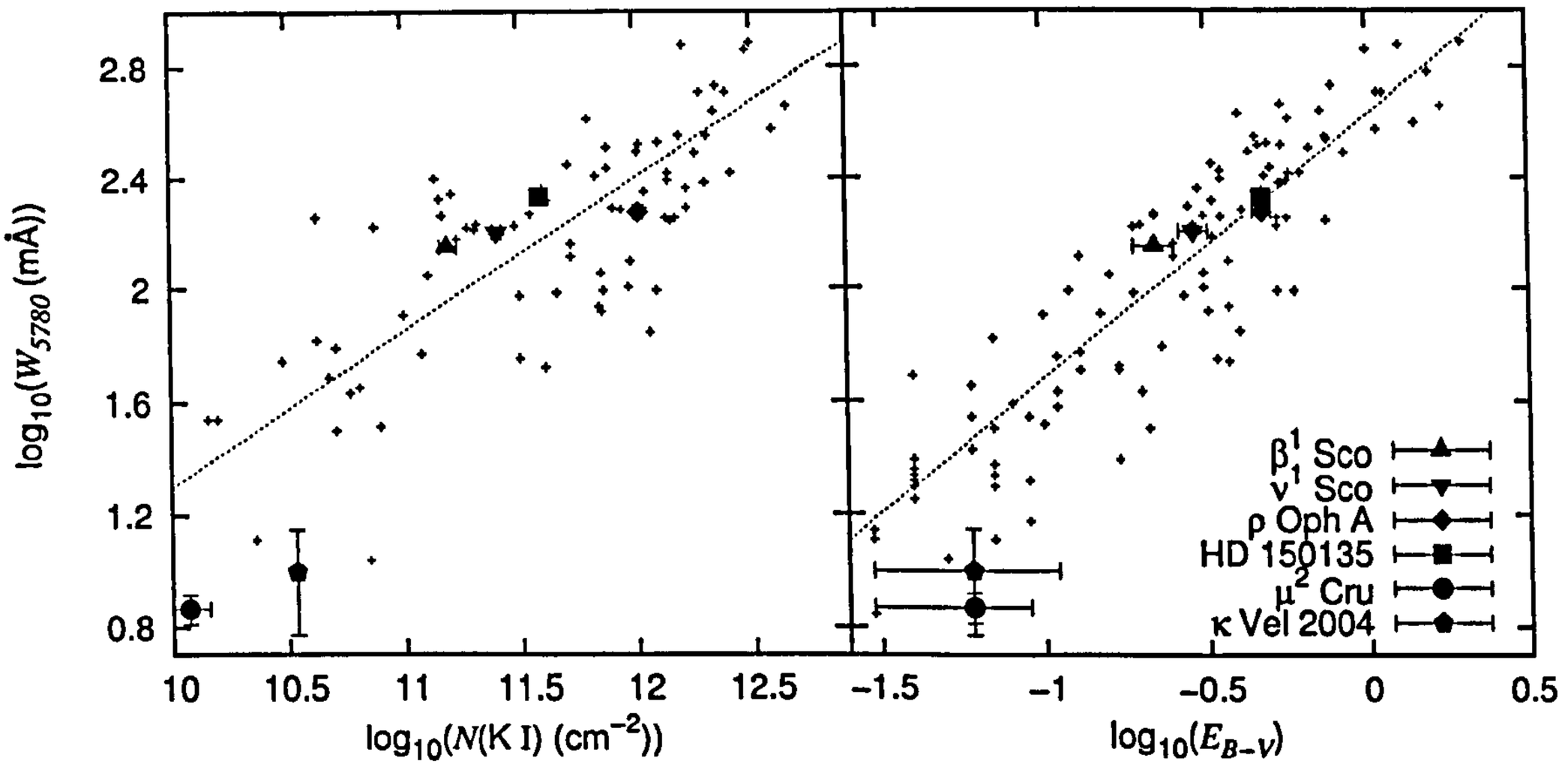

Figure 4.59: The equivalent width of the λ5780 diffuse interstellar band measured towards selected programme stars, plotted against N(K I) and E_{B-V} with data for other diffuse Galactic sightlines. The dotted line represents the line of best fit through the Galactic comparison data.

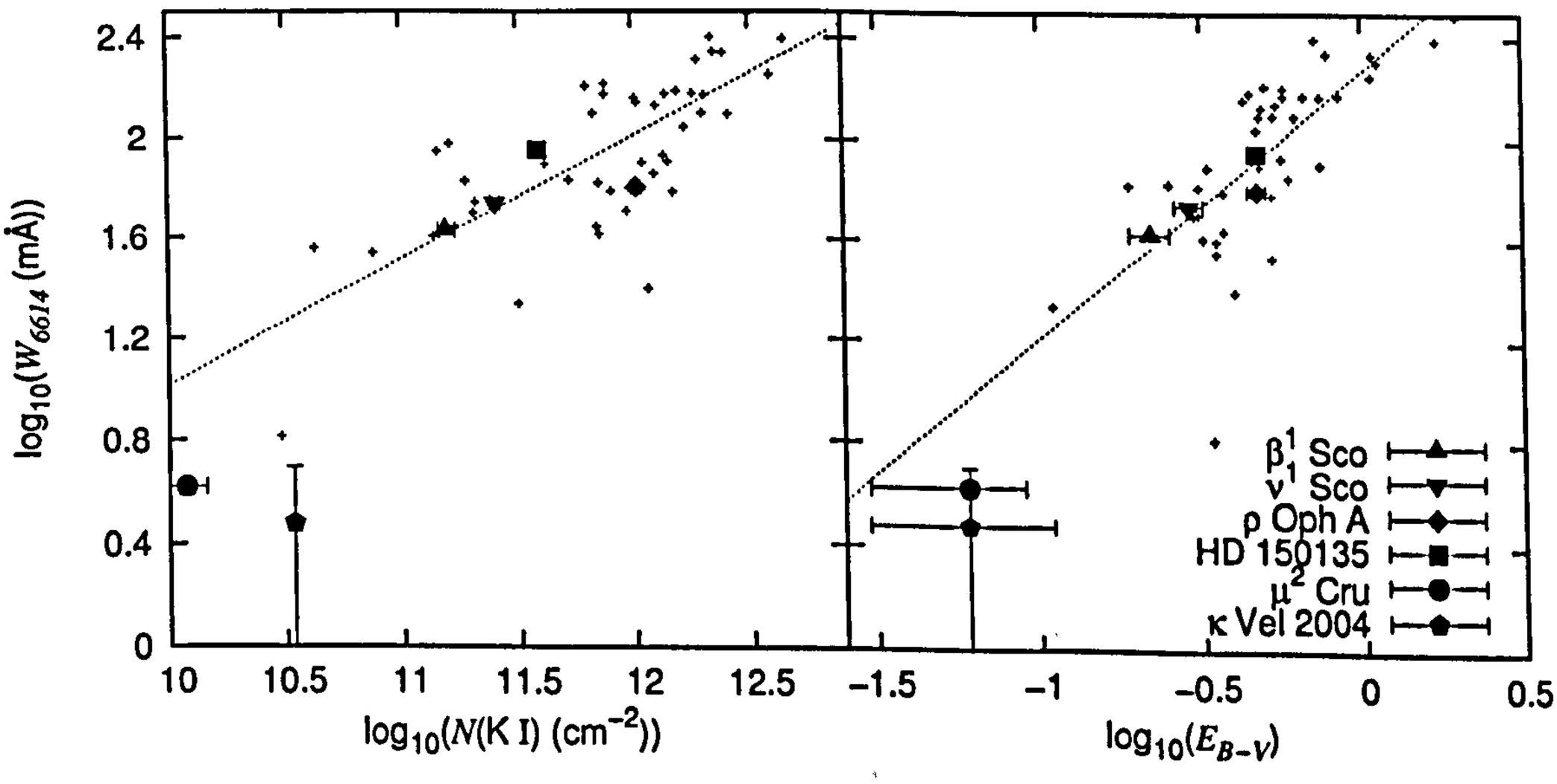

Figure 4.60: The equivalent width of the λ6614 diffuse interstellar band measured towards selected programme stars, plotted against N(K I) and E_{B-V} with data for other diffuse Galactic sightlines. The dotted line represents the line of best fit through the Galactic comparison data.

that stellar lines contaminate this result to a degree, but it is difficult to determine the magnitude of this effect when the DIBs are so weak.

DIB λ6196 is measured as being 80 ± 40% stronger towards μ^2 than μ^1 Cru, without significant stellar contamination in either sightline. The residual plot in Figure 4.54 shows three pixels at $\gtrsim 3\sigma$ below the relatively flat surrounding residual continuum within the narrow profile of the λ6196 DIB. λ6203 does not show any significant differences between the two sightlines.

Due to its relative broadness, λ6284 is a difficult DIB to measure when it is weak. A depression around 6284 Å can be seen in Figure 4.55, and is slightly stronger in the μ^2 Cru spectrum. Telluric and stellar contamination in the surrounding region make definitive measurements difficult, but it appears as though this DIB may not be as variable between these two sightlines as λ5780, λ6196 and λ6614.

The spectral region adjacent to λ6614 contains stellar features, but none are expected within the wavelength limits of this DIB. Figure 4.56 shows the spectra and residual plot, and the DIB appears to be substantially stronger towards μ^2 Cru. Within the S/N the DIB profile for μ^1 and μ^2 Cru is consistent with a standard λ6614 profile (see, *e.g.* Figure 4.47). From the residual plot, λ6614 is almost three times stronger towards μ^2 than μ^1 Cru, with a measured residual percentage excess of 180 ± 33%.

Other relatively strong DIBs such as λ5797, λ5850 (see Figures 4.52 and 4.53) and λ7224 were not detected. Strong stellar features in the vicinity of 6375 Å prevented any accurate measurements of the λ6376 and λ6379 DIBs.

4.3.6 HD 150135/6

Recently determined as host to our nearest O3 star (Niemela & Gamen 2005), the HD 150135/6 binary system resides approximately 1320 ± 120 pc distant (Perryman & ESA 1997) in NGC 6193, an open cluster in the Ara OB1 association. The cluster has associated H II nebulosity and star formation has occurred recently in the adjacent Ara R1 dust cloud (Herbst & Havlen 1977). It is reasonable to assume that the principal concentrations of interstellar matter are associated with the cluster, such that the SSS probe length is equal to the sky-projected separation of the binary of ~ 12,500 AU at the binary separation of 9.6″.

With a moderately high reddening of $E_{B-V} = 0.47$ (see Table 4.1), the observed DIB spectrum is strong enough to permit reasonable accuracy on equivalent width measurements. The early spectral type ensures that there are few species in the stellar atmospheres to contaminate the DIB spectra, though C IV absorption near 5800 Å prevents accurate measurements of λ5797 (seen in Figure 4.62).

The only DIB that shows significant variability in its strength between HD 150135 and HD 150136 is λ6614, whose spectra and residuals are shown in Figure 4.67. The residuals are consistent with a pure increase in the strength of this DIB towards HD 150136 compared to HD 150135, and given the broadness of the stellar lines in both stars (see Figures 4.62 and 4.66) it is extremely unlikely that the residual pattern is caused by overlapping stellar absorption or emission. The differences between the λ6614 spectra are highlighted in Figure 4.68.

Examples of the spectra and residuals in the region of other strong DIBs are shown in Figures 4.61 to 4.66. The flatness of the residual DIB spectra is remarkable for the case of λ5850, λ5780, λ6196, λ6284 and λ6376, so reliable statistical upper limits can be placed on their possible variation (see Table 4.8). From Figure 4.62, a residual 'bulge' near 5780 Å suggests that λ5780 could be slightly stronger towards HD 150135 than towards HD 150136, but the equivalent width difference measured from this bump (4.6 mÅ) lies within the error estimate of 5.2 mÅ. A summary of all of the equivalent width measurements is shown in Table 4.8. A kink in the λ6203 residual spectrum (see Figure 4.64) could indicate that this broad DIB exhibits a different profile between the two stars, being slightly stronger towards HD150135. The kink is not in the correct location to represent an increase in the strength of the narrow peak of λ6203, nor of the correct shape to represent an increase in the strength of the broader 'shoulder' component of this DIB located between 6204 and 6208 Å, so it is likely that this residual feature is due to differences in the stellar continua.

Both the Na I D_1 and K I λ7699 lines are slightly stronger towards HD 150136 than HD 150135 (spectra shown in Figures 4.69 and 4.70). The K I lines were modelled using VAPID, and required four clouds for a good fit. Least-squares model parameters are given in Table 4.9, from which there appears to be ~ 11% more K I towards HD 150136 than HD 150135, though this may not be significant considering the fact that the 1σ Monte Carlo error estimates on the total column densities are ±0.02 dex, and to the measured total difference in N(K I) between the sightlines is only 0.04 dex.

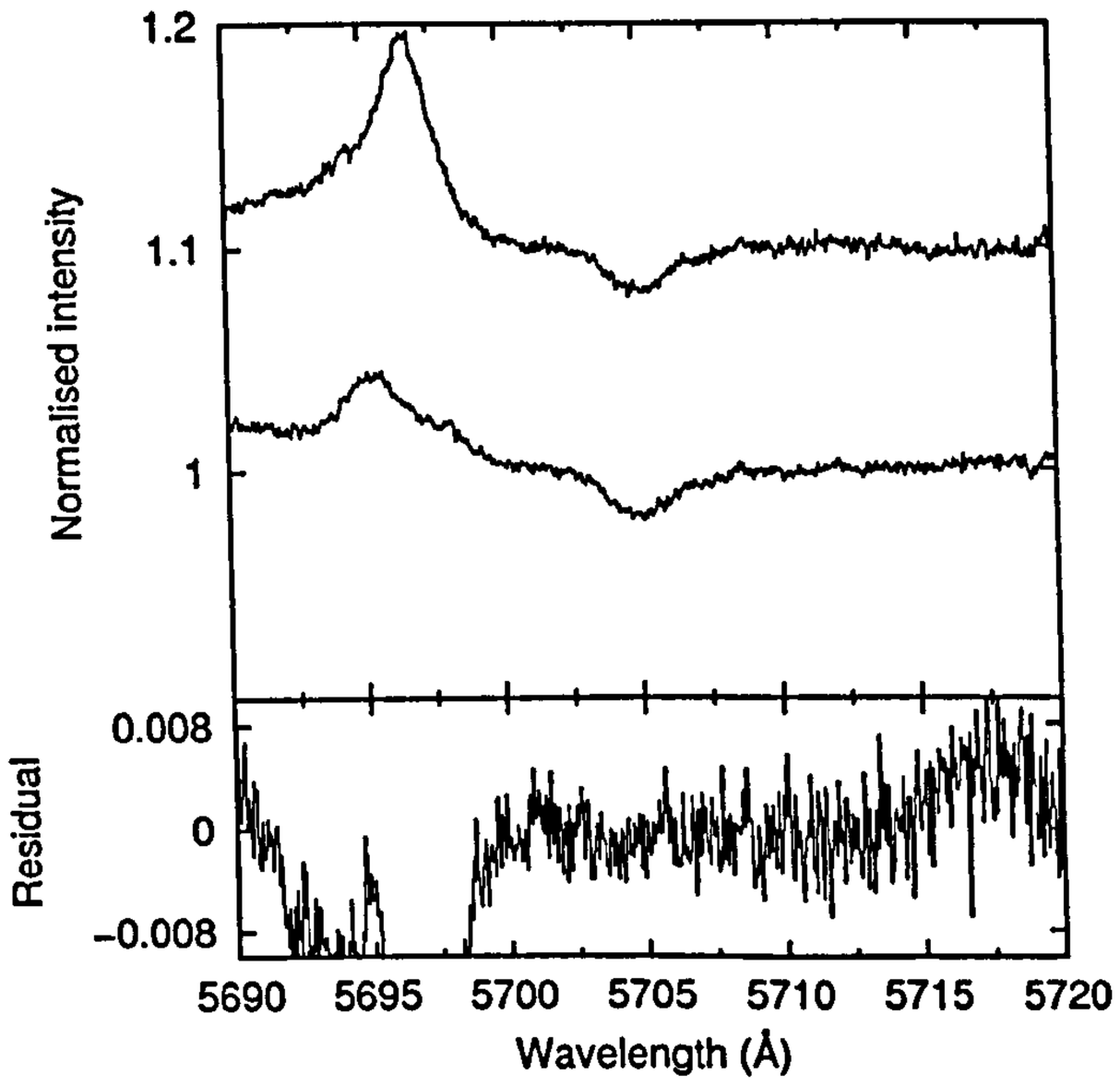

Figure 4.61: Spectra of λ5705 recorded towards HD 150135 (top) and HD 150136 (middle), telluric-corrected and normalised with straight line continua. Lower trace shows the residual intensities of HD 150136 – HD 150135.

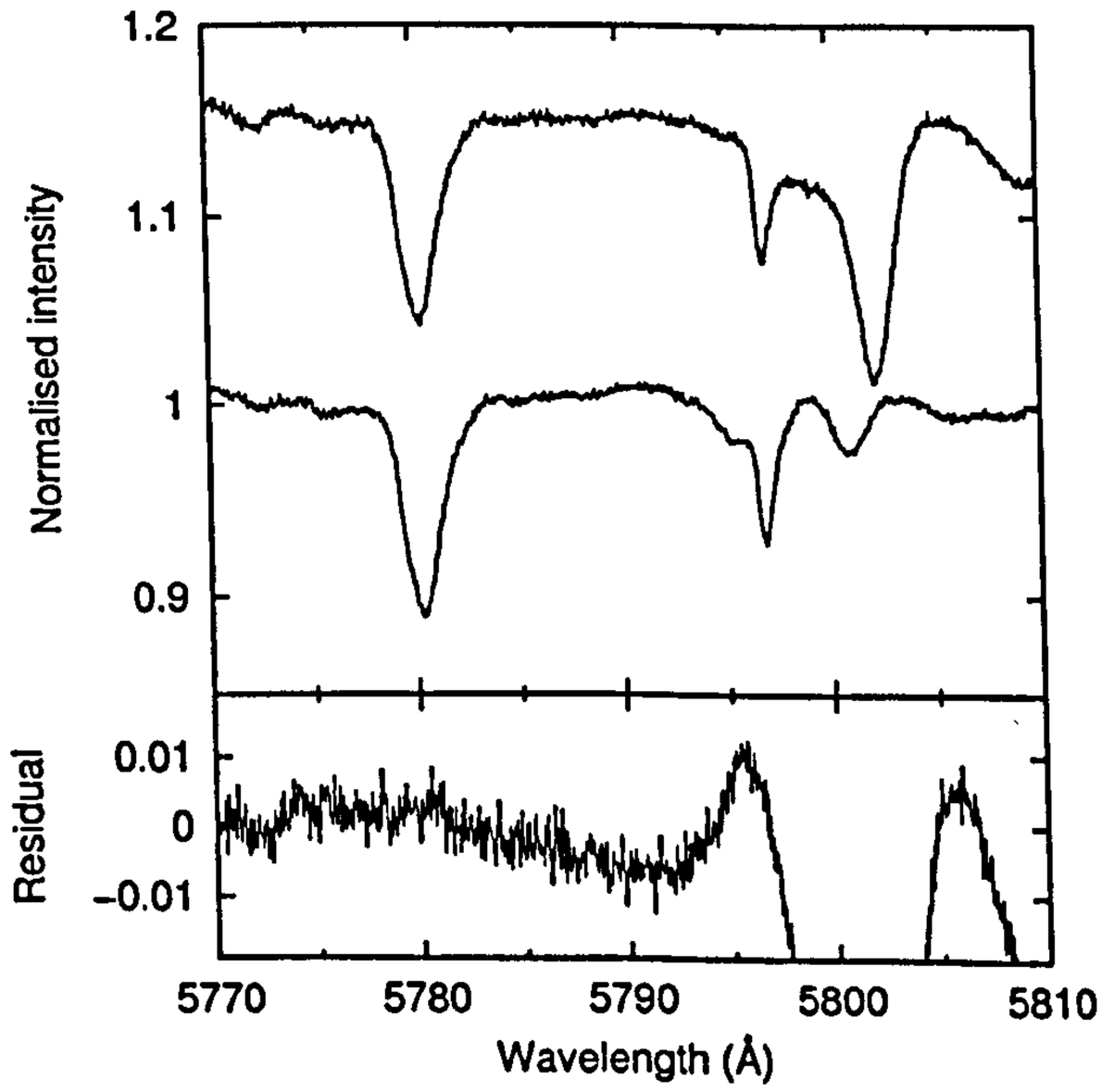

Figure 4.62: Spectra of λ5780 and λ5797 recorded towards HD 150135 (top) and HD 150136 (middle), telluric-corrected and normalised with straight line continua. Lower trace shows the residual intensities of HD 150136 – HD 150135.

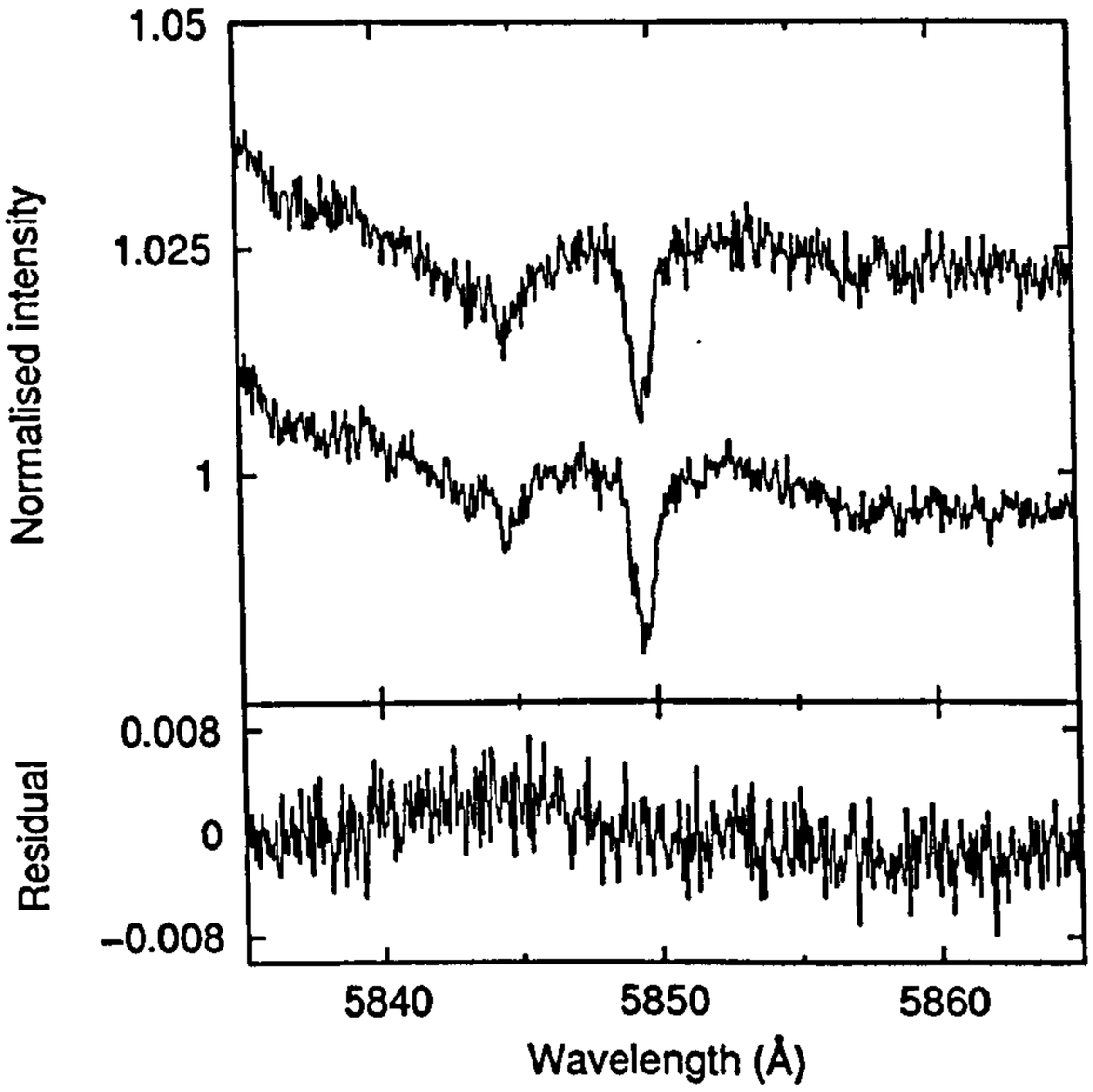

Figure 4.63: Spectra of λ5850 recorded towards HD 150135 (top) and HD 150136 (middle), telluric-corrected and normalised with straight line continua. Lower trace shows the residual intensities of HD 150136 – HD 150135.

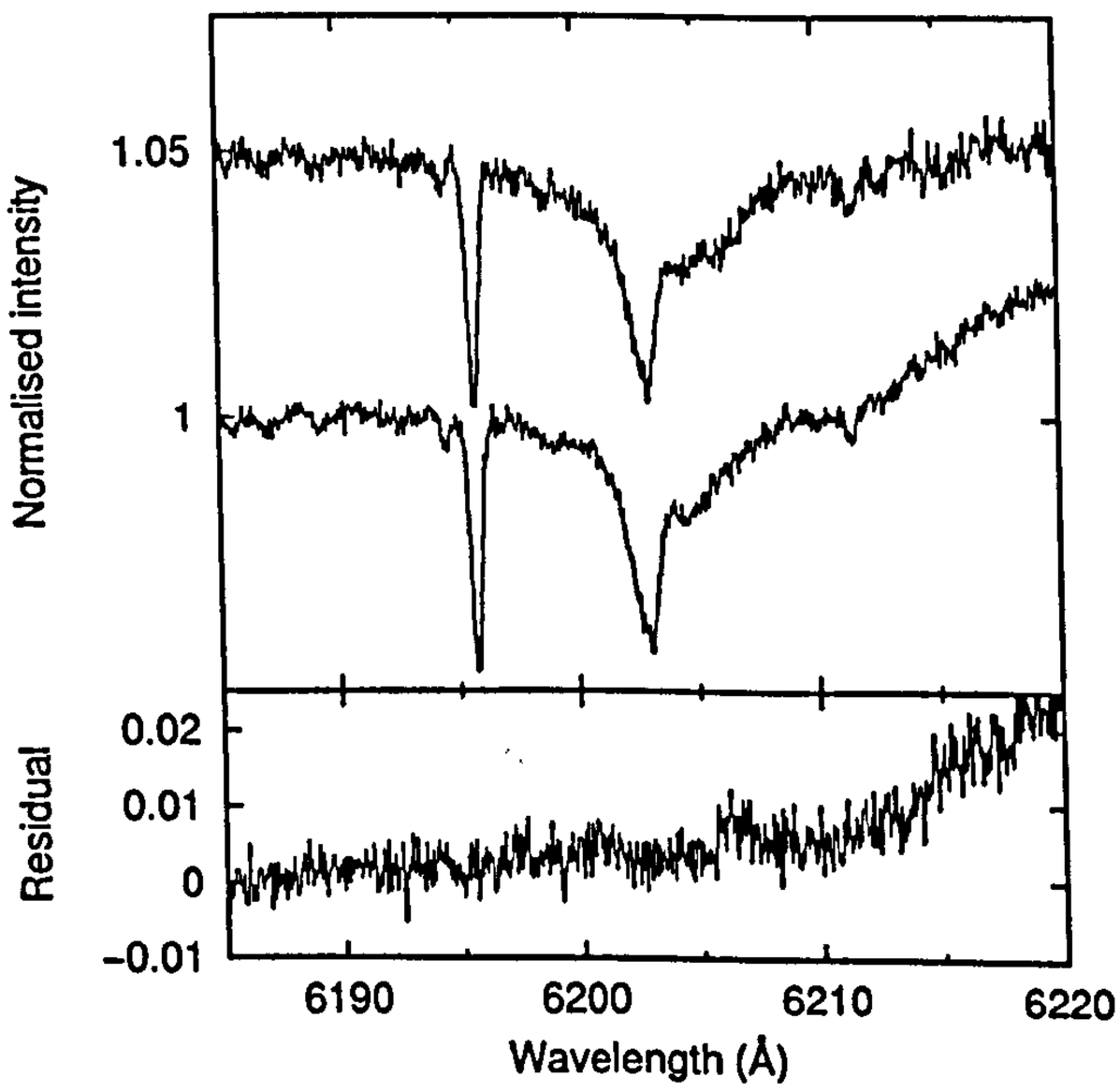

Figure 4.64: Spectra of λ6196 and λ6203 recorded towards HD 150135 (top) and HD 150136 (middle), telluric-corrected and normalised with low-order polynomial continua. Lower trace shows the residual intensities of HD 150136 – HD 150135.

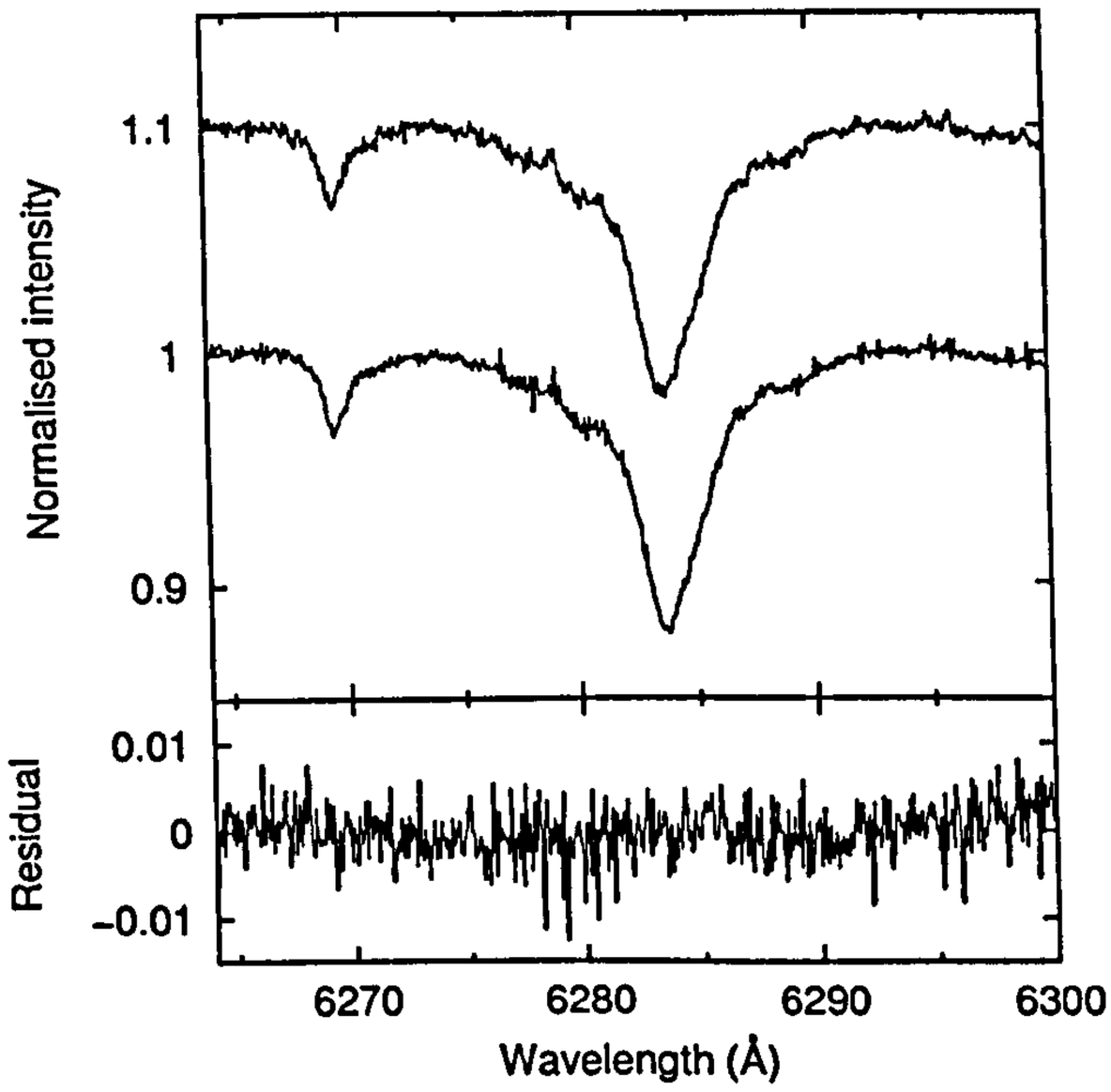

Figure 4.65: Spectra of λ6284 recorded towards HD 150135 (top) and HD 150136 (middle), telluric-corrected and normalised with straight line continua. Lower trace shows the residual intensities of HD 150136 – HD 150135.

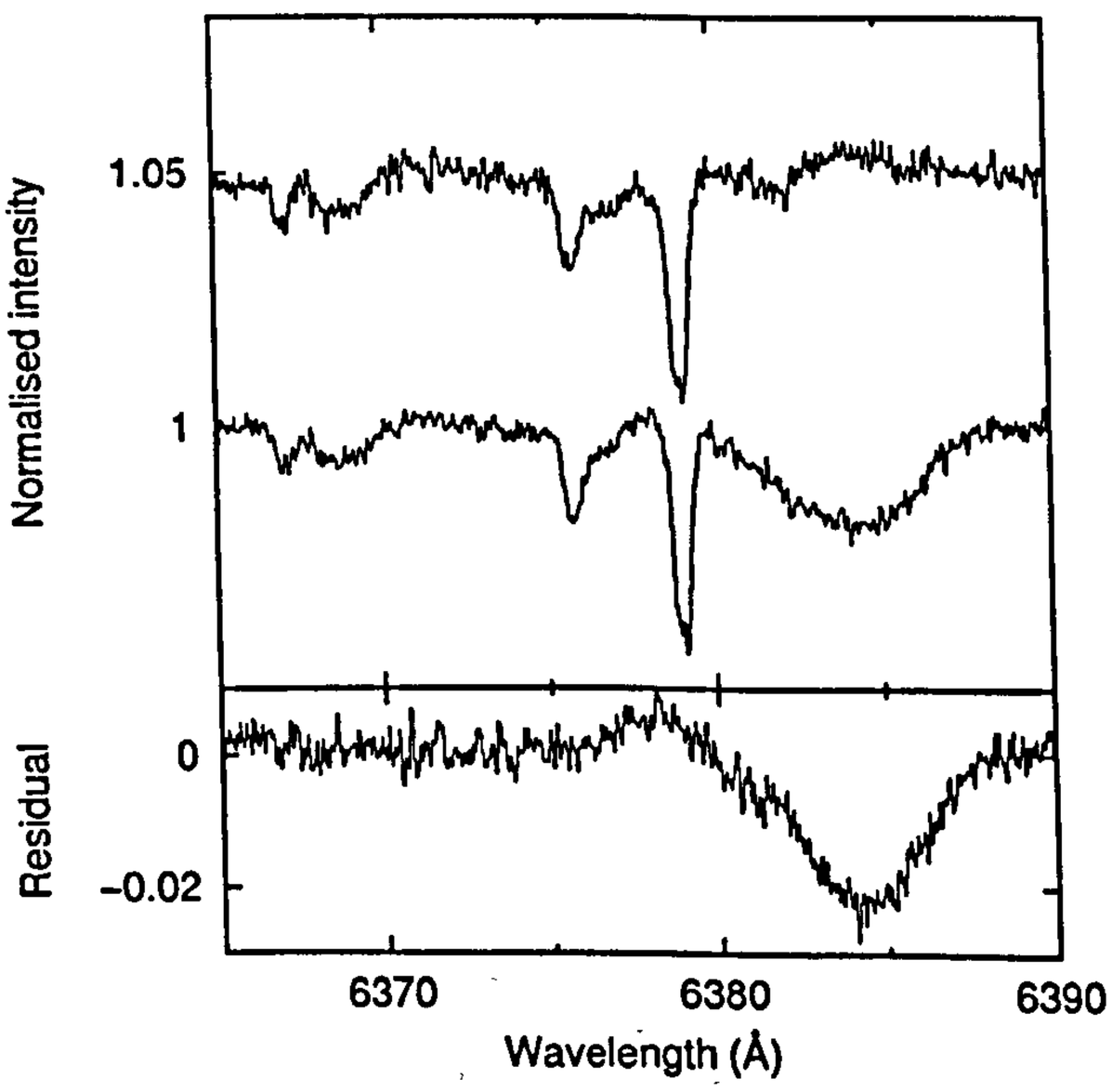

Figure 4.66: Spectra of λ6376 and λ6379 recorded towards HD 150135 (top) and HD 150136 (middle), telluric-corrected and normalised with straight line continua. Lower trace shows the residual intensities of HD 150136 – HD 150135.

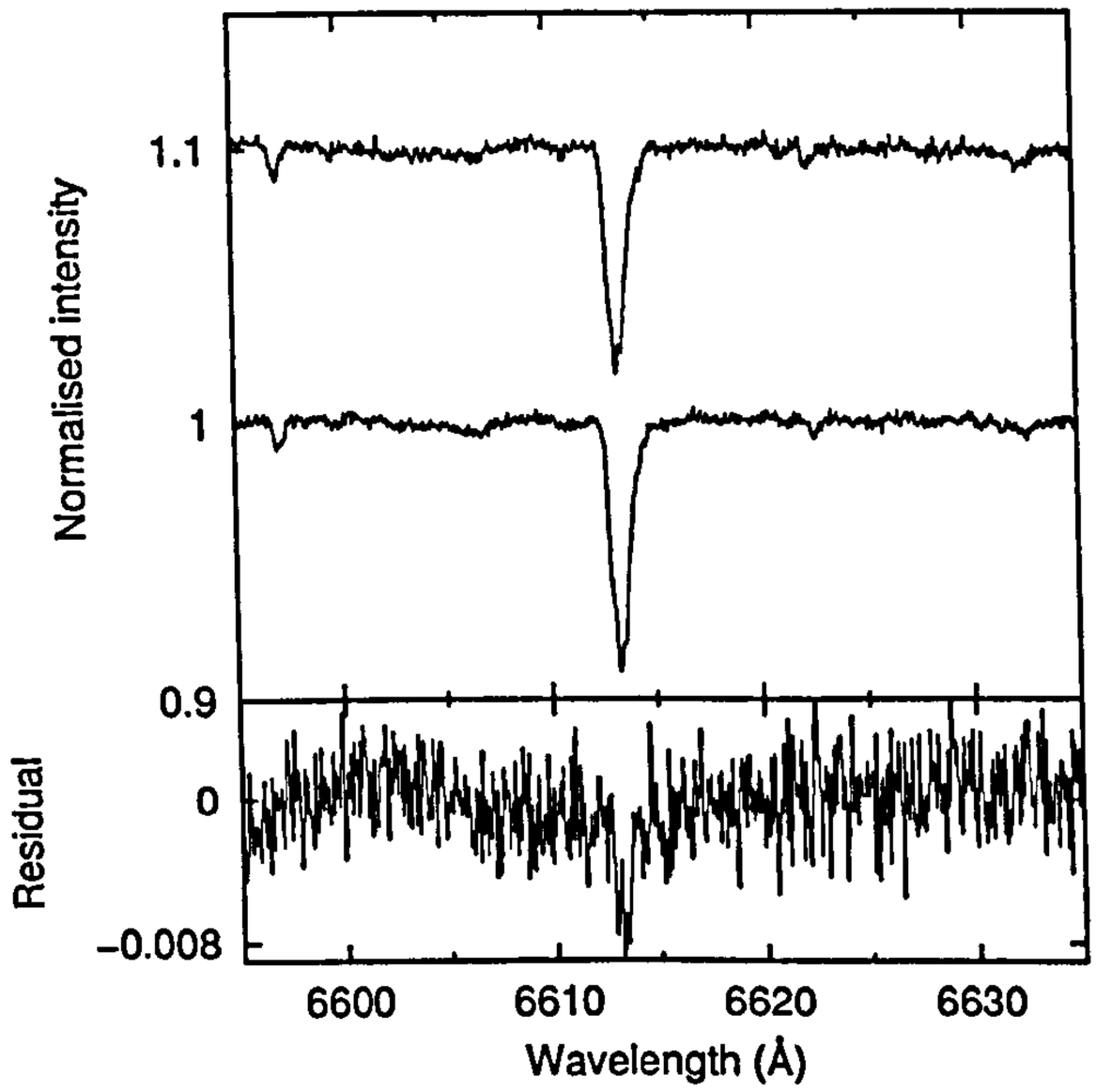

Figure 4.67: Spectra of λ6614 recorded towards HD 150135 (top) and HD 150136 (middle), telluric-corrected and normalised with straight line continua. Lower trace shows the residual intensities of HD 150136 – HD 150135.

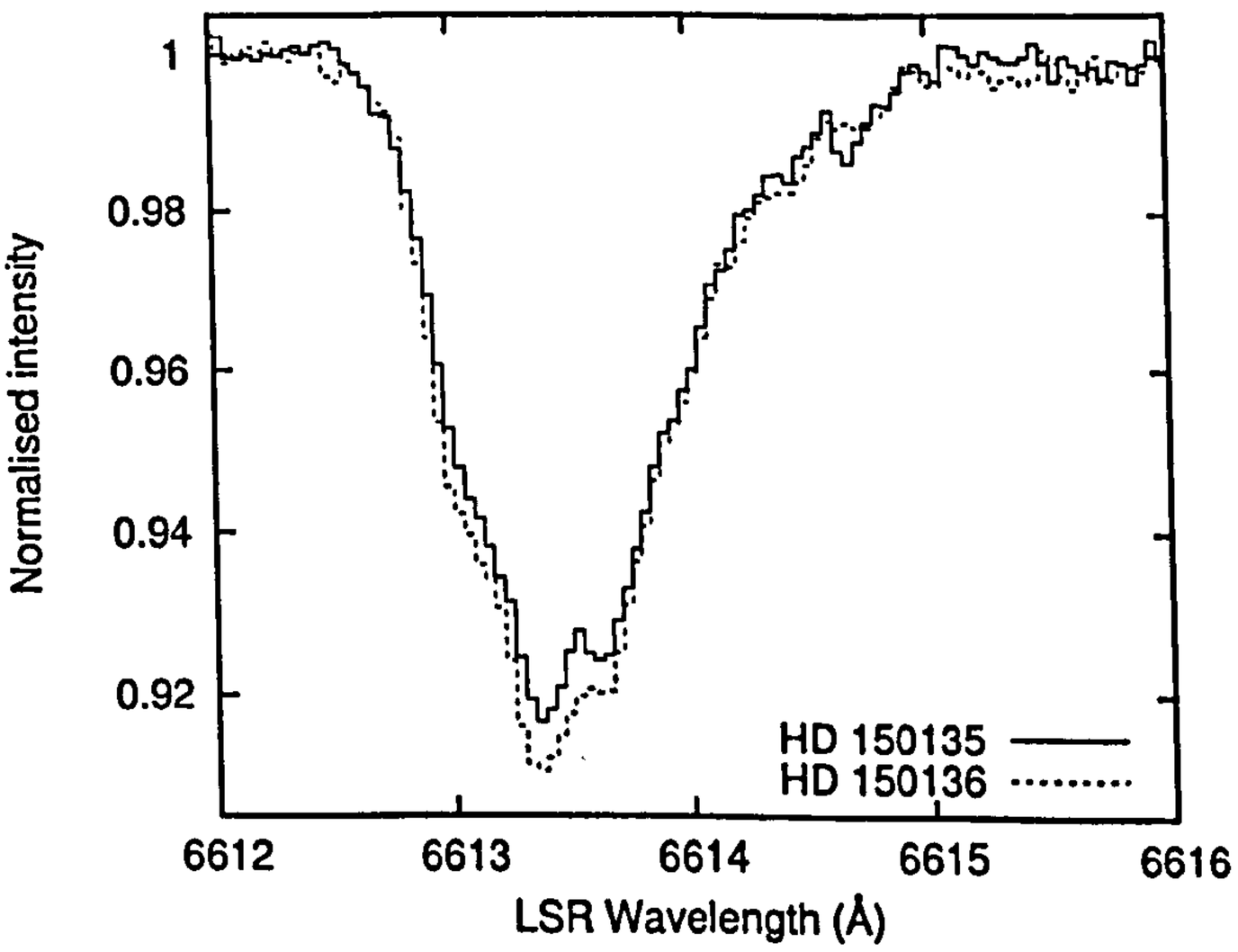

Figure 4.68: Overlaid HD 150135/6 λ6614 spectra, telluric-corrected and normalised with low-order polynomial continua.

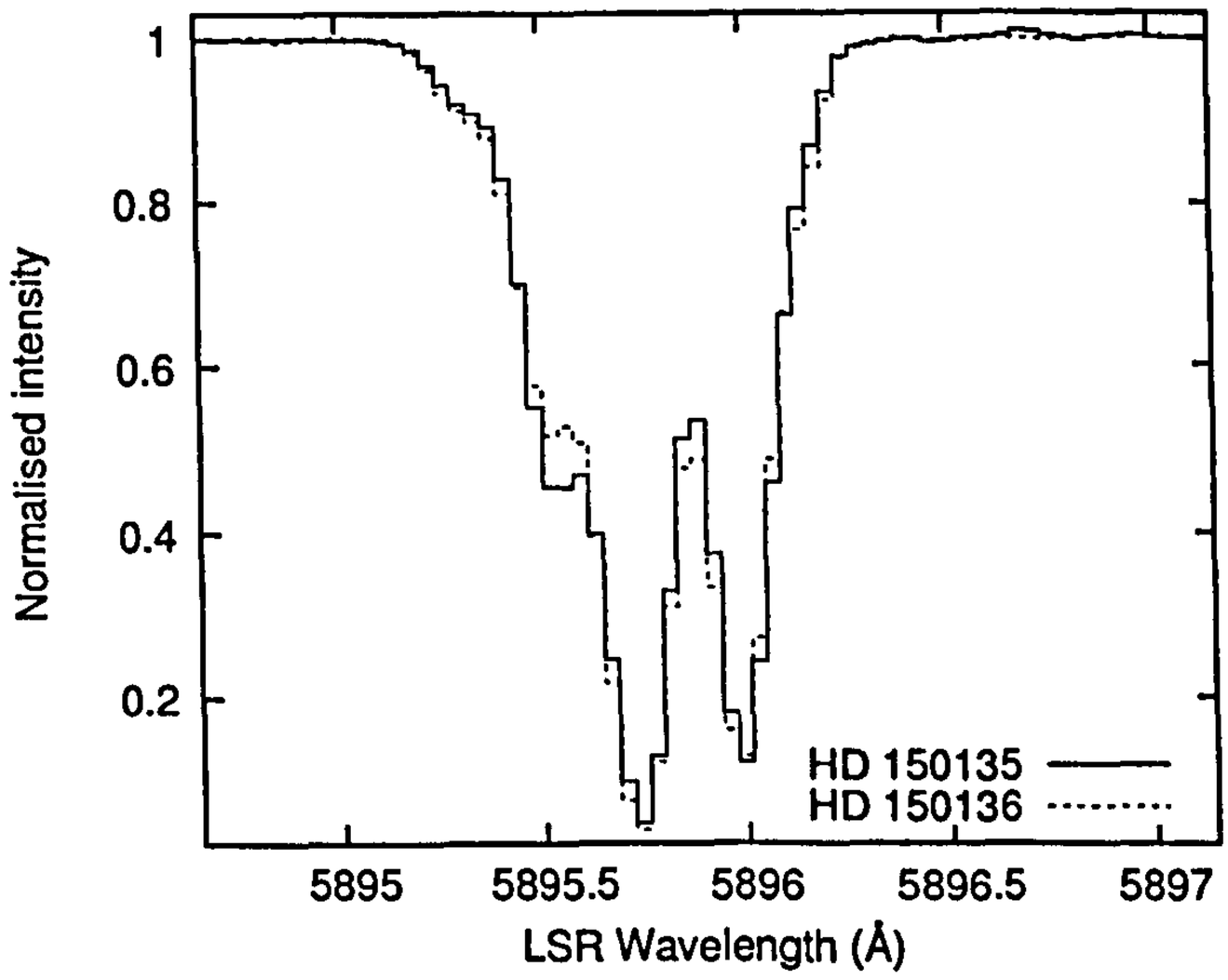

Figure 4.69: Overlaid HD 150135/6 Na I D_1 spectra, telluric-corrected and normalised with low-order polynomial continua.

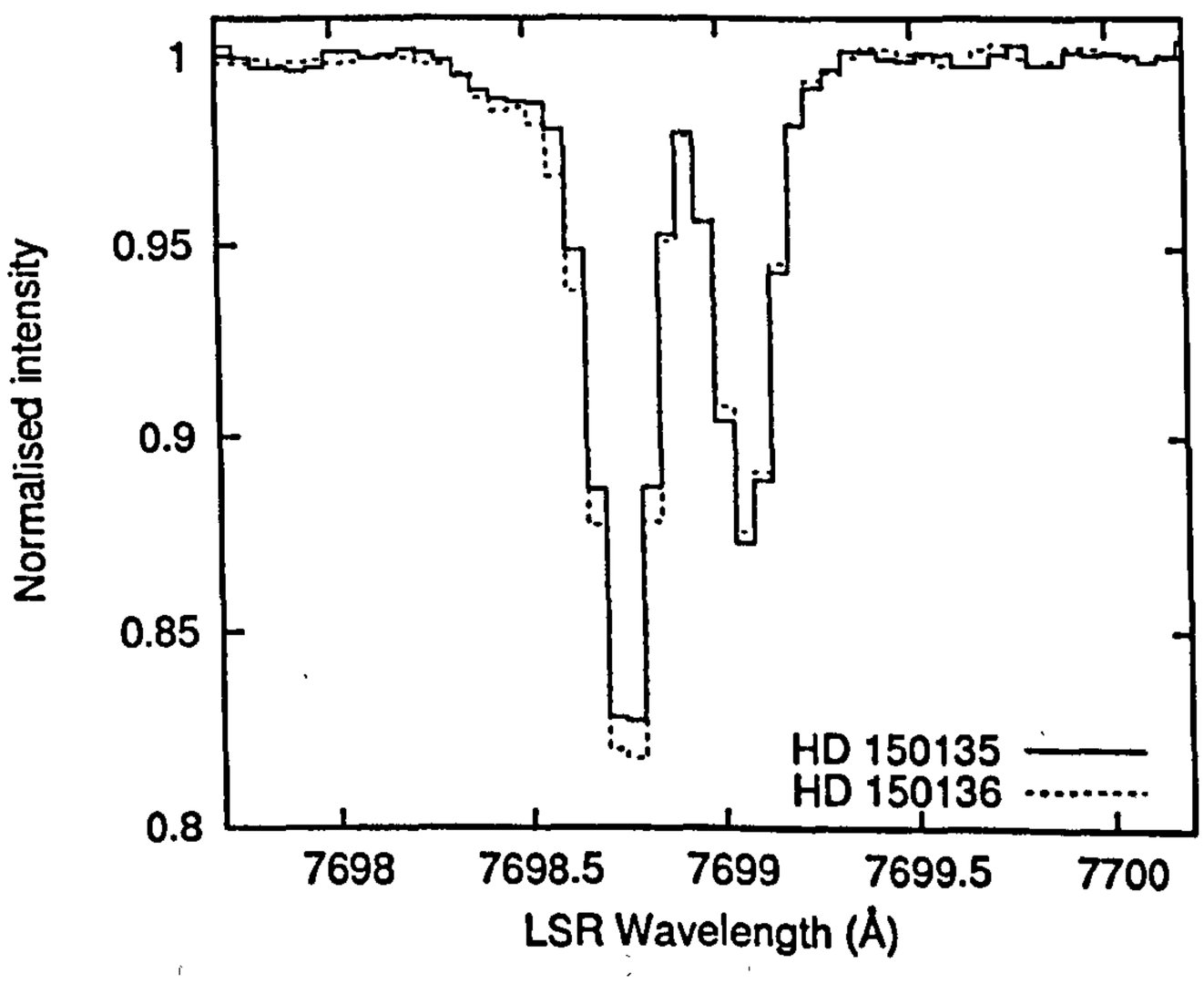

Figure 4.70: Overlaid HD 150135/6 K I λ7699 spectra, telluric-corrected and normalised with low-order polynomial continua.

	W_λ (mÅ)		δ(6/5)	
Feature	HD 150135	HD 150136	(%)	Blend?
λ5705	48	48	<12	N
λ5780	215	215	<2.4	N
λ5797	58	58	<3.4	Y
λ5850	25	25	<8.5	N
λ6196	25	25	<4.0	N
λ6203	120	120	<8.2	?
λ6284	620	620	<1.5	N
λ6376	18	18	<9.0	N
λ6379	31	31	<4.3	?
λ6426	4.8	4.8	<50	N
λ6439	4.5	4.5	<44	N
λ6445	11.7	11.7	<13.7	N
λ6614	89.9	95	5.7 (2.4)	N
λ6660	14	14	<9.1	N
λ7224	120	120	<2.1	T
λ7562	55	55	<8.2	N
K I λ7699	58.5	61.7	5.5 (3.6)	
Na I D_1	478.6	482	0.7 (0.3)	
log N(K I)	11.59	11.63	11 (10)	

Table 4.8: Equivalent widths of interstellar features measured towards HD 150135/6. δ(6/5) is the percentage *excess* of HD 150136 measurements compared to HD 150135, with error estimates given in parentheses. N(K I) data were measured using VAPID. In the last column, 'Y' indicates a definite or probable stellar blend contaminating the DIB spectra, 'N' indicates improbable or absent stellar blend and '?' is for indeterminate cases, 'T' indicates severe telluric contamination of results.

	v_{LSR} (km s^{-1})		Doppler b (km s^{-1})		log(N (cm^{-2}))	
	HD 150135	HD 150136	HD 150135	HD 150136	HD 150135	HD 150136
1	-19.6	-19.6	3.9 (1.1)	4.5 (1.4)	10.20 (0.07)	10.32 (0.07)
2	-10.0	-10.0	1.6 (0.2)	2.2 (0.3)	11.11 (0.01)	11.15 (0.01)
3	-7.3	-7.3	0.3 (0.1)	0.3 (0.1)	11.01 (0.05)	11.13 (0.04)
4	3.5	3.5	2.0 (0.2)	2.0 (0.3)	11.14 (0.01)	11.13 (0.01)

Table 4.9: Parameters of the least-squares VAPID interstellar K I models fits to the data shown in Figure 4.70 for HD 150135 and HD 150136. Cloud velocities were optimised for both sightlines, averaged, then fixed for the final model optimisation; all other parameters were free to vary. 1σ Monte Carlo errors (calculated using 100 replications) are given in parentheses.

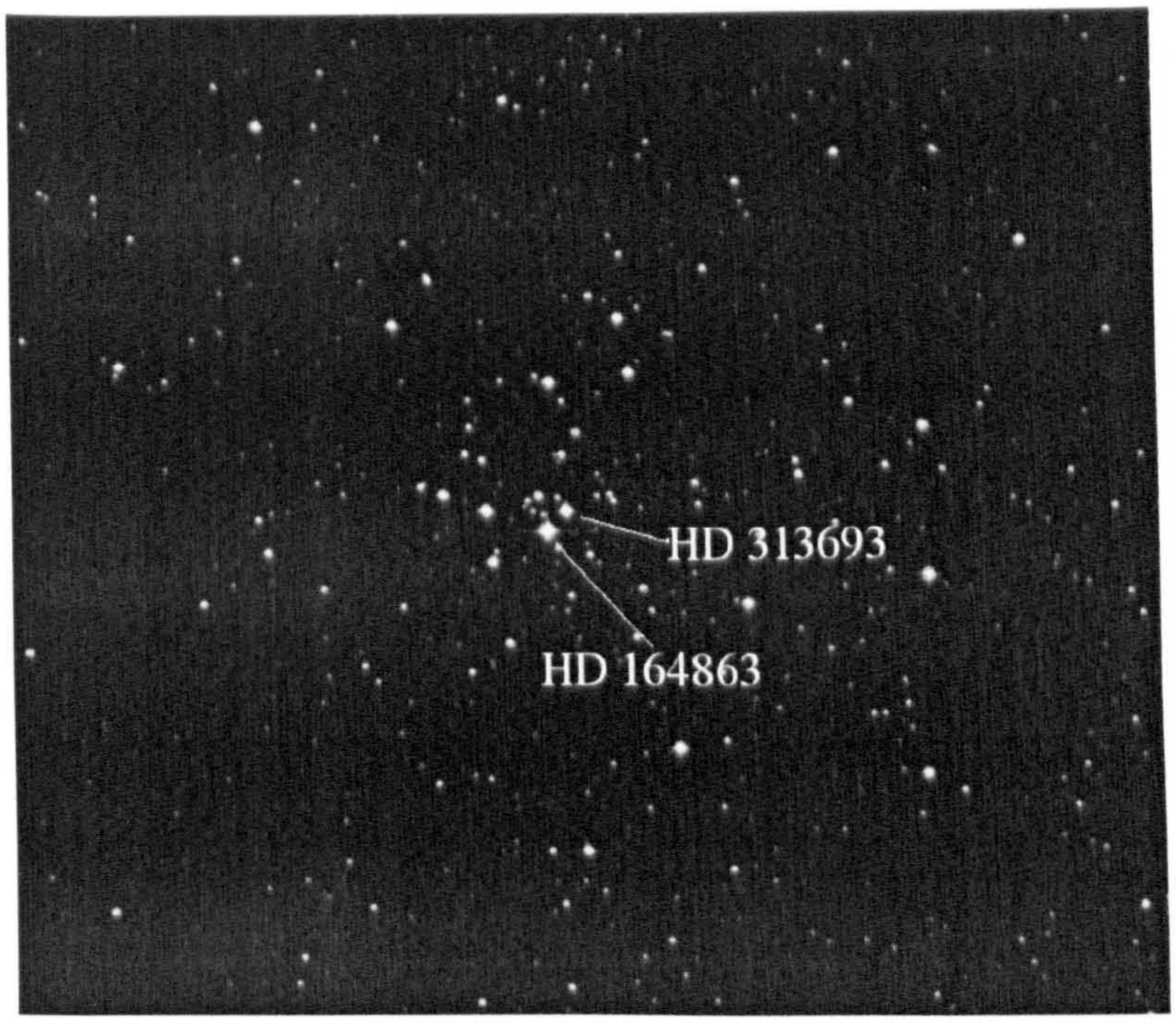

Figure 4.71: Annotated image of NGC 6531 (M 21) obtained from the Digitized Sky Survey. HD 164863 and HD 313693 are the brightest members of this young open cluster and are separated by 30.6″. The Digitized Sky Surveys were produced at the Space Telescope Science Institute under U.S. Government grant NAG W-2166. The images of these surveys are based on photographic data obtained using the Oschin Schmidt Telescope on Palomar Mountain and the UK Schmidt Telescope. The plates were processed into the present compressed digital form with the permission of these institutions.

4.3.7 HD 164863/313693

According to Forbes (1996) HD 164863 and HD 313693 are the brightest members of the young (~ 8 Myrs old) cluster NGC 6531 (M 21). The cluster is located towards the Galactic centre in a region of the Milky Way particularly rich in young objects, and is proposed to be a part of the star-forming region Sgr I. The distance to NGC 6531 is about 1400 pc, and no neutral or ionised gas is associated with the cluster itself such that the reddening of $E_{B-V} = 0.28$ arises in foreground material. The separation of 30.6″ between HD 164863 and HD 313693 produces a SSS probe length of $\lesssim 43,000$ AU due to the sky-projected separation of the stars. An annotated image of NGC 6531 is shown in Figure 4.71.

All of the strong DIBs recorded for β Sco, ν Sco and ρ Oph have been measured, and the early spectral type of these stars combined with the moderately low signal-to-

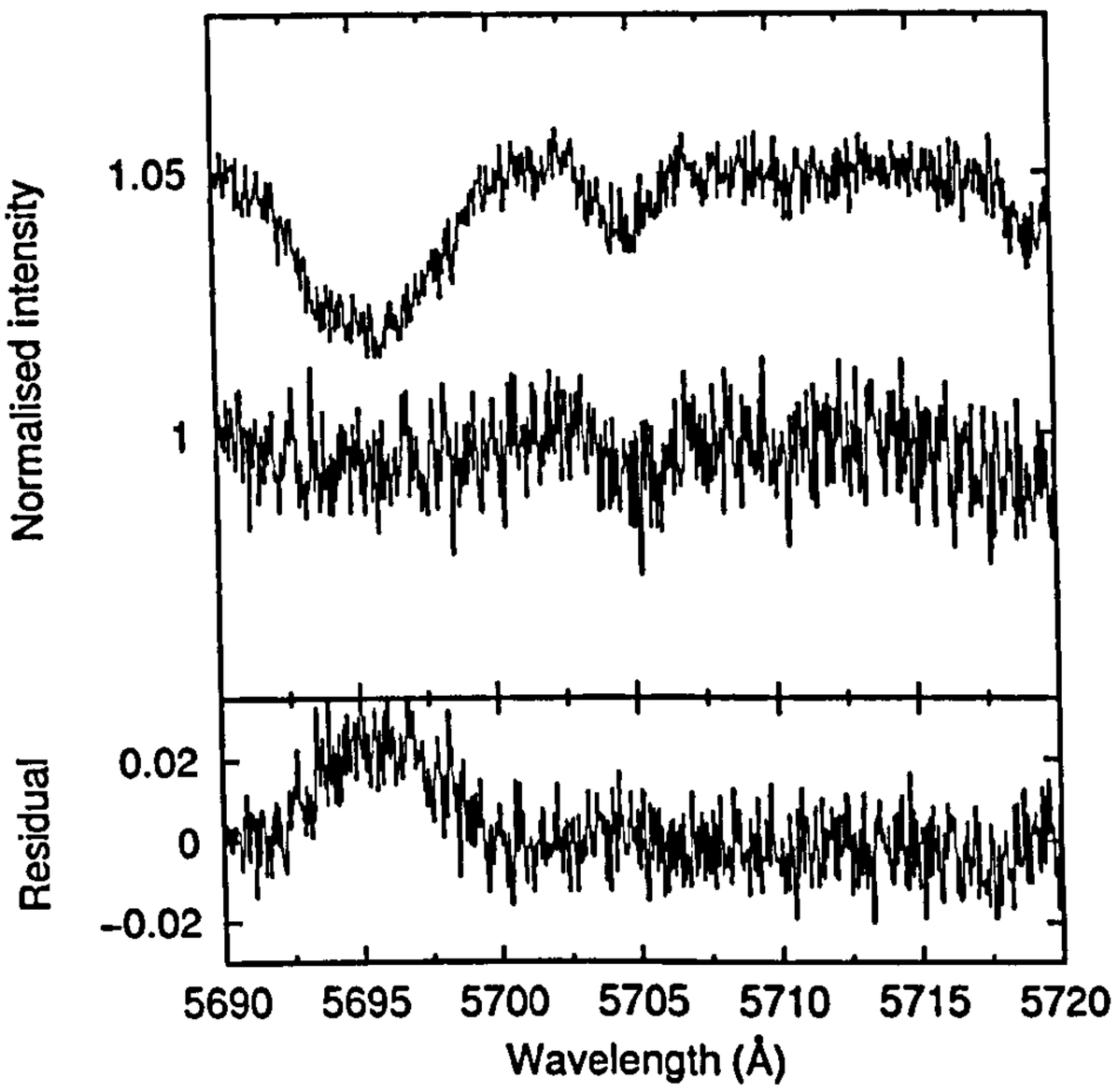

Figure 4.72: Spectra of λ5705 recorded towards HD 164863 (top) and HD 313693 (middle), telluric-corrected and normalised with straight line continua. Lower trace shows the residual intensities of HD 313693 – HD 164863.

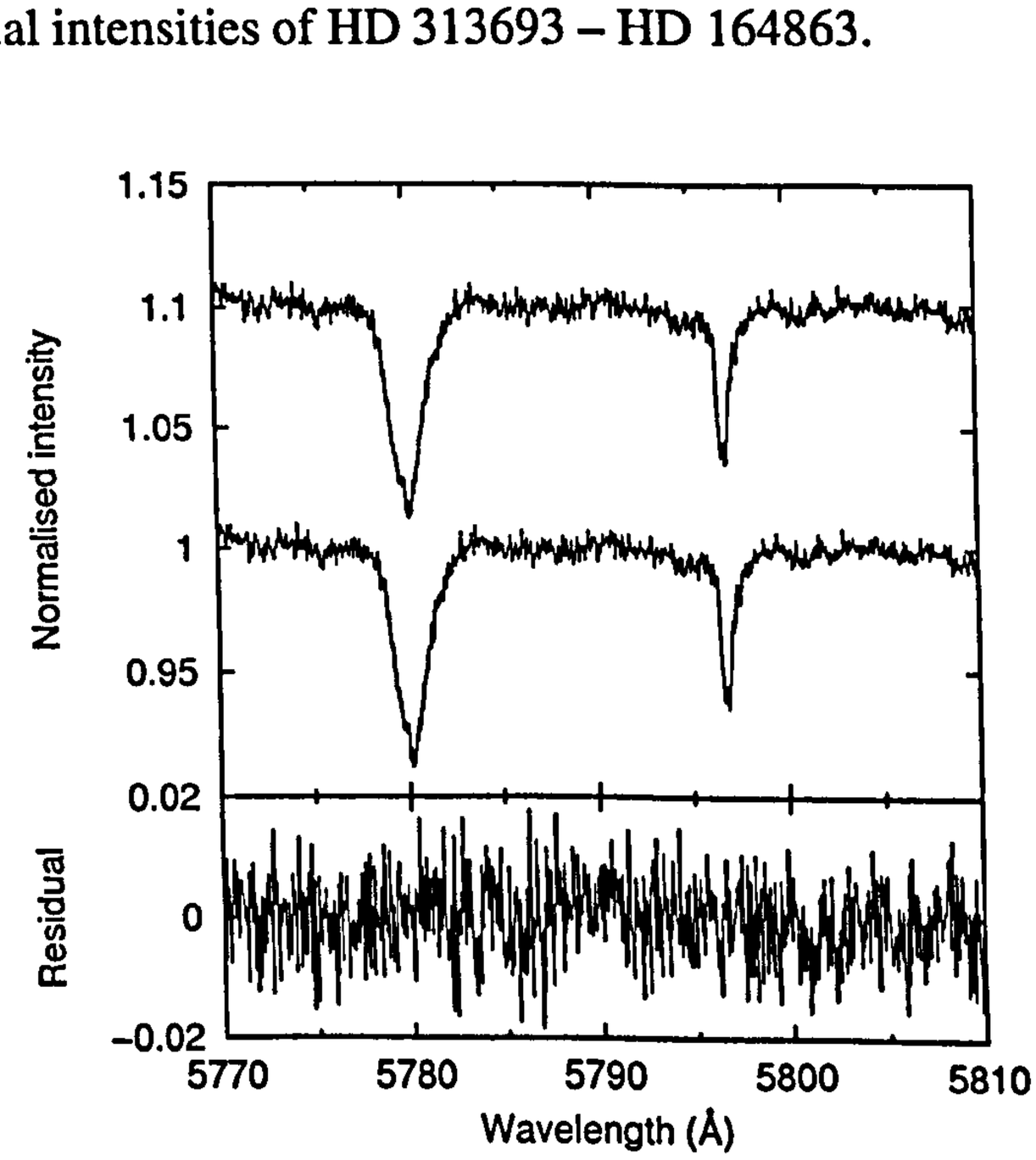

Figure 4.73: Spectra of λ5780 and λ5797 recorded towards HD 164863 (top) and HD 313693 (middle), telluric-corrected and normalised with straight line continua. Lower trace shows the residual intensities of HD 313693 – HD 164863.

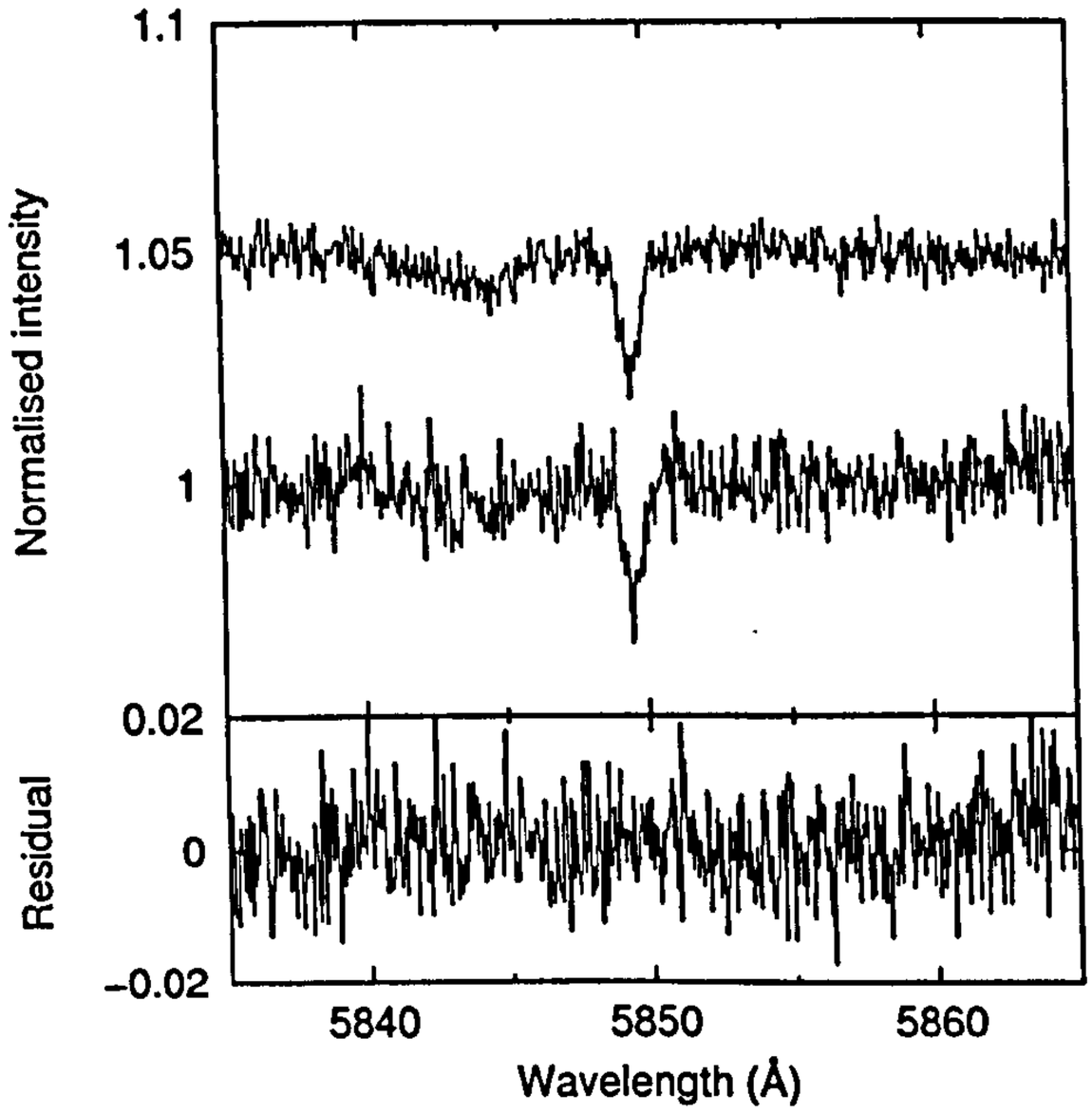

Figure 4.74: Spectra of λ5850 recorded towards HD 164863 (top) and HD 313693 (middle), telluric-corrected and normalised with straight line continua. Lower trace shows the residual intensities of HD 313693 – HD 164863.

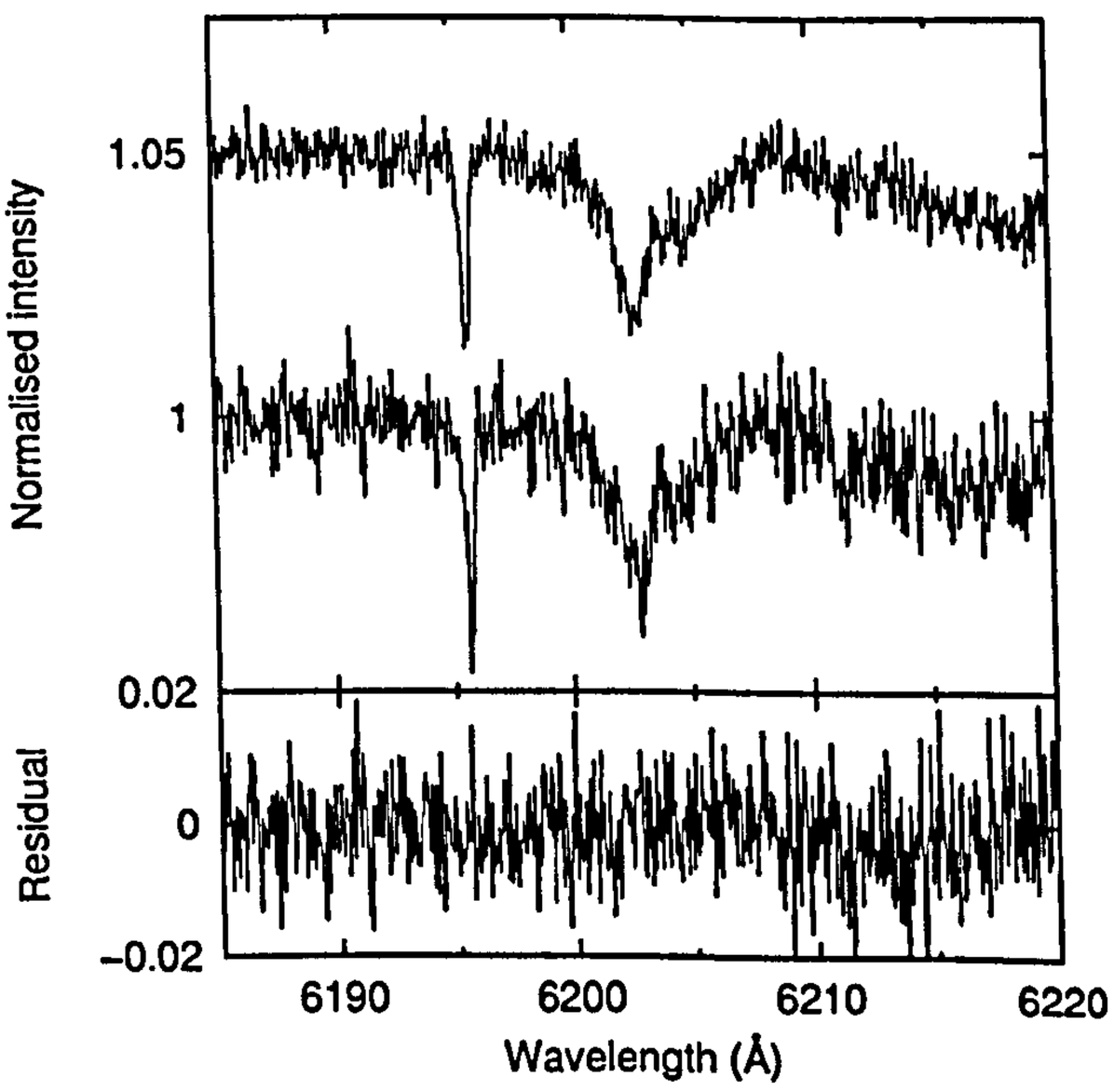

Figure 4.75: Spectra of λ6196 and λ6203 recorded towards HD 164863 (top) and HD 313693 (middle), telluric-corrected and normalised with low-order polynomial continua. Lower trace shows the residual intensities of HD 313693 – HD 164863.

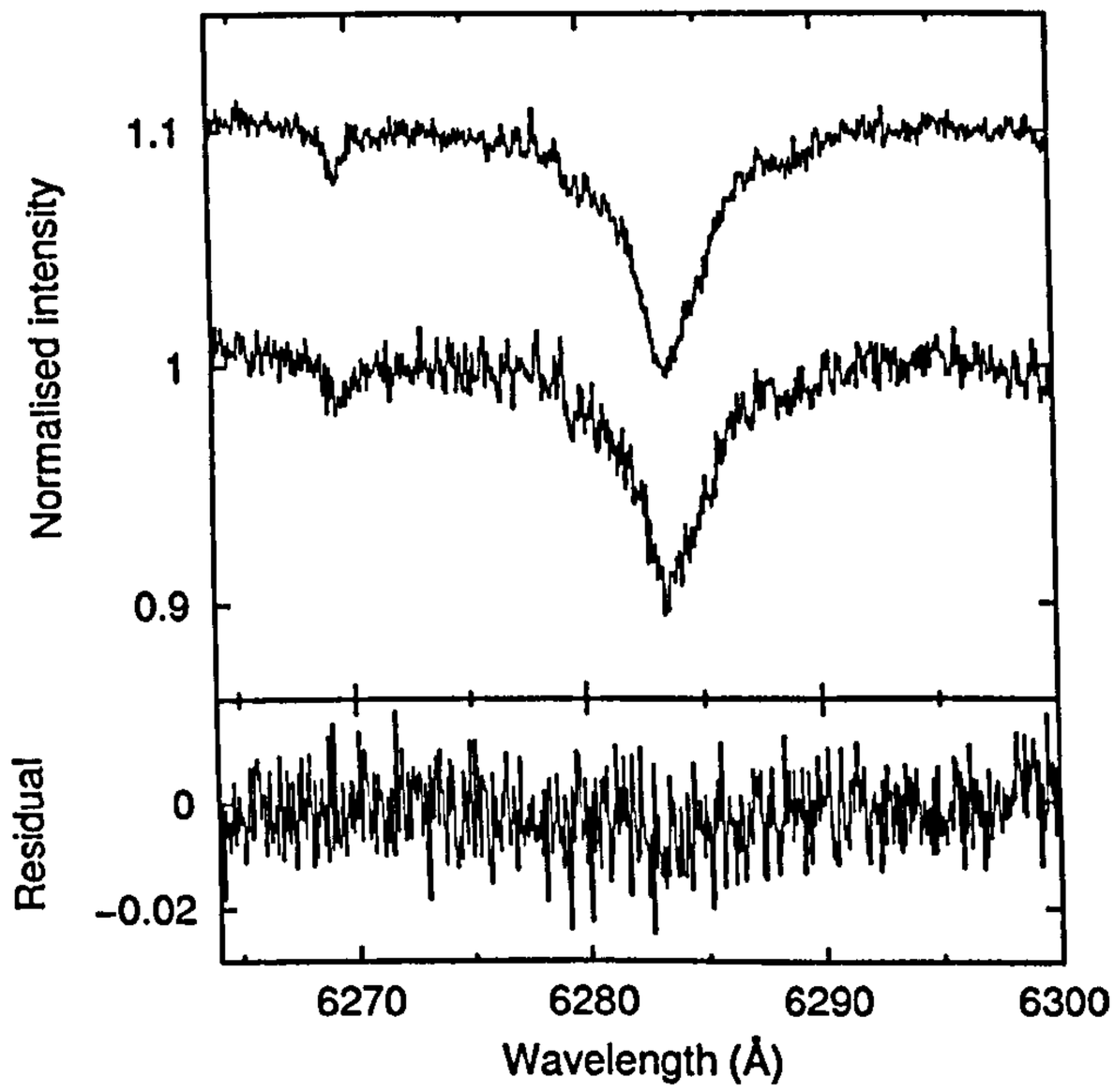

Figure 4.76: Spectra of λ6284 recorded towards HD 164863 (top) and HD 313693 (middle), telluric-corrected and normalised with straight line continua. Lower trace shows the residual intensities of HD 313693 – HD 164863.

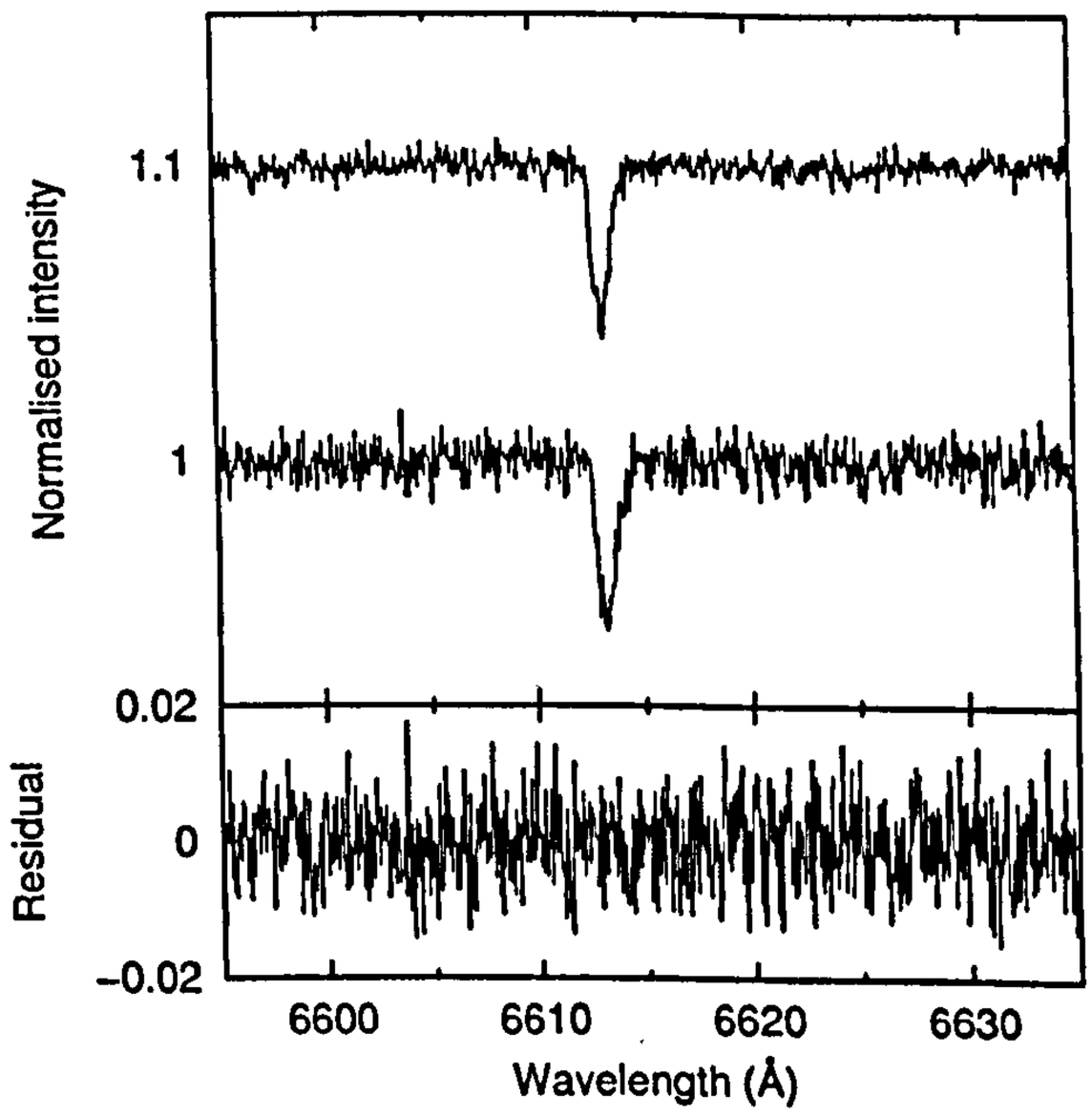

Figure 4.77: Spectra of λ6614 recorded towards HD 164863 (top) and HD 313693 (middle), telluric-corrected and normalised with straight line continua. Lower trace shows the residual intensities of HD 313693 – HD 164863.

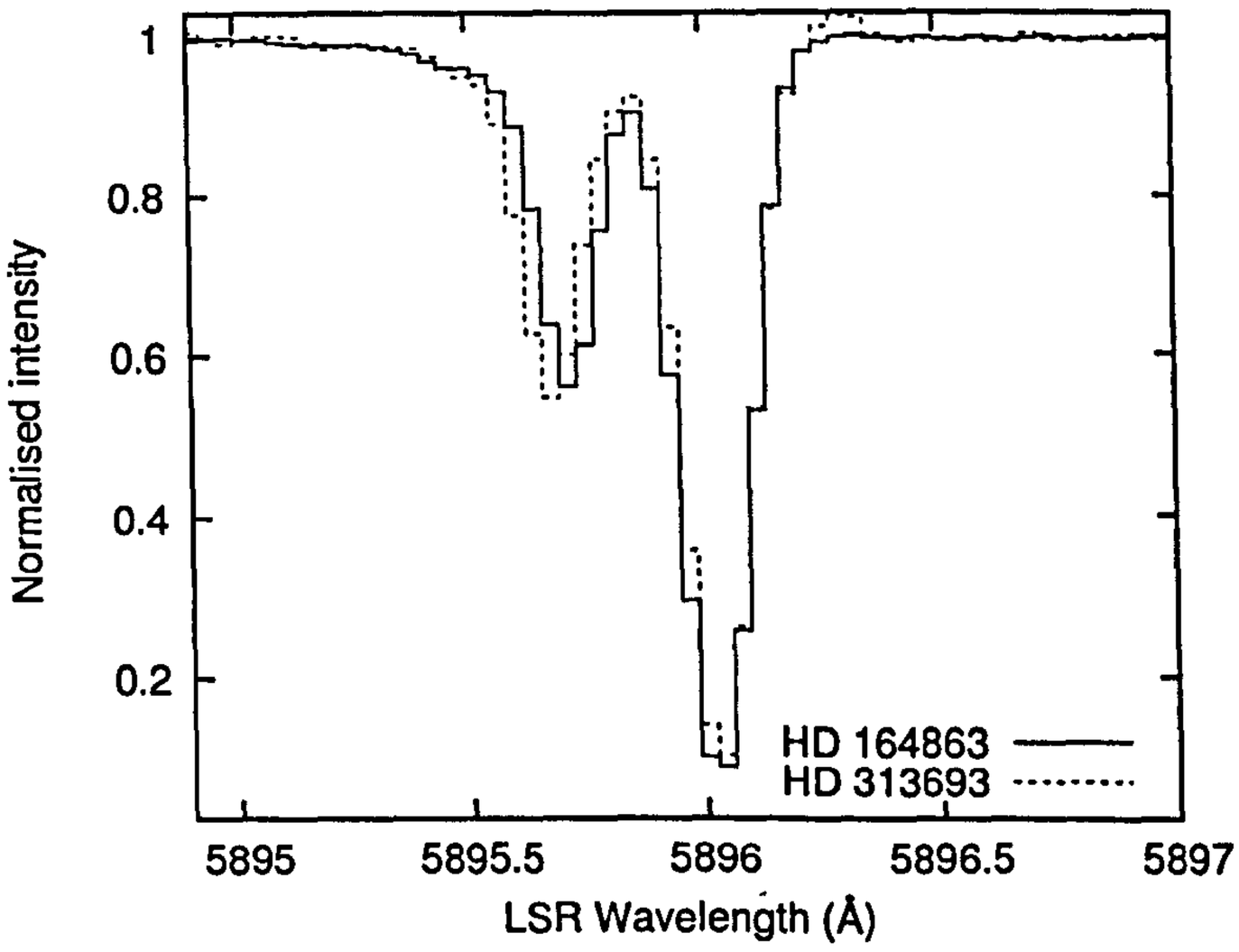

Figure 4.78: Overlaid HD 164863/313693 Na I D_1 spectra, telluric-corrected and normalised with low-order polynomial continua.

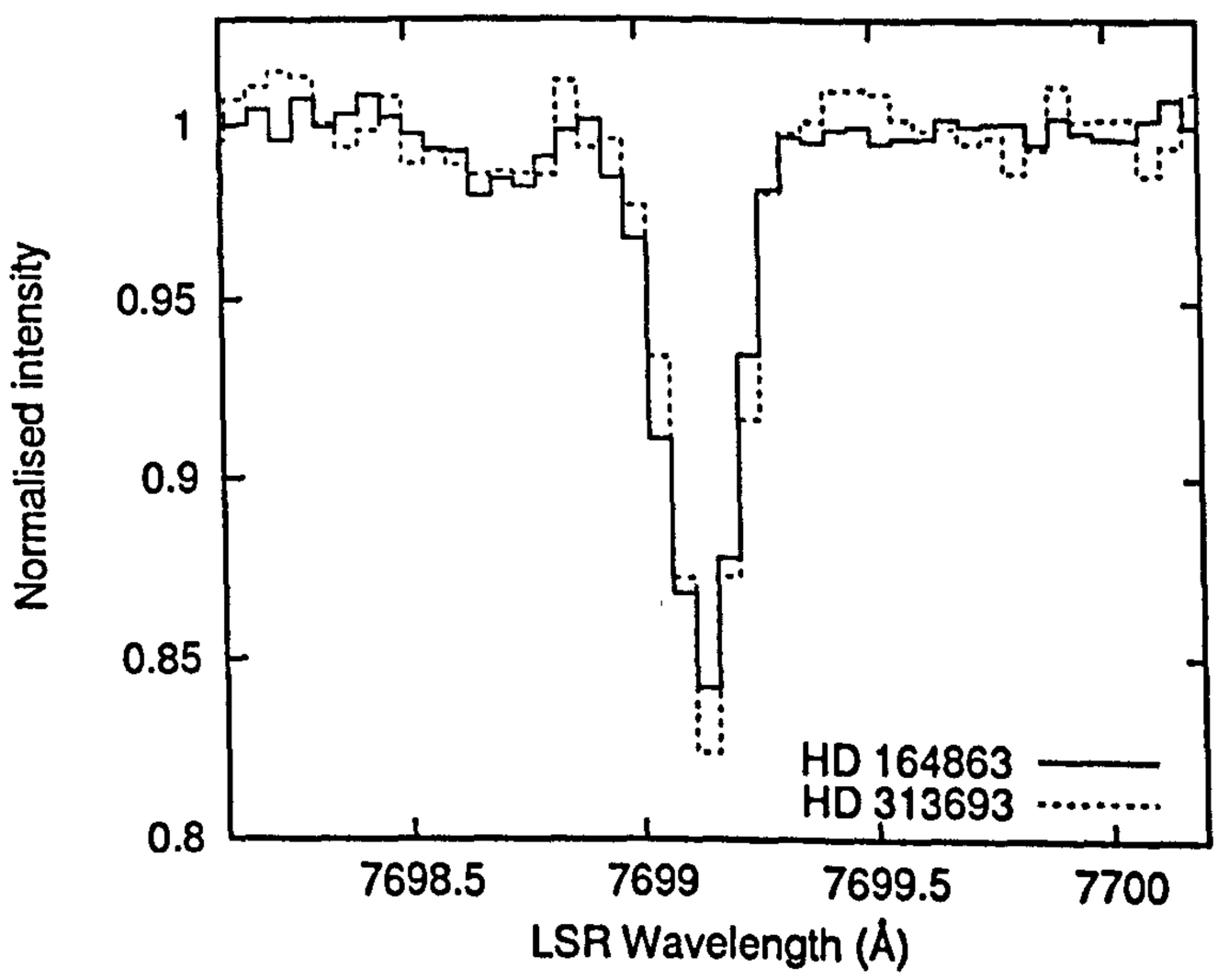

Figure 4.79: Overlaid HD 164863/313693 K I λ7699 spectra, telluric-corrected and normalised with low-order polynomial continua.

	W_λ (mÅ)		δ(B/A)	
Feature	HD 164863	HD 313693	(%)	Blend?
λ5705	31	31	<41	N
λ5780	168	168	<6.8	N
λ5797	49.5	49.5	<8.7	N
λ5850	20	20	<24	N
λ6196	15	15	<15	N
λ6203	102	102	<22	N
λ6284	495	495	<4.2	N
λ6376	8.5	8.5	<44	N
λ6379	17	17	<18	N
λ6426	3.7	3.7	<148	N
λ6439	6.4	6.4	<71	N
λ6445	4.6	4.6	<81	N
λ6614	52.5	52.5	<9.5	N
λ6660	5.9	5.9	<5.1	N
λ7224	82	82	<7.6	T
λ7562	29.5	29.5	<38	N
K I λ7699	34.9	36.2	3.7 (5.3)	
Na I D_1	254.6	250.1	-1.8 (0.5)	
log N(K I)	11.31	11.32	1.9 (12)	

Table 4.10: Equivalent widths of interstellar features measured towards HD 164863/313693. δ(B/A) is the percentage *excess* of HD 313693 measurements compared to HD 164863, all of which are approximate upper limits for this system. N(K I) data were calculated using VAPID. In the last column, 'Y' indicates a definite or probable stellar blend contaminating the DIB spectra, 'N' indicates improbable or absent stellar blend and '?' is for indeterminate cases, 'T' indicates severe telluric contamination of results.

noise of the observations (~ 300) means that no significant stellar features appear to contaminate the DIB profiles or the continua immediately adjacent to them. Examples of the recorded spectra and residual intensities of the stronger DIBs are plotted in Figures 4.73 to 4.77. The flatness of the residuals in each case leads to the result that no DIB variation has been observed between HD 164863 and HD 313693. Although the S/N is not as high as for other spectra in this study, upper limits of $\lesssim$ 10% have been determined for the possible difference in many of the measured DIB equivalent widths, as shown in Table 4.10. The most stringent upper limits on the amount of DIB variation are $\simeq$ 6.8% for λ5780, $\simeq$ 4.2% for λ6284 and $\simeq$ 5.1% for λ6660.

The Na I D_1 and K I λ7699 lines (Figures 4.78 and 4.79) show that $W_{\mathrm{Na\ I\ D_1}}$ is greater towards HD 164863 by almost 2% whereas $W_{\mathrm{K\ I\ \lambda 7699}}$ is almost 4% greater towards

	v_{LSR} (km s^{-1})		Doppler b (km s^{-1})		log(N (cm^{-2}))	
	HD 164863	HD 313693	HD 164863	HD 313693	HD 164863	HD 313693
1	-12.2	-12.2	3.0	3.0	10.33 (0.08)	10.24 (0.18)
2	6.5	6.5	2.5	2.5	11.26 (0.01)	11.28 (0.02)

Table 4.11: Parameters of the least-squares VAPID interstellar K I models fits to the data shown in Figure 4.79 for HD 164863 and HD 313693. Cloud velocities and Doppler b parameters were optimised for both sightlines, averaged, then held fixed in the final model optimisation; all column densities were free to vary. 1σ Monte Carlo errors (calculated using 100 replications) are given in parentheses.

HD 313693, though the measured K I variation is within the error estimate so may not be significant. Modelling the K I line-profiles in VAPID required two clouds and yielded logarithmic column densities with 1σ Monte Carlo error estimates of 11.31 ± 0.01 towards HD 164863 and 11.32 ± 0.02 towards HD 313693. The model parameters are given in Table 4.11. The column densities of the the saturated interstellar Na D lines could not be reliably modelled in these relatively low-resolution data.[6]

4.3.8 Small-scale spatial variation in the velocity structure of the ISM towards HD 164863/313693

Although there is no convincing evidence for a difference in the strengths of the DIBs or atomic lines between HD 164863 and HD 313693, there exists a difference in the *velocity* structure of the interstellar gas. Examination of the Na I spectra in Figure 4.78 reveals that the interstellar absorption profile consists of a strong and a weak component, Doppler-separated by about 2.3 Å. From measurements of the shifts in successive Th/Ar spectra, the UCLES wavelength calibration was found to be accurate to about 0.01 Å over time periods greater than the difference in time (about an hour) between which the exposures of HD 164863 and HD 313693 were obtained. The peak absorption wavelengths of the strong component match to within this accuracy (measured by cross-correlation of the line-profiles in IRAF). The peak absorption of the weaker component however, is shifted to the blue in the HD 313693 spectrum compared with HD 164863 by about 1 CCD pixel, or ≈ 0.04 Å.

VAPID was used to construct models of the Na I cloud structure in the two sightlines,

[6]Noise in saturated line profiles leads to large errors in the observed apparent optical depth, substantially reducing the accuracy of least-squares column densities.

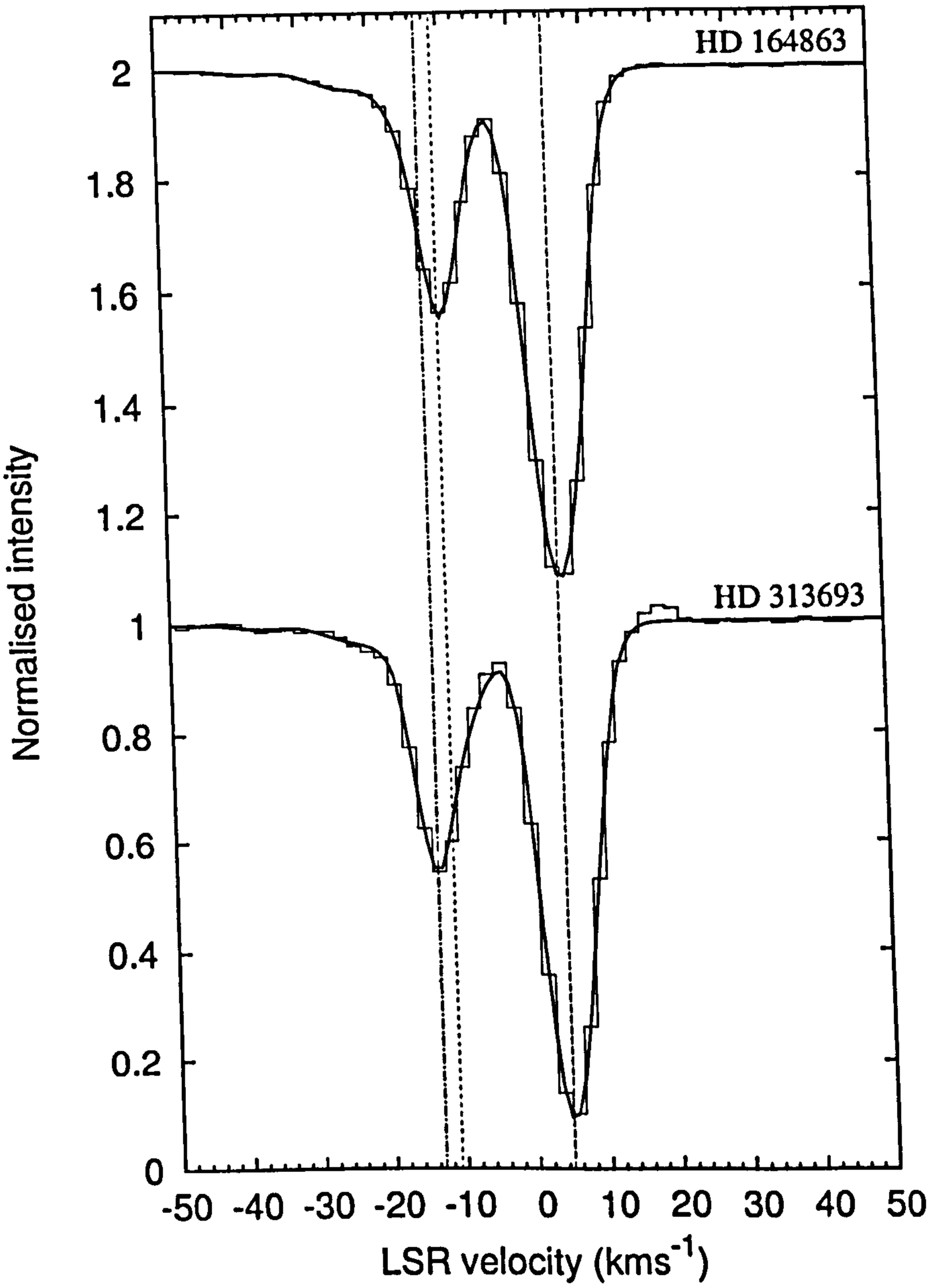

Figure 4.80: Normalised, telluric-corrected Na I D_1 spectra recorded towards HD 164863 (top histogram, shifted vertically for display) and HD 313693 (bottom histogram) in the LSR frame. VAPID model fits are overlaid (thicker smooth traces); model parameters (see Table 4.12) were kept identical between the two sightlines except for the velocity of the single variable cloud. Dashed lines show the VAPID least squares velocities of the variable cloud in the two sightlines; the velocity of the peak optical depth of the (fixed) dominant Na I cloud is also shown. HD 164863 spectra have been shifted vertically for display.

and the final fits are shown in Figure 4.80. The models required six clouds to produce an adequate fit to the spectra, and Na D_1 and D_2 lines were fitted simultaneously for increased accuracy. Allowing all parameters freedom to vary in the least-squares optimisation resulted in models for the two sightlines that differed slightly in every parameter $[v,\ b,\ N]_i$. Statistically however, the RMS variation between the two sightlines of these 'free' fits was small compared to the continuum RMS of the spectra. In order to determine a precise velocity shift of the variable component, the average of the parameters ($[v,\ b,\ N]_i$) for HD 164863 and HD 313693 was taken for each cloud in the model except for cloud 3 at $v_{LSR} \simeq -12$ km s^{-1} that showed the greatest velocity variation between the two sightlines, for which only the column density (N_3) was averaged. All of the model parameters were held fixed except for the velocity and Doppler b parameters of the 'variable cloud' (cloud 3), and the models were re-optimised to produce the fits that are shown in Figure 4.80. Fixing the parameters of all of the clouds except for the variable one did not significantly degrade the RMS of the fits from those obtained when all parameters were free to vary.

The resulting interstellar model parameters are shown in Table 4.12. With 2σ confidence, the variable cloud (cloud 3, at $v_{LSR} \simeq -12$ km s^{-1}) is moving at a radial velocity of $+2.8 \pm 0.4$ km s^{-1} in the HD 164863 sightline relative to its velocity in HD 313693 such that the cloud is apparently either (a) 'shearing' or (b) rotating, with an angular velocity component parallel to our sightline. Within the S/N of the spectra, the VAPID models are consistent with the total integrated Na I column density being identical for both sightlines. Cloud 3 also has a variable Doppler width (b), about 1/3 greater towards HD 313693 than HD 164863. Formally, the measured change in b is 0.4 ± 0.3 km s^{-1} with 2σ accuracy. The Doppler width of cloud 3 is small compared to the others modelled in these sightlines, indicating a low turbulent and/or kinetic velocity of the gas.

Although the tabulated model parameters (Table 4.12) accurately represent the spectra at the UCLES resolution of 5.2 km s^{-1}, the fitting of multiple closely spaced clouds in data of this resolution is prone to error. There is little doubt that there is a significant shift in the peak velocity of the weaker component of the profile (see Figure 4.80), but without properly resolving the intrinsic profiles of the Na I clouds, it is possible that the cause of the shift is the growing of one (or more) cloud components and the shrinking of one (or more) others between the two sightlines, such that when convolved to the

	v_{LSR} (km s^{-1})		Doppler b (km s^{-1})		log(N (cm^{-2}))	
	HD 164863	HD 313693	HD 164863	HD 313693	HD 164863	HD 313693
1	-37.7	-37.7	3.1	3.1	10.10	10.10
2	-23.9	-23.9	5.5	5.5	10.88	10.88
3	-11.0 (0.2)	-13.8 (0.2)	0.7 (0.1)	1.1 (0.2)	11.80	11.80
4	-11.2	-11.2	5.5	5.5	11.72	11.72
5	5.2	5.2	4	4	11.88	11.88
6	4.7	4.7	1.4	1.4	14.26	14.26

Table 4.12: Parameters of the VAPID interstellar Na I models shown in Figure 4.80 for HD 164863 and HD 313693. Na D_1 and D_2 lines were fit simultaneously for each sightline. All model parameters were optimised simultaneously for HD 164863 and HD 313693 except for the velocity and Doppler width of cloud 3 (the 'variable' component). 2σ Monte Carlo errors on the parameters of the variable component (calculated using 500 replications) are shown in parentheses.

instrumental resolving power, the effect is indistinguishable from an apparent shift in the wavelength of the line. This cannot be ruled out, but in any case, small-scale Na I structure is certainly present between these two sightlines to cause the observed profile variation.

In support of a pure velocity shift causing the profile variation it was found that the variable component (cloud 3) could be ascribed an identical column density between the two sightlines without reducing the quality of the model fits. It is very unlikely that this situation could arise if the profile change was caused by changes in the parameters of multiple blended, unresolved clouds. Thus, the velocity shift seems to be real, though this result can only be confirmed beyond doubt by obtaining spectra of high enough resolution ($\lesssim 0.5$ km s^{-1}) to resolve the profiles of the individual clouds in the two sightlines.

The presence of small-scale velocity structure towards HD 164863 and HD 313693 is a significant result and appears to be the first reported evidence for variation in the mean velocity of an interstellar cloud in studies of small-sale interstellar structure. This may be important because the velocity structure of interstellar clouds is often assumed by authors to be identical towards the different component sightlines in SSS cloud models. In addition, the velocity width (as determined from b) of the variable cloud towards HD 313693 appears to be significantly greater than towards HD 164863. Taken as evidence for an increased thermal and/or turbulent velocity in the gas, this result points towards an interpretation of the velocity shift as due to a supernova shock or wind-disruption from one or more massive stars in the cluster, of the cloud towards

HD 313693, 'pushing' it away from the cluster towards us. Further observations of molecular species such as CH^+ in this cloud could thus potentially provide a probe of the effects of shocks on diffuse cloud chemistry.

4.4 The time-variable sightline towards κ Vel

The bright B2 IV spectroscopic binary star κ Vel, with a proper motion of 15.5 ± 0.6 mas per year and a distance of 165 ± 14 pc (from the parallax data given by Perryman & ESA 1997), moves through space tangential to our sightline at approximately 2.5 AU per year. This section makes a comparison between past measurements of atoms and DIBs in the sightline towards κ Vel and new observations made at the AAO on UCLES in June 2004 ($R \simeq 58,000$, S/N ~ 2300). Spectra with S/N ~ 550 were obtained at $R \simeq 60,000$ by S. J. Fossey (private communication) in January 1995 at the Mount Stromlo Observatory in the wavelength range 5000 to 7000 Å which provide spectra for diffuse interstellar band comparisons. Past atomic and molecular line data are taken from the ultra-high resolution ($R \simeq 900,000$) spectroscopic work published by Crawford *et al.* (2000) and Crawford (2002), based on observations made at the AAO in June 1994, March 2000 and March 2002.

4.4.1 Interstellar K I column density variations

Analysis of the new telluric-corrected UCLES K I λ7699 spectrum obtained in June 2004 shows a significant increase in the equivalent width since March 2002. Crawford (2002) states $W_{\mathrm{K\,I}\ \lambda7699} = 4.21 \pm 0.26$ mÅ with 2σ accuracy for the March 2002 spectra. Using Crawford's single-cloud interstellar K I model parameters ($v_{\mathrm{HEL}} = 8.21$ km s^{-1}, corresponding to $v_{\mathrm{LSR}} = -6.5$ km s^{-1} with $b = 0.46$ km s^{-1} and $N(\mathrm{K\,I}) = 2.51 \times 10^{10}$ cm^{-2}), the 2002 κ Vel K I spectrum was modelled in VAPID at the UCLES resolution of 5.2 km s^{-1}. The model parameters were fixed to *simulate* the spectrum *i.e.* no least-squares parameter optimisation was performed. The June 1994 K I model was also modelled at a resolution of 5.2 km s^{-1} for comparison with the 2004 UCLES spectrum. The simulated spectra are shown in Figure 4.81, overlaid with the observed June 2004 spectrum and *optimised* VAPID fit.

The Doppler b value of 0.46 km s^{-1} was held fixed in the modelling of the June 2004

Epoch	$W_{\mathrm{K\,I}\ \lambda7699}$ (mÅ)	N(K I) (10^{10} cm^{-2})
June 1994	2.76	1.62 (0.08)
March 2000	3.83	2.29 (0.1)
March 2002	4.14	2.51 (0.1)
June 2004	5.45 (0.2)	3.38 (0.15)[a], 3.15 (0.1)[b], 3.43 (0.13)[c]

Table 4.13: The measurements of the κ Vel K I column density for June 1994, March 2000 and March 2002 published by Crawford (2002) are shown. Equivalent widths of the respective K I λ7699 lines were measured from spectra simulated using the least-squares model parameters given by Crawford (2002). The equivalent width of the June 2004 K I line was measured directly from the observed spectrum; N(K I) was calculated using three methods, labelled as follows:[a] — from the curve of growth (Figure 4.82), [b] — from integration of the K I λ7699 $N_v(v)$ (apparent optical depth) profile, and [c] — from the least-squares VAPID fit to the spectrum. 1σ error estimates are given in parentheses.

spectrum due to the fact that the line-width is not well resolved at the relatively low resolution of the UCLES spectra and so could not be measured as reliably as in the ultra-high resolution spectra used by Crawford. It has been assumed that the Doppler b parameter of the K I cloud has remained constant since 1994 (after Crawford 2002).

The equivalent width of the June 2004 K I λ7699 line was measured as 5.4 mÅ from direct integration of the spectrum. Statistical noise might have affected this result due to the weakness of the line, so a Monte Carlo error analysis with 1000 replications of the spectral Poisson noise was performed, re-fitting the VAPID model to each. A mean of $N(\mathrm{K\,I}) = 3.43 \pm 0.13 \times 10^{10}$ cm^{-2} was derived. All fits were statistically good to within the RMS noise of the spectra. Measuring the the equivalent widths of the mean N and $N \pm 1\sigma$ VAPID fits gave $W_{\mathrm{K\,I}\ \lambda7699} = 5.45^{+0.27}_{-0.10}$ mÅ. The equivalent widths of the VAPID simulations of the June 1994 to March 2002 data were also measured. The results are given in Table 4.13.

For increased rigour, two other methods were employed to determine N(K I) for June 2004. A curve of growth for the neutral potassium in the cloud (a plot of N(K I) *vs.* $W_{\mathrm{K\,I}\ \lambda7699}$) was generated numerically using VAPID: The equivalent width of the K I λ7699 line was computed for a range of K I column densities using a single absorbing cloud with Doppler $b = 0.46$ km s^{-1}. The curve of growth is shown in Figure 4.82; as expected, the data from Crawford (2002) coincides exactly with the curve. The black data point shows the position of the June 2004 measurement of $W_{\mathrm{K\,I}\ \lambda7699} = 5.45^{+0.27}_{-0.10}$ mÅ, which corresponds to $N(\mathrm{K\,I}) = 3.38 \pm 0.15 \times 10^{10}$ cm^{-2} on the curve of growth,

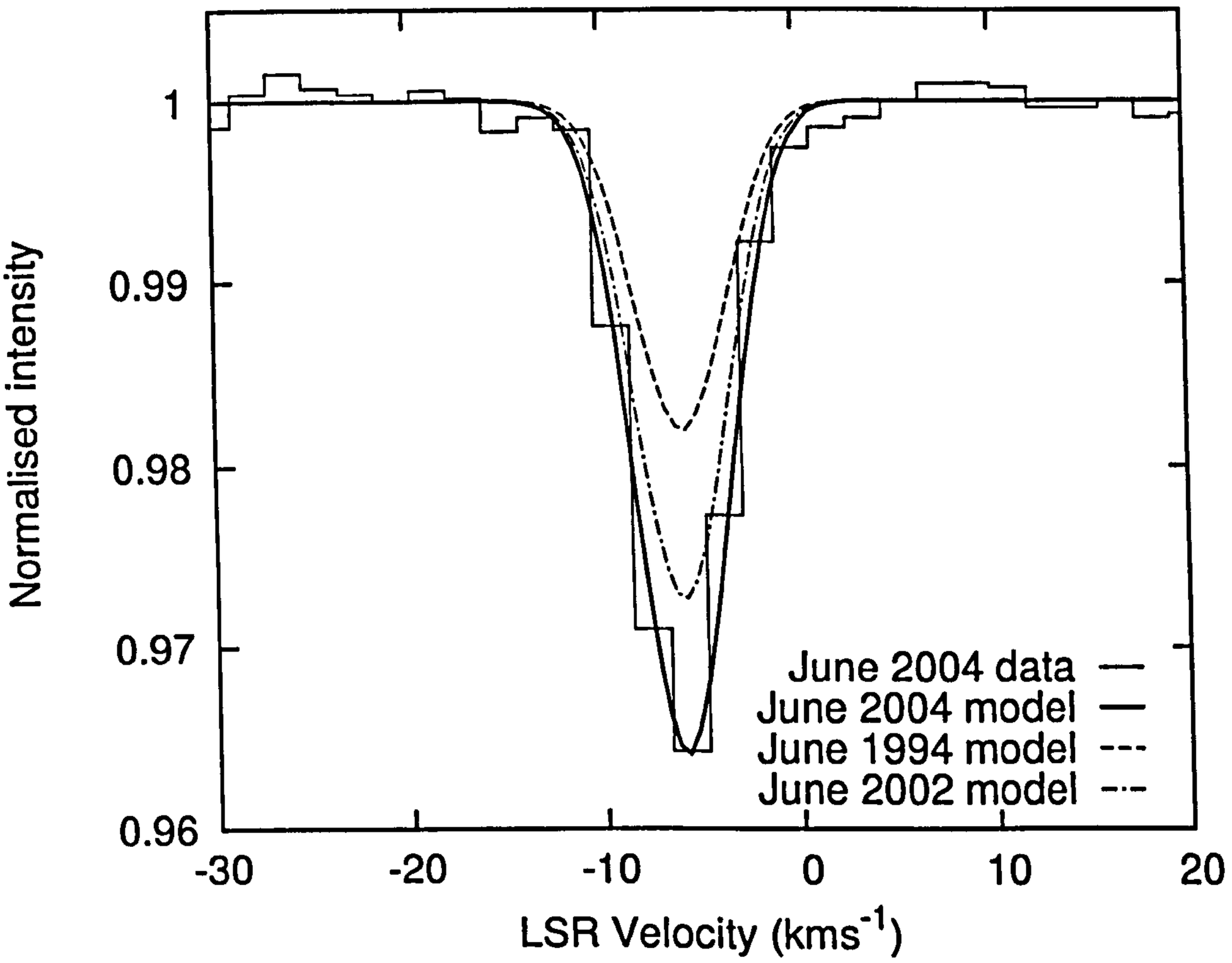

Figure 4.81: Comparison between the new (June 2004) κ Vel interstellar K I λ7699 line (continuum normalised and telluric-corrected histogram) and the past observations made by Crawford in 1994 and 2002. The VAPID model for the new spectrum is shown as the thicker trace. Using the single-cloud K I model parameters from Crawford (2002), the K I line profiles for the earlier epochs were simulated at the UCLES resolution of 5.2 km s^{-1}.

in good agreement with the result obtained from direct line modelling in VAPID.

Finally, the column density was calculated using an apparent optical-depth integral over the K I line profile (using $\tau(\lambda) = \tau_a(\lambda)$ in Equation (3.1), Section 3.5 and the K I λ7699 transition wavelength and oscillator strength from Morton (2003)). Subject to some degradation in core opacity due to unresolved saturated structure, integration of the optical depth profile gave $N(\mathrm{K\,I}) = 3.15 \pm 0.1 \times 10^{10}$ cm^{-2}, with error estimate based on apparent optical depth integrals of the $N \pm 1\sigma$ VAPID fits to the spectra. For further details of the use of the apparent optical depth method, see Section 3.5.1. This result is 8% lower than derived using VAPID modelling or the curve of growth, which can be explained as due to a reduction in the apparent core optical depth of the line due to the smearing caused by the spectrograph's PSF and the narrowness of the cloud's

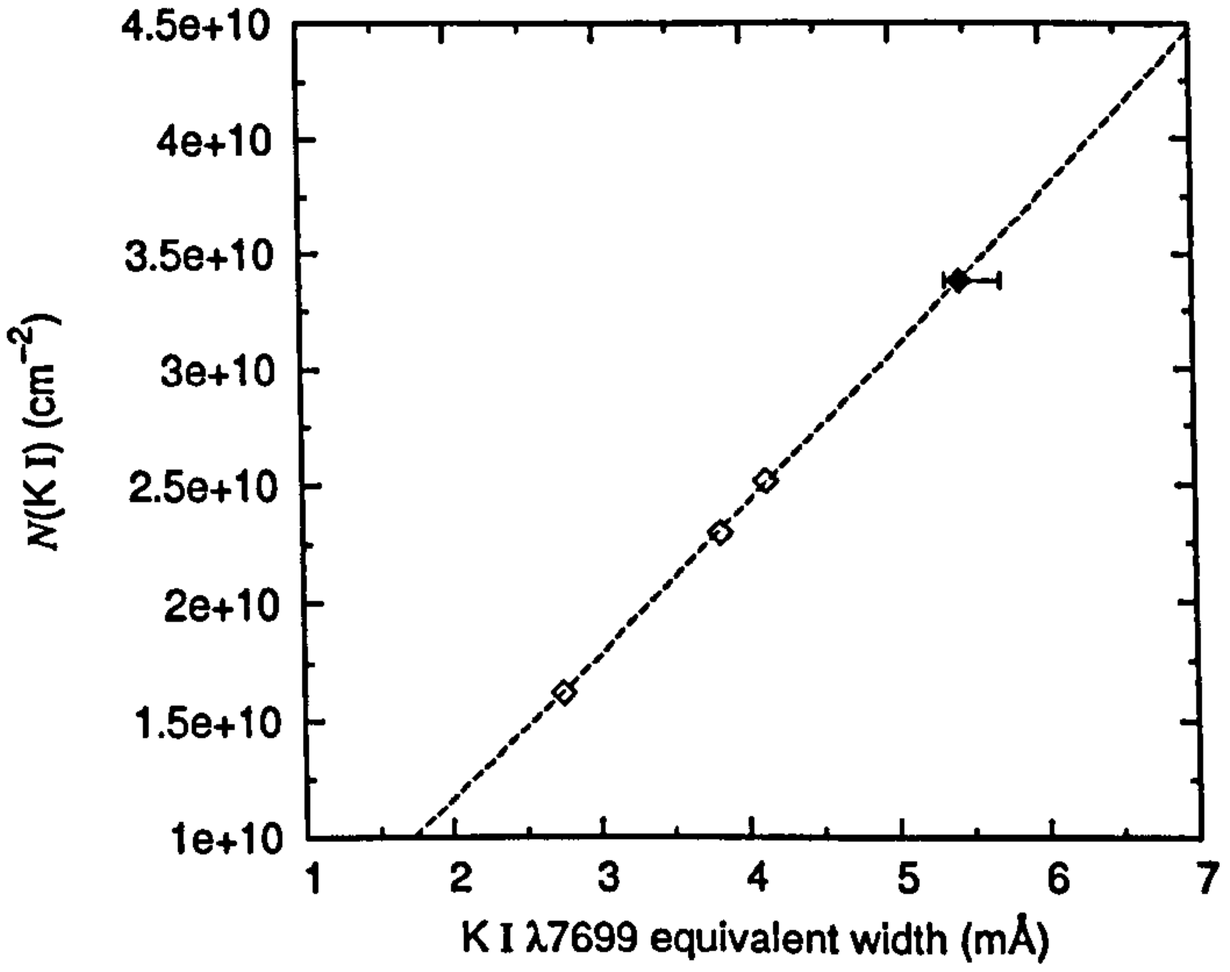

Figure 4.82: Curve of growth for the κ Vel interstellar K I λ7699 line (dashed curve), calculated in VAPID using a single-cloud model with $b = 0.46$ km s^{-1}. Open diamonds represent data from past epochs (1994, 2000, 2002) simulated from the least-squares model parameters given by Crawford (2002). The filled diamond shows the position of the new equivalent width measurement, with 1σ error bar.

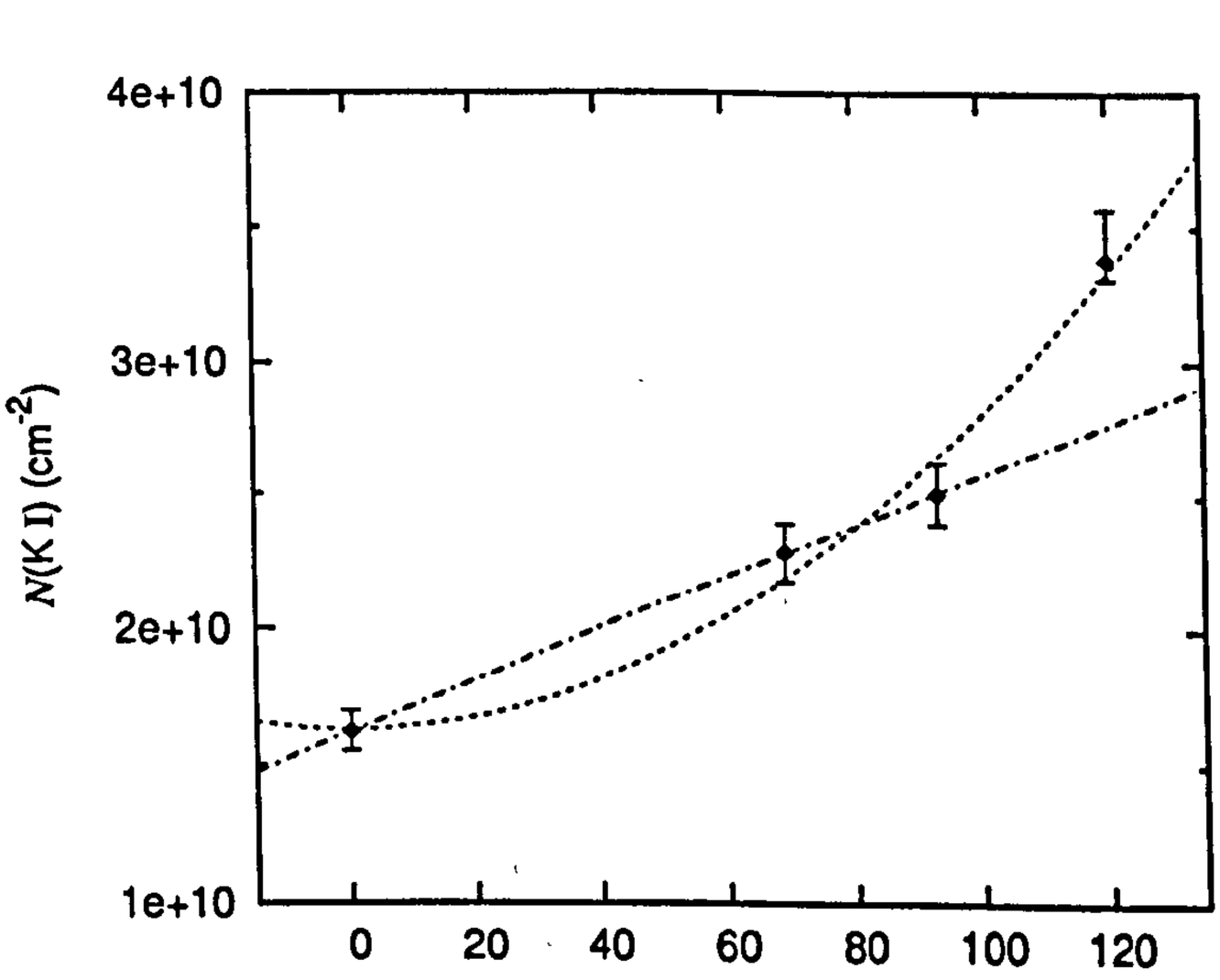

Figure 4.83: N(K I) plotted against time in months since June 1994. Filled diamonds represent the data from past epochs (1994, 2000, 2002) measured by Crawford *et al.* (2000); Crawford (2002) plus the new measurement, including 1σ error bars. The dashed curve is a quadratic least-squares fit, and the dot-dashed line shows a linear N(K I) increase at a rate of 1.15×10^{10} cm^{-2} yr^{-1} (similar to that found by Crawford (2002) who quotes a rate of 1.2×10^{10} cm^{-2} yr^{-1}) between June '94 and March '02.

Doppler width.

A remarkable time progression in the neutral potassium column density towards κ Vel occurred between June 1994 and March 2002 (Crawford 2002). Based on the results shown in Figure 4.81 and Table 4.13, an even more remarkable change has occurred between March 2002 and June 2004, with $\simeq 35\%$ increase in K I column density from 2.51×10^{10} to 3.4×10^{10} cm^{-2}. During the ten years since June 1994, the K I column density towards κ Vel has approximately doubled. The change in N(K I) over time is plotted in Figure 4.83. The assumed linear increase in N(K I) during the period of Crawford (2002)'s observations is plotted as a dot-dashed line. The present result is not compatible with an extrapolation of this rate to 2004. A least-squares fitted quadratic function (fit to all four data points), is shown as a dotted line. There is no particular physical justification to assume a quadratic increase in N(K I) with time, but this fit shows that a process resulting in a quadratic increase in N(K I) could plausibly account for the observed time-variability of N(K I) in this sightline.

Neglecting the possible effect of transverse motion of the cloud across our sightline (likely to be small compared to the proper motion of κ Vel), the sightline has traversed $\lesssim 5$ AU across the ISM since March 2002, providing evidence for significant interstellar structure on the smallest spatial scales yet probed by studies of this kind.

4.4.2 The search for time-variable DIBs

Extrapolating the initial linear increase in the K I column density (see Crawford (2002) and Figure 4.83) 7 months on from June 1994 gives N(K I) = 1.67×10^{10} cm^{-2} for January 1995 when the Mount Stromlo DIB spectra were recorded. Since then, the sightline towards κ Vel has swept across $\lesssim 25$ AU of interstellar space, and the amount of K I in the sightline has increased by $102 \pm 17.5\%$. This study reports the first detection of DIBs towards κ Vel and seeks to answer the question of whether the strengths of the diffuse interstellar bands have changed during the period from January 1995 to June 2004.

Plots of the 1995 and 2004 spectra in the wavelength range of some of the strongest DIBs are shown in Figures 4.84 to 4.85. The diffuse interstellar band spectrum is exceptionally weak in this sightline, highlighted by the relationship of the λ5780 and λ6614 DIB strengths with N(K I) and E_{B-V} — these DIBs are weak compared to the

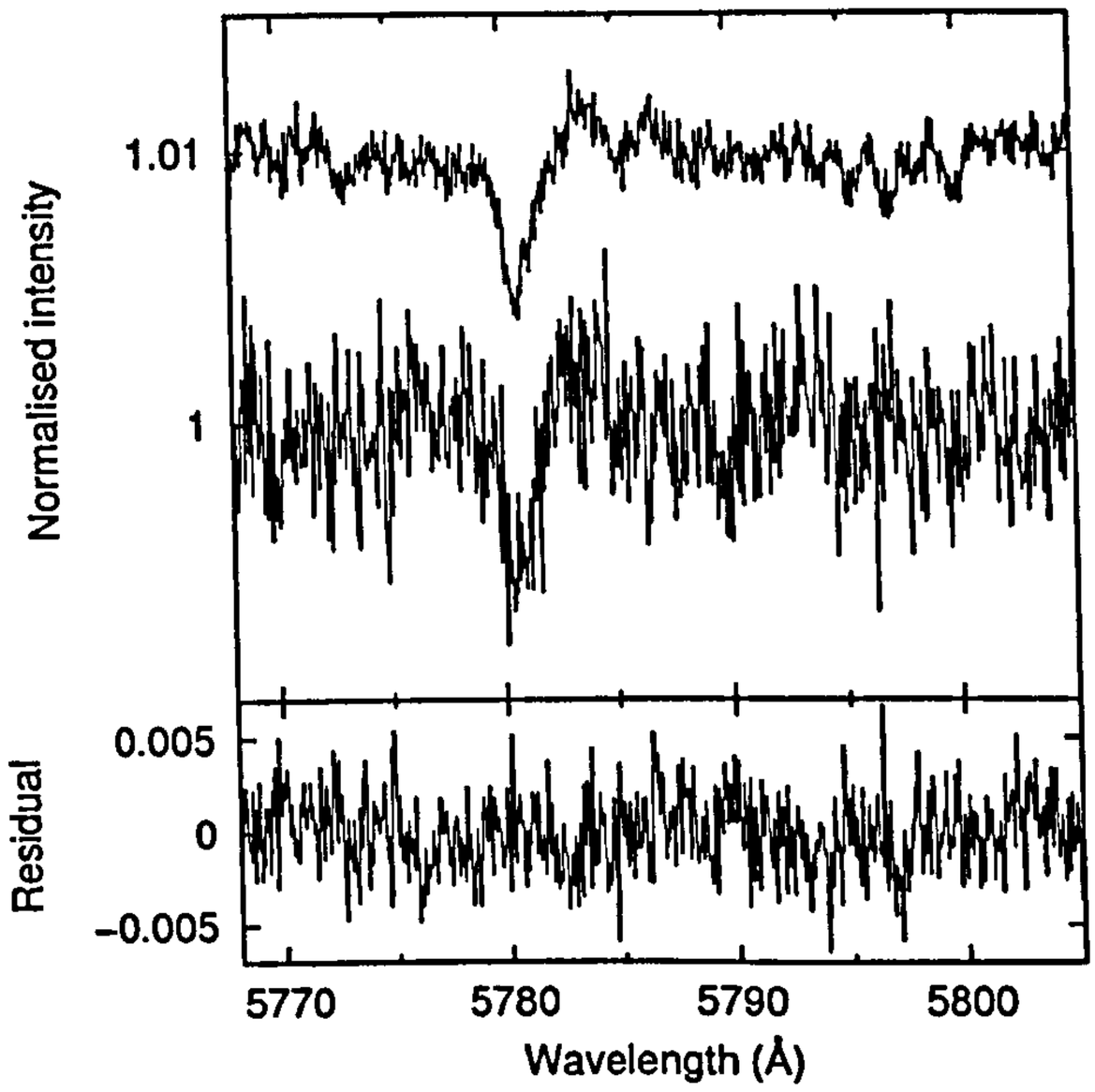

Figure 4.84: Spectra of λ5780 and λ5797 recorded towards κ Vel in 2004 (top) and 1995 (middle), telluric-corrected and normalised with low-order polynomial continua. Lower trace shows residual intensities of the 2004 minus the 1995 data.

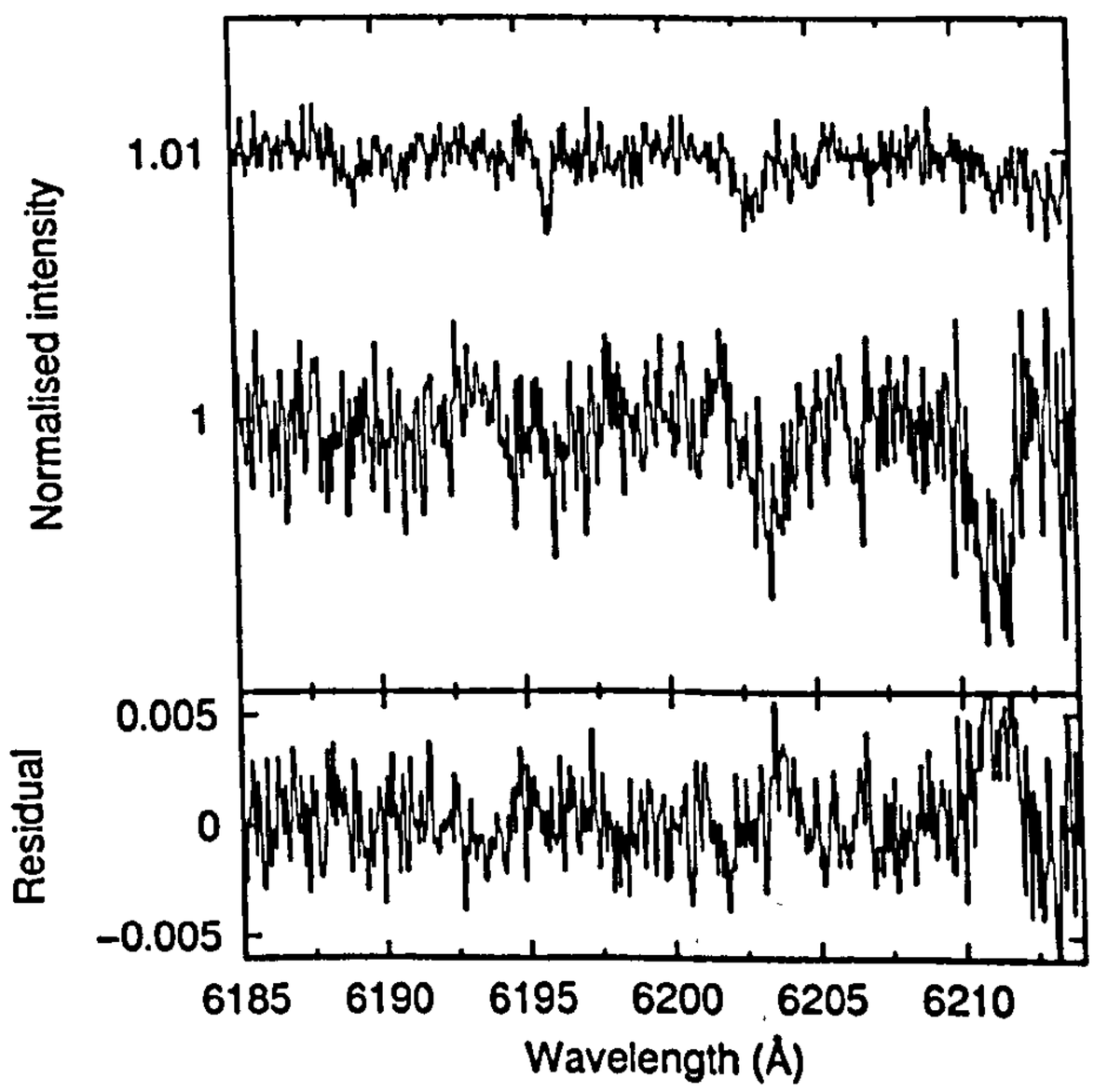

Figure 4.85: Spectra of λ6196 and λ6203 recorded towards κ Vel in 2004 (top) and 1995 (middle), telluric-corrected and normalised with low-order polynomial continua. Lower trace shows residual intensities of the 2004 minus the 1995 data.

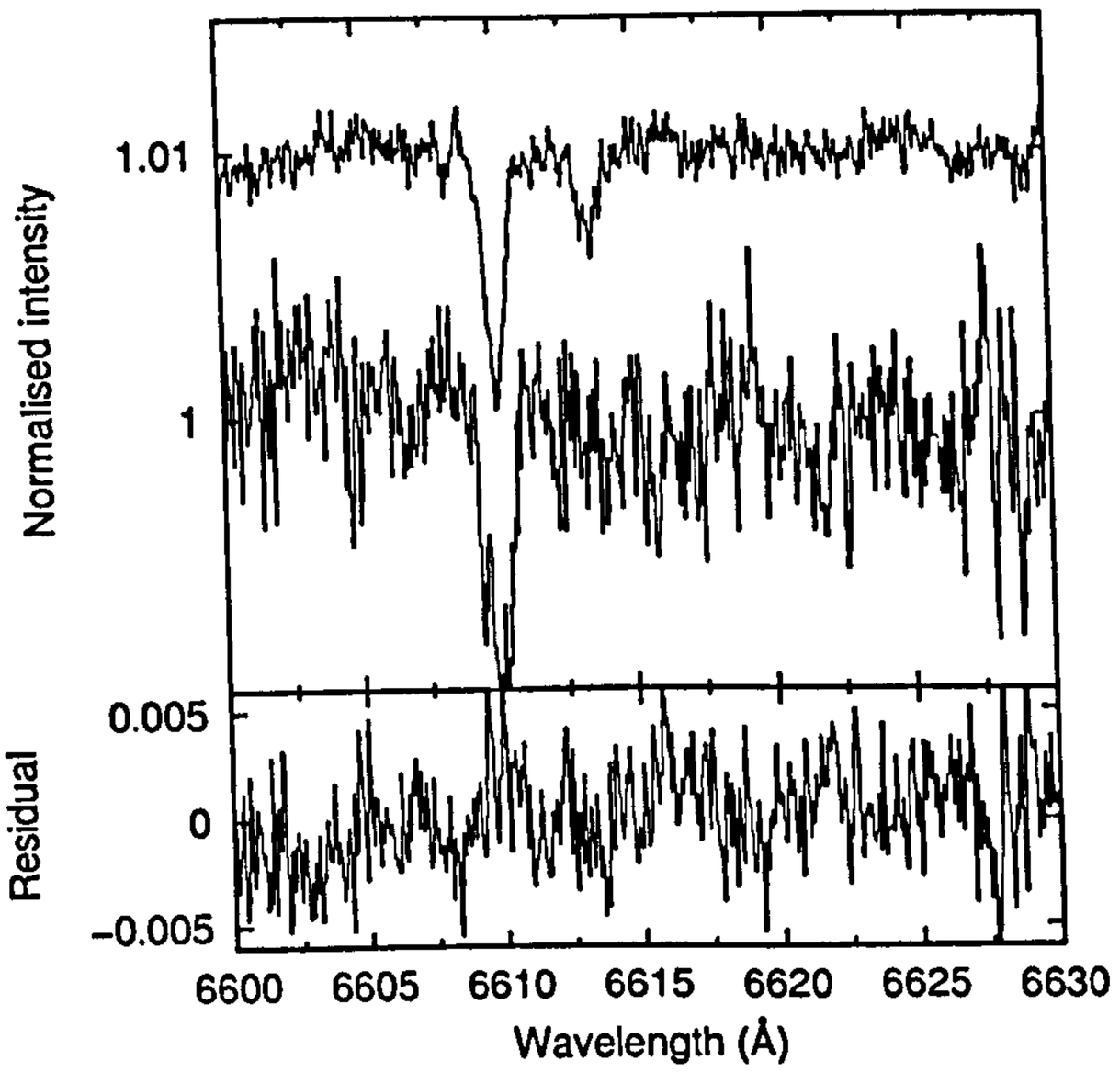

Figure 4.86: Spectra of λ6614 recorded towards κ Vel in 2004 (top) and 1995 (middle), telluric-corrected and normalised with low-order polynomial continua. Lower trace shows residual intensities of the 2004 minus the 1995 data.

	W_λ (mÅ)		δ(04/95)	
Feature	Jan 1995	June 2004	(%)	Blend?
λ5780	10 (4)	10 (1)	<41	?
λ5797	<1.5	<0.4	–	?
λ5850	<1.2	<0.4	–	N
λ6196	<0.6	1.1 (0.2)	–	N
λ6203	4.8 (6)	3 (2.1)	38 (82)	N
λ6284	–	15	–	Y
λ6614	0 (1.8)	3 (0.5)	–	N
K I λ7699	–	5.45	–	
Na I D_1	59.8	62.2	4.0 (0.8)	
log N(K I)	10.227	10.535	102 (17.5)	

Table 4.14: Equivalent widths of interstellar features measured towards κ Vel in January 1995 and June 2004. δ(04/95) is the percentage *excess* of the 2004 measurements compared to 1995, with a significant result obtained only for λ5780. N(K I) was calculated for Jan 1995 using the data from Crawford (2002), assuming a linear increase in N(K I) between June '94 and Jan '95 (at a rate of 6.7×10^8 cm^{-2} per month). N(K I) was calculated for June '04 using VAPID. In the last column, 'Y' indicates a definite or probable stellar blend contaminating the DIB spectra, 'N' indicates improbable or absent stellar blend and '?' is for indeterminate cases, 'T' indicates severe telluric contamination of results. Dashes indicate where no measurement was possible.

typical Galactic diffuse sightlines plotted in Figures 4.59 and 4.60 on page 208, for similar values of N(K I) and E_{B-V}. The only DIBs detected in the 1995 data were λ5780 and λ6203, and therefore these are the only ones from which meaningful results can be obtained. Unfortunately, λ6203 is rather broad, so the error estimate calculated from $\sigma\Delta_\lambda$ is greater than the equivalent width of the DIB. However, measurement of the residual spectrum (Figure 4.85) suggests that this DIB has decreased in strength since 1995 by about 38%.

The λ5780 spectrum is recorded clearly for both epochs, but as shown by Figure 4.84 there is a small feature that looks like emission on or adjacent to the red wing of the DIB absorption (also present in the μ^1 Cru spectrum). There are some small stellar features in this wavelength region as shown by the standard stars in Figure 4.1, and it is possible that the continuum is depressed by a blending of many weak features across the wavelength range shown in Figure 4.84, except for in the region around 5784 Å, where an apparent emission feature results. In any case, the 1995 and 2004 spectra look very similar. They have both been telluric-corrected using a combination of α Vir and α Eri spectra[7] (fast rotators), so any features present in the telluric standards should be common to both the 1995 and the 2004 spectra. Given the high rotation speed of the telluric standards, the 'emission' feature at 5784 Å is too narrow to have been introduced during telluric division, so it can be assumed to originate in the intrinsic stellar spectrum of κ Vel. Although the star is a spectroscopic binary, the stellar features appear at exactly the same wavelength in the spectra from both epochs. Figure 4.86 shows an example of this; the N II line at 6610 Å is identical in wavelength and almost identical in profile and strength between the two spectra. Thus, in subtraction of the spectra to form the residuals, good cancellation of stellar features occurs. To within the S/N for λ5780, all that remains in the residual spectrum is a flat line. There has apparently been no change in the strength of λ5780 between January 1995 and June 2004. Results are summarised in Table 4.14 and the estimated upper limit on the possible variation in λ5780 is ±41%.

[7]To obtain a very high S/N in the telluric standard spectrum, sufficient not to introduce extra noise into the κ Vel spectrum upon division, two telluric standard stellar spectra were co-added.

4.5 Discussion

4.5.1 Small-scale structure in the DIB-carrier distribution

Due to S/N constraints, only the stronger, narrower diffuse interstellar bands belonging to the KW II and III families (see Section 1.2.1) have been analysed for the presence of small-scale spatial variability. Variation in DIB strengths observed in the β Sco, ρ Oph and μ Cru systems show that small-scale structure is present in the gas that hosts both families of DIBs. The small-scale structure of the very broad and shallow bands such as λ4430, λ5778 and λ6177 (in the KW I group) may be analysed in future work.

Strong evidence for small-scale structure of the interstellar gas that contains the DIB carriers has been found in ten out of twelve sets of observations; the ρ Oph system is counted as six sets of observations due to the permutations available for comparison between its four component sightlines. The SSS length scales probed varied between $\sim$ 25 AU for the time-variable sightline κ Vel up to $\sim$ 43,000 AU for the pair of stars HD 164863/313693 in NGC 6531. Differences in the DIB strengths were observed over length scales $\sim$ 370 AU (ρ Oph A/B); $\sim$ 2200 AU ($\beta^{1,2}$ Sco); $\sim$ 4,500 AU ($\mu^{1,2}$ Cru); $\sim$ 5500 AU ($\nu^{1,3}$ Sco); $\sim$ 12,500 AU (HD 150135/6), and scales of $\gtrsim$ 20,000 AU for various sightline pairs in the ρ Oph system.

This work shows that structure is present in the gas in which the DIB carriers reside, on all spatial scales greater than a few hundred AU. This is not to rule out structure on smaller scales, but the κ Vel DIBs were too weak relative to the spectral S/N to identify any small variations in the DIB strengths. Some DIBs (such as λ6284 and λ7562) show very little or no evidence for small-scale variability, and in the systems HD 164863/313693, and HD 150135/6 (with the exception of λ6614), no evidence for any small-scale DIB variability was found.

The amount of small-scale variation between the DIB strengths ranged between 2.4 $\pm$ 1.4% for λ6614 towards β Sco to 180 $\pm$ 33% for λ6614 towards μ Cru, proving the existence of a broad range of degrees of small-scale DIB variability. The strictest upper limits on possible variations are for λ6284, apparently varying less than 1.5% between ρ Oph A, B and D, and between HD 150135 and HD 150136.

The observed variations in DIB strengths tend to follow the variations in the trace-neutral species K I (and therefore Na I, Li I and C I by their close correlations with K I;

see for example Welty & Hobbs (2001)). K I provides a good tracer for the behaviour of the abundances of species that are relatively undepleted and predominantly ionised in the ISM. According to Welty & Hobbs (2001), in the cold, relatively dense gas in which K I is typically observed, approximately 75% of the available potassium is depleted on to dust grains. Of the remainder, approximately 99% is ionised to form K II.[8] The ionised fraction generally diminishes with increasing density of interstellar clouds.

There is a $\gtrsim$ 50% difference in the K I and Na I column densities between μ^1 and μ^2 Cru, which is similar to the variation observed in the λ5780, λ6196 and λ6284 DIB strengths. λ6614 shows a greater difference than the others, similar to the behaviour of this DIB towards HD 150135/6. For the β Sco and ρ Oph systems, the N(K I) variations are around 5 to 20%, with observed variations in the DIB strengths of a comparable magnitude. The sightlines HD 150135/6 and HD 164863/313693 show no robust evidence for small-scale variations in the total K I column densities, which matches a lack of observation of SSS in the DIBs in these sightlines.

The SSS variations observed are relatively small so it is difficult to draw significant conclusions about the exact relationship of the small-scale structure of the DIB carrier distribution with that of K I. The general trend, however is for the DIB strengths to follow the small-scale K I variations. From the data presented here, it is not possible to determine whether this trend is (a) a reflection of a relationship between the ionisation state of K I and that of the DIB carriers or (b) simply that the mass of the column of gas and dust in the sightlines determines the strength of the interstellar absorption features. Further complicating the issue is the unknown nature of the DIB carriers and the extent to which they may be subject to spatially variable excitation, depletion, formation and destruction rates, all of which are presently undefined.

The dichotomy of whether ionisation or simple column density variations are responsible for the observed differences in K I and the DIBs could be resolved with the help of accurate measurements of a relatively undepleted, dominant-ion interstellar species such as Zn II, or indeed any other method that provides accurate data on the total quantity of gas down the sightlines in question. From the analysis of C I excitation (see

[8]Calculated assuming temperatures ~ 100 K and electron densities ~ 0.1 cm^{-3} typical of the diffuse ISM, utilising the K I photoionisation and recombination coefficients from Pequignot & Aldrovandi (1986) and Equation (1.5).

Section 4.1), evidence is mounting that, for many of the examples of SSS seen in K I and Na I, gas densities are low ($n_H \sim 100$ cm^{-3}), and that the observed SSS may be due to changes in electron recombination rates caused by subtle localised density fluctuations (Lauroesch & Meyer 1999). It is therefore hypothesised that such variations can also affect the abundance of the DIB carriers *via* changes in their ionisation balance and/or level of internal excitation. Other physical and chemical factors affecting DIB strengths are deemed to be less significant; depletion of titanium has been found not to correlate with the DIB strengths (Herbig 1993), and photodissociation of large PAH-type molecules is deemed to occur much more slowly than ionisation (see Sonnentrucker *et al.* 1997, and references therein). Differences in the elemental composition of the ISM should be negligible over the small spatial scales probed here, due to turbulent and kinetic mixing of the gases within a cloud. It is plausible that the observed differences between the small-scale behaviour of the different DIBs are due to differences in the density-dependent ionisation balances of the carriers and/or the radiation field strength.

Towards $\mu^{1,2}$ Cru, Lauroesch *et al.* (1998) found Ca II to vary substantially less than Na I. Further, they found no significant small-scale variations in the Zn II absorption profiles, supporting the idea that the Na I and K I variations are due to changes in ionisation balance. Therefore, towards μ Cru, it is suggested that the changes in the DIB strengths are caused by changes in the ionisation or excitation state of large gas-phase molecules responsible for the DIBs. The reduced photoionisation rate for Ca II compared to K I and Na I (Pequignot & Aldrovandi 1986) may explain why relatively little variation is seen in the Ca II profile. This fits with the observation that N(K I) apparently varies by around twice as much as N(Na I) towards $\mu^{1,2}$ Cru, the photoionisation rate for K I being significantly greater than for Na I. This trend suggests that the carriers of the DIBs that showed relatively less variation: λ5780, λ6196 DIBs (and possibly λ6284, though this DIB is contaminated by telluric and stellar features), may have photoionisation rates comparable to that of Na I, and the more variable λ6614 DIB may have an even larger photoionisation rate, comparable to that of K I, as inferred from its large variability between the two μ Cru sightlines. It is possible that this scenario could explain why λ6614 was the only DIB to show SSS towards HD 150135/6 and why λ6284 generally showed little or no evidence for small-scale variability in any of the sightlines.

Lauroesch & Meyer (2003) suggest that the magnitude of SSS variability exhibited by a species should depend on its photoionisation rate because it determines the distance that the species can travel from a site of density enhancement before being re-ionised. If photoionisation rate contributes towards the magnitude of SSS observed for a particular species, then the work of Sonnentrucker *et al.* (1997), Krełowski *et al.* (1998) and Weselak *et al.* (2004) who determine that the λ5780 and λ6284 (KW II) carriers are more resistant to UV flux than the λ5797, λ5850 and λ6379 (KW III) carriers, suggests that differing amounts of SSS should be observable for these two different families of DIBs. No such trends are immediately obvious in our data, though the extreme lack of apparent small-scale variation in λ6284 towards the β Sco, ρ Oph and HD 150135/6 sightlines does indicate that this DIB is resistant to the effects that cause SSS in the other DIBs. In the context of the present discussion, the λ6284 DIB carrier would have a lower photoionisation rate than all of the other DIBs analysed, possibly due to a high ionisation potential, approaching the 13.6 eV of H I.

Other explanations for the relative invariability of λ6284 include a reduced photodissociation rate or slow destruction rate through chemical reaction, allowing the carrier to travel further from its formation site before being destroyed.

Against the general trend for DIB strengths to follow K I, ρ Oph C shows significantly less K I than the other ρ Oph stars, yet most of the DIBs in this sightline are stronger than towards A or B, particularly λ6439. This shows that the DIB strengths are being influenced by a chemical process distinct from that which determines N(K I). Possibilities include a different shape, or 'hardness' of the interstellar UV field resulting in preferential K I ionisation towards ρ Oph C or, alternatively, density inhomogeneities in the cloud conducive to preferential shielding and/or recombination of the and/or excitation of the DIB carriers towards ρ Oph C. Another possibility is differing cloud dynamics, perhaps due to impinging stellar winds resulting in increased grain abrasion that could provide a larger source of material for DIB carrier formation. Perhaps related is the enhanced CN column density in this sightline that may indicate a greater gas density, though this is at odds with observations that show reductions in the strengths of many DIBs in higher density gas. No significant differences between the Doppler b values of the six species observed by Pan *et al.* (2004) were found between the members of the ρ Oph system.

The time-variable sightline towards κ Vel showed an approximately two-fold increase

in N(K I) between subsequent DIB observations. No such variation was observed in the strength of λ5780, which is at odds with the variations observed in other sightlines. It appears as though the cloud into which the sightline is moving does not contain a significantly greater column density of DIB carriers than the surrounding ISM. This result could be an example of the photoionisation rate of a species influencing the scale size of its small-scale structures (following the suggestion of Lauroesch & Meyer 2003, for ρ Leo), and that since 1995 the sightline towards κ Vel has moved into the edge of dense cloud, resulting in a progression from ionised to less ionised K I. Hypothetically, the λ5780 carrier, due to a relatively low photoionisation rate, was already predominantly in its 'preferred' ionisation state at the position of the sightline in Jan '95, such that further movement of the sightline into a denser part of the cloud did not result in any noticeable increase in DIB strength. This hypothesis could be tested by monitoring the strength of one of the DIBs believed to be less resistant to destruction by UV, such as λ5797 (Sonnentrucker *et al.* 1999b). Unfortunately, λ5797 has not been observed at either epoch, but it will be of interest to monitor the sightline for the presence of this DIB at future epochs. The lack of detection of λ5797 towards κ Vel indicates that the cloud that contains the DIBs is of σ type — diffuse and subject to high UV flux (Krełowski & Sneden 1995).

An alternative hypothesis is that a distinctly different cloud is moving into the κ Vel sightline that is rich in K I but contains negligible amounts of λ5780 carriers. The reality of this hypothesis hinges on there being multiple clouds in this very lightly-reddened sightline. Work by Krełowski & Westerlund (1988) showed that not all of the clouds in a given sightline produce DIB carriers in the same abundance. Thus it seems plausible that some clouds may contain negligibly small quantities of DIB carriers. Dense clouds, for example contain reduced DIB carrier abundances (Adamson *et al.* 1991) due either to lack of UV to excite the carriers, or to factors related to the growth of grain mantles (possibly the freezing out of DIB carriers onto grain surfaces). Crawford's work in 2002 lead to the conclusion that the cloud passing into the κ Vel sightline is indeed a very dense sheet or filament with $n_{\rm H} \gtrsim 10^3$ cm^{-3}. Additionally, *two* clouds with similar column densities were required to adequately model the κ Vel Na I absorption spectrum, which is consistent with the hypothesis that the DIBs arise in one cloud along the sightline, and that the time-variable K I column arises in the other cloud where negligible amounts of DIB carriers reside. For the amount of K I and the reddening of the sightline, the DIBs towards κ Vel are very weak (see Figures 4.59 and

4.60 on page 208), indicating that much of the sightline material is indeed inefficient at producing DIBs. Future observations examining the C I fine structure excitation along this sightline would help to constrain the cloud densities and determine whether this is correct.

The close correlation between λ5780, λ6196 and λ6284 in the Galactic ISM (Chlewicki *et al.* 1987) appears not to be upheld over small scales towards ρ Oph and β Sco: for ρ Oph, λ5780 shows large variations, whereas in most cases λ6196 and λ6284 do not. For β Sco, the variation of λ5780 and λ6196 are correlated, but to the apparent exclusion of λ6284. Given the expected similarities in physical and chemical conditions between the closely spaced sightlines studied, the lack of strong family behaviour indicates that over small interstellar distances, the factors that influence the DIB strengths are different from those that give rise to family behaviour on larger scales throughout the Galaxy. Based on the ubiquity of SSS density inhomogeneities in the ISM, density-dependent factors that affect DIB strengths offer the most likely cause of the DIB SSS. Variations in electron recombination rates and/or ionisation and/or excitation rates, and chemical pathways involving the DIB carriers that have a strong density-dependence appear to be good candidates to explain the SSS of the DIBs.

The diffuse interstellar bands λ5850 and λ5797 both correlate very well with N(K I) (Galazutdinov *et al.* 2004). In the ρ Oph system however, the λ5850 DIB is anticorrelated with N(K I) and N(Ca I), as shown by the plots in Figure 4.51. The strengths of λ5850 and λ5797 vary almost in the opposite sense to each other, as shown by Figures 4.43 and 4.42. This behaviour could be explained in a hypothesis whereby the the abundance of λ5797 carriers depend inversely on the abundance of λ5850 carriers. Such a situation could occur if the two species are chemically linked by an equilibrium reaction that creates one and destroys the other in approximately equal amounts. Alternatively, the two DIBs could be due to a single carrier molecule, but in a different level of internal excitation. For example, if excitation of the carrier of λ5850 results in the de-excitation of the carrier of λ5797, then the abundance of λ5850 carriers would go down as the abundance of λ5797 carriers went up. One possible scenario is that the carrier of λ5850 is a vibrationally excited state of the molecule that causes λ5797. The difference in wavelength of $\simeq$ 53 Å between λ5797 and λ5850 amounts to 0.02 eV difference in the vibrational energy levels. The excited state would have to be meta-stable in order to be significantly populated in the cold ISM.

4.5.2 DIBs as probes of SSS cloud conditions

Towards κ Vel, the lack of observed DIB variability leads to the interpretation that either no DIB carriers are present in the cloud responsible for the dramatic changes in K I, or that the variable K I cloud contains a non-variable amount of λ5780 DIB carriers over the length scale probed. Crawford (2002) reached the conclusion that the variable cloud has a very high density, which if true, means there must be a negligible amount of DIB carriers in this SSS cloud.

Towards ρ Oph, β Sco, μ Cru and HD 150135/6 the variations in the DIBs are at a similar level to the K I SSS. This is highly suggestive that the DIB carriers are located in the same cloud(s) that are responsible for the SSS observed in K I. The DIBs are too broad and the variations in strength too small to use a deconvolution analysis assign the variations to a particular cloud in velocity space. Given the apparent ubiquity of SSS in the ISM (Watson & Meyer 1996), it is possible that the 'DIB SSS' occurs in physically distinct clouds to those that cause atomic and molecular variability. Even for the relatively lightly-reddened sightlines studied here, multiple clouds are known to exist (see for example Welty & Hobbs 2001). It is difficult to assign *atomic* SSS to specific clouds because ultra-high resolution, high S/N observations are required, so to identify definitively which clouds cause DIB SSS is very challenging.

Assuming the DIB SSS does arise in the same clouds as the atomic SSS, certain properties of the clouds may be derived. The presence of the DIBs indicates a substantial dust content in the SSS cloud through the known correlation of DIB strengths with E_{B-V}. The small-scale DIB variations are similar to the K I variations, suggesting that the Galactic correlations between DIB strengths and atoms are upheld in the SSS clouds. Thus the SSS cloud conditions towards ρ Oph, β Sco and μ Cru must be similar to typical diffuse interstellar environments (*e.g.* $T \sim 100$ K, $n \sim 100$ cm^{-3}).

Due to stellar blends with λ5797 in many of the sightlines studied, the characteristic $\zeta - \sigma$ strength ratio of the SSS (for closely-separated sightlines X and Y),

$$F(X/Y) = \frac{W_{5780}(X) - W_{5780}(Y)}{W_{5797}(X) - W_{5797}(Y)} \tag{4.4}$$

could only be measured reliably for the ρ Oph system. From the residual intensities, and assuming a single SSS cloud, the following were obtained for different permuta-

tions of F in ρ Oph: F(B/A) = 3.6, F(DE/A) = 8.4, F(DE/B) = 16.3. From these ratios, the cloud causing a relative increase in DIB strengths in front of ρ Oph B compared to A is mid-way between ζ and σ type, for D compared to A, the cloud is of typical σ type, and for D compared to B, extreme σ type. Errors on the F(DE/B) value may be large due to the low value of W_{5797}(DE) − W_{5797}(B). Thus, the clouds responsible for SSS towards ρ Oph represent typical diffuse interstellar clouds as characterised by Krełowski & Walker (1987)'s $\zeta - \sigma$ scheme. The SSS cloud in front of ρ Oph DE has a λ5780/λ5797 ratio typical of very diffuse, high R_V, low FUV extinction, low molecular content, strongly UV-irradiated clouds. This is not consistent with hypotheses that the SSS in the diffuse ISM is caused by very dense, cool clouds or filaments where λ5780/λ5797 would be expected to be very low.

4.5.3 Small-scale structure and λ6614 profile variability

The profile of the λ6614 DIB has been shown by Walker *et al.* (2000) and Galazutdinov *et al.* (2002) to show significant variations in sub-structure pattern. Similar variations are clearly present in our data from comparison of the β Sco and ρ Oph spectra in Figures 4.17 and 4.47 respectively. Variations in the relative strengths of the substructure peaks within the λ6614 profile can also be seen between ρ Oph A and C (see Figures 4.47 and 4.48, Section 4.3.4). Thus, the factors that affect the λ6614 sub-structure also appear to operate over small distance scales in the ISM.

The origin of sub-structure within the λ6614 DIB is unknown, but work by Sarre *et al.* (1995) has shown that the DIB profile can be interpreted as a rotational contour: Three principal peaks in the λ6614 profile correspond to the P, Q and R rotational branches of an electronic transition in a large, symmetric molecule such as a PAH. Variations in the DIB profile could, in principle, be attributed to changes in the excitation of the rotational levels.

An alternative theory was developed by Webster (1996) (see also Webster 2004) that explains the profile as a sum of contributions from equally spaced, isotopically shifted Gaussian components. Each Gaussian component represents a rotationally broadened electronic transition in a large (50 – 100 atom), highly symmetrical carbon-based molecule, with an accompanying vibrational transition, the energy of which depends on the number of ^{13}C atoms in the molecule. Averaged over a large number of carriers

in space, the average number of ^{13}C atoms per molecule, $\bar{n}_{13}$, determines the relative strengths of the constituent Gaussian peaks. ^{13}C atoms are assumed to be substituted at random for ^{12}C atoms such that the number of ^{13}C atoms per molecule is determined by a Poisson distribution. Walker *et al.* (2000) successfully modelled the variations in λ6614 sub-structure for many sightlines exhibiting different λ6614 profiles. Variations in $\bar{n}_{13}$ were interpreted as resulting from quantifiable variations in the gas-phase interstellar ^{12}C to ^{13}C ratio ($[^{12}C]/[^{13}C]$) between sightlines.

In Webster's model, the wavelength shift and Gaussian FWHM of isotopically shifted components are set arbitrarily at ~ 0.3 Å to match the observed λ6614 spectra. Using a wavelength shift of 0.345 Å and a Gaussian FWHM of 0.326 Å, allowing the strength of each Gaussian to vary independently results in accurate fits to the λ6614 DIB towards ρ Oph A and C, shown in Figure 4.87. The residual RMS is approximately equal to the continuum RMS in both cases, albeit with a few relatively low magnitude apparent deviations from Poisson noise. Seven isotopic components were required, though more may be present, hidden in the noise in the red-degraded wing of the DIB.

Under the assumption that Webster's hypothesis is correct, to determine whether a difference in $\bar{n}_{13}$ could produce the sub-structure variation shown in Figure 4.48, the strengths of the individual Gaussian components that make up the λ6614 profile have been fit with Poisson distributions of the form given by Equation 3 of Webster (1996). In these fits, the only variable parameters are $\bar{n}_{13}$ and a constant scaling factor. The fits are shown as histograms in Figures 4.88 and 4.89 for ρ Oph A and C respectively. The best-fitting Poisson distributions have $\bar{n}_{13} = 1.68$ for ρ Oph A and $\bar{n}_{13} = 1.75$ for ρ Oph C.

Although the 'Webster model' fits provide a reasonable match to the strengths of the Gaussian components, they are not completely convincing. There is a systematic difference between the shapes of the Gaussian component distributions and the shapes of the least-squares Poisson distributions for the two sightlines. The observed DIB profiles fall to zero-intensity towards the red at a slower rate than the Poisson-law fits. The high S/N of the λ6614 spectra results in small errors on the Gaussian component strengths (less than the size of the data points in Figures 4.88 and 4.89) so improvements to the Webster model may be required for the successful modelling of high S/N λ6614 data; indeed, the assumption of invariant Gaussian profiles for each isotopic component may be invalid. Nevertheless, a difference in $\bar{n}_{13}$ is a plausible explanation

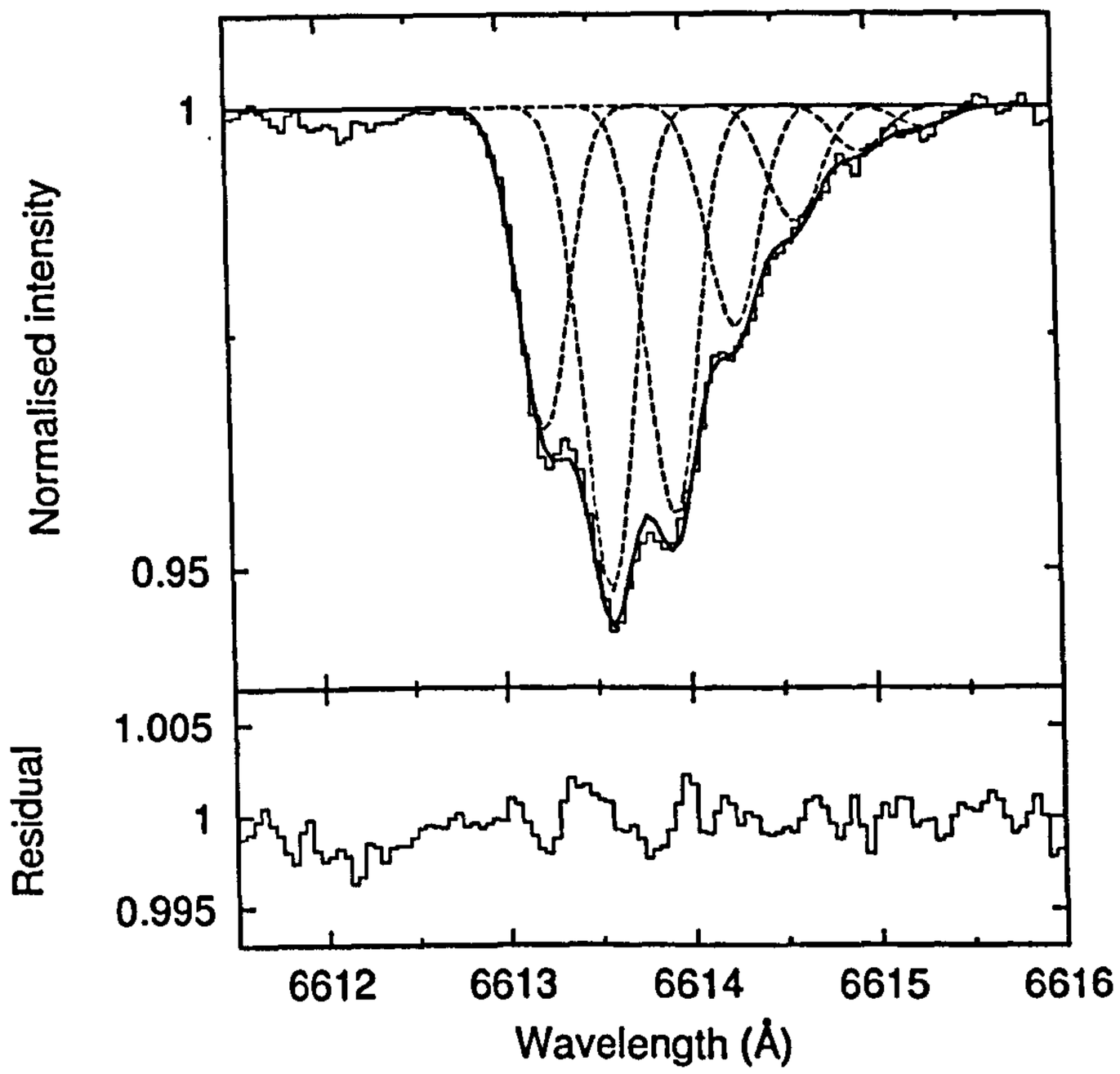

Figure 4.87: Telluric-corrected, normalised λ6614 DIB spectra observed towards ρ Oph A (top) and ρ Oph C (bottom), plotted as a histogram. Dotted lines show components of the 7-Gaussian least-squares fit. Gaussian FWHM was held fixed at 0.326 Å and the spacing between components was held fixed at 0.345 Å. The thick trace shows the total fit, with residual spectrum in the lower panel.

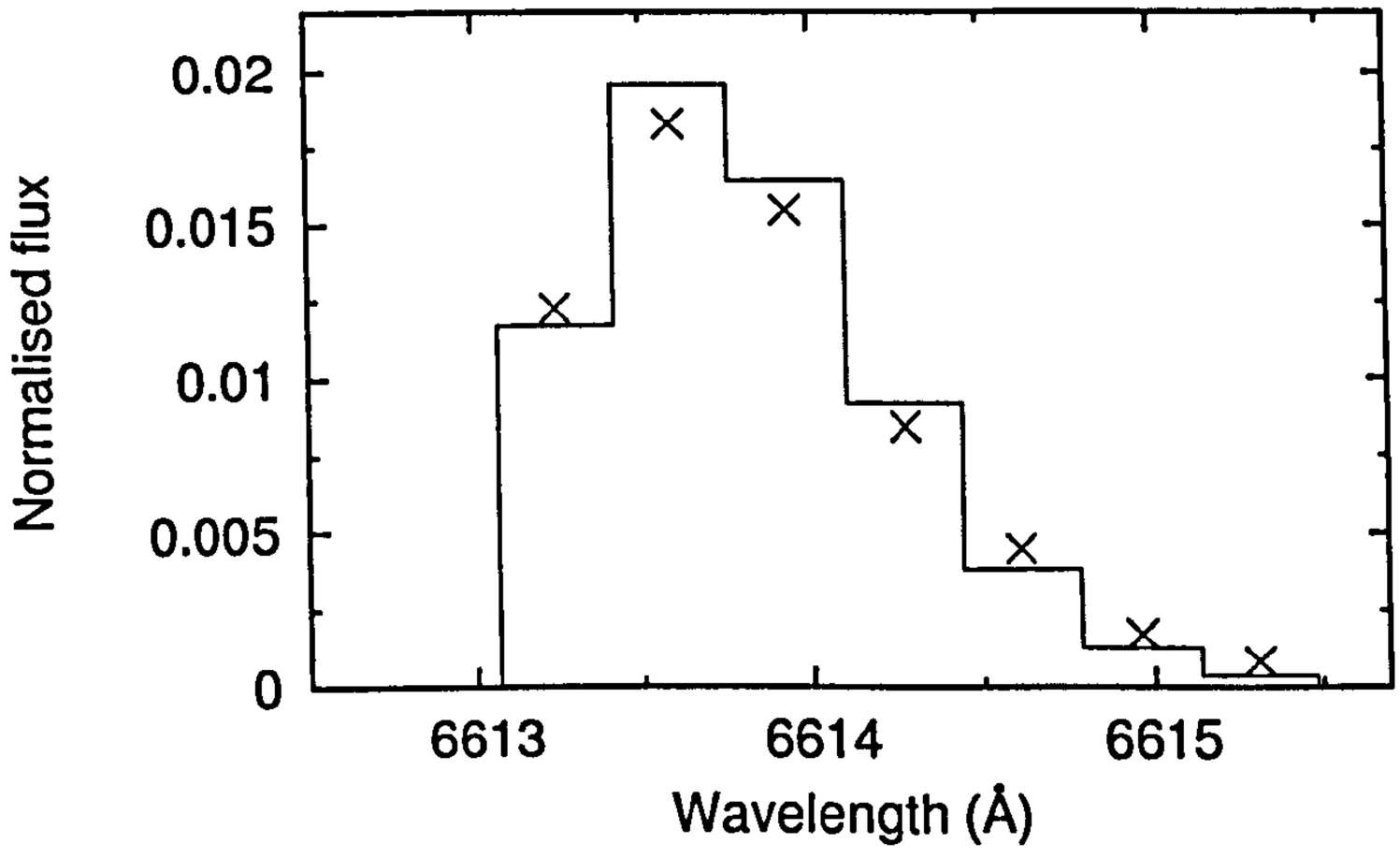

Figure 4.88: The histogram shows the least-squares fitted Poisson distribution for the Gaussian component strengths in the 'Webster model' of the λ6614 DIB sub-structure observed towards ρ Oph A. Gaussian component strengths are shown as crosses. The fit corresponds to $\bar{n}_{13} = 1.68$

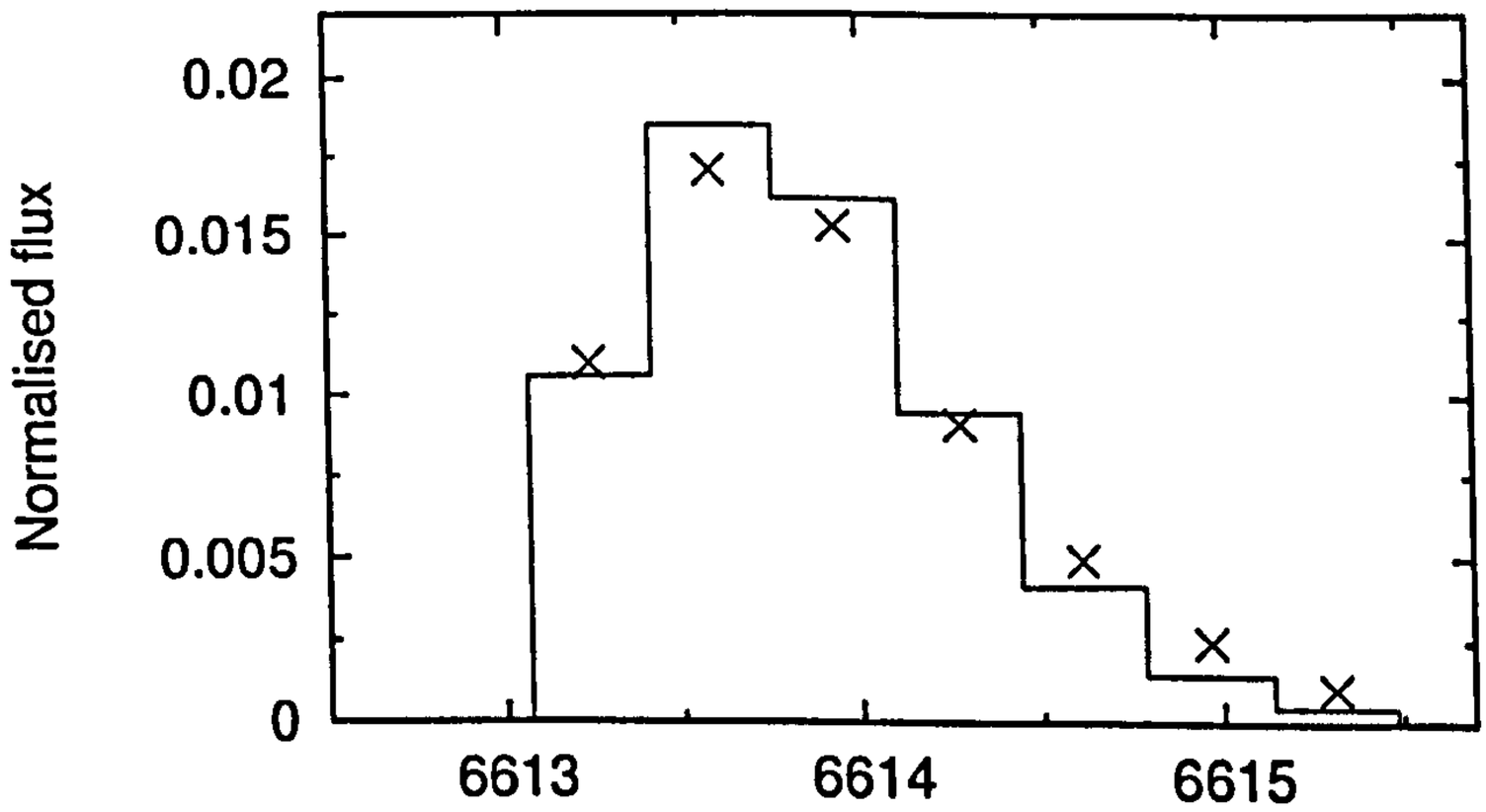

Figure 4.89: The histogram shows the least-squares fitted Poisson distribution for the Gaussian component strengths in the 'Webster model' of the λ6614 DIB sub-structure observed towards ρ Oph C. Gaussian component strengths are shown as crosses. The fit corresponds to $\bar{n}_{13} = 1.75$

for the observed changes in λ6614 between ρ Oph A and C.

Recent measurements of interstellar CH^+ by Federman *et al.* (2003) gave a value of $[^{12}C]/[^{13}C] = 109 \pm 36$ towards ρ Oph A, whereas in the nearby ρ Oph molecular cloud, Bensch *et al.* (2001) derived $[^{12}C]/[^{13}C] = 65.0 \pm 6.3$. Taking the mean of 87, the value of $\bar{n}_{13}$ towards ρ Oph A indicates that the λ6614 carrier molecule contains about 146 carbon atoms if Webster's hypothesis is correct. The difference in the least-squares $\bar{n}_{13}$ value between ρ Oph A and C indicates that $[^{12}C]/[^{13}C]$ should be about 4% greater towards ρ Oph A than ρ Oph C. Measuring such a small difference would be non-trivial, but provides motivation for future studies that might shed light on the nature of the λ6614 carrier.

4.6 Conclusion to Chapter 4

Variations have been discovered in the equivalent widths of fifteen out of sixteen measured diffuse interstellar bands observed between the component sightlines of nearby binary and multiple star systems. The sky-projected separation of sightline pairs ranged from $\lesssim 370$ AU to $\lesssim 43,000$ AU. Where the presence of contaminating stellar features could be ruled out, variations in the equivalent widths consistent with a change in overall DIB strength have been interpreted as resulting from small-scale spatial variations in the interstellar abundances of the DIB carriers. This constitutes the first firm evidence for small-scale structure in the spatial distribution of the DIB carriers.

The amount of small-scale variability observed in the DIB strengths was typically rather small, lying between about 5 and 20%. Much larger variations of $\sim$ 100% were observed towards μ Cru, over a distance of $\lesssim 4500$ AU, showing that the small-scale factors that govern DIB carrier abundance can produce a broad range of differing amounts of DIB SSS.

In such cases where contaminating stellar features were absent, variability in diffuse band profiles was generally not found, except for λ6614 towards ρ Oph C compared to ρ Oph A, B and DE. Interpreted within the framework of the hypothesis by Webster (1996), the variation in the λ6614 profile leads to the prediction of small-scale variability in the interstellar $[^{12}C]/[^{13}C]$ ratio, which would be expected to be enhanced by $\sim 4\%$ towards ρ Oph A compared to ρ Oph C.

Ten out of the twelve pairs of the closely separated sightlines observed showed evidence for small-scale structure in the material responsible for causing the DIBs. All ten showed differences in the K I λ7699 spectra. Of the two pairs that did not show DIB SSS, the HD 163864/313693 sightlines showed no evidence for significant variability in N(K I). Spectral S/N constraints could be responsible for a lack of observed DIB SSS in these two cases.

Evidence has been presented that, further to the increase in N(K I) towards the time-variable sightline towards κ Vel observed by Crawford (2002), N(K I) has since increased at an even faster rate, from 2.51×10^{10} cm^{-2} in March 2002 to 3.4×10^{10} cm^{-2} in June 2004. This constitutes a $\simeq 35\%$ increase in the interstellar K I column density during the passage of the sightline over a distance of $\lesssim 5$ AU through the ISM.

Between January 1995 and June 2004, the sightline towards κ Vel has traversed an interstellar distance of $\lesssim 25$ AU, accompanied by an approximately two-fold increase in N(K I). The lack of observed variability in the λ5780 diffuse interstellar band strength over this period shows that, if the strong K I small-scale variability is due to a dense ($n_{\rm H} \sim 10^3$ cm^{-3}) cloud (as inferred by Crawford *et al.* 2000; Crawford 2002), then this cloud must contain a negligible abundance of λ5780 carriers. This hypothesis is compatible with the theory that the DIB carriers are present at low abundances in denser interstellar media. However, if the variable K I cloud is of a density more typical of the diffuse medium, then the lack of small-scale λ5780 variation suggests that the conditions that favour the existence of the λ5780 carrier occur over a longer transverse distance scale than those that favour neutral potassium in this variable sightline. This hypothesis is compatible with a theory whereby the typical size of SSS of a given species is inversely related to its photoionisation rate (Lauroesch & Meyer 2003), such that the λ5780 carrier would have a lower photoionisation rate than K I.

Examples have been presented of the different DIBs varying by different amounts between the same pair of sightlines. The only DIB observed to show any variation between HD 150135 and HD 150136 was λ6614, which was about 5.7% stronger towards HD 150136 than HD 150135 whereas λ5780 and λ5797 showed less than 3.5% variation. Within the ρ Oph system, cases of one DIB increasing in strength where others decrease have been observed. For example, λ5797 is stronger towards ρ Oph DE than A, whereas λ5850 is stronger towards A than DE. Such patterns of variability are unlikely to have been caused purely by variations in the total amount of interstellar

material between the sightlines, caused for example by the presence of compact clouds or filaments. However, if the anomalous sightlines towards ρ Oph C and κ Vel are neglected, then the overall trend is that the DIB strengths follow roughly the small-scale variations observed in K I. In the ρ Oph system, the DIB strengths also tend to follow the variability observed in Ca I by Pan *et al.* (2004). Small-scale, density-dependent variations in the electron recombination, photoionisation and photodissociation rates are a likely explanation for the observed DIB variability patterns. It is likely that these variations are accompanied by significant variations in other interstellar parameters that govern the physics and chemistry that produce and destroy the DIB carriers. Such parameters may include dust grain abrasion rate, electron density, gas kinetic temperature and turbulent properties.

Within the ρ Oph system, no significant correlations were observed between DIB equivalent widths and the abundances of the species Ca II, CH, CH^+ or CN.

No good evidence for DIB family behaviour over small spatial scales has been observed. A breakdown of the usual family behaviour of λ5780, λ6196 and λ6284 is apparent towards the ρ Oph and β Sco systems, where the typically close correlations between the strengths of these three DIBs are not maintained. Therefore, the factors that cause DIB family behaviour appear to operate over larger scales in the interstellar medium than have been probed by this study.

Small-scale spatial variation in the velocity structure of the interstellar Na I D absorption profiles towards two stars in the cluster NGC 6531 (M 21) has been reported. Interpreted as due to a 2.8 ± 0.4 km s^{-1} velocity shift (at 2σ confidence) and an accompanying change in Doppler b of the $v_{\rm LSR} \simeq -12$ km s^{-1} cloud, this result implies the presence of small-scale variability in bulk interstellar cloud dynamics and in the internal kinetics and/or turbulence of the neutral sodium clouds towards HD 164863 and HD 313693.

The use of background stars with minimal stellar absorption and emission features has become obvious as one of the most important requirements for performing studies on DIB small-scale variability in multiple and binary systems. Variations in DIB strengths can only be measured accurately when no significant stellar features contaminate the DIB profiles.

In order to constrain the causes of the observed small-scale DIB variation, accurate

characterisation of interstellar cloud parameters is required. Measurements of the total column density and volume density of interstellar material, for example through detailed H I, Zn II and C I observations, would help to resolve the dichotomy of whether observed DIB variations are due to subtle changes in the factors that control the ionisation balance and chemistry of interstellar species, or to variations in the column density of the ISM caused by the presence of small (~ 10 AU), dense ($n \sim 10^4$ cm^{-3}) clouds. The observation of UV neutral-ion pairs such as Mg I and Mg II could be used to usefully measure the small-scale variability of electron density and determine its possible effects on 'DIB SSS'. Ultra-high resolution spectroscopy of two spatially co-existing species that differ significantly in mass (such as CN and CH or Na I and K I) could be used (see for example Crawford 2001) to calculate the kinetic and turbulent temperatures of the SSS clouds and determine whether chemical factors dependent on gas and dust kinetics are important for DIB SSS. Obtaining useful results from such observations will place exceptionally high demands on spectra in terms of S/N and resolution.

Chapter 5

CH_2CN^-: Possible carrier of the λ8037 diffuse interstellar band

5.1 Introduction to Chapter 5

5.1.1 Organic interstellar anions

The gas-phase chemistry of the diffuse ISM is dominated by the reactive elements that occur in the highest interstellar abundances: H, C, N and O. Presently, more than 125 molecules are known to exist in space, the majority of which are relatively small organic species, and contain between two and thirteen atoms. In the diffuse/translucent ISM where the diffuse interstellar band carriers reside, only a small fraction of the known molecules have been unambiguously detected. The conventional belief that the photodissociation rate in diffuse clouds is too high to allow molecules to exist in significant abundances is challenged by recent observations of molecules such as H_3^+ (McCall *et al.* 1998), HCO^+, HCN, H_2CO, C_2H and *c*-C_2H_3 (Lucas & Liszt 1996b, see for example) at high fractional abundances relative to H_2, similar to the fractional abundances found in dark molecular clouds. Conventional models of diffuse cloud chemistry are unable to explain such high molecular abundances.

As discussed by Duley & Williams (1984) and Hall & Williams (1995), the availability of erosion products from carbonaceous dust grains, including polyynes (C_n chains) or small hydrocarbons such as diacetylene (C_4H_2) in diffuse interstellar clouds could

provide a reservoir of reagents to fuel a complex network of organic chemistry. Species such as H_2O, C_4H and C_2H may thus be produced in appreciable abundances ($\sim 10^{-6}$ to $10^{-9} n_H$). Polyyne hydrogenation may occur *via*

$$C_n^+ + H_2 \longrightarrow C_nH^+ + H, \tag{5.1}$$

(Duley & Williams 1984), which generalises to

$$C_nH_m^+ + H_2 \longrightarrow C_nH_{m+1}^+ + H \tag{5.2}$$

and is efficient for $n < 5$ (Herbst & Leung 1989). Ketones and cyanopolyynes can be produced efficiently through reactions such as

$$C_2H_4^+ + O \longrightarrow C_2H_3O^+ + H \tag{5.3}$$

and

$$C_2H_4^+ + N \longrightarrow C_2H_3N^+ + H. \tag{5.4}$$

It is reasonable to expect such molecules to be found in the diffuse/translucent ISM where DIB carriers are found. The CH_4^+ molecule was proposed as a potential DIB carrier by Herzberg (1955b), and Douglas (1977) proposed that linear carbon-chain molecules were likely to exist in the diffuse ISM, with the potential to form DIBs. The argument put forward was that carbon chains should be able to resist break-up in the interstellar UV field by undergoing internal conversion. This is the process by which the energy of absorbed photons is redistributed into the vibrational modes of the molecule due to the high density of vibrational states. Although studies of neutral and cationic carbon chains (C_n) and cumulenic carbenes (C_nH) have yet proved fruitless in explaining any of the diffuse band absorptions, their anions have recently received significant attention.

The electronic spectrum of C_7^- was studied by Tulej *et al.* (1998) and five optical absorption bands were reported to match with the wavelengths of known diffuse interstellar bands. Models of diffuse cloud chemistry by Ruffle *et al.* (1999) that incorporated the gas-phase hydrocarbon reaction networks of Bettens & Herbst (1996) with time-dependent desorption of seed molecules from grain surfaces were able to reproduce the

required abundance of C_7^- (approximately $10^{-9}n_H$), and similarly high abundances of C_7H^-. The high electron affinity of C_7 permits rapid radiative electron capture, the rate of which was calculated by Ruffle *et al.* (1999) to proceed approximately two orders of magnitude faster than the C_7^- destruction mechanisms: photoionisation or associative electron detachment with neutral hydrogen.

The early promise of C_7^- as a potential DIB carrier was quashed when high resolution echelle spectroscopy by Galazutdinov *et al.* (1999) and McCall *et al.* (2001) identified that the match between the DIBs and the wavelengths, strengths and profiles of the C_7^- optical absorption bands was not good enough to constitute an assignment. Nevertheless, the work on C_7^- demonstrated the plausibility of small carbon-based molecules and their anions as possible DIB carriers.

In the past, the role of anions in interstellar reaction networks has generally been considered to be minimal. No reaction pathways involving anions were present in the comprehensive diffuse cloud models of van Dishoeck & Black (1986) (where ~ 500 reactions were modelled), and only a handful of atomic and diatomic anions are present in the UMIST 1999 database of ~ 4000 astrochemical reactions involving ~ 400 different species (Le Teuff *et al.* 2000). This is at least partly due to the lack of any direct observational evidence for anions in space, but also reflects the common belief that anions would be rapidly photoionised in the strong interstellar UV field. However, for species with high electron affinities such as radicals, photoionisation rates of their anions should be similar to those of other common interstellar molecules. The primary loss mechanisms for anions are generally considered to be (a) associative detachment (most likely with neutral hydrogen) and (b) mutual neutralisation with positively charged species (Dalgarno & McCray 1973; Herbst 1981; Petrie 1996).

Anions represent an attractive class of possible DIB carrier because, as noted by Herbig (1995) there is a distinct cutoff in the DIB spectrum at around 400 nm, corresponding to an energy of ~ 2.8 eV above which very few DIBs occur. The first ionisation energy of most ground-state anions lies below ~ 2.8 eV so that bound-bound electronic transitions occur only at wavelengths longer than ~ 400 nm. Without such photoionisation of the DIB carriers, it is difficult to explain why so few DIBs are seen in the NUV-UV.

The abundance of interstellar anions in relatively diffuse media depends predominantly on the balance between radiative electron attachment (Dalgarno & McCray 1973) and the processes that result in removal of the electron. Determining the electron attach-

ment rate requires knowledge of the electron attachment cross-section, the electron temperature of the ISM and the rate at which the 'temporary anion' stabilises. A temporary anion may be considered to form upon attachment of an electron into a vibrationally excited state of a molecule X (Herbst & Petrie 1997):

$$X + e \longrightarrow X^{-*} \tag{5.5}$$

which proceeds at a rate k_1. The excited electron may be lost at a rate k_{-1} in the reverse process

$$X^{-*} \longrightarrow X + e, \tag{5.6}$$

or may radiatively stabilise to form a ground-state anion at a rate k_r:

$$X^{-*} \longrightarrow X^- + h\nu. \tag{5.7}$$

Following the formalism of Herbst & Petrie (1997) the electron attachment cross-section for formation of a temporary anion by attachment of s-wave electrons[1] is given by

$$\sigma = \frac{\pi\hbar^2 G}{2\mu E} \tag{5.8}$$

where G is the ratio of the degeneracy of the ground state of the negative ion to that of the reactants; μ is the reduced mass and E is the collisional kinetic energy. Taking the thermal average and approximating the reduced mass to the mass of the electron,

$$k_1(T) = \hbar^2 G \left(\frac{2\pi}{m_e{}^2 k_B T}\right)^{\frac{1}{2}} \tag{5.9}$$

where k_B is the Boltzmann constant and T the kinetic temperature of the gas (assumed to be in thermal equilibrium). For radicals in doublet states forming negative ions in singlet states, $G = 1/4$ (Herbst & Petrie 1997) so substituting in the values of the constants, the expression becomes

[1]s-wave electrons have angular momentum quantum number $l = 0$. The electronic wavefunction may be expressed as a sum of 'partial waves' over the different possible values of l.

$$k_1(T) = 2.16 \times 10^{-6} T^{-1/2}. \tag{5.10}$$

For the typical temperature (100 K) of the diffuse medium, $k_1 = 2.16 \times 10^{-7}$ cm^{-3} s^{-1} is obtained.

The rate of electron detachment from the temporary ion is given by Herbst (1985) as

$$k_{-1} = c/\rho \tag{5.11}$$

where c is the speed of light and ρ the density of vibrational states (in cm) of the negative ion at the electron detachment threshold energy.

The temporary ion may stabilise through vibrational de-excitation at a rate given by Herbst (1982) as

$$k_r = \frac{E_{vib}}{hs} \sum_{i=1}^{s} \frac{A^i{}_{1\rightarrow 0}}{\nu_i} \tag{5.12}$$

where E_{vib}, the vibrational energy of the excited state can be set equal to the electron affinity, s is the number of vibrational degrees of freedom, ν_i are the vibrational frequencies of the anion and $A^i{}_{1\rightarrow 0}$ are the Einstein A coefficients of the fundamental transitions of the normal modes of the molecule.

Combining the above rates to form the 'overall anion formation' (electron capture) rate

$$k_{cap} = \frac{k_1 k_r}{k_{-1} + k_r}. \tag{5.13}$$

Thus, the rate at which stable anions form is dependent on the density of vibrational states ρ at the detachment threshold of the anion and on the electron affinity of the neutral species X. For linear carbon chains with more than 6 atoms, Terzieva & Herbst (2000) calculated that k_r is significantly greater than k_{-1} so, provided collisional electron detachment of the excited complex does not occur (by collisions with hydrogen for example), k_{cap} tends towards the value of k_1.

Fundamentally, formation of a negative ion requires that the excited temporary ion radiatively stabilises before the collisionally attached electron is lost back to the continuum. The rate k_r is increased by the presence of electronic states near the attachment

threshold that have strong electronic transitions to lower energy states.

If collisions with other species are neglected, in steady state, the fraction of anions relative to neutrals is given by

$$\frac{[X^-]}{[X]} = \frac{k_{cap} n_e}{k_d} \tag{5.14}$$

where n_e is the electron density and k_d the photoionisation rate of the anion. Using a typical value for the electron density of 0.1 cm^{-3} in the diffuse medium (*e.g.* Welty *et al.* 2003), and with values of k_d between 10^{-9} and 10^{-12} s^{-1} for a range of different simple molecules (Roberge *et al.* 1991), it is clear that as k_{cap} tends towards the value of $k_1 = 2.16 \times 10^{-7}$ cm^{-3} s^{-1} derived above for the diffuse medium, the fraction of anions can become large, even dominant.

Using similar arguments, Omont (1986) deduced that PAHs in the diffuse ISM should attain appreciable anionic fractions through radiative electron attachment. Lepp & Dalgarno (1988) reached a similar conclusion and determined that large PAHs (containing ~ 50 carbon atoms) could exist entirely as anions over a range of interstellar conditions, given a sufficiently high ratio of electron density to UV field strength. The combination of relatively high electron affinities and a high density of vibrational states due to the many vibrational degrees of freedom of the aromatic structures results in rapid electron capture and stabilisation for large PAHs. From extensive chemical modelling Bakes & Tielens (1994) determined that, under typical diffuse interstellar conditions the majority of small PAHs should be in the form of anions, a result that was supported by the studies by Dartois & D'Hendecourt (1997). PAH charge states were found by Salama *et al.* (1996) to vary as a function of their size and depth inside modelled clouds. In their models, small PAHs (~ 20 atoms) tended to be cationic, with larger PAHs becoming neutral, then anionic for very large PAHs ($\gtrsim$ 100 atoms); PAHs were seen to become increasingly negatively charged with distance towards the cloud interiors.

The expected high interstellar abundances of PAHs (~ $10^{-7} n_H$ as determined by Leger & Puget (1984)) leads to the prediction of the presence of a large population of negatively charged large molecules (LM^-) in the ISM. Capable of efficient donation of the excess electron to another species upon collision, LM^- are now becoming accepted as one of the major sources of 'spare' electrons in astrochemical reactions. The role of

LM^- in the formation of CN^- has been discussed in depth by Petrie (1996), and the importance of LM^- for models of diffuse cloud chemistry was shown by Bakes & Tielens (1998) who determined that charge transfer from PAH^- to atomic cations such as C II (and by inference Na II and K II), results in their rapid neutralisation and therefore significantly raises the abundances of neutral interstellar species. It is reasonable to expect that collisions of neutral molecules with LM^- may also expedite the production of small molecular anions.

5.1.2 Dipole-bound anionic states

Electron donation from LM^- is not the only method by which the abundances of molecular anions may be increased. Güthe *et al.* (2001) noted that the 'dipole-bound' electronic state of *l*-CH_2CC may assist this strongly polar radical to attach and stabilise an electron. The electric dipole potential between a free electron and polar neutral falls as $1/r^2$ whereas the polarisation interaction potential falls as $1/r^4$ (r is the distance of the electron from the molecule), so the electron attachment rate k_1 should be greater for molecules with dipole moments than those without (Desfrançois *et al.* 1996). Classically, the electron is attracted to the dipole field of the molecule over a longer range than is possible due to the polarisability (Van der Waals) interaction alone.

Dipole-bound electronic states were first predicted by Fermi & Teller (1947), whose calculations showed that a theoretical point-dipole with a sufficiently large dipole moment (> 1.625 D; see also Desfrançois *et al.* (1996)) can bind an extra electron in a very diffuse orbital to form a so-called 'dipole-bound' anion. The binding energy of the dipole-bound electron (typically ~ 10 – 100 cm^{-1}) depends predominantly on the magnitude of the dipole moment and the electron affinity of the neutral molecule. Theoretical studies (Crawford 1970; Garrett 1978; Gutsev & Adamowicz 1995a,b,c) and experimental work (Moran *et al.* 1987; Brinkman *et al.* 1995; Lykke *et al.* 1987; Desfrançois *et al.* 1996) has since shown that in practice, molecules with dipole moments $\mu \gtrsim 2.5$ D can support at least one dipole-bound electronic state. The discrepancy between the theoretical and experimental minimum dipole moment is caused by perturbations to the dipole-bound electronic wavefunction, mainly due to rotation and electron correlation and repulsion interactions of the molecule. The dipole-bound electron orbits mostly about the positive end of the molecular dipole, at a typical mean

distance of around 30 Å from the molecule, dependent on the binding energy of the state (Garrett 1978; Desfrançois *et al.* 1996).

Many molecules capable of forming dipole-bound anionic states also possesses a standard valence-anionic state, in which case the dipole-bound state (DBS) lies at an energy just below the threshold for ionisation of the valence anion. Figure 5.1 shows a schematic representation of the potential energy curves and levels for the neutral, valence anionic and dipole-bound anionic states of a diatomic molecule of this type. The cyanomethyl radical (CH_2CN) is an example of a molecule that can form stable valence and dipole-bound anionic states. It possesses a dipole moment of between approximately 3.6 and 4.0 D (Liu 2001; Gutsev & Adamowicz 1995a) and an electron affinity of 1.56 eV (Marks *et al.* 1986). The first dipole-bound state of CH_2CN^- lies only $\simeq$ 10 meV below the ionisation continuum (Lykke *et al.* 1987; Moran *et al.* 1987; Gutsev & Adamowicz 1995a). Given that the DBS lies almost at the detachment threshold, the electron affinity of the neutral (1.56 eV) is almost identical to the energy required to raise the *anion* from its ground state (GS) into the first dipole-bound state (DBS). Thus, the absorption transition (DBS $\longleftarrow$ GS) of CH_2CN^- occurs at a wavelength in the region of 800 nm. High resolution fast ion-beam autodetachment spectroscopy allowed Lykke *et al.* (1987) to derive the molecular parameters of CH_2CN^-. They determined that the DBS lies $12,428.665 \pm 0.002$ cm^{-1} (1.54 eV, or 8046 Å) above the GS.

Using the molecular parameters of Lykke *et al.* (1987), Sarre (2000) discovered that in the 0_0^0 origin band, the $^rQ_0(1)$ transition between the GS and DBS of CH_2CN^- occurs at an air wavelength of 8037.8 Å. The remarkable correspondence of this transition with the peak absorption wavelength of a diffuse interstellar band[2] located around 8037 Å, combined with the additional location of other DBS $\longleftarrow$ GS rotational lines involving low-lying rotational levels of CH_2CN^- within the DIB profile lead to the 'dipole-bound state' hypothesis: that some, possibly many of the unidentified diffuse interstellar bands are caused by transitions between the ground and dipole-bound states of polar molecules or small polar grains (Sarre 2000). It was also noted that the electron-dipole interaction could increase the radiative association rate of interstellar anions. The case for CH_2CN^- as possible carrier of the λ8037 DIB is explored as the main subject of this chapter.

Güthe *et al.* (2001) studied the molecule *l*-CH_2CC that possesses valence and dipole-

[2]Peak absorption wavelength 8037.9 ± 0.3 Å according to Galazutdinov *et al.* (2000b)

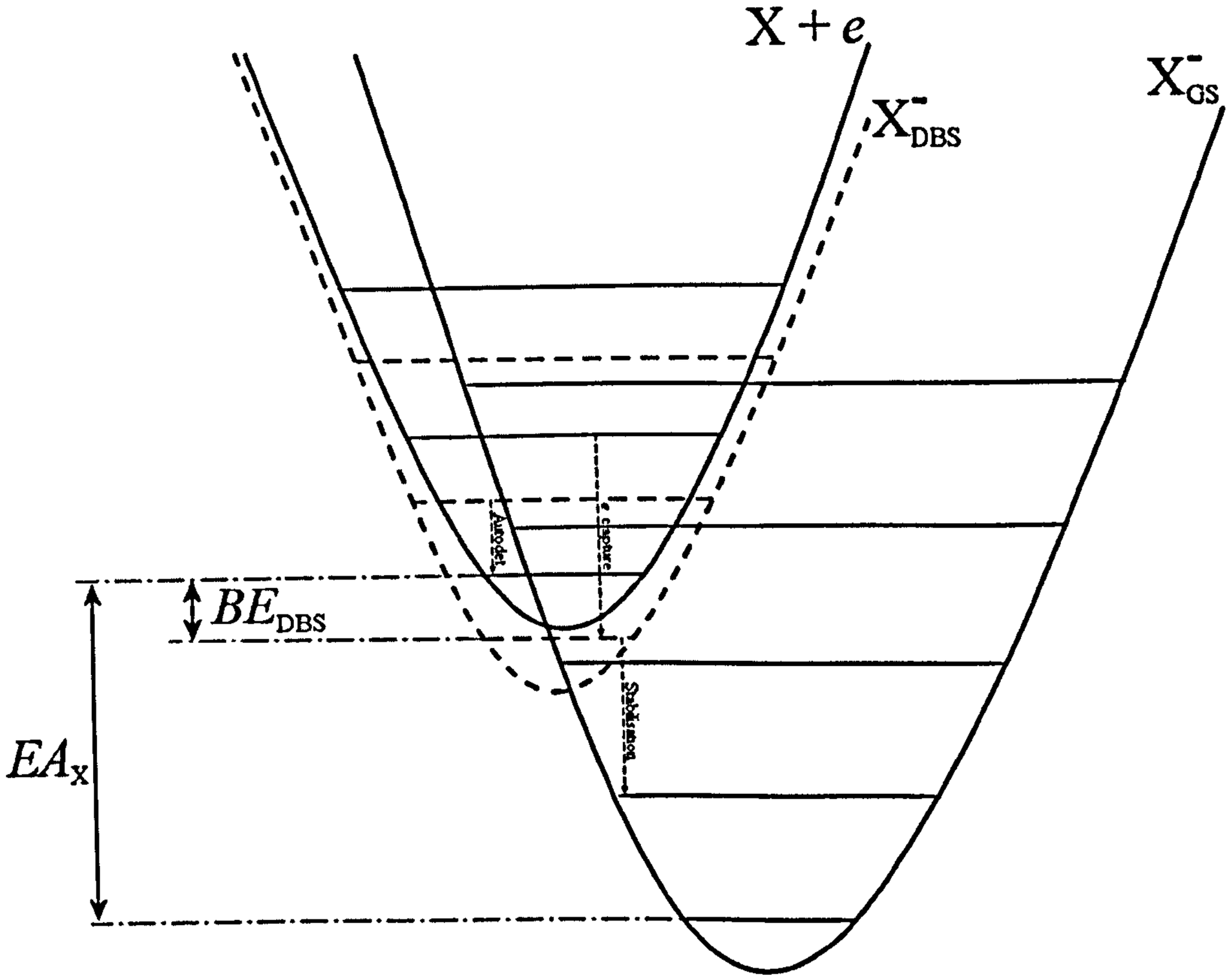

Figure 5.1: Schematic potential energy diagram for a dipolar neutral molecule (with $\mu \gtrsim 2.5$ D) and free electron 'X + e', its valence anionic state 'X^-_{GS}' and its dipole-bound anionic state 'X^-_{DBS}'. The electron affinity of the neutral molecule EA_X and the binding energy of the dipole-bound state BE_{DBS} are shown. The small dotted arrows represent various electronic transitions: autodetachment of an excited dipole-bound level (labelled 'Autodet'), continuum electron capture into a stable dipole-bound state ('e capture') and a transition DBS $\longrightarrow$ GS from the DBS to GS of the anion ('Stabilisation').

bound anionic states very similar to those of CH_2CN and noted the close correspondence between the wavelengths of the low-lying rotational DBS ⟵ GS transitions and the λ6993 DIB. The attractive dipole potential and the fact that the molecule undergoes strong transitions from GS to DBS (and *vice versa*) suggests that the *l*-CH_2CC^- anion could form in appreciable abundances in the diffuse ISM where electron densities are relatively high. However, a detailed study by McCall *et al.* (2002a) revealed ~ 1 Å mismatch between the wavelength of the λ6993 DIB and their modelled *l*-CH_2CC^- DBS ⟵ GS absorption contour, with the conclusion that there was no evidence to support the theory that this molecule is the carrier of the λ6993 DIB (or any others).

Evidence that molecular dipoles can assist electron capture and stabilisation is shown, for example in the studies of electron scattering by HCl performed by Domcke & Cederbaum (1980), where large increases in the total electron scattering cross-section were observed, attributable to near-threshold resonances. Although the dipole of HCl is too weak to support a DBS, the effects of the long-range electron-dipole interaction were strongly observed. Spectroscopy of the strongly dipolar nitromethane molecule (CH_3NO_2) by Compton *et al.* (1996) determined that the presence of a near-threshold dipole-bound state acts as a 'doorway' for electron capture, and that strong transitions occur from the DBS to the GS, resulting in rapid formation of a stable anion. Sommerfeld (2005) studied the coupling between the valence and dipole-bound anionic states of nitromethane, cyanoacetylene and uracil, concluding again that the DBS acts as efficient doorway to valence anion formation.

5.1.3 CH_2CN^- as possible carrier of the λ8037 DIB

The initial calculations by Sarre (2000) identified a very close correspondence between the wavelength of the λ8037 diffuse band and the origin band DBS ⟵ GS $^rR_0(0)$, $^rQ_0(1)$ and $^rP_0(2)$ transitions of CH_2CN^- (at air wavelengths of 8037.3 Å, 8037.8 Å and 8037.6 Å respectively). These transitions are from the lowest energy levels of the molecule, *i.e.* those likely to be populated assuming thermal equilibrium of the molecule with the 2.74 K cosmic microwave background (CMB) in the diffuse ISM, with a kinetic temperature of ~ 100 K. The spectroscopic match is shown in Figure 5.2 for the heavily-reddened sightline towards Cygnus OB2 8a. The spectrum has been Doppler-shifted to place the peak interstellar K I absorption wavelength at rest.

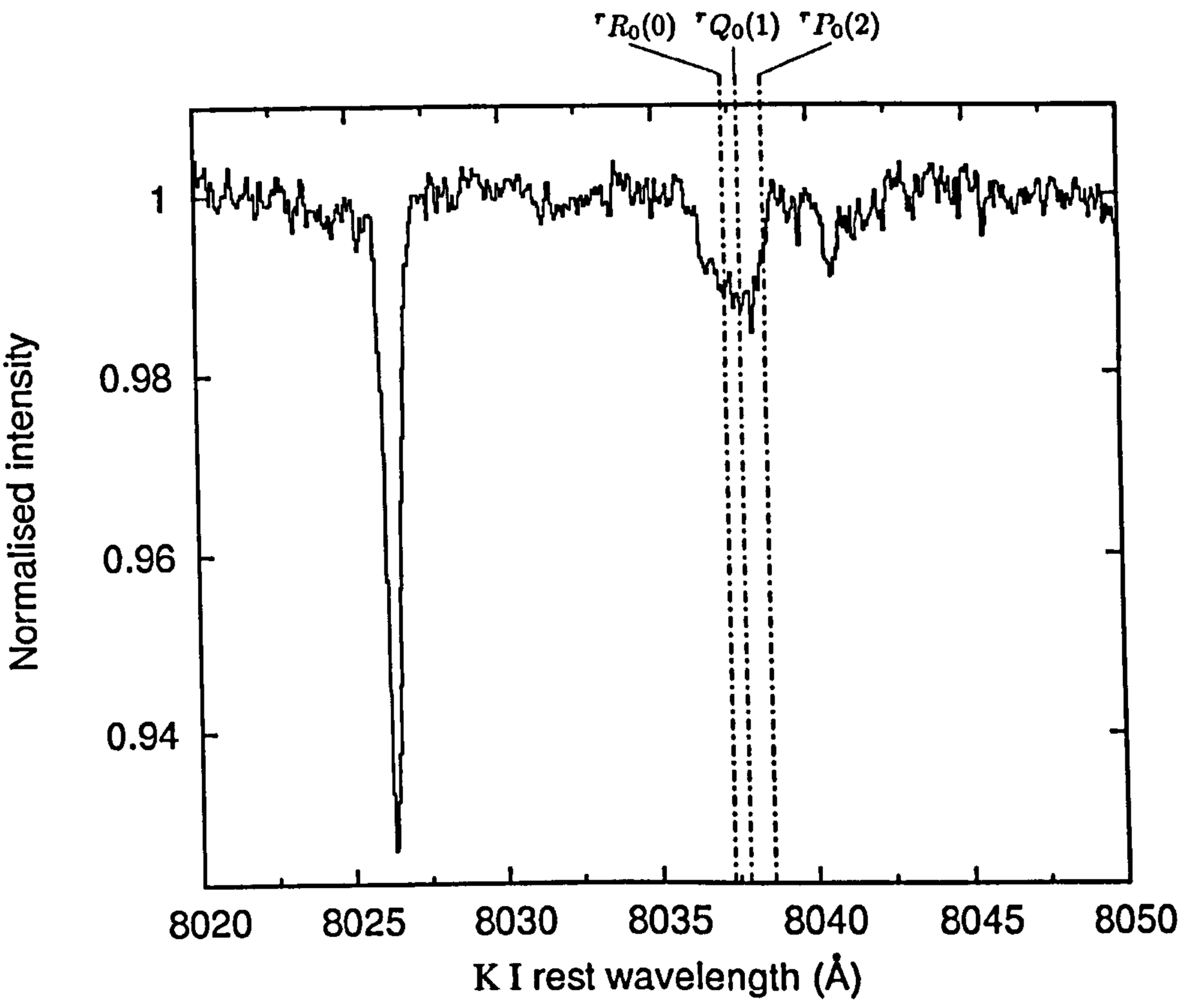

Figure 5.2: The interstellar spectrum towards Cyg OB2 8a (with interstellar K I at rest wavelength), in the region surrounding the λ8037 DIB. The narrow λ8026 DIB is also clearly seen. The wavelengths of the CH_2CN^- DBS ⟵ GS $^rR_0(0)$, $^rQ_0(1)$, $^rP_0(2)$ transitions are shown, assuming a rigid asymmetric prolate-top rotor. The asymmetry of CH_2CN^- introduces $\lesssim 0.5$ Å uncertainty in the calculated wavelengths.

To assess the possibility of CH_2CN^- being the carrier of the λ8037 DIB, rigorous modelling of its transition wavelengths and their relative intensities is required, taking into account the rotational temperature, asymmetry and centrifugal distortion of the molecule. Combined with high S/N, high-resolution spectra of the region around 8037 Å and knowledge of the velocity dispersion of the interstellar gas, the ability of CH_2CN^- to reproduce the observed λ8037 profile is assessed in this chapter.

5.2 Observations of the λ8037 DIB

A medium resolution survey of heavily-reddened Galactic sightlines was performed by G. H. Herbig and K. D Leka in 1996 and 1997 using the HIRES (High Resolution Echelle Spectrograph) facility at the W. M. Keck Observatory, Hawaii. The raw sci-

Sightline	Spectral Type	E_{B-V}
Cyg OB2 5	O7 e	1.94
Cyg OB2 8a	O6 e	1.59
Cyg OB2 12	B2 I – B8 Ia	2.8–3.4
HD 168112	O5.5	1.01
HD 169034	B5 Ia	1.30
HD 183143	B7 Ia	1.24
HD 186745	B8 Ia	0.96
HD 229196	O5	1.22
λ Cyg	B5 V	0.04
ζ Peg	B8.5 V	0.00

Table 5.1: Table showing sightline data for stars observed by G. H. Herbig (private communication). For the E_{B-V} values, spectral types and $B-V$ photometry were taken from, respectively, the modal and mean averages of all data referenced in the SIMBAD database (URL: http://simbad.u-strasbg.fr/sim-fid.pl); intrinsic stellar photometry from Wegner (1994) with the exception of Cyg OB2 5 and 8a for which photometry was taken from Massey & Thompson (1991) and Cyg OB2 12 whose uncertain spectral type and photometry have been discussed by Gredel & Munch (1994).

ence exposures, flat fields, Th/Ar and bias frames from four nights' observations were kindly made available to us by G. H. Herbig (private communication). Reductions were carried out as prescribed in Chapter 2. The S/N of the reduced spectra was typically between 400 and 800 per pixel, with resolving power $R \simeq 42,500$ measured from the average of several unblended Th/Ar lines. The wavelength range of the spectra was $\sim$ 7000 to 10,000 Å.

The λ8037 DIB is weak and cannot be observed easily in moderate-to-low E_{B-V} sightlines. The most-reddened sightlines were selected to provide the best comparisons with the CH_2CN^- DBS $\longleftarrow$ GS transitions. The CCD used during the observations was subject to fringing at red/NIR wavelengths, removed successfully in most cases by the flat-fielding process. However, some reduced spectra still showed significant fringing and were identified from the presence of periodic oscillations in spectral regions that were expected to be free of stellar or interstellar features; these sightlines were discarded. Details of the remaining set of sightlines are given in Table 5.1.

Low-opacity ($\tau < 0.1$) telluric absorption is present across the main regions of interest in this chapter (the λ8037 DIB and the K I λ7699 line) and was successfully removed by division by a scaled and shifted composite of the co-added λ Cyg and ζ Peg unreddened standard spectra (a composite was used so as to enhance the S/N of the standard star

spectrum).

5.3 The $^1B_1$ DBS ⟵ $^1A'$ GS transition of CH_2CN^-

5.3.1 Rotational spectroscopy of polyatomic molecules

For any molecule, three orthogonal axes (a, b, c) may be defined in rectangular coordinates that are fixed with respect to the molecular rest frame. Each axis (q) passes through the molecular centre of mass and has an associated moment of inertia I_q (with $q = a, b, c$). By convention, the direction of the a-axis is defined along the molecular axis with minimum moment of inertia. The directions of b and c are then defined according to $I_c \geq I_b \geq I_a$.

The classical rotational kinetic energy of the molecule is

$$KE = \frac{1}{2}\sum_q I_q {\omega_q}^2 = \sum_q \frac{{P_q}^2}{2I_q} \tag{5.15}$$

where ω_q and I_q are the angular frequency and moment of inertia about axis q, and the angular momentum $P_q = I_q\omega_q$.

For a rotating molecule described by a wavefunction ψ, the energy eigenvalues E_n of the rotational Hamiltonian $\hat{H}$ are given by the Schrödinger equation

$$\hat{H}\psi = E_n\psi \tag{5.16}$$

For a rigid rotor, $\hat{H}$ may be defined in terms of the angular momentum operators $\hat{P}_q$, for the q components of angular momentum, as

$$\hat{H} = \hbar^2\left(\frac{\hat{P}_a^2}{2I_a} + \frac{\hat{P}_b^2}{2I_b} + \frac{\hat{P}_c^2}{2I_c}\right). \tag{5.17}$$

The definition of the angular momentum operators $\hat{P}_q$ may be found in standard quantum mechanics or rotational spectroscopy texts (Gordy & Cook 1984, for example).

Introducing the 'rotational constants' of the molecule

$$A = \frac{\hbar^2}{2I_a},\ B = \frac{\hbar^2}{2I_b},\ C = \frac{\hbar^2}{2I_c}, \tag{5.18}$$

the Hamiltonian becomes

$$\hat{H} = A\hat{P}_a^2 + B\hat{P}_b^2 + C\hat{P}_c^2 \tag{5.19}$$

which may be re-arranged (Gordy & Cook 1984) to

$$\hat{H} = \frac{1}{2}(A + C)\hat{P}^2 + \frac{1}{2}(A - C)\hat{P}_b^2 H(\kappa) \tag{5.20}$$

where $\hat{H}(\kappa)$ is the 'Reduced Hamiltonian'

$$\hat{H}(\kappa) = \hat{P}_a^2 + \kappa\hat{P}_b^2 - \hat{P}_c^2. \tag{5.21}$$

The molecular constant κ is a measure of the asymmetry of the molecule, calculated from the rotational constants using

$$\kappa = \frac{2B - A - C}{A - C}. \tag{5.22}$$

The limiting cases of $\kappa = -1, +1$ represent 'prolate' ($B = C$) and 'oblate' ($A = B$) symmetric top molecules respectively. The total angular momentum of the molecule is $\hat{P} = \hat{P}_a^2 + \hat{P}_b^2 + \hat{P}_c^2$ so that in the prolate and oblate limits, the energy eigenvalues of the Hamiltonian may be obtained relatively easily. For example, for a prolate symmetric top molecule ($\kappa = -1$), from Equation (5.19), Equation (5.20), and Equation (5.21),

$$\hat{H} = B\hat{P}^2 + (A - B)\hat{P}_a^2. \tag{5.23}$$

Given the rotational constants, to calculate the energy levels of a prolate symmetric top all that need be known are the angular momentum eigenvalues of $\hat{P}^2$, given by $J(J+1)$, and the eigenvalues of $\hat{P}_a^2$, given by K_a^2. J and K_a are the quantum numbers that define the rotational energy levels[3]; K_a is the component of J projected along the molecular a-axis ($K_a = J \cdot \hat{a}$ where $\hat{a}$ is a unit vector along a).

[3] $J = 0, 1, 2, \ldots$ and $K_a = J, J-1, J-2 \ldots, -J$.

An additional consideration in describing the energy levels is that, when they spin, molecules experience distortion of their bonds due to centrifugal forces. The distortion modifies the axial moments of inertia I_q such that the rotational constants change. The amount of distortion depends on the rotational energy about the molecular axes, and may be parameterised in various different ways for inclusion in the Hamiltonian (see for example Gordy & Cook 1984).

When $\kappa \neq \pm 1$, the molecule is said to be an 'asymmetric rotor'. In such cases, the total rotational angular momentum quantum number J still defines the eigenvalues of $\hat{P}^2$, but K_a no longer correctly describes the component of J along a; it is no longer a 'good quantum number' for describing the eigenvalues of $\hat{P}_a^2$. In addition, levels corresponding to $|K_a| > 0$ that are degenerate for symmetric rotors now have different energies. The Schrödinger equation for the the asymmetric rotor cannot be solved directly except for the lowest J levels.

To obtain a solution to the Schrödinger equation of an asymmetric rotor, its wavefunction is commonly expressed as a linear combination of symmetric-rotor wavefunctions. The full treatment of the distortable asymmetric rotor is complex. For details the reader is referred to a standard rotational spectroscopy text such as Gordy & Cook (1984).

The rotational Hamiltonian of the distortable asymmetric rotor may be approximated in various ways. For near-prolate symmetric top molecules (with $A > B \approx C$), Watson's S-reduced Hamiltonian $\hat{H}^S$ (Watson 1977) is commonly used[4]. Including the centrifugal distortion terms (D_J, D_K, D_{JK}, d_1, d_2) up to fourth order,

$$\hat{H}^S = \left(A - \frac{B+C}{2}\right)\hat{P}_a^2 + \left(\frac{B+C}{2}\right)\hat{P}^2 - D_J\hat{P}^4 - D_{JK}\hat{P}^2\hat{P}_a^2 - D_K\hat{P}^4$$

$$+2\left(\frac{B-C}{4} + d_1\hat{P}^2\right)\hat{P}_c^2 + d_2\left((\hat{P}_c + i\hat{P}_b)^4 + (\hat{P}_c - i\hat{P}_b)^4\right). \qquad (5.24)$$

5.3.2 Spectroscopy of CH_2CN^-

The rotational spectroscopy of the neutral cyanomethyl radical CH_2CN has been discussed by Turner *et al.* (1990). It has a planar ground state configuration corresponding to C_{2v} symmetry with a $^2B_1$ electronic ground state (Moran *et al.* 1987; Gutsev &

[4] 'S' stands for near-symmetric.

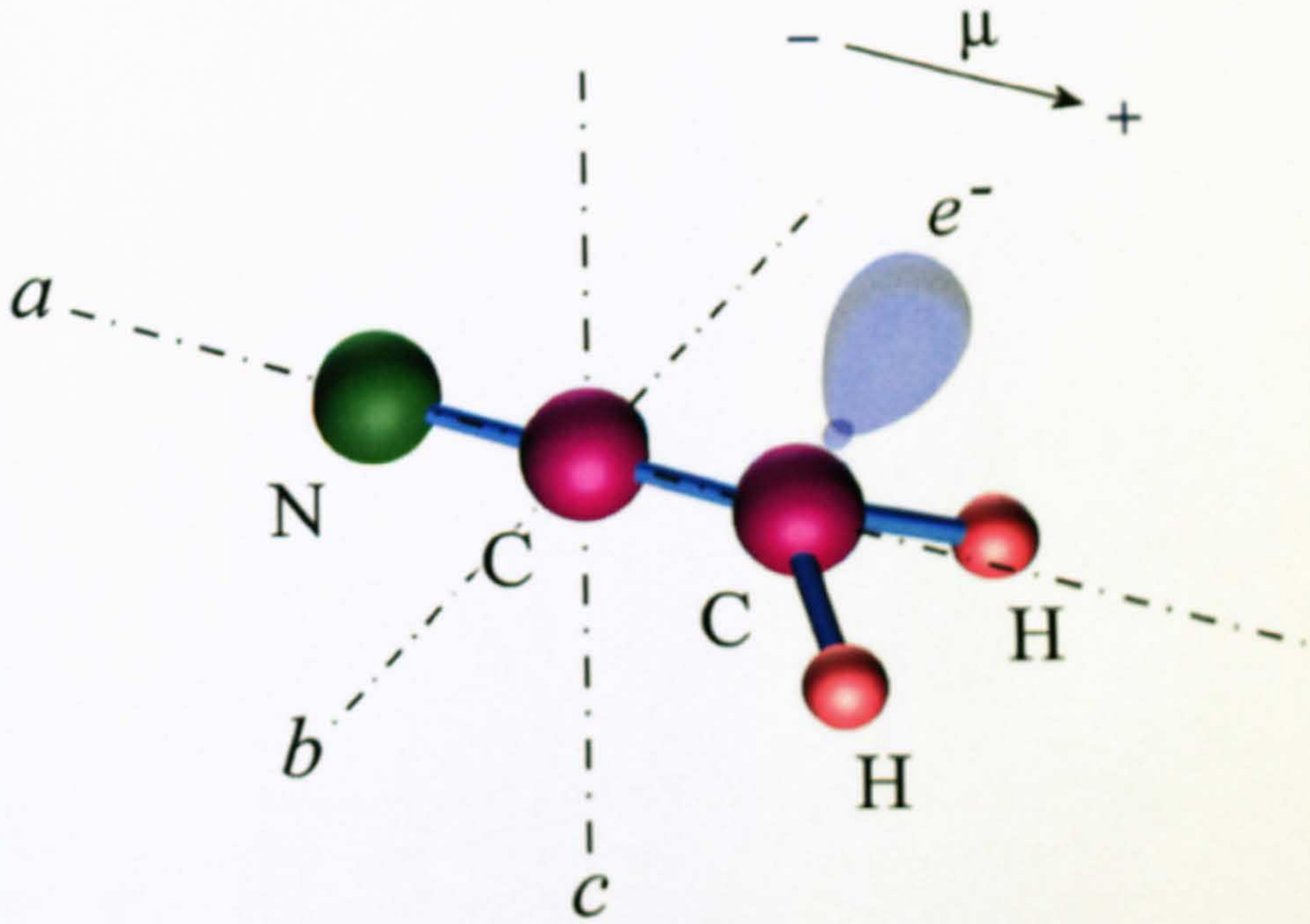

Figure 5.3: Structure of the CH_2CN^- molecule. The principal rotational axes and direction of the dipole moment of the molecule are labelled. A schematic representation of the sp^3 hybridised orbital that contains the majority of the 'extra' electron of the anion in the $^1A'$ ground state is shown.

Adamowicz 1995a). CH_2CN consists of a CH_2 methylene group bonded to a CN radical with the hydrogens in-plane, and the unpaired electron resides on the methylene carbon atom. Upon attachment of an additional electron to this unpaired π electron system, the in-plane methylene sp^2 orbitals become sp^3 hybridised and the planar molecular geometry becomes slightly distorted into a pyramidal geometry. The hydrogen atoms move out of plane by 30 ± 5 degrees, resulting in a $^1A'$ electronic ground state in C_s symmetry (Gutsev & Adamowicz 1995a). The mirror plane lies along the C-C-N backbone. 'Inversion' of the out-of-plane H atoms is the process by which they tunnel to the opposing configuration, reversing the sign of the out-of-plane angle. The energy barrier for such an inversion is small (100 ± 50 cm^{-1}; see Moran *et al.* (1987)) and the molecule readily tunnels between the two possible conformations (Lykke *et al.* 1987). A diagram of the structure of CH_2CN^- is shown in Figure 5.3 with the principal rotational axes and the direction of the molecular dipole moment indicated.

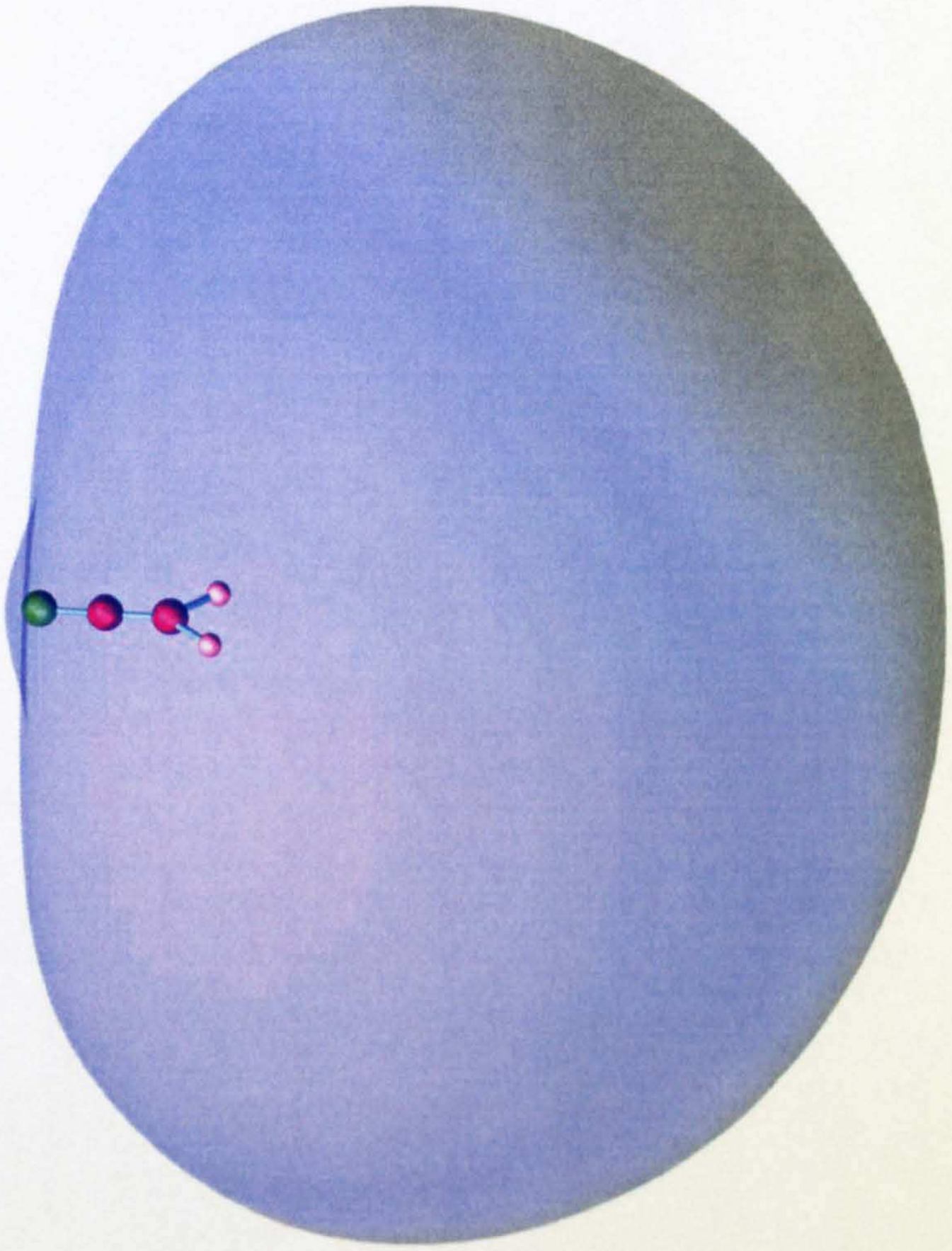

Figure 5.4: Artist's impression of the CH_2CN^- molecule and dipole-bound electronic orbital. The size and shape of the DBS is based on the HCN^- dipole-bound electron 90% charge probability contour published by Abdoul-Carime & Desfrançois (1998). The HCN dipole moment of $\mu \sim 3$ D is comparable to the $3.6 \sim 4$ D value for CH_2CN.

When CH_2CN^- is excited into its DBS, the dipole-bound electron is very weakly bound and diffuse. Its interaction with the rest of the molecule becomes only weakly perturbative — effectively, the electron orbits at such a distance that its effect on the rest of the molecule is minimal. Therefore in the dipole-bound state, the CH_2CN^- nuclear framework assumes an almost identical geometry to that of the neutral radical. Consequently, the electronic transition from the GS to the DBS involves a change in the symmetry of the molecule from $\{C_s, {}^1A'\}$ to $\{C_{2v}, {}^1B_1\}$ (Gutsev & Adamowicz 1995a). The probability distribution of the dipole-bound orbital is well described by the functional form of an sp^1 hybrid, symmetric with respect to rotation about *a* (Desfrançois *et al.* 1996). The DBS ⟵ GS transition corresponds to a 'perpendicular type' transition (Lykke *et al.* 1987) with the transition dipole-moment orientated along the molecular *c* axis. A diagram of the dipole-bound state configuration of the molecule is shown in Figure 5.4.

The rotational constants of the cyanomethyl anion were determined to very high accuracy by Lykke *et al.* (1987) using high-resolution autodetachment spectroscopy of a beam of pure CH_2CN^-. Rovibronic transitions were observed from the GS to autodetaching levels of the DBS, and the energy of the lowest observed autodetaching level corresponded to $J = 9$, $K_a = 2$. The rotational constants of the molecule were determined through least-squares fitting of the energy eigenvalues of Watson's S-reduced Hamiltonian (Equation (5.24)) to the energy levels of the observed spectra. Transitions obey the rotational selection rules $\Delta J = 0, \pm 1$ and $\Delta K_a = \pm 1$. A diagram of the rotational energy level structure and some examples of ${}^1B_1$ DBS ⟵ ${}^1A'$ GS transitions are shown in Figure 5.5.

The selection rule $\Delta K_a = \pm 1$ is consistent with the *c*-polarised transition dipole-moment and the change in symmetry of the electronic wavefunction from ${}^1A'$ to ${}^1B_1$.

Nuclear spin statistics (see for example Atkins & Friedman 1997) dictate that there exist two separate forms of the ground state cyanomethyl radical and its anion, distinguished by the spin symmetry of the fermionic (*i.e.* spin 1/2) hydrogen nuclei. The nuclear spin statistics of NH_2CN, which is isoelectronic with CH_2CN^- and has an almost identical structure has been discussed by Millen *et al.* (1962). Assuming the different modes of motion of CH_2CN^- can be separated, the total molecular wavefunction ψ may be factorised into electronic (E), vibrational (V), rotational (R) and nuclear spin (S) components:

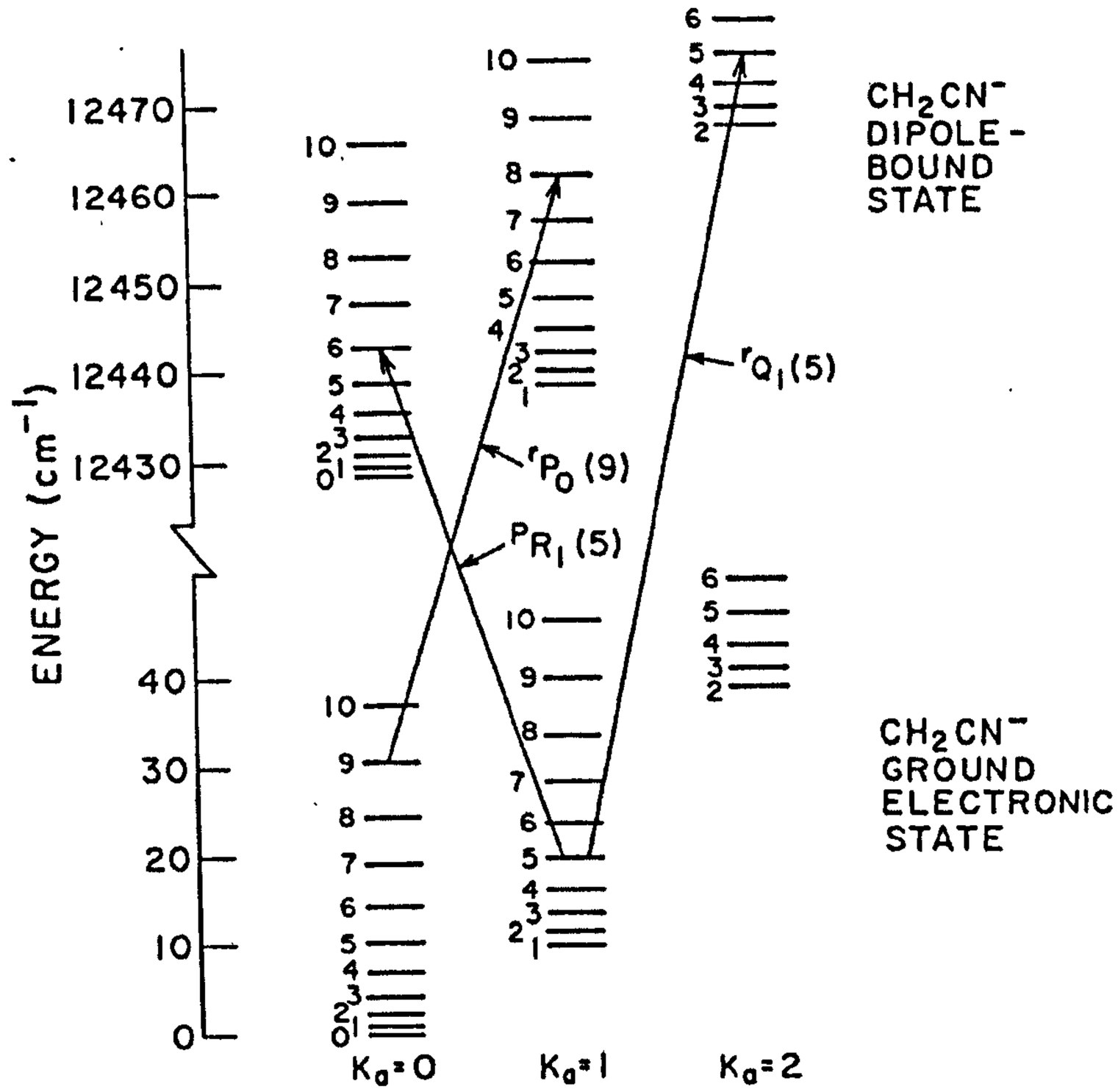

Figure 5.5: Rotational energy level diagram for the CH_2CN^- DBS ⟵ GS transition (reproduced with permission, from Lykke *et al.* (1987)) showing some of the J levels (arranged vertically) and K_a stacks (arranged horizontally) of the origin band. Arrows correspond to the transitions $^1B_1$ DBS ⟵ $^1A'$ GS. The asymmetry doubling of the J levels is not shown.

$$\psi = \psi^E \psi^V \psi^R \psi^S . \tag{5.25}$$

The Pauli principle states that the interchange of identical fermions causes an inversion of the symmetry of the total wavefunction: $\psi \rightarrow -\psi$. Interchange of the H nuclei requires a reflection of ψ in the mirror plane ac, which causes the nuclear spin wavefunction's symmetry to invert ($\psi^S \rightarrow -\psi^S$) when the H nucleic spins are antiparallel, but not when the spins are parallel ($\psi^S \rightarrow \psi^S$). Upon exchange of the nuclei, the $^1A'$ electronic wavefunction preserves symmetry ($\psi^E \rightarrow \psi^E$). The behaviour of the vibrational and rotational wavefunctions depends on the level of excitation: For rotational wavefunctions, the symmetry is preserved for levels with even K_a and inverts for levels with odd K_a such that $\psi^R \rightarrow (-1)^{K_a}\psi^R$. The vibrational wavefunctions associated with the inversion of a pyramidal molecule such as CH_2CN^- (and NH_2CN; see Millen *et al.*

(1962)) transform according to a point group including the symmetry operation $C_2{}^a$ (involving π rotations about the a axis), and conserve symmetry for evenly numbered vibrational levels (with quantum number $v = 0$ representing no vibrational excitation), whereas the symmetry inverts for the odd numbered vibrational levels. Thus, the vibrational wavefunction symmetry goes as $\psi^v \rightarrow (-1)^v\psi^v$. Multiplying the symmetry factors of the different components of the wavefunction, when the H nuclear spins are parallel, to achieve $\psi \rightarrow -\psi$, even v wavefunctions must be paired with odd K_a wavefunctions and *vice versa*. When the spins are antiparallel, odd v wavefunctions must be paired with odd K_a wavefunctions and even with even.

The transition dipole-moment for the hydrogen nucleus spin-flip transition is small so that interconversion between the spins-parallel and spins-antiparallel forms of isolated CH_2CN^- will occur very slowly. This is analogous to the situation for the H_2 molecule (see Atkins & Friedman 1997, for example), where the spins-parallel version of the molecule is referred to as 'ortho' and the spins-antiparallel version 'para'. The consequence of nuclear spin statistics is that the ground state of the ortho form has a degeneracy of three compared to the singly degenerate para form, manifested in laboratory rotational spectra as a 3 : 1 strength ratio in those transitions originating from odd J levels compared to those from even J. The three to one ratio occurs because there are three degenerate ways to combine spins in parallel (for the ortho form), but only one way to combine the spins in antiparallel (for para). Nuclear spin statistics dictate that para H_2 exists only in even J levels and ortho H_2 only in odd J levels.

For H_2, the rate of the spin-flip transition is very small ($\sim 10^{-20}$ s^{-1}; see Dodelson (1986)), but when molecular hydrogen is cooled to within a few degrees of absolute zero, conversion of the ortho to the para form may occur. The ground state $J = 0$ level represents the lowest energy level of H_2, so because ortho H_2 exists only in the odd J levels (1, 3, 5, ...), to achieve the lowest energy state, cooling from $J = 1 \longrightarrow 0$ requires the conversion of H_2 from ortho to para. The spin-flip transitions of pure H_2 are unlikely, so a cold metal surface may be provided as a catalyst to speed the process: H_2 adsorbs onto the surface where re-orientation of the nuclei may occur rapidly upon bond breakage, forming a distribution of energy levels in thermal equilibrium with the surface, followed by desorption of the molecule.

H_2 is observed in the interstellar medium with a range of ortho : para (o : p) ratios consistent with collisional proton exchange being the dominant mechanism for inter-

conversion. According to Flower & Watt (1984), the reaction o-H_2 + H^+ $\longrightarrow$ p-H_2 + H^+ + hν occurs efficiently, allowing the rotational energy levels to reach thermal equilibrium with the incident protons, skewing o : p away from 3 : 1 according to the relative populations of the thermalised odd and even J levels.

For other molecules with identical H nuclei, if collisional proton exchange cannot occur efficiently, then the observed distribution of rotational levels (and correspondingly skewed o : p ratios) can give clues as to the chemical reactions in which the molecule participates. For example, if a molecule is formed by reaction with H_2, then the molecular o : p ratio may reflect the o : p ratio of the H_2 (see for example the case of c-C_3H_2, studied by Takakuwa *et al.* (2001)). According to Dickens & Irvine (1999), the thermally skewed o : p ratio of H_2CO, which has the same nuclear spin statistical properties as H_2 and CH_2CN^-, indicates that the molecule probably formed in thermal equilibrium with cold dust grains. The enthalpy of molecular formation is important however, because if it is large with respect to the energy spacing between the distinct rotational levels of the ortho and para forms, then the molecular formation mechanism will not favour one form or the other, and the statistical 3 : 1 ratio occurs. If the enthalpy of formation is very small and the rotational level spacing becomes significant in the energetics of the reaction, then production of the lower energy ($J = 0$) para form is favoured.

The formation mechanisms for interstellar CH_2CN^-, particularly for its production in the diffuse ISM, are not firmly established. It is unclear whether complete thermalisation of the rotational energy levels would take place, or whether the molecule would be found with the statistical o : p ratio of 3 : 1. CH_2CN^-, due to its 'bent' pyramidal geometry has a small dipole moment along the c axis that may assist the thermalisation of the K_a levels through radiative rotational transitions that couple with the spin-flip transition of the H nuclei. If CH_2CN^- forms on cold grain surfaces or through a reaction with very low enthalpy, then thermal equilibrium of the rotational levels may dictate a very low o/p ratio. If however, CH_2CN^- is formed in the gas phase at a relatively warm temperature or in a high enthalpy reaction, then the $\sim$ 9 cm^{-1} spacing between the ortho and para levels would be insignificant in the molecular formation process such that the statistical 3 : 1 ratio of o : p level degeneracies would result.

Turner *et al.* (1999) noted that unsaturated hydrocarbon molecules such as H_2CO, H_2CS and CH_3CN typically exhibit thermal rotational energy level populations, with

no dependence on nuclear spin statistics, whereas saturated hydrocarbons (including H_2C_4, H_2CCO and CH_3CCH) exhibit rotational level populations governed by nuclear-spin statistical ortho to para ratios. It was suggested that this may be due to the lower affinity of the unsaturated species with grain surfaces, making them easier to desorb once the rotational level populations have thermalised.

Chemical modelling of the o : p ratio to deduce the possible populations of the K_a levels of CH_2CN^- in its $^1A'$ ground state is beyond the scope of this thesis. However, from observations of o : p ratios in other molecules (*e.g.* Flower & Watt 1984; Takakuwa *et al.* 2001; Dickens & Irvine 1999; Turner *et al.* 1999), it is likely that the K_a levels should be populated by a distribution that lies somewhere between the extremes of a thermal Boltzmann distribution and the 3 : 1 ratio of populations of the odd : even K_a levels imposed by nuclear-spin statistics.

5.4 Modelling CH_2CN^- as the λ8037 DIB carrier

5.4.1 Rotational contour calculations

The $^1B_1$ DBS $\longleftarrow$ $^1A'$ GS transitions of CH_2CN^- were modelled for an initial distribution of J level populations described by a 2.74 K Boltzmann distribution. This is the temperature of the cosmic microwave background radiation with which dipolar molecules are expected to reach thermal equilibrium in the diffuse ISM. The low density of the diffuse ISM means that collisional excitation of the molecule should be small enough to have a negligible effect on the energy level populations (see for example Lucas & Liszt 2000). Over time, the molecule should have relaxed down through the K_a rotational levels due to the finite dipole moment along the molecular c axis. Quadrupolar transitions will also assist relaxation process such that, in the absence of processes that modify the o : p ratio, para CH_2CN^- should occur predominantly in the $K_a = 0$ levels, and ortho CH_2CN^- in $K_a = 1$. From the A rotational constant (see Table 5.2), the energy spacing between the lowest K_a levels is ~ 9 cm^{-1}, so that thermal equilibrium of the K_a levels with the CMB (with $k_BT \sim 2$ cm^{-1}) would not cause significant excitation of any K_a levels above $K_a = 1$.

Using the ASYROT routine (Briss & Ramsay 1984), the CH_2CN^- rotational constants from Lykke *et al.* (1987) (see Table 5.2), and the selection rules outlined in Section

	GS (cm^{-2})	DBS (cm^{-2})
A	9.29431(14)	9.51035(17)
B	0.338427(20)	0.341049(21)
C	0.327061(21)	0.328764(21)
D_J	$1.65(10)\times10^{-7}$	$2.19(10)\times10^{-7}$
D_{JK}	$1.297(15)\times10^{-5}$	$1.499(14)\times10^{-5}$
D_K	$1.0028(21)\times10^{-3}$	$0.7546(36)\times10^{-3}$
T	0	12428.665(2)

Table 5.2: Molecular parameters used in the modelling of the origin band CH_2CN^- $^1B_1$ DBS $\longleftarrow$ $^1A'$ GS transitions, taken from Lykke *et al.* (1987). 1σ uncertainties on the last two digits are given in parentheses.

5.3.2, the origin band CH_2CN^- $^1B_1$ DBS $\longleftarrow$ $^1A'$ GS transition wavelengths and relative intensities were calculated for $K_a = 1 \longleftarrow 0$, corresponding to the transitions of para CH_2CN^-. The transition wavelengths and strengths are shown in Table 5.3 and Figure 5.6. The use of the 'bad' quantum numbers K_a and K_c to characterise the rotational levels is instructive due to the very nearly prolate symmetry of CH_2CN^-. They represent the quantum numbers of those rotational levels of the prolate symmetric top rotor (with $B = C = (B + C)/2$), that lie closest to the energies of the asymmetric top rotor. The small asymmetry of CH_2CN^- means that the energy differences from the prolate symmetric rotor are small.

The ortho CH_2CN^- transitions originating from $K_a'' = 1$ occur at $\simeq \pm 19.5$ cm^{-1} with respect to the para transitions (corresponding to $\simeq \pm 12.5$ Å at 8037 Å). Assuming a 2.74 K Boltzmann distribution of J levels, the ortho transitions occur at wavelengths of $\sim$ 8025 and $\sim$ 8050 Å and do not overlap the wavelengths of the para ($K_a = 1 \longleftarrow 0$) transitions near 8037 Å.

A model for the interstellar CH_2CN^- $^1B_1$ DBS $\longleftarrow$ $^1A'$ GS origin band absorption spectrum was constructed assuming a single cloud of CH_2CN^- with a Gaussian internal velocity distribution. The distribution of initial (J'', K_a'') rotational levels was assumed to be in *full thermal equilibrium* with the 2.74 K CMB. At this temperature, the $K_a'' = 1$ levels are negligibly populated such that the $K_a = 1 \longleftarrow 0$ transitions dominate the spectrum. Free parameters in the model were the Doppler width of the CH_2CN^- velocity distribution (expressed as a b value), the mean radial velocity of the cloud and the equivalent width of the resulting absorption feature.

The transition vacuum wavelengths λ_{vac} and relative intensities S_r from Table 5.3 were

λ_{vac} (Å)	S_r	J'	K'_a	K'_c	J''	K''_a	K''_c	Transition
8037.259	0.02	6	1	5	5	0	5	$^rR_0(5)$
8037.730	0.09	5	1	4	4	0	4	$^rR_0(4)$
8038.194	0.31	4	1	3	3	0	3	$^rR_0(3)$
8038.650	0.70	3	1	2	2	0	2	$^rR_0(2)$
8039.101	1.06	2	1	1	1	0	1	$^rR_0(1)$
8039.544	1.00	1	1	0	0	0	0	$^rR_0(0)$
8039.983	1.06	1	1	1	1	0	1	$^rQ_0(1)$
8039.985	0.88	2	1	2	2	0	2	$^rQ_0(2)$
8039.988	0.43	3	1	3	3	0	3	$^rQ_0(3)$
8039.994	0.14	4	1	4	4	0	4	$^rQ_0(4)$
8039.999	0.03	5	1	5	5	0	5	$^rQ_0(5)$
8040.835	0.17	1	1	0	2	0	2	$^rP_0(2)$
8041.252	0.12	2	1	1	3	0	3	$^rP_0(3)$
8041.662	0.05	3	1	2	4	0	4	$^rP_0(4)$
8042.065	0.01	4	1	3	5	0	5	$^rP_0(5)$

Table 5.3: List of the strongest CH_2CN^- $^1B_1$ DBS $\longleftarrow$ $^1A'$ GS $K_a = 1 \longleftarrow 0$ origin band transitions at $T = 2.74$ K (thermal equilibrium with the CMB) calculated using ASYROT (Briss & Ramsay 1984) and the CH_2CN^- molecular parameters from Lykke *et al.* (1987). Vacuum transition wavelengths λ_{vac} given are accurate to within ~ 0.01 Å (~ 0.4 km s^{-1}) based on the 1σ errors given for the molecular parameters. S_r is the relative transition strength, proportional to the transition dipole-moment. To convert λ_{vac} to wavelengths in air at 15° C and standard pressure, subtract ≃ 2.210 Å. Transitions go as $(J', K'_a, K'_c) \longleftarrow (J'', K''_a, K''_c)$. J is the total angular momentum quantum number; K_a and K_c are shown, but their precise physical meaning is undefined for the transitions calculated — they represent the components of J along the a and c molecular axes upon extrapolation of the molecular geometry to the prolate symmetric-top limit ($B = C = (B + C)/2$).

convolved with a Lorentzian profile of width 0.01 Å to simulate the intrinsic natural line-broadening of the transition, assuming a relatively high transition strength (with an upper state lifetime of ~ 10^{-9} s), typical of resonant atomic transitions. The resulting 'intrinsic' transition profile was then convolved with the Gaussian interstellar CH_2CN^- cloud model (parameterised by b and v), with an arbitrary intensity scaling factor to ensure line optical depths were $\ll 1$ such that the lines remained optically thin. The resulting optical depth spectrum[5] was transformed to an air wavelength scale using the formula given by Edlen (1966):

[5]Relative transition strengths S_r obtained from ASYROT are proportional to the total line optical depths.

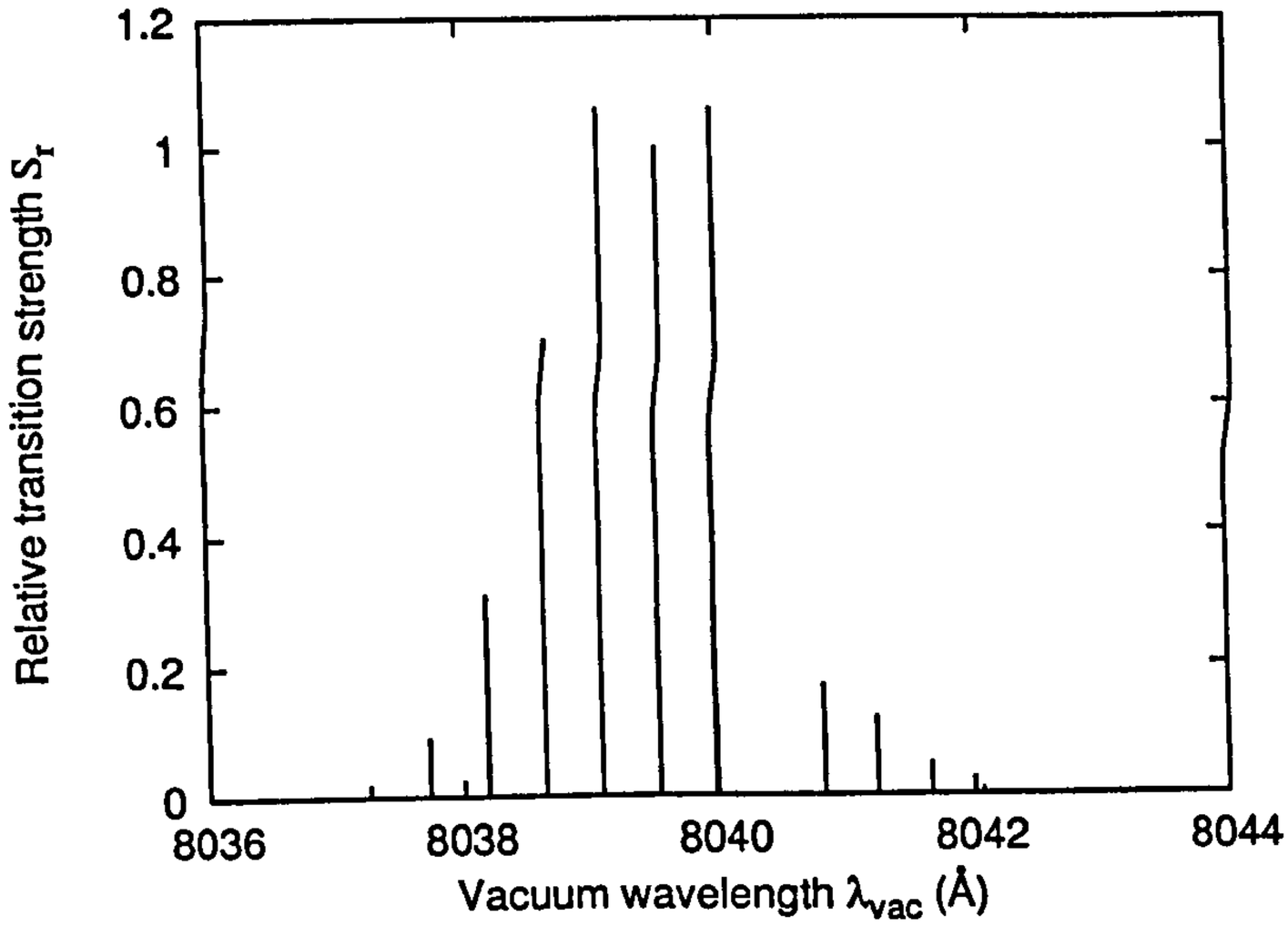

Figure 5.6: Plot of the strongest CH_2CN^- DBS ⟵ GS origin band transition wavelengths and strengths at $T = 2.74$ K, shown in Table 5.3. Note that the Q branch transitions overlap in this plot.

$$(n-1)\times 10^8 = 8342.13 + \frac{2406030}{130-\epsilon^2} + \frac{15997}{38.9-\epsilon^2} \tag{5.26}$$

applicable to air with standard composition at 15°C and standard pressure (760 mmHg). The substitution $\epsilon = 10^4/\lambda_{vac} \simeq 10^4/\lambda_{air}$ was used in the calculation of λ_{air}, introducing a negligible ($\lesssim 0.1$ mÅ) error into the air wavelengths. The Edlen (1966) formula has been used for calculation of air wavelengths by many authors of astronomical spectroscopic data since 1966 (see de Cuyper & Hensberge 1998, and references therein), including all of the Th/Ar wavelength calibration line lists employed in this thesis, and in the internal line lists used in the IRAF **identify** tasks.

The exponential of the optical depth spectrum was taken and the resulting absorption spectrum convolved to the resolving power ($R \simeq 42,500$) of the HIRES spectra using a Gaussian with FWHM = 7 km s^{-1}.

5.4.2 Comparison of model with observations

The initial CH_2CN^- $^1B_1$ DBS ⟵ $^1A'$ GS model considered a single interstellar cloud at rest with $b = 1$ km s^{-1}, representative of a typical cool diffuse interstellar cloud (see

Welty 1998). The result is shown at the top of Figures 5.7 and 5.8 for comparison with the λ8037 DIB spectra. The observed λ8037 spectra have been shifted to set the peak of the interstellar K I distribution at rest. Where the K I distribution was multi-peaked, the weighted mean K I velocity was taken, with component weights determined from their equivalent widths. Thus, provided the λ8037 DIB carriers reside at a similar line-of-sight velocity to the K I clouds, then the spectra in Figures 5.7 and 5.8 show this DIB at rest. The peak absorption wavelength of the 'rest' CH_2CN^- model is at 8037.78 Å, which is closely co-incident with the peak absorption wavelength of the 'rest' λ8037 DIB at 8037.8 ± 0.15 Å (measured by repeated fitting of a Gaussian function to the co-added λ8037 spectrum shown in Figure 5.15). The K I spectra can be seen in Figures 5.13 and 5.14.

The peak wavelength match is excellent, but the model CH_2CN^- spectrum clearly contains significant fine structure that is not present in any of the observed λ8037 profiles. The Q branch of the transition creates the strong peak at 8037.78 Å, with the P branch of rather low intensity compared to the R branch that provides a 'blue shoulder' of transitions. Evidence for a blue degradation of the λ8037 DIB can be seen in the spectra towards all three Cyg OB2 sightlines and towards HD 183143, HD 186745 and HD 229196. The band appears more symmetrical towards HD 168112 and HD 169034, and shows significant evidence for profile variability across all of the sightlines, especially in comparison of HD 186745 and HD 183143 with the Cyg OB2 sightlines. Suggestive of a Doppler origin for some of the profile variability is the fact that HD 169034 has the broadest λ8037 profile and the broadest, most complex K I velocity structure (see top right panel of Figure 5.14).

Examination of the unreddened λ Cyg spectrum (Figures 5.7 and 5.8) shows no evidence for significant stellar lines, fringing artifacts or telluric residuals across the wavelength region. Apparently all of the structure present in the reddened sightline spectra represents interstellar absorption. The most prominent features are the λ8026 DIB, which is among the narrowest diffuse bands known, and an absorption feature around 8037 Å, which is apparently a composite of overlapping features. The λ8037 DIB, as considered by this study, is relatively narrow (with a FWHM $\sim$ 1.3 – 2 Å) but is partially overlapped by a broader absorption centered at around 8040 Å (noted by Herbig & Leka 1991) that is most prominent towards HD 183143. This broad component has a FWHM of around 4 Å and forms an absorption peak at about 8040.7 ± 0.3

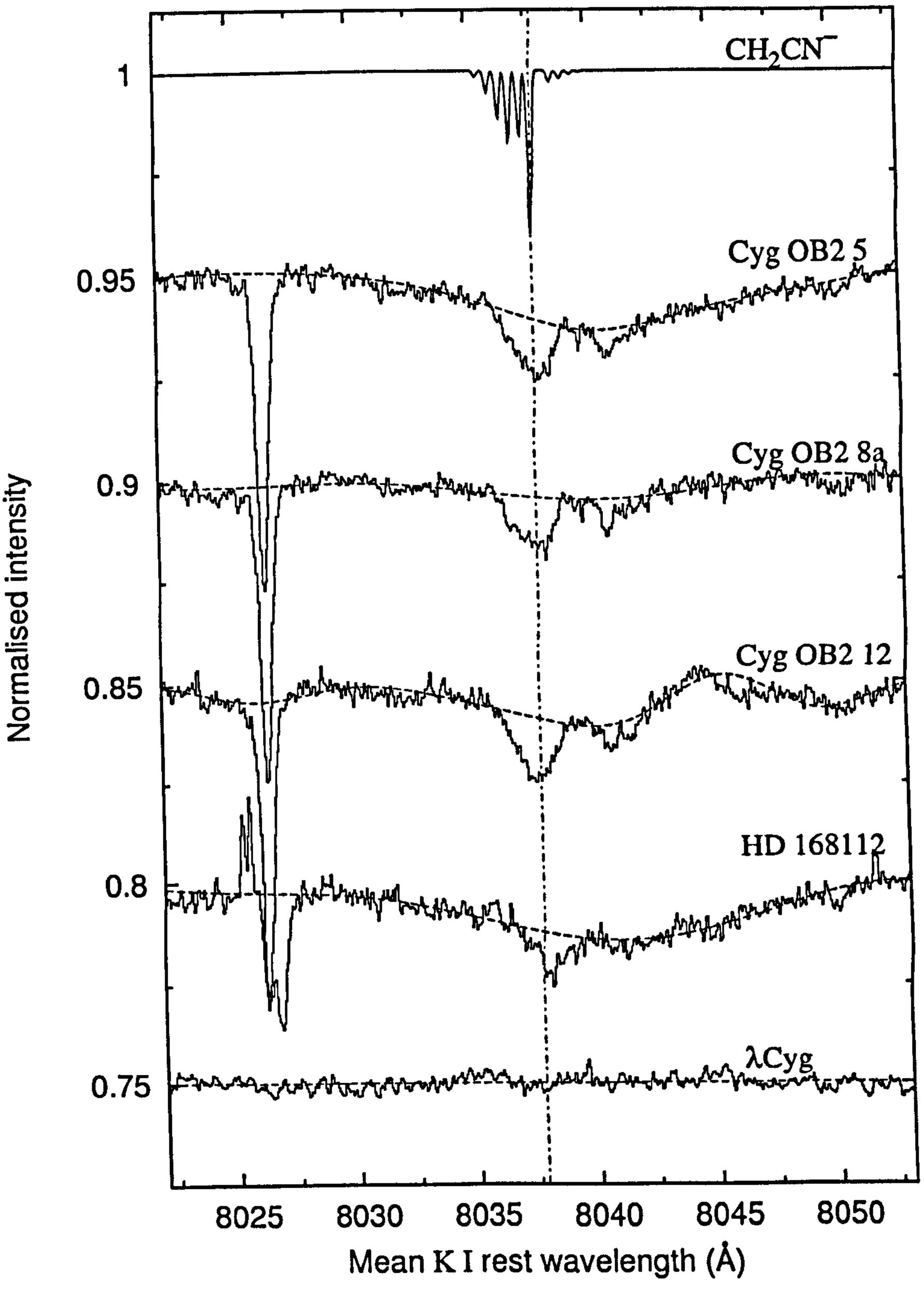

Figure 5.7: Normalised (second order Chebyshev polynomial), telluric-corrected Keck HIRES spectra of the region around λ8037 observed towards heavily-reddened stars. Dependent on the interstellar K I velocity structure, spectra have been Doppler shifted to place the peak or mean K I wavelength at rest (using $\lambda_{\mathrm{K\ I\ rest}} = 7698.9645$ Å (Morton 2003). λ Cyg is shown as an unreddened standard. Fitted 'continua' are shown as dotted lines. The CH_2CN^- $^1B_1$ DBS $\longleftarrow$ $^1A'$ GS origin band $K_a = 1 \longleftarrow 0$ modelled absorption spectrum is shown, calculated assuming a single cloud at rest ($v(CH_2CH^-) = v(\mathrm{K\ I}) = 0$ km s^{-1}) with Doppler $b = 1$ km s^{-1} and convolved to the resolving power $R = 42,500$ of the HIRES spectra.

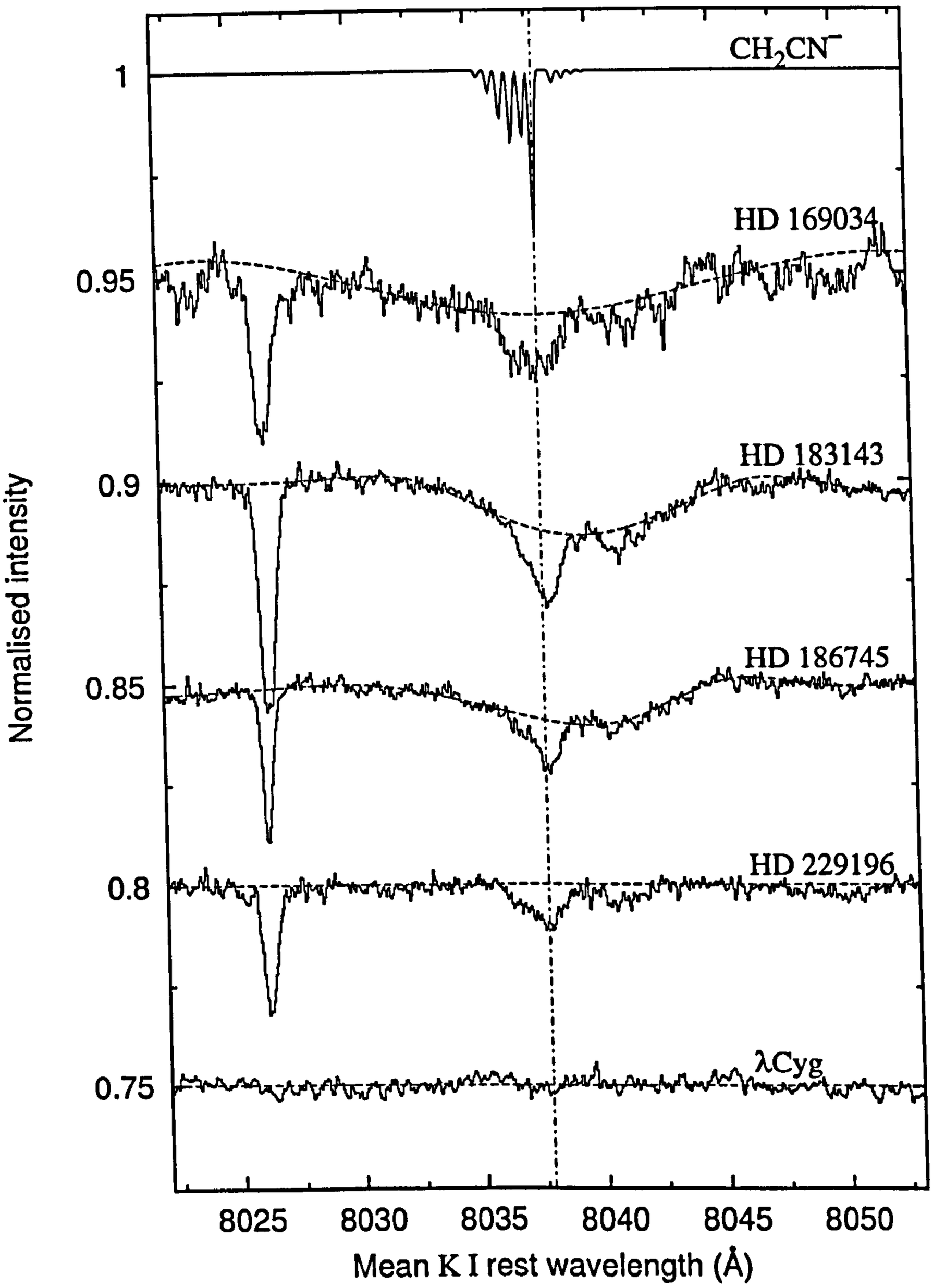

Figure 5.8: Normalised (second order Chebyshev polynomial), telluric-corrected Keck HIRES spectra of the region around λ8037 observed towards heavily-reddened stars. Dependent on the interstellar K I velocity structure, spectra have been Doppler shifted to place the peak or mean K I wavelength at rest (using $\lambda_{\mathrm{K\,I\ rest}} = 7698.9645$ Å (Morton 2003). λ Cyg is shown as an unreddened standard. Fitted 'continua' are shown as dotted lines. The CH_2CN^- $^1B_1$ DBS $\longleftarrow$ $^1A'$ GS origin band $K_a = 1 \longleftarrow 0$ modelled absorption spectrum is shown, calculated assuming a single cloud at rest ($v(CH_2CH^-) = v(\mathrm{K\,I}) = 0$ km s^{-1}) with Doppler $b = 1$ km s^{-1} and convolved to the resolving power $R = 42,500$ of the HIRES spectra.

Å. It is very weak towards Cyg OB2 8a and HD 229196.

The variability of the λ8040 DIB strength with respect to λ8037 suggests that it is probably caused by a different carrier. Towards Cyg OB2 5 and HD 168112, the λ8040 DIB has FWHM ~ 11.5 Å, which is much broader than in the other sightlines, perhaps indicating the presence of *another* broad DIB centered on this region. To isolate the narrow λ8037 DIB for analysis is non-trivial among these other contaminating DIBs. However, the narrowness of λ8037 assists its rejection in continuum fitting algorithms such that a consistently repeatable 'continuum' could be fit to all of the spectra, allowing the 'fitting out' of the broad λ8040 DIB(s), using the well-defined λ8037 profiles towards the Cyg OB 2 and HD 229196 sightlines as a guide for the wavelength extent of this narrow DIB.

5.4.3 Velocity structure of the interstellar gas towards HD 183143

The initial CH_2CN^- λ8037 model shown in Figures 5.7 and 5.8 does not adequately reproduce the shape of the λ8037 DIB in any of the sightlines observed. Given the apparent variability of the DIB profile, to obtain a better fit to the data, the most obvious model parameter to adjust is the velocity structure of the interstellar CH_2CN^-. According to the high resolution interstellar K I survey by Welty & Hobbs (2001) who measured a median reddening of $\approx$ 0.03 per interstellar cloud, one might reasonably expect to find of the order of 50 clouds in the sightlines towards such heavily-reddened stars as those in Table 5.1, with E_{B-V} ~ 1 to 3.

Although the Keck HIRES spectra contain the K I λ7699 line, the likely velocity distribution of interstellar CH_2CN^- is unknown. Towards heavily-reddened stars, the complexity of interstellar absorption lines is considerable and the velocity structure varies between different species (see for example McCall *et al.* (2002b) and the interstellar atomic data presented for LMC sightlines in Chapter 3). It is well known that different interstellar species reside preferentially in different interstellar clouds dependent on ionisation balance, depletion and other physical and chemical variables. For example, interstellar Ca II velocity profiles are typically broader and smoother than K I because Ca II is found in abundance in hotter, higher velocity, more energetic clouds where K I is relatively scarce. Given that interstellar CH_2CN^- has never been observed, to determine its possible velocity structure requires spectra of species that are expected

to co-exist with this molecular anion. However, the CH_2CN^- formation mechanism is also unknown, so one cannot say with certainty with which species the anion would be associated. H I is the most widely distributed interstellar gas, but its velocity structure is difficult to observe in Lyman α due to saturation of the absorption line, and it is difficult to be sure that the gas is not in the background when observing 21 cm emission spectra. Observation of other atomic and molecular species in UV-visible absorption should provide information on the different possibilities for the velocity distribution of the postulated interstellar CH_2CN^-.

During the LMC observing run using the VLT UVES instrument from September 25^{th} to 27^{th} 2001 (see Section 3.3), spectra of HD 183143 were recorded in the wavelength range from ~ 3000 Å to 10,000 Å. The data were reduced according to the methods explained in Chapter 2, producing spectra of the Ti II lines at 3242.0 and 3383.8 Å, the Na I UV doublet at 3302.4 and 3303.0 Å, the Ca II H and K lines, CN at 3874.6 Å, CH at 4300.3 Å, CH^+ at 3957.6 and 4232.5 Å, and Ca I at 4226.7 Å. The S/N per pixel of the co-added spectra was typically ~ 175 with a velocity resolution of $\simeq$ 3.5 km s^{-1}.

The velocity structure of the spectra was analysed in the LSR frame using VAPID (see Section 2.4.2). Ti II, Ca II, Ca I and Na I transition wavelength and oscillator strength data were taken from Morton (2003), CN and CH data from Crawford (1997) and CH^+ data from Centurion & Vladilo (1991). The models utilised the minimum number of cloud components required to obtain good fits to the spectra, and the results of the fitting process are shown graphically in Figure 5.9. Optimised model parameters are shown in Table 5.4. CH is not shown in the plot — its spectrum is very similar to that of Na I, K I and CH. The Na I, Ti II and CH^+ models were each optimised with respect to two different transitions to increase accuracy; for Ca II, only the stronger K line was fitted due to a broad stellar He II absorption overlapping the Ca II H line.

Consistent with the results published by Herbig & Soderblöm (1982), two dominant, narrow components of K I are present, separated by 15.0 km s^{-1} at v_{LSR} = 7.5 km s^{-1} and v_{LSR} = 22.5 km s^{-1}. The components are of comparable strength, though the redder of the two is slightly stronger. Na I has almost identical structure, but Ca II and Ti II are markedly different with much more complex cloud structure. The Ca II profile is consistent with that published by McCall *et al.* (2002b). Resolution of all the individual clouds could not be achieved at the $\simeq$ 3.5 km s^{-1} instrumental resolution, so many components have unfeasibly large Doppler widths. Nevertheless, the model profile fits

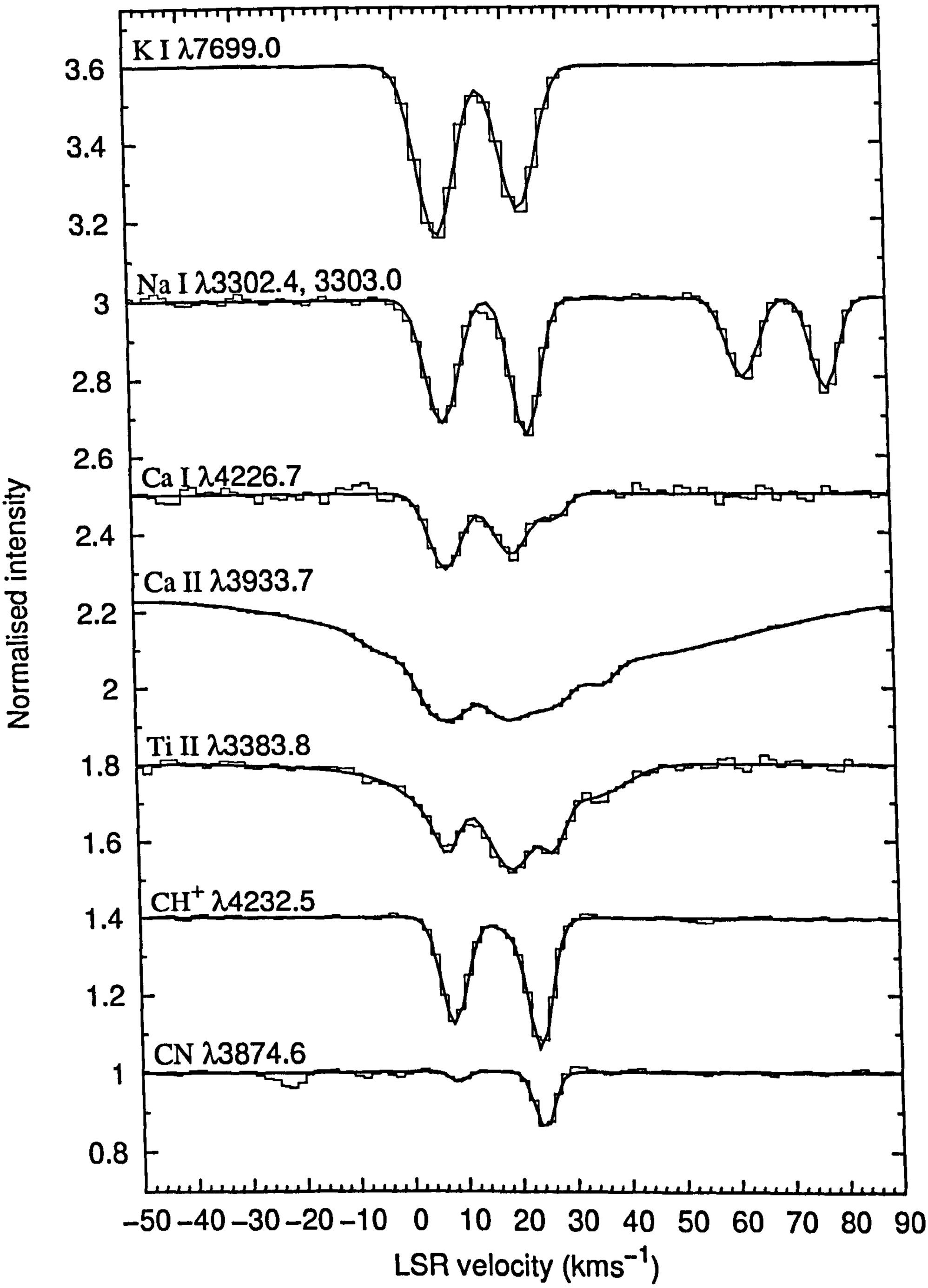

Figure 5.9: HD 183143 interstellar atomic and diatomic spectra (shown as histograms), plotted in LSR velocity space, telluric-corrected where necessary, normalised, and shifted vertically for display. VAPID least-squares cloud model fits overlaid as thicker traces. The Ca II spectrum is scaled by a factor of 1/3, Ca I spectrum scaled by a factor of 4, Na I spectrum scaled by a factor of 2, for clarity of display.

Ca II λ3934			Ti II λ3242, λ3384			K I λ7699			Na I λ3302, λ3303			Ca I λ4227			CN λ3875			CH λ4300			CH^+ λ3958, λ4233		
v_{LSR}	b	N	v_{LSR}	b	N	v_{LSR}	b	N	v_{LSR}	b	N	v_{LSR}	b	N	v_{LSR}	b	N	v_{LSR}	b	N	v_{LSR}	b	N
-4.1	4.6	11.35	6.8	3.1	11.51	7.5	2.6	11.90	7.9	3.2	13.93	8.0	3.6	10.27	8.4	0.8	11.44	7.9	4.1	13.31	7.6	2.6	13.50
7.4	4.4	12.58	12.4	20.1	12.07	22.5	2.4	11.79	23.3	2.5	13.95	20.1	4.3	10.23	24.2	1.3	12.30	23.5	2.9	13.51	23.5	2.0	13.51
18.6	3.8	12.44	19.2	4.5	11.79							28.4	1.9	9.57							20.4	5.0	12.94
23.5	18.6	11.49	26.8	2.3	11.43																		
24.4	37.1	12.83	34.9	7.0	11.39																		
26.3	4.8	12.23																					
36.2	2.4	11.52																					
59.5	29.9	11.93																					

Table 5.4: Results of least-squares VAPID analysis of HD 183143 interstellar atomic and diatomic spectra as derived from VLT UVES and Keck HIRES spectra. LSR velocity v_{LSR}, and Doppler b of cloud model components given in kms^{-1}. N given as $\log_{10}$(Column density / cm^{-2}). Wavelengths of the transitions used in the fits are shown to one decimal place; in the cases of Ti II, Na I and CH^+ two different transitions were fit simultaneously to improve accuracy of the cloud models. v_{LSR} is accurate to $\sim \pm 1$ kms^{-1} and N should be accurate to around ± 0.1 dex. Doppler b errors are ~ 0.5 km s^{-1}. Uniqueness of cloud model parameters is not certain.

give an accurate representation of the absorption spectra. The Ca II has several very broad components upon which are superimposed some narrower components of similar structure to those present in Ti II. The very broad structure is present in both the H and K lines and is perhaps indicative of circumstellar material, broadened by temperature, pressure and rotation effects. One might also expect these broad components to be present in the Ti II profile, but they may be too weak to show up clearly. Most of the Ca II is contained in the narrower components centered around $v_{LSR} \simeq 7.5$, 18.5 and 25 km s^{-1}, which is similar to the triple-cloud structure determined for the Ca I. The molecular material (CH, CH^+ and CN) appears to be confined to within the two 'trace neutral' clouds (with strong Na I and K I), indicating that these clouds are rather dense and well shielded from dissociating and ionising UV radiation. The broader distribution of Ca I, Ca II and Ti II is indicative of the Routly-Spitzer effect, suggesting that these (typically highly depleted) species have been liberated from dust grains into the gas phase following an energetic grain-shocking event that propelled the clouds to high velocities.

The K I, Ca II and Ti II VAPID cloud models shown in Table 5.4 were employed in the CH_2CN^- λ8037 DIB model as 'postulated interstellar CH_2CN^- distributions'. The oscillator strength of the $^1B_1$ DBS $\longleftarrow$ $^1A'$ GS transition is not known, so a multiplicative intensity-scaling of the model spectrum (in optical depth space) was carried out in order to achieve the best match with the DIB spectrum. The multiplicative factor was determined by searching for the factor that produced the minimum RMS difference between the model and the spectrum. An additive continuum height offset was also incorporated in the fitting to allow for possible errors in the continuum definition. The continuum of the HD 183143 λ8037 DIB spectrum was defined as in Figure 5.8. Results are shown in Figures 5.10, 5.11 and 5.12.

Assuming the interstellar CH_2CN^- distribution to be the same as the K I (and by their profile similarities, Na I, CH and CH^+), produces the model DIB profile shown in Figure 5.10. The relative strengths of the absorption peaks results in a good match on the blue side of the DIB, but the lack of any comparable structure in the observed DIB profile, combined with the poorness of fit on the red side leads to the conclusion that if CH_2CN^- is preferentially located in the same clouds as K I, then the origin band $^1B_1$ DBS $\longleftarrow$ $^1A'$ GS, $K_a = 1 \longleftarrow 0$ transitions at 2.74 K cannot be responsible for the λ8037 DIB.

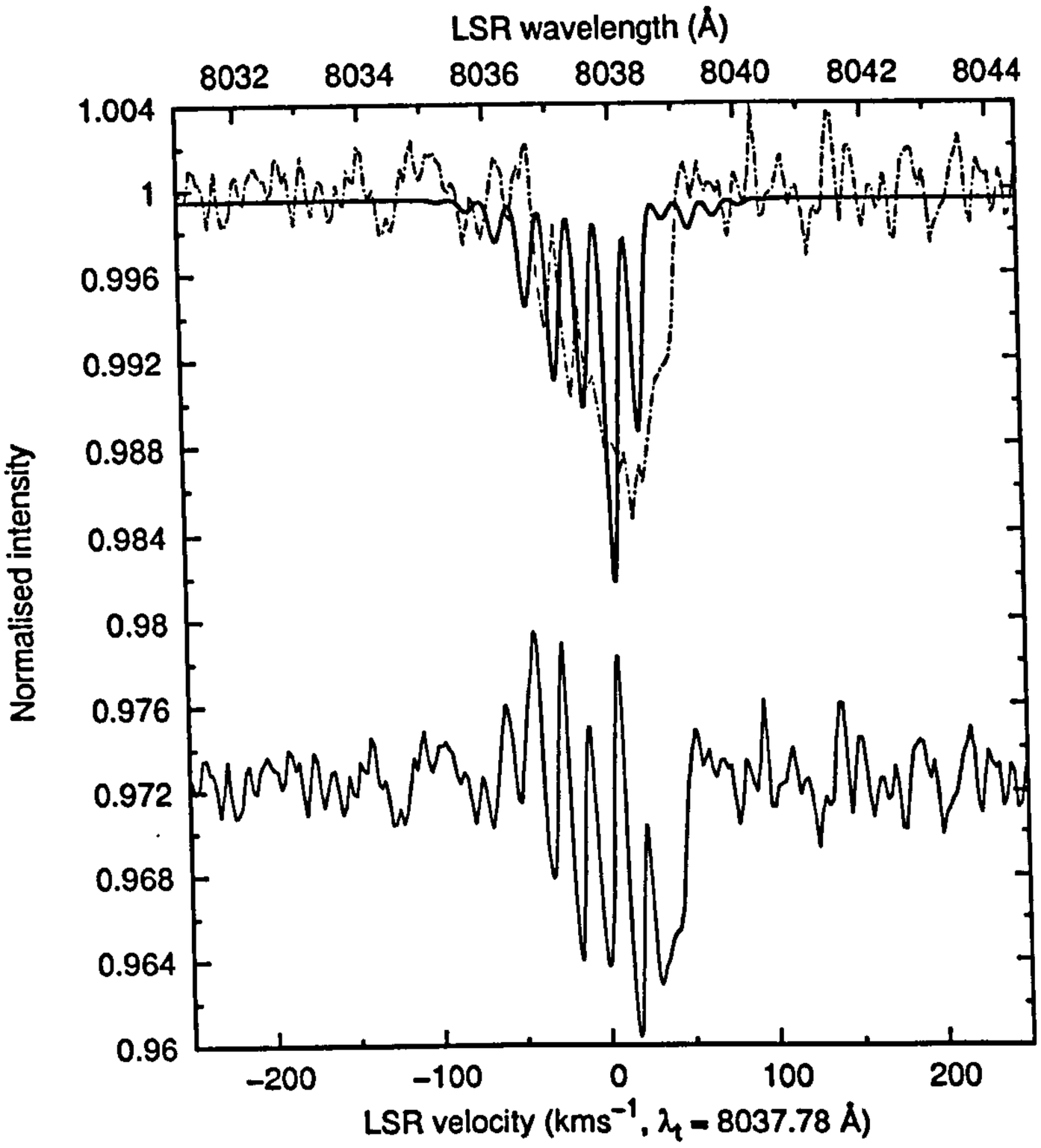

Figure 5.10: The dot-dashed trace is the telluric-corrected, normalised λ8037 diffuse band spectrum observed towards HD 183143. The thick trace is the CH_2CN^- DIB model: origin band $^1B_1$ DBS $\longleftarrow$ $^1A'$ GS, $K_a = 1 \longleftarrow 0$ transitions at 2.74 K convolved with the HD 183143 VAPID least-squares interstellar K I cloud model (see Figure 5.9 and Table 5.4). Lower trace gives residuals of DIB spectrum minus model spectrum. The velocity scale of the figure is set arbitrarily with $v_{LSR} \simeq 0$ km s^{-1} at the peak of the model profile shown in Figures 5.7 and 5.7, with $\lambda_t = 8037.78$ Å.

Examining the DIB model under the assumption that the CH_2CN^- is associated with Ca II however (Figure 5.11), shows that the origin band $^1B_1$ DBS $\longleftarrow$ $^1A'$ GS, $K_a = 1 \longleftarrow 0$ transition is capable of reproducing the λ8037 profile towards HD 183143 to within a remarkable degree of similarity. Fine structure is apparent in the model DIB profile that could feasibly be masked by the spectral noise, and the blue sides match very closely. The greatest discrepancy lies on the red side where the model degrades too slowly towards the red compared to the observed DIB profile.

If the postulated CH_2CN^- distribution is taken to be the same as that of Ti II, the match between the model and the observed DIB spectrum is exceptionally good (Figure 5.12). From the residuals, the model DIB clearly represents a good fit across the

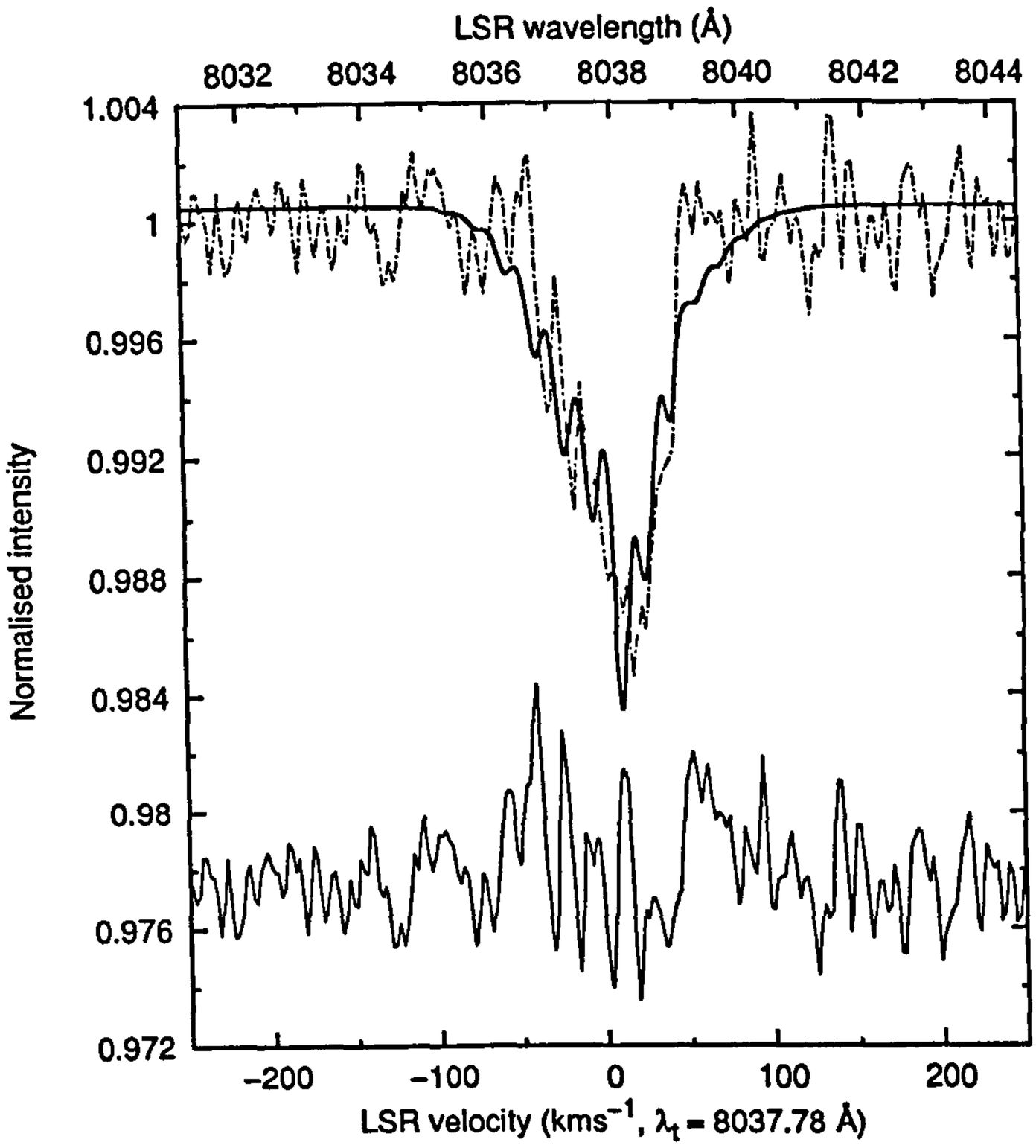

Figure 5.11: The dot-dashed trace is the telluric-corrected, normalised λ8037 diffuse band spectrum observed towards HD 183143. The thick trace is the CH_2CN^- DIB model: origin band $^1B_1$ DBS ⟵ $^1A'$ GS, K_a = 1 ⟵ 0 transitions at 2.74 K convolved with the HD 183143 VAPID least-squares interstellar Ca II cloud model (see Figure 5.9 and Table 5.4). Lower trace gives residuals of DIB spectrum minus model spectrum.The velocity scale of the figure is set arbitrarily with $v_{LSR} \simeq 0$ km s^{-1} at the peak of the model profile shown in Figures 5.7 and 5.7, with λ_t = 8037.78 Å.

whole absorption profile.

Within the S/N constraints, the model fit in Figure 5.12 represents almost the best match possible between a diffuse interstellar band and a proposed carrier. The quality of fit implies that the origin band CH_2CN^- $^1B_1$ DBS ⟵ $^1A'$ GS, K_a = 1 ⟵ 0 transition at 2.74 K is capable of reproducing the narrow λ8037 DIB towards HD 183143 provided that the postulated CH_2CN^- carrier molecule is distributed in velocity space in approximately the same way as the interstellar Ti II.

Several caveats apply to this comparison; the unknown transition strength necessitates the use of an arbitrary intensity scaling factor in the model to achieve the intensity match between the observed and model DIB. Clearly, the interstellar CH_2CN^- abun-

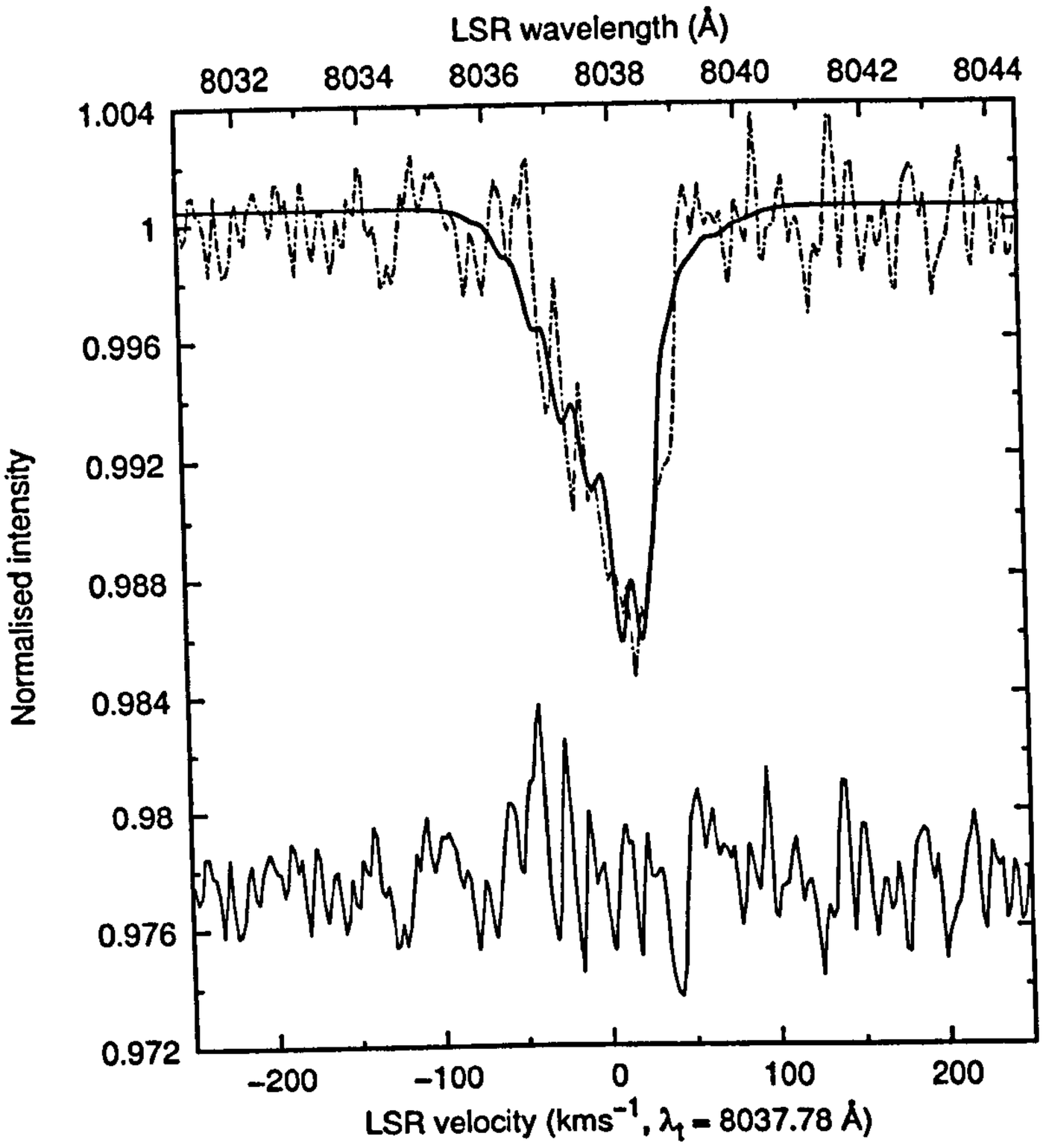

Figure 5.12: The dot-dashed trace is the telluric-corrected, normalised λ8037 diffuse band spectrum observed towards HD 183143. The thick trace is the CH_2CN^- DIB model: origin band $^1B_1$ DBS $\longleftarrow$ $^1A'$ GS, $K_a = 1 \longleftarrow 0$ transitions at 2.74 K convolved with the HD 183143 VAPID least-squares interstellar Ti II cloud model (see Figure 5.9 and Table 5.4). Lower trace gives residuals of DIB spectrum minus model spectrum.The velocity scale of the figure is set arbitrarily with $v_{LSR} \simeq 0$ km s^{-1} at the peak of the model profile shown in Figures 5.7 and 5.7, with $\lambda_t = 8037.78$ Å.

dance would be expected to be low based on the measured abundances of molecules with three or more atoms in the diffuse ISM, necessitating a very high oscillator strength for the transition (see discussion in Section 5.5). Also, the narrow DIB is overlapped by at least one broader feature such that the continuum definition is subject to a degree of ambiguity. In addition, towards HD 183143, the λ8037 has a rather smooth absorption intensity drop-off on the blue side which, during continuum-fitting, was assumed to be caused by the broader λ8040 absorption feature (see Figure 5.8). If this is not the case, then the quality of fit with the 'Ti II-convolved' model may be significantly lower. Overall however, the fits in Figures 5.11 and 5.12 are certainly intriguing, and provide motivation to examine the spectroscopy of CH_2CN^- further and to consider

the different possibilities for its interstellar velocity distribution.

5.4.4 Interstellar CH_2CN^- velocity structure

The near-perfect reproduction of the λ8037 profile towards HD 183143 may be coincidental. It is clear that basing the CH_2CN^- distribution on the K I velocity profile cannot reproduce the DIB profile adequately. Unfortunately, digital Ti II and Ca II spectra were not immediately available for the other sightlines studied, so the hypothesis that CH_2CN^- with a similar interstellar distribution as Ti II and Ca II causes the λ8037 DIB is difficult to assess. Nevertheless, using the observed λ8037 DIB profiles (in Figures 5.7 and 5.8), it is possible to work backwards and determine the shape of the interstellar CH_2CN^- velocity distribution required to produce the observed absorption features, based on the assumption that the narrow λ8037 DIB is caused by the origin band $^1B_1$ DBS $\longleftarrow$ $^1A'$ GS, $K_a = 1 \longleftarrow 0$ transitions of CH_2CN^- at 2.74 K.

A **C** algorithm was written to carry out the vacuum-air wavelength conversion, natural line broadening and instrumental resolution convolution of the DBS $\longleftarrow$ GS transitions, outlined in Section 5.4.2. The computed absorption spectrum was fed into a least-squares analysis routine whereby it was subjected to convolution with a single Gaussian interstellar cloud model. The Doppler b, mean radial velocity (v_{LSR}) and equivalent width of the final model DIB ($W_{CH_2CN^-}$) were floated as free parameters. A fourth free parameter was included as an additive constant to vertically shift the continuum between 0.998 and 1.002 if necessary. In the algorithm, b was taken to lie between 10 and 50 km s^{-1}, v between -50 and 50 km s^{-1}, and $W_{CH_2CN^-}$ between 15 and 50 mÅ. The entire parameter space was explored, comparing the sum of squares of the differences between the model and observed DIB spectrum (χ^2) for every combination of parameters. Care was taken to ensure that the parameter space was large enough to contain the global χ^2 minimum for each fit. The least-squares parameters for each sightline were recorded, shown in Table 5.5, and the corresponding CH_2CN^- velocity distribution and DIB model spectrum were output for display. The quality of the fits was monitored by comparing the normalised continuum RMS of the observed spectra (σ_c) with the normalised RMS of the model fit residuals σ_f (where $\sigma_f = \sqrt{\chi^2}/N_p$, and N_p is the number of spectral data points used for the calculation of χ^2). Comparing the fit and continuum RMS's, $\sigma_c \approx \sigma_f$ was found for each sightline, indicating that the fits

Sightline	v_{LSR}	b	$W_{CH_2CN^-}$	σ_c	σ_f
Cyg OB2 5	13.9	21.6	32.5	0.0020	0.0014
Cyg OB2 8a	12.3	21.0	30.2	0.0024	0.0016
Cyg OB2 12	9.4	24.0	38.3	0.0024	0.0013
HD 168112	29.9	26.4	24.5	0.0018	0.0021
HD 169034	13.6	33.0	38.7	0.0036	0.0024
HD 183143	25.0	18.0	37.5	0.0022	0.0012
HD 186745	19.3	16.2	24.3	0.0014	0.0013
HD 229196	14.1	21.6	22.0	0.0020	0.0012

Table 5.5: Least-squares fit parameters of the λ8037 CH_2CN^- models for each sightline. The mean LSR velocity (v_{LSR} / km s^{-1}), Doppler cloud width (b / km s^{-1}) and equivalent width of the model λ8037 DIB ($W_{CH_2CN^-}$ / mÅ) are given along with the normalised continuum RMS of the observed spectra (σ_c), and the RMS of the model fit residuals (σ_f).

were statistically good.

The least-squares λ8037 model fits are shown in Figure 5.13 and Figure 5.14. The postulated interstellar CH_2CN^- LSR velocity distributions are plotted in the right-hand panes above the telluric-corrected LSR K I spectra for each sightline. For HD 183143, the VLT UVES Ti II and Ca II profiles are shown, and for HD 186745 the Ca II spectrum published Galazutdinov *et al.* (2000a) (used with permission) has been digitally reproduced, scaled and shifted to the LSR wavelength scale of the figure.

The model fits match the spectra to an exceptional degree of accuracy for each of the eight sightlines. Variations in the width and structure of the DIB profile are reproduced in each case, highlighted by the progression of the λ8037 FWHM from narrow to wide in the sequence HD 186745 → HD 183143 → Cyg OB2 12 → HD 169034. The progression corresponds to a sequential increase in the Doppler b of the cloud model: 16.2 km s^{-1} → 18.0 km s^{-1} → 24.0 km s^{-1} → 33.0 km s^{-1}. Such large b values would require unphysically large kinetic and/or turbulent gas velocities and clearly cannot arise in a single cloud; typically diffuse clouds have $b \lesssim 1$ km s^{-1} (Welty & Hobbs 2001; Welty *et al.* 2003), which places doubt on the validity of the single-cloud model used here. Given the S/N of the spectra, there is no statistical justification for employing more than one cloud in the model, and introducing more degrees of freedom would result in the noise being fitted. Also, the Gaussian cloud model fits the DIB well (as shown by $\sigma_c \approx \sigma_f$), implying that if CH_2CN^- is the λ8037 carrier, its interstellar velocity distribution must be approximately Gaussian.

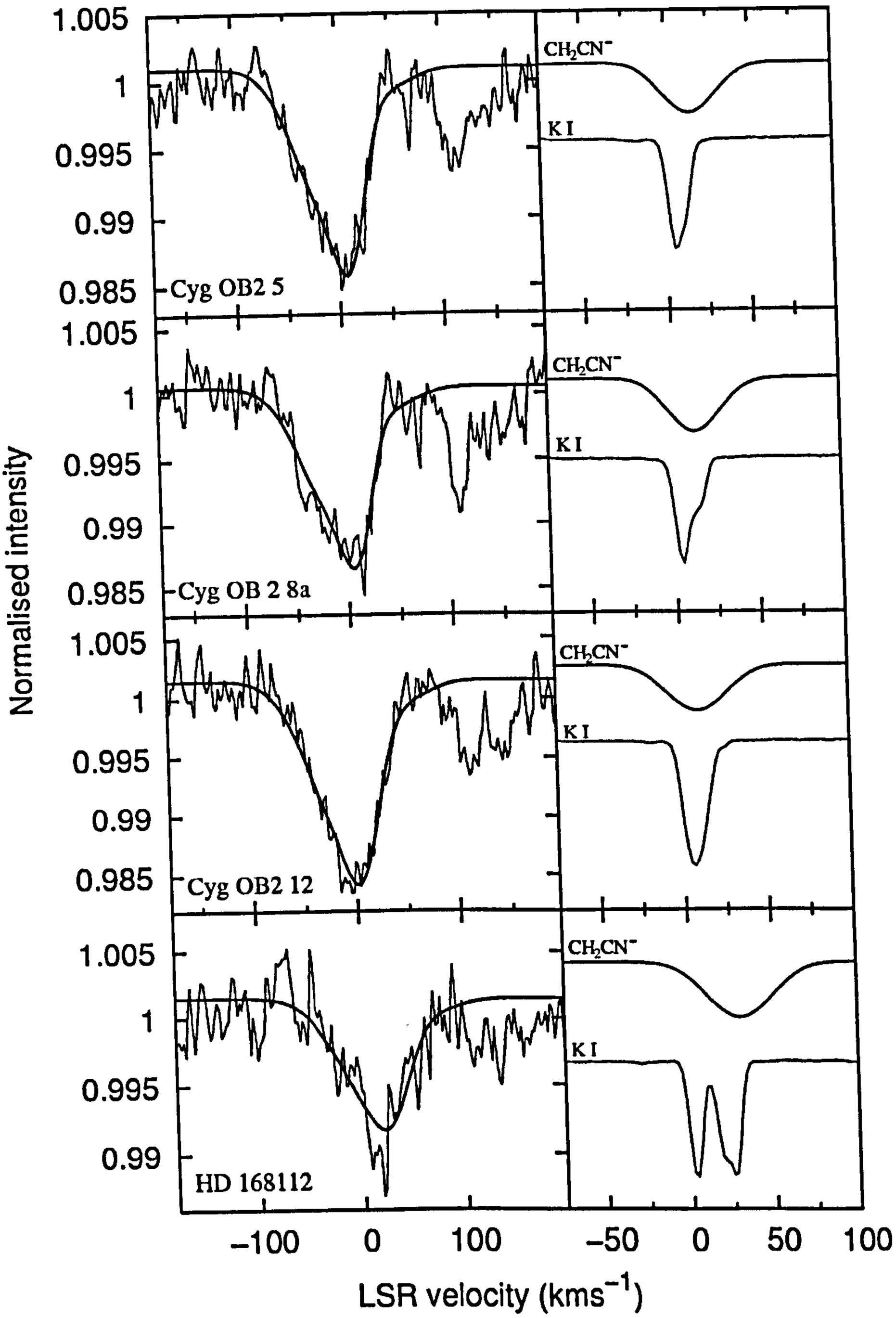

Figure 5.13: Telluric-corrected, normalised DIB λ8037 spectra (thin traces) and least-squares fitted CH_2CN^- $^1B_1$ DBS $\longleftarrow$ $^1A'$ GS, $K_a = 1 \longleftarrow 0$ models (thick traces). Models employed a single cloud. Radial velocity shift, Doppler width, central depth and continuum height were free parameters in the fits. The corresponding postulated CH_2CN^- gas velocity distributions are shown in the right-hand panels compared with the interstellar K I λ7699 distributions (on an arbitrary intensity scale). The DIB rest wavelength was set at $\lambda_{CH_2CH^-} = 8037.78$ Å for λ8037's display LSR velocity scale.

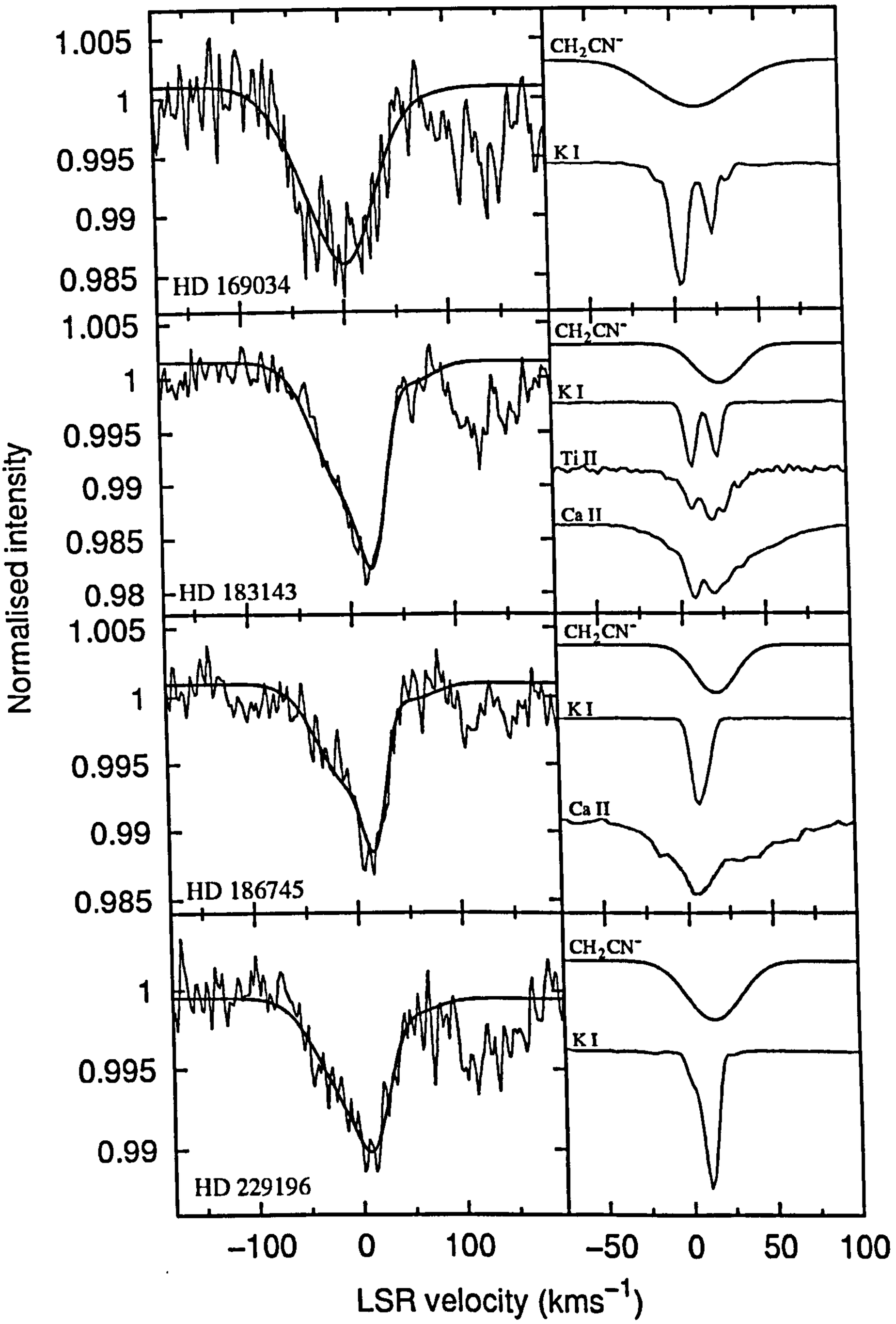

Figure 5.14: See caption for Figure 5.13. For HD 183143 the UVES Ti II λ3384 and Ca II H velocity distributions are shown in addition to the K I λ7699 line. For HD 186745 the Ca II K profile published by Galazutdinov *et al.* (2000a) has been digitally reproduced (with permission) on the same velocity scale as the interstellar K I and postulated CH_2CN^- gas distributions.

The HD 183143 least-squares model CH_2CN^- distribution in Figure 5.14 shows gross similarities with the Ti II and Ca II in profiles, and even though the profiles of these atomic ions are non-Gaussian due to the presence of narrow cloud components, their overall profiles could be modelled as Gaussians to a first approximation. From Table 5.5, $\sigma_c > \sigma_f$ for HD 183143 shows that the CH_2CN^- cloud model fits the observed DIB slightly too well, such that deviations of the model cloud shape from Gaussian would likely have the effect of statistically improving the fit.

Comparing the postulated CH_2CN^- velocity structures with the observed K I lines shown in the right-hand panes of Figures 5.13 and 5.14 shows that, in every sightline, the velocities of the modelled CH_2CN^- distributions closely match those of interstellar clouds traced by K I. The K I profiles are, however, significantly narrower in every case. The Ti II and Ca II profiles are generally unknown, but from the study of interstellar gas towards HD 183143 (Section 5.4.3), it is probable that these refractory species have markedly different distributions to K I — predominantly due to their variable depletions and ionisation potentials.

Comparison of the HD 186745 K I and Ca II gives further evidence for remarkable differences between the distribution of these species in heavily-reddened sightlines. Although the peak CH_2CN^- model distribution fails to match the K I peak velocity, it lies entirely within the extent of the Ca II profile. From inspection of the figure, the centre of mass of the Ca II velocity distribution lies near the peak of the postulated interstellar CH_2CN^- distribution.

For the Cyg OB2 sightlines and for HD 229196, although the CH_2CN^- models are significantly broader than the interstellar K I profiles, their peak velocities match closely. For HD 169034, the CH_2CN^- model is very broad, but overlaps the complex K I profile such that most of the postulated CH_2CN^- lies within the velocity range spanned by the multiple K I clouds.

It is interesting to note that the least-squares mean LSR velocity (v_{LSR}) of the postulated CH_2CN^- is positive for every sightline, which is also true for the interstellar K I (see Figures 5.13 and 5.14). The sightlines studied all lie close to the Galactic plane between 0 and 90 degrees Galactic longitude at distances $\gtrsim$ 1 kpc. The bias of the mean LSR velocities of the interstellar gas towards the red could be explained as a consequence of Galactic rotation: The sightlines towards these stars lie at an acute angle relative to the (away-pointing) Galactic rotational velocity vectors, introducing

a positive velocity spread in the gas along the sightlines.

Other interstellar species must be observed at high resolution to assess the plausibility of the postulated CH_2CN^- distributions. However, the presence of interstellar gas over the full velocity ranges of the model CH_2CN^- distributions has been confirmed for the sightlines towards HD 183143 (in Ti II and Ca II) and HD 186745 (in Ca II). To determine whether this is true for the other sightlines will require further literature study and new observations. The HD 183143 and HD 186745 results raise the important question of whether the CH_2CN^- molecule can be formed and maintained in detectable abundances in the interstellar medium traced by Ca II and Ti II.

5.4.5 'Ortho' CH_2CN^- transitions

The λ8037 DIB modelling has so far focussed only on the narrow interstellar absorption feature at 8037.8 Å and the $K_a = 1 \longleftarrow 0$ rotational sub-band of the CH_2CN^- $^1B_1$ DBS $\longleftarrow$ $^1A'$ GS origin band transition. A 'hot band', corresponding to a transition originating from a level with one quantum of vibrational excitation (424.770 cm^{-1} above the origin band; see Lykke *et al.* (1987)) will not be significantly populated at the kinetic temperature (~ 100 K) of the diffuse ISM.

As explained in Section 5.4.1, CH_2CN^- is expected to exist in the ISM in 'para' and 'ortho' forms, with lowest occupied rotational levels of $\{J'' = 0,\ K_a'' = 0\}$ and $\{J'' = 1,\ K_a'' = 1\}$ respectively. The $K_a = 1 \longleftarrow 0$ transitions occur around 8037.7 Å, whereas the $K_a = 0 \longleftarrow 1$ and the $K_a = 2 \longleftarrow 1$ transitions occur at peak absorption wavelengths of 8049.6 and 8024.8 Å. Discussed in Section 5.3.2, the population of the different K_a levels in similar molecules depends on the chemistry that forms and modifies them in the ISM. Based on the nuclear spin statistics of CH_2CN^-, assuming that the molecule occurs in the ISM with the equilibrium $o : p$ ratio of 3 : 1, the ortho transitions would be expected to be three times stronger than the para. However, as is observed for other similar molecules, it is plausible that the K_a level populations exhibit a purely thermal Boltzmann population distribution, irrespective of the nuclear spin statistics.

A co-added λ8037 spectrum is plotted in Figure 5.15 with the 'para'+'ortho' CH_2CN^- $^1B_1$ DBS $\longleftarrow$ $^1A'$ GS transitions, convolved with a rest cloud model ($v_{LSR} = 0$ km s^{-1}) with Doppler $b = 18$ km s^{-1} and an arbitrary intensity scaling. The two extreme cases

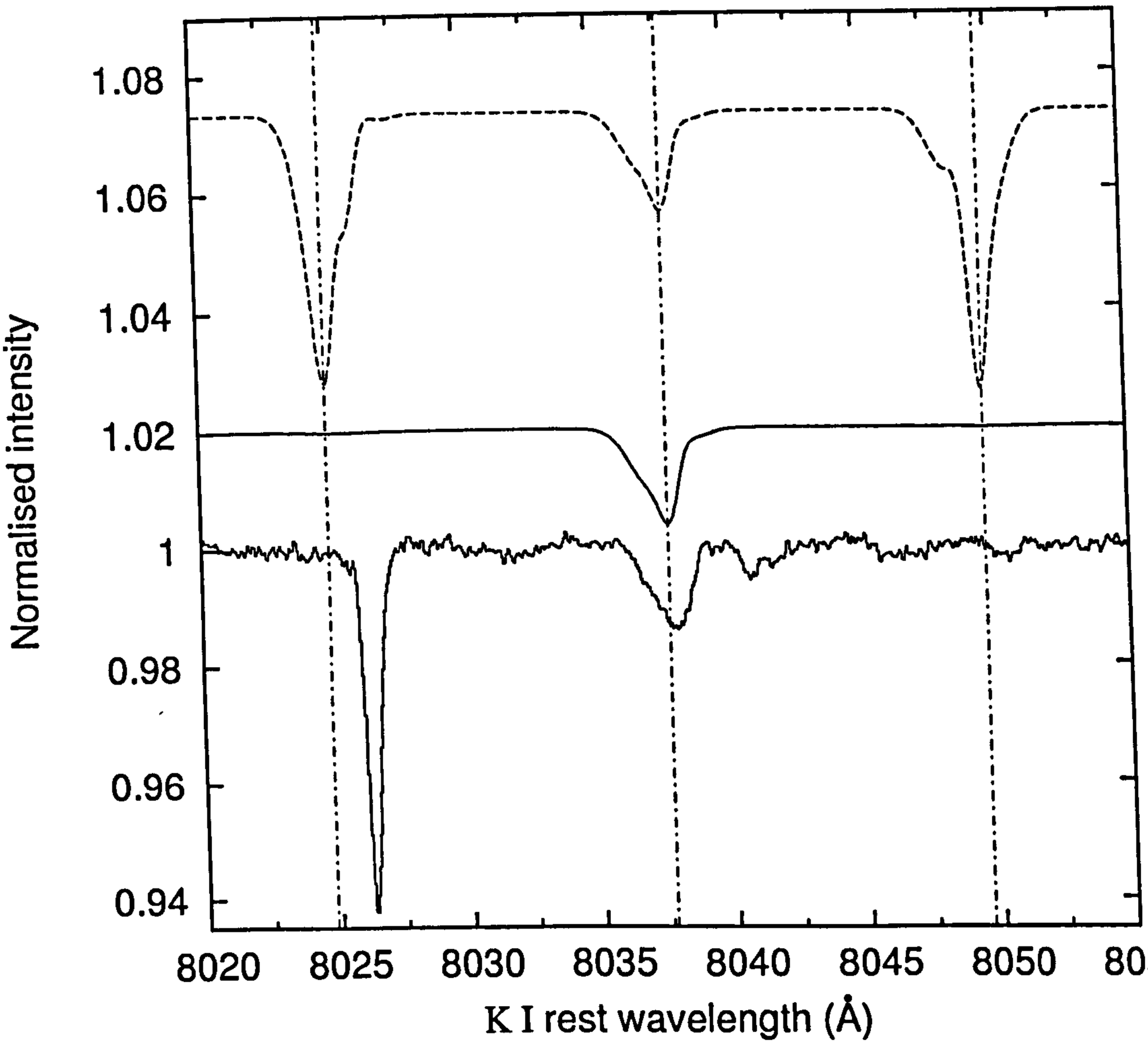

Figure 5.15: The lower trace shows the *co-added*, normalised (see Figures 5.7 and 5.8), telluric-corrected Keck HIRES spectrum of the region around λ8037 observed towards the heavily-reddened stars in Table 5.1. Dependent on the interstellar K I velocity structure, spectra were Doppler shifted to place the peak or mean K I wavelength at rest (using $\lambda_{\text{K I rest}} = 7698.9645$ Å (Morton 2003) before co-addition. The $^1B_1$ DBS $\longleftarrow$ $^1A'$ GS, $\{K_a = 2 \longleftarrow 1, K_a = 1 \longleftarrow 0, K_a = 0 \longleftarrow 1\}$ modelled absorption spectrum is shown, and includes the sub-bands arising from para *and* ortho CH_2CN^-. The middle spectrum (solid line) was calculated assuming a (thermal) Boltzmann distribution of K_a level populations. The upper spectrum (dotted line) shows the calculation for a 3 : 1 'equilibrium' nuclear spin-statistical ortho : para ratio of odd : even K_a'' levels. The interstellar CH_2CN^- model utilised a single cloud at rest ($v = 0$ km s^{-1}) with Doppler $b = 18$ km s^{-1} convolved to the resolving power $R = 42,500$ of the HIRES spectra. The respective peak absorption wavelengths of the three Doppler-broadened K_a sub-bands are 8024.8, 8037.7, and 8049.6 Å, shown as dot-dashed lines, corresponding to 'ortho', 'para' and 'ortho' CH_2CN^- respectively.

of K_a population are plotted: (1) a 3 : 1 population ratio of odd : even K_a'' levels and (2) a 2.74 K Boltzmann distribution of K_a'' levels.

The $K_a = 2 \longleftarrow 1$ transitions (with peak absorption at ~ 8024.8 Å) partially overlap the narrow λ8026 DIB. There is some evidence for a small blue shoulder on this DIB, at a wavelength slightly red of the peak $K_a = 2 \longleftarrow 1$ absorption wavelength. The $K_a = 0 \longleftarrow 1$ feature (with peak absorption at ~ 8049.6 Å) coincides with a small absorption feature in the co-added spectrum, again slightly red of the expected wavelength. In the co-added spectrum, the central depth of the λ8037 feature is $1.35 \pm 0.16\%$ and the central depth of the λ8049 feature is $0.3 \pm 0.16\%$. The 2σ error estimates were derived from the RMS of the continuum. The ratio of central the depth of the λ8037 to λ8049 features is consistent with a ~ 4.5 : 1 ratio of the relative $K_a = 1 \longleftarrow 0$ (para) and $K_a = 0 \longleftarrow 1$ (ortho) transition strengths.

From Figure 5.15, it is clear that if interstellar CH_2CN^- has a 3 : 1 'equilibrium' ratio of $o : p$ states, it cannot be the carrier of the λ8037 DIB due to the lack of the ortho transitions at the expected strengths in the observed spectra. The λ8026 DIB is too red relative to the Q branch (main peak) of the $K_a = 2 \longleftarrow 1$ transition to constitute a spectroscopic match with the model calculation. If however the K_a level populations have, or approach, a Boltzmann distribution, then the transitions originating in $K_a = 1$ are sufficiently weak for CH_2CN^- to be a plausible carrier for the λ8037 diffuse interstellar band.

The lack of evidence for the existence of the $K_a'' = 1$ sub-bands suggests that if CH_2CN^- is the carrier of λ8037, then mechanisms must exist to allow thermalisation of the K_a'' levels, with a corresponding skewing of the $o : p$ ratio towards para as the dominant form (*i.e.* $o : p = 3 : 1 \longrightarrow 1 : \sim 4.5$). Higher S/N ($\gtrsim$ 2000) spectra of this region must be obtained to further analyse the presence or absence of the 'ortho' sub-bands. Confirming their presence would add significant weight to the proposal that the CH_2CN^- is the carrier of the λ8037 diffuse interstellar band. Measurement of their strengths to derive an ortho : para ratio would provide insight into the possible CH_2CN^- formation mechanisms.

5.5 Discussion

To fit the observed λ8037 diffuse interstellar band profiles with the $^1B_1$ DBS $\longleftarrow$ $^1A'$ GS, $K_a = 1 \longleftarrow 0$ transitions of CH_2CN^- requires a shifting and broadening of the intrinsic absorption spectrum. The amount of broadening exceeds the K I Doppler width in every instance, though the required wavelength shift closely matches the peak or mean K I wavelength in most cases.

This study considers the most likely broadening mechanism to be due to the velocity distribution of the interstellar CH_2CN^-. Other broadening mechanisms may, in principle operate, such as lifetime broadening (see for example Snow (2002) for the case of the λ4430 DIB) for very short-lived upper states. Dipole-bound state transitions probably have moderately long lifetimes such that this type of broadening is expected to be negligible. Future studies may consider other possible broadening mechanisms.

Under the assumption that the CH_2CN^- distribution is the same as that of Ti II — with the inference that CH_2CN^- co-exists with gas-phase Ti II — the model fit to the observed λ8037 spectrum towards HD 183143 is excellent. This result leads to two possibilities for the type of gas with which the postulated CH_2CN^- might be most closely associated: (1) The warm, shocked 'intercloud' medium; for the ~ 50 interstellar clouds expected to be present in the heavily-reddened sightlines studied in this chapter, the warm, low density, shocked clouds with low depletions should dominate the Ti II profiles (*e.g.* Crinklaw *et al.* 1994). (2) H I regions; neglecting variations in depletion, the ionisation potential of TiII in its ground state (~ 13.6 eV) makes it an excellent tracer of neutral hydrogen gas (Stokes 1978). In Chapter 3, Section 3.5.1, reasonable agreement between the Ti II and H I 21 cm profiles was observed for every LMC sightline studied. Without knowledge of the H I velocity profiles, the possibility that the postulated CH_2CN^- co-exists with neutral hydrogen gas cannot be ruled out.

By volume, neutral hydrogen constitutes the main component of the ISM. All of the galactic H I is in regions dominated by FUV (6 eV $\lesssim h\nu \lesssim$ 13.6 eV) photons (Tielens 1995). The general association of dust grains with H I gas (as is implied by the good correlation of N(H I) with E_{B-V} found by Bohlin *et al.* (1978)) indicates that if CH_2CN^- production is heavily dependent on a dust-grain assisted chemistry, then the interstellar CH_2CN^- and H I profiles would be expected to be very similar, accompanied by a correlation between $N(CH_2CN^-)$ and N(H I). Diffuse cloud CH_2CN^-

chemistry must be studied further to ascertain the plausibility of such a link. It is an intreaguing possibility that CH_2CN^- might arise as a result of dust grain-dependent chemistry.

The absence of neutral potassium across most of the velocity range of the postulated CH_2CN^- profiles indicates that the gas is of low density, consistent with the observations of atomic species towards HD 183143 and HD 186745. K I/Ca II ratios are zero across most of the CH_2CN^- velocity range, suggesting that the postulated CH_2CN^- resides predominantly in the warm ($T \sim 8000$ K; Tielens (1995)), shocked intercloud medium with $n_{\rm H} \sim 0.1 - 1$ cm^{-3} (Spitzer 1985) and $n_e \sim 0.001 - 0.1$ cm^{-3} (Stokes 1978). As is typical of molecular material in diffuse sightlines (see for example McCall *et al.* 2002b), the CN, CH and CH^+ towards HD 183143 are concentrated in velocity space within a few narrow, isolated clouds, suggesting that the postulated CH_2CN^- does not preferentially reside within the cold diffuse/translucent molecular material (with $n \gtrsim 100$ cm^{-3}) along this sightline.

It is difficult to envisage how appreciable abundances of a small polyatomic anion could arise in the broadly distributed, warm, low density intercloud gas. The neutral radical CH_2CN has been observed in the dense TMC-1 and Sgr B2 molecular clouds (see Irvine *et al.* 1988; Turner *et al.* 1990) by its pure rotational transitions. Fractional abundances are $\sim 5 \times 10^{-9}$ to 5×10^{-11} relative to H_2, and CH_2CN was found by Irvine *et al.* (1988) to be similarly distributed to the species' CH_3CN and C_4H. In TMC-1 ($T \sim 15$ K, $n \sim 5 \times 10^4$ cm^{-3}), CH_2CN was found to be similarly distributed to CH_3CN by Turner *et al.* (1990), who found a CH_2CN/CH_3CN ratio of about 10, whereas in the SGR B2 molecular core ($T \sim 90$ K, $n \sim 10^6$ cm^{-3}) the ratio was around 0.05. Towards SGR B2(N), the survey by Nummelin *et al.* (2000) revealed (relative to H_2), fractional abundances for many organic molecules including: $N(CH_2CN) = 3 \times 10^{-11} n_{H_2}$, $N(CH_2CO) = 2 \times 10^{-10} n_{H_2}$, $N(CO) = 4 \times 10^{-8} n_{H_2}$, $N(H^{13}CO^+) = 4 \times 10^{-12} n_{H_2}$ (which corresponds to $N(HCO^+) = 2.4 \times 10^{-10} n_{H_2}$ assuming an $H^{12}CO^+/H^{13}CO^+$ ratio of 60 after Lucas & Liszt (1998)), and $N(C_2H) = 2 \times 10^{-10} n_{H_2}$. Turner (2000) tabulated the fractional abundances of many molecules in TMC-1, including $N(HCN) = 3 \times 10^{-8} n_{H_2}$, $N(HCO^+) = 5 \times 10^{-9} n_{H_2}$ and $N(C_2H) = 5 \times 10^{-8} n_{H_2}$. To within a couple of orders of magnitude it is apparent that simple organic polyatomic species reside in dense clouds with abundances of $\sim 5 \times 10^{-9} n_{H_2}$, but CH_2CN has never been observed in the diffuse ISM.

The diffuse interstellar medium has generally been considered a hostile environment for the production of polyatomic molecules in appreciable abundances due to the low density (resulting in few collisions between atoms to fuel a gas-phase chemistry), and the high dissociating UV photon flux. This applies to an even greater extent in the warm neutral medium. However, polyatomic species have recently been discovered in diffuse and translucent clouds where models of conventional diffuse cloud chemistry predict their abundances should be much lower. The millimetre absorption studies by Lucas and Liszt (1996a; 1996b; 2000; 2001) identified a plethora of simple polyatomic molecules including HCO^+, HCN, C_2H, c-C_3H_2 and H_2CO. It seems likely that CH_2CN would also be detectable.

Even at the very low visual extinction of $A_V \simeq 0.25$, HCO^+ was found in high abundance in low Galactic-latitude sightlines, occurring at a similar fractional abundance to that found in dark clouds. The HCN/HCO^+ ratio was measured to be about two, showing HCN to be as widespread as HCO^+ in the diffuse ISM. C_2H was found to be more widespread than HCO^+, with $N(C_2H) \sim 10^{13}$ cm^{-2} ($\sim 10^{-10} n_{H_2}$), about $2-3$ times less abundant than CN and C_2, and relatively speaking, even more abundant than in many dark clouds. c-C_3H_2 was found at a fractional abundance of $\sim 10^{-10} n_{H_2}$. The similarities between translucent and dark cloud molecular abundances have also been studied by Turner (2000), who found a smooth transition of abundance ratios from dense to translucent to diffuse cloud regimes. The possible importance of dust grain-catalysed chemistry has been considered by Lucas & Liszt (1996b) and Turner (2000) as a means to explain the large abundances of polyatomic molecules in diffuse gas.

The rich polyatomic chemistry of the diffuse ISM may be fueled by the products of dust grain erosion and destruction. The effects of supernova shock-induced gain-grain collisions are likely to result in the release of hydrocarbons (C_nH_m, for example) *via* sputtering and shattering of carbonaceous grains (Duley & Williams 1984; Hall & Williams 1995). Such processes may provide a sufficient source of small molecules to fuel the chemistry required for the formation of CH_2CN^- in the diffuse ISM (see Section 5.1.1).

According to Herbst & Leung (1990), a likely route to the formation of CH_2CN in molecular clouds is as follows:

$$C_2H_4^+ + N \longrightarrow C_2H_3N^+ + H \qquad (5.27)$$

followed by

$$C_2H_3N^+ + e \longrightarrow CH_2CN + H \tag{5.28}$$

or

$$C_2H_3N^+ + CO \longrightarrow CH_2CN + HCO^+. \tag{5.29}$$

Alternatively,

$$CH_3^+ + HCN \longrightarrow CH_3CNH^+ + h\nu \tag{5.30}$$

then

$$CH_3CNH^+ + e \longrightarrow CH_2CN + H_2. \tag{5.31}$$

The most obvious pathway for production of the cyanomethyl anion CH_2CN^- is by radiative attachment:

$$CH_2CN + e \longrightarrow CH_2CN^- + h\nu, \tag{5.32}$$

though an alternative route exists *via* dissociative attachment to CH_3CN:

$$CH_3CNH^+ + e \longrightarrow CH_3CN + H \tag{5.33}$$

$$CH_3CN + e \longrightarrow CH_2CN^- + H. \tag{5.34}$$

The last step was studied by Sailer *et al.* (2003) in the laboratory. The dissociative electron attachment cross-section peaked at 4×10^{-23} m^2 for an electron energy of 3.2 eV, providing a highly efficient route to the formation of CH_2CN^- from CH_3CN. The cyanomethyl anion production channel is ~ 500 times more efficient than those of the other possible anionic fragments ($CHCN^-$, CCN^-, CN^- and CH_3^-) upon attachment of electrons with energies < 10 eV to CH_3CN.

Is it possible that CH_2CN^- could be produced in the diffuse ISM *via* these mechanisms? With a rate coefficient of $\sim 10^{-10}$ cm^3 s^{-1}, given a sufficient abundance of C_2H_4 — perhaps as a product of grain erosion — reaction 5.27 could proceed rapidly enough to produce sufficient quantities of $C_2H_3N^+$ to allow the electron capture step to occur, provided electron densities are sufficiently high. In diffuse clouds, the neutral hydrogen density exceeds the electron density by several orders of magnitude however, so it is possible that $C_2H_3N^+$ would be destroyed by reacting with H before electron capture takes place.

The main destruction mechanisms of CH_2CN and CH_3CN are by reaction with H^+, C^+ and He^+ which are also likely to be rapid in the diffuse ISM, further reducing the possibility of finding CH_2CN^- in the diffuse or warm ISM.

Plausible mechanisms for the production of CH_2CN^- exist, but whatever the precise details, they must proceed very efficiently if the molecule is to survive in the diffuse or warm interstellar media. The work by Lucas and Liszt (1996a; 1996b; 2000; 2001) shows that polyatomics do exist in the diffuse medium in abundances that cannot be explained by conventional gas-phase chemical models. Apparently, the existence of CH_2CN^- cannot yet be ruled out. It is difficult to see how CH_2CN^- could arise in the gas traced by Ti II without significant hydrocarbon input from dust grain erosion/destruction. If further studies confirm a correlation between the distribution of Ti II and the postulated cyanomethyl anion, a critical examination of the role of dust grain abrasion products in astrochemistry will be required.

Based on the apparent unity between dense and diffuse cloud abundance ratios (Turner 2000), what might be the expected interstellar CH_2CN^- abundance in sightlines that exhibit the λ8037 DIB? Polyatomic molecules are likely to be present in all of the heavily-reddened sightlines towards which λ8037 was observed. Cyg OB 12, Cyg OB2 5 and HD 183143 have been studied in depth by McCall *et al.* (1998, 2002b), particularly with reference to interstellar H_3^+, detected in all three sightlines with a Doppler b of ~ 10 km s^{-1}. Apparently, the H_3^+ is not closely associated with the other molecular material along these sightlines; Scappini *et al.* (2000, 2002) observed ^{13}CO and HCO^+ with narrow velocity components at $v_{LSR} \simeq 7$ km s^{-1} and $v_{LSR} \simeq 12$ km s^{-1} towards Cyg OB2 12. They inferred a CO density of $\sim 4 \times 10^3$ cm^{-3}, a column density of $N(CO) = 3 \times 10^{16}$ cm^{-2} and an HCO^+ column density of $\sim 10^{11}$ cm^{-2}. Scappini *et al.* (2002) determined a likely total number density of $n \gtrsim 10^4$ cm^{-3} for the gas

containing the CO and HCO^+, with the inference of dense, compact molecular clumps within a more diffuse medium; McCall *et al.* (2002b) determined $n \sim 4.8$ cm^{-3} for the broadly distributed gas containing the H_3^+. For Cyg OB2 5 and 12, Gredel *et al.* (2001) determined that the gas containing the C_2 molecules has a density of $n \sim 600$ cm^{-3}.

The approximate molecular hydrogen column density towards Cyg OB2 12 (from McCall *et al.* 2002b) is 6.5×10^{21} cm^{-2} such that the fractional HCO^+ abundance is $\sim 1.5 \times 10^{-11} n_{H_2}$. The equivalent width of the λ8037 DIB is 38.3 mÅ (see Table 5.5) which, from Equation (2.22) requires a CH_2CN^- column density of $N(CH_2CN^-) = 6.7 \times 10^{10}$ cm$^{-2}/f$ where f is the oscillator strength of the transition. Transitions between the ground and dipole-bound states are strongly observed in the lab (Lykke *et al.* 1987), suggesting that the value of f should be relatively large. Possible reasons for a large f (of between about 0.1 and 1) include the unusually large distance over which the electron travels in the transition, and the fact that the DBS orbital encompasses the whole of the GS electronic (π) orbital system; both factors should give rise to a large transition dipole-moment[6].

If $f = 0.5$ then $N(CH_2CN^-) = 1.3 \times 10^{11}$ cm^{-2} is required towards Cyg OB2 12 to produce the observed λ8037 equivalent width. Assuming a relatively efficient rate of formation of the anion by radiative electron attachment to neutral cyanomethyl, an anionic fraction of 10% yields $N(CH_2CN) = 1.3 \times 10^{12}$ cm^{-2}, which corresponds to a molecular fraction of $2 \times 10^{-10} n_{H_2}$. Thus, provided the $^1B_1$ DBS $\longleftarrow$ $^1A'$ GS transition is strong, the required interstellar CH_2CN fractional abundance is comparable to that of HCO^+ in the Cyg OB2 12 sightline, and very similar to the relative HCO^+ abundance in the Sgr B2 molecular cloud. The interstellar CH_2CN fractional abundance is bracketed by the values found by Irvine *et al.* (1988) and Turner *et al.* (1990) in dense molecular clouds ($\sim 5 \times 10^{-9}$ to $5 \times 10^{-11} n_{H_2}$). If diffuse and dense cloud molecular abundances are similar, then enough CH_2CN^- can probably be produced to create the λ8037 DIB along heavily-reddened sightlines. The required CH_2CN fractional abundance is also about the same as that of the simple hydrocarbon C_2H in the diffuse/translucent ISM ($\sim 10^{-10} n_{H_2}$), that may arise through erosion/destruction of carbonaceous dust grains and large molecules such as PAHs (Lucas & Liszt 1996a; Duley & Williams 1984).

[6]The transition dipole-moment (TDM) is the overlap integral of the electronic transition dipole between the upper and lower state wave-functions: TDM = $\langle \Psi_{GS} | \, er \, | \Psi_{DBS} \rangle$, where r is the electronic co-ordinate and e the electronic charge.

5.6 Conclusion to Chapter 5

Using the very accurate rotational constants published by Lykke *et al.* (1987), the absorption spectrum arising from the $^1B_1$ DBS $\longleftarrow$ $^1A'$ GS $K_a = 1 \longleftarrow 0$ transition of CH_2CN^- has been calculated with a distribution of J rotational level populations in equilibrium with the CMB at 2.74 K. The peak of the intrinsic absorption profile (at 8037.78 Å) matches the peak of the unidentified diffuse interstellar absorption feature at 8037.8 ± 0.15 Å found in the spectra of heavily-reddened stars in the Galactic plane. Spectra were telluric-corrected, shifted to set the peak or weighted mean K I wavelength at rest, and continuum-normalised, including the removal of the broad diffuse interstellar band centered around 8040 Å.

Considering transitions from $K_a'' = 1$, if CH_2CN^- occurs in the ISM with the 'equilibrium' statistical ortho : para abundance ratio of 3 : 1, the $^1B_1$ DBS $\longleftarrow$ $^1A'$ GS transitions with $K_a = 0 \longleftarrow 1$ and $K_a = 2 \longleftarrow 1$ produce strong spectral features at wavelengths of ~ 8024.8 Å and ~ 8049.6 Å that are not present in the observed interstellar spectra. If the $K_a'' = 1$ level is populated based on a Boltzmann distribution at 2.74 K, then the $K_a = 0 \longleftarrow 1$ and $K_a = 2 \longleftarrow 1$ sub-bands are sufficiently weak to be compatible with their absence in the observed spectra. A thermal (Boltzmann) distribution of K_a'' levels would be expected if an efficient mechanism exists for conversion between the ortho and para forms of CH_2CN^-. Alternatively, the formation mechanism for CH_2CN^- may introduce a 'non-equilibrium' (*i.e.* non 3 : 1) ratio of ortho and para forms that allows sufficiently small population of the $K_a'' = 1$ level for the CH_2CN^- anion to be the carrier of λ8037. Higher S/N ($\gtrsim$ 2000) observations of the λ8037 region may assist in the search for the $K_a'' = 1$ sub-bands.

The cyanomethyl anion CH_2CN^- is thus a plausible candidate for the carrier of the narrow diffuse interstellar band located at 8037.8 Å, provided a spectral line-broadening mechanism can be accounted for that produces an approximately Gaussian broadening corresponding to a Doppler b of between 16 and 33 km s^{-1} dependent on the specific sightline observed.

Measurement of the oscillator strength of the $^1B_1$ DBS $\longleftarrow$ $^1A'$ GS transition would enable the calculation of the interstellar column density of CH_2CN^- required to produce the λ8037 DIB. Assuming the transition is strong ($f \sim 0.5$) and the fraction of anions high (~ 10%), towards Cyg OB2 12 the required abundance of neutral CH_2CN

(relative to H_2) is similar to the HCO^+ abundance observed by Scappini *et al.* (2000). The required fractional abundance is also very similar to the typical diffuse/translucent medium C_2H fractional abundance observed by Lucas & Liszt (2000), and within a couple of orders of magnitude of the fractional abundance of small polyatomic hydrocarbons in typical dense/translucent molecular clouds.

There seems to be good evidence for a 'multi-component' ISM along heavily-reddened sightlines, consisting of dense, clumpy molecular material and a diffuse, rarefied, broadly distributed molecular component in which H_3^+ is found. More broadly distributed still is the shocked, high velocity gas traced by Ti II and Ca II as shown for the case of HD 183143. If interstellar CH_2CN^- is responsible for the λ8037 DIB, in the absence of any other broadening mechanisms, it must be distributed with an approximately Gaussian velocity spread similar to that exhibited by Ti II and Ca II towards HD 183143 and HD 186745. Observations of Ti II and Ca II are required for all of the sightlines in this study to test this hypothesis.

It is also plausible that the CH_2CN^- co-exists with interstellar dust, a hypothesis that could be examined by analysis of the correlation between W_{8037} and E_{B-V}. Such a study would require the observation of λ8037 towards many more sightlines than have been presented here. The issue may be somewhat clouded however, by the presence of other interstellar absorption features (predominantly centered around 8040 Å) that overlap this relatively narrow diffuse interstellar band and contaminate its profile.

Bibliography

Abdoul-Carime, H., Desfrançois, C., 1998, Eur. Phys. J. D, **2**, 149.

Abt, H. A., Levato, H., Grosso, M., 2002, ApJ, **573**, 359.

Adams, W. S., 1943, PASP, **55**, 217.

Adams, W. S., 1943, ApJ, **97**, 105.

Adamson, A. J., Whittet, D. C. B., 1992, ApJ, **398**, L69.

Adamson, A. J., Whittet, D. C. B., Duley, W. W., 1991, MNRAS, **252**, 234.

Albert, C. E., Blades, J. C., Morton, D. C., Lockman, F. J., Proulx, M., Ferrarese, L., 1993, ApJS, **88**, 81.

Anders, E., Grevesse, N., 1989, Geochim. Cosmochim. Acta, **53**, 197.

André, M. K., Le Petit, F., Sonnentrucker, P., Ferlet, R., Roueff, E., Civeit, T., Désert, J.-. M., Lacour, S., Vidal-Madjar, A., 2004, A&A, **422**, 483.

Ardeberg, A., Brunet, J. P., Maurice, E., Prevot, L., 1972, A&AS, **6**, 249.

Atkins, P. W., Friedman, R. S., 1997. *Molecular Quantum Mechanics*. Oxford University Press, third edition edition.

Bakes, E. L. O., Tielens, A. G. G. M., 1994, ApJ, **427**, 822.

Bakes, E. L. O., Tielens, A. G. G. M., 1998, ApJ, **499**, 258.

Bell, T. A., Viti, S., Williams, D. A., Crawford, I. A., Price, R. J., 2005, MNRAS, **357**, 961.

Bensch, F., Pak, I., Wouterloot, J. G. A., Klapper, G., Winnewisser, G., 2001, ApJ, **562**, L185.

Bernacca, P. L., Perinotto, M., 1970, Contributions dell'Osservatorio Astrofisica dell'Universita di Padova in Asiago, **239**, 1.

Bertin, P., Lallement, R., Ferlet, R., Vidal-Madjar, A., 1993, A&A, **278**, 549.

Bettens, R. P. A., Herbst, E., 1996, ApJ, **468**, 686.

Black, J. H., Dalgarno, A., 1973, Astrophys. Lett., **15**, 79.

Black, J. H., van Dishoeck, E. F., 1991. Chemistry and Small-Scale Structure of Diffuse and Translucent Clouds. In *IAU Symp. 147: Fragmentation of Molecular Clouds and Star Formation*, page 139.

Blades, J. C., Madore, B. F., 1979, A&A, **71**, 359.

Blades, J. C., Meaburn, J., 1980, MNRAS, **190**, 59P.

Blair, W. P., 2005. Kepler's Supernova Remnant: The View at 400 Years. In M. Turatto, S. Benetti, L. Zampieri, and W. Shea, editors, *ASP Conf. Ser. 342: 1604-2004: Supernovae as Cosmological Lighthouses*, page 416.

Bohlin, R. C., Savage, B. D., Drake, J. F., 1978, ApJ, **224**, 132.

Bolatto, A. D., Jackson, J. M., Ingalls, J. G., 1999, ApJ, **513**, 275.

Breysacher, J., 1981, A&AS, **43**, 203.

Breysacher, J., Azzopardi, M., Testor, G., 1999, A&AS, **137**, 117.

Brinkman, E. A., Berger, S., Marks, J., Brauman, J. I., 1995, J. Chem. Phys., **99**(10), 7586.

Briss, F. W., Ramsay, D. A., 1984, Computer Physics Communications, **38**, 83.

Burstein, D., Heiles, C., 1978, ApJ, **225**, 40.

Calura, F., Matteucci, F., Vladilo, G., 2003, MNRAS, **340**, 59.

Cami, J., Sonnentrucker, P., Ehrenfreund, P., Foing, B. H., 1997, A&A, **326**, 822.

Cami, J., Salama, F., Jiménez-Vicente, J., Galazutdinov, G. A., Krełowski, J., 2004, ApJ, **611**, L113.

Cappa de Nicolau, C. E., Poeppel, W. G. L., 1986, A&A, **164**, 274.

Cardelli, J. A., Clayton, G. C., Mathis, J. S., 1989, ApJ, **345**, 245.

Carruthers, G. R., 1970, ApJ, **161**, L81.

Caulet, A., Newell, R., 1996, ApJ, **465**, 205.

Centurion, M., Vladilo, G., 1991, A&A, **251**, 245.

Cheung, A. C., Rank, D. M., Townes, C. H., Thornton, D. D., Welch, W. J., 1969, Nature, **221**, 626.

Chlewicki, G., de Groot, M. S., van der Zwet, G. P., Greenberg, J. M., Alvarez, P. P., Mampaso, A., 1987, A&A, **173**, 131.

Churchwell, E., Wood, D. O. S., Felli, M., Massi, M., 1987, ApJ, **321**, 516.

Clayton, G. C., Martin, P. G., 1985, ApJ, **288**, 558.

Compton, R. N., Carman, H. S., Desfrançois, C., Abdoul-Carime, H., Scherman, J. P., 1996, J. Chem. Phys., **105**, 6126.

Cox, N. L. J., Cordiner, M. A., Cami, J., Ehrenfreund, P., Foing, B. H., Sarre, P. J., Kaper, L., 2005, Accepted for publication by A&A.

Crawford, I. A., 1992, MNRAS, **259**, 47.

Crawford, I. A., 1997, MNRAS, **290**, 41.

Crawford, I. A., 2001, MNRAS, **328**, 1115.

Crawford, I. A., 2002, MNRAS, **334**, L33.

Crawford, I. A., 2003, Ap&SS, **285**, 661.

Crawford, I. A., Howarth, I. D., Ryder, S. D., Stathakis, R. A., 2000, MNRAS, **319**, L1.

Crawford, M. K., Tielens, A. G. G. M., Allamandola, L. J., 1985, ApJ, **293**, L45.

Crawford, O. H., 1970, Mol. Phys., **20**, 585.

Crinklaw, G., Federman, S. R., Joseph, C. L., 1994, ApJ, **424**, 748.

Dalgarno, A., McCray, R. A., 1973, ApJ, **181**, 95.

Dartois, E., D'Hendecourt, L., 1997, A&A, **323**, 534.

Davies, R. D., Elliott, K. H., Meaburn, J., 1976, MmRAS, **81**, 89.

Davis, R. J., Diamond, P. J., Goss, W. M., 1996, MNRAS, **283**, 1105.

de Boer, K. S., 1991. Review: the Interstellar Medium of the Magellanic Clouds from Absorption Lines. In *IAU Symp. 148: The Magellanic Clouds*, page 401.

de Boer, K. S., Koornneef, J., Savage, B. D., 1980, ApJ, **236**, 769.

de Cuyper, J. P., Hensberge, H., 1998, A&AS, **128**, 409.

Desért, F.-X., Boulanger, F., Puget, J. L., 1990, A&A, **237**, 215.

Desért, F.-X., Jenniskens, P., Dennefeld, M., 1995, A&A, **303**, 223.

Desfrançois, C., Abdoul-Carime, H., Scherman, J. P., 1996, Int. J. Mod. Phys., **10(12)**, 1339.

Diamond, P. J., Goss, W. M., Romney, J. D., Booth, R. S., Kalberla, P. M. W., Mebold, U., 1989, ApJ, **347**, 302.

Dickens, J. E., Irvine, W. M., 1999, ApJ, **518**, 733.

Dickey, J. M., Lockman, F. J., 1990, ARA&A, **28**, 215.

Dieter, N. H., Welch, W. J., Romney, J. D., 1976, ApJ, **206**, L113.

Dodelson, S., 1986, J. Phys. B: At. Mol. Phys., **19**, 2871.

Domcke, W., Cederbaum, L. S., 1980, J. Phys. B, **14**, 149.

Dommanget, J., Nys, O., 1994, Communications de l'Observatoire Royal de Belgique, **115**, 1.

Douglas, A. E., 1977, Nature, **269**, 130.

Douglas, A. E., Herzberg, G., 1941, ApJ, **94**, 381.

Draine, B., 1989. On the Interpretation of the λ 2175 Å Feature. In *IAU Symp. 135: Interstellar Dust*, page 313.

Draine, B. T., Katz, N., 1986, ApJ, **306**, 655.

Draine, B. T., Lee, H. M., 1984, ApJ, **285**, 89.

Draine, B. T., Salpeter, E. E., 1979, ApJ, **231**, 438.

Draine, B. T., Roberge, W. G., Dalgarno, A., 1983, ApJ, **264**, 485.

Dufour, R. J., Shields, G. A., Talbot, R. J., 1982, ApJ, **252**, 461.

Duley, W. W., Williams, D. A., 1984, MNRAS, **211**, 97.

Dunham, T., 1937, PASP, **49**, 26.

Dyson, J. E., Williams, D. A., 1997. *The Physics of the Interstellar Medium.* Institute of Physics Publishing.

Edlen, B. P., 1966, Metrologia, **2**, 71.

Ehrenfreund, P., Foing, B. H., 1997, Advances in Space Research, **19**, 1033.

Ehrenfreund, P., Jenniskens, P., 1995. *The Environment Dependence of Diffuse Interstellar Bands*, page 105. ASSL Vol. 202: The Diffuse Interstellar Bands.

Evershed, J., 1924, The Observatory, **47**, 53.

Faison, M. D., Goss, W. M., Diamond, P. J., Taylor, G. B., 1998, AJ, **116**, 2916.

Feast, M. W., 1961, MNRAS, **122**, 1.

Feast, M. W., Thackeray, A. D., Wesselink, A. J., 1960, MNRAS, **121**, 337.

Federman, S. R., Lambert, D. L., Sheffer, Y., Cardelli, J. A., Andersson, B.-G., van Dishoeck, E. F., Zsargó, J., 2003, ApJ, **591**, 986.

Feitzinger, J. V., Isserstedt, J., 1983, A&AS, **51**, 505.

Feitzinger, J. V., Hanuschik, R. W., Schmidt-Kaler, T., 1984, MNRAS, **211**, 867.

Fermi, E., Teller, E., 1947, Phys. Rev., **72**, 406.

Fiedler, R. L., Dennison, B., Johnston, K. J., Hewish, A., 1987, Nature, **326**, 675.

Fitzpatrick, E. L., 1985, ApJ, **299**, 219.

Fitzpatrick, E. L., 1986, AJ, **92**, 1068.

Fitzpatrick, E. L., 1988, ApJ, **335**, 703.

Fitzpatrick, E. L., 2004. Interstellar Extinction in the Milky Way Galaxy. In *ASP Conf. Ser. 309: Astrophysics of Dust*, page 33.

Fitzpatrick, E. L., Massa, D., 1990, ApJS, **72**, 163.

Fitzpatrick, E. L., Savage, B. D., 1984, ApJ, **279**, 578.

Flower, D. R., Watt, G. D., 1984, MNRAS, **209**, 25.

Forbes, D., 1996, AJ, **112**, 1073.

Fossey, S., Somerville, W., 1995. *The Diffuse Interstellar Bands Towards Southern Stars*, page 31. ASSL Vol. 202: The Diffuse Interstellar Bands.

Frail, D. A., Weisberg, J. M., Cordes, J. M., Mathers, C., 1994, ApJ, **436**, 144.

Güthe, F., Tulej, M., Pachkov, M. V., Maier, J. P., 2001, ApJ, **555**, 466.

Galazutdinov, G., Moutou, C., Musaev, F., Krełowski, J., 2002, A&A, **384**, 215.

Galazutdinov, G. A., Krełowski, J., Moutou, C., Musaev, F. A., 1998, MNRAS, **295**, 437.

Galazutdinov, G. A., Krełowski, J., Musaev, F. A., 1999, MNRAS, **310**, 1017.

Galazutdinov, G. A., Krełowski, J., Musaev, F. A., 2000, MNRAS, **315**, 703.

Galazutdinov, G. A., Musaev, F. A., Krełowski, J., Walker, G. A. H., 2000, PASP, **112**, 648.

Galazutdinov, G. A., Musaev, F. A., Bondar, A. V., Krełowski, J., 2003, MNRAS, **345**, 365.

Galazutdinov, G. A., Manicò, G., Pirronello, V., Krełowski, J., 2004, MNRAS, **355**, 169.

Garrett, W. R., 1978, J. Chem. Phys., **69**(6), 2621.

Garrison, R. F., 1967, ApJ, **147**, 1003.

Gochermann, J., Schmidt-Kaler, T., Goudfrooij, P., 1989, A&A, **213**, 333.

Gordon, K. D., Clayton, G. C., Misselt, K. A., Landolt, A. U., Wolff, M. J., 2003, ApJ, **594**, 279.

Gordy, W., Cook, R. L., 1984. *Microwave Molecular Spectra*. John Wiley and Sons, third edition edition.

Gredel, R., Munch, G., 1994, AA, **285**, 640.

Gredel, R., Black, J. H., Yan, M., 2001, AA, **375**, 553.

Greenberg, J. M., Stoeckly, R., 1971, Nature, **230**, 15.

Greisen, E. W., Liszt, H. S., 1986, ApJ, **303**, 702.

Guarinos, J., 1988, Bulletin d'Information du Centre de Donnees Stellaires, **35**, 161.

Gutsev, G. L., Adamowicz, L., 1995, Chem. Phys. Lett., **246**, 245.

Gutsev, G. L., Adamowicz, L., 1995, J. Phys. Chem., **99**, 13412.

Gutsev, G. L., Adamowicz, L., 1995, Chem. Phys. Lett., **235**, 377.

Hall, P., Williams, D. A., 1995, Ap&SS, **229**, 49.

Hartmann, J., 1904, ApJ, **19**, 268.

Hartquist, T. W., Williams, D. A., 1998. *The Molecular Astrophysics of Stars and Galaxies.* Clarendon Press, Oxford.

Heckman, T. M., Lehnert, M. D., 2000, ApJ, **537**, 690.

Heger, M. L., 1922, Lick Observatory Bulletin, **10**, 141.

Heiles, C., 1967, ApJS, **15**, 97.

Heiles, C., 1997, ApJ, **481**, 193.

Herbig, G. H., 1975, ApJ, **196**, 129.

Herbig, G. H., 1993, ApJ, **407**, 142.

Herbig, G. H., 1995, Annu. Rev. Astophys., **33**, 19.

Herbig, G. H., Leka, K. D., 1991, ApJ, **382**, 193.

Herbig, G. H., Soderblöm, D. R., 1982, ApJ, **252**, 610.

Herbst, E., 1981, Nat, **289**, 656.

Herbst, E., 1982, A&A, **65**, 185.

Herbst, E., 1985, A&A, **153**, 151.

Herbst, E., 1995, Annu. Rev. Astrophys., **33**, 19.

Herbst, E., Klemperer, W., 1973, ApJ, **185**, 505.

Herbst, E., Leung, C. M., 1989, ApJS, **69**, 271.

Herbst, E., Leung, C. M., 1990, A&A, **233**, 177.

Herbst, E., Petrie, S., 1997, ApJ, **491**, 210.

Herbst, W., Havlen, R. J., 1977, A&AS, **30**, 279.

Herzberg, G., 1955, Mem. Soc. R. Sci. Liege, Ser. 4, **15**, 115.

Herzberg, G., 1955, J. Opt. Soc. Am., **55**, 229.

Herzberg, G., 1988, JRASC, **82**, 115.

Hill, V., Andrievsky, S., Spite, M., 1995, A&A, **293**, 347.

Hobbs, L. M., 1974, ApJ, **191**, 381.

Hobbs, L. M., 1978, ApJS, **38**, 129.

Houk, N., Smith-Moore, M., 1988. Michigan catalogue of Two-Dimensional spectral types for the HD stars,vol. 4 : -26 to -12 degrees. In *Michigan Spectral Survey, Ann Arbor, Dept. of Astronomy, Univ. Michigan (Vol. 4) (1988)*, page 0.

Houziaux, L., Nandy, K., Morgan, D. H., 1980, A&A, **84**, 377.

Howarth, I. D., Price, R. J., Crawford, I. A., Hawkins, I., 2002, MNRAS, **335**, 267.

Hutchings, J. B., 1966, MNRAS, **131**, 299.

Irvine, W. M., Friberg, P., Hjalmarson, A., Ishikawa, S., Kaifu, N., Kawaguchi, K., Madden, S. C., Matthews, H. E., Ohishi, M., Saito, S., Suzuki, H., Thaddeus, P., Turner, B. E., Yamamoto, S., Ziurys, L. M., 1988, ApJ, **334**, L107.

Israel, F. P., 1997, A&A, **328**, 471.

Issa, M. R., MacLaren, I., Wolfendale, A. W., 1990, A&A, **236**, 237.

Jenkins, E., 1989. Insights on Dust Grain Formation and Destruction Provided by Gas-Phase Element Abundances. In *IAU Symp. 135: Interstellar Dust*, page 23.

Jenkins, E. B., 1986, ApJ, **304**, 739.

Jenkins, E. B., 1996, ApJ, **471**, 292.

Jenniskens, P., Desért, F.-X., 1994, A&AS, **106**, 39.

Joblin, C., D'Hendecourt, L., Leger, A., Maillard, J. P., 1990, Nature, **346**, 729.

Johnson, H. L., Morgan, W. W., 1953, ApJ, **117**, 313.

Johnston, S., Koribalski, B., Wilson, W., Walker, M., 2003, MNRAS, **341**, 941.

Kaplan, S. A., Pikelner, S. B., 1970. *The Interstellar Medium*. Harvard University Press.

Kerr, T. H., Hibbins, R. E., Miles, J. R., Fossey, S. J., Somerville, W. B., Sarre, P. J., 1996, MNRAS, **283**, L105.

Kim, S., Staveley-Smith, L., Dopita, M. A., Sault, R. J., Freeman, K. C., Lee, Y., Chu, Y., 2003, ApJS, **148**, 473.

Koornneef, J., 1982, A&A, **107**, 247.

Koornneef, J., 1984. Gas-to-dust ratios in the Magellanic Clouds. In *IAU Symp. 108: Structure and Evolution of the Magellanic Clouds*, page 333.

Koornneef, J., Mathis, J. S., 1981, ApJ, **245**, 49.

Krełowski, J., Schmidt, M., 1997, ApJ, **477**, 209.

Krełowski, J., Sneden, C., 1995. *Diffuse Interstellar Bands in Individual Sightlines*, page 13. ASSL Vol. 202: The Diffuse Interstellar Bands.

Krełowski, J., Walker, G. A. H., 1987, ApJ, **312**, 860.

Krełowski, J., Westerlund, B. E., 1988, A&A, **190**, 339.

Krełowski, J., Snow, T. P., Seab, C. G., Papaj, J., 1992, MNRAS, **258**, 693.

Krełowski, J., Galazutdinov, G. A., Musaev, F. A., 1998, ApJ, **506**, 926.

Krełowski, J., Ehrenfreund, P., Foing, B. H., Snow, T. P., Weselak, T., Tuairisg, S. Ó., Galazutdinov, G. A., Musaev, F. A., 1999, A&A, **347**, 235.

Lauroesch, J. T., Meyer, D. M., 1999, ApJ, **519**, L181.

Lauroesch, J. T., Meyer, D. M., 2003, ApJ, **591**, L123.

Lauroesch, J. T., Meyer, D. M., Watson, J. K., Blades, J. C., 1998, ApJ, **507**, L89.

Lauroesch, J. T., Meyer, D. M., Blades, J. C., 2000, ApJ, **543**, L43.

Lawton, B., Churchill, C. W., 2004, American Astronomical Society Meeting Abstracts, **205**.

Le Teuff, Y. H., Millar, T. J., Markwick, A. J., 2000, A&AS, **146**, 157.

Leger, A., D'hendecourt, L., 1985, A&A, **146**, 81.

Leger, A., Puget, J. L., 1984, A&A, **137**, L5.

Lepp, S., Dalgarno, A., 1988, ApJ, **324**, 553.

Lequeux, J., 2005. *The Interstellar Medium*. Springer.

Levenberg, K., 1944, Quart. Appl. Math., **2**, 164.

Lipman, K., Pettini, M., 1995, ApJ, **442**, 628.

Liszt, H., Lucas, R., 2001, A&A, **370**, 576.

Liu, X., 2001. *Electronic Structre of Molecules of potential Astrophysical importance*. Master's thesis, University of Nottingham.

Lodén, L. O., 1973, Ap&SS, **24**, 511.

Lucas, R., Liszt, H., 1996, A&A, **307**, 237.

Lucas, R., Liszt, H., 1998, A&A, **337**, 246.

Lucas, R., Liszt, H. S., 1996. Millimeter-wave observations of diffuse clouds. In *IAU Symp. 178: Molecules in Astrophysics: Probes & Processes*, page 421.

Lucas, R., Liszt, H. S., 2000, A&A, **358**, 1069.

Lykke, K. R., Neumark, D. M., Andersen, T., Trapa, V. J., Lineberger, W. C., 1987, J. Chem. Phys., **87**(12), 6842.

Münch, G., Unsöld, A., 1962, ApJ, **135**, 711.

Maíz-Apellániz, J., Walborn, N. R., Galué, H. Á., Wei, L. H., 2004, ApJS, **151**, 103.

Marks, J., Wetzel, D. M., Comita, P., Brauman, J. I., 1986, J. Chem. Phys., **84**(10), 5284.

Marquardt, D., 1963, SIAM J. Appl. Math., **11**, 431.

Marscher, A. P., Moore, E. M., Bania, T. M., 1993, ApJ, **419**, L101.

Martin, N., Maurice, E., Lequeux, J., 1989. The Structure of the Small Magellanic Cloud. In *Recent Developments of Magellanic Cloud Research. A European Colloquium, held in Paris, France, May 9-11, 1989. Editors, K.S. de Boer, F. Spite, G. Stasinska; Publisher, Observatoire de Paris, Section Astrophysique de Meudon, Meudon, France, 1989. LC # QB858.5.M33 R42 1989. ISBN # NONE. P.157, 1989*, page 157.

Martin, P. G., Angel, J. R. P., 1974, ApJ, **188**, 517.

Marx-Zimmer, M., Herbstmeier, U., Dickey, J. M., Zimmer, F., Staveley-Smith, L., Mebold, U., 2000, A&A, **354**, 787.

Massey, P., Hunter, D. A., 1998, ApJ, **493**, 180.

Massey, P., Thompson, A. B., 1991, AJ, **101**(4), 1408.

McCall, B. J., Geballe, T. R., Hinkle, K. H., Oka, T., 1998, Science, **279**, 1910.

McCall, B. J., Thorburn, J., Hobbs, L. M., Oka, T., York, D. G., 2001, ApJ, **559**, L49.

McCall, B. J., Oka, T., Thorburn, J., Hobbs, L. M., York, D. G., 2002, ApJ, **567**, L145.

McCall, B. J., Hinkle, K. H., Geballe, T. R., Moriarty-Schieven, G. H., Evans, N. J., Kawaguchi, K., Takano, S., Smith, V. V., Oka, T., 2002, ApJ, **567**, 391.

McGee, R. X., Newton, L. M., Morton, D. C., 1983, MNRAS, **205**, 1191.

McKellar, A., 1940, PASP, **52**, 187.

Merrill, P. W., 1934, Publ. Astron. Soc. Pac., **46**, 206.

Merrill, P. W., Wilson, O. C., 1938, ApJ, **87**, 9.

Meyer, D. M., 1990, ApJ, **364**, L5.

Meyer, D. M., Blades, J. C., 1996, ApJ, **464**, L179.

Meyer, D. M., Lauroesch, J. T., 1999, ApJ, **520**, L103.

Millen, D. J., Topping, G., Lide, D. R. J., 1962, J. Molo. Spec., **8**, 153.

Molaro, P., Vladilo, G., Monai, S., D'Odorico, S., Ferlet, R., Madjar, A. V., Dennefeld, M., 1993, A&A, **274**, 505.

Moran, S., Ellis, B. J., Defrees, D. J., Mclean, A. D., Ellison, G. B., 1987, J. Am. Chem. Soc, **109**, 5996.

Morgan, D. H., 1987, QJRAS, **28**, 328.

Morton, D. C., 2003, ApJS, **149**, 205.

Nandy, K., Morgan, D. H., Houziaux, L., 1982, Ap&SS, **85**, 159.

Niemela, V. S., Gamen, R. C., 2005, MNRAS, **356**, 974.

Nummelin, A. *et al.*, 2000, ApJ SS, **128**, 213.

Oestreicher, M. O., Gochermann, J., Schmidt-Kaler, T., 1995, A&AS, **112**, 495.

Olano, C. A., 2004, A&A, **423**, 895.

Omont, A., 1986, A&A, **164**, 159.

Pan, K., Federman, S. R., Cunha, K., Smith, V. V., Welty, D. E., 2004, ApJS, **151**, 313.

Pequignot, D., Aldrovandi, S. M. V., 1986, A&A, **161**, 169.

Perryman, M. A. C., ESA, 1997. *The HIPPARCOS and TYCHO catalogues. Astrometric and photometric star catalogues derived from the ESA HIPPARCOS Space Astrometry Mission.* The Hipparcos and Tycho catalogues. Astrometric and photometric star catalogues derived from the ESA Hipparcos Space Astrometry Mission, Publisher: Noordwijk, Netherlands: ESA Publications Division, 1997, Series: ESA SP Series vol no: 1200, ISBN: 9290923997 (set).

Petrie, S., 1996, MNRAS, **281**, 137.

Pettini, M., Dodorico, S., 1986, ApJ, **310**, 700.

Pfenniger, D., Combes, F., 1994, A&A, **285**, 94.

Pfenniger, D., Combes, F., Martinet, L., 1994, A&A, **285**, 79.

Plaskett, J. S., 1923, MNRAS, **84**, 80.

Poglitsch, A., Krabbe, A., Madden, S. C., Nikola, T., Geis, N., Johansson, L. E. B., Stacey, G. J., Sternberg, A., 1995, ApJ, **454**, 293.

Price, R. J., Crawford, I. A., Barlow, M. J., Howarth, I. D., 2001, MNRAS, **328**, 555.

Richter, P., Sembach, K. R., Howk, J. C., 2003, A&A, **405**, 1013.

Roberge, W. G., Jones, D., Lepp, S., Dalgarno, A., 1991, ApJS, **77**, 287.

Rohlfs, K., Kreitschmann, J., Feitzinger, J. V., Siegman, B. C., 1984, A&A, **137**, 343.

Rolleston, W. R. J., Trundle, C., Dufton, P. L., 2002, A&A, **396**, 53.

Rollinde, E., Boissé, P., Federman, S. R., Pan, K., 2003, A&A, **401**, 215.

Romani, R. W., Blandford, R. D., Cordes, J. M., 1987, Nature, **328**, 324.

Routly, P. M., Spitzer, L. J., 1952, ApJ, **115**, 227.

Royer, F., Grenier, S., Baylac, M.-O., Gómez, A. E., Zorec, J., 2002, A&A, **393**, 897.

Rudkjøbing, M., 1969, Ap&SS, **3**, 102.

Ruffle, D. P., Bettens, R. P. A., Terzieva, R., Herbst, E., 1999, ApJ, **523**, 678.

Ruiterkamp, R., Halasinski, T., Salama, F., Foing, B. H., Allamandola, L. J., Schmidt, W., Ehrenfreund, P., 2002, A&A, **390**, 1153.

Russell, S. C., Dopita, M. A., 1990, ApJS, **74**, 93.

Sailer, W., Pelc, W., Limao-Vieira, P., Mason, N. J., Limtrakul, J., Scheier, P., Probst, M., Mark, T. D., 2003, Chem. Phys. Lett., **381**, 216.

Salama, F., Allamandola, L., 1994. PAHs; DIBs and Interstellar Extinction. In *ASP Conf. Ser. 58: The First Symposium on the Infrared Cirrus and Diffuse Interstellar Clouds*, page 279.

Salama, F., Bakes, E. L. O., Allamandola, L. J., Tielens, A. G. G. M., 1996, ApJ, **458**, 621.

Salama, F., Galazutdinov, G. A., Krełowski, J., Allamandola, L. J., Musaev, F. A., 1999, ApJ, **526**, 265.

Sarre, P. J., 2000, MNRAS, **313**, L14.

Sarre, P. J., Miles, J. R., Kerr, T. H., Hibbins, R. E., Fossey, S. J., Somerville, W. B., 1995, MNRAS, **277**, L41.

Savage, B. D., de Boer, K. S., 1981, ApJ, **243**, 460.

Savage, B. D., Jenkins, E. P., 1972, ApJ, **172**, 491.

Savage, B. D., Sembach, K. R., 1991, ApJ, **379**, 245.

Scappini, F., Cecchi-Pestellini, C., Codella, C., Dalgarno, A., 2000, MNRAS, **317**, L6.

Scappini, F., Casu, S., Cecchi-Pestellini, C., Olberg, M., 2002, MNRAS, **337**, 495.

Scarrott, S. M., Watkin, S., Miles, J. R., Sarre, P. J., 1992, MNRAS, **255**, 11P.

Schmidt-Kaler, T., Feitzinger, J. V., 1976, Ap&SS, **41**, 357.

Schwering, P. B. W., Israel, F. P., 1991, A&A, **246**, 231.

Seab, C. G., Snow, T. P., 1995, ApJ, **443**, 698.

Seaton, M. J., 1979, MNRAS, **187**, 73P.

Sembach, K. R., Danks, A. C., 1994, A&A, **289**, 539.

Sembach, K. R., Danks, A. C., Savage, B. D., 1993, A&AS, **100**, 107.

Shapiro, P. R., Holcomb, K. A., 1986, ApJ, **310**, 872.

Slipher, V. M., 1912, Lowell Obs. Bull, **12**, 26.

Smith, L. F., 1968, MNRAS, **140**, 409.

Smith, L. F., Shara, M. M., Moffat, A. F. J., 1990, ApJ, **348**, 471.

Smith, V. V., Hinkle, K. H., Cunha, K., Plez, B., Lambert, D. L., Pilachowski, C. A., Barbuy, B., Meléndez, J., Balachandran, S., Bessell, M. S., Geisler, D. P., Hesser, J. E., Winge, C., 2002, AJ, **124**, 3241.

Snow, T. P., 2002, ApJ, **567**, 407.

Snow, T. P., Krełowski, J., 1994. A Comparison of the Diffuse Clouds in Front of Zeta OPH and Sigma SCO. In *Astronomical Society of the Pacific Conference Series*, page 64.

Sofia, U. J., Meyer, D. M., 2001, ApJ, **554**, L221.

Sollerman, J., Cox, N., Mattila, S., Ehrenfreund, P., Kaper, L., Leibundgut, B., Lundqvist, P., 2005, A&A, **429**, 559.

Sommerfeld, T., 2005, Journal of Physics: Conference Series, **4**, 245.

Songaila, A., 1981, ApJ, **248**, 945.

Songaila, A., Blades, J. C., Hu, E. M., Cowie, L. L., 1986, ApJ, **303**, 198.

Sonnentrucker, P., Cami, J., Ehrenfreund, P., Foing, B. H., 1997, A&A, **327**, 1215.

Sonnentrucker, P., Foing, B. H., Breitfellner, M., Ehrenfreund, P., 1999, A&A, **346**, 936.

Sonnentrucker, P., Foing, B. H., Ehrenfreund, P., 1999, Advances in Space Research, **24**, 519.

Spitzer, L., 1985, ApJ, **290**, L21.

Spitzer, L. J., 1978. *Physical Processes in the Intersteallar Medium*. Wiley.

Stanimirović, S., Weisberg, J. M., Hedden, A., Devine, K. E., Green, J. T., 2003, ApJ, **598**, L23.

Staveley-Smith, L., Kim, S., Calabretta, M. R., Haynes, R. F., Kesteven, M. J., 2003, MNRAS, **339**, 87.

Stokes, G. M., 1978, ApJS, **36**, 115.

Struve, F. G. W., 1847. *Etudes d'Astronomie Stellaire : Sur la voie lactee et sur la distance des etoiles fixes*. St. Petersburg : Tip. Acad. Imper., 1847; IV, 165 p. ; in 8.; DCCC.4.211.

Swings, P., 1942, ApJ, **95**, 270.

Swings, P., Rosenfeld, L., 1937, ApJ, **86**, 483.

Takakuwa, S., Kawaguchi, K., Mikami, H., Saito, M., 2001, PASJ, **53**, 251.

Terzieva, R., Herbst, E., 2000, International Journal of Mass Spectrometry, **201**, 135.

Thorburn, J. A., Hobbs, L. M., McCall, B. J., Oka, T., Welty, D. E., Friedman, S. D., Snow, T. P., Sonnentrucker, P., York, D. G., 2003, ApJ, **584**, 339.

Thorndike, S. L., 1930, PASP, **42**, 99.

Tielens, A. G. G. M., 1995. The Interstellar Medium. In *ASP Conf. Ser. 73: From Gas to Stars to Dust*, page 3.

Torres, V. A., Conti, P. S., P., M., 1986, ApJ, **300**, 379.

Tripp, T. M., Cardelli, J. A., Savage, B. D., 1994, AJ, **107**, 645.

Trumpler, R. J., 1930, PASP, **42**, 214.

Tuairisg, S. Ó., Cami, J., Foing, B. H., Sonnentrucker, P., Ehrenfreund, P., 2000, A&AS, **142**, 225.

Tulej, M., Kirkwood, D. A., Pachkov, M., Maier, J. P., 1998, ApJ, **506**, L69.

Tumlinson, J., Shull, J. M., Rachford, B. L., Browning, M. K., Snow, T. P., Fullerton, A. W., Jenkins, E. B., Savage, B. D., Crowther, P. A., Moos, H. W., Sembach, K. R., Sonneborn, G., York, D. G., 2002, ApJ, **566**, 857.

Turner, B. E., 1989, ApJS, **70**, 539.

Turner, B. E., 2000, ApJ, **542**, 837.

Turner, B. E., Friberg, P., Irvine, W. M., Saito, S., Yamamoto, S., 1990, ApJ, **355**, 546.

Turner, B. E., Terzieva, R., Herbst, E., 1999, ApJ, **518**, 699.

Turner, D. G., 1982. Preliminary results of a new study of the intrinsic properties of Wolf-Rayet stars. In *IAU Symp. 99: Wolf-Rayet Stars: Observations, Physics, Evolution*, page 57.

Uesugi, A., Fukuda, I., 1970. *Catalogue of rotational velocities of the stars*. Contributions from the Institute of Astrophysics and Kwasan Observatory, University of Kyoto, Kyoto: University, Kwasan Observatory, Institute of Astrophysics, 1970.

van de Hulst, H. C., 1948, Rech. Astron. Obs. Uttrecht, **11**, pt. 2.

van der Marel, R. P., Alves, D. R., Hardy, E., Suntzeff, N. B., 2002, AJ, **124**, 2639.

van Dishoeck, E. F., Black, J. H., 1986, ApJS, **62**, 109.

van Loon, J. T., 2000, A&A, **354**, 125.

Vidal-Madjar, A., Andreani, P., Cristiani, S., Ferlet, R., Lanz, T., Vladilo, G., 1987, A&A, **177**, L17.

Vladilo, G., Crivellari, L., Molaro, P., Beckman, J. E., 1987, A&A, **182**, L59.

Vladilo, G., Molaro, P., Monai, S., D'Odorico, S., Ferlet, R., Madjar, A. V., Dennefeld, M., 1993, A&A, **274**, 37.

Vogt, S. S., Penrod, G. D., 1988. HIRES - a High Resolution Echelle Spectrometer for the Keck 10-METER Telescope. In *Instrumentation for Ground-Based Optical Astronomy, Present and Future. The Ninth Santa Cruz Summer Workshop in Astronomy and Astrophysics, July 13- 24, 1987, Lick Observatory. Editor, L.B. Robinson; Publisher, Springer-Verlag, New York, NY, 1988. LC # QB856 .S26 1987. ISBN # 0-387-96730-3. P. 68, 1988*, page 68.

Wagenblast, R., Williams, D. A., Millar, T. J., Nejad, L. A. M., 1993, MNRAS, **260**, 420.

Walborn, N. R., 1972, AJ, **77**, 312.

Walborn, N. R., Blades, J. C., 1997, ApJS, **112**, 457.

Walker, G. A. H., Bohlender, D. A., Krełowski, J., 2000, ApJ, **530**, 362.

Walker, M., Wardle, M., 1998, ApJ, **498**, L125.

Watson, J. K., Meyer, D. M., 1996, ApJ, **473**, L127.

Watson, J. K. G., 1977, Vib. Spectra Struct., **6**, 1.

Watson, J. K. G., 2001, ApJ, **555**, 472.

Wayte, S. R., 1990, ApJ, **355**, 473.

Webster, A., 1996, MNRAS, **282**, 1372.

Webster, A., 2004, MNRAS, **349**, 263.

Wegner, W., 1994, MNRAS, **270**, 229.

Weinreb, S., Barrett, A. H., Meeks, M. L., Henry, J. C., 1963, Nature, **200**, 829.

Welsh, B. Y., Sasseen, T., Craig, N., Jelinsky, S., Albert, C. E., 1997, ApJS, **112**, 507.

Welty, D., 1998, LNP Vol. 506: IAU Colloq. 166: The Local Bubble and Beyond, **506**, 151.

Welty, D. E., Fitzpatrick, E. L., 2001, ApJ, **551**, L175.

Welty, D. E., Hobbs, L. M., 2001, ApJS, **133**, 345.

Welty, D. E., Hobbs, L. M., Kulkarni, V. P., 1994, ApJ, **436**, 152.

Welty, D. E., Morton, D. C., Hobbs, L. M., 1996, ApJS, **106**, 533.

Welty, D. E., Frisch, P. C., Sonneborn, G., York, D. G., 1999, ApJ, **512**, 636.

Welty, D. E., Lauroesch, J. T., Blades, J. C., Hobbs, L. M., York, D. G., 2001, ApJ, **554**, L75.

Welty, D. E., Hobbs, L. M., Morton, D. C., 2003, ApJS, **147**, 61.

Welty, D. E., Lauroesch, J. T., Hobbs, L. M., York, D. G., 2004, American Astronomical Society Meeting Abstracts, **205**.

Weselak, T., Galazutdinov, G. A., Musaev, F. A., Krełowski, J., 2004, A&A, **414**, 949.

Westerlund, B. E., 1997. *The Magellanic Clouds*. Book,.

Westerlund, B. E., Krełowski, J., 1988, A&A, **203**, 134.

Westerlund, B. E., Krełowski, J., 1989, A&A, **218**, 216.

Whittet, D. C. B., 2003. *Dust in the Galactic Environment*. Institute of Physics Publishing.

Wilson, R. W., Jefferts, K. B., Penzias, A. A., 1970, ApJ, **161**, L43.

List of Figures

1 Image of the night sky towards Sco-Oph 12

1.1 Example UV extinction curves for various values of R_V 20

2.1 Schematic diagram of Keck HIRES 42

2.2 Example of an echellogram 43

3.1 LMC and Galactic UV extinction curves from Fitzpatrick (1986) . . . 60

3.2 LMC UV extinction curves from Gordon *et al.* (2003) 60

3.3 Annotated optical image of the LMC and zoom-in of the 30 Dor region 68

3.4 Acquisition image for Sk −69°223 72

3.5 LMC Ca II K spectra with VAPID fits 74

3.6 LMC Na D spectra with VAPID fits 75

3.7 LMC Na UV spectra 76

3.8 LMC DIBs: λ4430 and λ5705 81

3.9 LMC DIBs: λ5780 and λ5797 82

3.10 LMC DIBs: λ5850 83

3.11 LMC DIBs: λ6196 and λ6203 84

3.12 LMC DIBs: λ6270 and λ6284 85

3.13 LMC DIBs: λ6379 and λ6614 86

3.14 Sk −67°2 atomic column densities plotted as a function of LSR velocity, DIB velocities labelled 92

3.15 Sk −67°5 atomic column densities plotted as a function of LSR velocity 93

3.16 Sk −68°135 atomic column densities plotted as a function of LSR velocity, DIB velocities labelled 94

3.17 Sk −69°223 atomic column densities plotted as a function of LSR velocity, DIB velocities labelled 95

3.18 Sk −69°243 atomic column densities and plotted as a function of LSR velocity, DIB velocities labelled 96

3.19 Sk −70°120 atomic column densities plotted as a function of LSR velocity 97

3.20 Galactic λ6614 sub-structure variation velocity fits 100

3.21 Sk −69°223 λ5780 VAPID intrinsic profile fit 103

3.22 Key for LMC/Galactic atomic/DIB W_λ/E_{B-V} comparison plots 116

3.23 LMC K I, H I and Ti II column denisties compared with Galactic data as a function of E_{B-V} 117

3.24 Galactic and LMC λ5780 and λ5797 DIB equivalent widths plotted against E_{B-V} and N(K I) 118

3.25 Galactic and LMC λ5705 DIB equivalent widths plotted against E_{B-V} and N(K I) 119

3.26 Galactic and LMC λ5850 DIB equivalent widths plotted against E_{B-V} and N(K I) 119

3.27 Galactic and LMC λ6196, λ6203 and λ6284 DIB equivalent widths plotted against E_{B-V} and N(K I) 120

3.28 Galactic and LMC λ6379 and λ6614 DIB equivalent widths plotted against E_{B-V} and N(K I) 121

3.29 W_{6284} *vs.* N(H I) for LMC targets compared with Galactic 134

3.30 LMC λ6284 and λ6614 equivalent widths plotted against R_V 137

4.1 SSS spectral type standards I 156

4.2 SSS spectral type standards II 157

4.3 SSS spectral type standards III 158

4.4 $\beta^{1,2}$ Sco λ5705 spectra and residual intensities 160

4.5 $\beta^{1,2}$ Sco λ5780 and λ5797 spectra and residual intensities 160

4.6 $\beta^{1,2}$ Sco λ5850 spectra and residual intensities 161

4.7 $\beta^{1,2}$ Sco λ6196 and λ6203 spectra and residual intensities 161

4.8 $\beta^{1,2}$ Sco λ6284 spectra and residual intensities 162

4.9 $\beta^{1,2}$ Sco λ6376 and λ6379 spectra and residual intensities 162

4.10 $\beta^{1,2}$ Sco λ6426, λ6439 and λ6445 spectra and residual intensities . . . 163

4.11 $\beta^{1,2}$ Sco λ6614 spectra and residual intensities 163

4.12 $\beta^{1,2}$ Sco λ6660 spectra and residual intensities 164

4.13 $\beta^{1,2}$ Sco λ7224 spectra and residual intensities 164

4.14 $\beta^{1,2}$ Sco λ7562 spectra and residual intensities 165

4.15 Overlaid $\beta^{1,2}$ Sco λ5780 spectra 167

4.16 Overlaid $\beta^{1,2}$ Sco λ6196 spectra 168

4.17 Overlaid $\beta^{1,2}$ Sco λ6614 spectra 168

4.18 Overlaid $\beta^{1,2}$ Sco Na I D_1 spectra 169

4.19 Overlaid $\beta^{1,2}$ Sco K I λ7699 spectra 169

4.20 $\nu^{1,3}$ Sco λ5705 spectra and residual intensities 172

4.21 $\nu^{1,3}$ Sco λ5780 and λ5797 spectra and residual intensities 172

4.22 $\nu^{1,3}$ Sco λ5850 spectra and residual intensities 173

4.23 $\nu^{1,3}$ Sco λ6196 and λ6203 spectra and residual intensities 173

4.24 $\nu^{1,3}$ Sco λ6284 spectra and residual intensities 174

4.25 $\nu^{1,3}$ Sco λ6376 and λ6379 spectra and residual intensities 174

4.26 $\nu^{1,3}$ Sco λ6614 spectra and residual intensities 175

4.27 Overlaid $\nu^{1,3}$ Sco λ5780 spectra 175

4.28 Overlaid $\nu^{1,3}$ Sco Na I D_1 spectra 176

4.29 Overlaid $\nu^{1,3}$ Sco K I λ7699 spectra 176

4.30 DSS image of the ρ Oph system 178

4.31 ρ Oph A, B, C, DE λ5705 spectra and residual intensities 180

4.32 ρ Oph A, B, C, DE λ5780 and λ5797 spectra and residual intensities . 181

4.33 ρ Oph A, B, C, DE λ5850 spectra and residual intensities 182

4.34 ρ Oph A, B, C, DE λ6196 and λ6203 spectra and residual intensities . 183

4.35 ρ Oph A, B, C, DE λ6284 spectra and residual intensities 184

4.36 ρ Oph A, B, C, DE λ6376 and λ6379 spectra and residual intensities . 185

4.37 ρ Oph A, B, C, DE λ6426, λ6439 and λ6445 spectra and residual intensities 186

4.38 ρ Oph A, B, C, DE λ6614 spectra and residual intensities 187

4.39 ρ Oph A, B, C, DE λ6660 spectra and residual intensities 188

4.40 ρ Oph A, B, C, DE λ7224 spectra and residual intensities 189

4.41 ρ Oph A, B, C, DE λ7562 spectra and residual intensities 190

4.42 Overlaid ρ Oph A, B, C, DE λ5780 spectra 195

4.43 Overlaid ρ Oph A, B, C, DE λ5797 spectra 196

4.44 Overlaid ρ Oph A, B, C, DE λ5850 spectra 196

4.45 Overlaid ρ Oph A, B, C, DE λ6196 spectra 197

4.46 Overlaid ρ Oph A, B, C, DE λ6376 and λ6379 spectra 197

4.47 Overlaid ρ Oph A, B, C, DE λ6614 spectra 198

4.48 Overlaid, peak-absorption scaled ρ Oph A & C λ6614 spectra 198

4.49 Overlaid ρ Oph A, B, C, DE Na I D_1 spectra 199

4.50 Overlaid ρ Oph A, B, C, DE K I λ7699 spectra 199

4.51 ρ Oph DIB atomic and diatomic correlation plots 201

4.52 $\mu^{1,2}$ Cru λ5780 and λ5797 spectra and residual intensities 204

4.53 $\mu^{1,2}$ Cru λ5850 spectra and residual intensities 204

4.54 $\mu^{1,2}$ Cru λ6196 and λ6203 spectra and residual intensities 205

4.55 $\mu^{1,2}$ Cru λ6284 spectra and residual intensities 205

4.56 $\mu^{1,2}$ Cru λ6614 spectra and residual intensities 206

4.57 Overlaid $\mu^{1,2}$ Cru Na I D_1 spectra 206

4.58 Overlaid $\mu^{1,2}$ Cru K I λ7699 spectra 207

4.59 W_{5780} *vs.* N(K I) and E_{B-V} for SSS targets 208

4.60 W_{6614} *vs.* N(K I) and E_{B-V} for SSS targets 208

4.61 HD 150135/6 λ5705 spectra and residual intensities 211

4.62 HD 150135/6 λ5780 and λ5797 spectra and residual intensities 211

4.63 HD 150135/6 λ5850 spectra and residual intensities 212

4.64 HD 150135/6 λ6196 and λ6203 spectra and residual intensities 212

4.65 HD 150135/6 λ6284 spectra and residual intensities 213

4.66 HD 150135/6 λ6376 and λ6379 spectra and residual intensities 213

4.67 HD 150135/6 λ6614 spectra and residual intensities 214

4.68 Overlaid HD 150135/6 λ6614 spectra 214

4.69 Overlaid HD 150135/6 Na I D_1 spectra 215

4.70 Overlaid HD 150135/6 K I λ7699 spectra 215

4.71 DSS image of NGC 6531 (M 21) 217

4.72 HD 164863/313693 λ5705 spectra and residual intensities 218

4.73 HD 164863/313693 λ5780 and λ5797 spectra and residual intensities 218

4.74 HD 164863/313693 λ5850 spectra and residual intensities 219

4.75 HD 164863/313693 λ6196 and λ6203 spectra and residual intensities 219

4.76 HD 164863/313693 λ6284 spectra and residual intensities 220

4.77 HD 164863/313693 λ6614 spectra and residual intensities 220

4.78 Overlaid HD 164863/313693 Na I D_1 spectra 221

4.79 Overlaid HD 164863/313693 K I λ7699 spectra 221

4.80 HD 164863/313693 interstellar Na I D_1 velocity comparison 224

4.81 New κ Vel interstellar K I λ7699 spectrum and model fit compared with past data 229

4.82 κ Vel K I λ7699 curve of growth 230

4.83 κ Vel N(K I) *vs.* time 230

4.84 κ Vel 1995 and 2004 λ5780 and λ5797 spectra and residual intensities 232

4.85 κ Vel 1995 and 2004 λ6196 and λ6203 spectra and residual intensities 232

4.86 κ Vel 1995 and 2004 λ6614 spectra and residual intensities 233

4.87 ρ Oph A and C λ6614 spectra with 'Webster hypothesis' Gaussian fits 244

4.88 'Webster hypothesis' Poisson-law fit to λ6614 component strengths for ρ Oph A 245

4.89 'Webster hypothesis' Poisson-law fit to λ6614 component strengths for ρ Oph C 245

5.1 Schematic potential energy diagram for 'X + e', 'X^-_{GS}' and 'X^-_{DBS}' . 258

5.2 Cyg OB2 8a λ8037 DIB spectroscopic match with CH_2CN^- $^rR_0(0)$, $^rQ_0(1)$, $^rP_0(2)$ origin band DBS ⟵ GS transitions 260

5.3 CH_2CN^- structure and principal axes 265

5.4 Schematic picture of the CH_2CN^- dipole-bound state 266

5.5 Rotational energy level diagram for selected DBS ⟵ GS transitions of CH_2CN^- 268

5.6 Plot of CH_2CN^- $^1B_1$ DBS ⟵ $^1A'$ GS origin band $K_a = 1 \longleftarrow 0$ vacuum transition wavelengths and strengths calculated at $T = 2.74$ K 274

5.7 λ8037 spectra compared with CH_2CN^- DBS ⟵ GS calculated spectrum I 276

5.8 λ8037 spectra compated with CH_2CN^- DBS ⟵ GS calculated spectrum II 277

5.9 HD 183143 interstellar atomic and diatomic spectra and VAPID fits . . . 280

5.10 HD 183143 λ8037 profile with K I-convolved CH_2CN^- model 283

5.11 HD 183143 λ8037 profile with Ca II-convolved CH_2CN^- model . . . 284

5.12 HD 183143 λ8037 profile with Ti II-convolved CH_2CN^- model 285

5.13 Interstellar CH_2CN^- λ8037 fits I 288

5.14 Interstellar CH_2CN^- λ8037 fits II 289

5.15 λ8037 spectrum compared with CH_2CN^- DBS ⟵ GS calculated spectrum including 'ortho' transitions 292

List of Tables

1.1 Comparison of ζ and σ-type interstellar clouds 31

3.1 LMC programme target data 69

3.2 LMC DIB equivalent widths 79

3.3 Galactic and LMC and atomic and ionic column densities and ratios . 105

3.4 LMC sightline characteristics 110

3.5 LMC cloud properties 113

4.1 SSS DIB main programme stars 152

4.2 Telluric and spectral type standard stars for SSS DIB programme . . . 153

4.3 $\beta^{1,2}$ Sco SSS DIB equivalent widths 166

4.4 $\nu^{1,3}$ Sco SSS DIB equivalent widths 177

4.5 ρ Oph SSS DIB and atom equivalent widths 191

4.6 ρ Oph SSS DIB and atom equivalent width percentage excesses . . . 192

4.7 $\mu^{1,2}$ Cru SSS DIB equivalent widths 207

4.8 HD 150135/6 SSS DIB equivalent widths 216

4.9 VAPID cloud model parameters for HD 150135/150136 K I lines 216

4.10 HD 164863/6 SSS DIB equivalent widths 222

4.11 VAPID cloud model parameters for HD 164863/313693 K I lines 223

4.12 VAPID cloud model parameters for HD 164863/313693 Na D lines . . 226

4.13 κ Vel time variation of N(K I) 228

4.14 κ Vel DIB equivalent widths 1995 & 2004 233

5.1 Heavily-reddened stars observed by G. H. Herbig 261

5.2 CH_2CN^- ground and dipole-bound state molecular parameters 272

5.3 CH_2CN^- DBS ⟵ GS, $K_a = 1 \longleftarrow 0$ origin band transitions calculated at $T = 2.74$ K 273

5.4 HD 183143 interstellar atomic and diatomic VAPID model parameters . 281

5.5 Interstellar CH_2CN^- λ8037 fit parameters 287